國立中央大學天文研究所
鹿林天文台年報

2020

No.18

國立中央大學天文研究所 編

目錄

研究論文

Solar System/Exoplanets

Stars/Star Clusters

Star Formation and Evolution

High Energy Astrophysical Phenomena

Instrumentation and Methods

工作報告

新聞報導

研究論文

Planetary and Space Science 180 (2020) 104763

Contents lists available at ScienceDirect

Planetary and Space Science

journal homepage: www.elsevier.com/locate/pss

The current development of the Taiwan Meteor Detector System (TMDS) with a dedication to the Geminids 2017 and 2018

Zhong-Yi Lin [a,*], Hsin-Chang Chi [b], Bo-Hao Wang [c], Zong-Yi Lin [b], Chih-Cheng Liu [c], Jim Lee [d], Hung-Chin Lin [a], Bingsyun Wu [e], Xue-Hui Ma [f], Chia-Hsien Liao [f]

[a] *Institute of Astronomy, NCU, No. 300, Zhongda Rd., Zhongli Dist., Taoyuan City, 32001, Taiwan*
[b] *Department of Physics, NDHU, No. 1, Sec. 2, Da Hsueh Rd. Shoufeng, Hualien, 97401, Taiwan*
[c] *Department of Applied Mathematics, NDHU, No. 1, Sec. 2, Da Hsueh Rd. Shoufeng, Hualien, 97401, Taiwan*
[d] *Taipei Astronomical Museum, Taipei, Taiwan*
[e] *Taichung municipal Hui-Wen High School, Taichung, Taiwan*
[f] *Ken-Ting Observatory, NTU, Taiwan*

ARTICLE INFO

Keywords:
Geminids
Orbits
(3200) Phaethon

ABSTRACT

We summarize the outcomes of the first 2-year period observations using the Taiwan Meteor Detector System (TMDS) since its establishment in August 2016. The TDMS is an automated four-station video meteor system equipped to record meteors as well as obtain the meteor orientations in space. The multi-station observations of an individual meteor make feasible determination of the orbital parameters corresponding to the meteor. The associated parent bodies of individual meteors are consequently identified from the orbital information. To demonstrate, we also present an analysis of the results from the Geminid meteor stream in 2017 and 2018 with the magnitude and velocity distribution being provided. In addition, a conclusive interrelation is verified while applying the Southworth-Hawkins D-criterion (D_{sh}) to compare the similarities between Geminids and the asteroid 3200 Phaethon orbits. The newly established TMDS can perform real-time as well as long-term synchronous surveillance of meteor events.

1. Introduction

A meteor occurs when a meteoroid (comet debris or asteroid fragment) strikes Earth's atmosphere at high speeds. Active combustions, which leads to evaporation of the meteoroid in the atmosphere, generally occur due to the instantaneous compressions of the air confronting a meteoroid. Such a scenario usually displays a familiar white "shooting star" to show up in the sky. In fact, every year, 30000 tons of interplanetary dust fall in the Earth's atmosphere. Studying meteors and meteoroids can provide a clue about their parent objects: comets (Trigo-Rodriguez et al., 2009) and asteroids (Porubcan et al., 2004). The strength of the meteoroids, for instance, provides information as to the structure and evolution of the parent body. Through meteor studies, the relation between the properties of comets and asteroids can be further investigated. Studying meteors also gives us a better understanding of the near Earth environment, and detail information on the dynamical, physical and chemical properties of comets, asteroids and their evolution in the solar system (Prakash et al., 2009).

Motion activated video recording is one of the most convenient detection techniques for meteor observations. Under the collaboration among three institutions: the Graduate Institute of Astronomy at National Central University (NCU), the Department of Physics at National Dong-Hua University (NDHU), and the Taipei Astronomical Museum (TAM), the Taiwan Meteor Detector System (TMDS) is founded and started operations in late-July of 2016. The TDMS, to accompany with other meteor observing systems around the world, is aiming at the determination of the physical properties of meteoroids. Particular attention of the TDMS is paid to improve the understanding of poorly studied showers and their associated parent bodies. As is well known, the International Astronomical Union's Meteor Data Center has accomplished a catalog to list 957 proposed showers, in which 112 meteor showers are certain to exist. Nevertheless, in fact, only 32 of the 112 existing meteor showers are associated with identified parent bodies. The Geminids is one of the largest showers belonging to the catalogued meteor database; especially,

* Corresponding author.
E-mail addresses: zylin@astro.ncu.edu.tw (Z.-Y. Lin), hsinchang@mail.ndhu.edu.tw (H.-C. Chi).

https://doi.org/10.1016/j.pss.2019.104763
Received 31 July 2018; Received in revised form 20 September 2019; Accepted 29 September 2019
Available online 10 October 2019

it has been studied using various observation techniques by plenty of researchers over a long time. For example, a comprehensive review of observational and theoretical studies of the Geminid stream has been presented by Neslusan (2015). Moreover, using video technique, several authors have reported observations on the Geminid meteor shower in the recent past. Among them, there are Ueda and Fujiwara (1993); De Lignie et al., 1993; Elliott and Bone (1993); Andreic and Segon (2008); Jenniskens et al. (2010, 2011, 2016); Trigo-Rodriguez et al. (2010); Toth et al. (2011, 2012); Rudawska et al. (2013); Madiedo et al. (2013); Molau et al. (2015, 2016), Hajdukova et al. (2017), etc.

In the following paragraphs, we introduce, in Sec. 2, the TMDS along with several examples, which demonstrate the capabilities of the system. In Sec. 3, we present the statistical outcomes and analyses of the data sets acquired by the TDMS from its startup in 2016 to end of 2018. Preliminary results from the observations of the Geminids meteor shower 2017 and 2018 are given in Sec. 4. Furthermore, Sec. 5 is devoted to discussion and summary.

2. Instrumentation and data analysis

Since its start into operation in August 2016, the TDMS routinely monitors the sky to search for luminous near-earth objects, especially meteors. With the intention to record as many meteors as possible by adopting a multi-station configuration, the TMDS consists of ten cameras distributed at four different locations in Taiwan at present (Mt. Yangmingshan, Fushoushan Farm, Lulin Observatory, and Kenting Observatory, see Fig. 1). The geographic coordinates of the four sites are listed in Table 1. For obtaining better precision determinations of a meteor trajectory, the four observing stations are located between 93.6 km and 250.7 km apart. The hardware facilities for observations and software programs for data analysis are described below in detail.

2.1. System specifications

Individual observation stations of the TDMS use Watec or Starlight cameras for data recordings. The limiting magnitudes and fields of view of the cameras are listed in Table 2. The data recordings are sampled at a rate 33 FPS (frame per second), which corresponds to an approximately 0.03s resolution of each frame. Besides, timing information is calibrated from invoking the Network Time Protocol (NTP) services supported by the U.S. government. Instead of simply correcting the system clock times periodically, NTP responds to adjust the clock rates of local systems to ensure the clock is always accurate to better than one frame time.

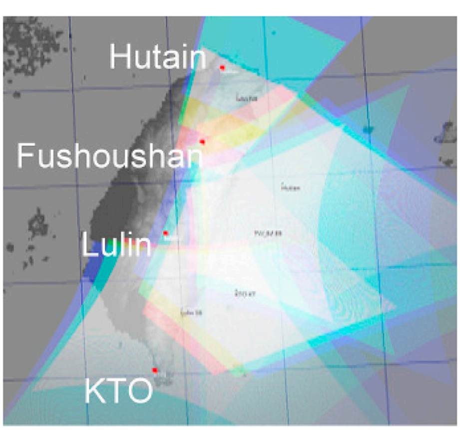

Fig. 1. The locations of the 4 observing stations currently affiliated with the Taiwan Meteor Detection System (TMDS). From northern to southern Taiwan, the locations of the 4 installed stations are at Hutain elementary school inside Yang-Ming-Shan National Park, Fushoushan Farm, Lulin observatory, and Kenting observatory, respectively.

Table 1
Location of TMDS observing sites.

Sation	Latitude° (N)	Longitude° (E)	Altitude (m)	In (year/moth)
Lulin (E1)	120.8736	23.5833	2862	2016/7 - present
Lulin (S1,N1)	120.8736	23.5833	2862	2017/12 - present
Hutain	121.5420	25.1700	660	2016/8–2018/12
KTO	120.6982	22.0500	38.4	2017/11 - present
Fushoushan FSS (E,S)	121.2424	23.2345	2500	2018/5 - present

2.2. Software and data analysis

The present TDMS employs the UFO Capture software version 4.272 (SonotaCo, 2009) for video recordings of meteor events. The UFO Capture tool set consists of 3 sub-packages; UFO Capture, UFO Analyser and UFO Orbit. Here, we give a brief outline of the sub-packages as follows: First, the UFO Capture is designed to accomplish motion-activated detections. Second, the UFO Analyser performs classifications of detected motional objects based on features in brightness, size and duration, respectively. In addition, it best conforms the sky video-snapshot to a standard star map under superimposition; parameters for astrometry and photometry are estimated. Third, the UFO Orbit is implemented for determining meteor orbits by analyzing data sets acquired from simultaneous multi-station detections.Since no automatic reduction or calculation software is applicable for filtering detected events at present, significant data sets are reduced from manual examinations of the raw database periodically. Confirmed meteor events are further analyzed using the UFO software package, which generates uniformly formatted data loggings suitable for compilations in spite of a vast detection acquired from distinct stations.

3. Results and analyses

From August 2016 to December 2018, successive operations of the TDMS have registered about twenty thousand meteor trails. Among the detected trails, only about 7% (see Fig. 2) are successfully providing definite orbit information. This deficiency in achieving meteor orbits is attributable to the relatively unfavorable weather conditions around the observing stations Hutain, KTO and the most recently installed Fushoushan (FSS). It is initially anticipated that the Fushoushan station should operate as efficient as the Lulin observatory since the geographical conditions are comparable. However, the actual situation is not so because of several uncertain weather factors. Table 3 shows the accumulated detections in each station whereas Table 4 gives the meteor orbits determined using multi-station orientations of a meteor captured by at least 2 individual stations. Since FSS was online just a few months, the number of the meteor orbits has been increasing dramatically in late 2018. The reason might be due to the relatively good weather condition compared to Hutain and KTO.

The knowledge of the meteor magnitudes is an important and complicated subject deserving advanced studies. Factors affecting the magnitudes include meteor velocity, height, compositions, size, mass, et cetera. In addition, atmospheric conditions also play an influential role. We use an empirical formula to analyze the event distributions depending on magnitudes. The prescription is given as the following

$$N(m) = \frac{A(m_c - m)^2}{e^{B(m_c-m)} - 1}. \quad (1)$$

where m_c is the detection magnitude cutoffs (Mag_{limit}) specified by a camera, m is meteor magnitude, and N(m) represents the amount of meteor events depending on magnitude m. The parameters A and B, obtained from optimization processes to best fit the raw-data

Table 2
System specifications.

Stations	Lulin E1	Lulin S1	Lulin N1	Hutain	KTO	FSS (S)	FSS (E)
	E1	S1	N1	Hutain		S	E
Cameras	902H2U	902H2U	910HX	902H2U	STARLIGHT EX27	902H2U	902H2U
Mag_{limit}	3.0	3.6	6.3	1.9	3.4	3.2	3.3
FOV	69.5	88.9	28.3	64.7	64.6	69.6	58.3

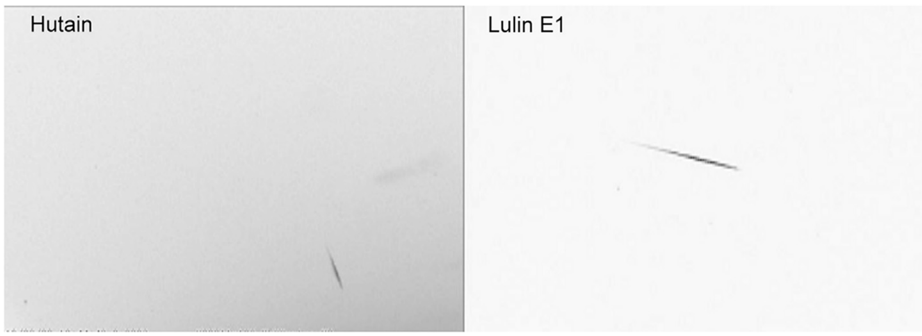

Fig. 2. On September 22, 2016, two Meteor Cameras being operated 200 km apart mutually captured a common meteor.

Table 3
The accumulated detections in Taiwan Meteor Detection System (TMDS) from July 2016 to December 2018.

Sation	Lulin	Hutain	KTO	FSS
(direction)	(E.N.S)	(SE)	(NE)	(E.S)
Events	17978	886	821	926

Table 4
The orbits in Taiwan Meteor Detection System (TMDS) from August 2017 to December 2018.

Stations	Lulin	Hutain	KTO	FSS (S)	FSS (E)	FSS (E)
	Hutain	KTO	Lulin	KTO	Lulin	KTO
Orbits	105	11	263	46	311	18

distributions, describe the characteristics of the magnitude distributions. The apparent magnitude cutoffs for cameras installed at individual stations are given in Table 2 with regard to the sensitivities of corresponding cameras. We have applied the above empirical formula to analyze the magnitude distribution of full-calibrated meteor events captured from late 2016 to 2018. Fig. 3 presents the results from our analyses. Because of the detecting restrictions on magnitude, the faintest meteors to be detectable are, for example, with magnitudes around +2 at Hutain and +7 at Lulin N1B. As it is shown in Fig. 3, positions of the high-magnitude ends of the magnitude distributions are consistently put by the limits of camera detecting capabilities.

The computations of orbits are mainly performed using the UFOOrbit software. UFOOrbit allows multiple parameter settings. Our database accommodates all the unfiltered data obtained by setting Q0. Commonly detected meteors are assumed when the occurrences of a monitored meteor differ with an interval shorter than 3 s. The Q0 parameter provides all possible combinations, and the interval of dt = 3s is pre-chosen to account for 2 inevitable causes: The first arises from the difficulty to

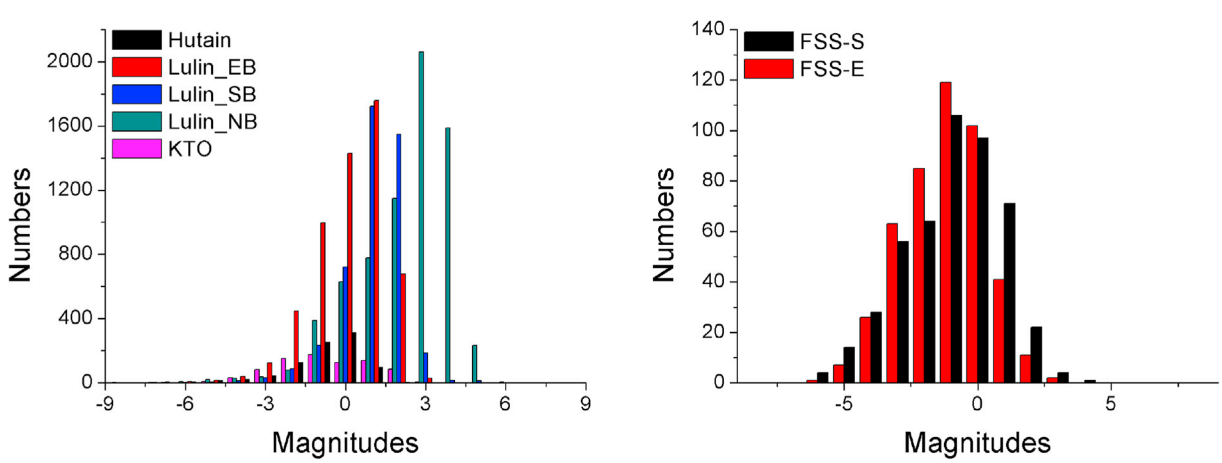

Fig. 3. Histogram comparing the magnitude distribution of the detected meteor events at Lulin observatory (E1, N1, and S1), KTO, Hutain in left-panel and FSS (E, and S) in right-panel respectively, between 2016 and 2018. For a few of them, the magnitude can not be determined due to readout noise from the recorded files. The deviations among different stations are owing to several factors: the start-up time, camera sensitivity, weather condition, and so on.

Table 5
The classified meteor showers detected using the TMDS from August 2017 to 2018.

Meteor Showers	Active Period	Max (Date)	Orbit Amount
J5etA (Eta Aquarids)	Apr 21–May 12	May 5–6	11
J5sdA (South Delta Aquarids)	Jul 12–Aug 19	July 28	12
J5Eri (Eta Eridanids)	Aug 3–Aug 14	Aug 9	4
J5Per (Perseids)	Jul 23–Aug 22	Aug 12–13	58
J5sPe (September Perseids)	Sep 5–Sep 21	Sep 9	3
J5Ori (Orionids))	Oct 15–Oct 29	Oct 21	25
J5sTa (Southern Taurids)	Sep 17–Nov 27	Oct 30 ~ Nov 7	15
J5nTa (North. Taurids)	Oct 12–Dec 2	Nov 4–7	11
J5Leo (Leonids)	Nov 13–Nov 20	Nov 17–18	14
J5noO (Nov. Orionids)	Nov 13–Dec. 6	Nov 28	5
J5Hyd (Sigma Hydrids)	Dec 3–Dec 15	Dec 12	11
J5Gem (Geminids)	Dec 6–Dec 19	Dec 13–14	53
J5Com (Comae Berenicids)	Dec 8–Dec 23	Dec 18–Jan 6	13

synchronize precisely the multi-station time settings. The second is, depending on the camera sensitivities, the desynchronized triggers of event recordings at distinct observation stations. Positions and velocities of simultaneously detected meteors from multi-stations are calculated subsequently by applying the triangulation method. Practical properness of using the pre-set dt = 3s is justified since very few false-detections of concurrent meteor events are found from operations. To proceed further, with the position and velocity components of individual meteors, the meteor orbits are determined. To sum up, there are 676 orbits identified from two or three separate stations (78 orbits) but only 36% of the meteor orbits can be classified. Table 5 presents the detected 235 orbits with more than one detection in known meteor showers. In other words, about 64% of identified orbits are sporadic or unclassifiable.

4. Observations of the Geminids in 2017 and 2018

The Geminid meteor shower, happening around December 13 and 14, is one of the most familiar and prominent showers, which annually yields a maximum zenith hourly rate over 100. Our observations of the Geminid meteor shower were mainly performed at Lulin, KTO, and FSS stations proceeded for each year December 13 until dawn local time December 15 in 2017 and 2018. Unfortunately, we have only one night data because the adverse weather condition in the island of Taiwan during the 2017 Geminid period. Meanwhile, Hutain station acquired no data of Geminids in 2017 and 2018 because the weather was extremely unfavorable even for a single-night observation in Northern Taiwan where the Hutain station is located. Fig. 4 summarizes the detected meteors obtained only on the day of December 14 in 2017 and 2018 from these three stations. In 2017, most meteor detections were triggered after midnight because of

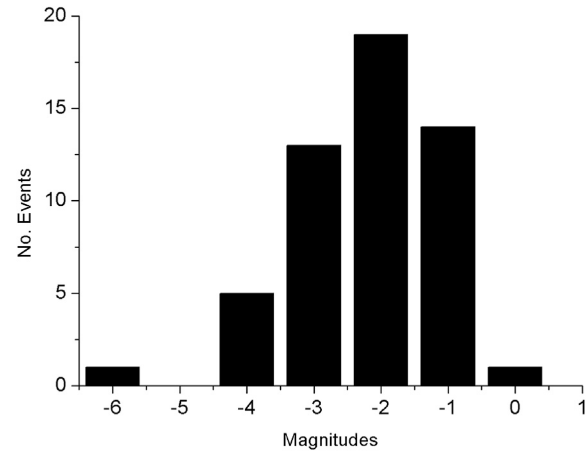

Fig. 5. The magnitude distribution range of Geminids of 53 detections in 2017 and 2018.

cirrus cloud in the beginning of night. The observing condition in 2018 was relatively good and then we have more detections of meteor events.To achieve meteoroid orbits, we combined the data obtained from 2 frameworks of pairwise stations, Lulin E1 together with KTO (framework E1+KTO), Lulin S1 along with KTO (framework S1+KTO), Lulin N1 as well as FSS (framework N1+FSS (East and South)) requiring that the video cameras installed are apart farther than ~ 100 km to ensure the triangulation method is applicable for determining the trajectory across the Earth's atmosphere. That trajectory can then be recast into a Heliocentric orbit using prescribed techniques (Ceplecha, 1987; Jenniskens et al., 2011). The orbits obtained from the two individual frameworks E1+KTO, N1+ FSS(E), FSS (S),and S1+KTO are 53 in total. On top of that, the number distribution during the night on December 14 in 2017 and 2018 is shown in Fig. 4 as well. In Fig. 5, we present the magnitude distribution of these detected orbits in 2017 and 2018. We find that the brightness of the Geminid meteors scatters a wide range from −6 to 0 magnitudes. In general, the size of the meteoroid (comet debris or asteroid fragment) is in scales from mm to cm. The Geminid meteors, on average, are brighter than the meteors of sporadic background or statistics results and this is in accord with previous observations (Evans and Bone, 1993). In Fig. 6, we show the event distribution as a function of meteor velocity. More than 74% of Geminids have velocity between 35 and 39 km s^{-1}. The peak and mean velocity are 36.5 and 37.1 km s^{-1} which is consistent with the IMO (International Meteor Organization) values.

In addition to statistics analysis, we employed orbit similarity criteria to justify the interrelated asteroid by using the JPL asteroid orbit database. The Southworth-Hawkins D-criterion (D_{sh}) is employed to seek the

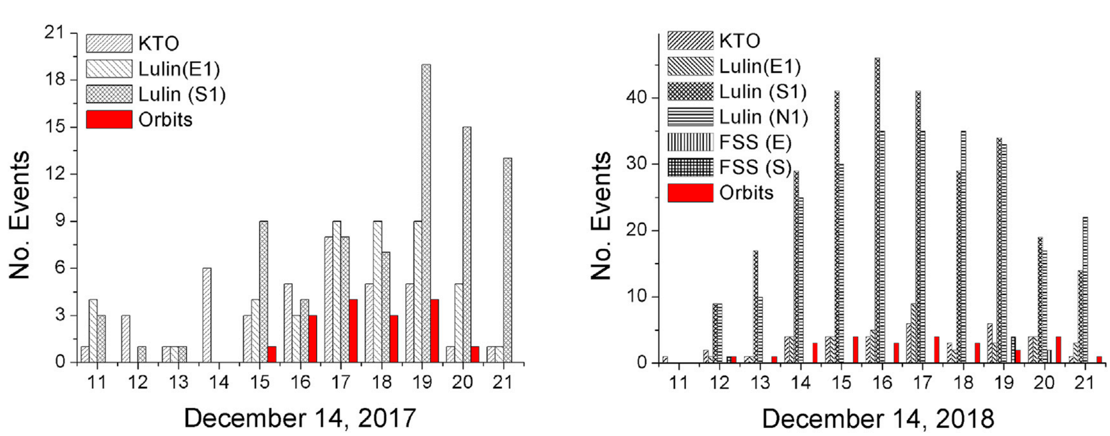

Fig. 4. The summarized amount of detections from Lulin (East 1, and South 1), KTO and FSS (East and South) stations on December 14, 2017 and 2018.

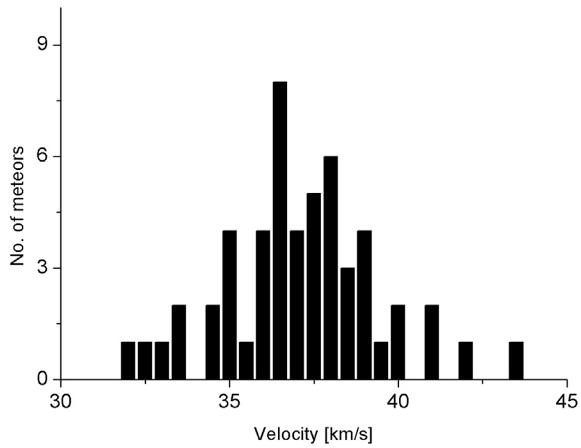

Fig. 6. Velocity distribution for Geminids.

Table 6
The results of D_{sh} criterion with respect to the Phaethon-Geminid complex.

Asteroids	D_{sh} (mean)	D_{sh} distribution range in 39 orbits
3200 Phaethon	0.087	0.028–0.146
2005 UD	1.392	1.275–1.446
1999 YC5	2.801	2.728–2.843

similarity of two orbits (Southworth and Hawkins, 1963). A smaller D_{sh} represents a better similarity between 2 orbits. For comparison, the asteroids 2005 UD and 1999 YC from the IAU database are also proposed for similarity tests because former ground-based observations estimated that about 10^{12}~10^{13} kg of mass had been dispensed to the Geminid meteor shower (Jenniskens, 1994), which is in excess of the mass of 3×10^5 kg ejected from each encounter of Phaethon at the perihelion (Jewitt et al., 2013). Jewitt and Hsieh (2006) suggested that the mass loss of Geminid stream may arise from the Phaethon-Geminid complex (asteroid Phaethon, (155140) 2005 UD and asteroid (225416) 1999 YC5) which originated from one breakup event and was associated with one of the big asteroid, 2 Pallas (de León et al., 2010). The calculated D_{sh} of these three asteroids are given in Table 6. Notice that although there were identified 53 meteor orbits belonging to Geminids, only 39 orbits were selected using iterative method with $D_{sh}\leq 0.15$. The detailed orbital elements of these 39 orbits can be found in Table A.7. However, if we take a look carefully in Appendix A.7, we find that some orbits with relatively low and high inclination angle, corresponding to the D_{sh} about 0.090 ~ 0.146, to asteroid (3200) Phaethon's orbit still remain. In other words, the orbits with high-threshold (a low D_{sh}) have to be taken into account in the future analysis. From Table 6 and Appendix A.7, where the average value and the individual value of D_{sh} is actually smaller than the 0.15 matching criterion, it is concluded that the observed orbits of Geminid meteor shower and the Phaethon's orbit are in positive interrelation.

The elements used for the D_{sh} criterion estimation of asteroids 3200 Phaethon, 2005 UD, and 1999 YC5 are from JPL small body database.

5. Discussion and summary

Recent operations of the TDMS have advanced a growing database, which provides profuse data sets readily available for examining the linkages connecting the meteor orbital characteristics with their associated parent asteroids. By taking the Geminids as a proto-typical practice, it is shown that the comparison of the orbital elements of the Geminid meteoroids with its parent 3200 Phaethon shows good agreement. Although the results of the orbital elements with the other 2 asteroids, 2005 UD and asteroid 1999 YC show inconsistency, we still cannot rule them out as the candidates of the shower's progenitor. While stringent constrains on the orbit evolution are essential for gaining accurate knowledge about the mechanism behind the breakup, captures of sufficient meteors with precise orbit elements are fundamental for desired orbital analyses. It is noticed that since its start into operation, from an around 2-year session of observations, TDMS acquired just about 7% of meteors detected with orbital elements. To deal with this circumstance, we have set up a new site in mid-2018, Fushoushan Farm, where the observation conditions, including historical weather records and geographical aspects, are comparable with Lulin observatory. Indeed, the efficiency of the network was increasing dramatically in late-2018 from 1% to 7%. We hope, in the future, to accomplish observations with more meteor detections and orbit determinations for improving our knowledge of the orbital characteristics of meteor showers.

In summary, we arrive at the following concluding remarks:

1. The TMDS gathered 676 precise orbits of meteors captured during operations from 2016 to 2018. Analyzes of the orbit data sets provide an effective approach to attain information of relevance to activities of the meteor parent bodies (i.e. Near-Earth Asteroids or Comets).
2. The present conduction of the TDMS to observations in the 2017 an 2018 Geminid meteor shower yielded 39 precisely determined meteor orbits. From analyzes of the D_{sh} parameters in these orbits, the associated parent body is uniquely identified: namely, the 3200 Phaethon. A result agrees with the finding unfolded from former investigations of Geminid in the literature. It is worthwhile to note that the TDMS proved to be highly efficacious in deciding the parent bodies of meteor showers, though it is not satisfactorily efficient for capturing meteors with deterministic orbits. Once the efficiency in determining meteor orbits can be substantially increased, it is anticipatable that the TDMS will be capable of providing prolific meteor-shower events for advanced studies. For improving the efficiency of the TDMS to detect meteor events in conjunction with orbits, the site locations selected for installations play a crucial role. Deployment of additional observation stations at suitable locations to achieve sufficient concurrent meteor detections with orbital information is one of the primary tasks called for the future development of the TDMS.

Acknowledgements

We specially acknowledge that the Lulin staff, Chi-Sheng Lin and Hsiang-Yao Hsiao have provided assistance in observations. This publication has made use of data collected at Lulin Observatory, partly supported by MOST grant 105-2112-M-008-024-MY3. This work was also supported by MOST 105-2112-M-008-002-MY3 from the Ministry of Science and Technology of Taiwan.

Appendix B. Supplementary data

Supplementary data to this article can be found online at https://doi.org/10.1016/j.pss.2019.104763.

Appendix A. Orbital elements

Table A.7
The Geminid orbital elements including the six basic parameters and orbital period are all derived by the UFOOrbit software. The standard deviation for these 39 orbits in semi-major axis, perihelion distance, eccentricity, orbital period, argument of perihelion, longitude of the ascending node, and inclination are 0.32, 0.02, 0.02, 0.67, 2.3, 0.6, 3.5 respectively.

Orbit no. (stations)	MJD	semi-major axis (au)	perihelion distance (au)	eccentricity	orbital period (year)	argument of perihelion (deg)	longitude of the ascending node (deg)	inclination (deg)	D_{sh} Phaethon
1 (Lulin, KTO)	58101.66	1.53	0.13	0.92	1.90	324.8	262.6	21.6	0.03
2 (Lulin, KTO)	58101.67	1.71	0.14	0.92	2.23	323.0	262.6	27.8	0.11
3 (Lulin, KTO)	58101.67	1.93	0.13	0.93	2.68	322.9	262.6	25.6	0.08
4 (Lulin, KTO)	58101.67	1.50	0.13	0.91	1.83	324.7	262.6	23.8	0.04
5 (Lulin, KTO)	58101.71	1.62	0.15	0.91	2.05	321.4	262.7	17.5	0.09
6 (Lulin, KTO)	58101.72	1.91	0.13	0.93	2.64	323.4	262.7	22.9	0.05
7 (Lulin, KTO)	58101.73	1.77	0.12	0.93	2.36	324.9	262.7	28.9	0.13
8 (Lulin, KTO)	58101.76	1.76	0.12	0.94	2.34	325.9	262.7	28.8	0.13
9 (Lulin, KTO)	58101.76	1.90	0.11	0.94	2.62	326.6	262.7	28.6	0.13
10 (Lulin, KTO)	58101.77	2.07	0.13	0.94	2.98	323.1	262.7	24.7	0.07
11 (Lulin, KTO)	58101.77	1.54	0.12	0.92	1.91	326.1	262.7	27.6	0.10
12 (Lulin, KTO)	58101.82	1.72	0.14	0.92	2.26	321.8	262.8	24.0	0.05
13 (Lulin, KTO)	58101.83	1.87	0.12	0.93	2.56	324.2	262.8	27.2	0.10
14 (Lulin, KTO)	58101.83	1.61	0.14	0.91	2.04	322.5	262.8	27.5	0.10
15 (Lulin, FSS)	58464.75	1.41	0.17	0.88	1.67	320.5	260.4	18.9	0.10
16 (Lulin, KTO)	58464.75	1.15	0.14	0.88	1.23	327.0	260.4	14.6	0.14
17 (Lulin, KTO)	58465.52	1.32	0.14	0.90	1.52	325.0	261.2	24.1	0.04
18 (Lulin, KTO)	58465.67	1.84	0.13	0.93	2.50	323.8	261.3	23.9	0.06
19 (Lulin, KTO)	58466.53	1.34	0.14	0.90	1.54	324.8	262.2	24.2	0.04
20 (Lulin, KTO)	58466.56	1.44	0.13	0.91	1.73	324.8	262.2	22.9	0.03
21 (Lulin, KTO)	58466.60	1.55	0.13	0.92	1.92	324.9	262.3	27.6	0.10
22 (Lulin, KTO)	58466.59	1.52	0.13	0.91	1.87	324.6	262.3	24.0	0.04
23 (Lulin, KTO)	58466.62	1.98	0.11	0.94	2.79	325.3	262.3	29.5	0.14
24 (Lulin, KTO)	58466.65	1.89	0.11	0.94	2.59	325.8	262.3	26.7	0.10
25 (Lulin, KTO)	58466.66	1.89	0.11	0.94	2.59	325.8	262.3	26.7	0.09
26 (Lulin, KTO)	58466.67	1.96	0.11	0.94	2.75	325.8	262.4	28.1	0.12
27 (Lulin, KTO)	58466.67	1.27	0.10	0.92	1.44	330.5	262.4	25.7	0.10
28 (Lulin, KTO)	58466.68	1.27	0.11	0.95	2.81	325.9	262.4	29.7	0.15
29 (Lulin, KTO)	58466.69	1.41	0.10	0.93	1.68	329.9	262.4	21.3	0.08
30 (Lulin, KTO)	58466.74	1.76	0.12	0.93	2.33	325.2	262.4	28.6	0.12
31 (Lulin, KTO)	58466.74	1.66	0.11	0.94	2.14	327.5	262.4	26.7	0.10
32 (Lulin, KTO)	58466.75	1.91	0.14	0.93	2.64	321.3	262.4	25.6	0.08
33 (Lulin, KTO)	58466.78	1.52	0.12	0.92	1.87	326.3	262.5	26.3	0.08
34 (Lulin, KTO)	58466.80	1.63	0.12	0.93	2.08	326.3	262.5	26.7	0.09
35 (Lulin, KTO)	58466.81	2.67	0.11	0.96	4.35	324.5	262.5	26.0	0.10
36 (Lulin, KTO)	58466.84	1.13	0.14	0.88	1.21	327.1	262.5	19.2	0.06
37 (Lulin, FSS)	58466.84	1.39	0.16	0.89	1.65	321.8	262.5	20.6	0.05
38 (Lulin, FSS)	58466.88	2.59	0.14	0.95	4.17	320.2	262.6	27.9	0.13

(continued on next column)

Table A.7 (*continued*)

Orbit no.	MJD	semi-major axis	perihelion distance	eccentricity	orbital period	argument of perihelion	longitude of the ascending node	inclination	D_{sh}
(stations)		(au)	(au)		(year)	(deg)	(deg)	(deg)	Phaethon
39 (Lulin, FSS)	58466.78	1.43	0.14	0.91	1.70	324.6	264.5	21.6	0.03

References

Andreić, Ž., Šegon, D., 2008. 2006-2007 Geminids from Croatian meteor network video data, WGN. J. Int. Meteorol. Organ. 36, 99–104.

Ceplecha, Z., 1987. Geometric, dynamic, orbital and photometric data on meteoroids from photographic fireball networks. Bull. Astron. Inst. Czechoslov. 38, 222–234.

de León, J., Campins, H., Tsiganis, K., Morbidelli, A., Licandro, J., 2010. Origin of the near-Earth asteroid Phaethon and the Geminids meteor shower. Astron. Astrophys. 513, A26. https://doi.org/10.1051/0004-6361/200913609.

De Lignie, M., Jobse, K., Schievink, R., 1993. In: Ocenas, D., Zimnikoval, P. (Eds.), Proceedings of the International Meteor Conference, p. 59.

Elliott, A.J., Bone, N.M., 1993. Video observations of the Geminid meteor shower in 1990. J. Br. Astron. Assoc. 103, 181–183.

Evans, S.J., Bone, N.M., 1993. Photographic and visual observations of the Geminid meteor shower in 1991. J. Br. Astron. Assoc. 103, 300–304.

Hajduková Jr., M., Koten, P., Kornoš, L., Tóth, J., 2017. Meteoroid orbits from video meteors. The case of the Geminid stream. Planet. Space Sci. 143, 89–98. https://doi.org/10.1016/j.pss.2017.01.004 arXiv:1704.03750.

Jenniskens, P., 1994. Meteor stream activity I. The annual streams. Astron. Astrophys. 287, 990–1013.

Jenniskens, P., Mameta, K., Nakano, S., Koop, M., Trigo-Rodriguez, J.M., Madiedo, J.M., Pujols, P., Millan, J.C., Azcarate, J.A., Zamorano, J., Ocaña, F., 2010. Geminid Meteors. Central Bureau Electronic Telegrams, p. 2593.

Jenniskens, P., Gural, P.S., Dynneson, L., Grigsby, B.J., Newman, K.E., Borden, M., Koop, M., Holman, D., 2011. CAMS: cameras for Allsky Meteor Surveillance to establish minor meteor showers. Icarus 216, 40–61. https://doi.org/10.1016/j.icarus.2011.08.012.

Jenniskens, P., Nénon, Q., Albers, J., Gural, P.S., Haberman, B., Holman, D., Morales, R., Grigsby, B.J., Samuels, D., Johannink, C., 2016. The established meteor showers as observed by CAMS. Icarus 266, 331–354. https://doi.org/10.1016/j.icarus.2015.09.013.

Jewitt, D., Hsieh, H., 2006. Physical observations of 2005 UD: a mini-Phaethon. Astron. J. 132, 1624–1629. https://doi.org/10.1086/507483.

Jewitt, D., Li, J., Agarwal, J., 2013. The dust tail of asteroid (3200) Phaethon. Astrophys. J. 771, L36. https://doi.org/10.1088/2041-8205/771/2/L36 arXiv:1306.3741.

Madiedo, J.M., Trigo-Rodríguez, J.M., Castro-Tirado, A.J., Ortiz, J.L., Cabrera-Caño, J., 2013. The Geminid meteoroid stream as a potential meteorite dropper: a case study. Mon. Not. R. Astron. Soc. 436, 2818–2823. https://doi.org/10.1093/mnras/stt1777 arXiv:1309.6465.

Molau, S., Kac, J., Crivello, S., Stomeo, E., Barentsen, G., Goncalves, R., Saraiva, C., Maciewski, M., Maslov, M., 2015. Results of the IMO video meteor network - December 2014, WGN. J. Int. Meteorol. Organ. 43, 62–68.

Molau, S., Crivello, S., Goncalves, R., Saraiva, C., Stomeo, E., Kac, J., 2016. Results of the IMO video meteor network - December 2015, WGN. J. Int. Meteorol. Organ. 44, 51–56.

Neslušan, L., 2015. A summary of the research of Geminid meteoroid stream. Contrib. Astronomical Obs. Skalnaté Pleso 45, 60–82.

Porubčan, V., Williams, I.P., Kornoš, L., 2004. Associations between asteroids and meteoroid streams. Earth Moon Planets 95, 697–712. https://doi.org/10.1007/s11038-005-2243-5.

Prakash, A., 2009. Doctor's Thesis, Armagh Observatory.

Rudawska, R., Daassou, A., Ait Moulay Larbi, M., Benkhaldoun, Z., Vaubaillon, J., Colas, F., Baratoux, D., Bouley, S., 2013. Birth of meteor network in Morocco - analysis for the 2012 Geminids, WGN. J. Int. Meteorol. Organ. 41, 121–128.

SonotaCo, 2009. A meteor shower catalog based on video observations in 2007-2008, WGN. J. Int. Meteorol. Organ. 37, 55–62.

Southworth, R.B., Hawkins, G.S., 1963. Statistics of meteor streams. Smithson. Contrib. Astrophys. 7, 261.

Tóth, J., Kornoš, L., Piffl, R., Koukal, J., Gajdoš, S., Popek, M., Majchrovic, I., Zima, M., Világi, J., Kalmancok, D., Vereš, P., Zigo, P., 2012. In: Gyssens, M., Roggemans, P. (Eds.), Proceedings of the International Meteor Conference.

Tóth, J., Veres, P., Kornoš, L., Piffl, R., Koukal, J., Gajdoš, S., Majchrovic, I., Zigo, P., Zima, M., Világi, J., Kalmancok, D., 2011. Video observation of Geminids 2010 and Quadrantids 2011 by VMN and CEMeNt, WGN. J. Int. Meteorol. Organ. 39, 34–38 arXiv:1106.0595.

Trigo-Rodríguez, J.M., Madiedo, J.M., Williams, I.P., Castro-Tirado, A.J., Llorca, J., Vítek, S., Jelínek, M., 2009. Observations of a very bright fireball and its likely link with comet C/1919 Q2 Metcalf. Mon. Not. R. Astron. Soc. 394, 569–576. https://doi.org/10.1111/j.1365-2966.2008.14363.x.

Trigo-Rodriguez, J.M., Madiedo, J.M., Pujols, P., Millan, J.C., Azcarate, J.A., Zamorano, J., Ocana, F., 2010. Geminid Meteors 2010, vol. 2593. Central Bureau Electronic Telegrams, p. 2.

Ueda, M., Fujiwara, Y., 1993. TV observations of the 1991 Geminid meteor shower., WGN. J. Int. Meteorol. Organ. 21, 215–217.

L3-1

Publ. Astron. Soc. Japan (2020) 72 (2), L3 (1–6)
doi: 10.1093/pasj/psaa003
Advance Access Publication Date: 2020 March 2
Letter

Letter

Long-term activity of Comet C/2007 N3 (Lulin) as monitored by the SLT at the Lulin Observatory

Zhong-Yi Lin*†

Institute of Astronomy, National Central University, No. 300, Zhongda Road, Zhongli District, Taoyuan City 32001, Taiwan

*E-mail: zylin@astro.ncu.edu.tw

†This work was based on observations obtained at Taiwan's Lulin Observatory.

Received 2019 November 1; Accepted 2020 January 13

Abstract

The green comet C/2007 N3 (Lulin) is a new Oort cloud comet that has a retrograde orbit (inclination of 178°). It reached its perihelion on 2009 January 10, and its closest distance to Earth was 0.411 astronomical units (au) on February 24. Soon after its discovery on 2007 July 11, the coma activity of Comet Lulin was monitored closely by an Super Light Telescope 41 cm telescope until 2009 April. After long-term monitoring of Comet Lulin, the dust production rate [$A(\theta)f\rho$] was estimated. An unexpected increase in the $A(0)\ f\rho$ near the perigee appears to indicate an opposition effect. By investigating the surface brightness profiles, dust-to-gas ratios, and magnitudes, we ruled out the influences of gas and ion contamination and the outburst phenomenon. We discovered the anti-tail in late December 2008 but were unsure of the composition. We found that this abnormal tail lasted for a considerable time because of the effect of the orbital geometry. We also found that the jet activity coincided with the peak $A(\theta)\ f\rho$ values, and this clue helped us realize what was happening in the dust coma of Comet Lulin.

Key words: comets: general — comets: individual (C/2007 N3 (Lulin))

1 Introduction

Comet Lulin was discovered on 2007 July 11 as the Lulin Sky Survey (LUSS) program was carried out using the 16″ Ritchey-Chrétien telescope. This new comet was named "Comet Lulin" after the Lulin Observatory (officially designated comet C/2007 N3; Green 2007) and was the first discovery made in Taiwan using the local telescope there. The discovery of Comet Lulin was one of the major achievements of the LUSS project, the aim of which was to explore the various populations of small bodies in the solar system, and especially to study near-Earth asteroids (NEAs) that might present serious damage to the Earth.

The orbit of Comet Lulin measured $1/a_0$ of 0.00022, corresponding to an aphelion distance ($2a_0$) of $\sim$ 90000 astronomical units (au),[1] meaning Comet Lulin was entering the inner solar system for the first time. The dynamically new (Oort cloud) Comet Lulin reached its perihelion on 2009 January 10, at a distance of 1.211 au from the Sun and approached the Earth, reaching its nearest point (0.411 au) on 2009 February 24 (Bair et al. 2018). An interesting finding was that the orbit of Comet Lulin was very nearly a parabola and that it occupied a very low inclination orbit

[1] See Nakano Note, No. 1754 (2009) ⟨http://www.oaa.gr.jp/oaacs/nk/nk1754.htm⟩.

of approximately 1°.6 from the ecliptic plane. A low inclination orbit is always found in short-period comets (SPCs), meaning Jupiter family comets. However, their Tisserand parameters (with respect to Jupiter, T_J), as proposed by Levison (1996), and their origins are completely different. Short-period comets have a T_J of between 2 and 3, whereas long-period comets (LPCs) have a T_J of < 2. Previous studies on the origin and evolution had suggested that SPCs originate in the Edgeworth–Kuiper belt, which surrounds the Sun at distances between about 30 au (the distance of Neptune) and 50 au, but SPCs are now thought to originate in the scattered disc associated with the Kuiper belt because this belt is relatively stable (Horner et al. 2004). In contrast, LPCs, or Oort cloud comets such as Comet Lulin (with a T_J of approximately ~ 1.365), are thought to originate in a spherical cloud of debris that surrounds the Sun at distances of between 20000 and 100000 au. However, Comet Lulin moves around the Sun in a retrograde orbit, which is different from other LPCs. This retrograde orbit means that the comet orbits the Sun in the opposite direction of the planets, or clockwise when viewed from above the Sun's north pole. A similar orientation has been found in SPCs (the famous Halley's Comet also orbits backwards), so the retrograde orbit is currently a puzzle. One possible explanation is the tidally driven precession (Levison et al. 2006), when comets orbit in a disk-shaped inner Oort cloud that is located between a spherical outer Oort cloud and the Kuiper belt and scattered disc. Another probability is that when the comet was ejected from the solar system by planetary perturbation, some comets may have assumed a retrograde orbit (Fouchard et al. 2014).

2 Observations and data reduction

The Super Light Telescope (SLT) 41 cm (16″ Ritchey–Chrétien) telescope , which was the telescope used for the Comet Lulin monitoring program, was installed by the Institute of Astronomy of the National Central University in 2005 March on the summit of Mt. Front Lulin (120°52′25″ E, 23°28′7″ N, at a height of 2862 m) in central Taiwan. A charge-coupled device (CCD) imaging camera was attached to the Cassegrain focus of the telescope. The U42 CCD camera was manufactured by Apogee Instruments, Inc.[2] The focal length of the SLT was 2500 mm (with a 0.75× reducer), resulting in a 1 × 1 pixel scale binning of 1.1 arcsec pixel^{-1}. The field of view (FOV) of this system was 38′ × 38′. The CCD was cooled by thermoelectric cooling, and the system could reach an operative temperature of −20 °C. The CCD images were acquired with the software Maxim DL provided by Diffraction Limited, Inc., running on a Windows operating system.[3]

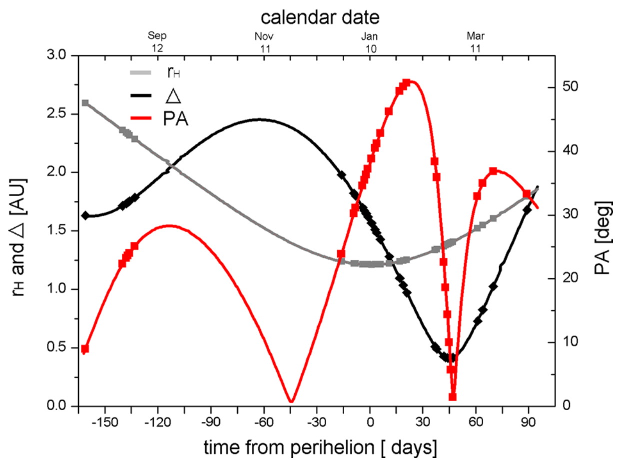

Fig. 1. Behavior of heliocentric distance r_H(au), geocentric distance △(au), and phase angle α. The symbols depict the UT dates when observations are acquired from Lulin observatory. The opposition is shown in the data between February 25 and 26, meaning about 46 days after perihelion. (Color online)

Comet Lulin was monitored at the Lulin Observatory from 2008 July to 2009 April, for a total of 33 observation nights, with a broadband Bessel R filter (central wavelength of 634.9 nm, full width at half maximum [FWHM] of 120 nm). The observation log is shown in figure 1. Data reduction followed the standard procedures. In brief, the procedure began with the dark-frame subtraction and flat-field correction of all frames. The night-sky contribution was then subtracted by using the part of an image where the contamination from the nucleus and the coma brightness were relatively smaller. To convert the measured counting rates into physical units in the R filter, we observed both Landolt standard star fields (Landolt 1992) and stars selected from the European Southern Observatory (ESO) catalog of optical spectrophotometric standard stars (Hamuy et al. 1992, 1994; Oke 1990). Measurements of the photometric standards were carried out every 1 to 1.5 hr, and the results yielded information on the sky conditions. If the sky was stable or close to a photometric night meaning the atmospheric transparency was stable within ~ 0.02 mag over several minutes, we moved to the calibration step. The step-by-step process for conversion was as follows. First, we needed to acquire the transmission curves for both the Bessel R filter and the U42 CCD camera and the flux units of energy, erg cm^{-2}s^{-1} Å^{-1}, versus wavelength (A), for the flux of the standard star (e.g., GD71). (The transmission curves could be measured and calculated at Thin Film Technology Center, National Central

[2] Camera specifications can be found at ⟨https://www.apogeeinstruments.com/⟩.

[3] Additional details regarding this software can be found at ⟨http://diffractionlimited.com/product/maxim-dl/⟩.

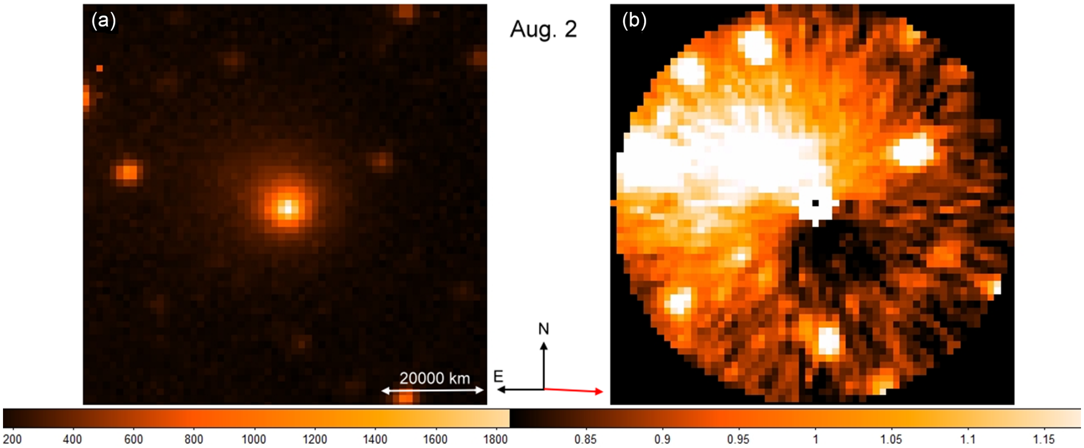

Fig. 2. Images of Comet Lulin taken on 2008 August 2. (a) The original image, acquired with an R filter, shows a nearly circular coma. (b) The same scale as (a) but enhanced by azimuthal median masking to show the curved jet clearly. The orientation is given in the figure, and the red arrow indicates the direction of the Sun. The field of view (FOV) is 1.′1 × 1.′1, corresponding to 79000 × 79000 km. (Color online)

University, and the flux information was downloaded directly from the ESO website.) We then used the information above to obtain the theoretical flux in the R filter. For GD71, the value was approximately 120000 erg cm^{-2}. Secondly, we measured the extinction coefficient from the Landolt standard star field (GD71, PG0918, PG1047, and PG1323; Landolt 1992) to verify the weather conditions, and at the same time, we observed the spectrophotometric standard star (GD71) at different air masses. The extinction coefficient could be used and the optical spectrophotometric standard stars normalized to an air mass of 1. Up to this point, we could easily measure how many counts were in the optical spectrophotometric standard stars at an air mass of 1. In other words, we could have the total counts ($\sim$ 1300) of GD71. Finally, we obtained the conversion factor, which was used to convert the counts into the real flux between the theoretical flux and instrumental counts. This factor, also called the count rate in our calculation, was in the range of 89 to 93. Generally speaking, if we knew how many counts were in a cometary coma with a fixed projected distance (10000 km), we could use this value to multiply and obtain the real flux in the cometary coma. Notice that the typical seeing during the observations ranged from 1.″5 to 2.″5.

3 Data analysis and results

3.1 Large-scale morphology

The imaging was processed to enhance the coma structure by using radial and azimuthal masking. This method can be briefly described as follows. In the first step, the mean radial brightness profile of the cometary coma, averaged over all azimuthal angles, was determined. The comet image was then divided by the mean brightness profile to enhance deviations from the mean coma (Lin et al. 2007). The dust jet feature first appeared on 2008 August 2, when we began our long-term monitoring program. The jet feature was spiral-like rather than straight, and its position angle, measured from north through east, was nearly perpendicular to the anti-solar direction (figure 2b). This phenomenon, the curved jet, may have been caused by a rotational effect from the cometary nucleus. The position angle of the jet feature changed from time to time because of the different orbital geometry and viewing angles (i.e., the phase angle or Sun–comet–Earth angle, α, changed from 20° to 90° from the beginning to the end of August 2008). Unfortunately, the cadence was not high enough to be used to estimate the rotation period of the comet by using the time-resolving relationship of the dust feature and its position angle. In addition, the dust jet may not have been very sensitive to the cometary rotation. Knight and Schleicher (2009) instead reported a tentative rotation period of 42 ± 0.5 hr based on the mapping of cyanogen gas jet features. Further discussion of dust and gas jets is deferred to a future publication.

The elevation of Comet Lulin began to decrease after August, and it was not available for further observation until the end of 2008 December. On 2008 December 19, we detected the anti-tail of Comet Lulin at a very low elevation. Two days later, we were finally able to obtain good-quality anti-tail imaging. Figure 3 shows the anti-tail lying in the sunward direction. The anti-tail is actually only part of the dust tail, and this rare phenomenon is an illusion caused by the viewing geometry as the comet orbits in nearly the same plane as the Earth. This phenomenon is usually rather rare and of short duration; however, the anti-tail of Comet Lulin lasted for a considerable time after it was detected in 2008 December.

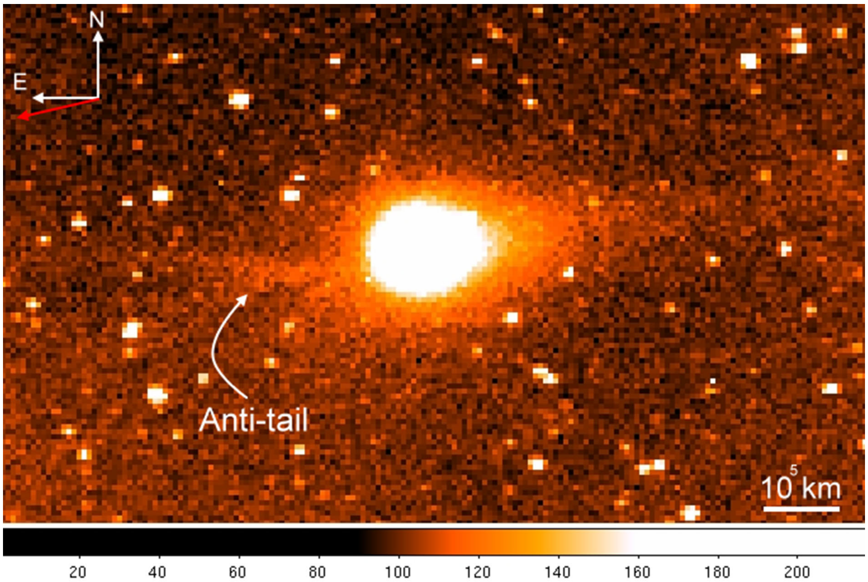

Fig. 3. Comet Lulin presented an anti-tail in a sunward direction on 2008 December 21. This unusual tail lasted for a considerable time and did not dissipate during our observations from 2008 December to 2009 April. The orientation is given in the figure, and the red arrow indicates the direction of the Sun. The field of view (FOV) is 12′ × 7′.5 corresponding to $(1.12 \times 10^6) \times (6.7 \times 10^5)$ km. (Color online)

3.2 Dust production rate

The dust production rate, $A(\theta)\,f\rho$, is the product of the dust Bond albedo at a given phase angle, $A(\theta)$, the filling factor of the dust within the aperture, f, and the projected aperture radius, ρ. It was first described by A'Hearn et al. (1984) to characterize the dust activity of a comet. The dust production rate is related to a stationary model that assumes a uniform and constant dust expansion within the coma. According to this model, the dust column density varies as ρ^{-1}. In this case, $A(\theta)\,f\rho$ becomes independent of ρ. The $Af\rho$ (in cm) is given in equation (1):

$$A(\theta)\,f\rho = \frac{(2r_{\mathrm{H}}\triangle)^2}{\rho}\frac{F_{\mathrm{com}}}{F_{\mathrm{sun}}}. \tag{1}$$

Here, r_{H} (au) is the comet's heliocentric distance, $\triangle$ (au) is the comet's geocentric distance, ρ (cm) is the radius of the aperture at the comet (we used 10000 km in this work), F_{com} (erg cm^{-2}s^{-1}) is the cometary flux measured in a continuum filter, and F_{sun} (erg cm^{-2}s^{-1}) is the solar flux at 1 au. The solar flux can be computed by using a high-resolution solar spectrum (Kurucz et al. 1984) for the conversion; see Lin et al. (2007, 2009) for a detailed explanation. Additionally, because cometary magnitudes are observed to follow similar phase angle effect as asteroids, we applied the phase angle correction shown in equation (2):

$$m_{\mathrm{comet}}(\alpha = 0) = m_{\mathrm{comet}}(\alpha) - C\alpha \tag{2}$$

where α is the phase angle in degrees and C is the correction factor of 0.03 mag degree^{-1}, the mean of the correction

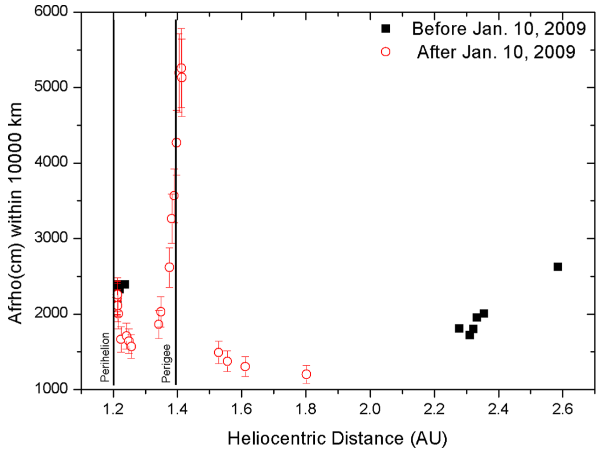

Fig. 4. Variation of the $Af\rho$ with heliocentric distance. Shown are the upper limit $Af\rho$ values within an aperture of radius ρ of 10000 km for Comet Lulin from 2008 August 2 (~ 2.6 au) to 2009 March 12 (~ 2.1 au). The square symbols (black) indicate the days before the perihelion (~ 1.2 au), and the open circles (red) were determined after Comet Lulin passed through its perihelion. Uncertainty in the data was about 5%–10% because of errors in the absolute flux calibration of the images. (Color online)

factors derived by Meech and Jewitt (1987). The resulting values are given in figure 4. The $A(0)\,f\rho$ values measured here were affected by an error of ~ 5% to 10% because of errors in the absolute flux calibration of the images.

4 Discussion and summary

Anti-tails are rare phenomena in comets, but they are mostly observed in brighter comets, such as C/1995 O1

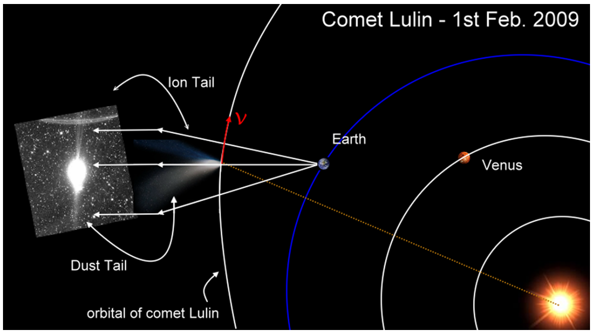

Fig. 5. Illustration of the anti-tail, viewed edge-on, from Earth on 2009 February 1. (Color online)

(Hale-Bopp), C/2000 WM1 (LINEAR), C/2006 P1 (McNaught), and C/2007 N3 (Lulin). The appearance of a spike or neckline has been interpreted as evidence of heavy grains released previously (on the order of many months to years) crossing the orbital plane of a comet at 180° of true anomaly from their emission, or as a projected effect as the Earth crosses the comet's orbital plane (Boehnhardt 2004). Comet Lulin is not the former case because we could find no needle or neck-line feature. Instead, we found some fine features ahead of the cometary nucleus (figure 5). Unfortunately, the images were acquired only from broad-band filters, and we were unable to determine their composition (i.e., ion or dust tail). Fortunately, Comet Lulin traveled along the ecliptic plane and crossed it, which is unusual for the comets mentioned above. Because of this coincidence of orbital geometry, the anti-tail lasted for a considerable time. Figure 5 shows how the anti-tail was caused by the effect of the orbital geometry as well as our viewing angle here on Earth.

In addition to the anti-tail structure, Comet Lulin showed a nearly circular coma, approximately $1'$ in diameter, and was slightly elongated in a west–east direction (figure 2a) as we began our long-term monitoring program in early August 2008. The unusual jet structure, which was similar to Comet Machholz, was extremely curved (Lin et al. 2007). We found it interesting that the jet spiraled toward the tail-ward direction in late August and could no longer be found in images obtained after late 2008 December. The most interesting finding was that the $A(0)\,f\rho$ value in this month was slightly higher than expected. We think this high value may have been caused by the inner curved jet in its coma. Furthermore, our measurement of $A(0)\,f\rho$ increased as Comet Lulin was on the way to its perihelion, and it obviously increased dramatically at the perihelion ($r_{\mathrm{H}} \sim 1.21$ au in early January 2009) and perigee ($r_{\mathrm{H}} \sim 1.40$ au in late 2009 February). These phenomena seemed to be consistent with the light curve of Comet Lulin presented by Dr. Yashida.[4]

[4] ⟨http://www.aerith.net/comet/catalog/2007N3/2007N3.html⟩.

One explanation for these unexpected values, meaning that the $A(0)\,f\rho$ did not follow the normal trend of decreasing or increasing as the heliocentric distance increased or decreased, may be a cometary outburst. During an outburst, the brightness of a comet increases dramatically by 2 to 3 mag on average. A few days after an outburst takes place, the brightness of the comet decreases smoothly to the previous state. Unfortunately, no outburst reports were addressed near early August of 2008 or at the perigee (February 24.3) of 2009, although the comet was 4 mag brighter at the perigee than at the perihelion (January 10.64). Instead, an outburst of Comet Lulin was detected around late 2009 January ($r_{\mathrm{H}} \sim 1.25$ au), as reported by Bodewits et al. (2011). We therefore think these detections may not be associated with a cometary outburst.

Another possibility is the contamination from gas and ion species such as C_2 at 5141 Å and H_2O^+ at 6190 Å. Thus, we checked the surface brightness profile of Comet Lulin to find any deviation from the conical $1/\rho$ profile. Given the seeing of 1.5–2.5 FWHM, the surface brightness of Comet Lulin was entirely consistent with a simple $\rho{-}1$ dependence, meaning that this unexpected increase in values did not come from the contribution of gas and ion species. Even though the faintly visible ion tail had been found on February 21, four days before the opposition, the slope of the comet surface brightness did not change much. In addition to checking the contamination, we checked the dust-to-gas ratio and found that the results from Bair, Schleicher, and Knight (2018) stayed approximately constant during this period. Furthermore, the dust-to-gas ratio seemed to indicate an overall increase as a function of the heliocentric distance, but such an overall trend was not consistent with our results.

An alternative explanation for this unexpected increase in brightness or $A(0)\,f\rho$ may be the opposition effect, meaning that the reflectance increased nonlinearly as the phase angle decreased (Hapke et al. 1993). A'Hearn et al. (1984) and Millis et al. (1982) have reported observations of opposition surges in comets P/Ashbrook-Jackson, Bowell (1982I), and P/Stephan-Oterma when these comets were all in near-backscattering geometry. Additionally, Joshi, Ganesh, and Baliyan (2011) observed a significant brightness enhancement with the decreasing phase angle in Comet Lulin around the perigee.

In summary, we performed photometric observations of Comet Lulin from early 2008 August to 2009 April with the 0.4 m telescope at the Lulin Observatory in Taiwan. After image processing, a curved jet and an anti-tail were found in 2008 August and December, respectively. The anti-tail images acquired from the broad-band filters did not provide any information on the composition (i.e., ion or dust tail). The unexpected increase in $A(0)\,f\rho$ near the perigee may be an opposition effect. We excluded the effects of gas and ion contamination and the outburst phenomenon by investigating the surface brightness profiles, dust-to-gas ratios, and magnitudes, respectively.

Acknowledgment

This work was based on observations obtained at Taiwan's Lulin Observatory. We thank the staff members for their assistances with the observations. This work was supported by grant numbers MOST 105-2112-M-008-002-MY3, MOST 107-2119-M-008-012, MOST 108-2112-M-008-004, and MOST 108-2112-M-008-001 from the Ministry of Science and Technology of Taiwan.

References

A'Hearn, M. F., Schleicher, D. G., Millis, R. L., Feldman, P. D., & Thompson, D. T. 1984, AJ, 89, 579
Bair, A. N., Schleicher, D. G., & Knight, M. M. 2018, AJ, 156, 159
Bodewits, D., Villanueva, G. L., Mumma, M. J., Landsman, W. B., Carter, J. A., & Read, A. M. 2011, AJ, 141, 12
Boehnhardt, H. 2004, in Comets II, ed. M. C. Festou et al. (Tucson: University of Arizona Press), 301
Green, D. W. E. 2007, IAU Circ., 8857
Fouchard, M., Rickman, H., Froeschlé, C., & Valsecchi, G. B. 2014, Icarus, 231, 110
Hamuy, M., Suntzeff, N. B., Heathcote, S. R., Walker, A. R., Gigoux, P., & Phillips, M. M. 1994, PASP, 106, 566
Hamuy, M., Walker, A. R., Suntzeff, N. B., Gigoux, P., Heathcote, S. R., & Phillips, M. M. 1992, PASP, 104, 533
Hapke, B. W., Nelson, R. M., & Smythe, W. D. 1993, Sci, 260, 509
Horner, J., Evans, N. W., & Bailey, M. E. 2004, MNRAS, 355, 321
Joshi, U. C., Ganesh, S., & Baliyan, K. S. 2011, MNRAS, 412, L58
Knight, M., & Schleicher, D. 2009, IAU Circ., 9025, 1
Kurucz, R. L., Furenlid, I., Brault, J., & Testerman, L. 1984, Solar Flux Atlas from 296 to 1300 nm (Sunspot: National Solar Observatory)
Landolt, A. U. 1992, AJ, 104, 340
Levison, H. F. 1996, in ASP Conf. Ser., 107, Completing the Inventory of the Solar System, ed T. W. Rettig et al. (San Francisco: ASP), 173
Levison, H. F., Duncan, M. J., Dones, L., & Gladman, B. J. 2006, Icarus, 184, 619
Lin, Z.-Y., Lin, C.-S., Ip, W.-H., & Lara, L. M. 2009, AJ, 138, 625
Lin, Z. Y., Weiler, M., Rauer, H., & Ip, W. H. 2007, A&A, 469, 771
Meech, K. J., & Jewitt, D. C. 1987, A&A, 187, 585
Millis, R. L., A'Hearn, M. F., & Thompson, D. T. 1982, AJ, 87, 1310
Oke, J. B. 1990, AJ, 99, 1621

The Astronomical Journal, 160:26 (16pp), 2020 July https://doi.org/10.3847/1538-3881/ab9305

Characterization of the Nucleus, Morphology, and Activity of Interstellar Comet 2I/Borisov by Optical and Near-infrared GROWTH, Apache Point, IRTF, ZTF, and Keck Observations

Bryce T. Bolin[1,2], Carey M. Lisse[3], Mansi M. Kasliwal[1], Robert Quimby[4,5], Hanjie Tan[6], Chris M. Copperwheat[7], Zhong-Yi Lin[6], Alessandro Morbidelli[8], Lyu Abe[9], Philippe Bendjoya[9], Kevin B. Burdge[1], Michael Coughlin[10,37], Christoffer Fremling[1], Ryosuke Itoh[11], Michael Koss[12], Frank J. Masci[2], Syota Maeno[11], Eric E. Mamajek[13,14], Federico Marocco[2,13], Katsuhiro Murata[15], Jean-Pierre Rivet[9], Michael L. Sitko[16,17], Daniel Stern[13], David Vernet[18], Richard Walters[1], Lin Yan[1], Igor Andreoni[1], Varun Bhalerao[19], Dennis Bodewits[20], Kishalay De[1], Kunal P. Deshmukh[21], Eric C. Bellm[22], Nadejda Blagorodnova[23], Derek Buzasi[24], S. Bradley Cenko[25,26], Chan-Kao Chang[6], Drew Chojnowski[27], Richard Dekany[28], Dmitry A. Duev[1], Matthew Graham[1], Mario Jurić[29], Shrinivas R. Kulkarni[1], Thomas Kupfer[30], Ashish Mahabal[1,31], James D. Neill[1], Chow-Choong Ngeow[6], Bryan Penprase[32], Reed Riddle[28], Hector Rodriguez[28], Roger M. Smith[28], Philippe Rosnet[33], Jesper Sollerman[34], and Maayane T. Soumagnac[35,36]

[1] Division of Physics, Mathematics and Astronomy, California Institute of Technology, Pasadena, CA 91125, USA; bbolin@caltech.edu
[2] IPAC, Mail Code 100-22, Caltech, 1200 E. California Blvd., Pasadena, CA 91125, USA
[3] Johns Hopkins University Applied Physics Laboratory, Laurel, MD 20723, USA
[4] Department of Astronomy, San Diego State University, 5500 Campanile Dr., San Diego, CA 92182, USA
[5] Kavli Institute for the Physics and Mathematics of the Universe (WPI), The University of Tokyo Institutes for Advanced Study, The University of Tokyo, Kashiwa, Chiba 277-8583, Japan
[6] Institute of Astronomy, National Central University, 32001, Taiwan
[7] Astrophysics Research Institute Liverpool John Moores University, 146 Brownlow Hill, Liverpool L3 5RF, UK
[8] Université Côte d'Azur, Observatoire de la Côte d'Azur, CNRS, Laboratoire Lagrange, Boulevard de l'Observatoire, CS 34229, F-06304 Nice cedex 4, France
[9] Université Côte d'Azur, Observatoire de la Côte d'Azur, CNRS, Laboratoire Lagrange, France
[10] LIGO Laboratory, West Bridge, Rm. 257, California Institute of Technology, MC 100-36, Pasadena, CA 91125, USA
[11] Bisei Astronomical Observatory, 1723-70 Ohkur a, Bisei, Ibara, Okayama, 714-1411, Japan
[12] Eureka Scientific, 5248 Valley View Rd., El Sobrante, CA 94803, USA
[13] Jet Propulsion Laboratory, California Institute of Technology, 4800 Oak Grove Dr., Pasadena, CA 91109, USA
[14] Department of Physics & Astronomy, University of Rochester, Rochester, NY 14627, USA
[15] Tokyo Institute of Technology, 2 Chome-12-1 Ookayama, Meguro City, Tokyo 152-8550, Japan
[16] Department of Physics, University of Cincinnati, Cincinnati, OH 45221-0011, USA
[17] Space Science Institute, Boulder, CO 80301, USA
[18] Université Côte d'Azur, Observatoire de la Côte d'Azur, UMS Galilée, France
[19] Department of Physics, Indian Institute of Technology Bombay, Powai, Mumbai-400076, India
[20] Physics Department, Leach Science Center, Auburn University, Auburn, AL 36832, USA
[21] Department of Metallurgical Engineering and Materials Science, Indian Institute of Technology Bombay, Powai, Mumbai-400076, India
[22] DIRAC Institute, Department of Astronomy, University of Washington, 3910 15th Ave. NE, Seattle, WA 98195, USA
[23] Department of Astrophysics/IMAPP, Radboud University, Nijmegen, The Netherlands
[24] Department of Chemistry and Physics, Florida Gulf Coast University, 10501 FGCU Blvd. S, Fort Myers, FL 33965, USA
[25] Astrophysics Science Division, NASA Goddard Space Flight Center, 8800 Greenbelt Rd., Greenbelt, MD 20771, USA
[26] Joint Space-Science Institute, University of Maryland, College Park, MD 20742, USA
[27] Department of Astronomy, New Mexico State University, PO Box 30001, MSC 4500, Las Cruces, NM 88001, USA
[28] Caltech Optical Observatories, California Institute of Technology, Pasadena, CA 91125, USA
[29] Department of Astronomy, University of Washington, 3910 15th Ave. NE, Seattle, WA 98195, USA
[30] Kavli Institute for Theoretical Physics, University of California, Santa Barbara, CA 93106, USA
[31] Center for Data Driven Discovery, California Institute of Technology, Pasadena, CA 91125, USA
[32] Soka University of America, 425 Pauling Hall, 1 University Drive, Aliso Viejo, CA 92656, USA
[33] Université Clermont Auvergne, CNRS/IN2P3, LPC, Clermont-Ferrand, France
[34] Department of Astronomy, Stockholm University, SE-106 91 Stockholm, Sweden
[35] Lawrence Berkeley National Laboratory, 1 Cyclotron Rd., Berkeley, CA 94720, USA
[36] Department of Particle Physics and Astrophysics, Weizmann Institute of Science, Rehovot 76100, Israel
Received 2019 November 5; revised 2020 May 7; accepted 2020 May 12; published 2020 June 17

Abstract

We present visible and near-infrared (NIR) photometric and spectroscopic observations of interstellar object (ISO) 2I/Borisov taken from 2019 September 10 to 2019 December 20 using the GROWTH, the Apache Point Observatory Astrophysical Research Consortium 3.5 m, and the NASA Infrared Telescope Facility 3.0 m combined with pre- and postdiscovery observations of 2I obtained by the Zwicky Transient Facility from 2019 March 17 to 2019 May 5. Comparison with imaging of distant solar system comets shows an object very similar to mildly active solar system comets with an outgassing rate of $\sim10^{27}$ mol s^{-1}. The photometry, taken in filters spanning the visible and NIR range, shows a gradual brightening trend of $\sim$0.03 mag day^{-1} since 2019 September 10 UTC for a reddish object becoming neutral in the NIR. The light curve from recent and prediscovery data reveals a brightness trend suggesting the recent onset of significant H_2O sublimation with the comet being active with super volatiles such as CO at heliocentric distances >6 au consistent with its extended morphology. Using the

[37] David and Ellen Lee Prize Postdoctoral Fellow.

advanced capability to significantly reduce the scattered light from the coma enabled by high-resolution NIR images from Keck adaptive optics taken on 2019 October 4, we estimate a diameter for 2I's nucleus of $\lesssim$1.4 km. We use the size estimates of 1I/'Oumuamua and 2I/Borisov to roughly estimate the slope of the ISO size distribution, resulting in a slope of $\sim$3.4 $\pm$ 1.2, similar to solar system comets and bodies produced from collisional equilibrium.

Unified Astronomy Thesaurus concepts: Comets (280); Minor planets (1065)

1. Introduction

The study of interstellar objects (ISOs) is presently the best opportunity to directly observe the contents of extrasolar circumstellar disks at larger than centimeter-sized scales. Present-day observations are limited to observing the micron-sized (e.g., Lisse et al. 2012, 2017) to millimeter-sized (MacGregor et al. 2019) dust contents of extrasolar disks. Indirect observations of macroscopic objects and their volatile contents in debris disks can be obtained through the massive amounts of dust produced by their collision with each other (Meng et al. 2014; Su et al. 2019), their presence around young stars (Chen et al. 2006), or sometimes by their transit of stars (Rappaport et al. 2018), but observing and obtaining the physical properties and volatile contents of specific bodies from other stars has remained elusive.

The second example of a macroscopic body with a definitive interstellar origin to be discovered is 2I/Borisov (2I). Discovered on 2019 August 30 by amateur astronomer Gennadiy Borisov, the hyperbolic orbit with $e \simeq 3.35$ was confirmed on 2019 September 11 (Williams 2019a). Unlike the first ISO to be discovered, 1I/'Oumuamua (Williams 2017), which did not have a cometary appearance in ground-based (Jewitt et al. 2017b; Bolin et al. 2018) or space-based images (Micheli et al. 2018), 2I has a distinct comet-like appearance with a diffuse coma (Jewitt & Luu 2019). This provides an opportunity to characterize the properties of a cometary interstellar body for the first time.

Initial spectroscopic observations have revealed the presence of CN and C_2 gas in the coma of 2I with gas production rates comparable to solar system comets at similar heliocentric distances, r_h (Fitzsimmons et al. 2019; Kareta et al. 2020; Opitom et al. 2019). Using solar system comets as a guide, the production rate of CN observed in 2I implies a nuclear diameter of $\sim$6 km. The measured size combined with canonical models describing the brightness of 2I driven by H_2O or CO sublimation produces very different results versus heliocentric distance, as a body dominated by CO sublimation will be active much farther away from the Sun due to CO's much lower enthalpy of sublimation (Meech & Svoren 2004; Fitzsimmons et al. 2019). Therefore, it may be possible to distinguish between different compositional models of 2I by measuring its brightness at different heliocentric distances covering a wide span of times (e.g., Jewitt et al. 2017a; Meech 2017). This indeed appears to be the case, with Zwicky Transient Facility (ZTF) precovery observations of 2I strongly favoring the activity of the comet being driven by more volatile species than H_20, such as CO or CO_2 (Ye et al. 2020). In this paper, we build upon these ZTF results and present visible and near-infrared (NIR) observations of 2I and its morphology; the null result for variability on short-term timescales; estimates of the comet's size, afρ, and dust mass-loss rate; strengthened evidence for activity driven by CO and H_2O; and an estimate of the ISO cumulative size distribution slope.

2. Observations

Since before the official announcement of the hyperbolic orbit of 2I, optical observations were being taken to characterize the object's brightness and refine its orbit. We used the rapid-response capability of the Global Relay of Observatories Watching Transients Happen (GROWTH) network to organize and schedule observations of 2I. Observations were done at different observatories around the world, all conducted at high airmass, $\gtrsim$2, just before or during astronomical twilight owing to the small, 43° solar elongation of the comet in 2019 mid-September. In addition to the difficulty of observing near twilight and at high airmass, the comet had a fast sky motion of $\sim$1″ minute^{-1}, necessitating the use of nonsidereal tracking for the majority of the observations.

We present here the observations of a monitoring campaign led by the GROWTH collaboration (Kasliwal et al. 2019) combined with data from the Apache Point Observatory (APO) Astrophysical Research Consortium (ARC) 3.5 m telescope, the NASA Infrared Telescope Facility (IRTF) 3.0 m telescope, ZTF, and Keck Observatory. The time span of our observations is between 2019 March 17 and 2019 December 20 UTC.

2.1. SED Machine

The first observations of 2I used in this study were made with the Spectral Energy Distribution Machine (SEDM), operating on the P60 telescope on Palomar (Blagorodnova et al. 2018; Rigault et al. 2019). The SEDM possesses a multiband CCD camera that we used to obtain Sloan Digital Sky Survey (SDSS) *r*-band images in 60 s exposures of 2I on 2019 September 10 and 11 UTC. The telescope was tracked nonsidereally according to the sky motion of 2I, resulting in background stars that were trailed $\sim$2″. The astrometric positions of 2I were computed and submitted to the MPC to refine the object's orbit (Williams 2019b). The airmass at the time of the observations was $\sim$2, and the seeing was $\sim$1″.4 in the images taken for the object. This facility is a member of the GROWTH collaboration.

2.2. APO ARC 3.5 m

Immediately following the MPC's announcement of the discovery of 2I, we obtained director's discretionary time to observe 2I with the APO ARC 3.5 m. The first observations with the ARC 3.5 m were made on 2019 September 12 UTC in photometric conditions with the ARCTIC large-format optical CCD camera (Huehnerhoff et al. 2016). The camera was used in full-frame, quad-amplifier readout, 2 $\times$ 2 binning mode, resulting in a pixel scale of 0″.228. Exposures were each 120 s long; made in a rotating order of four filters, SDSS *griz*, in order to mitigate the potential effects of rotational variability on the color calculations (e.g., Hanuš et al. 2018); and dithered by 20″ between exposures of the same filter. In total, five *g*, eight *r*, one *i*, and two *z* exposures were obtained. The telescope was tracked at the sky motion rate of the comet, resulting in stars that were trailed by $\sim 2''$. Additional observations were made on 2019 September 27 UTC using the Aspen Apogee Camera in the *R* band and 2019 October 12 UTC using the ARCTIC camera with *Bgriz* filters. Seeing was exceptionally good, $\sim 0\farcs55$ in the images taken for the object, on the night of 2019 September 12 UTC; however, the observations were conducted at high airmass and into astronomical twilight, reducing the sensitivity of the observations.

The ARC 3.5 m was also used to obtain SDSS/Maunakea *zJHK* photometry of 2I on 2019 September 19 and 27 UTC with the NIC-FPS NIR camera (Vincent et al. 2003). A revolving *zJHK* filter sequence was used with a five-point dither pattern. To avoid the effects of the high sky background in the NIR, 40 and 20 s exposures were used for the *H* and *K* filter images, respectively, and 120 and 60 s exposures were used for the *z* and *J* filter images. Up to eight Fowler samples were used per readout to limit readout noise. Seeing was $\sim 1''$ or better during the nights of 2019 September 12, 19, and 27 and October 12 and 21 UTC.

2.3. LOT

Also soon after the discovery of 2I, imaging data were obtained on 2019 September 12 UTC with the 1 m Lulin Optical Telescope (LOT) using the 2K $\times$ 2K SOPHIA camera (Kinoshita et al. 2005) at Lulin Observatory. Data were taken in Johnson–Cousins *V*, *B*, *R*, and *I* bands, and the telescope was tracked nonsidereally at the comet's sky motion rate. The seeing during the observations was $\sim 3\farcs5$ in the images taken for the object, and the airmass was ~ 2.36.

2.4. Bisei Observatory 101 cm

Images of 2I were obtained at Bisei Observatory[38] on 2019 September 15 UTC using the 101 cm reflecting telescope. Images with 60 s exposure in the Johnson–Cousins *R* band were obtained using the Astrocam optical camera, and the telescope was tracked at a sidereal rate. Seeing at the time of observations was typically $\sim 2''$ in the images taken for the object, and the airmass was ~ 2. This facility is a member of the GROWTH collaboration.

2.5. Liverpool Telescope

On eight separate nights between 2019 September 18 and 2019 October 15 UTC, observations of 2I were obtained with the 2 m Liverpool Telescope located at the Observatorio del Roque de los Muchachos. Images were obtained using the IO:O wide-field camera with a 2 $\times$ 2 binning and the SDSS *g* and *r* filters (Steele et al. 2004). A 30 s exposure time was used with the telescope tracking the target in a nonsidereal mode. Debiasing and flat-fielding of the data were performed using the automated IO:O pipeline software. Seeing was typically $\sim 1''$ in the images taken for the object during the observations, and the airmass was ~ 1.8–2.0. This facility is a member of the GROWTH collaboration.

2.6. Mount Laguna Observatory 40 inch Telescope

Optical images were obtained with the 1.0 m telescope at the Mount Laguna Observatory (Smith & Nelson 1969) on 2019 September 19 and 30 and October 4, 8, 12, and 17 UTC. The E2V 42-40 CCD camera was used to obtain typically six 90 s exposures in each of the Johnson–Cousins *V* and *R* filters each night. Both sidereal and nonsidereal tracking was used, and these produced similar results due to the shortness of the exposures. The seeing during observations was typically $\lesssim 3''$, as measured using stars in the images, and the airmass was ~ 1.5–2.0. This facility is a member of the GROWTH collaboration.

2.7. NASA/IRTF

On 2019 September 20, 22, and 29 and October 2 UTC, observations of 2I were obtained with the 3 m NASA/IRTF located at Maunakea, Hawaii. Images in the *H* filter and NIR spectra were obtained with a wide $0\farcs8$ slit and the low-resolution prism mode of the SpeX prism instrument (Rayner et al. 2003), and *r*-band imagery was also obtained with the MORIS guider camera. The telescope was tracked at comet rate, and long 120 s exposures were used. The slit was rotated to the optimal azimuth angle in order to reduce differential atmospheric refraction, which would affect the shortest wavelengths in the spectrum the most, when taking prism data for 2I and the standard star. Because of the comet's brief time above the horizon, only four ABBA pairs were obtained on a typically good weather night; the evening of 2019 September 22 UTC was clouded out and little useful data obtained. The most useful data came from the observations on 2019 September 29 UTC, which are described below. The airmass during the time of observation was ~ 1.5–2.0. The seeing was $\sim 0\farcs8$ measured at zenith and worse by $\sim 30\%$ at the airmass of our observations.

2.8. ZTF

The ZTF is a wide-field all-sky survey using Palomar Observatory's P48 Oschin Schmidt telescope (Bellm et al. 2019b). The mission of the ZTF survey is to discover transients, which include asteroids and comets (Graham et al. 2019). The ZTF camera has a 47 deg^2 field of view and can reach $r \sim 20.5$ to a signal-to-noise ratio (S/N) = 5 depth in a 30 s exposure, enabling the survey to cover 3800 deg^2 hr^{-1}. In addition to the GROWTH and APO data, we use prediscovery observations found in the ZTF database to extend the time range of our observations (Masci et al. 2019). Seeing was typically $\sim 2''$, and the airmass was ~ 2.

Using the latest orbital solution for 2I that was available on 2019 October 2 UTC (Williams 2019c), we used the ZTF database search tool (Masci et al. 2019) to locate images that had overlapping coverage with the trajectory of 2I. The positional uncertainty of 2I in images as far back as 2019 March and May was less than $10''$–$30''$. With such a small search area, it became viable to visually spot the detections of the comet in the images where automated software would have missed these detections, i.e., for being too faint, S/N $\simeq$ 2–3. Therefore, we searched for the detections of 2I by eye in each set of images between 2019 March 17 and 2019 May 5 UTC using the nominal position from JPL HORIZONS as a starting point. The individual detections were very weak, of the order of S/N 2–3, and in a high sky background owing to the fact that some of them came from observations taken during astronomical twilight.

We identified the prediscoveries on the dates 2019 March 17 and 18 and May 2 and 5 UTC during the public and partnership

[38] http://www.bao.city.ibara.okayama.jp/eng/sisetu.htm

surveys (Bellm et al. 2019a). We used images that were taken with a 30 s r-filter exposure for the prediscovery images. We used two exposures taken on 2019 March 17 UTC, two exposures taken on 2019 March 18 UTC, six exposures taken on 2019 May 2 UTC, and four exposures taken on 2019 May 5 UTC (Ye et al. 2020). In addition to the prediscovery detections, we identified additional postdiscovery detections of 2I in ZTF survey data between 2019 September 11 and 2019 December 20 UTC that were taken in SDSS-like g and r filters (Graham et al. 2019). Seeing was typically $\sim2''$ in the images taken for the object, and the airmass ranged between 1.2 and 2 in the prediscovery images.

2.9. Keck I Telescope

We obtained high-resolution images of 2I on 2019 October 4 UTC with the Keck I instrument OSIRIS in imaging mode using laser guide star adaptive optics (AO; Larkin et al. 2006), the first time this instrument and telescope combination had been used to track and observe a comet. The comet was at a heliocentric distance of 2.48 au, a topocentric distance of 2.96 au, and a phase angle of $18\overset{\circ}{.}65$ during our observations. Four 60 s exposures were made in the K_p band using the laser guide system with an $r\sim15$ mag star within $60''$ of the comet during the observations. Because of Keck I's 33° elevation constraint in the azimuth range of 2I, observations had to wait for astronomical twilight to begin. The K_p filter[39] is an NIR filter similar to the Two Micron All Sky Survey (2MASS) K_s filter with a central wavelength of 2114.45 nm and an FWHM bandpass of 307.03 nm. A nearby $r\sim15$ star was used with the laser guidance system for AO correction while tracking at the sky motion rate of 2I; however, the high airmass of the observations and performance of the laser system resulted in lower image quality than usual. The point-spread function (PSF) FWHM of background stars in OSIRIS images is $0\overset{''}{.}22$–$0\overset{''}{.}26$ measuring in the perpendicular direction of the direction of motion of 2I. The airmass during the time of the observations was ~1.6.

2.10. C2PU Facility 1.04 m Omicron Telescope

Observations of 2I were obtained with the Observatoire de la Côte d'Azur's C2PU 1.04 m telescope located at Calern on 2019 November 29 UTC. Images were obtained using the 4096 × 4096 SBIG STX-16803 CCD camera with a $0\overset{''}{.}6$ pixel scale in the R bands. A 30 s exposure time was used with the telescope tracking the target in nonsidereal mode, and the airmass of the observation was ~2.4. The atmospheric seeing was $\sim1\overset{''}{.}88$ in the images taken for the object. Debiasing and flat-fielding was performed on the data using automated software.

3. Results

3.1. Optical Photometry and Colors

Data collected with the GROWTH and ARC 3.5 m telescopes were processed using flattened and dark-subtracted images produced by basic methods. Photometric measurements were obtained by using a circular aperture with a projected radius of 10,000 km at the topocentric distance of the comet, typically $\sim5''$. The typical seeing at our observing locations was well under $\sim5''$, measured in the images as described in Table 1. The brightness of the comet was calibrated using the PanSTARRS catalog (Tonry et al. 2012; Flewelling et al. 2016). Johnson–Cousins photometry was calibrated using the PanSTARRS catalog and the filter transformations described in Tonry et al. (2012). We calibrated the photometry with in a frame stars, thus accounting for varying conditions at the high airmass of our observations. Sky subtraction was done using annuli with an inner radius exceeding the extent of the coma by $\gtrsim10''$.

Our team regularly monitored the comet's brightness between 2019 September 10 UTC and 2019 December 20 UTC with telescopes in the GROWTH network at observatories from around the world as described above. The photometric observations cover a span of wavelengths from the V band to I and z. To put the photometric measurements on the same scale for comparison, individual Johnson–Cousins filters were converted to the SDSS magnitude system using the colors measured here in $griz$ and $VBRI$ filters (Jordi et al. 2006). The resulting magnitudes are listed in Table 1.

A mosaic of composite images showing the detections of 2I taken by the ARC 3.5 m on 2019 September 12 UTC in the g, r, i, and z filters is shown in Figure 1. The comet has a clearly extended appearance with a diffuse tail $\sim6\overset{''}{.}7$ long pointing in the $\sim315°$ position angle. Using the stacked images taken by the ARC 3.5 m on 2019 September 12 UTC, the SDSS $griz$ filter colors of 2I are $g-r=0.54\pm0.06$, $r-i=0.20\pm0.04$, and $i-z=-0.23\pm0.04$. Immediately after the ARC 3.5 m observations on 2019 September 12 UTC, $BVRI$ observations were obtained with the LOT, resulting in the following colors: $B-V=0.76\pm0.12$, $V-R=0.55\pm0.09$, and $R-I=0.37\pm0.08$. Converting the ARC 3.5 m $griz$ colors for 2I to $BVRI$ colors using the transformations in Jordi et al. (2006) results in $B-V=0.69\pm0.09$, $V-R=0.40\pm0.1$, and $R-I=0.41\pm0.07$, which are in good agreement with the LOT $BVRI$ colors and the $BVRI$ colors obtained by Fitzsimmons et al. (2019) and Jewitt & Luu (2019). An additional observing run on the ARC 3.5 m was conducted on 2019 October 12 UTC, where $Bgriz$ filtered observations were obtained of 2I with similar colors as measured from data obtained with the ARC 3.5 m on 2019 September 12 UTC: $g-r=0.63\pm0.05$, $r-i=0.20\pm0.05$, and $i-z=-0.23\pm0.02$. In addition, we calculate $B-V$ colors for data taken on 2019 October 12 UTC by converting our g and r measurements to a V magnitude using the filter transformations for converting SDSS to Johnson–Cousins magnitudes. This results in $B-V=0.68\pm0.04$, similar to the $B-V$ colors obtained by the LOT on 2019 September 12 UTC and by Jewitt & Luu (2019).

We extend our color analysis redward of the SDSS i and Cousins I filters, centered at 762 and 880 nm, respectively, to 913 nm with the inclusion of the SDSS z filter. While the visual spectrum reported by de León et al. (2019) and Hui et al. (2020) shows an overall red appearance, our $g-r$ versus $r-z$ colors of 2I show similarity with neutral and bluish solar system bodies, and 2I does not appear to be as red as outer solar system bodies, such as comets and Kuiper Belt objects (KBOs), with the inclusion of the longer-wavelength z-filter data, as seen in Figure 2. This is in contrast with the apparently slightly red color of 2I in $B-V$ versus $V-R$ color space, as seen in Figure 5 of Jewitt & Luu (2019), which only goes as red as 635 nm for the R versus 913 nm for the z-filter $g-r$ versus

[39] https://www2.keck.hawaii.edu/inst/osiris/technical/filters/filter_index.html

Table 1
Summary of Comet 2I Photometry

Date[1] UTC (1)	Telescope[2] (2)	r_h^3 (au) (3)	Δ^4 (au) (4)	α^5 (deg) (5)	ν^6 (deg) (6)	Filter[7] (7)	Mag.[8] (8)	$\sigma_{\rm mag}^9$ (9)	θ_s^{10} (arcsec) (10)	$\chi_{\rm am}^{11}$ (11)
2019 Mar 17	ZTF	6.0	6.1	9.3	277.6	*r*	20.71	0.37	2.37	1.32
2019 Mar 18	ZTF	6.0	6.1	9.3	277.7	*r*	21.01	0.37	2.18	1.27
2019 May 2	ZTF	5.2	5.8	8.2	281.8	*r*	20.30	0.18	2.11	1.90
2019 May 5	ZTF	5.1	5.8	8.0	282.0	*r*	20.66	0.31	2.53	2.01
2019 Sep 10	SEDM	2.8	3.48	13.9	308.6	*r*	17.91	0.05	2.11	1.89
2019 Sep 11	SEDM	2.8	3.45	14.1	309.2	*r*	17.71	0.04	1.74	1.68
2019 Sep 11	ZTF	2.8	3.45	14.1	309.2	*g*	18.43	0.06	1.92	1.40
2019 Sep 12	ARC 3.5 m	2.78	3.43	14.3	309.6	*g*	18.29	0.04	0.66	2.34
2019 Sep 12	ARC 3.5 m	2.78	3.43	14.3	309.6	*r*	17.75	0.04	0.62	2.15
2019 Sep 12	ARC 3.5 m	2.78	3.43	14.3	309.6	*i*	17.55	0.01	0.58	2.32
2019 Sep 12	ARC 3.5 m	2.78	3.43	14.3	309.6	*z*	17.78	0.03	0.56	2.21
2019 Sep 12	LOT	2.78	3.43	14.3	309.6	*V*	18.01	0.05	3.50	2.36
2019 Sep 12	LOT	2.78	3.43	14.3	309.6	*B*	18.77	0.1	3.50	2.36
2019 Sep 12	LOT	2.78	3.43	14.3	309.6	*R*	17.47	0.04	3.50	2.36
2019 Sep 12	LOT	2.78	3.43	14.3	309.6	*I*	17.09	0.04	3.50	2.36
2019 Sep 15	Bisei	2.73	3.37	14.9	310.7	*R*	17.41	0.06	2.05	2.11
2019 Sep 18	Liverpool	2.69	3.30	15.5	311.9	*g*	18.23	0.17	1.03	2.25
2019 Sep 19	MLO 1.0 m	2.68	3.27	15.7	312.3	*r*	17.86	0.02	3.53	2.08
2019 Sep 21	ZTF	2.65	3.23	16.0	313.1	*r*	17.82	0.04	1.76	1.76
2019 Sep 22	ZTF	2.64	3.21	16.2	313.6	*g*	17.72	0.06	2.53	1.72
2019 Sep 22	ZTF	2.64	3.21	16.2	313.6	*r*	18.33	0.13	2.16	2.21
2019 Sep 27	ARC 3.5 m	2.56	3.11	17.2	315.7	*R*	17.45	0.04	1.87	2.25
2019 Sep 30	MLO 1.0 m	2.52	3.04	17.8	317.1	*r*	17.51	0.02	3.49	2.32
2019 Oct 1	ZTF	2.51	3.02	18.0	317.5	*r*	17.36	0.03	2.20	2.35
2019 Oct 2	ZTF	2.50	2.99	18.2	318.0	*g*	17.83	0.04	2.24	2.20
2019 Oct 2	ZTF	2.50	2.99	18.2	318.0	*r*	17.25	0.04	1.94	1.80
2019 Oct 4	MLO 1.0 m	2.47	2.95	18.64	318.9	*V*	17.80	0.02	3.75	1.99
2019 Oct 4	MLO 1.0 m	2.47	2.95	18.64	318.9	*r*	17.32	0.01	3.62	1.95
2019 Oct 4	Liverpool	2.47	2.95	18.64	318.9	*g*	17.89	0.02	1.12	1.97
2019 Oct 4	Liverpool	2.47	2.95	18.64	318.9	*r*	17.31	0.01	1.17	1.94
2019 Oct 5	ZTF	2.46	2.94	18.85	319.4	*r*	17.19	0.04	1.97	2.02
2019 Oct 8	MLO 1.0 m	2.42	2.87	19.45	320.8	*V*	17.73	0.03	2.82	2.17
2019 Oct 8	MLO 1.0 m	2.42	2.87	19.45	320.8	*r*	17.21	0.01	2.95	2.22
2019 Oct 8	Liverpool	2.42	2.87	19.45	320.8	*g*	17.75	0.03	1.03	2.01
2019 Oct 8	Liverpool	2.42	2.87	19.45	320.8	*r*	17.15	0.01	1.07	1.99
2019 Oct 10	Liverpool	2.40	2.83	19.85	321.8	*g*	17.61	0.01	0.99	1.98
2019 Oct 10	Liverpool	2.40	2.83	19.85	321.8	*r*	17.13	0.01	1.08	1.93
2019 Oct 11	ZTF	2.38	2.81	20.1	322.4	*g*	17.71	0.04	2.99	2.03
2019 Oct 12	ARC 3.5 m	2.37	2.79	20.25	322.9	*B*	18.04	0.04	0.88	1.56
2019 Oct 12	ARC 3.5 m	2.37	2.79	20.25	322.9	*g*	17.74	0.05	0.73	1.71
2019 Oct 12	ARC 3.5 m	2.37	2.79	20.25	322.9	*r*	17.11	0.05	0.78	2.02
2019 Oct 12	ARC 3.5 m	2.37	2.79	20.25	322.9	*i*	16.94	0.02	0.82	2.12
2019 Oct 12	ARC 3.5 m	2.37	2.79	20.25	322.9	*z*	17.14	0.05	0.75	1.62
2019 Oct 12	MLO 1.0 m	2.37	2.79	20.25	322.9	*V*	17.55	0.04	2.78	1.74
2019 Oct 12	MLO 1.0 m	2.37	2.79	20.25	322.9	*r*	17.27	0.04	2.56	1.83
2019 Oct 14	Liverpool	2.35	2.76	20.66	323.9	*r*	17.14	0.04	1.10	1.9
2019 Oct 14	ZTF	2.35	2.76	20.66	323.9	*g*	17.74	0.08	2.00	1.37
2019 Oct 14	ZTF	2.35	2.76	20.66	323.9	*r*	17.16	0.04	2.01	1.77
2019 Oct 15	ZTF	2.34	2.74	20.86	324.4	*r*	17.18	0.05	3.84	1.79
2019 Oct 17	MLO 1.0 m	2.32	2.70	21.26	325.5	*V*	17.46	0.04	2.93	1.68
2019 Oct 17	MLO 1.0 m	2.32	2.70	21.26	325.5	*r*	17.19	0.04	3.12	1.76
2019 Oct 21	ARC 3.5 m	2.28	2.62	22.04	327.7	*r*	16.99	0.02	2.21	2.13
2019 Oct 29	ZTF	2.20	2.48	23.56	332.4	*r*	16.84	0.01	1.92	1.59
2019 Nov 3	ARC 3.5 m	2.16	2.40	24.46	335.5	*r*	16.76	0.02	0.96	2.58
2019 Nov 5	ZTF	2.14	2.37	24.79	336.7	*r*	16.61	0.03	1.74	1.68
2019 Nov 8	ZTF	2.12	2.32	25.29	338.7	*r*	16.76	0.03	1.92	1.40
2019 Nov 12	ZTF	2.09	2.26	25.91	341.3	*r*	16.76	0.04	2.13	2.20
2019 Nov 17	ZTF	2.06	2.20	26.62	344.7	*r*	16.88	0.04	2.67	1.40
2019 Nov 27	ZTF	2.02	2.08	27.76	351.7	*g*	17.29	0.0	4.18	1.65
2019 Nov 29	C2PU	2.01	1.99	27.93	353.1	*r*	16.88	0.03	1.88	2.40
2019 Dec 20	ZTF	2.03	1.94	28.63	8.2	*g*	17.50	0.06	2.51	1.90

Note. Columns: (1) observation date, (2) observatory, (3) heliocentric distance, (4) topocentric distance, (5) phase angle, (6) true anomaly, (7) filter, (8) 10^4 km aperture mag, (9) 1σ mag uncertainty, (10) in-image seeing of observations, (11) airmass of observations.

$r - z$ color space. We must caution that the comparison of the colors between 2I and known solar system comets can be affected by the fact that comet dust for active comets can modify their apparent color compared to inactive bodies (Li et al. 2013). We also further caution that although 2I appears neutral to reddish with the addition of longer wavelengths in the $g - r$ versus $r - z$ color space compared to $B - V$ versus $V - R$ color space, the interpretation of the colors of small bodies is limited by the fact that many solar system bodies appear neutral in optical colors spanning wavelengths of 477–913 nm for filters g to z (Bus & Binzel 2002). However, solar system objects that appear to be neutral in optical wavelengths can be revealed to be much redder with the inclusion of even longer wavelength data in the NIR range (e.g., DeMeo et al. 2009; Schwamb et al. 2019), as further discussed in Section 3.2. We wish to reiterate that this comparison of colors with inactive bodies is for reference only. In addition, 2I exhibits colors that are markedly different from active solar system objects, being less red in $r - z$ color, which may indicate that the color of the dust of 2I is different from solar system comets.

We increased the range of our long-term light curve by using prediscovery observations of 2I found in r-filter images from the ZTF survey spanning 2019 March to May. Ye et al. (2020) presented these measurements and analysis; here we repeat their extraction from raw data both as a cross-check and for methodological consistency reasons.

The prediscovery detections from ZTF were stacked in the individual images, increasing their S/N by locating detections in several overlapping images taken on the same night that were processed to remove static sources. The limiting magnitude in the image stacks was $r \sim 21.5$ for the 60 s equivalent exposure time image stacks taken in 2019 March and $r \sim 22.5$ and 22 for the 180 and 120 s equivalent exposure time image stacks taken on 2019 May 2 and 5, respectively. The image stacks showing the individual detections taken on 2019 March 17 UTC and 2019 May 2 UTC are shown in the bottom panels of Figure 1. In addition to the photometry, the prediscovery detections were measured astrometrically and submitted to the MPC, allowing for the orbital arc to be significantly extended by several months, improving its accuracy, and for use by the community to study 2I. The photometry from the postdiscovery observations by the GROWTH and ZTF telescopes is listed in Table 1.

3.2. NIR Photometry and Spectrum

From our VisNIR observations with the ARC 3.5, cometary morphology is evident in the z image, but the cometary appearance is suppressed in the longer-wavelength JHK images as seen in Figure 3 due to light scattering by cometary dust being less efficient at longer wavelengths (Fernández et al. 2013; Bauer et al. 2017). The z and JHK photometry were calibrated using the PanSTARRS (Chambers et al. 2016) and 2MASS (Skrutskie et al. 2006) catalogs. We measure magnitudes $z = 17.57 \pm 0.05$, $J = 16.80 \pm 0.05$, $H = 16.01 \pm 0.09$, and $K = 15.81 \pm 0.10$. Combined with the R-filter observation also taken on 2019 September 27 UTC, the resulting colors are, after converting the R measurement to $r = 17.60 \pm 0.04$, $r - z = 0.03 \pm 0.06$, $r - J = 0.80 \pm 0.06$, $z - J = 0.77 \pm 0.07$, $J - H = 0.79 \pm 0.10$, and $H - K = 0.20 \pm 0.13$, similar to neutral solar system objects and distinct from very red outer solar system objects (Schwamb et al. 2019). As seen in Figure 3 from Bannister et al. (2017), the rough dividing line in $r - J$ separating outer solar system objects from inner solar system objects is $r - J \gtrsim 1.2$, where the $r - J$ of 2I is $\sim$0.8.

We made a pair-subtracted stack of the four 120 s ABBA sequence SpeX prism exposures of 2I, resulting in the composite spectrum seen in the top panel of Figure 3. The full compliment of gri and $zJHK$ photometry from 2019 October 12 and 2019 September 27 UTC are overplotted on top of the NIR spectrum, showing agreement with the visible portion with the visible spectrum of de León et al. (2019). The spectrum was adjusted to the photometric points. The IR color of 2I, as determined by the continuum slope of the prism spectra, was found to be neutral gray, in agreement with the $rzJHK$ colors, in contrast with Yang et al. (2019). No definitive absorption or emission lines were found within the errors of the measurements, similar to the lack of emission lines seen in the spectra of solar system comets and asteroids in the 0.7–2.5 μm range (Feldman et al. 2004).

The colors are typical of optically reddish objects containing refractory organics and silicates that become NIR-neutral because of the presence of water ice (Yang et al. 2009; Snodgrass et al. 2017). Because the flux of 2I is dominated by its coma, as discussed in Section 3.1, we can infer, by analogy with solar system comet spectra, that the 2I NIR spectrum coma dust contains silicates, refractory organics, and water ice (Protopapa et al. 2014; Bockelée-Morvan et al. 2017), though recent observations suggest that the main driver of the activity is CO and is likely responsible for driving the dust production (Bodewits et al. 2020).

From our OSIRIS observations with Keck I, a composite stack of the K_p images of 2I is shown in Figure 4. No extended coma or tail features are evident in the OSIRIS images taken on 2019 October 4 UTC owing to the low surface brightness of these features in K-band wavelengths similar to the NIR wavelength images taken by the ARC 3.5 m on 2019 September 27 UTC, as seen in the bottom panel of Figure 3. We estimate the apparent brightness of 2I in the AO K_p images measured to be $m_{K_p} = 15.68 \pm 0.06$ using a $4''\!.7$ circular aperture with a projected radius of 10,000 km at the topocentric distance of the comet of 2.96 au on 2019 October 4 and the zero-point of 27.6 determined for the K_p of the OSIRIS instrument.[40]

3.3. Long-term Light Curve and Volatile-driven Activity

Due to the density and slow crossing time of dust within 2I's coma at the scale of our ground-based observations, as discussed in Jewitt & Luu (2019), measuring any short-term light-curve variations on the order of hours to tens of hours caused by the rotation of the comet's nucleus is difficult. However, other effects on the comet's brightness can happen on longer time spans of weeks to months, such as outbursts, seasonal effects, or changes in its activity due to the sublimation of different volatile species that become active at different heliocentric distances along the comet's orbit (Hughes 1990; Li et al. 2016; Keller et al. 2017; Womack et al. 2017). Because these effects can take weeks to months, a comet needs to be monitored over a long time period, requiring the dedication of observers to make regular observations of the comet. A detailed discussion of the long-term light curve's implication for the activity of 2I follows.

[40] https://www2.keck.hawaii.edu/inst/osiris/OSIRIS_Manual_v2.2.pdf

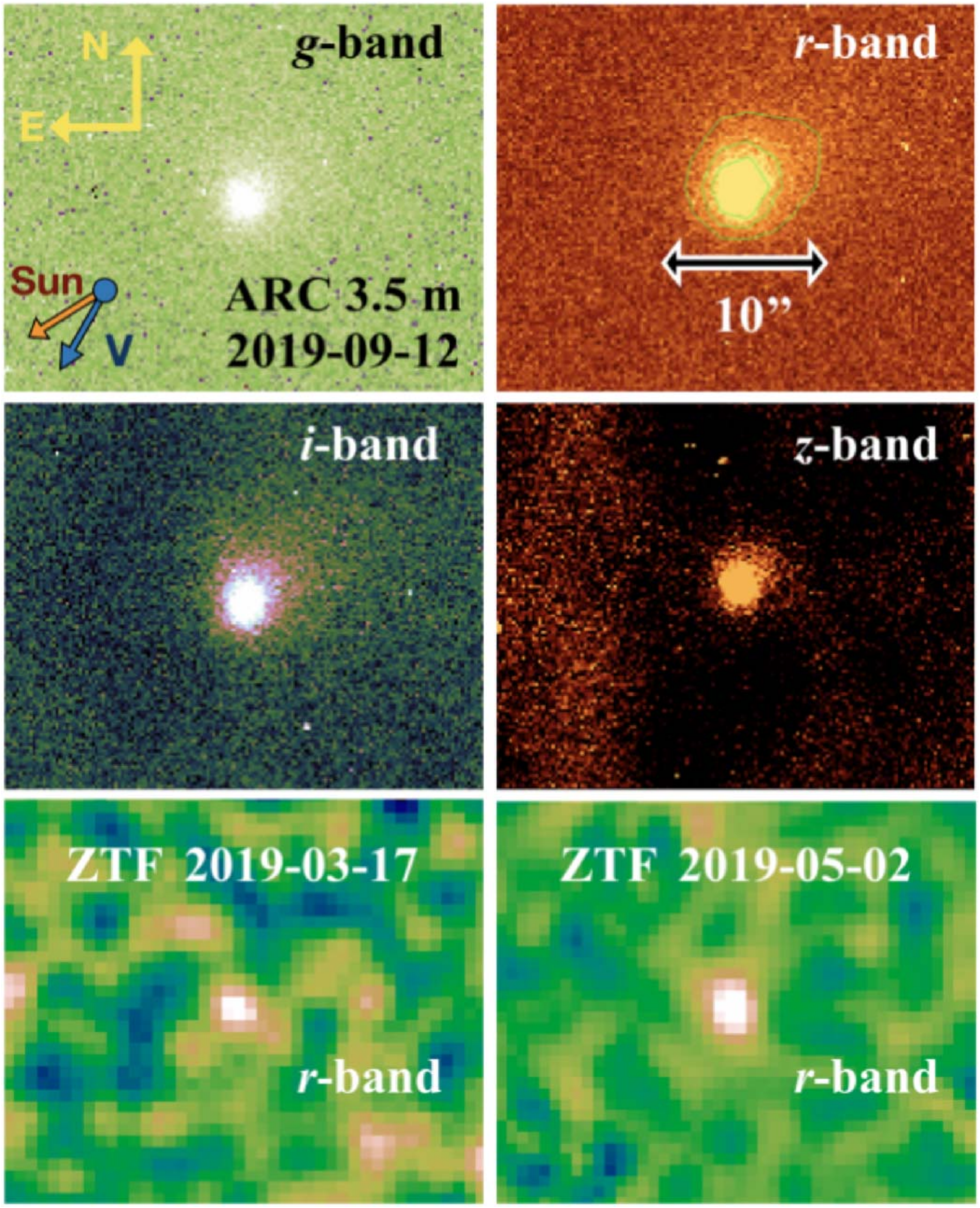

Figure 1. Mosaic of g, r, i, and z images of 2I taken with the ARC 3.5 m on 2019 September 12 UTC and prediscovery ZTF images from 2019 March 17 and 2019 May 2 UTC. Top left panel: composite stack of five 120 s g-filter exposures with the orbital velocity and solar directions. Top right panel: composite stack of eight 120 s r-filter exposures and showing the extent of the comet's tail limited by sky background. Middle left panel: single 120 s i-filter exposure. Middle right panel: stack of two z-filter exposures. The nearby background is irregular due to incomplete removal of fringes. Calibration stars were carefully chosen that were not affected by these fringe removal artifacts. Bottom left and right panels: prediscovery detections of 2I from 2019 March 17 and 2019 May 2 UTC. The 2019 March 17 UTC data is a stack of two images with an equivalent exposure time of 60 s. The 2019 May 2 UTC data is a stack of six images with an equivalent exposure time of 180 s. Both of these ZTF image stacks have been spatially smoothed to enhance faint features in the image. The artifact at the bottom of the 2019 March 17 UTC image is a star subtraction artifact. No extended coma or tail features are evident in the prediscovery image stacks owing to the low surface brightness of these features at the time of observation. A green color scale was chosen for the ZTF r-filter observations to more clearly highlight these faint detections compared to the surrounding background.

The light curve of equivalent r magnitudes is plotted in Figure 5. As of writing, the brightness of 2I, plotted as orange squares, appears to follow the trend predicted by Fitzsimmons et al. (2019) for an H_2O-dominated comet, plotted as a blue line, best seen in the inset plot zoomed in on $-52°$ to $-32°$ in Figure 5. The activity for a CO_2-dominated comet is plotted as an orange line. Both of these activity models from Fitzsimmons et al. (2019) are based on assuming a nucleus diameter of $\sim$1 km and activity consistent with solar system comets using the measured CN activity to estimate the production rate of other volatile species (A'Hearn et al. 1995). In addition, the activity model assumes that 100% of the comet's surface is active and dust grain properties are similar to solar system comets. There was a recent rise in brightness as 2I approached the water-ice line at heliocentric distance $r_h = 2.5$ au on 2019 October 2 UTC that may correspond to the increase in the sublimation rate of H_2O as the comet approaches the Sun (Meech & Svoren 2004; Jewitt et al. 2015).

Extrapolating the H_2O brightness model backward to the prediscovery data taken by ZTF in 2019 March and May, when the comet was at a heliocentric distance of 6.03 and 5.09 au, respectively, predicts a much fainter magnitude of $r \sim 26$ than

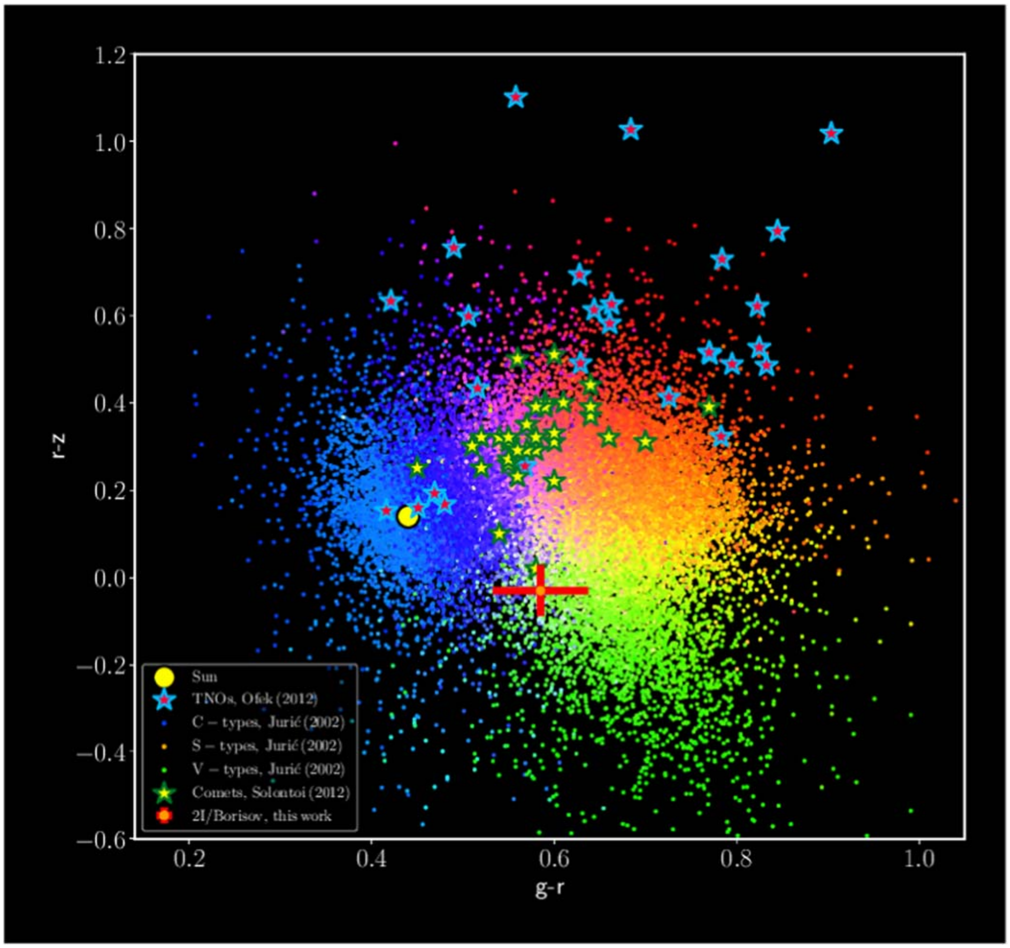

Figure 2. The $g - r$ vs. $r - z$ colors of 2I plotted with the $g - r$ and $r - z$ colors of other solar system bodies, including inner solar system asteroids such as C, S, and V types (Ivezić et al. 2001; Jurić et al. 2002; DeMeo & Carry 2013); active comets (Solontoi et al. 2012); and KBOs (Ofek 2012). The colorization scheme of data points for asteroids by their *griz* colors is adapted from Ivezić et al. (2002). We note that the comparison of the colors of 2I to active comets in Solontoi et al. (2012) is the most appropriate comparison, rather than inactive bodies, since the colors of 2I are most representative of its dust, rather than bare nucleus. The colors of inactive bodies are present for comparison only.

the observed magnitude of $r = 20.5$–21.0. As shown by Ye et al. (2020) and confirmed by our work, the actual observed prediscovery r magnitudes are much closer to the brightness model predicted for a comet that has its activity dominated by CO than H_2O (Fitzsimmons et al. 2019). This is supported by the fact that H_2O is very weakly sublimating at temperatures $\lesssim$150 K at a heliocentric distance >3.5 au, while CO can become volatile much further from the Sun at heliocentric distances exceding 10–100 au (Meech & Svoren 2004).

However, the prediscovery photometry may also be compatible with CO_2-driven activity where CO_2 can become active at >13 au (Womack et al. 2017; Ye et al. 2020). As discussed in Section 3.4, a significant production rate of H_2O is inferred from the observed production of CN and C_2 gas (Fitzsimmons et al. 2019; Kareta et al. 2020) and is ∼100 kg s^{-1} comparable, though larger than the $H_2O \sim 20$ kg s^{-1} production inferred from the detection of the [O I] 6300 Å line taken at further heliocentric distances (McKay et al. 2020). Since our photometric light curve suggests that the activity of 2I is partially driven by CO, we expect the mass loss of CO to also be much higher than the mass loss from dust in the ∼10–100 kg s^{-1} range as it approaches perihelion. The ratio of CO to H_2O has been shown to be >130%, as revealed by recent Hubble Space Telescope (HST) and Atacama Large Millimeter/submillimeter Array observations (Bodewits et al. 2020; Cordiner et al. 2020), much higher than the typical <30% of solar system comets (Paganini et al. 2014; Meech 2017).

The difference between the observed brightness of 2I in the prediscovery data is even larger for a bare, inactive ∼1.4 km diameter nucleus, as seen from the black dashed–dotted line in Figure 5. In addition, there appears to be an ∼0.2 mag change in brightness in the light curve between 2019 September 20 and 2019 October 3 UTC corresponding to true anomaly angles $-47°$ and $-42°$, deviating from the trend predicting the brightness for an H_2O-dominated comet as seen in Figure 5, and possibly indicating a change in the activity of the comet. We must caution that the height of the curves is also dependent on the size of the nucleus, and the activity could be compatible with a slight increase in nucleus size and a corresponding decrease in the water production rate.

Concerning the outgassing models used to constrain the activity, it is important to note that our suggestion of initial CO-driven outgassing activity transitioning to H_2O-driven activity is not dependent on 2I's nucleus size or fractional active outgassing area. The fractional active outgassing scales the CO + H_2O model; once set, this scale is fixed. It is the relative shape of our measured 2I long-term light curve and the upward

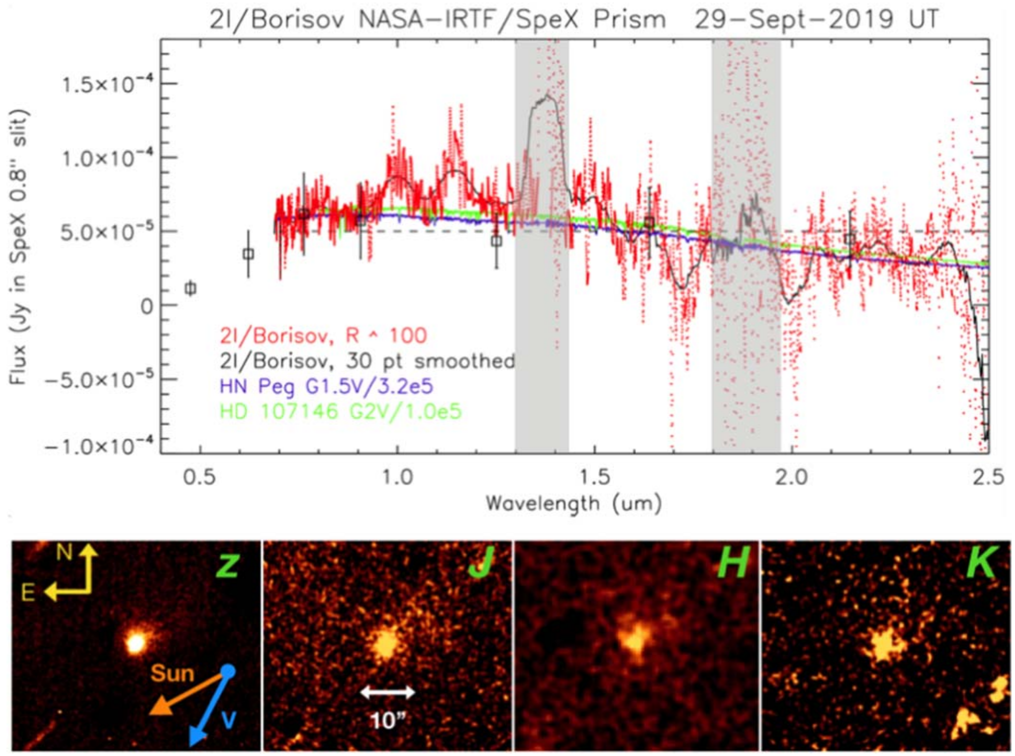

Figure 3. Top panel: scaled flux IRTF SpeX spectrum of 2I taken on 2019 September 29 UTC. The red line is an $R \sim 100$ spectrum between 0.7 and 2.5 μm from two ABBA 120 s pair subtractions. The black line is the smoothed spectrum of 2I with a 30 pt (∼50 nm) running mean. The blue and green lines correspond to G1.5V and G2V analog stars HN Peg and HD 107146. The SED is overall reddish-neutral with some slight deviations in the 0.9–1.2 μm range. The *gri* fluxes obtained in observations on 2019 October 12 and the *zJHK* fluxes obtained in observations on 2019 September 27 with the ARC 3.5 m are overplotted on the spectrum and in rough agreement with the spectrum. Emission features at ∼1.4 and ∼1.8 μm are of terrestrial atmospheric origin. Bottom panel: *zJHK* image stacks of 2I taken on 2019 September 27 UTC with NIC-FPS on the ARC 3.5 m. The *z* and *J* images are a 600 s robust mean stack, and the *H* and *K* images are 200 s robust mean stacks. All images have been spatially smoothed to enhance faint features. The north and south directions and the solar and orbital velocity directions are indicated on the *z*-band panel. Regions of the spectrum degraded by sky absorption are grayed out.

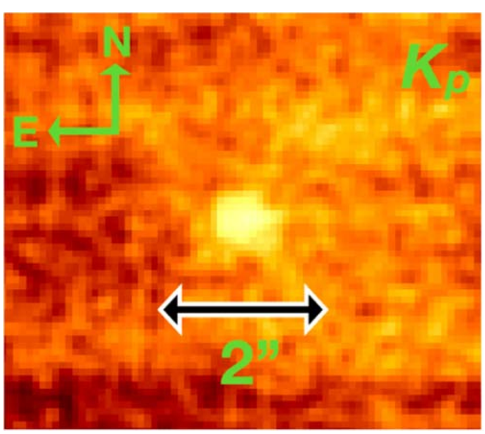

Figure 4. The K_p image of 2I taken with the OSIRIS AO instrument on Keck I tracking at the sky motion rate of the comet. The image is a composite stack of four 60 s K_p exposures stacked on the position of the comet in each individual exposure. The image has been 4 × 4 binned, giving it a pixel scale of 0″08. The FWHM of the background stars measured perpendicular to the rate of motion of 2I is ∼0″2. The detection is PSF-like without an extended appearance or a tail visible in the image. The image has been Gaussian smoothed by 2 binned pixels.

inflection point in the light curve seen at distances $r_h < 3$ au that tell us that additional water outgassing has turned on and started to dominate the activity of the object. This latter finding, of water outgassing dominance, again tells us that 2I appears to be acting like a normal solar system comet, as water is by far the most abundant ice found in solar system comets.

3.4. Mass Loss

Using the *g*, *r*, *i*, and *z* photometry obtained by the ARC 3.5 m on 2019 September 12 UTC, we place estimates on 2I's $Af\rho$ parameter, a proxy for dust production rate (A'Hearn et al. 1984). We find $(Af\rho)_g = 113 \pm 5$ cm, $(Af\rho)_r = 185 \pm 7$ cm, $(Af\rho)_i = 223 \pm 8$ cm, and $(Af\rho)_z = 180 \pm 8$ cm, typical values for solar system comets (A'Hearn et al. 1995; Kelley et al. 2013), implying an outgassing rate of $\sim 10^{27}$ mol s^{-1} (Fink & Rubin 2012). The recently taken data from between 2019 September 11 UTC and 2019 December 20 UTC seen in Table 1 and Figure 5 show a brightening trend of ∼0.03 mag day^{-1}, consistent with the enhancement in brightness expected for the evolving viewing geometry of the comet according to the equation

$$m_V = H_{\rm abs} + 2.5\log_{10}(r_h\Delta) + \Phi(\alpha), \quad (1)$$

where m_V is the apparent magnitude; $H_{\rm abs}$ is the absolute magnitude; r_h is the heliocentric distance in au; Δ is the observercentric distance in au; $\Phi(\alpha)$ is a function describing the brightening of the comet, which we approximate with $\Phi(\alpha) = -0.04\alpha$ (Jewitt 1991); and α is the phase angle of the comet measured in degrees, appropriate for comets at smaller phase angles than ∼20° (Bertini et al. 2017). We translate the $H_{\rm abs}$ magnitude computed from Equation (1) into an effective cross section, *C*, in units of km^2 within a 10,000 km aperture using

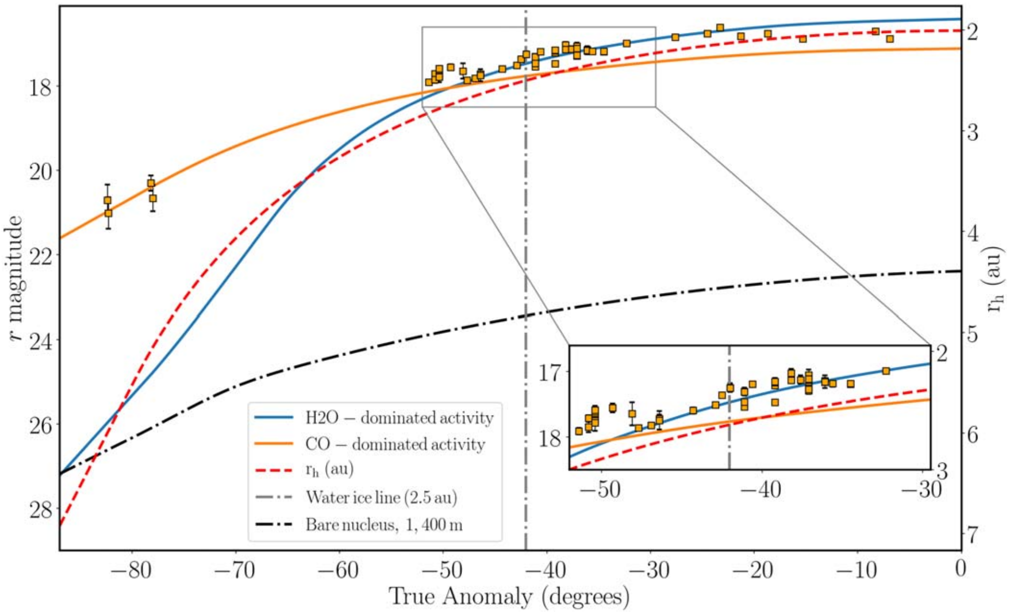

Figure 5. The r magnitude of 2I as a function of the true anomaly using photometry translated to r magnitudes for data taken between 2019 March 17 (Ye et al. 2020) and 2019 November 29 (this campaign) and tabulated in Table 1. The blue and orange lines are the predicted brightness as a function of true anomaly angle for H_2O- and CO-dominated activity for a comet with a diameter of 1.4 km and 100% active surface area from the outgassing model of 2I from Fitzsimmons et al. (2019). The brightness prediction assumes a 5″ aperture, comparable to the aperture size used to measure the brightness of 2I in this study. The dashed–dotted black line is the predicted brightness as a function of true anomaly angle assuming an inactive bare nucleus, a 1.4 km diameter, and a 0.04 albedo, the lower limit on the estimate of 2I's nucleus size from the detection of CN gas (Fitzsimmons et al. 2019). The red dashed line shows the heliocentric distance, r_h, as a function of true anomaly for 2I. The vertical gray dashed–dotted line is positioned on the true anomaly where 2I crosses the water-ice line at 2.5 au. True anomaly = 0° corresponds to 2I's perihelion passage on 2019 December 8 UTC.

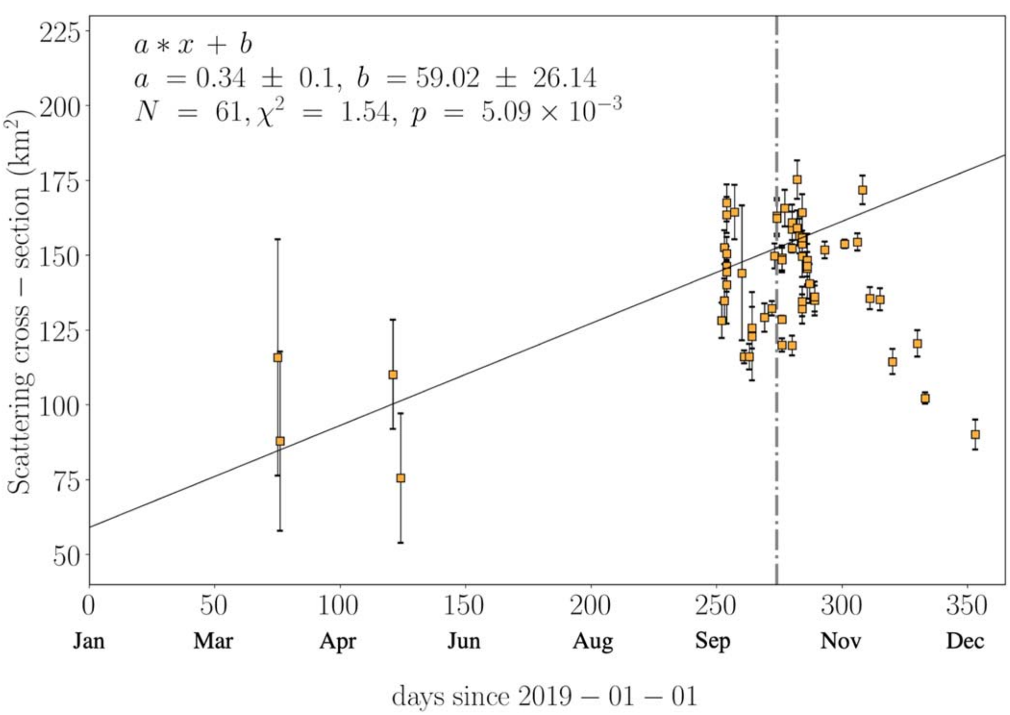

Figure 6. Effective cross section of 2I calculated from Equation (2) as a function of days since 2019 January 1 UTC. The black line shows the minimized χ^2 fit to the cross-section measurements, and the vertical dashed–dotted line corresponds to the date when 2I crossed the water-ice line at 2.5 au.

the formula

$$C = 1.5 \times 10^6\, p_v^{-1}\, 10^{-0.4H} \tag{2}$$

from Jewitt et al. (2016), where p_v is the albedo of the comet, assumed to be 0.10, typical for comet dust (Jewitt & Meech 1986; Kolokolova et al. 2004). We caution that uncertainties of $H_{\rm abs}$ inferred from Equation (1) are lower limits on the overall photometric uncertainty because they should also include a component from the phase function, which is unknown at the present time for 2I.

We plot the effective cross section over the baseline of available 2I photometry,including the ZTF prediscovery data taken in 2019 March and May, as seen in Figure 6. The median cross section from these data is $\sim 145\,\mathrm{km}^2$. A linear fit is applied to the data with the minimized χ^2 fit corresponding to a slope of $0.34 \pm 0.10\,\mathrm{km}^{-2}\,\mathrm{day}^{-1}$, suggesting that the cross section doubled since the earliest observations from the ZTF prediscovery images in 2019 March 17 and will exceed $\sim 200\,\mathrm{km}^2$ by the time 2I reaches perihelion on 2019 December 8 UTC, assuming the slope is constant. We note that the data point corresponding to the 2019 November 29 UTC and 2019 December 20 UTC data may be due to 2I increasing in brightness at a slower rate than expected as the comet reaches perihelion, so we do not include it with our linear fit.

There appears to be a sudden, $\sim 50\,\mathrm{km}^2$ jump in the effective cross section between 2019 September 20 and 2019 October 3 UTC, as seen in Figure 6, corresponding to the drop in the overall trend for brightness seen in the light curve plotted in Figure 5 between true anomaly angles $-47°$ and $-42°$. As discussed in Section 3.3, the deviation in brightness may indicate a change in the comet's activity. The location of the vertical dashed–dotted line in Figure 6 indicates when 2I crossed the water-ice line, which is near an observed steep increase in the cross section, possibly connected to the sublimation of H_2O discussed further in Section 3.3. There is also another, earlier $\sim 50\,\mathrm{km}^2$ jump in the cross section starting around the onset of our observations on 2019 September 10 UTC, though we caution that the variability can also be due to the large errors of the individual data points.

3.5. Diameter Estimate

A rough upper limit to the diameter of 2I of $\sim$5–10 km was found using our conventional ground-based observations, typically on the order of $\sim 1''$ resolution, similar to the size upper limit estimate of $\sim$8 km from Jewitt & Luu (2019). Coma-subtraction techniques that remove the dust component from the total effective cross section of the comet (i.e., Fernández et al. 2013; Bauer et al. 2017) proved to be only partially effective due to the density of the coma at the resolution afforded by ground-based observations.

A more accurate upper limit can be inferred by measuring the effective cross section using high-resolution data from high-resolution ground-based AO and space-based observations from Keck (e.g., Marchis et al. 2006). Using a $0\farcs48$ aperture with a contiguous median sky-subtraction annulus from $0\farcs48$ to $0\farcs96$, we obtain $Kp = 19.63 \pm 0.09$. We use our visible and NIR colors determined for 2I to transform the K_p magnitude measured in the OSIRIS images taken on 2019 October 4 UTC to $V = 21.95 \pm 0.16$ from our combined VisNIR photometry and IRTF spectrum presented in Sections 3.1 and 3.2. We use the V magnitude to calculate $H_{\mathrm{abs}} = 16.88 \pm 0.16$ using Equation (1) with the $r_h = 2.48$ au, $\Delta = 2.96$ au, and $\alpha = 18\fdg65$ that the comet had on 2019 October 4 UTC. As mentioned in Section 3.4, the uncertainty on the H_{abs} calculation is a lower limit due to the unknown phase function of the comet.

We converted the H_{abs} magnitude determined with the $0\farcs48$ aperture into an effective cross section using Equation (2), resulting in an effective cross section of $2.65 \pm 0.39\,\mathrm{km}^2$, assuming an albedo equal to 0.1, typical for comet dust, and resulting in a value of $6.63 \pm 0.97\,\mathrm{km}^2$, assuming an albedo equal to 0.04, typical for comet nuclei (Fernández et al. 2001; Bauer et al. 2017). A higher albedo could also be used to calculate the cross section corresponding to an icy, more reflective composition (Yang et al. 2009), but the NIR spectra presented here, as well as additional NIR spectra (Yang et al. 2019), do not show strong evidence for the presence of ice in the coma of 2I.

Using the equation $D = 2\sqrt{C/\pi}$ to calculate the diameter from C, we obtain the values 1.84 ± 0.13 and 2.90 ± 0.21 km for $pv = 0.1$ and 0.04, respectively, implying a mass of $\lesssim 10^{12}$ kg, assuming a comet nucleus density of $400\,\mathrm{kg\,m}^{-3}$ (e.g., Pätzold et al. 2016). In addition to the advantages of using higher-resolution AO imaging compared to conventional ground-based observations, observing comets in longer wavelengths such as the K_p band has the advantage of avoiding much of the scattered light from micron-sized dust that is more prevalent in visible wavelengths. This effect of using less dust-contaminated wavelengths in the photometry of comets has already been demonstrated to produce robust diameter estimates of comets, even at spatial resolutions approaching or worse than in the K_p AO images presented here (Fernández et al. 2013; Bauer et al. 2017).

We caution that the estimates of the nucleus size are strictly rough upper limits (Bolin 2020). Profiles through the imagery, especially the high spatial resolution Keck images, do not show a discernible signal due to a point-source nucleus, arguing for an object dominated in brightness by scattered light from its surrounding coma (e.g., Jewitt & Luu 2019; Kim et al. 2020) and suggesting a small (less than a few km diameter) nucleus at the 2.9 au distance at which 2I was observed by Keck.

We thus resort to estimating its nucleus size in three different ways: (1) a very optimistic method that includes all the flux detected in the central PSF, in order to determine a hard upper limit for the nucleus' size; (2) a more realistic method that involves extrapolating the run of coma brightness versus distance from the nucleus into the central PSF, allowing us to model the coma in the entire image and then remove it; and (3) a hybrid approach whereby we take the flux from method (1) and modify it for known observations of hyperactive solar system comets.

The first method yields an object with a diameter of $\sim$3 km, giving us a hard upper limit to 2I's size; it cannot be on the order of 20 km diameter or greater, as some initial estimates have stated. The second method is much more constraining, as we do not detect a nucleus residual after modeling and removing the coma (assuming a stellar PSF derived from cuts through highly trailed stars perpendicular to the trailing direction). Adopting a 2σ upper limit from the noise level of the coma removal ($\sim$10% of the central PSF flux), we find an upper limit to the 2I diameter of $\sim$1.4 km, similar to the prediction of 2I's size by the thermal model presented in Fitzsimmons et al. (2019). The third method takes note of the fact that a small 2I nucleus size implies a very high outgassing rate per unit km^2 of nucleus surface area, a phenomenon seen for "hyperactive" solar system comets like 103P Hartley 2 (Lisse et al. 2009; A'Hearn et al. 2011; Harker et al. 2018) and 46P/Wirtannen (Lis et al. 2019) to be due to large amounts of ice-rich dust expulsion into the surrounding coma, greatly increasing the active surface area receiving solar insolation. Using the ratio of $\sim$4:1 coma:nucleus surface brightness seen for comet 103P during the Deep Impact mission in situ flyby, we can scale the total flux in the central PSF by a factor of $1/(1+4) = 0.2$ and then proceed as if we have measured the nucleus's flux. Doing so, we arrive again at an estimated nucleus diameter upper limit of ∼1.4 km, similar to nucleus measurements from high-resolution space-based observations (Jewitt et al. 2020).

4. Discussion and Conclusions

The second ISO, 2I, seems on all accounts like an ordinary comet compared to the comets of the solar system, though it is depleted in some chemical species relative to solar system comets (Kareta et al. 2020; Opitom et al. 2019; Bannister et al. 2020) and has an excess of CO (Bodewits et al. 2020; Cordiner et al. 2020). If it were not for its significantly hyperbolic orbit, 2I probably would not have warranted an in-depth scientific investigation. However, given its special status as a comet of extrasolar origin, it presents a unique opportunity to study the cometary components of other star systems, since a likely outcome of the evolution of planetary systems is the ejection of many cometary bodies (Raymond et al. 2018a, 2018b). In our own solar system, the comet population is a record of its formation properties and evolution (Morbidelli & Nesvorny 2020), so by studying objects that were ejected from their home systems, like 1I and 2I, we can directly observe the consequences of planetary system evolution.

One of the salient properties of 2I is that it contains significant amounts of volatiles such as CN and C_2 gas (Fitzsimmons et al. 2019; Kareta et al. 2020; Opitom et al. 2019), and there is evidence in this work from the photometry presented in Section 3.3 that the comet also contains H_2O, unlike the super-rich CO/N2/CH4, H_2O-depleted comet C/2016 R2 (Cochran & McKay 2018; McKay et al. 2020). Instead, it is acting like an Oort cloud comet on a megayear-period orbit like C/1995 O1 (Hale–Bopp), C/2013 S1 (ISON), or C/2017 K2 (Jewitt et al. 2017a; Meech et al. 2017), which commonly demonstrate outgassing abundances of CO with respect to water in the 0.2%–20% range (Bockelée-Morvan et al. 2004). The presence of moderately abundant CO and H_2O on 2I (Ye et al. 2020 and this work) suggests that while 2I has not been heated so thoroughly by its home Sun (as solar system Jupiter family comets and likely 1I have), it could have been ejected from its home system or placed into its star's equivalent of the solar system's Oort cloud more than a few Myr of its formation after its home system's protoplanetary disk midplane had cleared enough to heat its surface above 30 K (Lisse et al. 2019). This assumes that in comparison with the solar system comet C/2016 R2, has never been heated above 20K before encountering the Sun, where it is in the process of losing its hypervolatiles but not its H_2O ice due to hypervolatile supercooling (Biver et al. 2018; Lisse et al. 2019). Additionally, the host star of 2I may have a higher stellar iron abundance that has been shown to have an effect on the water-ice fraction solid building blocks in the protoplanetary disk favoring a higher concentration of CO/CO_2 relative to water ice (Bitsch & Battistini 2020).

Compared to 2I, 1I had only marginal levels of activity. The activity of 1I was not seen in direct imaging of the comet or in its spectra (Meech et al. 2017; Fitzsimmons et al. 2018), only being evident via detailed astrometry of the small trajectory deviations from inertial-solar gravitation caused by low levels of outgassing (Micheli et al. 2018). So, if it was actively outgassing, its coma was very faint and below the noise level in any of the detection images, including imaging from HST. One explanation for the lack of activity of 1I is that it had a mantle built up by cosmic-ray bombardment during its interstellar travel, trapping its volatiles inside its structure (Fitzsimmons et al. 2018). On the other hand, the specific outgassing rate per unit body surface area implied by the nongravitational force model of Micheli et al. (2018) is on the upper bound of Jupiter family comet activity (Fernández et al. 2013). With an ∼250 m diameter (Meech et al. 2017; Trilling et al. 2018), 1I was small compared to the typical km scale for a JFC comet, so it took very little force from outgassing to significantly accelerate it.

The activity of 2I can possibly be used to distinguish between the "large" or "small" size estimates for 2I discussed in Section 3.5, especially in comparison to 1I, by constraining the effect of nongravitational forces due to outgassing on its orbital trajectory. Moderate nongravitational force parameters have been measured for the orbit of 2I in prediscovery data when the comet's activity was weaker (Ye et al. 2020), as has been done for solar system comets (e.g., Moreno et al. 2017). If 2I has a similar size as 1I, then its small total volume and mass mean that it could also be accelerated much more by nongravitationally outgassing jet forces compared to 1I, given the apparent much larger outgassing rate for 2I than 1I. However, if 2I is much larger than 1I where the mass ratio between 2I and 1I scales as $(3\,\mathrm{km}/0.25\,\mathrm{km})^3$, ∼1000 times more massive than 1I, then 2I can be outgassing ∼1000 times more than 1I and still suffer the same amount of jet acceleration. Thus, monitoring the astrometric position of 2I throughout the next few months will be critical for understanding the size regime of 2I's nucleus as its activity grows and its orbit can be potentially more affected by nongravitational forces.

Other estimates of size distribution for the ISO population have included upper limits on both the nondetection of ISOs (Engelhardt et al. 2017) and the sole detection of 1I (Trilling et al. 2017; Raymond et al. 2018b). We estimate the size distribution of the ISO population updated with the detection of 2I and the upper limit on its diameter from high-resolution images. We calculate the number of 250 m ISOs to be ∼13 objects within 3 au of the Sun by scaling the density of 250 m ISOs, ∼one ISO within 1 au of the Sun at any given time (Meech et al. 2017), to a sphere of radius 3 au, accounting for the gravitational focusing of the Sun and assuming a velocity at infinity of 32 km s^{-1} for ISOs as for comet 2I. Assuming a slightly lower velocity at infinity of 26 m s^{-1} as for 1I does not significantly change the results.

We calculate the relative number of 250 m diameter ISOs like 1I to 1.4 km ISOs like 2I by the fraction of time 2I was observable within 3 au over the total survey lifetime of the past 15 yr. We consider 15 yr to be the amount of time that the search for objects like 2I by amateur astronomers was active due to the difficulty in obtaining sensitive CCD cameras at the consumer level before this time (Copandean et al. 2017). This translates into 13 ± 13 ISOs with a diameter of ∼250 m to $\sim 4 \times 10^{-2} \pm 4 \times 10^{-2}$ ISOs with a diameter of ∼2–3 km within 3 au of the Sun, where the uncertainties are estimated from the allowable range in number of 1I-like and 2I-like objects assuming Poissonian statistics. The resulting cumulative size distribution inferred from the ratio of the number of 250 m objects to 1.5–3 km objects is shown in Figure 7. The slope of the cumulative size distribution is $\sim -3.38 \pm 1.18$, which is comparable to the cumulative size distribution slope of collisionally evolved solar system bodies (Dohnanyi 1969) and

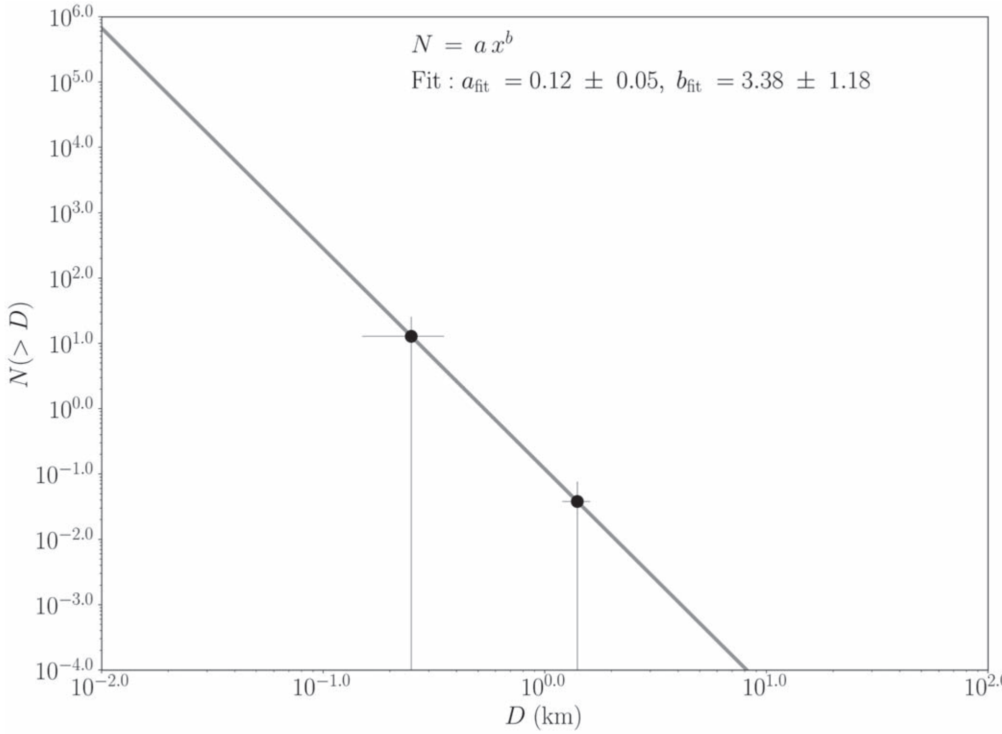

Figure 7. Size distribution of ISOs within 3 au of the Sun estimated from the detection of 1I with $D \simeq 250$ m and 2I with $D \sim 1.4$ km. The number of ISOs in the size range of 1I is estimated to be ~340 from the rate of occurrence of 1I-sized objects. The solid gray line is fit to data with the function $y = ax^b$ and is based on the estimated size of 1I from the literature and the average of the upper limits on the diameter of 2I assuming 0.04 and 0.1 albedo. The error bars on the numbers of 1I and 2I objects are estimated to be $\sim 10^{-2}$ and $\sqrt{13}$, respectively. The errors on the parameters are determined within the allowable range by the errors on the diameter of 1I and 2I (Trilling et al. 2018, this work) and the number of 1I-like and 2I-like objects assuming Poissonian statistics.

comets measured in the kilometer diameter range (Meech & Svoren 2004; Fernández et al. 2013; Boe et al. 2019a).

The size estimates we have derived for 2I above bear on the question of why "asteroidal" object 1I/Oumuamua was detected before an active, bright object like cometary 2I. Cognizant of the dangers of extrapolating size distributions and population statistics from a sample of $N = 2$ purportedly related objects, we do so here because these arguments will likely be valuable in the fullness of time as we collect more and more detections of ISOs over the next decades. Naively, one would have expected active, ~3 mag brighter 2I-like objects to have been detected first modulo selection effects (e.g., Jedicke et al. 2016; Vokrouhlický et al. 2017) because they can be seen out to much farther distances (the detectability distance scales as the object's D, so the volume of space it can be detected in goes as the objects D^2). If 2I is substantially bigger than 1I, then for a steep enough ISO size distribution (slope steeper than -3), there can be many more 1Is in the volume of space than 2I-like objects, enough so that 1I-like objects will be seen more frequently. For a size distribution scaling with $\sim D^{-3}$ and $D_{1\rm I} \simeq 250$ m, $D_{2\rm I} \simeq 2.0$ km, there would be several hundred 1I-like objects for every one 2I in a given volume of space, overwhelming the 100 times larger volume that a 2 km diameter 2I-like object could be detected in.

Recent evidence suggests that the slope of active comets goes from steeper to shallower at a transition boundary of $D \sim 3$ km (see Figure 5 of Boe et al. 2019a). In the $D \lesssim 3$ range, the cumulative size distribution slope is significantly shallower than objects $\gtrsim 3$ km in size, which seems to contradict the slope of the size distribution that we measure for the ISOs. However, work in preparation on the size distribution of inactive comets in the subkilometer range shows a steeper size distribution than compared to subkilometer active comets and more closely resembles the slope of the ISO size distribution from this work (Boe et al. 2019b). Assuming that the properties of the size distributions of active and inactive comets in the solar system are shared with those in extrasolar systems, 1I may be a representative of the inactive comet population, given its lack of activity, and may come from a population with a steep size distribution, explaining its small size. In addition, a steeper size distribution for ISOs may indicate more ISOs being on retrograde orbits as they pass through the Solar System (Marčeta & Novaković 2020). The observed activity of 2I suggests that it comes from an active comet population that has a shallower size distribution which would be consistent with 2I having a larger size than 1I. Alternatively, if 2I actually has a size comparable to 1I, its apparent activity might indicate that it comes from a shallower size distribution compared to the size distribution of inactive objects. Thus, the relative numbers of active and inactive objects from correspondingly shallower and steeper size distributions may explain the relative frequency of inactive objects like 1I compared to inactive objects.

The ISO size distribution that we are observing may be a hybrid of both active and inactive comet populations from the ensemble of comet-ejecting extrasolar systems producing a mixed active and inactive observed ISO population resulting in a size distribution slope steeper than ~ -3. Although the error bars from our measurement of the ISO size distribution slope from the occurrence of 1I and 2I are large, future observations of ISOs could refine the measurement of the slope. A shallower slope would be more consistent with production from a population in collisional equilibrium (e.g., Dohnanyi 1969), while a steeper slope may indicate that the ISO population is fed partially by additional fragmentation events, such as tidal disruption (Bolin et al. 2018; Raymond et al. 2018a; Zhang & Lin 2020). In any case, the existence of subkilometer interstellar comets like 1I suggests that the size distribution of objects in extrasolar Kuiper Belts, the progenitors of extrasolar comets, is not truncated at 1–2 km, challenging the claim that the size distribution of objects in the solar system's Kuiper Belt is effectively truncated at 1–2 km in diameter (Singer et al. 2019). The arrival of additional ISOs will provide further constraints on their physical properties and size distribution, enhancing our understanding of comets in extrasolar systems.

We would like to thank the anonymous reviewers for helpful comments in substantially improving the manuscript.

This work was supported by the GROWTH project, funded by the National Science Foundation under PIRE grant No. 1545949.

Our work includes observations obtained with the Apache Point Observatory 3.5 m telescope, which is owned and operated by the Astrophysical Research Consortium. We thank the Director (Nancy Chanover) and Deputy Director (Ben Williams) of the Astrophysical Research Consortium (ARC) 3.5 m telescope at Apache Point Observatory for their enthusiastic and timely support of our Director's Discretionary Time (DDT) proposals. We also thank Russet McMillan, Ted Rudyk, Candace Gray, Jack Dembicky, and the rest of the APO technical staff for their assistance in performing the observations on the same day our DDT proposals were submitted.

Based on observations obtained with the Samuel Oschin Telescope 48 inch and the 60 inch telescope at the Palomar Observatory as part of the Zwicky Transient Facility project. The ZTF is supported by the National Science Foundation under grant No. AST-1440341 and a collaboration including Caltech, IPAC, the Weizmann Institute for Science, the Oskar Klein Center at Stockholm University, the University of Maryland, the University of Washington, Deutsches Elektronen-Synchrotron and Humboldt University, Los Alamos National Laboratories, the TANGO Consortium of Taiwan, the University of Wisconsin at Milwaukee, and Lawrence Berkeley National Laboratories. Operations are conducted by COO, IPAC, and UW.

Some of the data presented herein were obtained at the W. M. Keck Observatory, which is operated as a scientific partnership among the California Institute of Technology, the University of California, and the National Aeronautics and Space Administration. The Observatory was made possible by the generous financial support of the W. M. Keck Foundation.

We thank Jim Lyke and Carlos Alvarez for guiding the planning and executing the AO observation with the OSIRIS instrument on Keck I.

C.-C.N. is thankful for the funding from MoST grant 104-2923-M-008-004-MY5.

The work of D.S. was carried out at the Jet Propulsion Laboratory, California Institute of Technology, under a contract with NASA.

SED Machine is based upon work supported by the National Science Foundation under grant No. 1106171.

This publication has made use of data collected at Lulin Observatory, partly supported by MoST grant 108-2112-M-008-001.

The results presented in this paper are based in part on observations collected with the Liverpool Telescope, which is operated on the island of La Palma by Liverpool John Moores University in the Spanish Observatorio del Roque de los Muchachos of the Instituto de Astrofisica de Canarias with financial support from the UK Science and Technology Facilities Council.

Visiting Astronomer at the Infrared Telescope Facility, which is operated by the University of Hawaii under contract NNH14CK55B with the National Aeronautics and Space Administration.

The authors wish to recognize and acknowledge the very significant cultural role and reverence that the summit of Maunakea has always had within the indigenous Hawaiian community. We are most fortunate to have the opportunity to conduct observations from this mountain.

F.M. is supported by an appointment to the NASA Postdoctoral Program at the Jet Propulsion Laboratory, administered by the Universities Space Research Association under contract with NASA.

The authors would like to thank E. Turner, B. Draine, S. Tremaine, and M. Mac-Low for many useful discussions concerning the nature and provenance of 1I and 2I. In addition, the authors would like to thank R. Jedicke and G. Helou for helpful discussion on the size distribution of comets. We would also like to thank J. Bauer and Y. Fernandez for fruitful discussion on comet nuclei.

The authors would like to thank the astrophysics masters students of the Université Côte d'Azur who recorded the data taken by the C2PU telescope at Observatoire de la Côte d'Azur, Calern observing site.

Facilities: Astrophysical Research Consortium 3.5 m, C2PU Omicron telescope, Bisei Observatory 101 cm, Lulin Optical Telescope, Keck:I (LRIS, OSIRIS), Liverpool Telescope, Mount Laguna Observatory 40 inch, NASA/Infrared Telescope Facility, Zwicky Transient Facility, SED Machine.

ORCID iDs

Bryce T. Bolin https://orcid.org/0000-0002-4950-6323
Carey M. Lisse https://orcid.org/0000-0002-9548-1526
Mansi M. Kasliwal https://orcid.org/0000-0002-5619-4938
Robert Quimby https://orcid.org/0000-0001-9171-5236
Chris M. Copperwheat https://orcid.org/0000-0001-7983-8698
Kevin B. Burdge https://orcid.org/0000-0002-7226-836X
Michael Coughlin https://orcid.org/0000-0002-8262-2924
Christoffer Fremling https://orcid.org/0000-0002-4223-103X
Ryosuke Itoh https://orcid.org/0000-0002-1183-8955
Michael Koss https://orcid.org/0000-0002-7998-9581
Frank J. Masci https://orcid.org/0000-0002-8532-9395
Eric E. Mamajek https://orcid.org/0000-0003-2008-1488
Federico Marocco https://orcid.org/0000-0001-7519-1700
Michael L. Sitko https://orcid.org/0000-0003-1799-1755
Daniel Stern https://orcid.org/0000-0003-2686-9241
Lin Yan https://orcid.org/0000-0003-1710-9339
Igor Andreoni https://orcid.org/0000-0002-8977-1498
Varun Bhalerao https://orcid.org/0000-0002-6112-7609
Dennis Bodewits https://orcid.org/0000-0002-2668-7248

Eric C. Bellm https://orcid.org/0000-0001-8018-5348
Nadejda Blagorodnova https://orcid.org/0000-0003-0901-1606
Derek Buzasi https://orcid.org/0000-0002-1988-143X
S. Bradley Cenko https://orcid.org/0000-0003-1673-970X
Chan-Kao Chang https://orcid.org/0000-0003-1656-4540
Dmitry A. Duev https://orcid.org/0000-0001-5060-8733
Shrinivas R. Kulkarni https://orcid.org/0000-0001-5390-8563
Thomas Kupfer https://orcid.org/0000-0002-6540-1484
Chow-Choong Ngeow https://orcid.org/0000-0001-8771-7554
Reed Riddle https://orcid.org/0000-0002-0387-370X
Jesper Sollerman https://orcid.org/0000-0003-1546-6615
Maayane T. Soumagnac https://orcid.org/0000-0001-6753-1488

References

A'Hearn, M. F., Belton, M. J. S., Delamere, W. A., et al. 2011, Sci, 332, 1396
A'Hearn, M. F., Millis, R. C., Schleicher, D. O., Osip, D. J., & Birch, P. V. 1995, Icar, 118, 223
A'Hearn, M. F., Schleicher, D. G., Millis, R. L., Feldman, P. D., & Thompson, D. T. 1984, AJ, 89, 579
Bannister, M. T., Opitom, C., Fitzsimmons, A., et al. 2020, arXiv:2001.11605
Bannister, M. T., Schwamb, M. E., Fraser, W. C., et al. 2017, ApJL, 851, L38
Bauer, J. M., Grav, T., Fernández, Y. R., et al. 2017, AJ, 154, 53
Bellm, E. C., Kulkarni, S. R., Barlow, T., et al. 2019a, PASP, 131, 068003
Bellm, E. C., Kulkarni, S. R., Graham, M. J., et al. 2019b, PASP, 131, 018002
Bertini, I., la Forgia, F., Tubiana, C., et al. 2017, MNRAS, 469, S404
Bitsch, B., & Battistini, C. 2020, A&A, 633, A10
Biver, N., Bockelée-Morvan, D., Paubert, G., et al. 2018, A&A, 619, A127
Blagorodnova, N., Neill, J. D., Walters, R., et al. 2018, PASP, 130, 035003
Bockelée-Morvan, D., Crovisier, J., Mumma, M. J., & Weaver, H. A. 2004, in Comets II, ed. M. C. Festou, H. U. Keller, & H. A. Weaver (Tucson, AZ: Univ. Arizona Press), 391
Bockelée-Morvan, D., Rinaldi, G., Erard, S., et al. 2017, MNRAS, 469, S443
Bodewits, D., Noonan, J. W., Feldman, P. D., et al. 2020, NatAs, in press
Boe, B., Jedicke, R., Meech, K. J., et al. 2019a, Icar, 333, 252
Boe, B., Jedicke, R., Wiegert, P., et al. 2019b, EPSC-DPS Joint Meeting, 2019, EPSC-DPS2019-626
Bolin, B. T. 2020, arXiv:1912.07386
Bolin, B. T., Weaver, H. A., Fernandez, Y. R., et al. 2018, ApJL, 852, L2
Bus, S. J., & Binzel, R. P. 2002, Icar, 158, 146
Chambers, K. C., Magnier, E. A., Metcalfe, N., et al. 2016, arXiv:1612.05560
Chen, C. H., Sargent, B. A., Bohac, C., et al. 2006, ApJS, 166, 351
Cochran, A. L., & McKay, A. J. 2018, ApJL, 854, L10
Copandean, D., Vaduvescu, O., & Gorgan, D. 2017, in 13th IEEE Int. Conf. Intelligent Computer Communication and Processing, ed. R. Potolea & R. Razvan Slavescu (Piscataway, NJ: IEEE), 377
Cordiner, M. A., Milam, S. N., Biver, N., et al. 2020, NatAs, in press
de León, J., Licandro, J., Serra-Ricart, M., et al. 2019, RNAAS, 3, 131
DeMeo, F. E., Binzel, R. P., Slivan, S. M., & Bus, S. J. 2009, Icar, 202, 160
DeMeo, F. E., & Carry, B. 2013, Icar, 226, 723
Dohnanyi, J. S. 1969, JGR, 74, 2531
Engelhardt, T., Jedicke, R., Vereš, P., et al. 2017, AJ, 153, 133
Feldman, P. D., Cochran, A. L., & Combi, M. R. 2004, in Comets II, ed. M. C. Festou, H. U. Keller, & H. A. Weaver (Tucson, AZ: Univ. Arizona Press), 425
Fernández, Y. R., Jewitt, D. C., & Sheppard, S. S. 2001, ApJL, 553, L197
Fernández, Y. R., Kelley, M. S., Lamy, P. L., et al. 2013, Icar, 226, 1138
Fink, U., & Rubin, M. 2012, Icar, 221, 721
Fitzsimmons, A., Hainaut, O., Meech, K. J., et al. 2019, ApJL, 885, L9
Fitzsimmons, A., Snodgrass, C., Rozitis, B., et al. 2018, NatAs, 2, 133
Flewelling, H. A., Magnier, E. A., Chambers, K. C., et al. 2016, arXiv:1612.05243
Graham, M. J., Kulkarni, S. R., Bellm, E. C., et al. 2019, PASP, 131, 078001
Hanuš, J., Delbo, M., Alí-Lagoa, V., et al. 2018, Icar, 299, 84
Harker, D. E., Woodward, C. E., Kelley, M. S. P., & Wooden, D. H. 2018, AJ, 155, 199
Huehnerhoff, J., Ketzeback, W., Bradley, A., et al. 2016, Proc. SPIE, 9908, 99085H
Hughes, D. W. 1990, QJRAS, 31, 69
Hui, M.-T., Ye, Q.-Z., Föhring, D., Hung, D., & Tholen, D. J. 2020, arXiv:2003.14064
Ivezić, Ž., Lupton, R. H., Jurić, M., et al. 2002, AJ, 124, 2943
Ivezić, Ž., Tabachnik, S., Rafikov, R., et al. 2001, AJ, 122, 2749
Jedicke, R., Bolin, B., Granvik, M., & Beshore, E. 2016, Icar, 266, 173
Jewitt, D. 1991, in IAU Coll. 116: Comets in the post-Halley Era 167, Astrophysics and Space Science Library, ed. R. L. Newburn, Jr., M. Neugebauer, & J. Rahe, 19
Jewitt, D., Hsieh, H., & Agarwal, J. 2015, in Asteroids IV, ed. P. Michel, F. E. DeMeo, & W. F. Bottke (Tucson, AZ: Univ. Arizona Press), 221
Jewitt, D., Hui, M.-T., Kim, Y., et al. 2020, ApJL, 888, L23
Jewitt, D., Hui, M.-T., Mutchler, M., et al. 2017a, ApJL, 847, L19
Jewitt, D., & Luu, J. 2019, ApJL, 886, L29
Jewitt, D., Luu, J., Rajagopal, J., et al. 2017b, ApJL, 850, L36
Jewitt, D., & Meech, K. J. 1986, ApJ, 310, 937
Jewitt, D., Mutchler, M., Weaver, H., et al. 2016, ApJL, 829, L8
Jordi, K., Grebel, E. K., & Ammon, K. 2006, A&A, 460, 339
Jurić, M., Ivezić, Ž., Lupton, R. H., et al. 2002, AJ, 124, 1776
Kareta, T., Andrews, J., Noonan, J. W., et al. 2020, ApJL, 889, L38
Kasliwal, M. M., Cannella, C., Bagdasaryan, A., et al. 2019, PASP, 131, 038003
Keller, H. U., Mottola, S., Hviid, S. F., et al. 2017, MNRAS, 469, S357
Kelley, M. S., Fernández, Y. R., Licandro, J., et al. 2013, Icar, 225, 475
Kim, Y., Jewitt, D., Mutchler, M., et al. 2020, ApJL, 895, L34
Kinoshita, D., Chen, C.-W., Lin, H.-C., et al. 2005, ChJAA, 5, 315
Kolokolova, L., Hanner, M. S., Levasseur-Regourd, A.-C., & Gustafson, B. Å S. 2004, in Comets II, ed. M. C. Festou, H. U. Keller, & H. A. Weaver (Tucson, AZ: Univ. Arizona Press), 577
Larkin, J., Barczys, M., Krabbe, A., et al. 2006, Proc. SPIE, 6269, 62691A
Li, J.-Y., Besse, S., A'Hearn, M. F., et al. 2013, Icar, 222, 559
Li, J.-Y., Samarasinha, N. H., Kelley, M. S. P., et al. 2016, ApJL, 817, L23
Lis, D. C., Bockelée-Morvan, D., Güsten, R., et al. 2019, A&A, 625, L5
Lisse, C. M., Fernandez, Y. R., Reach, W. T., et al. 2009, PASP, 121, 968
Lisse, C. M., Sitko, M. L., Marengo, M., et al. 2017, AJ, 154, 182
Lisse, C. M., Wyatt, M. C., Chen, C. H., et al. 2012, ApJ, 747, 93
Lisse, C. M., Young, L. A., Cruikshank, D., et al. 2019, AGU Meeting, 2019, P33I-3540
MacGregor, M. A., Weinberger, A. J., Nesvold, E. R., et al. 2019, ApJL, 877, L32
Marčeta, D., & Novaković, B. 2020, MNRAS, in press
Marchis, F., Kaasalainen, M., Hom, E. F. Y., et al. 2006, Icar, 185, 39
Masci, F. J., Laher, R. R., Rusholme, B., et al. 2019, PASP, 131, 018003
McKay, A. J., Cochran, A. L., Dello Russo, N., & DiSanti, M. 2020, ApJL, 889, L10
Meech, K. J. 2017, RSPTA, 375, 20160247
Meech, K. J., & Svoren, J. 2004, in Comets II, ed. M. C. Festou, H. U. Keller, & H. A. Weaver (Tucson, AZ: Univ. Arizona Press), 317
Meech, K. J., Weryk, R., Micheli, M., et al. 2017, Natur, 552, 378
Meng, H. Y. A., Su, K. Y. L., Rieke, G. H., et al. 2014, Sci, 345, 1032
Micheli, M., Farnocchia, D., Meech, K. J., et al. 2018, Natur, 559, 223
Morbidelli, A., & Nesvorny, D. 2020, in The Trans-Neptunian Solar System, ed. D. Prialnik, M. Antoinetta Barucci, & L. Young (Amsterdam: Elsevier)
Moreno, F., Pozuelos, F. J., Novaković, B., et al. 2017, ApJL, 837, L3
Ofek, E. O. 2012, ApJ, 749, 10
Opitom, C., Fitzsimmons, A., Jehin, E., et al. 2019, A&A, 631, L8
Paganini, L., Mumma, M. J., Villanueva, G. L., et al. 2014, ApJ, 791, 122
Pätzold, M., Andert, T., Hahn, M., et al. 2016, Natur, 530, 63
Protopapa, S., sunshine, J. M., Feaga, L. M., et al. 2014, Icar, 238, 191
Rappaport, S., Vanderburg, A., Jacobs, T., et al. 2018, MNRAS, 474, 1453
Raymond, S. N., Armitage, P. J., & Veras, D. 2018a, ApJL, 856, L7
Raymond, S. N., Armitage, P. J., Veras, D., Quintana, E. V., & Barclay, T. 2018b, MNRAS, 476, 3031
Rayner, J. T., Toomey, D. W., Onaka, P. M., et al. 2003, PASP, 115, 362
Rigault, M., Neill, J. D., Blagorodnova, N., et al. 2019, A&A, 627, A115
Schwamb, M. E., Fraser, W. C., Bannister, M. T., et al. 2019, ApJS, 243, 12
Singer, K. N., McKinnon, W. B., Gladman, B., et al. 2019, Sci, 363, 955
Skrutskie, M. F., Cutri, R. M., Stiening, R., et al. 2006, AJ, 131, 1163
Smith, C. E., & Nelson, B. 1969, PASP, 81, 74
Snodgrass, C., Agarwal, J., Combi, M., et al. 2017, A&ARv, 25, 5
Solontoi, M., Ivezić, Ž., Jurić, M., et al. 2012, Icar, 218, 571
Steele, I. A., Smith, R. J., Rees, P. C. T., et al. 2004, Proc. SPIE, 5489, 679
Su, K. Y. L., Jackson, A. P., Gáspár, A., et al. 2019, AJ, 157, 202
Tonry, J. L., Stubbs, C. W., Lykke, K. R., et al. 2012, ApJ, 750, 99
Trilling, D. E., Mommert, M., Hora, J. L., et al. 2018, AJ, 156, 261
Trilling, D. E., Robinson, T., Roegge, A., et al. 2017, ApJL, 850, L38

Vincent, M. B., Morse, J. A., Beland, S., et al. 2003, Proc. SPIE, 4841, 367
Vokrouhlický, D., Pravec, P., Durech, J., et al. 2017, A&A, 598, A91
Williams, G. V. 2017, MPEC, U183
Williams, G. V. 2019a, MPEC, R106
Williams, G. V. 2019b, MPEC, S09
Williams, G. V. 2019c, MPEC, S25
Womack, M., Sarid, G., & Wierzchos, K. 2017, PASP, 129, 031001
Yang, B., Jewitt, D., & Bus, S. J. 2009, AJ, 137, 4538
Yang, B., Keane, J., Kelley, M., Protopapa, S., & Meech, K. J. 2019, CBET, 4672
Ye, Q., Kelley, M. S. P., Bolin, B. T., et al. 2020, AJ, 159, 77
Zhang, Y., & Lin, D. N. C. 2020, NatAs, in press

The Astronomical Journal, 160:73 (18pp), 2020 August https://doi.org/10.3847/1538-3881/ab9a32

The Asteroid Rotation Period Survey Using the China Near-Earth Object Survey Telescope (CNEOST)

Ting-Shuo Yeh[1], Bin Li[2,3], Chan-Kao Chang[1], Hai-Bin Zhao[2,4,5], Jiang-Hui Ji[2,4], Zhong-Yi Lin[1], and Wing-Huen Ip[1,6,7]
[1] Institute of Astronomy, National Central University, Zhongli, Taiwan; tsyeh@astro.ncu.edu.tw, rex@astro.ncu.edu.tw
[2] CAS Key Laboratory of Planetary Sciences, Purple Mountain Observatory, Chinese Academy of Sciences, Nanjing 210008, People's Republic of China
[3] University of Science and Technology of China, Hefei 230026, People's Republic of China
[4] CAS Center for Excellence in Comparative Planetology, Hefei, People's Republic of China
[5] CAS Key Laboratory of Infrared System Detection and Imaging Technology, Shanghai Institute of Technical Physics, Chinese Academy of Sciences, People's Republic of China
[6] Institute of Space Science, National Central University, Zhongli, Taiwan
[7] Space Science Institute, Macau University of Science and Technology, Macau MSAR
Received 2019 June 25; revised 2020 May 18; accepted 2020 May 31; published 2020 July 23

Abstract

We initiated the bilateral collaboration between the Lulin Observatory and the Purple Mountain Observatory to collect asteroid lightcurves using the Chinese Near-Earth Object Survey Telescope at the Xuyi Observation Station. The primary goal of this collaboration was to discover super-fast rotators (SFRs) and study their physical properties. Two campaigns have been conducted: (a) a survey of $\sim$45 deg^2 using 8 minute cadence during 2017 February 26–March 2, and (b) a survey of $\sim$60 deg^2 using 10 minute cadence during 2018 March 9–12. Our samples are mainly main-belt asteroids and some Hildas and Jupiter Trojans. Out of 4522 collected lightcurves, 506 reliable rotation periods were obtained. Among the reliable rotation periods, we found 16 candidates with a possible rotation period of <2.2 hr, in which (134291) 2006 DZ6 shows a very convincing folded lightcurve and the other 15 candidates only have a likely trend. Further confirmation is needed for the rotation periods of these SFR candidates. In addition, (2280) Kunikov seems to have an eclipsing feature on its lightcurve with a relatively long rotation period suggesting that it is likely a fully synchronized binary asteroid. When the preliminary spin-rate distributions were carried out for asteroids using different sizes, no obvious difference was found.

Unified Astronomy Thesaurus concepts: Asteroids (72); Period determination (1211)

Supporting material: extended figures, machine-readable tables

1. Introduction

Several important physical properties of an asteroid can be derived from its lightcurve. For example, the rotation period can be measured from lightcurves (Harris et al. 1989), the general shape can be estimated from the lightcurve amplitude (Pravec & Harris 2000; Lacerda & Luu 2003), the detailed shape model can be obtained from lightcurve inversion (Kaasalainen et al. 1992a, 1992b), and the albedo can be roughly inferred from the phase–curve relation (Bowell et al. 1989, and reference therein). Moreover, the statistics for the asteroid spin rate and pole orientation are also important to understand how the rotational state was affected by various mechanisms. As shown by Warner et al. (2009), the spin-rate distribution of asteroids with diameters larger than $\sim$10 km have a Maxwellian distribution and smaller ones have a non-Maxwellian form. This suggests that larger asteroids could be in a collisional equilibrium (Salo 1987) and smaller ones are probably dominated by the Yarkovsky–O'Keefe–Radzievskii–Paddack (YORP) effect, which disperses the spin-rate distribution from Maxwellian (Rubincam 2000). Indeed, the YORP effect works more efficiently on small asteroids (McNeill et al. 2016, and the references therein) and, therefore, some variation should be expected in the spin-rate distributions of asteroids of different sizes and locations.

Another important application using asteroid rotation periods is for the study of their interior structures through an overall spin-rate limit. Harris (1996) and Pravec et al. (2002) pointed out a 2.2 hr spin-rate limit for asteroids of $D > 150$ m, which suggests that asteroids with diameters of few hundred meters or larger have a rubble-pile structure (i.e., gravitationally bounded aggregations). Under the assumption of a rubble-pile structure, the 2.2 hr spin-rate limit is set by the equilibrium between the self-gravity and the centrifugal force from the spinning and, therefore, an upper limit on the bulk density of $\sim$3 g cm^{-3} was estimated for the asteroids (Harris 1996). However, a special kind of asteroid, called a large super-fast rotator (SFR; i.e., asteroids in a size of a couple hundred meters or larger and with a rotation period shorter than $\sim$2 hr), was first found by Pravec et al. (2002), which if considered to be a rubble-pile (strengthless) structure would require an unreasonably high bulk density. Therefore, cohesion was suggested to be present inside these asteroids to allow super-fast rotation without disruption (Holsapple 2007). In the past few years, more than two dozens of large SFRs were discovered using wide-field surveys (Chang et al. 2014, 2016, 2017, 2019; Lo et al. 2020). Except for the super-fast spinning and a likely trend that smaller asteroids possibly harbor have more SFRs (Lo et al. 2020), no common property was found in these SFRs (Chang et al. 2019). To have a better understanding for this group and also for asteroid interior structure, more large SFRs need to be identified, especially those with a diameter up to few kilometers, which place an important constraint on the cohesion value.

Along this line, we initiated a bilateral collaboration between the Lulin Observatory and the Purple Mountain Observatory (PMO) to search for SFRs. In this work, we report our first joint asteroid rotation period survey using the Chinese Near-Earth Object Survey Telescope (CNEOST), a wild-field telescope.

Table 1
Observation Information of 2017 February 27–March 2

Field No.	R.A. α (hms)	Decl. δ (°)	February 26 N_{exp}, Δt	February 27 N_{exp}, Δt	February 28 N_{exp}, Δt	March 1 N_{exp}, Δt	March 2 N_{exp}, Δt
1	10:22:31.07	+07:50:10	41, 4.9	53, 6.3	43, 4.5	43, 4.4	36, 5.3
2	10:43:13.56	+07:52:22	41, 4.9	53, 6.3	43, 4.5	43, 4.4	36, 5.3
3	10:53:42.06	+07:54:32	41, 4.9	53, 6.3	43, 4.5	43, 4.4	36, 5.3
4	10:32:54.75	+07:53:42	41, 4.9	53, 6.3	43, 4.5	43, 4.4	36, 5.3
5	10:36:51.22	+04:51:11					36, 5.3

Note. N_{exp} is the total number of exposures for each field and each night, and Δt is the observing duration each day in hours.

Table 2
Observation Information of 2018 March 8–12

Field No.	R.A. α (hms)	Decl. δ (°)	March 8 N_{exp}, Δt	March 9 N_{exp}, Δt	March 11 N_{exp}, Δt	March 12 N_{exp}, Δt
1	11:36:57.85	+08:04:16	35, 6.2	35, 6.2	28, 5.7	28, 5.7
2	11:36:53.53	+04:08:27	35, 6.2	35, 6.2	28, 5.7	28, 5.7
3	11:25:19.51	+04:05:33	35, 6.2	35, 6.2	28, 5.7	28, 5.7
4	11:13:45.04	+04:14:10	35, 6.2	35, 6.2	28, 5.7	28, 5.7
5	11:16:54.52	+06:58:12	35, 6.2	35, 6.2	28, 5.7	28, 5.7
6	11:27:59.00	+07:08:37	35, 6.2	35, 6.2	28, 5.7	28, 5.7
7	11:39:28.47	+06:51:14			28, 5.7	28, 5.7

Note. N_{exp} is the total number of exposures for each field and each night, and Δt is the observing duration each day in hours.

Details of the telescope and our observations can be found in Section 2.1, the results and discussion are given in Section 3, and the summary is shown in Section 4.

2. The Observation, Data Reduction, Lightcurve Extraction, and Rotation Period Analysis

2.1. Observation

The main goal of this cooperative project between the Lulin Observatory and the PMO is to discover SFRs. Therefore, we used the CNEOST to conduct the survey. The CNEOST is a 1.2 m telescope located at the XuYi station, which is equipped with a wide-field camera to create a field of view (FOV) $\sim 9\ \mathrm{deg}^2$. A wide-field facility, like the CNEOST, is very useful to collect hundreds of asteroid lightcurves within a short period of time. Two surveys were conducted. The first survey was carried in 2017 February 26–March 2, which covered a total survey area of $\sim 45\ \mathrm{deg}^2$ close to the ecliptic plane. We continuously scanned on four main fields in a cadence of ∼8 minutes using the R band for the first four nights and another additional field was added in the last night for the follow-up observation of near-Earth asteroids of the other proposal. The second survey was conducted in 2018 March 8, 9, 11, and 12, which had a total survey area of $\sim 60\ \mathrm{deg}^2$. In this survey, six fields were repeatedly observed in a cadence of ∼10 minutes using the I band and, moreover, an extra field was added in the last two nights to follow up other targets of another proposal. Both surveys used 90 s exposures, which had limiting magnitudes of ∼20.1 and ∼19.9 mag in the R and I bands, respectively. The field configurations and the details of the observations are summarized in Tables 1 and 2.

2.2. Data Reduction

All the images were processed with standard image reduction (i.e., bias correction, dark subtraction, and flat-field calibration). Then, we extracted all of the sources using SExtractor (Bertin & Arnouts 1996) and calibrated them against the UCAC4 (Zacharias et al. 2013).

To extract asteroid lightcurves, we used the orbital elements obtained from the Minor Planet Center (hereafter MPC[8]) to calculate the ephemerides of known asteroids of our observing epoches and then matched the detections in the source catalogs with the ephemerides using a radius of 2″. In the end, there were 1650 and 2872 lightcurves obtained from each of the two surveys.

2.3. Rotation Period Analysis

To derive the rotation periods, we correct the light-travel time for each data point and fit the lightcurves with a second-order Fourier series (Harris et al. 1989),

$$M_{i,j} = \sum_{k=1,2}^{N_k} B_k \sin\left[\frac{2\pi k}{P}(t_j - t_0)\right] + C_k \cos\left[\frac{2\pi k}{P}(t_j - t_0)\right] + Z_i, \quad (1)$$

where $M_{i,j}$ is the R-band or I-band magnitude measured at the epoch of t_j; B_k and C_k are the Fourier coefficients; P is the rotation period; t_0 is an arbitrary epoch; and Z_i is the offset of the measurements taken in different nights.

The derived rotation periods were then visually reviewed and assigned a quality code "U" according to the criteria of the the Lightcurve Database (LCDB),[9] where $U = 3$, 2, and 1 means highly reliable, some ambiguity, and low reliability, respectively. Figure 1 shows the lightcurve examples of different quality codes. The amplitude was estimated from the peak-to-peak difference of the lightcurve after rejecting the upper and lower 5% outliers which are probably contaminated by nearby sources or artifacts.

[8] ⟨https://www.minorplanetcenter.net⟩

[9] The LCDB (Warner et al. 2009); http://www.minorplanet.info/lightcurvedatabase.html.

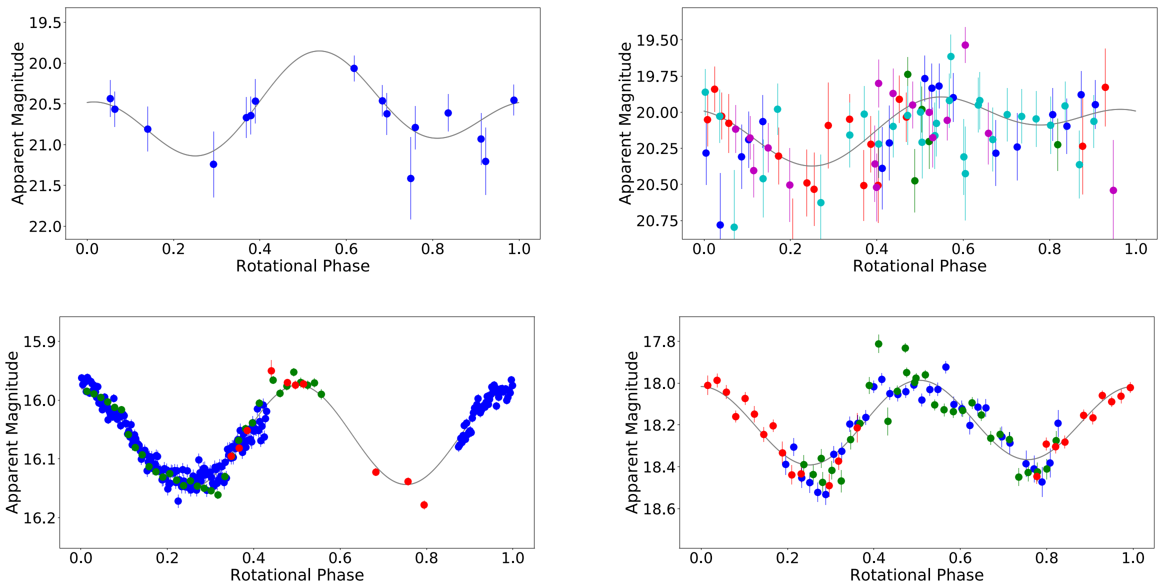

Figure 1. Example lightcurves of different quality codes. From upper-left to lower-right no periods are detected and $U = 1$, 2, and 3, respectively. The colors represent data points obtained from different dates and the gray line is the fitting result.

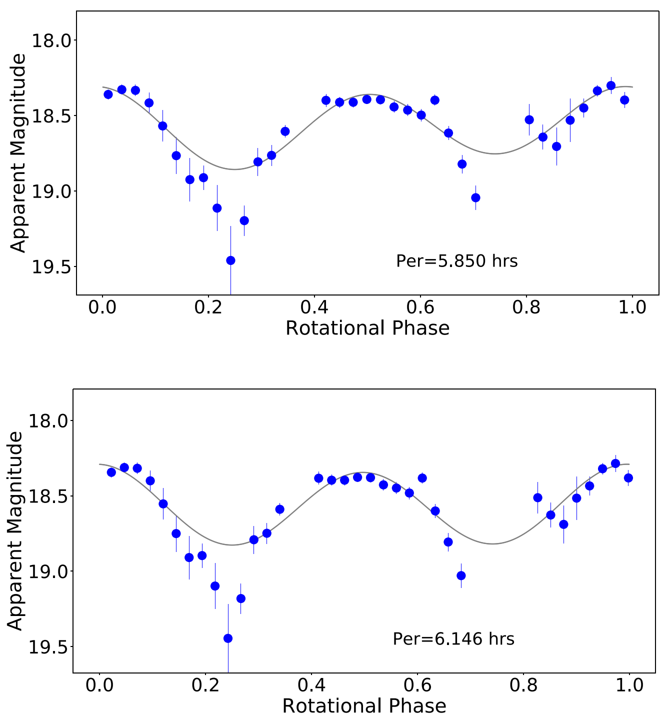

Figure 2. Lightcurve of asteroid (12614) Hokusai folded to 5.85 hr (top) and 6.146 hr (bottom).

We estimated the diameters of asteroids using

$$\log D = 0.2 m_{\odot} + \log 2 r_{\oplus} - 0.5 \log p - 0.2 H_x, \qquad (2)$$

where $m_{\odot}$ is the apparent magnitude of the Sun, $2r_{\oplus}$ the heliocentric distance of Earth in the same unit as D, p is the geometric albedo, and H_x is the absolute magnitude in the observed filter band (i.e., R or I band). We adopted $m_{\odot} = -27.15$ in the R band and -27.47 in the I band from Willmer (2018) and used three empirical albedo values, $p = 0.20$, 0.08, and 0.04, for the asteroids in the inner ($2.1 < a < 2.5$ au), mid ($2.5 < a < 2.8$ au), and outer ($a > 2.8$ au) main belt, respectively (Tedesco et al. 2005).[10] Moreover, the absolute magnitudes in the observed filter band were estimated simply by applying a slope of 0.15 in the $H - G$ system (Bowell et al. 1989).

Table 3
Comparison of the Rotation Period for the 13 Objects Listed in the LCDB with $U \geqslant 2+$

Object	Quality	LCDB Period (hr)	Derived Period (hr)
(62) Erato	3	9.22	9.23 ± 0.04
(1492) Oppolzer	3	3.77	3.77 ± 0.01
(2216) Kerch	3	9.46	9.47 ± 0.02
(3983) Sakiko	3	10.53	10.53 ± 0.00
(4417) Lecar	3	3.18	3.00 ± 0.00
(6479) Leoconnolly	3	5.11	5.11 ± 0.01
(6709) Hiromiyuki	3	6.83	6.83 ± 0.01
(8120) Kobe	3	5.86	5.88 ± 0.03
(8479) 1987 HD2	3	2.68	2.68 ± 0.00
(61479) 2000 QH39	2	4.89	4.90 ± 0.01
(173748) 2001 RW30	2	5.30	5.30 ± 0.04
(2280) Kunikov	2	21.45	12.97 ± 0.07
(12614) Hokusai	2	5.84	6.15 ± 0.01

Note. Columns: asteroid designation, quality code of our rotation period, the LCDB rotation period, and our rotation period. The lightcurve of (2280) Kunikov and (12614) Hokusai in this work do not cover a full rotation of these two objects and introduces ambiguity in their rotation period fitting. More explanations can be found in the context.

3. Results and Discussion

In total, 506 reliable rotation periods were obtained (i.e., $U \geqslant 2$), which are listed in Tables 5 and 6. Figures 7 and 8

[10] The albedo in the R and I band could have a few percent difference from the visual band depending on asteroid colors and this would only cause a slight change in the diameter estimation.

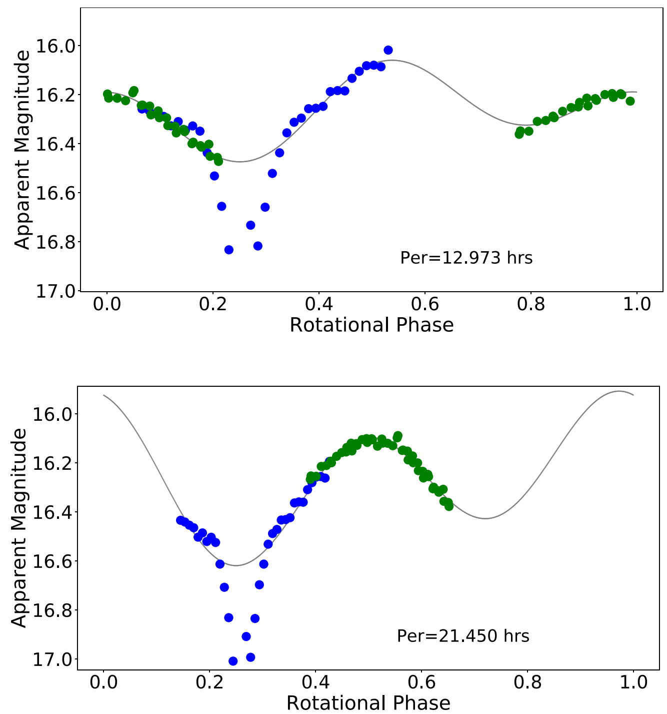

Figure 3. Lightcurve of asteroid (2280) Kunikov folded to 12.97 (top) and 21.45 hr (bottom), where both cases show a possible eclipsing feature of the binary system.

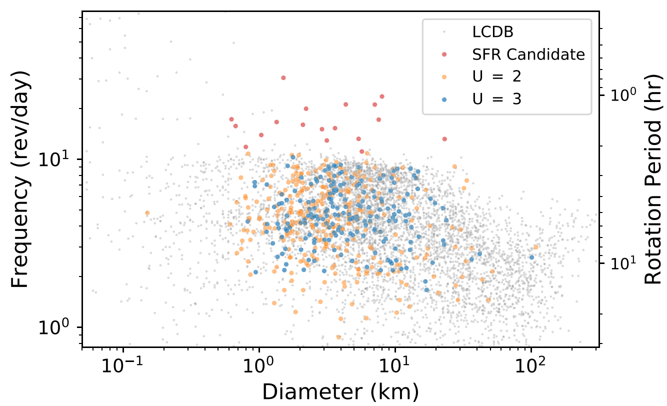

Figure 4. Plot of the asteroid diameters vs. rotation periods. The red, blue, and orange dots are the SFR candidates, $U = 3$, and $U = 2$ objects in our samples, respectively. The gray dots are the LCDB objects of $U = 3$.

show the folded lightcurves for the objects of $U = 3$ and 2, respectively. Among the 506 reliable rotation periods, 13 of them also have published rotation periods with $U \geqslant 2+$ in the LCDB. Table 3 shows the comparison of rotation period for the 13 objects. Most of the cases have consistent results, except for two cases, (2280) Kunikov and (12614) Hokusai, which show ambiguity in our period fitting and are discussed below. For (12614) Hokusai, the time coverage of our lightcurve is slightly shorter than its reported rotation period (i.e., 5.85 hr), which causes some ambiguity in the rotation period fitting. When we fold the lightcurve of (12614) Hokusai to 5.85 hr, it gives an equally good result to that of our best fit of 6.146 hr (see Figure 2). For (2280) Kunikov, the published rotation period is 21.45 hr (Linville et al. 2017), which is a relatively long rotation period and our four-night observation could not obtain a lightcurve to fully cover its entire rotation. Therefore, our measurement has a relatively large uncertainty in this fitting. Similarly, when we fold our lightcurve of (2280) Kunikov to the reported period of 21.45 hr and our best-fit value of 12.97 hr, we find that both results look equally good (see Figure 3). Considering the time coverage and completeness of the published lightcurves for (2280) Kunikov and (12614) Hokusai, the previous reported rotation periods should be more secure. The ambiguity in our rotation period fitting for (12614) Hokusai and (2280) Kunikov should be relieved when a denser lightcurve with a better time coverage is available. Therefore, we conclude that our rotation period measurements are trustworthy in general.

Figure 4 shows the plot of the diameters versus the rotation periods of our objects with reliable rotation periods on top of the

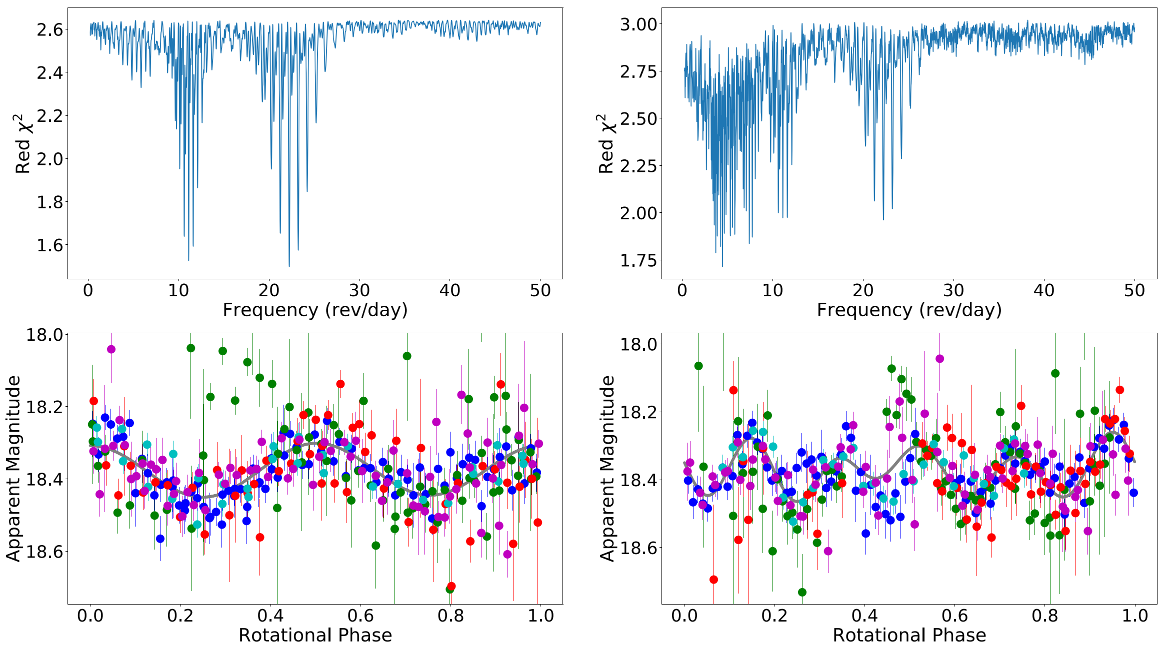

Figure 5. Periodogram (top) and folded lightcurve (bottom) of the SRF candidate, (134291) 2006 DZ6, for the fittings of second- (left) and sixth- (right) order Fourier series, respectively.

Table 4
Super-fast Rotator Candidates

Object	Diameter (km)	Period (hr)	H_x (mag)	Filter	Magnitude	Amplitude (mag)	Semimajor Axis (au)	Phase Angle (°)
(21709) Sethmurray	3.8	1.59 ± 0.00	14.49	*I*	16.45	0.05	2.26	1.6
(22512) Cannat	7.0	1.81 ± 0.00	14.14	*I*	17.28	0.08	2.53	1.4
(65768) 1995 DR6	8.5	1.39 ± 0.00	14.47	*R*	19.69	0.28	3.14	0.8
(94734) 2001 XM70	2.0	0.79 ± 0.00	15.91	*I*	18.66	0.12	2.45	1.3
(134291) 2006 DZ6	6.4	2.16 ± 0.00	15.09	*R*	18.36	0.15	3.15	1.0
(144459) 2004 EW43	10.4	1.01 ± 0.00	14.03	*I*	19.86	0.62	3.18	0.7
(181563) 2006 UQ329	4.1	1.86 ± 0.01	16.06	*I*	19.88	0.38	2.91	1.5
(193434) 2000 WZ115	2.9	1.20 ± 0.00	16.07	*I*	19.28	0.18	2.56	1.0
(202533) 2006 DY32	1.2	1.72 ± 0.01	17.04	*R*	19.29	0.29	2.4	2.3
(207364) 2005 JR162	2.7	1.50 ± 0.00	16.18	*I*	20.0	0.5	2.76	0.6
(236724) 2007 GL48	0.9	2.03 ± 0.01	17.61	*R*	20.19	0.37	2.3	1.6
(243282) 2008 CJ86	7.9	1.13 ± 0.03	14.61	*R*	20.22	0.43	3.09	12.8
(266653) 2008 TS30	4.9	1.13 ± 0.00	15.68	*R*	20.09	0.38	3.22	0.6
(513920) 2014 BY16	0.8	1.39 ± 0.00	17.81	*I*	19.96	0.41	2.4	2.7
2017 DL83	0.8	1.52 ± 0.00	17.98	*R*	20.1	0.36	2.32	1.2
2017 DU80	1.5	1.44 ± 0.00	17.47	*R*	19.87	0.36	2.7	2.6

Note. Columns: asteroid designation, estimated diameter, derived rotation period, absolute magnitude in the observed filter band, filter, apparent magnitude, lightcurve amplitude, semimajor axis, and mean phase angle.

objects of $U = 3$ in the LCDB, where all our samples are below 2.2 hr following the prediction of rubble-pile structure, except for (134291) 2006 DZ6. 2006 DZ6 has a rotation period of 2.15 hr, slightly shorter than the 2.2 hr spin-rate limit. Since its best-fit period is outstanding on the periodogram and its folded lightcurve is very concentrated (see the left panel of Figure 5), we identify 2006 DZ6 as a very likely SFR. Using the Drucker–Prager model shown in Holsapple (2007), Rozitis et al. (2014), Polishook et al. (2016), and Chang et al. (2017), a preliminary estimation of cohesion to survive 2006 DZ6 under this condition is about the order of hundred Pa. To further search subtle features on the lightcurve of 2006 DZ6, we ran a sixth-order Fourier series fitting and the best-fit period became 5.39 hr. Figure 5 shows the folded lightcurve of 5.39 hr using the sixth-order Fourier series fitting, in which the oscillations have insignificant differences from each other. It is hard to tell whether the difference is a real detection or just a false signal from noise. Therefore, the 2.15 hr rotation period of (134291) 2006 DZ6 needs a follow-up confirmation.

In addition to (134291) 2006 DZ6, we also found another 16 objects with possible rotation periods of <2.2 hr. Their rotation

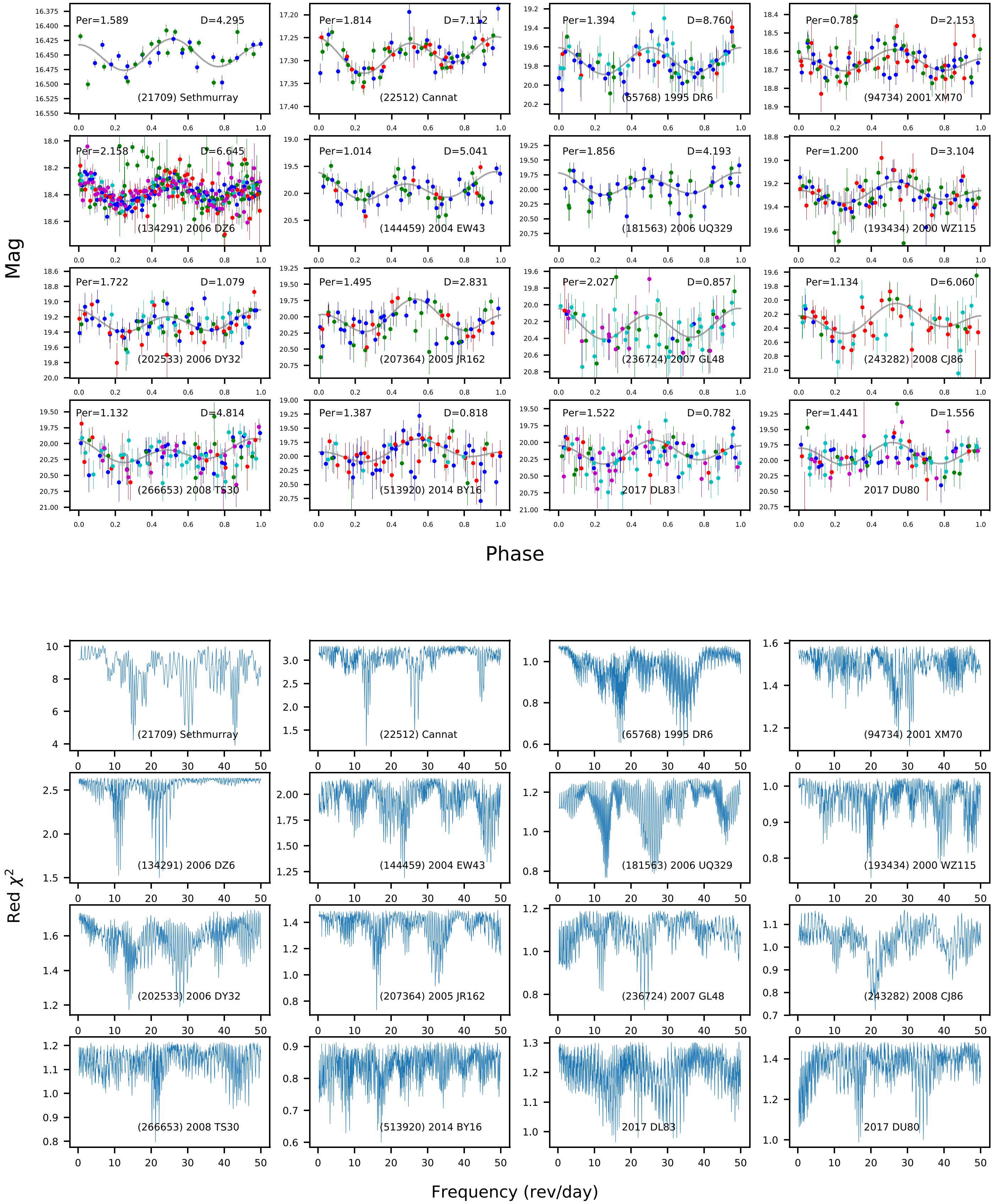

Figure 6. Folded lightcurves (top) and periodograms (bottom) of 16 SFR candidates. The colors represent data points obtained from different dates and the gray line is the fitting result.

Table 5
List of $U = 3$ Asteroids

Object	Diameter (km)	Period (hr)	H (mag)	Filter	Magnitude	Amplitude (mag)	Semimajor Axis (au)	Phase Angle (°)
(62) Erato	100.9	9.23 ± 0.04	8.85	R	13.36	0.28	3.14	0.7
(936) Kunigunde	41.8	8.79 ± 0.00	10.44	I	15.42	0.26	3.13	1.2
(1492) Oppolzer	5.9	3.77 ± 0.01	12.95	I	14.79	0.1	2.17	3.4
(2097) Galle	22.5	7.32 ± 0.00	12.1	R	17.51	0.33	3.14	0.7
(2216) Kerch	36.5	9.47 ± 0.02	11.05	R	15.59	0.33	3.02	0.7
(2256) Wisniewski	18.2	4.13 ± 0.00	12.25	I	16.99	0.12	3.09	0.5
(2385) Mustel	5.6	4.59 ± 0.00	13.06	I	16.39	0.45	2.24	0.9
(2996) Bowman	16.7	12.83 ± 0.07	12.0	R	15.75	0.25	2.78	1.4
(3765) Texereau	13.0	2.73 ± 0.00	12.98	I	16.78	0.11	2.84	1.4
(3811) Karma	17.1	14.41 ± 0.04	11.95	R	15.29	0.5	2.58	0.6
(3983) Sakiko	6.2	10.53 ± 0.00	13.16	R	15.45	0.53	2.45	0.8
(4073) Ruianzhongxue	22.9	7.74 ± 0.05	11.74	I	16.92	0.17	3.17	0.6
(4417) Lecar	13.8	3.00 ± 0.00	12.1	I	15.26	0.17	2.76	1.3
(4588) Wislicenus	22.5	4.70 ± 0.01	12.1	R	15.73	0.21	2.95	0.9
(4839) Daisetsuzan	5.4	3.38 ± 0.05	13.13	I	16.35	0.19	2.43	0.7
(5315) Bal'mont	3.4	4.35 ± 0.02	14.14	I	17.39	0.18	2.26	0.7
(5826) Bradstreet	23.8	5.54 ± 0.01	11.99	R	16.05	0.54	3.07	0.9
(5915) Yoshihiro	3.5	5.84 ± 0.25	14.1	I	16.46	0.1	2.25	3.9
(6287) Lenham	12.0	5.62 ± 0.01	13.15	I	16.91	0.34	3.14	0.6
(6378) 1987 SE13	13.2	6.10 ± 0.02	12.95	I	17.81	0.38	3.17	1.1
(6479) Leoconnolly	12.7	5.11 ± 0.01	12.6	R	15.2	0.59	2.61	2.2
(6581) Sobers	4.7	6.64 ± 0.01	13.44	I	16.63	0.6	2.3	1.1
(6709) Hiromiyuki	3.7	6.83 ± 0.01	13.98	I	16.46	0.71	2.35	1.5
(7024) 1992 PA4	19.6	4.38 ± 0.00	12.4	R	17.28	0.16	3.12	0.5
(7365) Sejong	4.0	2.59 ± 0.01	13.8	I	17.24	0.11	2.21	1.4
(7502) Arakida	14.7	2.84 ± 0.00	13.03	R	17.09	0.25	2.84	2.5
(7668) Mizunotakao	3.5	3.36 ± 0.00	14.38	R	16.93	0.17	2.37	2.0
(7935) Beppefenoglio	14.7	3.60 ± 0.01	13.04	R	16.96	0.07	3.09	0.5
(8096) Emilezola	3.7	3.63 ± 0.00	13.96	I	17.77	0.16	2.39	1.5
(8120) Kobe	2.6	5.88 ± 0.03	14.7	I	18.53	0.52	2.42	1.2
(8343) Tugendhat	11.6	4.21 ± 0.00	13.55	R	17.4	0.12	2.84	1.3
(8479) 1987 HD2	5.4	2.68 ± 0.00	13.46	R	15.86	0.08	2.43	0.7
(8549) Alcide	3.7	3.70 ± 0.09	14.29	R	17.41	0.23	2.44	1.5
(9126) Samcoulson	4.0	3.42 ± 0.01	14.81	I	17.81	0.23	2.54	0.7
(9216) Masuzawa	4.2	5.02 ± 0.32	14.02	R	17.25	0.15	2.25	2.2
(9291) Alanburdick	14.2	3.11 ± 0.00	13.1	R	17.56	0.12	3.07	0.5
(9310) 1987 SV12	11.9	5.19 ± 0.03	13.17	I	18.46	0.17	3.14	1.0
(9848) Yugra	3.0	2.80 ± 0.00	14.38	I	18.27	0.42	2.38	1.3
(10008) Raisanyo	7.1	8.65 ± 0.02	13.53	I	17.12	0.13	2.74	1.2
(10177) Ellison	4.5	7.27 ± 0.02	13.88	R	17.26	0.32	2.31	1.2
(11446) Betankur	11.1	10.79 ± 0.02	13.32	I	18.23	0.47	3.06	0.5
(11462) Hsingwenlin	3.6	3.65 ± 0.01	15.04	I	18.51	0.31	2.57	0.6
(11535) 1992 EQ27	9.8	4.58 ± 0.00	13.92	R	18.07	0.2	2.92	0.7
(12357) Toyako	12.9	8.32 ± 0.01	13.0	I	17.63	0.57	3.13	1.1
(12474) 1997 CZ19	3.3	2.74 ± 0.00	14.23	I	17.28	0.1	2.3	2.1
(12621) Alsufi	8.8	4.72 ± 0.01	13.81	I	18.64	0.59	3.11	0.6
(12947) 3099 T-1	3.5	3.27 ± 0.01	14.38	R	16.5	0.06	2.22	0.9
(13158) 1995 UE	2.5	8.48 ± 0.00	15.09	R	17.11	0.35	2.24	0.9
(13209) Arnhem	2.5	9.68 ± 0.00	14.77	I	16.92	0.36	2.32	3.1
(13396) Midavaine	6.1	5.93 ± 0.01	13.87	I	17.37	0.21	2.59	1.4
(13706) 1998 QF3	3.3	3.85 ± 0.00	14.52	R	17.02	0.52	2.27	3.1
(14387) 1990 QE5	2.3	9.56 ± 0.00	14.98	I	18.18	0.4	2.36	0.9
(14398) 1990 VT6	4.2	3.36 ± 0.01	14.68	I	18.5	0.23	2.65	1.2
(14561) 1997 WC34	10.7	4.91 ± 0.00	13.73	R	18.7	0.37	3.25	0.7
(14754) 4806 P-L	3.9	2.92 ± 0.01	15.16	R	17.84	0.2	2.61	1.4
(14875) 1990 WZ1	2.5	5.26 ± 0.00	14.79	I	18.21	0.55	2.38	0.9
(15959) 1998 BQ40	7.1	4.03 ± 0.00	13.87	R	17.92	0.3	2.79	0.6
(16306) 6797 P-L	2.2	5.50 ± 0.01	15.13	I	17.56	0.39	2.39	1.6
(16484) 1990 QJ9	8.5	7.16 ± 0.11	13.9	I	17.86	0.21	2.91	1.4
(17274) 2000 LC16	5.2	5.50 ± 0.01	14.19	I	18.28	0.55	2.73	28.1
(17574) 1994 PT13	9.8	2.82 ± 0.01	13.6	I	18.02	0.24	3.01	0.8
(18175) Jenniferchoy	8.2	2.99 ± 0.00	13.98	I	18.17	0.34	2.89	1.2
(19198) 1992 ED8	9.3	3.70 ± 0.00	14.03	R	17.59	0.23	2.92	0.6
(19741) Callahan	3.3	7.27 ± 0.00	14.55	R	17.39	0.65	2.25	2.4
(20030) 1992 EN30	2.6	7.23 ± 0.00	15.08	R	18.52	0.35	2.34	2.2
(20105) 1995 OS1	3.1	5.79 ± 0.01	14.65	R	17.75	0.23	2.48	0.8
(20131) 1996 BP3	12.3	3.88 ± 0.00	13.41	R	17.36	0.44	3.01	1.0
(20514) 1999 RD34	8.0	4.29 ± 0.00	14.03	I	18.72	0.54	3.06	0.6
(22329) 1991 VT5	4.0	8.92 ± 0.10	14.78	I	18.39	0.15	2.58	1.2
(22418) 1995 WM4	5.7	3.21 ± 0.01	14.03	I	18.15	0.22	2.59	2.4
(22501) 1997 PR3	1.6	4.20 ± 0.01	15.79	I	18.22	0.22	2.37	1.3

Table 5
(Continued)

Object	Diameter (km)	Period (hr)	H (mag)	Filter	Magnitude	Amplitude (mag)	Semimajor Axis (au)	Phase Angle (°)
(22984) 1999 VP36	10.0	5.59 ± 0.01	13.54	*I*	17.28	0.39	3.17	1.3
(22990) Mattbrenner	3.6	2.65 ± 0.01	14.98	*I*	17.55	0.23	2.62	1.5
(23157) 2000 DH19	10.2	9.62 ± 0.02	13.82	*R*	18.84	0.61	3.14	0.5
(23879) Demura	9.6	11.01 ± 0.05	13.63	*I*	18.48	0.55	3.18	0.6
(24345) Llaverias	5.2	6.47 ± 0.00	14.51	*R*	17.53	0.4	2.54	1.4
(24496) 2001 AV17	3.3	6.11 ± 0.00	15.21	*I*	17.43	0.7	2.62	1.1
(24548) Katieeverett	1.5	8.79 ± 0.00	15.95	*I*	18.28	0.58	2.25	1.3
(25303) 1998 XE17	14.9	6.95 ± 0.01	13.0	*R*	17.32	0.32	3.18	1.9
(26018) 2695 P-L	7.8	6.50 ± 0.01	14.41	*R*	18.31	0.49	3.1	0.6
(28161) Neelpatel	1.6	6.39 ± 0.01	16.1	*R*	18.91	0.69	2.29	0.6
(28420) 1999 VC78	9.4	3.10 ± 0.01	13.68	*I*	18.29	0.24	3.11	0.8
(28961) 2001 FO64	2.2	5.76 ± 0.03	15.11	*I*	18.61	0.54	2.27	1.4
(29391) Knight	3.6	5.13 ± 0.00	15.33	*R*	18.82	0.43	2.66	0.9
(29398) 1996 RM5	4.3	4.18 ± 0.00	14.63	*I*	18.7	0.12	2.79	1.4
(29857) 1999 FS28	7.9	4.13 ± 0.00	14.06	*I*	17.84	0.37	2.86	1.3
(30213) 2000 GW124	3.2	4.79 ± 0.00	14.3	*I*	17.82	0.39	2.4	1.0
(30584) 2001 PF9	7.1	6.37 ± 0.01	13.86	*R*	16.76	0.1	2.7	1.3
(32315) Clarezhu	6.9	3.72 ± 0.00	14.35	*I*	18.27	0.73	2.9	1.0
(32562) Caseywarner	4.7	5.46 ± 0.01	14.75	*R*	18.45	0.51	2.71	1.1
(33354) 1998 YZ16	1.8	3.71 ± 0.00	15.48	*I*	17.71	0.36	2.41	1.7
(34243) 2000 QR100	10.4	2.74 ± 0.01	13.47	*I*	17.6	0.16	2.97	2.0
(34728) 2001 QM30	7.3	5.28 ± 0.01	13.78	*R*	17.67	0.48	2.75	1.6
(35596) 1998 HZ117	5.2	3.45 ± 0.00	14.2	*I*	16.45	0.08	2.54	2.8
(35752) 1999 GW36	2.3	6.76 ± 0.02	15.26	*R*	17.17	0.12	2.37	2.0
(36176) 1999 SR9	2.3	4.75 ± 0.00	14.95	*I*	18.19	0.36	2.23	1.0
(37260) 2000 XR4	9.8	3.31 ± 0.00	13.59	*I*	17.82	0.28	3.04	2.5
(38301) 1999 RH92	9.4	10.02 ± 0.02	13.99	*R*	18.03	0.4	2.95	0.6
(38773) 2000 RY9	2.4	3.37 ± 0.01	15.21	*R*	18.86	0.55	2.45	0.8
(38975) 2000 TH66	4.1	6.58 ± 0.00	14.08	*R*	18.57	0.52	2.27	14.5
(39649) 1995 SM15	3.5	2.61 ± 0.01	15.04	*I*	18.46	0.23	2.56	0.5
(40497) 1999 RR78	6.6	5.25 ± 0.01	14.46	*I*	18.4	0.39	3.04	1.0
(40580) 1999 RN135	3.1	4.92 ± 0.01	15.34	*I*	19.21	0.78	2.55	1.4
(40628) 1999 RV173	3.6	6.58 ± 0.02	15.03	*I*	18.97	0.56	2.56	1.9
(40641) 1999 RV181	2.4	5.08 ± 0.02	15.89	*I*	19.54	0.61	2.55	0.5
(41234) 1999 XP23	6.5	5.61 ± 0.01	14.47	*I*	18.57	0.39	3.15	0.9
(41620) 2000 SU160	3.8	4.68 ± 0.01	14.92	*I*	18.41	0.44	2.57	1.3
(41872) 2000 WJ100	3.4	4.14 ± 0.01	15.15	*I*	18.44	0.27	2.56	2.0
(42130) 2001 BW19	8.2	7.43 ± 0.00	13.97	*I*	17.96	0.59	3.11	1.4
(42754) 1998 SN60	9.0	5.59 ± 0.01	14.09	*R*	18.68	0.39	3.08	1.1
(44765) 1999 TP122	1.4	4.44 ± 0.07	16.07	*I*	18.81	0.58	2.28	1.1
(45325) 2000 AD70	3.8	6.35 ± 0.02	14.88	*I*	17.41	0.15	2.67	1.0
(45605) 2000 DM28	10.0	8.18 ± 0.01	13.86	*R*	18.44	0.51	3.16	0.6
(46885) 1998 RR18	3.3	3.21 ± 0.00	15.54	*R*	19.39	0.54	2.6	1.0
(47767) 2000 DR103	4.8	3.07 ± 0.01	14.4	*I*	18.51	0.22	2.71	2.5
(47894) 2000 GS21	3.4	3.44 ± 0.01	15.15	*I*	18.81	0.31	2.76	1.3
(48507) 1993 FS11	2.5	7.55 ± 0.00	14.77	*I*	17.24	0.22	2.34	1.3
(49445) 1998 YS8	4.8	9.68 ± 0.04	14.7	*R*	18.28	0.61	2.64	2.3
(49587) 1999 CL145	18.8	9.92 ± 0.00	12.49	*R*	18.58	0.61	3.16	16.7
(49755) 1999 VO172	1.6	2.63 ± 0.01	15.75	*I*	18.55	0.19	2.3	0.7
(50197) 2000 AS198	4.1	2.86 ± 0.01	14.75	*I*	17.84	0.14	2.7	0.6
(50388) 2000 CM92	7.8	11.01 ± 0.10	14.4	*R*	17.92	0.28	3.19	0.7
(50496) 2000 DA94	3.5	3.80 ± 0.01	15.06	*I*	18.51	0.28	2.71	1.5
(53620) 2000 CN93	2.6	3.15 ± 0.02	14.71	*I*	17.31	0.54	2.36	3.6
(53657) 2000 DG53	3.1	5.21 ± 0.02	14.31	*I*	18.82	0.59	2.18	3.4
(54264) 2000 JN33	1.7	6.13 ± 0.01	15.67	*I*	17.41	0.18	2.38	0.9
(55181) 2001 QD280	13.0	7.48 ± 0.02	12.22	*I*	18.23	0.43	2.63	10.3
(56755) 2000 OT12	1.5	4.39 ± 0.00	15.97	*I*	18.93	0.5	2.41	1.0
(57315) 2001 QC233	2.9	5.45 ± 0.01	14.45	*I*	18.38	0.53	2.36	16.9
(57490) 2001 ST175	1.6	8.21 ± 0.01	15.83	*I*	17.7	0.62	2.41	2.4
(58328) 1994 ST9	1.4	9.16 ± 0.00	16.44	*R*	18.46	0.57	2.32	1.5
(59008) 1998 SS63	4.3	4.61 ± 0.02	14.93	*R*	18.59	0.81	2.62	0.7
(59115) 1998 XG3	2.3	4.32 ± 0.00	15.3	*R*	18.4	0.63	2.31	1.0
(60314) 1999 XU226	6.4	4.64 ± 0.02	14.51	*I*	19.54	0.61	3.18	1.0
(61839) 2000 QA198	1.5	3.89 ± 0.00	15.97	*I*	18.82	0.47	2.42	2.7
(62188) 2000 SK41	6.0	5.63 ± 0.00	14.66	*I*	18.49	0.49	2.96	2.3
(63201) 2000 YH129	5.8	6.85 ± 0.01	14.71	*I*	18.49	0.54	3.11	1.3
(68311) 2001 FN112	7.1	6.26 ± 0.01	14.62	*R*	18.88	0.5	3.08	0.6
(68479) 2001 TX40	8.8	9.54 ± 0.02	13.38	*R*	18.48	0.44	2.58	4.5
(70783) Kenwilliams	3.6	3.67 ± 0.00	15.04	*I*	18.62	0.4	2.62	0.5
(73773) 1994 PZ18	5.8	4.26 ± 0.01	14.31	*R*	16.99	0.17	2.57	3.2
(74194) 1998 RL48	12.1	10.67 ± 0.00	12.38	*I*	18.03	0.58	2.74	19.3

Table 5
(Continued)

Object	Diameter (km)	Period (hr)	H (mag)	Filter	Magnitude	Amplitude (mag)	Semimajor Axis (au)	Phase Angle (°)
(74348) 1998 VT53	3.6	8.33 ± 0.06	15.03	I	18.92	0.65	2.71	2.5
(75923) 2000 CL65	3.8	5.18 ± 0.01	15.2	R	17.51	0.21	2.62	0.9
(79157) 1993 FE16	1.6	6.26 ± 0.04	15.81	I	18.7	0.36	2.35	1.8
(79616) 1998 RV57	1.6	5.21 ± 0.01	15.78	I	18.18	0.56	2.3	2.0
(81534) 2000 HM15	2.7	3.25 ± 0.01	15.67	I	19.0	0.32	2.76	0.5
(81613) 2000 HE69	3.5	4.59 ± 0.00	15.08	I	18.8	0.46	2.78	1.5
(81709) 2000 JY23	3.6	3.02 ± 0.01	15.03	I	18.11	0.14	2.76	0.6
(84748) 2002 XQ9	1.1	6.50 ± 0.01	16.53	I	19.5	0.81	2.33	2.0
(85244) 1993 QB9	1.4	6.17 ± 0.47	16.08	I	18.64	0.44	2.41	1.6
(85333) 1995 SN13	4.9	5.39 ± 0.03	15.12	I	19.67	0.66	2.91	0.9
(86241) 1999 TE120	9.9	5.11 ± 0.01	13.58	I	17.59	0.16	3.05	0.5
(90268) 2003 CT8	1.3	7.61 ± 0.01	16.3	I	18.9	0.56	2.39	1.2
(90352) 2003 GK49	4.9	6.81 ± 0.01	15.42	R	19.48	0.69	2.87	1.1
(90483) 2004 DM4	2.7	5.44 ± 0.00	15.62	I	19.05	0.36	2.76	1.4
(90879) 1996 WB1	2.5	4.25 ± 0.01	15.13	R	18.71	0.38	2.47	0.7
(90890) 1997 AT12	3.9	6.11 ± 0.76	14.84	I	17.92	0.18	2.58	1.8
(91613) 1999 TO31	7.7	4.79 ± 0.01	14.12	I	17.89	0.26	3.08	0.7
(92502) 2000 NP15	2.0	5.73 ± 0.00	15.59	R	18.45	0.63	2.35	1.8
(92959) 2000 RA47	2.1	10.93 ± 0.07	15.48	R	19.03	0.39	2.42	0.9
(93763) 2000 WH19	3.3	4.12 ± 0.00	15.22	I	17.86	0.49	2.57	1.9
(95260) 2002 CS59	7.7	3.13 ± 0.00	14.43	R	18.6	0.28	2.94	0.7
(98114) 2000 RQ95	2.3	5.22 ± 0.00	15.99	I	19.14	0.74	2.53	2.6
(10233) Le Creusot	9.2	9.78 ± 0.02	13.29	R	17.37	0.34	2.73	2.3
(103429) 2000 AJ159	1.5	10.98 ± 0.03	16.19	R	17.45	0.53	2.25	1.3
(106943) 2000 YX72	2.8	3.06 ± 0.01	15.54	I	18.53	0.2	2.57	2.8
(109504) 2001 QV233	1.5	6.97 ± 0.01	15.96	I	18.5	0.53	2.42	1.1
(116804) 2004 EJ70	4.6	5.11 ± 0.00	14.48	I	19.06	0.62	2.7	25.0
(117343) 2004 XR38	2.5	5.33 ± 0.01	15.84	I	19.28	0.37	2.56	2.3
(118641) 2000 HU95	1.1	3.40 ± 0.00	16.52	I	18.44	0.27	2.37	0.8
(123699) 2000 YF105	9.6	5.34 ± 0.01	13.63	I	18.0	0.24	3.18	1.0
(126923) 2002 EC135	2.0	3.08 ± 0.00	16.24	I	19.15	0.37	2.53	0.6
(127801) 2003 FL77	1.6	5.80 ± 0.01	16.07	R	19.24	0.65	2.33	1.2
(130320) Maherrassas	5.4	4.49 ± 0.01	15.22	R	18.8	0.43	3.19	0.9
(130583) 2000 RS75	4.6	5.45 ± 0.00	14.46	I	16.72	0.19	2.56	1.5
(131869) 2002 AJ155	1.6	10.15 ± 0.02	16.12	R	18.78	0.63	2.41	1.5
(135551) 2002 ED43	1.3	4.62 ± 0.00	16.56	R	18.77	0.28	2.43	0.8
(138048) 2000 DG32	3.0	7.24 ± 0.01	15.71	R	19.01	0.75	2.62	0.8
(14019) Pourbus	2.0	4.25 ± 0.00	15.61	R	18.21	0.47	2.27	1.0
(141110) 2001 XY62	5.0	5.35 ± 0.00	15.39	R	18.98	0.55	2.87	1.2
(142769) 2002 UB6	3.0	11.11 ± 0.15	15.4	I	18.47	0.2	2.78	1.2
(144251) 2004 CU83	2.0	8.30 ± 0.06	16.25	I	19.79	0.64	2.76	0.7
(147618) 2004 HG10	0.9	3.29 ± 0.00	16.96	I	18.56	0.31	2.34	1.0
(15316) Okagakimachi	3.2	2.65 ± 0.00	14.57	R	16.66	0.09	2.29	1.9
(154452) 2003 CO10	0.9	3.47 ± 0.01	16.96	I	18.67	0.26	2.4	1.2
(161079) 2002 LP61	4.0	3.91 ± 0.01	15.55	I	18.89	0.35	3.14	0.7
(162836) 2001 CY22	2.6	5.25 ± 0.00	15.68	I	18.4	0.48	2.59	1.6
(166087) 2002 CR123	1.1	5.84 ± 0.00	16.83	R	19.36	0.6	2.4	0.8
(179762) 2002 RB242	2.6	4.70 ± 0.02	16.08	R	18.53	0.56	2.64	2.8
(195054) 2002 CZ74	0.9	11.29 ± 0.03	17.24	R	19.24	0.72	2.4	1.3
(200543) 2001 FH71	1.4	5.82 ± 0.01	17.11	I	18.84	0.57	2.63	3.5
(225707) 2001 QN242	1.8	2.34 ± 0.01	15.55	I	18.62	0.41	2.43	1.4
(251886) 1999 VV86	5.2	5.27 ± 0.00	15.27	R	18.87	0.45	3.11	1.5
(307883) 2004 BT107	2.2	7.10 ± 0.00	16.41	R	18.58	0.46	2.64	1.4
(380499) 2004 DC34	0.8	5.63 ± 0.00	17.22	I	18.5	0.64	2.31	1.3

Note. Columns are the same as those in Table 4.

(This table is available in its entirety in machine-readable form.)

periods were clearly detected in the periodograms and, however, their folded lightcurves are relatively scattered (see Figure 6). We only list them as possible SFR candidates in Table 4 for further confirmation. These objects are of special interests because it requires relatively large cohesion to survive them under such super-fast rotation considering that they are relatively large in size (i.e., few kilometers). Therefore, learning their physical properties is important to study the asteroid interior structure.

Some asteroids in our samples show large amplitudes suggesting that they are potential binary/contact binary asteroids (see Tables 5 and 6), among which (2280) Kunikov seems to display an eclipsing feature, with a very deep minimum with a very sharp and obvious transition in the beginning and the end (see Figure 3 as an example). To confirm the binarity, it requires densely covered lightcurves to reveal the detailed features. Therefore, we leave these large-amplitude objects for further follow-up observations.

Table 6
List $U = 2$ Asteroids

Object	Diameter (km)	Period (hr)	H (mag)	Filter	Magnitude	Amplitude (mag)	Semimajor Axis (au)	Phase Angle (°)
(178) Belisana	37.6	16.55 ± 0.11	9.49	*I*	12.48	0.39	2.46	1.5
(269) Justitia	54.6	16.55 ± 0.11	9.67	*R*	13.24	0.22	2.62	1.1
(772) Tanete	121.6	8.03 ± 0.03	8.69	*R*	14.92	0.34	3.02	14.8
(833) Monica	40.5	12.06 ± 0.00	11.07	*I*	15.54	0.19	3.01	0.6
(890) Waltraut	56.7	12.50 ± 0.00	10.34	*I*	14.36	0.27	3.02	1.1
(1465) Autonoma	29.5	6.11 ± 0.02	11.76	*R*	15.31	0.12	3.03	2.0
(2280) Kunikov	6.8	12.97 ± 0.07	13.2	*I*	16.25	0.41	2.18	2.4
(3269) Vibert-Douglas	16.6	18.11 ± 0.07	12.26	*I*	16.46	0.33	2.78	0.8
(4156) Okadanoboru	30.7	2.65 ± 0.01	10.93	*R*	16.9	0.03	2.7	9.8
(4195) Esambaev	18.7	4.70 ± 0.00	12.75	*I*	16.63	0.59	2.83	0.3
(4306) Dunaevskij	41.6	3.57 ± 0.03	11.02	*I*	15.85	0.24	3.13	0.8
(4347) Reger	25.0	12.00 ± 0.00	12.12	*I*	16.02	0.39	3.05	0.6
(4723) Wolfgangmattig	8.0	4.01 ± 0.00	13.83	*I*	18.03	0.23	2.68	1.3
(4985) Fitzsimmons	16.1	9.25 ± 0.02	13.08	*R*	17.82	0.07	3.25	0.9
(5375) Siedentopf	13.9	4.04 ± 0.02	13.39	*I*	18.5	0.16	3.17	1.0
(6229) Tursachan	14.0	16.55 ± 0.00	13.38	*I*	18.28	0.48	3.08	0.7
(7150) McKellar	3.7	7.23 ± 0.02	14.5	*I*	18.36	0.28	2.42	2.1
(7217) Dacke	31.2	13.56 ± 0.00	11.64	*R*	16.85	0.21	3.22	1.3
(7221) Sallaba	2.9	2.82 ± 0.21	15.04	*R*	18.89	0.28	2.41	0.4
(7423) 1992 PT2	3.3	3.51 ± 0.00	14.79	*R*	19.03	0.48	2.3	3.8
(7820) Ianlyon	3.8	4.10 ± 0.03	14.46	*I*	18.25	0.1	2.37	0.9
(9184) Vasilij	4.2	6.11 ± 0.00	14.27	*I*	16.57	0.2	2.31	0.5
(9740) 1987 ST11	4.6	10.30 ± 0.00	14.05	*I*	17.27	0.74	2.36	3.1
(10021) Henja	5.0	3.11 ± 0.00	13.86	*R*	17.13	0.11	2.35	2.3
(10214) 1997 RT9	7.6	10.55 ± 0.02	13.96	*R*	17.46	0.43	2.73	1.7
(11677) 1998 DY4	3.5	3.10 ± 0.01	14.64	*I*	17.28	0.08	2.22	3.0
(12175) Wimhermans	13.3	19.67 ± 0.92	13.49	*I*	18.52	0.57	3.1	1.1
(12546) 1998 QJ21	13.4	10.23 ± 0.02	13.48	*I*	18.05	0.64	3.08	0.6
(12614) Hokusai	2.8	6.15 ± 0.01	15.15	*R*	18.52	0.54	2.18	1.7
(12693) 1989 EZ	13.9	11.11 ± 0.00	12.64	*I*	16.06	0.18	2.55	2.5
(12763) 1993 UQ2	14.9	5.56 ± 0.45	13.25	*R*	17.95	0.3	3.06	1.7
(12857) 1998 HQ97	12.7	2.69 ± 0.01	13.59	*R*	17.82	0.1	2.91	0.7
(12904) 1998 RB65	19.1	8.89 ± 0.00	12.7	*R*	19.25	0.43	3.21	14.6
(12957) 2258 T-2	4.3	2.97 ± 0.01	15.2	*I*	18.91	0.19	2.62	0.6
(13046) Aliev	5.1	5.44 ± 0.04	14.82	*R*	19.27	0.31	2.55	1.8
(13065) 1991 PG11	4.0	7.91 ± 0.01	14.33	*I*	17.87	0.43	2.3	1.0
(13430) 1999 VM36	5.0	8.08 ± 0.00	14.88	*I*	19.25	0.83	2.62	0.8
(13677) Alvin	11.0	11.21 ± 0.00	13.91	*R*	18.61	0.17	3.15	2.2
(15121) 2000 EN14	2.6	5.80 ± 0.00	15.28	*I*	18.74	0.65	2.35	0.9
(15618) Lorifritz	1.4	17.27 ± 0.24	16.56	*R*	18.43	0.73	2.29	1.1
(16625) Kunitsugu	3.3	4.61 ± 0.00	14.8	*I*	16.67	0.06	2.15	0.8
(17035) Velichko	5.6	2.90 ± 0.00	13.63	*I*	17.32	0.22	2.44	1.2
(17108) Patricorbett	8.0	2.52 ± 0.01	14.6	*I*	18.37	0.09	2.89	0.5
(17314) Aisakos	42.9	9.74 ± 0.02	10.95	*I*	17.67	0.23	5.17	0.5
(17634) 1996 NM3	2.9	5.41 ± 0.65	15.08	*I*	17.65	0.08	2.44	1.1
(17696) Bombelli	14.5	12.97 ± 0.14	13.31	*I*	17.38	0.2	3.02	0.5
(17697) Evanchen	12.7	2.99 ± 0.00	13.6	*I*	17.46	0.13	3.0	0.5
(18161) Koshiishi	23.4	5.99 ± 0.00	12.27	*I*	16.81	0.09	3.0	1.2
(18387) 1992 GN3	2.7	5.91 ± 0.03	15.18	*R*	18.51	0.77	2.36	0.8
(18406) 1993 FT14	5.4	6.27 ± 0.21	14.72	*I*	16.97	0.3	2.6	3.2
(18554) 1997 BO1	12.8	2.75 ± 0.02	13.58	*I*	17.98	0.15	2.97	1.0
(19947) 1981 EE39	8.0	21.24 ± 0.73	14.6	*I*	18.98	0.78	3.03	0.5
(20218) Dukewriter	8.7	4.99 ± 0.00	14.41	*I*	18.07	0.15	3.04	1.1
(20409) 1998 QP43	17.2	4.05 ± 0.02	12.93	*I*	16.93	0.03	3.15	1.0
(20439) 1999 JM28	4.2	9.09 ± 4.32	14.23	*R*	16.96	0.18	2.4	1.4
(20515) 1999 RO34	47.2	8.14 ± 0.56	10.74	*I*	14.57	0.38	3.06	1.2
(20724) 1999 XO116	10.1	9.90 ± 0.02	14.09	*I*	18.38	0.36	3.13	0.6
(21537) Frechet	8.4	5.02 ± 0.22	14.49	*I*	18.22	0.43	3.07	0.8
(22460) 1997 AJ2	3.8	5.91 ± 0.00	14.44	*I*	17.01	0.06	2.29	3.4
(22784) Theresaoei	5.2	21.43 ± 0.00	13.79	*I*	16.21	0.24	2.47	1.4
(22891) 1999 SO11	2.5	4.91 ± 0.01	15.35	*R*	18.51	0.14	2.17	0.8
(23017) Advincula	6.9	11.51 ± 0.14	14.17	*R*	17.91	0.15	2.52	2.3
(25508) 1999 XC96	10.8	5.13 ± 0.43	12.2	*I*	15.51	0.47	2.29	1.7

Table 6
(Continued)

Object	Diameter (km)	Period (hr)	H (mag)	Filter	Magnitude	Amplitude (mag)	Semimajor Axis (au)	Phase Angle (°)
(26013) Amandalonzo	2.4	8.92 ± 0.00	15.44	*R*	18.67	0.34	2.2	2.3
(27012) 1998 FZ46	2.1	19.51 ± 0.31	15.78	*R*	18.18	0.19	2.17	1.1
(27138) 1998 XU42	3.0	6.45 ± 0.02	14.95	*R*	17.58	0.12	2.32	0.8
(27469) 2000 GN72	37.6	3.21 ± 0.01	11.24	*R*	17.27	0.08	3.04	14.0
(27545) 2000 JX16	10.0	11.43 ± 0.11	13.37	*I*	17.9	0.31	2.79	1.7
(27984) Herminefranz	3.5	7.69 ± 0.00	15.65	*R*	19.67	0.61	2.75	0.7
(28122) 1998 SJ74	4.5	7.92 ± 0.08	15.08	*I*	19.12	0.38	2.68	2.3
(29081) Krymradio	3.0	4.71 ± 0.00	14.98	*I*	18.78	0.42	2.43	1.6
(29740) 1999 BS9	10.0	11.65 ± 0.00	13.37	*R*	17.35	0.22	2.68	0.8
(30024) Neildavey	2.0	3.00 ± 0.01	15.87	*R*	18.28	0.12	2.25	0.8
(30097) Traino	2.9	10.02 ± 0.02	15.06	*I*	18.15	0.34	2.36	2.3
(30475) 2000 OA32	23.4	15.00 ± 0.09	12.27	*R*	18.01	0.51	3.17	13.3
(30506) 2000 RO85	35.9	8.00 ± 0.03	11.33	*I*	18.44	0.56	5.13	0.6
(30554) 2001 OP57	2.4	3.40 ± 0.01	15.43	*I*	19.0	0.17	2.39	1.4
(30566) Stokes	2.5	2.70 ± 0.00	15.38	*I*	19.21	0.26	2.38	1.8
(30910) 1993 FP52	1.7	2.82 ± 0.01	16.24	*I*	18.56	0.19	2.34	2.1
(31146) 1997 UV3	3.9	8.16 ± 0.06	14.4	*I*	18.02	0.32	2.45	1.5
(31478) 1999 CJ45	4.6	6.24 ± 0.01	14.06	*R*	17.52	0.11	2.34	1.0
(31652) 1999 HS2	3.2	3.44 ± 0.02	14.86	*I*	16.73	0.29	2.44	0.5
(31777) Amywinegar	10.0	6.48 ± 0.01	14.11	*I*	18.17	0.25	2.9	1.3
(32226) Vikulgupta	3.4	2.60 ± 0.18	14.74	*R*	17.5	0.24	2.32	2.0
(32577) 2001 QC87	5.9	5.27 ± 0.00	14.49	*I*	19.4	0.68	2.54	10.0
(34381) 2000 RW55	18.6	9.32 ± 0.02	12.77	*R*	18.77	0.59	3.19	9.5
(34789) 2001 SC2	2.6	10.30 ± 0.09	15.32	*R*	17.01	0.46	2.31	2.3
(34874) 2001 UU9	7.0	3.05 ± 0.01	14.89	*I*	18.79	0.18	2.84	0.6
(34902) 2728 P-L	8.1	2.21 ± 0.01	14.58	*I*	18.22	0.17	2.93	2.5
(35137) Meudon	2.2	2.27 ± 0.00	15.66	*R*	18.61	0.21	2.4	1.0
(35334) Yarkovsky	8.4	5.70 ± 0.03	14.48	*I*	18.6	0.28	3.02	1.6
(35373) 1997 UT25	1.9	4.82 ± 0.06	15.96	*R*	19.47	0.63	2.36	2.1
(35384) 1997 WK37	2.3	4.90 ± 0.01	15.59	*R*	19.34	0.45	2.36	0.6
(35612) 1998 HR137	8.5	8.00 ± 0.00	14.47	*I*	18.37	0.25	2.95	1.6
(35992) 1999 NF12	8.7	8.16 ± 0.08	14.41	*I*	18.94	0.56	3.0	1.3
(36040) 1999 PF6	6.4	5.50 ± 0.04	15.1	*I*	19.26	0.67	2.99	2.0
(36195) 1999 TG90	7.8	3.49 ± 0.06	14.64	*I*	19.5	0.69	2.89	23.8
(36538) 2000 QD91	3.1	4.85 ± 0.03	14.94	*R*	17.31	0.17	2.43	2.7
(37956) 1998 HO53	3.7	16.96 ± 0.06	15.54	*I*	17.83	0.15	2.54	0.8
(37956) 1998 HO53	3.7	2.71 ± 0.01	15.54	*I*	18.1	0.23	2.54	0.8
(38031) 1998 QN36	14.5	8.57 ± 0.12	13.31	*I*	18.05	0.26	3.17	1.6
(38418) 1999 RW218	4.4	3.14 ± 0.00	15.16	*I*	18.66	0.18	2.53	1.2
(38557) 1999 VV92	13.6	3.16 ± 0.01	13.44	*I*	18.77	0.37	2.96	20.5
(39295) 2001 DF95	9.2	2.68 ± 0.10	14.29	*I*	18.37	0.21	3.09	2.5
(39987) 1998 HJ33	2.1	2.65 ± 0.00	15.73	*R*	18.2	0.15	2.45	1.2
(40177) 1998 RU28	9.6	11.57 ± 0.03	14.19	*I*	19.21	1.24	3.12	1.1
(40649) 1999 RY186	5.7	8.39 ± 4.00	14.59	*I*	16.72	0.11	2.55	1.9
(41255) 1999 XV43	5.2	3.73 ± 0.01	14.8	*I*	18.74	0.16	2.58	1.0
(41450) Medkeff	1.6	2.59 ± 0.01	16.29	*I*	18.54	0.16	2.39	1.6
(41663) 2000 TK16	1.5	4.12 ± 0.04	16.45	*I*	18.42	0.18	2.19	1.6
(41949) 2000 XB8	2.6	3.80 ± 0.24	15.32	*I*	18.12	0.2	2.2	1.2
(42536) 1995 VX13	3.8	3.85 ± 0.16	15.48	*I*	18.62	0.58	2.59	1.1
(43595) 2001 QT101	7.6	3.64 ± 0.00	13.96	*R*	18.84	0.26	2.62	20.1
(44578) 1999 GL25	2.7	3.72 ± 0.00	15.23	*I*	18.18	0.29	2.44	1.7
(44658) 1999 RD168	1.7	7.28 ± 0.01	16.22	*R*	19.04	0.3	2.15	1.3
(45714) 2000 FV58	14.1	10.17 ± 0.17	13.37	*I*	18.73	0.6	3.01	4.4
(45786) 2000 OE20	5.3	4.36 ± 0.02	14.76	*R*	18.57	0.18	2.76	2.1
(46145) 2001 FC63	18.8	3.66 ± 0.00	12.74	*R*	18.56	0.23	2.89	18.1
(47732) 2000 DR51	8.8	2.97 ± 0.01	14.39	*R*	19.43	0.75	3.18	0.9
(47739) 2000 DD69	5.0	7.68 ± 0.01	14.87	*R*	17.85	0.81	2.63	2.3
(48612) 1995 FX6	4.7	11.51 ± 0.08	14.99	*I*	18.06	0.15	2.77	1.3
(48735) 1997 CX19	2.3	2.27 ± 0.00	15.6	*I*	17.33	0.14	2.3	1.9
(49173) 1998 SQ63	2.9	4.42 ± 0.00	15.07	*I*	18.21	0.14	2.34	2.1
(49319) 1998 VT25	3.9	12.97 ± 0.00	15.39	*I*	19.89	0.68	2.68	1.2
(51078) 2000 GZ163	19.4	8.18 ± 0.01	12.67	*R*	18.69	0.65	2.99	9.7
(52509) 1996 GP9	3.8	6.83 ± 0.03	15.47	*R*	19.23	0.37	2.64	1.9

Table 6
(Continued)

Object	Diameter (km)	Period (hr)	H (mag)	Filter	Magnitude	Amplitude (mag)	Semimajor Axis (au)	Phase Angle (°)
(53159) Myslivecek	2.2	9.20 ± 0.00	15.64	*I*	18.43	0.37	2.41	1.7
(55364) 2001 ST180	6.7	5.12 ± 0.01	14.97	*I*	18.58	0.24	2.81	1.0
(55666) 6631 P-L	1.7	14.46 ± 0.26	16.19	*R*	18.95	0.28	2.28	0.9
(56044) 1998 XU17	2.3	4.97 ± 0.00	15.6	*I*	18.72	0.44	2.4	1.6
(56232) 1999 JM31	2.4	5.71 ± 0.01	15.46	*I*	18.8	0.44	2.19	1.7
(57186) 2001 QK30	3.1	4.40 ± 0.02	14.88	*I*	18.45	0.22	2.41	2.2
(57758) 2001 VW20	7.0	4.26 ± 0.03	14.9	*I*	18.75	0.21	2.89	1.6
(57915) 2002 EB110	58.2	11.19 ± 0.03	10.29	*R*	18.34	0.12	5.23	9.1
(59466) 1999 GE54	1.4	5.84 ± 0.03	16.59	*I*	18.78	0.3	2.44	1.4
(60406) Albertosuci	2.3	2.94 ± 0.01	15.57	*R*	18.26	0.1	2.26	1.4
(60657) 2000 FT47	7.0	11.65 ± 0.00	14.14	*I*	17.94	0.15	2.75	2.3
(60780) 2000 GA164	2.3	5.65 ± 0.59	15.58	*I*	18.36	0.21	2.38	3.3
(60814) 2000 HG32	1.7	10.53 ± 0.14	16.15	*I*	18.02	0.28	2.37	1.9
(61362) 2000 PO19	2.5	6.63 ± 0.00	15.39	*I*	18.93	0.77	2.45	2.9
(61479) 2000 QH39	2.3	4.90 ± 0.01	15.59	*R*	18.92	0.37	2.39	2.7
(61486) 2000 QQ42	6.8	3.29 ± 0.02	14.94	*I*	19.36	0.27	2.92	1.1
(61796) 2000 QM183	7.0	4.80 ± 0.04	14.89	*I*	18.97	0.48	2.94	0.6
(61863) 2000 QJ208	1.9	6.02 ± 0.03	16.01	*R*	19.27	0.51	2.43	0.6
(62409) 2000 SR177	10.3	4.40 ± 0.00	14.04	*I*	18.53	0.63	2.98	0.8
(63123) 2000 WB174	7.0	10.88 ± 0.02	14.9	*I*	19.23	0.4	3.02	0.7
(63970) 2001 SG72	2.8	5.24 ± 0.36	15.11	*R*	17.56	0.17	2.35	2.4
(63997) 2001 SX110	2.3	9.76 ± 0.00	15.59	*R*	18.66	0.77	2.34	1.4
(64030) 2001 SQ168	39.3	6.30 ± 0.05	11.14	*I*	17.86	0.7	5.19	1.5
(64345) 2001 UY77	6.5	2.94 ± 0.02	15.04	*I*	19.28	0.21	2.9	1.1
(64897) 2001 YX81	2.2	5.01 ± 0.03	15.66	*R*	18.58	0.18	2.38	0.9
(65714) 1992 VR	2.4	9.64 ± 0.08	15.49	*R*	18.74	0.6	2.47	0.5
(65858) 1997 GL35	3.0	9.47 ± 0.02	15.98	*R*	19.24	0.26	2.55	1.0
(65917) 1998 FG38	2.0	5.87 ± 0.04	15.89	*R*	18.64	0.67	2.44	3.1
(67193) 2000 CY57	16.1	3.10 ± 0.01	13.08	*R*	17.28	0.1	3.2	1.5
(67221) 2000 DP73	1.9	3.87 ± 0.02	15.94	*I*	18.72	0.15	2.35	1.0
(68724) 2002 DH12	1.6	3.02 ± 0.02	16.35	*I*	17.78	0.13	1.91	0.8
(68941) 2002 PX124	3.5	4.25 ± 0.02	15.63	*I*	20.0	0.68	2.72	1.1
(70347) 1999 RA178	4.1	3.86 ± 0.03	15.27	*I*	19.09	0.32	2.53	1.2
(72128) 2000 YW72	1.4	3.19 ± 0.09	16.67	*I*	19.96	0.5	2.2	2.2
(73428) 2002 LP45	9.0	9.30 ± 0.18	14.34	*I*	18.48	0.53	3.15	0.9
(75563) 1999 YA23	4.2	2.50 ± 0.00	15.27	*R*	18.18	0.09	2.56	0.9
(76027) 2000 DK40	4.4	2.68 ± 0.01	15.15	*R*	18.3	0.22	2.62	1.9
(76200) 2000 EL50	11.3	6.76 ± 0.00	13.85	*R*	18.69	0.22	3.22	0.6
(78709) 2002 TV183	5.1	3.75 ± 0.01	14.83	*R*	18.32	0.14	2.57	0.9
(79392) 1997 GC15	1.7	4.55 ± 0.01	16.15	*I*	19.1	0.15	2.32	0.6
(79538) 1998 QN34	2.3	2.92 ± 0.01	15.56	*R*	18.93	0.21	2.25	0.8
(80293) 1999 XS56	2.1	3.19 ± 0.01	15.77	*R*	17.96	0.11	2.22	1.3
(82377) 2001 MG16	3.9	6.53 ± 0.01	15.4	*R*	19.03	0.5	2.67	1.3
(82875) 2001 QB67	5.6	4.48 ± 0.02	14.62	*I*	19.3	0.33	2.8	0.5
(83542) 2001 SP166	5.0	5.45 ± 0.05	15.63	*I*	19.31	0.24	2.84	0.7
(83582) 2001 SJ233	4.0	3.98 ± 0.01	15.34	*I*	18.87	0.34	2.79	0.9
(84024) 2002 PB42	1.8	3.81 ± 0.51	16.04	*I*	19.52	0.32	2.29	2.9
(85485) 1997 RJ2	1.9	5.02 ± 0.00	16.01	*R*	19.1	0.15	2.38	1.2
(86570) 2000 EH38	2.2	3.06 ± 0.00	15.68	*R*	17.82	0.16	2.27	1.2
(88146) Castello	6.0	10.86 ± 0.10	15.21	*R*	18.93	0.62	2.94	1.1
(88601) 2001 QF284	8.5	3.19 ± 0.03	13.71	*I*	19.23	0.47	2.58	1.9
(88765) 2001 SY67	1.9	9.23 ± 0.00	15.99	*R*	19.2	0.65	2.32	0.9
(88790) 2001 SS110	2.6	5.08 ± 0.00	15.29	*I*	18.25	0.12	2.4	1.2
(88848) 2001 ST202	1.7	3.66 ± 0.01	16.16	*R*	18.12	0.16	2.31	2.9
(94195) 2001 BU13	7.9	6.34 ± 1.36	14.63	*I*	19.05	0.27	3.12	2.4
(95284) 2002 CH83	6.5	3.42 ± 0.01	15.06	*I*	19.19	0.34	3.02	1.7
(95971) 2004 LU8	2.3	6.43 ± 0.02	15.57	*I*	19.38	0.71	2.43	1.5
(98291) 2000 SS229	2.0	3.23 ± 0.01	15.89	*R*	18.76	0.37	2.42	1.8
(100257) 1994 SF9	2.7	3.68 ± 0.02	16.22	*I*	19.72	0.36	2.65	0.6
(100724) 1998 BM38	3.6	5.76 ± 0.01	15.6	*R*	19.21	0.27	2.78	1.2
(100997) 1998 QF41	1.4	11.19 ± 0.03	16.56	*R*	19.89	0.99	2.27	1.3
(101375) 1998 UA10	2.8	9.36 ± 0.05	16.09	*R*	19.34	0.55	2.62	2.6
(104010) 2000 DH105	4.2	3.02 ± 0.01	15.25	*R*	19.13	0.31	2.64	1.3

Table 6
(Continued)

Object	Diameter (km)	Period (hr)	H (mag)	Filter	Magnitude	Amplitude (mag)	Semimajor Axis (au)	Phase Angle (°)
(104582) 2000 GX83	4.0	7.54 ± 0.06	15.34	*I*	18.6	0.34	2.73	1.7
(105184) 2000 OZ30	1.6	4.73 ± 0.06	16.28	*R*	20.19	0.89	2.38	0.7
(107681) 2001 FO11	8.4	4.09 ± 0.03	14.5	*R*	18.73	0.11	3.11	1.6
(107879) 2001 FP89	6.7	9.90 ± 0.02	14.99	*I*	18.82	0.51	3.21	1.7
(107929) 2001 FV106	1.9	4.66 ± 0.02	16.94	*R*	19.49	0.45	2.53	2.2
(108174) 2001 HH11	2.7	14.46 ± 0.00	16.17	*I*	18.85	0.69	2.65	1.2
(108639) 2001 NW7	3.1	5.47 ± 0.10	15.89	*I*	19.81	0.8	2.75	1.9
(110088) 2001 SG120	3.4	5.71 ± 0.80	15.68	*R*	19.31	1.21	2.69	2.2
(113040) 2002 RL49	3.2	4.29 ± 0.02	15.84	*R*	19.07	0.19	2.57	1.2
(113104) 2002 RT76	3.4	4.42 ± 0.02	15.7	*I*	18.59	0.25	2.65	0.6
(113326) 2002 RT205	4.2	2.93 ± 0.00	15.24	*I*	18.67	0.18	2.69	1.1
(114967) 2003 QM62	4.0	4.97 ± 0.05	15.37	*I*	19.06	0.22	2.65	1.4
(119085) 2001 NW15	1.7	6.20 ± 0.72	16.22	*I*	19.65	0.78	2.35	1.0
(119920) 2002 EW88	7.1	2.84 ± 0.01	14.86	*I*	18.47	0.12	3.08	1.0
(120884) 1998 RY50	7.0	11.19 ± 0.03	14.9	*R*	19.11	0.6	3.09	1.0
(120988) 1998 XM18	5.1	3.77 ± 0.01	15.57	*R*	19.38	0.35	3.18	0.6
(122035) 2000 GP68	1.5	4.80 ± 0.03	16.5	*I*	19.55	0.57	2.38	1.1
(124497) 2001 RF45	2.6	5.63 ± 0.04	15.33	*I*	18.51	0.2	2.43	1.5
(124636) 2001 SS65	1.9	3.98 ± 0.00	15.98	*R*	18.55	0.16	2.35	1.4
(127472) 2002 RD113	8.5	3.82 ± 0.02	14.46	*R*	18.77	0.16	3.11	1.7
(128914) 2004 TV53	5.5	5.42 ± 0.01	15.43	*R*	19.72	0.69	3.07	1.8
(129501) 1995 HJ5	1.7	5.69 ± 0.04	16.17	*R*	19.66	0.51	2.42	1.8
(132395) 2002 GA97	2.8	5.76 ± 0.04	16.1	*I*	19.13	0.26	2.55	1.7
(134494) 1998 XV67	4.3	27.59 ± 0.00	15.18	*R*	18.37	0.49	2.68	1.0
(137111) 1999 AX18	3.2	8.96 ± 1.81	15.84	*I*	19.54	0.77	2.77	2.0
(140311) 2001 SR319	3.8	4.44 ± 0.02	16.22	*I*	19.79	0.69	2.84	0.5
(140555) 2001 TV203	2.9	7.06 ± 0.04	16.02	*R*	19.49	0.49	2.71	1.0
(140637) 2001 UX21	3.6	4.85 ± 0.00	15.59	*R*	18.89	0.31	2.79	2.1
(141460) 2002 CM111	5.9	3.62 ± 0.02	15.24	*I*	18.88	0.2	3.05	1.2
(141474) 2002 CM219	4.3	4.05 ± 0.01	15.96	*I*	19.58	0.32	3.05	1.5
(146945) 2002 EC20	4.6	6.05 ± 0.05	15.81	*I*	18.89	0.33	3.04	0.6
(147363) 2003 CH10	3.7	3.74 ± 0.01	15.54	*R*	18.3	0.16	2.79	1.8
(147829) 2005 SM261	3.3	3.50 ± 0.01	15.76	*R*	19.28	0.27	2.77	2.0
(148028) 1998 EY12	7.1	4.00 ± 0.02	14.86	*I*	18.89	0.3	2.93	1.5
(150631) 2001 AK48	5.9	5.78 ± 0.00	15.26	*I*	19.36	0.45	3.07	1.5
(151321) 2002 CY133	5.5	13.75 ± 0.04	15.4	*I*	18.96	0.53	3.06	0.6
(151409) 2002 EX125	4.9	5.93 ± 0.04	15.64	*I*	19.63	0.33	3.0	0.5
(154054) 2002 CP148	5.0	5.13 ± 0.05	15.6	*I*	19.58	0.35	3.01	1.5
(154174) 2002 GH86	6.2	5.35 ± 0.02	15.14	*I*	19.15	0.5	3.11	0.6
(154249) 2002 KQ11	5.9	4.62 ± 0.03	15.24	*I*	19.93	0.78	3.16	1.1
(154941) 2004 TP54	7.0	9.02 ± 0.10	14.88	*I*	19.29	0.36	3.24	1.1
(155322) 2006 AR56	6.3	17.52 ± 0.13	15.13	*I*	18.92	0.59	3.17	1.2
(156076) 2001 SJ140	1.4	6.58 ± 0.04	16.64	*I*	19.3	0.58	2.44	1.2
(156087) 2001 SO185	1.4	6.20 ± 0.03	16.57	*I*	19.23	0.63	2.41	1.2
(156664) 2002 JQ98	3.9	3.55 ± 0.01	16.14	*R*	19.2	0.17	2.97	1.4
(156823) 2003 BV60	1.1	4.65 ± 0.03	17.2	*I*	19.76	0.55	2.39	1.4
(156892) 2003 EK22	1.6	6.14 ± 0.08	16.41	*I*	18.32	0.13	2.41	1.9
(157434) 2004 TR358	5.3	2.74 ± 0.00	15.48	*I*	18.94	0.15	3.15	1.5
(158235) 2001 SV293	1.1	11.68 ± 0.03	17.12	*I*	19.43	0.9	2.42	1.8
(158812) 2003 TX57	6.6	3.05 ± 0.00	15.0	*R*	19.58	0.41	3.15	1.1
(164818) 1999 RR41	2.3	7.29 ± 2.20	16.54	*I*	19.7	0.8	2.53	1.6
(165042) 2000 DE110	4.0	3.53 ± 0.02	15.34	*I*	18.81	0.27	2.73	0.6
(166085) 2002 CU117	1.1	5.44 ± 0.04	17.11	*R*	19.27	0.36	2.42	0.8
(167070) 2003 RQ2	2.8	5.37 ± 0.04	16.13	*I*	19.51	0.44	2.6	0.9
(168617) 2000 BH26	2.3	3.31 ± 0.00	16.51	*R*	18.26	0.11	2.61	0.9
(170539) 2003 WJ114	2.6	2.91 ± 0.02	16.3	*R*	18.5	0.07	2.56	1.2
(173748) 2001 RW30	4.4	5.30 ± 0.03	15.92	*I*	19.97	0.65	2.8	0.6
(177083) 2003 FO56	4.4	3.29 ± 0.02	15.89	*I*	19.68	0.39	2.92	1.2
(179273) 2001 UX203	3.1	7.29 ± 0.04	15.91	*R*	19.46	0.89	2.79	2.4
(184738) 2005 SS207	6.5	7.17 ± 0.03	15.06	*I*	18.93	0.44	2.99	1.3
(187654) 2007 EQ61	6.8	6.23 ± 0.00	14.94	*I*	19.71	0.44	3.12	1.3
(191466) 2003 SB273	6.4	4.89 ± 0.02	15.07	*R*	19.8	0.74	3.11	0.6
(198537) 2004 XR111	2.1	3.29 ± 0.00	16.71	*I*	19.34	0.29	2.61	2.5

Table 6
(Continued)

Object	Diameter (km)	Period (hr)	H (mag)	Filter	Magnitude	Amplitude (mag)	Semimajor Axis (au)	Phase Angle (°)
(204498) 2005 CM19	1.8	4.88 ± 0.03	17.09	*I*	19.47	0.46	2.63	1.1
(206443) 2003 SY234	2.5	3.25 ± 0.01	16.33	*I*	19.51	0.46	2.6	1.5
(207264) 2005 EW266	2.7	5.12 ± 0.03	16.17	*I*	19.64	0.58	2.7	0.9
(209739) 2005 EY184	3.0	3.59 ± 0.02	16.01	*I*	18.95	0.31	2.68	1.4
(210634) 2000 FM47	2.3	12.70 ± 0.00	16.59	*I*	18.98	0.53	2.74	3.2
(212122) 2005 EK197	2.1	3.95 ± 0.01	16.7	*R*	19.47	0.36	2.54	0.8
(213447) 2002 AK144	1.0	3.09 ± 0.02	17.47	*I*	19.39	0.34	2.15	1.4
(213705) 2002 TQ377	1.9	6.61 ± 0.00	16.97	*R*	19.77	0.48	2.6	1.3
(213940) 2003 WN72	1.9	8.25 ± 0.00	17.02	*R*	19.36	0.58	2.59	0.9
(223517) 2004 CF80	1.6	3.50 ± 0.02	16.38	*I*	18.66	0.21	2.3	1.7
(224708) 2006 BX114	5.1	4.96 ± 0.01	15.57	*R*	19.77	0.47	3.09	0.6
(225145) 2008 GC	1.1	9.76 ± 0.00	17.2	*I*	19.24	0.59	2.27	0.9
(226311) 2003 CX7	1.2	6.50 ± 0.03	17.01	*I*	19.34	0.73	2.41	2.7
(227807) 2007 BL18	1.0	3.98 ± 0.00	17.31	*I*	19.03	0.21	2.35	2.2
(227828) 2007 CA38	1.1	5.53 ± 0.00	17.17	*I*	19.1	0.24	2.36	2.5
(230532) 2002 XE76	1.5	5.18 ± 0.47	16.45	*R*	19.08	0.57	2.26	2.7
(234712) 2002 JY18	2.1	6.61 ± 0.04	16.77	*I*	19.67	0.66	2.56	1.4
(236426) 2006 DS114	2.2	5.98 ± 0.01	16.61	*I*	19.38	0.51	2.53	2.7
(245906) 2006 QT113	3.2	6.01 ± 0.01	15.82	*I*	19.24	0.65	2.68	0.6
(248012) 2004 EH94	3.3	8.12 ± 0.01	15.74	*I*	19.09	0.66	2.79	2.2
(250039) 2002 CH164	4.0	6.83 ± 0.12	16.09	*I*	19.93	0.5	3.0	2.1
(257594) 1999 RA31	2.2	11.43 ± 0.11	15.61	*I*	18.04	0.37	2.3	1.2
(262158) 2006 SX87	0.8	5.85 ± 0.07	17.86	*I*	20.21	0.56	2.26	0.6
(263058) 2007 HW67	3.9	10.67 ± 0.05	16.18	*R*	19.58	0.62	3.01	1.3
(267938) 2004 EQ19	1.0	6.35 ± 0.00	17.37	*I*	19.32	0.21	2.3	0.9
(271477) 2004 FN20	1.3	5.35 ± 0.06	16.77	*I*	18.63	0.16	2.31	1.4
(272245) 2005 QO125	1.1	6.38 ± 0.03	17.23	*I*	19.38	0.66	2.37	1.3
(275201) 2009 WN159	4.9	3.68 ± 0.03	15.68	*R*	20.07	0.86	3.11	0.5
(281947) 2011 GG31	0.9	4.34 ± 0.04	17.62	*I*	19.41	0.27	2.35	0.9
(289050) 2004 TN172	6.0	5.42 ± 0.02	15.21	*R*	19.48	0.56	3.03	0.8
(293336) 2007 DW86	3.9	6.09 ± 0.02	16.14	*R*	19.79	0.42	2.9	1.0
(305811) 2009 DH105	1.9	7.02 ± 0.06	16.98	*I*	19.75	0.64	2.75	1.2
(305835) 2009 DE137	3.2	5.24 ± 0.03	14.86	*R*	19.78	0.41	2.37	23.5
(307180) 2002 ES65	4.1	5.59 ± 0.01	16.02	*I*	19.08	0.79	3.07	1.5
(317640) 2003 ER23	1.1	7.25 ± 0.04	17.12	*I*	19.17	0.31	2.41	1.9
(319356) 2006 CX59	4.0	2.43 ± 0.01	16.08	*I*	20.22	0.52	3.29	0.7
(320005) 2007 DJ35	5.5	13.04 ± 0.21	15.43	*I*	19.62	0.89	3.11	1.2
(320125) 2007 EQ185	5.2	5.81 ± 0.03	15.55	*R*	19.48	0.36	3.01	0.7
(320796) 2008 EU153	1.9	4.35 ± 0.10	16.92	*R*	19.34	0.25	2.76	1.5
(326169) 2012 BT111	3.9	3.90 ± 0.02	16.18	*R*	19.78	0.38	2.88	1.4
(331451) 2012 HM16	6.2	4.76 ± 0.02	15.16	*R*	19.71	0.5	3.17	0.8
(338477) 2003 GQ49	1.1	2.22 ± 0.01	17.2	*I*	19.82	0.5	2.44	2.6
(338875) 2004 BM50	0.9	5.38 ± 0.02	17.48	*R*	19.77	0.77	2.18	3.0
(340262) 2006 BH156	15.7	13.45 ± 0.26	13.14	*I*	19.58	0.47	5.19	0.3
(347333) 2012 BV19	5.9	4.48 ± 0.02	15.27	*I*	19.37	0.44	3.14	2.7
(348341) 2005 EO51	2.4	2.89 ± 0.02	16.42	*I*	18.9	0.19	2.67	1.0
(348680) 2006 BO75	1.2	4.30 ± 0.04	16.89	*I*	20.03	0.55	2.47	2.1
(349944) 2010 CH32	0.8	7.34 ± 0.04	17.74	*R*	19.28	0.37	2.33	1.1
(351687) 2006 BL46	0.9	4.09 ± 0.00	17.61	*R*	19.63	0.59	2.37	1.3
(351743) 2006 DB74	1.4	2.60 ± 0.01	16.7	*R*	19.32	0.37	2.38	1.2
(359430) 2010 LJ115	2.3	7.20 ± 0.05	16.59	*R*	19.84	0.47	2.56	1.2
(362740) 2011 UE310	1.8	6.81 ± 0.01	17.09	*R*	19.92	0.71	2.64	1.9
(386736) 2010 AZ45	0.9	8.70 ± 0.00	17.61	*I*	19.88	0.46	2.45	1.6
(396362) 2014 DF89	2.3	2.67 ± 0.03	16.53	*I*	19.8	0.26	2.63	1.4
(404441) 2013 GF101	2.8	3.57 ± 0.03	16.9	*I*	19.65	0.31	3.07	1.5
(473304) 2015 RV70	3.9	6.45 ± 0.07	16.18	*I*	20.21	0.9	3.01	0.8
2017 DC73	0.8	8.22 ± 0.00	17.77	*R*	19.61	0.63	2.28	2.3
2018 DH1	0.2	5.01 ± 0.02	20.9	*I*	17.68	0.1	2.1	5.8

Note. Columns are the same as those in Table 4.

(This table is available in its entirety in machine-readable form.)

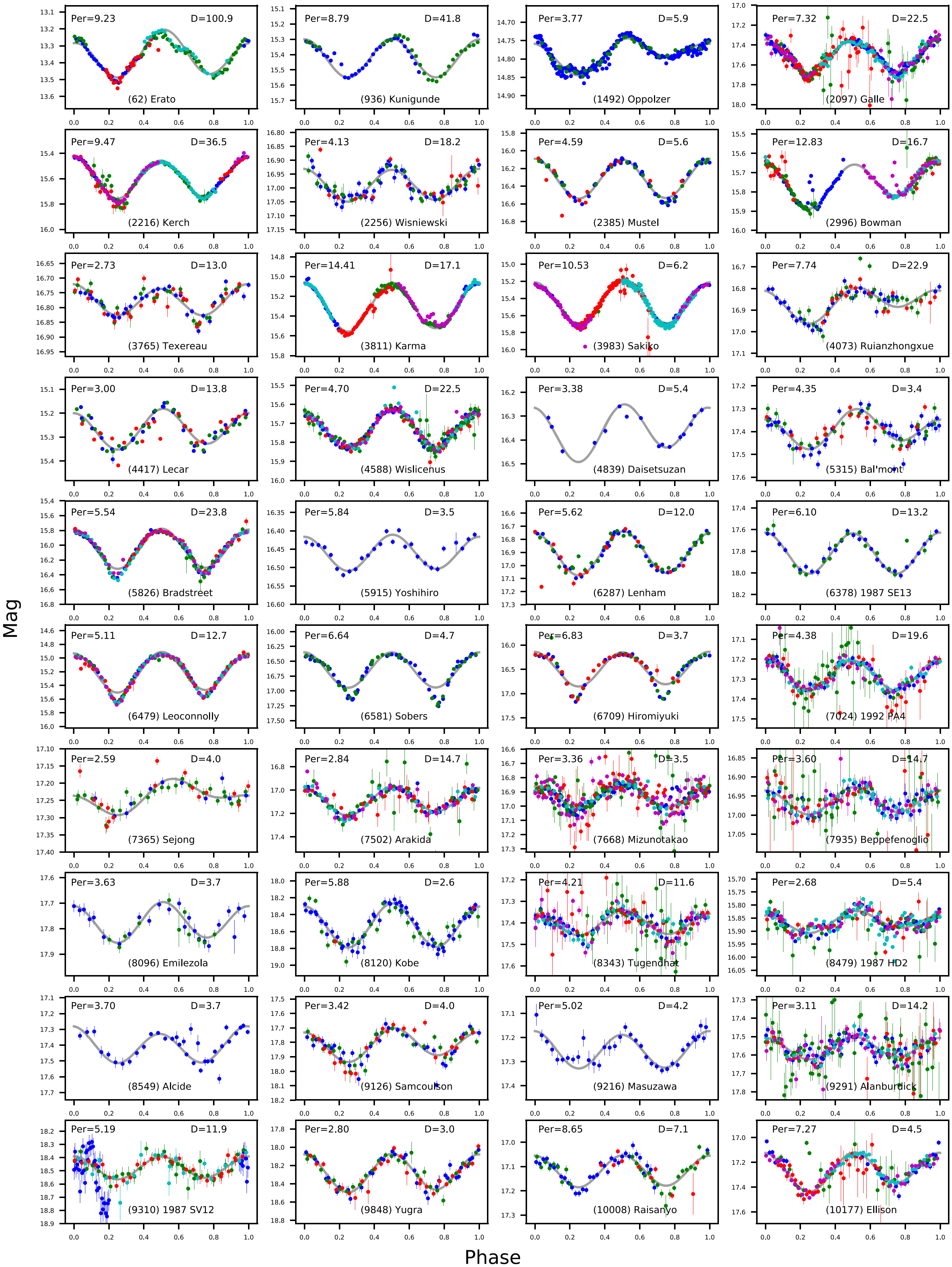

Figure 7. Set of 40 folded lightcurves for $U = 3$ asteroids. The colors represent data points obtained from different dates and the gray line is the fitting result. (An extended version of this figure is available.)

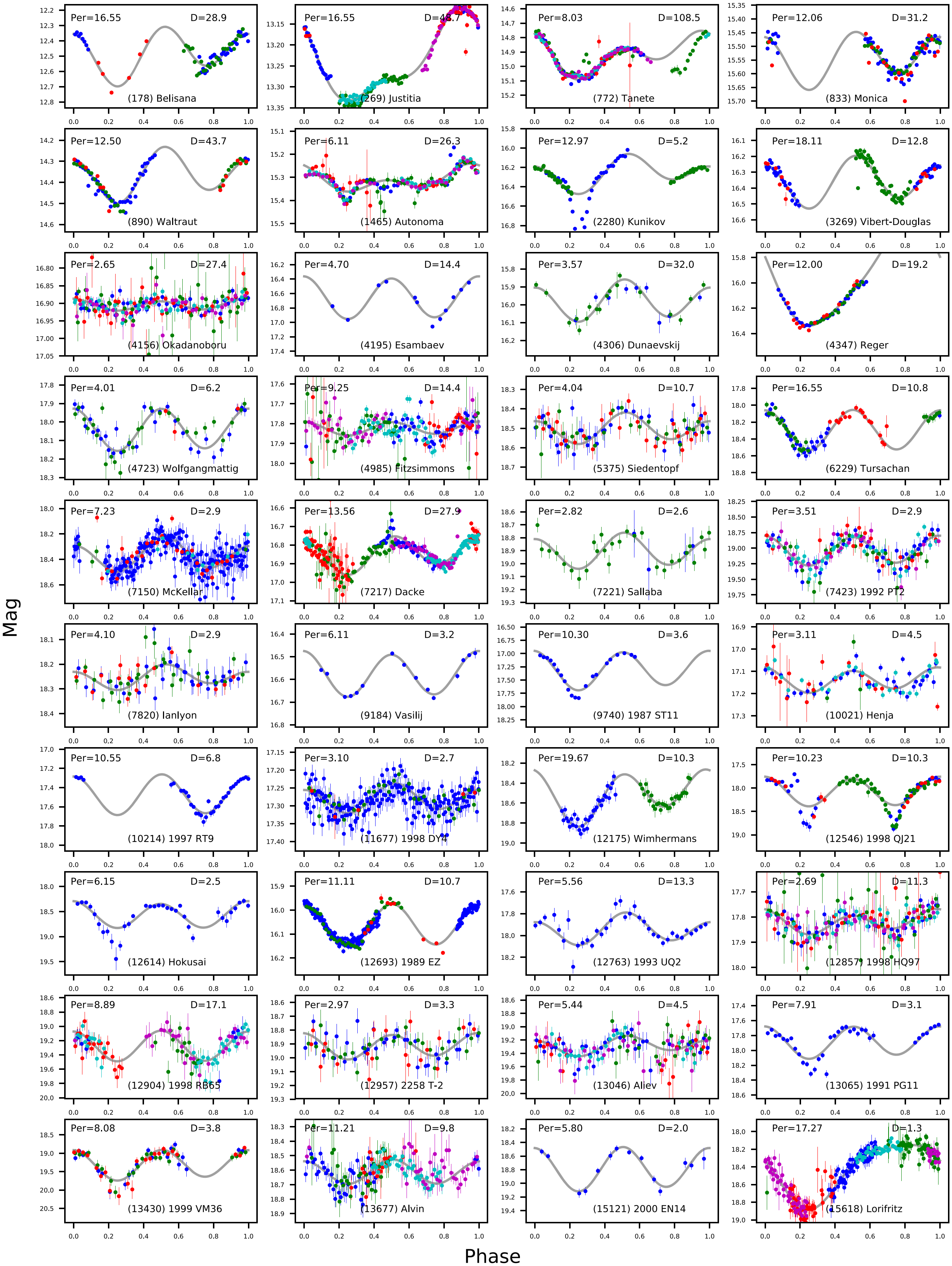

Figure 8. Set of 40 folded lightcurves for objects of $U = 2$. The colors represent data points obtained from different dates and the gray line is the fitting result. (An extended version of this figure is available.)

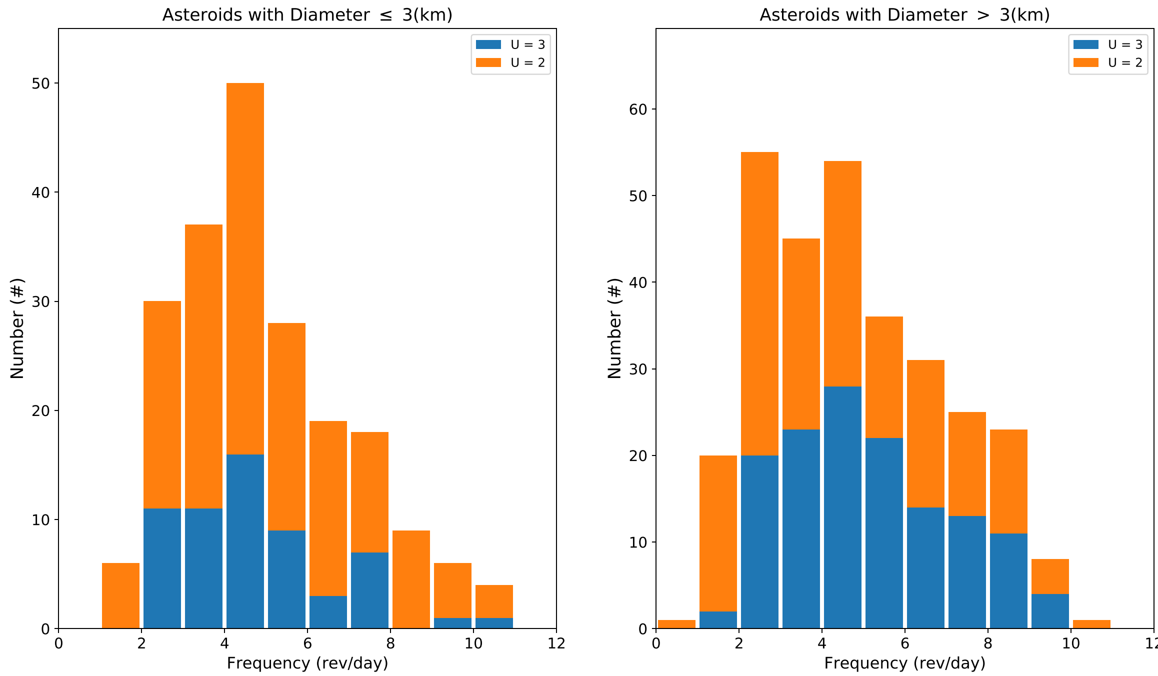

Figure 9. Spin-rate distributions of asteroids of $D \leqslant 3$ (left) and $D > 3$ km (right). The blue and orange colors represent the rotation periods of $U = 3$ and 2, respectively.

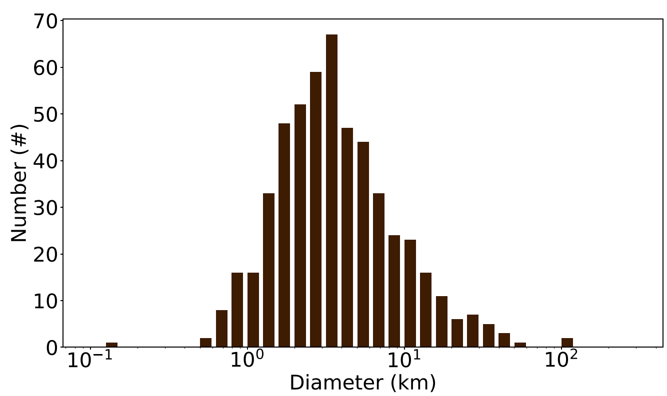

Figure 10. Size distribution of asteroids with $U \geqslant 2$.

Using the 506 reliable rotation periods, the spin-rate distributions were carried out for the asteroids of different sizes (i.e., $D > 3$ and $D \leqslant 3$ km). As seen in Figure 9, our survey is very insensitive to long periods (i.e., frequency of $\leqslant 2$ rev day^{-1}) due to the limited time span for each campaign (i.e., a few days). Moreover, the relatively short period (i.e., period in the order of tens of minutes or shorter) is very unlikely to be detected in our survey due to the deployed cadence. Despite these two factors, no obvious difference is shown between the spin-rate distributions in different diameter ranges. Using the K-S test, we obtained a p-value of 0.4889, which indicates that the distributions cannot be distinguished from each other (i.e., p-value > 0.05). Although the YORP is expected to affect more efficiently on small-sized asteroids, a sample of rotation period of asteroids with a limited size range, like ours (see Figure 10 for the size distribution of our samples in which the diameters of the majority are between 1 and 20 km), is probably unable to reveal the difference in the spin-rate distributions of asteroids with different sizes.

4. Summary

Two surveys of asteroid rotation period were carried out using the CNEOST during 2017 February 26–March 2 and 2018 March 8–12. In total, 4522 asteroid lightcurves were extracted and 506 reliable rotations were obtained from the surveys. In our samples, 13 asteroids have previously published rotation periods in the LCDB and the rotation period comparison shows that our measurements are reliable in general. A very likely SFR candidate, (134291) 2006 DZ6, along with anothr other 15 less likely ones were found. However, their rotation periods need further confirmation. In addition, no obvious difference was found when the preliminary spin-rate distributions were carried out for asteroids using different sizes.

This work is supported in part by the Ministry of Science and Technology of Taiwan under the grants MOST 107-2112-M-008-009-MY2 and MOST 105-2119-M-008-029-MY3, and by the National Natural Science Foundation of China (grants No.11661161013 and 11633009). H.-B.Z. is also supported by the B-type Strategic Priority Program of the Chinese Academy of Sciences (grant No. XDB41000000) and the civil aerospace pre-research project (grant No. D020302), the CAS Key Laboratory of Infrared System Detection and Imaging Technology, Shanghai Institute of Technical Physics, Chinese Academy of Sciences, and the Minor Planet Foundation of Purple Mountain Observatory. J.-H.J. also appreciates the Strategic Priority Research Program on Space Science, the Chinese Academy of Sciences, (grant No. XDA15020302), and the CAS Interdisciplinary Innovation Team.

ORCID iDs

Chan-Kao Chang https://orcid.org/0000-0003-1656-4540

References

Bertin, E., & Arnouts, S. 1996, A&AS, 117, 393
Bowell, E., Harpke, B., & Domingue, D. 1989, in Asteroids II, ed. R. P. Binzel, T. Gehrels, & M. S. Matthews (Tucson, AZ: Univ. Arizona Press), 524
Chang, C.-K., Lin, H.-W., Ip, W.-H., et al. 2016, ApJS, 227, 20
Chang, C.-K., Lin, H.-W., Ip, W.-H., et al. 2017, ApJL, 840, L22
Chang, C.-K., Lin, H.-W., Ip, W.-H., et al. 2019, ApJS, 241, 6
Chang, C.-K., Waszczak, A., Lin, H.-W., et al. 2014, ApJL, 791, L35
Harris, A. W. 1996, LPI, 27, 493
Harris, A. W., Young, J. W., Bowell, E., et al. 1989, Icar, 77, 171
Holsapple, K. A. 2007, Icar, 187, 500
Kaasalainen, M., Lamberg, L., Lumme, K., et al. 1992a, A&A, 259, 318
Kaasalainen, M., Lamberg, L., & Lumme, K. 1992b, A&A, 259, 333
Lacerda, P., & Luu, J. 2003, Icar, 161, 174
Linville, D., Jiang, H., Michalik, D., Wilson, S., & Ditteon, R. 2017, MPBu, 44, 173
Lo, K.-J., Chang, C.-K., Lin, H.-W., et al. 2020, AJ, 159, 25
McNeill, A., Fitzsimmons, A., Jedicke, R., et al. 2016, MNRAS, 459, 2964
Polishook, D., Moskovitz, N., Binzel, R. P., et al. 2016, Icar, 267, 243
Pravec, P., & Harris, A. W. 2000, Icar, 148, 12
Pravec, P., Kušnirák, P., Šarounová, L., et al. 2002, in Proc. Asteroids, Comets, Meteors, ACM 2002, ed. B. Warmbein (Noordwijk: ESA), 743
Rozitis, B., Maclennan, E., & Emery, J. P. 2014, Natur, 512, 174
Rubincam, D. P. 2000, Icar, 148, 2
Salo, H. 1987, Icar, 70, 37
Tedesco, E. F., Cellino, A., & Zappalá, V. 2005, AJ, 129, 2869
Warner, B. D., Harris, A. W., & Pravec, P. 2009, Icar, 202, 134
Willmer, C. N. A. 2018, ApJS, 236, 47
Zacharias, N., Finch, C. T., Girard, T. M., et al. 2013, AJ, 145, 44

Publ. Astron. Soc. Japan (2020) 72 (5), 79 (1–10)
doi: 10.1093/pasj/psaa069
Advance Access Publication Date: 2020 July 27

A study of the physical properties of an active asteroid (6478 Gault)

Zhong-Yi Lin,[1,*] Yu-Li Cheng,[2] Jean-Baptiste Vincent,[3] Xi-Liang Zhang,[4,5] Wing Huen Ip,[1] and Hsin-Chang Chi[2]

[1]Institute of Astronomy, National Central University, Taoyuan, 32001, Taiwan
[2]Department of Physics, National Dong Hwa University, No. 1, Sec. 2, Da Hsueh Rd. Shoufeng, Hualien 97401, Taiwan
[3]DLR Institute of Planetary Research, Berlin, Germany
[4]Yunnan Observatories (YNAO), Chinese Academy of Sciences, Kunming 650216, China
[5]Key Laboratory of the Structure and Evolution of Celestial Objects, Chinese Academy of Sciences, Kunming 650216, China

*Email: zylin@gm.astro.ncu.edu.tw

Received 2020 April 29; Accepted 2020 June 30

Abstract

In 2019 January, the appearance of asteroid 6478 Gault immediately attracted attention because this object exhibited a long and thin tail that was quite different from the usual asteroids. This unexpected morphology placed asteroid 6478 Gault into the catalogue of active asteroids. We acquired photometric and spectroscopic observations on 37 nights from 2019 January to April using several telescopes, including LOT (1 m telescope) and SLT (40 cm telescope) at Lulin Observatory, and the 2.4 m telescope at Lijiang station of Yunnan Observatory. We did not find any reliable value for the rotational period of Gault during 2.5 hr and 5 hr observations on 2019 January 26 at Lijiang station and March 25 at Lulin Observatory, respectively. We classified 6478 Gault as a Q-type asteroid using visible spectrum and photometric measurements, including colors ($B - V_{\rm avg} = 0.764 \pm 0.045$, $V - R_{\rm avg} = 0.450 \pm 0.023$), and relative reflectance. By using Finson–Probstein analysis, the grain size for Gault's tail 2 is larger than 20 μm.

Key words: minor planets, asteroids: general — minor planets, asteroids: individual (6478 Gault)

1 Introduction

Discovered in 1988, 6478 Gault (formerly 1998 JC1, and simply "Gault" hereafter), with the orbital elements $e = 0.194$, $a = 2.305$ au, $i = 22\overset{\circ}{.}8$, is a main-belt asteroid. Gault has an absolute magnitude of 16.11 in the V band (Ferrín et al. 2019) and a diameter ranging from 2 km to 4 km depending on the assumption of a geometric albedo of 0.2 (for S-type) or 0.04 (for C-type). It was an unremarkable object until late 2018, when the Hawaii ATLAS survey first noticed that it had suddenly brightened and developed a tail (Tonry et al. 2018). This made it a rare member of the class of active asteroids which is intermediate between asteroids and comets. These active asteroids have asteroid-like semi-major axes and Tisserand parameters (TJ > 3.0), but they can also exhibit comet-like mass loss, manifested optically as resolved comae and tails (Jewitt 2015). Until early 2020, about two dozen known active asteroids have been found, and some have been observed to repeat their activity during multiple orbit passages: 133P/Elst–Pizarro (Elst et al. 1996; Hsieh et al. 2004), 238P/Read (Hsieh et al. 2009,

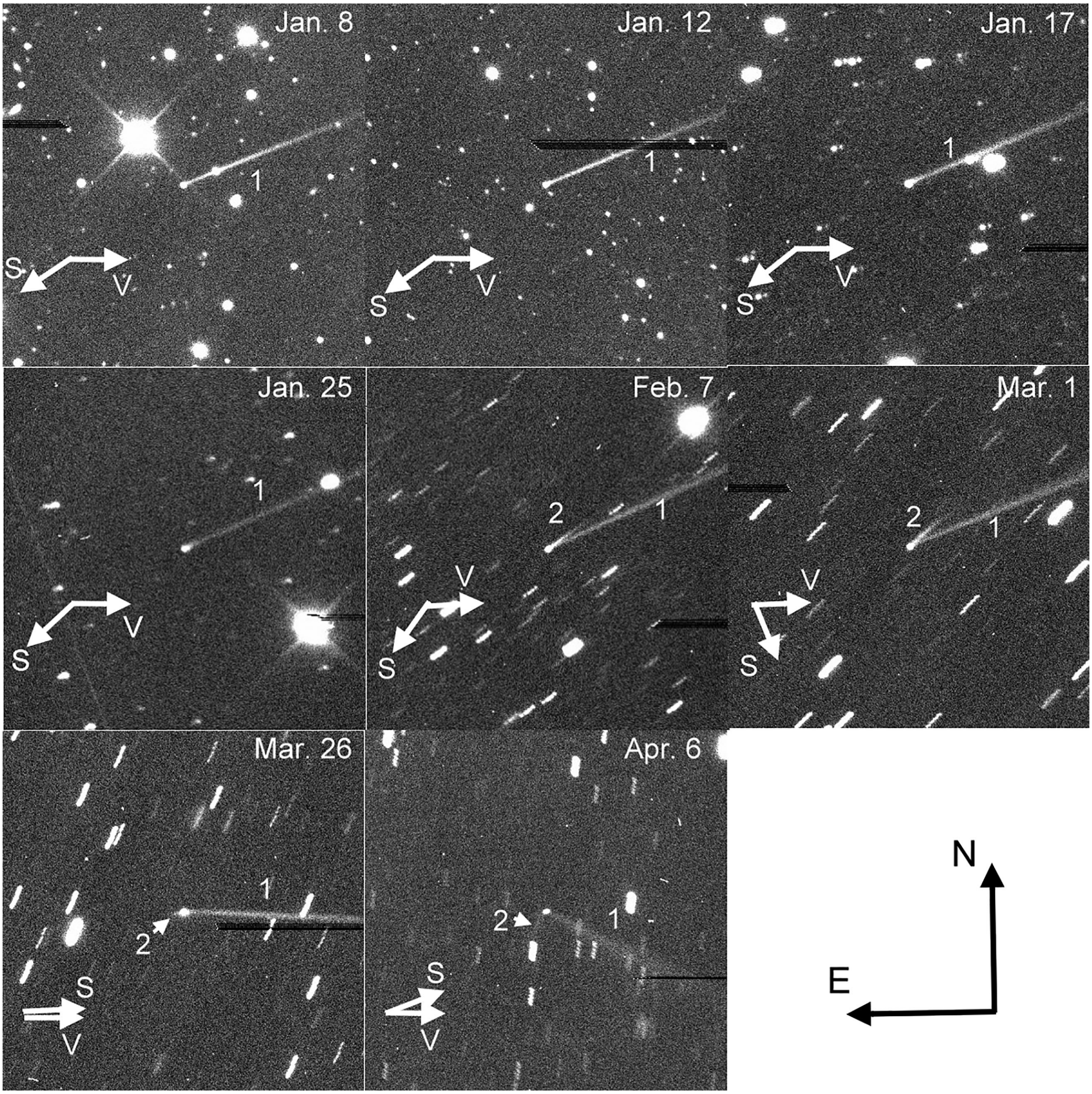

Fig. 1. Monitoring images of the evolution of the 6478 Gault dust tail by SLT of Lulin Observatory from 2019 January to April. The field of view is about 2.′6 and the arrows indicate the solar direction (S) and the negative of Gault's velocity (V). The tails are identified with numbers (1, 2, and 3) in order of discovery.

2011, 2018b), 288P (Hsieh et al. 2012b, 2018b; Agarwal et al. 2016), 259P/Garradd (Jewitt et al. 2009; Hsieh & Chavez 2017), 313P/Gibbs (Hsieh et al. 2015; Hui & Jewitt 2015), 324P/La Sagra (Hsieh et al. 2012a; Hsieh & Sheppard 2015), and 358P/PANSTARRS (Hsieh et al. 2018b). Several mechanisms have been proposed to explain such transient phenomena, including rotational breakup (e.g., 311P/PanSTARRS, Jewitt et al. 2013), asteroid impact (e.g., 596 Schelia; Bodewits et al. 2011; Moreno et al. 2011) and sublimation of subsurface ice in main belt comets (e.g., 133P/Elst–Pizarro; Hsieh et al. 2010). Studying each active asteroid to understand its mechanism of activity is therefore necessary because it can provide clues to solar system phenomena such as primordial volatiles from MBC sublimation and material composition from rotation and impacts (Kleyna et al. 2019).

Monitoring images of Gault exhibiting its long, thin tail are shown in figure 1. A debris tail from Gault was first spotted on 2019 January 5 (Smith et al. 2019). The tail also turned up in archival data in 2018 December from the ATLAS and Pan-STARRS telescopes in Hawaii. In mid-January, a second, shorter, tail was detected by the Canada–France–Hawaii Telescope in Hawaii and the Isaac Newton Telescope in Spain, as well as by other observers (Hale et al. 2019a, 2019b; Jehin et al. 2019; Lee 2019a; Ye et al. 2019b). The third one was detected by the NOT telescope after Earth passed through the projected orbital plane of Gault in early 2019 April (Jewitt et al. 2019). An analysis of the first two tails suggested the sudden release of tens of millions of kilograms of dust between 2018 October 28 and December 30 (Hui et al. 2019; Jewitt et al. 2019; Moreno et al. 2019; Ye et al. 2019a). The very low velocity of the ejected dust grains (Hui et al. 2019; Jewitt et al. 2019; Kleyna et al. 2019; Moreno et al. 2019; Ye et al. 2019a) and the absence of detectable gas in visible spectra (Jewitt et al. 2019) imply that the activity was not driven by the sublimation effect. Interestingly, Kleyna et al. (2019) determined that Gault has a rotation period of about 2 hr from their photometric data obtained in early 2019 February. Note that their lightcurve might not be derived directly from the nucleus because of coma contamination. But, it is noteworthy that this value is close to the spin barrier of ∼2.2 hr estimated for a rubble pile asteroid, meaning its internal strength is too weak to sustain a fast rotation (e.g., Pravec & Harris 2000). As the archival data back in 2013 revealed an earlier phase of dust activity (Chandler et al. 2019), these authors therefore ruled out a single-impact collision as the origin of the activity and suggested instead that the most likely scenario to explain the activity of this asteroid is breakup of the surface material or landslides resulting from a YORP-induced rotational disturbance (Chandler et al. 2019; Hui et al. 2019; Jewitt et al. 2019; Kleyna et al. 2019; Marsset et al. 2019; Moreno et al. 2019; Ye et al. 2019a).

Although Gault is dynamically linked to the 25 Phocaea collisional family of S-type classification, its spectral and compositional similarity with this family had not been fully investigated (Sanchez et al. 2019). For example, near-infrared spectroscopy revealed that Gault is a silicate-rich (Q- or S-type) object (Marsset et al. 2019), but broadband colors and some visible spectra revealed that this active asteroid is more similar to C-type asteroids than S-types (Ye et al. 2019a; Jewitt et al. 2019; Lee 2019b). The purpose of our work is to perform detailed time-series photometric measurements with spectroscopic data obtained from the Lulin and Lijiang Observatories to determine the rotation period and exact taxonomic class of Gault. In section 2 the observation and data reduction will be described. The results of the data analysis and discussions in rotation period and taxonomic identification will be given in section 3. In section 4, we constrain the grain size of Gault's tail using a Finson–Probstein analysis of the comprehensive dataset from 2019 January to April, and this is followed by a summary in section 5.

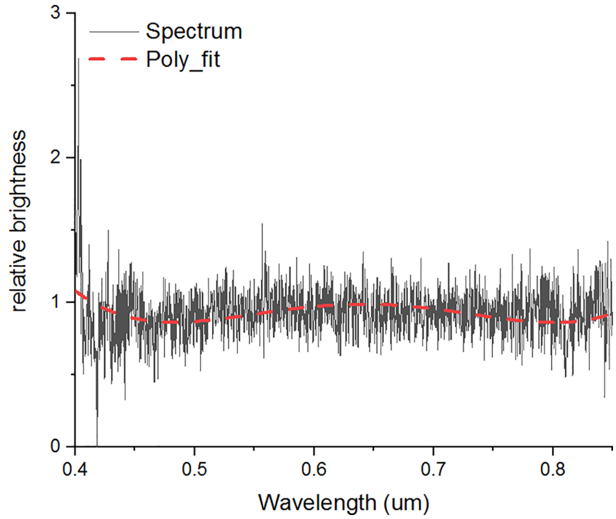

Fig. 2. A YFOSC spectrum of Gault obtained at the Lijiang 2.4 m telescope showing how it reflected light as a function of wavelength. To minimize the standard deviation of the errors, we smooth our asteroid spectrum by the polynomial curve shown with a dashed line. (Color online)

2 Observations

2.1 Spectrum and lightcurve

The optical spectrum of Gault was taken on 2019 March 15 using the Lijiang 2.4 m telescope at Lijiang station of Yunnan Observatories. The longitude, latitude, and altitude of the Lijiang station are 100°01′48″, 26°42′42″, and 3193 m, respectively. The Yunnan Faint Object Spectrograph and Camera (YFOSC) mounted on the Cassegrain telescope of 2.4 m aperture can quickly switch from photometry to spectroscopy. The detailed parameters of the telescope and YFOSC can be found in Wang et al. (2019). We used Grism 3, which provides a relatively low dispersion ($R \sim 2000$ at 600 nm pixel^{-1}) and wide wavelength coverage (3400 ∼ 9100 Å). The resulting spectrum divided by a standard solar analog star (G5 IV, SA 102-1081) and normalized at 550 nm is shown in figure 2. To minimize the standard deviation of the errors for attempting taxonomic classification, we smoothed our data by curve fitting with polynomial functions. This was done using poly fitting from the IDL routine. The degree of the polynomial was selected to be four, such that the fit produces the smallest least squares fitting residuals. The obtained fitting curve is also shown as dashed lines in figure 2.

Time-series photometry with 1 min and 2 min cadences were also acquired with the Johnson-*R* filter in YFOSC on 2019 January 26 and in LOT on 2019 March 25. The field of view (FOV) of YFOSC is about 10′, with a plate scale of 0.″57 pixel^{-1}. The time duration for the January 26 observation was about 2.5 hr, and the airmass varied between

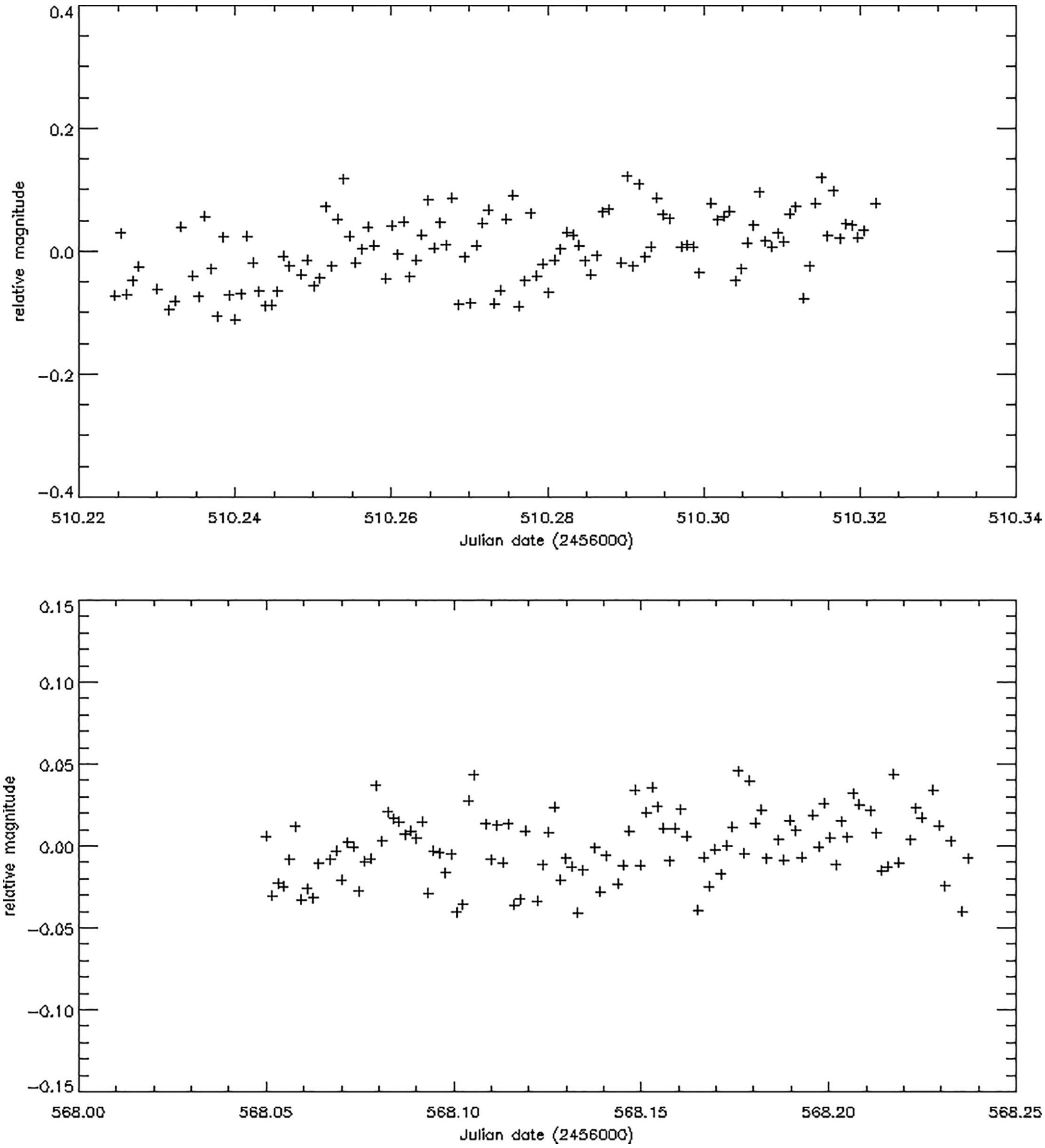

Fig. 3. Lightcurves of Gault obtained at Lijiang 2.4 m telescope (upper panel) on 2019 January 16 and the Lulin 1 m telescope (bottom panel) on 2019 March 25. The observational durations at the Lijiang and Lulin observatories werre 2.5 hr and 5 hr, respectively. We cannot find the reliable rotational period as suggested by Kleyna et al. (2019).

1.29 and 1.67. The time span in the March observation was about 5 hr, and the images were acquired at a variety of airmasses from 1.10 to 2.11. Differential photometry using at least seven reference stars on all images was carried out by means of IDL routines based on DAOPHOT. For aperture photometry of both Gault and the reference stars, the mean value of the full-width half-maximum (FWHM) of the point spread functions of the reference stars in each image was used. In other words, the flux of the asteroid and those of the reference stars were computed using the same aperture size. The normalized lightcurves of Gault at Lijiang and Lulin observatories are shown in figure 3.

2.2 Imaging and colors

The photometric observations of Gault were made using the 1 m telescope (LOT) and the 16″ Ritchey–Chrétien telescope (SLT) at the Lulin Observatory, Taiwan. The LOT with a FOV of 11′ was installed in 2002 by the Institute of Astronomy, National Central University. The 2K × 2K charge-coupled device (CCD) camera, Sophia, manufactured by Apogee Instruments has a pixel scale of 0.″39 pixel^{-1}. The SLT with a U42 CCD imaging camera was attached to the Cassegrain focus of the telescope. The focal length of the SLT was 2500 mm (with a 0.75× reducer), resulting in a 1 × 1 pixel-scale binning of 0.″79 pixel^{-1}. The FOV of this system was

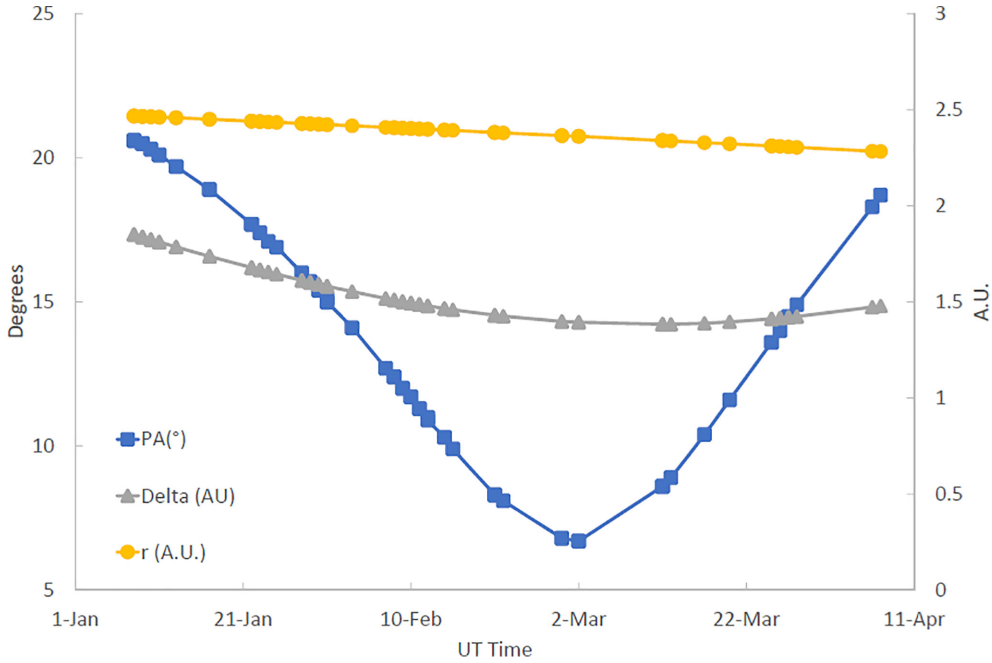

Fig. 4. Behavior of Δ (triangle), the distance from the observer to the object, *r* (circle), the distance from the sun to the object, and *PA* (square), the phase angle of the object. The symbols depict the UT dates when observations were acquired from Lulin Observatory. (Color online)

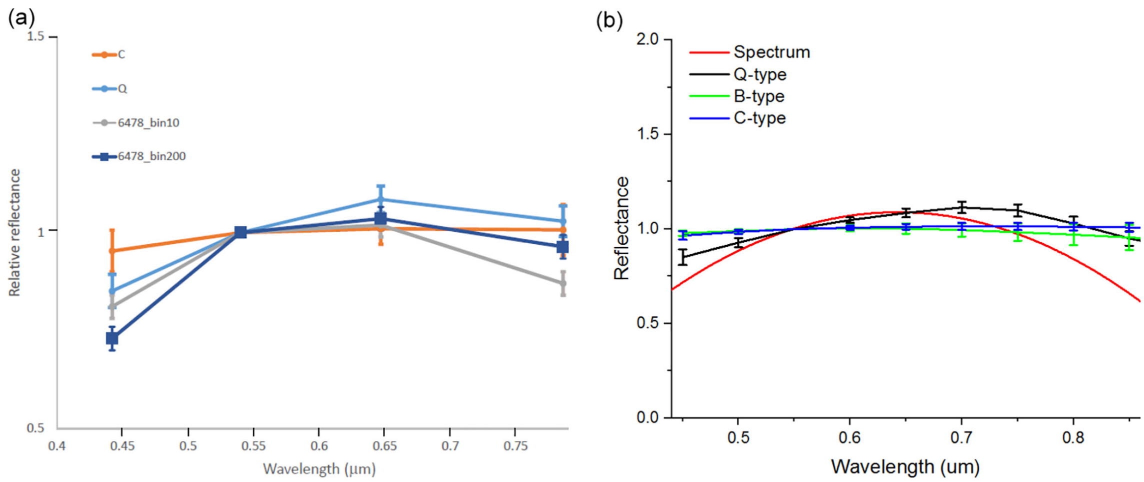

Fig. 5. Reflectance spectrum of 6478 Gault from Lijiang station normalized to 0.55 μm in the range 0.45–0.9 μm. Left panel: the smoothed asteroid spectrum with a 1 nm (bin10) and 20 nm (bin200) boxcar average and comparison to that of the C- and Q-type asteroids (Bus–DeMeo taxonomy). We note that a better match in this smoothed spectrum between 6478 Gault and Q-type asteroids is to rely on *R*- and *I* filters. Right panel: the result of the M4AST online tool; the Gault spectrum after polynomial curve fitting is much closer to Q-type classification than the other two classes (B and C). (Color online)

$27' \times 27'$. At LOT, Gault was observed for 39 nights from 2019 January to April with *B*, *V*, *R*, and *I* Johnson filters centered at 0.45, 0.55, 0.67, and 0.81 μm, respectively. At SLT, we mostly observed in the same time slot as LOT did through a Bessel R-filter with some additional *B*, *V*, and *I* images. The observational details of the color photometric measurements are shown as dots in figure 4. The asteroid phase angle and geocentric and heliocentric distances changed in the ranges 20°.7 to 17°.4, 1.85 to 1.38 au, and 2.47 to 2.28 au, respectively. The data reduction followed standard procedures, including bias and dark-frame subtraction and flat-field correction. The dark frames and the flat frames were taken at the beginning and the end of each observation night. To calibrate the resulting magnitudes and colors in LOT, a number of photometric standard fields selected from the list of Landolt (1992) were also observed during the photometric nights.

Table 1. M4AST results relative to the first three curve matches.*

Type	χ^2	Standard error	Mean squared error
Q	0.0026425	0.0482152	0.0022594
B	0.0027270	0.0546955	0.0026987
C	0.0036647	0.0628235	0.0035658

*Computed by normalizing the spectrum and the taxonomic type to their median values.

3 Results and discussion

3.1 Spectroscopic results

To assign a taxonomic type for the Gault spectra presented in this paper we used the Bus–DeMeo taxonomy (DeMeo et al. 2009). This taxonomy is based on principal component analysis of the *VNIR* spectra. We classified our spectra in this taxonomy using two methods: (i) by smoothing the spectrum comparing with reflectance values (see sub-subsection 3.2.2) computed from the Bus–DeMeo photometry, and (ii) by performing curve matching with the 25 classes defined by the taxonomy (using the M4AST website; Popescu et al. 2012). These two methods were used to determine how closely the asteroid spectra can be fitted by the standard spectrum of each class. The first method is to smooth the asteroid spectrum with the 1 nm and 20 nm boxcar average and then to compare this curve to the standard spectrum. The smoothed spectrum (figure 5a) shows a curved spectrum (within the limits of noise) in agreement with the Q-type classification indicated in the literature (a visible spectrum by Bus & Binzel 2002). The second one involves first fitting the spectrum with a polynomial curve and then comparing this curve to the standard spectrum at the wavelengths given in the taxonomy. In our approach to fitting, we decided to use the chi-square (χ^2) test for goodness of fit (Bevington & Robinson 1992). Table 1 displays the first three curve matches by the lowest standard deviation. After using the M4AST online tool, Gault can also be associated with Q-type asteroids (figure 5b). This taxonomic classification is consistent with the results from near-infrared spectra exhibiting deep absorption bands near 1 and 2 μm consistent with an S- or Q-type surface composition (Marsset et al. 2019; Sanchez et al. 2019) and from our visible photometric measurements (see sub-subsection 3.2.1). It is noteworthy that the other two possibilities (B- and C-class) have been reported by Lee (2019b) and Jewitt et al. (2019), the spectrum in short wavelengths is very noisy (figure 5), and the chi-square values in table 1 for those three classes are very close to each other if we take the errors into account. We therefore need photometric data (i.e., colors) to tell us whether Gault is S-complex or C-complex.

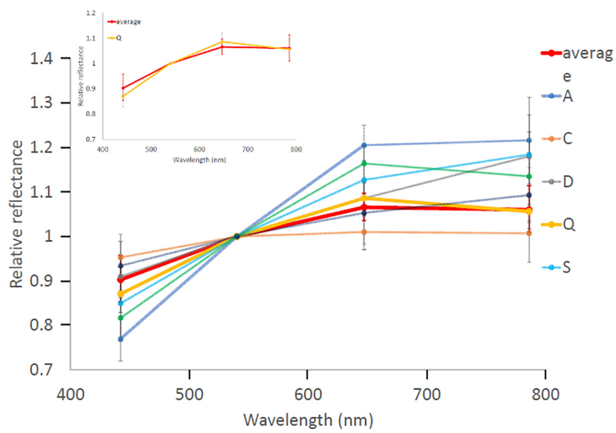

Fig. 6. The averaged and comparison-relative reflectance of Gault shows that the Q-type relative reflectance is the best fit (upper left panel). (Color online)

3.2 Photometric results

3.2.1 Spectral class and colors

The measurements of Gault at Lulin were carried out with *B*, *V*, *R*, and *I* filters with the aim of deriving its taxonomic type according to its surface colors. The Gault images using the sequence *R*–*B*–*R*–*V*–*R*–*I*–*R* were acquired to remove the effect of magnitude variation due to the asteroid's rotation, but the effect of phase angle was not corrected because the change of phase angle is small ($\sim 3^\circ\!.2$), and the correction of phase reddening was not done here. By subtracting the standard solar colors ($B - V = 0.665$, $V - R = 0.367$, and $V - I = 0.705$; Howell 1995), we obtained the averaged relative reflectance of Gault in figure 6. The relative reflectance is normalized to 1 at 0.55 μm (*V*-band). Through comparing with the known relative reflectance (i.e., the Bus–DeMeo system), we classified Gault as a Q-type asteroid.

The colors of Gault are compared with those of other asteroid spectral types from Dandy, Fitzsimmons, and Collander-Brown (2003), and all the data points and averaged values are shown in figure 7. Gault is closer to S-complex. A silicate-rich object (S- or Q-type) is consistent with the result from the near-infrared spectrum (Marsset et al. 2019; Sanchez et al. 2019) and makes Gault a slight relative of the 25 Phocaea collisional family.

3.2.2 Rotational period

Kleyna et al. (2019) had an extensive series of observations but they found no convincing lightcurve, meaning the rotational period could only be estimated at ~1 hr for one peak, and ~2 hr for two peaks. Moreno et al. (2019) also did not get a rotational signature from their long series of observations acquired at the TRAPPIST North and South telescopes. Instead, Ferrín, Fornari, and Acosta (2019) found a rotational period of $P_{\rm rot} = 3.360 \pm 0.005$ hr and showed

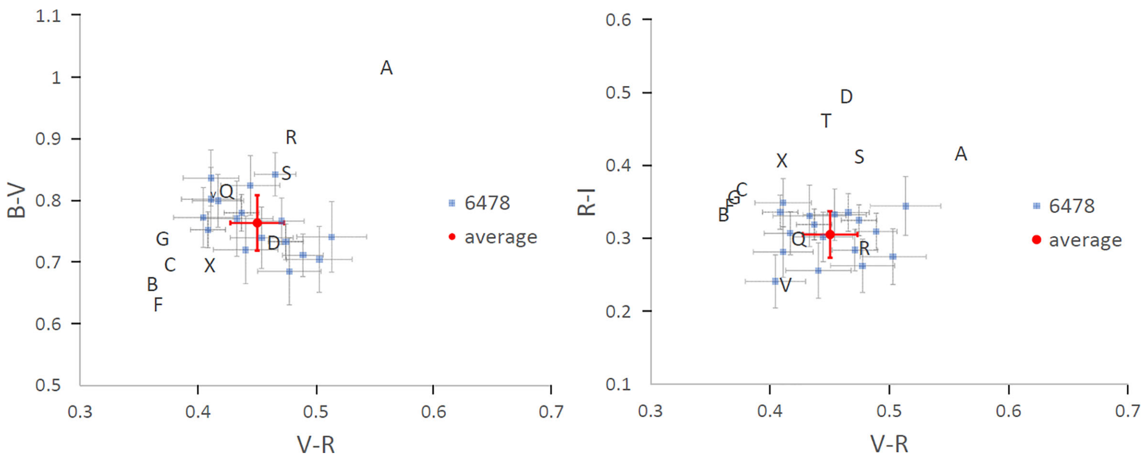

Fig. 7. Obtained asteroid Gault colors (marked with error bars) in color diagrams ($R-I$) vs. ($V-R$) in the left panel and ($B-V$) vs. ($V-R$) in the right panel. The blue dots are the data from 2019 January to April, and the red dot is the average value. (Color online)

evidence that 6478 might be a binary from their comprehensive dataset acquired on 41 nights from 2019 January to June. Jewitt et al. (2019) did not get any reliable period via their 3 hr observations. They claimed that the lack of a measurable lightcurve is consistent with Gault having a shape that is close to azimuthally symmetric, or a rotation vector parallel to the line of sight, or with the scattering cross-section being dominated by dust (Jewitt et al. 2019; Sanchez et al. 2019). Our photometric time-series data shown in figure 3 uses 5000 km ($\sim 6\farcs6$) as a measured radius on 2019 January 26 and March 25. Using the Lomb–Scargle method (Lomb 1976) to analyze these data, we did not find any reliable value for the rotational period of Gault. The same invariance of the photometry is observed using 10000 km ($\sim 13\farcs2$). In addition, we used 2 hr and 3.36 hr as the folding interval to represent the original lightcurve, but still could not get any meaningful values. Expect for the explanation made by Jewitt et al. (2019) and Sanchez et al. (2019), the non-repeating short-term variation in our dataset might possibly be caused by low-level cometary activity hiding the nucleus.

4 Tails

We report the detection of several dust tails in our dataset; their measured positions are given in table 2.

Tail 1 is the most prominent and can be observed in all images. It extends in the anti-velocity direction, with a lag of about 22° until the beginning of 2019 March. Afterwards, the tail direction migrates up to 29° ahead of the anti-velocity vector. This is due to the rapid change of observing geometry as the object reaches closest approach to Earth on March 11.

Tail 2 is only visible for a few weeks. We detected it for the first time on February 7, and it had almost completely faded away by April 6.

We interpret these tails as signatures of dust emission from the asteroid from at least two independent events. In order to constrain the timeline and physical properties of the dust grains present in those tails, we performed a Finson–Probstein analysis of the tail geometry (Finson & Probstein 1968). This model describes the motion of dust particles ejected from a cometary nucleus, accounting for solar gravity and radiation pressure. It leads to a geometric description of the dust environment, typically a grid of *synchrones* and *syndynes* which represent respectively the locations of particles released at the same time, or with the same size. Although simple, this model is commonly used in cometary science and leads to a robust description of the particles present in cometary tails, as well as good constraints on their time of emission. We use here the implementation described in Vincent (2014), with the code available at *www.comet-toolbox.com*.

At first, the Finson–Probstein analysis shows that dust emitted continuously from the asteroids in the last three months of 2018 would lead to a broad tail encompassing both tails 1 and 2. In order to reproduce the observations, we need to consider several discrete events. Each event creates one tail, and the width of each tail informs us about the duration of the dust release.

By fitting tail width/orientation over the full dataset, we get consistent constraints that can explain all the observations. Our analysis shows that dust was emitted during two separate events:

- Tail 1 (the longer) was created over a period of two weeks, from 2018-10-25 to 2018-11-9.
- Tail 2 (the shorter) was created over a period of 10 d, from 2018-12-29 to 2019-1-8.

Table 2. Position of tails in the active asteroid 6478 Gault.

Date (UT)	r_h* (au)	Δ* (au)	PsAng* (°)	PsAMV* (°)	Tail 1	Tail 2
January 8.75	2.468	1.853	303.4	269.7	~292	
January 12.83	2.461	1.799	305.2	269.9	~292	
January 17.87	2.451	1.737	307.5	270.1	~293	
January 25.75	2.435	1.645	312.1	270.7	~293	
February 7.83	2.409	1.518	323.5	271.7	~295	~310
March 1.58	2.364	1.396	21.4	272.7	~292	~307
March 26.58	2.310	1.416	92.6	271.1	~267	~90
Aprl 6.67	2.285	1.473	101.0	269.5	~243	~150

*r_h and Δ are the geocentric and heliocentric distances in au. PsAng is the position of the extended Sun–comet vector, measured from north toward east. PsAMV is the negative of the target's heliocentric velocity vector, measured from north toward east.

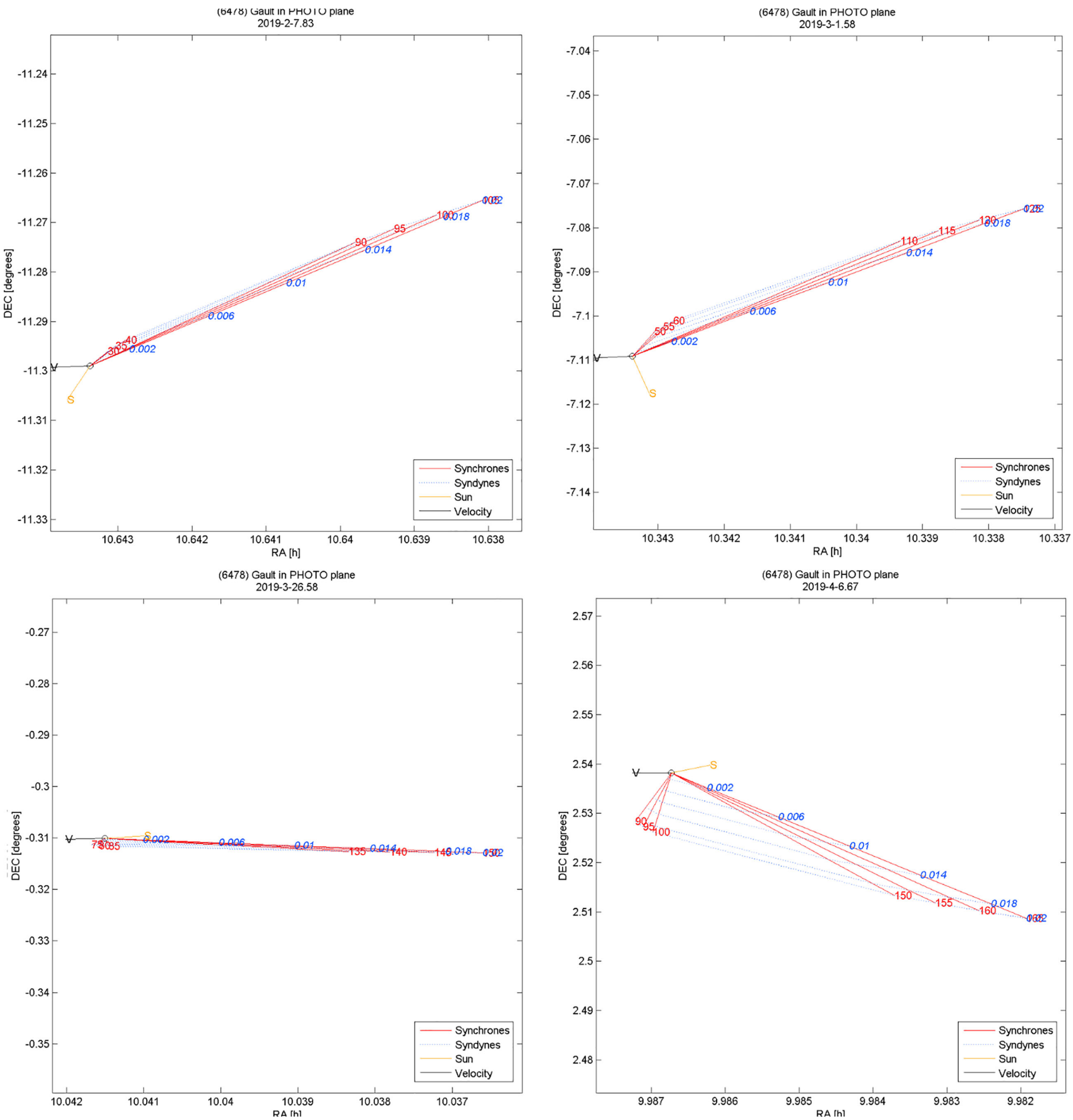

Fig. 8. Best-fitting Finson–Probstein diagrams for dates showing both tails (see figure 1). (Color online)

Figure 8 shows the best-fitting Finson–Probstein diagrams for dates showing both tails. Our model can reproduce both tails, and is consistent with the results published by Hui, Kim, and Gao (2019).

Tail 1 always extends beyond the borders of our images, and we cannot accurately constrain the size of its grains. However, tail 2 is finite in our dataset and extends to at most 0.4 arcmin from the asteroid. Beyond that, the tail photometric signal cannot be distinguished from the image background. This puts a strong upper limit on the beta ratio of the particles, which describes their sensitivity to the radiation pressure and is a function of their size: above 0.1 μm, smaller particles are more easily swept away than larger ones.

From the extent of tail 2, and within the limits of the instrument sensitivity at the edge of the tail, we derive a maximum beta value of 0.02, which for typical material would indicate a grain size larger than 20 μm (Burns et al. 1979). This falls within the range determined by Hui, Kim, and Gao (2019).

Our model assumes that dust grains leave the nucleus with zero relative velocity. It is possible that larger grains were also emitted with some velocity above the escape speed of Gault, but this cannot be constrained from our observations.

5 Summary

We acquired photometric and spectroscopic observations on 37 nights from 2019 January to April using several telescopes, LOT (1 m telescope) and SLT (40 cm telescope) at Lulin Observatory, and the 2.4 m telescope at Lijiang station of Yunnan Observatory. The results are summarized as follows:

(i) The low amplitude of our lightcurve data cannot confirm the rotation period of ~2 hr (Kleyna et al. 2019) or ~3.36 hr (Ferrín et al. 2019) for Gault. These results are compatible with an asteroid observed pole-on or an object having a spherical shape, akin to asteroid Ryugu and Bennu, or low-level cometary activity at the time of observation.

(ii) Through comparing the known relative reflectance (i.e., the Bus–DeMeo system) and average colors ($B - V_{avg} = 0.764 \pm 0.045$, $V - R_{avg} = 0.450 \pm 0.023$), Gault can be classified as a Q-type asteroid.

(iii) By comparing the spectrum of Gault with known classes defined by the Bus–Demeo taxonomy, we confirmed that our spectrum is very similar to Q-type asteroids. As a result of photometric and spectroscopic measurements, Gault's physical properties is closer to the Phocaea collisional family instead of the Tamara family.

(iv) By using Finson–Probstein analysis, the grain size for tail 2 is larger than 20 μm. Unfortunately, we cannot accurately constrain the size of tail 1's grains due to the limitation of the FOV.

Acknowledgments

We particularly acknowledge the staffs of the Lijiang 2.4 m telescope and the Lulin 1.0 m telescope for providing assistance with our observations. This publication has made use of data collected at Lulin Observatory, partly supported by MOST grant 108-2112-M-008-001. This work was supported by MOST 105-2112-M-008-002-MY3, MOST 107-2119-M-008-012, and MOST 108-2112-M-008-004 from the Ministry of Science and Technology of Taiwan. Analysis of the project also funded by the National Science Foundation of China (NSFC, No. U1731122).

References

Agarwal, J., Jewitt, D., Weaver, H., Mutchler, M., & Larson, S. 2016, CBET, 4306, 1
Bevington, P. R., & Robinson, D. K. 1992, Data Reduction and Error Analysis for the Physical Sciences (New York McGraw-Hill)
Bodewits, D., Kelley, M. S., Li, J.-Y., Landsman, W. B., Besse, S., & A'Hearn, M. F. 2011, ApJ, 733, L3
Burns, J. A., Lamy, P. L., & Soter, S. 1979, Icarus, 40, 1
Bus, S. J., & Binzel, R. P. 2002, Icarus, 158, 146
Chandler, C. O., Kueny, J., Gustafsson, A., Trujillo, C. A., Robinson, T. D., & Trilling, D. E. 2019, ApJ, 877, L12
Dandy, C. L., Fitzsimmons, A., & Collander-Brown, S. J. 2003, Icarus, 163, 363
DeMeo, F. E., Binzel, R. P., Slivan, S. M., & Bus, S. J. 2009, Icarus, 202, 160
Elst, E. W., Pizarro, O., Pollas, C., Ticha, J., Tichy, M., Moravec, Z., Offutt, W., & Marsden, B. G. 1996, IAU Circ., 6456, 1
Ferrín, I., Fornari, C., & Acosta, A. 2019, MNRAS, 490, 219
Finson, M. L., & Probstein, R. F. 1968, ApJ, 154, 353
Hale, A., Berry, R., & Weiland, H. 2019a, CBET, 4594, 2
Hale, A., Weiland, H., & Berry, R. 2019b, CBET, 4597, 1
Howell, E. S. 1995, PhD thesis, University of Arizona
Hsieh, H. H., et al. 2012a, AJ, 143, 104
Hsieh, H. H., et al. 2012b, ApJ, 748, L15
Hsieh, H. H., et al. 2015, ApJ, 800, L16
Hsieh, H. H., et al. 2018a, AJ, 156, 223
Hsieh, H. H., & Chavez, J. 2017, CBET, 4388, 1
Hsieh, H. H., Ishiguro, M., Knight, M. M., Micheli, M., Moskovitz, N. A., Sheppard, S. S., & Trujillo, C. A. 2018b, AJ, 156, 39
Hsieh, H. H., Jewitt, D. C., & Fernández, Y. R. 2004, AJ, 127, 2997
Hsieh, H. H., Jewitt, D., & Ishiguro, M. 2009, AJ, 137, 157
Hsieh, H. H., Jewitt, D., Lacerda, P., Lowry, S. C., & Snodgrass, C. 2010, MNRAS, 403, 363
Hsieh, H. H., Meech, K. J., & Pittichová, J. 2011, ApJ, 736, L18
Hsieh, H. H., & Sheppard, S. S. 2015, MNRAS, 454, L81
Hui, M.-T., & Jewitt, D. 2015, AJ, 149, 134

Hui, M.-T., Kim, Y., & Gao, X. 2019, MNRAS, 488, L143
Jehin, E., Ferrais, M., & Moulane, Y. 2019, CBET, 4606, 1
Jewitt, D. 2015, AJ, 150, 201
Jewitt, D., Agarwal, J., Weaver, H., Mutchler, M., & Larson, S. 2013, ApJ, 778, L21
Jewitt, D., Kim, Y., Luu, J., Rajagopal, J., Kotulla, R., Ridgway, S., & Liu, W. 2019, ApJ, 876, L19
Jewitt, D., Yang, B., & Haghighipour, N. 2009, AJ, 137, 4313
Kleyna, J. T., et al. 2019, ApJ, 874, L20
Landolt, A. 1992, AJ, 104, 340
Lee, C.-H. 2019a, Astronomer's Telegram, 12468, 1
Lee, C.-H. 2019b, AJ, 158, 92
Lomb, N. R. 1976, Ap&SS, 39, 447
Marsset, M., et al. 2019, ApJ, 882, L2
Moreno, F., et al. 2011, ApJ, 738, 130
Moreno, F., et al. 2019, A&A, 624, L14
Popescu, M., Birlan, M., & Nedelcu, D. A. 2012, A&A, 544, A130
Pravec, P., & Harris, A. W. 2000, Icarus, 148, 12
Sanchez, J. A., Reddy, V., Thirouin, A., Wright, E. L., Linder, T. R., Kareta, T., & Sharkey, B. 2019, ApJ, 881, L6
Smith, K. W., Denneau, L., Vincent, J.-B., & Weryk, R. 2019, CBET, 4594, 1
Tonry, J. L., et al. 2018, PASP, 130, 064505
Vincent, J. 2014, in Asteroids, Comets, Meteors 2014, ed. K. Muinonen et al. (New York: Association for Computing Machinery), 565
Wang, C.-J., et al. 2019, Res. Astron. Astrophys., 19, 149
Ye, Q., et al. 2019a, ApJ, 874, L16
Ye, Q., Kelley, M. S. P., Bodewits, D., Bolin, B., Chang, C.-K., & Lin, Z.-Y. 2019b, Astronomer's Telegram, 12450, 1

Planetary and Space Science 195 (2021) 105131

Contents lists available at ScienceDirect

Planetary and Space Science

journal homepage: www.elsevier.com/locate/pss

Low dispersion spectra of lunar impact flashes in 2018 Geminids

Masahisa Yanagisawa [a,*], Yuki Uchida [a], Seiya Kurihara [a], Shinsuke Abe [b], Ryota Fuse [b], Satoshi Tanaka [c], Keisuke Onodera [c,d], Fumi Yoshida [e], Hsin-Chang Chi [f], Zhong-Yi Lin [g], Jim Lee [h], Taichi Kawamura [i], Ryuhei Yamada [j]

[a] Department of Engineering Science, The University of Electro-Communications, Japan
[b] Department of Aerospace Engineering, Nihon Univ, Japan
[c] Institute of Space and Astronautical Science, Japan Aerospace Exploration Agency, Japan
[d] School of Physical Sciences, Department of Space and Astronautical Science, The Graduate University for Advanced Studies (SOKENDAI), Japan
[e] Planetary Exploration Research Center, Chiba Institute of Technology, Japan
[f] Department of Physics, National Dong Hwa University, Taiwan
[g] Graduate Institute of Astronomy, National Central University, Taiwan
[h] Taipei Astronomical Museum, Taiwan
[i] Institut de Physique du Globe de Paris, University of Paris Diderot, France
[j] School of Computer Science and Engineering, Aizu University, Japan

ARTICLE INFO

Keywords:
Visible and near-infrared spectrum
Lunar impact flash
Geminids

ABSTRACT

Lunar impact flashes have been observed at collisions of meteoroids against the non-sunlit lunar surface at speeds exceeding 10 km s^{-1}. We detected 13 flash candidates between 6.2 and 9.9 in R-magnitude on December 15, 2018 during the Geminids meteor activity. Two or three observatories confirmed eleven of them. We obtained their spectra in the wavelength range between 400 and 870 nm. They are continuous and red, with best-fitted single blackbody spectra indicating the temperatures of about 2000–4000 K. The temperatures for a few successive movie frames at 16 ms or 25 ms intervals decrease with time. Incandescent ejecta, consisting of melt droplets or dust, and the radiant floor of an impact crater could be the source of these flashes, except for the initial stages. At the beginning of some flashes, we found an excess of fluxes at short wavelengths of less than about 600 nm. The composites of two blackbody spectra may fit the spectra better where their temperatures are about 2000 K and 6000 K. The contribution of a high-temperature vapor plume, generated at the very beginnings of the impact phenomena, could be important.

1. Introduction

At collisions in the solar system, there are many cases where the collisions occur at speeds exceeding 10 km s^{-1}, which almost cannot be reproduced in laboratory experiments (e.g., Kurosawa et al., 2012a). In such a collision, melting, evaporation, and ionization of silicates occur, which do not occur at speed lower than this. Understanding of high-speed collisions accompanying such processes is an essential issue in planetary sciences. Not only numerical simulations (e.g., Nemtchinov et al., 1998a; Nemtchinov et al., 1998; Artemieva et al., 2000) but also many laboratory experiments have been conducted to reveal the nature of impact vaporizations (e.g., Schultz 1996; Sugita et al., 2003; Schultz and Eberhardy 2015). They use proxy target materials such as dolomite or calcite that evaporate at lower impact velocities (Kurosawa et al., 2012b). The knowledge obtained through these experiments was successfully applied to interpreting the phenomena at the spacecraft's impact on Comet 9P/Tempel 1 at 10 km s^{-1} (Deep Impact). It was used to derive the surface properties of the comet (Schultz et al., 2007; Ernst and Schultz 2007). However, our knowledge about the impact phenomena at much higher velocities is still limited. We can approach this problem from the observation of lunar impact flashes.

Spectral information is important to study the mechanism of lunar impact flashes. Madiedo et al. (2018) observed a flash on March 25, 2015 at both near-infrared and visible wavelengths in their MIDAS project (Madiedo et al., 2019a). Its V-band magnitude was about 7 at the beginning, then the brightness decreased with time, and their cameras recorded the flash for about 0.2 s. They assumed blackbody radiation and estimated its temperature to be about 4000 K at the initial phase,

* Corresponding author. 5-37-6-202 Tsurumaki, Tama-shi, Tokyo, 206-0034, Japan.
E-mail address: yanagi.uec@gmail.com (M. Yanagisawa).

https://doi.org/10.1016/j.pss.2020.105131
Received 15 November 2019; Received in revised form 27 July 2020; Accepted 27 October 2020
Available online 4 November 2020

followed by temperatures of about 3200 K after the peak of its brightness. Unfortunately, the exposure timings of their two cameras, one for the visible and the other for the near-infrared wavelengths, were not synchronized. Each frame is time-stamped with an accuracy of 0.01 s. However, the difference of the exposure timings less than 0.01 s could lead to a non-negligible error in their temperature derivation because the time constant of the brightness variation of lunar flashes is generally not so long, especially at their beginnings.

A lunar monitoring project NELIOTA (Xilouris et al., 2018), launched by ESA, started observations in 2017. Two cameras attached to a telescope of 1.2 m in aperture at the National Observatory of Athens observe the flashes at the R- and I-bands almost simultaneously. Derivations of temperatures assuming blackbody radiation are possible. As the first scientific result from the project, Bonanos et al. (2018) obtained temperatures between 1600 and 3100 K for ten flashes. Avdellidou and Vaubaillon (2019) then analyzed 55 flashes in the NELIOTA database. They found the temperature ranging between approximately 1300 and 5800 K with the typical value of about 2500–2600 K. Liakos et al. (2020) summarized results of the first 30 months of the NELIOTA project and showed that the temperatures distribute between 1700 and 5700 K and two-thirds of them were 2000–3500 K. These groups also reported a decrease in temperature with time. The problem of synchronization of the cameras remains though they describe that the synchronization is better than 6 ms (Bonanos et al., 2018; Liakos et al., 2019). For example, one of the flashes (ID 21 in Avdellidou and Vaubaillon 2019, ID28 in Liakos et al., 2020) appears first only in the I-band, then in both bands. The I-band magnitude is almost the same in the successive two frames. The exposure of the R-band camera probably ended before the I-band, then the flash appeared and raised to its peak, and the I-band camera accumulated about half of that total light energy. After the end of the exposure of the I-band camera, the I-band camera accumulated another half of the total light energy in the next frame. The R-band camera accumulated light energy only in the second frame. Typical lunar impact flashes are characterized by sudden brightening and decay, and its time constant is roughly the frame interval of the NELIOTA cameras (33 ms), except for the bright ones such as about 6 in magnitude or brighter. Therefore, even a small difference in exposure timing (e.g., 6 ms) could result in a non-negligible error in the temperature estimation. The scatter of the temperatures in a wide range may be due to the non-perfect synchronization.

The analyses of frames recorded by a color digital camera that was set to a movie mode at 50 frames s^{-1} also made the temperature estimation possible (Madiedo et al., 2019b). For a bright flash of about 4 in magnitude in visible wavelengths on January 21, 2019, they calculated the B-, V-, and R-magnitude of the flash from the images in the red-, green-, and blue-channel of the image data. Based on the assumption of blackbody radiation and the effective wavelengths of these bands, they obtained 5700 K for the temperature of the flash. There is no problem in the synchronization in this observation. They do not report the temporal evolution of its temperature, probably because of the small aperture (100 mm in diameter) of the telescope to which the camera was attached. At the same time, the flash was recognized for 0.28 s by their other observing system. The temperature is the same as the highest ones obtained by NELIOTA. We will discuss the high temperature later.

Spectral observation of lunar impact flashes, however, has not been conducted yet. As part of the Japan-France collaborative project, that is, the joint observation of meteoroids' impacts as lunar seismic sources (Yamada et al. 2011, 2019), an observation campaign was conducted during the December Geminids activities in 2018. In the campaign, we detected 13 flashes by simple spectral cameras for visible and near-infrared wavelengths (Yanagisawa and Kakinuma, in prep.). Though the resolution of the spectra is quite low, we will examine whether the single blackbody approximation adopted in the multi-band observations is appropriate or not. Further, we will discuss what the dominant source of the lunar impact flashes is.

As one of the major annual meteor showers, the characteristics of Geminids have been well-studied. Their density, 2.9×10^3 kg m^{-3}, is the highest among the meteoroids associated with major showers and the sporadic background (Babadzhanov 2002). Their tensile strength of $\sim 10^5$ Pa (Beech 2002) suggests that Geminids would not be fluffy aggregates as expected for cometary materials. Spectral observations of meteors show the depletion of sodium in Geminids, probably due to the solar heating during their perihelion passage (Kasuga and Jewitt 2019, Abe et al., 2020). The orbital similarity between Geminids and an asteroid 3200 Phaethon indicates that the meteoroids result from debris shed from the asteroid (reviewed in Vaubaillon et al., 2019). Its perihelion distance is only 0.14 AU, and it is classified as one of the active asteroids (Jewitt et al., 2015). A project of a flyby mission to the asteroid is also in progress for launch in 2022 (Arai etal., 2018). Many lunar impact flashes during the Geminid meteor shower activities have been reported (e.g., Cooke et al., 2007; Yanagisawa et al., 2008; Suggs et al., 2014; Ortiz et al., 2015; Madiedo et al., 2019c; Liakos et al., 2020). The increase of dust around the moon due to the Geminids' lunar impacts was also found by a dust detector onboard the LADEE lunar orbiter in 2013 (Szalay et al., 2018). Spectral observation of Geminid lunar impact flashes would contribute importantly to the studies in these fields.

We describe our observations in Chapter 2 and explain how to derive spectra in Chapter 3. We show the spectra and brightness magnitudes of the lunar impact flashes in Chapter 4. The temperatures of the flashes and meteoroids' masses are also shown in Chapter 4. We discuss the possible problem in a single blackbody model and the source of the flashes in Chapter 5. The conclusions are described in Chapter 6.

2. Observations

2.1. Observations by spectral cameras

At the University of Electro-Communications (UEC) in Tokyo, Japan (35°39′28″ N in latitude, 139°32′37″ E in longitude, and 80 m in elevation), observations were made with two spectral cameras. One was attached to a Newtonian telescope of an aperture of 450 mm and a focal length of 2025 mm. The other was attached to a Schmidt-Cassegrain telescope with a focal reducer of an aperture of 280 mm and an effective focal length of 940 mm.

The camera attached to the 450 mm telescope is an ASI174MM manufactured by the ZWO company. We removed the cover glass of the camera and glued a blazed type grating on the cover glass of a CMOS image sensor (SONY IMX174MM). The grating has 70 grooves per mm and sold as "Transmission Grating Beamsplitters" by the Edmund Optics company. The other one attached to the 280 mm telescope is a GS3-U3-15S5M-C manufactured by the Point Grey company. We removed the cover glass of the camera and glued the same type of gratings on the cover glass of a CCD image sensor (SONY ICX825). We call the observing system with the 450 mm telescope "System1" and the other "System2" from now on.

We do not apply collimators that make the converging light from the primary mirrors of the telescopes into parallel light rays before the gratings. The converging light directly enters the gratings, passes through them, and is focused on the image planes of the silicon sensor arrays. The no-collimator is not a standard way to use gratings but makes spectral images bright. Spectral resolutions are about 23.9 and 26.5 nm $pixel^{-1}$ for the System1 and System2, respectively.

For Sytem1, the pixel size of the image sensor is 5.86×5.86 μm, and its resolution, 1936×1216 pixels, makes its frame size 11.3×7.13 mm. Its field of view is 19.2×12.1 arc-minutes when it is attached to the telescope. The gain and exposure time of the camera were set to 40 dB and 16 ms, respectively. Inter-frame durations are negligible, and the frame interval was almost the same as the exposure time, that is, 16 ms. The camera was connected to a personal computer with a USB3.0 cable, and an application, "Fire Capture 2.4," developed by Torsten Edelmann, was used for capturing movies in the 16bit-SER format while the bit depth of the camera signal is 12 bits. For the observations of the Flashes A to F described below, movies were stored into a solid-state drive. Then

Table 1
Summary of observations.

Flash	Time (UT) on December 15, 2018	latitude[a]	longitude[a]	Impact angle[b]	number of frames[c]	Observatories[d]
A	08 h 17 m 08s	−21	−39	47	4	1, 2
B	08 h 29 m 35s	30	−57	67	10	1, 2, NU
C	08 h 58 m 50s	30	−40	56	2	1, NU
D	09 h 09 m 48s	−5	−50	66	2	1, NU
E	09 h 44 m 05s	−26	−49	50	2#	2, NU
F	09 h 46 m 16s	5	−70	85	2	1
G	10 h 23 m 07s	−15	−35	48	2	1, NU, Lu
H	10 h 25 m 42s	−60	−71	20	4#	2, NU, Lu
I	10 h 28 m 47s	−12	−48	60	6	1, 2, NU, Lu
J	10 h 35 m 56s	30	−50	63	1	1, NU
K	10 h 54 m 34s	25	−55	70	2	1, NU
L	11 h 22 m 13s	−3	−74	76	4	1, 2, NU, Lu
M	11 h 35 m 52s	23	−29	50	1	1, 2, NU

[a] Selenographic latitude and east longitude.
[b] Measured from local horizons.
[c] The number of frames, where each flash is recognized, observed by System1. Those observed by System2 are shown with #.
[d] Systems or observatories that detected each flash. 1: System1, 2: System2, NU: Nihon Univ, and Lu: Lulin observatory.

the pixels were binned into 2 × 2, and movies were stored into a hard disk drive for the other flashes. The binning makes the spectral resolution about 47.8 nm pixel^{-1}.

For Sytem2, the pixel size of the image sensor is 6.45 × 6.45 μm, and its resolution, 1384 × 1032 pixels, makes its frame size 8.93 × 6.66 mm. Its field of view is 32.7 × 24.2 arc-minutes when it is attached to the telescope. The gain and exposure time of the camera were set to 24 dB and 25 ms, respectively. The frame interval was 25 ms. The camera was connected to a personal computer with a USB3.0 cable, and “Fire Capture 2.5” captured movies into a hard disk drive in the 16bit-SER format while the bit depth of the camera signal is 14 bits. No binning was applied.

An observation campaign expecting lunar impact flashes due to Geminids was conducted between 10th and December 16, 2018. The weather was fine at UEC only in the night on the 15th. The age of the moon was 8.0–8.2 (a waxing moon). System1 and System2 were operated for 08:04:08–13:08:56 UT and for 07:58:10–13:11:38 UT, respectively. After the observations, an application, “ser_scan” developed by us, scanned the SER movies and found 13 flash candidates in the movies recorded by System1 and System2. We named them A to M flashes (Table 1). Supplementary video (online version only) shows the movie of Flash I. Madiedo et al., 2019c observed at least 11 lunar impact flashes on 13th and December 14, 2018 from two different sites in Spain. They calculated the probability of these flashes being associated with Geminids to be 90%. The flashes we observed on 15th December, therefore, must be generated due to the impacts of the Geminids’ meteoroids onto the lunar surface.

Fire Capture stamps the time of a computer clock on each frame in a movie. The intervals of the stamped times should be constant and the same as the exposure time if the stamped times are exact and there is no frame drop. The frame drops occur when image data transferred through the USB3.0 cable and stored into the disk exceeds the capability of the systems. We examined the intervals of the stamped times in successive frames over plus-minus 1 min around the times of the flashes. They fluctuate around 16 ms for System1, and 25 ms for System2. However, a longer interval is followed by a shorter one. Therefore, the average of the intervals over some frames is constant. We decided that the recording speed into the drive is fast enough and there is no frame drop. The application seems to stamp time when it stores a frame in a drive. It is slightly different from the time of the start or the end of the exposure of the camera. The difference would lead to the fluctuation of the intervals of stamped times.

2.2. Observations at the other observatories

Observations with normal digital movie cameras were conducted at Nihon University (NU) in Chiba-prefecture, Japan (35°43′31″ N in latitude, 140°03′32″ E in longitude, and 28 m in elevation) by a telescope of 400 mm in aperture. At Lulin Astronomical Observatory, Taiwan (23°28′07″ N in latitude, 120°52′25″ E in longitude, and 2862 m in elevation), they observed by two telescopes of 152 mm and 200 mm in apertures and normal digital movie cameras.

All the flashes, except A and F, were detected simultaneously at NU, which was located 47 km east of UEC. They did not start observations at the time of Flash A. Flash F was out of the field of view of their camera. Lulin observatory, which was located 2300 km south-west of UEC along the earth’s surface, started observations later at 10:16 UT due to the local time difference between Japan and Taiwan. Flashes G to M were expected to be found, and we confirmed four of them (Flashes G, H, I, and L). They paused observations at the times of Flashes J and M. Flash K was not detected probably due to the frame drop described in the previous section.

The most significant source of the false-positive detections of lunar impact flashes is the reflection of sunlight by artificial satellites or space debris. The best way to distinguish the lunar flashes from the satellite glints is by examining the movies obtained at least two observatories separated far enough. Most of the human-made objects are orbiting in and below the geosynchronous orbit. The distance to them from observatories is at most about 40,000 km, while the moon is about ten times far away. Their positions on the lunar disk are therefore different between the observatories, while a lunar flash appears at the same position. Simultaneous detections of the G, H, I, and L flashes both in Japan and Taiwan clearly show that they were the lunar phenomena. For the other flashes, we calculated the parallax of a satellite located at 40,000 km in the lunar direction between the observations at UEC and NU. It is about one-tenth of the angular diameter of the moon. We examined the positions of the flash-images on the lunar disk on the frames obtained by the two observatories. They agree with the accuracy of one-hundredth of the lunar angular diameter despite the blurred images due to the spectral dispersion of images obtained by the spectral cameras. The possibility of satellite glints thus is discarded completely for the eleven flashes. For the other two flashes, we examined whether cataloged satellites or space debris passed in front of the lunar disk accidently. We examined the positions of 17,754 satellites or space debris listed in the two-line element orbital datasets downloaded from Space-Track[1] on both 15th and December 17, 2018 using an application “StellaNavigator 10” by the Astro Arts company. We found no human-made object around the moon that moved slowly enough to be misinterpreted as a lunar flash at the times of Flash A. A geostationary satellite, Gorizont 23, was found at 0.5° from the lunar disk center in the celestial south-east direction at the time of Flash F. It was close to the south-eastern edge of the disk 1 min before

[1] Space-track: https://www.space-track.org/, last access on 4th March. 2020.

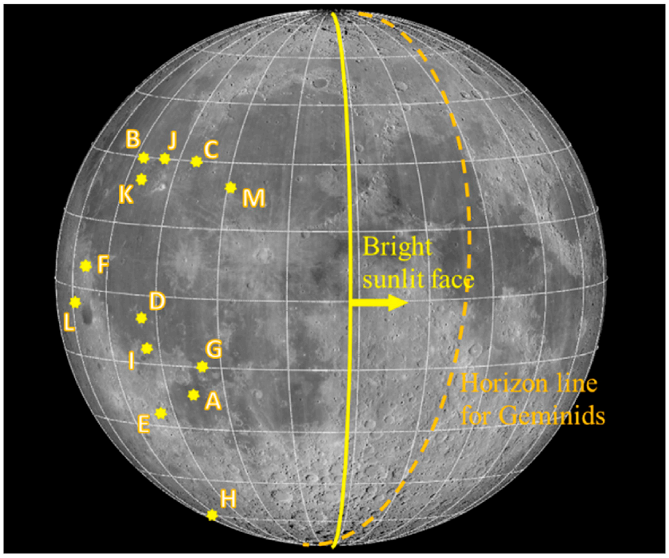

Fig. 1. Locations of the lunar impact flashes observed on 15th December. 2018. Geminids could hit the lunar surface to the left side of the orange broken line. The sunlight illuminated the right side of the solid yellow line. The lunar image was obtained by using the Virtual Moon Atlas[2]. (For interpretation of the references to color in this figure legend, the reader is referred to the Web version of this article.)

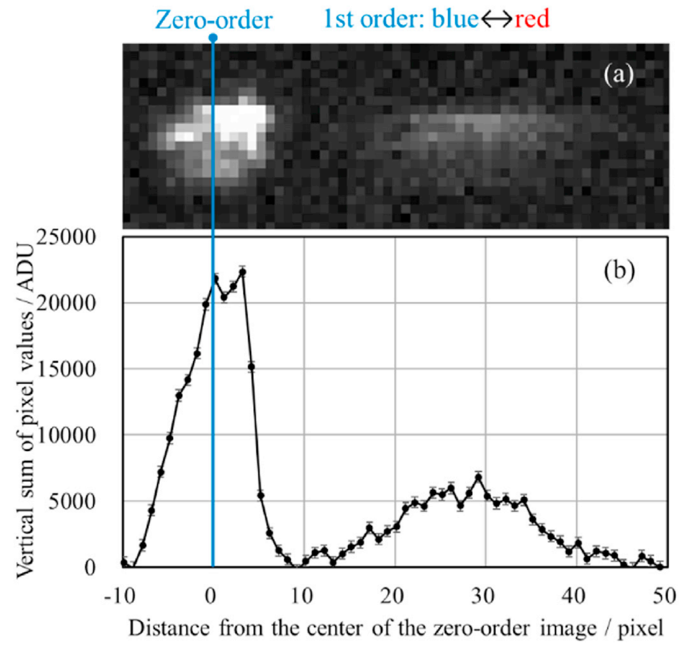

Fig. 2. The spectral image (a) and its count profile (b). The pixel values along each vertical column are added and plotted in the count profile. We convert the distance from the center of brightness of the zero-order image to a wavelength, after some corrections described in the text. The image (a) is a portion of the 1st frame of Flash B after the background subtraction (flipped horizontally).

the flash. We do not know the accuracy of the orbital data and the calculations in the application; however, the sudden brightening and an afterglow of this event support it to be a lunar impact flash.

The selenographic latitudes and longitudes of the flashes (Table 1 and Fig. 1) were determined on the images recorded at NU. For the flashes that were not recorded there, the locations were determined on the images by System1 or System2. Despite no sunlight illumination, we can recognize the bright Aristarchus region and the dark Grimaldi crater on the night side images of the moon illuminated by the earth (earthshine). Based on the positions of the flashes relative to them, we determined the latitudes and longitudes on the maps generated by an application "Virtual Moon Atlas"[2]. The impact angles measured from local lunar horizons in the table were calculated assuming the Geminids impacts, the radiant of which is 112° and 33°, respectively in right ascension and declination.

The flashes appear brightest in the 1st frames of frame sequences where they are recognized. The times at the 1st frames are listed in Table 1. The computer clock at NU was adjusted through an internet signal, while those at UEC were adjusted manually. The stamped times of System1 and System2 were therefore corrected to agree to those at NU, and shown in the table.

3. Spectral analyses

The spectral flux densities $\overline{F}_{flash}(\lambda)$ at wavelength λ of a flash is calculated as

$$\overline{F}_{flash}(\lambda) = N_{flash}(\lambda) \Big/ N_{star}(\lambda) \cdot k \cdot \pi B_{T\_star}(\lambda) \tag{1}$$

where $N_{flash}(\lambda)$ and $N_{star}(\lambda)$ are count numbers as shown in Fig. 2b after the corrections described below. Their subscripts represent a flash and a comparison star. $B_{T\_star}(\lambda)$ represents the Planck function at temperature T_star, and k is a non-dimensional value related to the brightness of the star. T_star is the effective temperature of the star derived from its color index, $B-V$, and Table 3 in Flower (1996), where B and V denote respectively the B- and V-magnitudes. We obtained B and V from the SIMBAD[3] database. It should be noted that $\overline{F}_{flash}(\lambda)$ is a temporal average of the flux $F_{flash}(\lambda, t)$ over an exposure time of the cameras Δt as

$$\overline{F}_{flash}(\lambda) = \frac{1}{\Delta t}\int_{t}^{t+\Delta t} F_{flash}(\lambda, t)\cdot \mathrm{d}t \tag{2}$$

Therefore, when the duration of the peak at the beginning of a flash is shorter than the exposure time, $\overline{F}_{flash}(\lambda)$ underestimates its real flux. We applied the following corrections to $N_{flash}(\lambda)$ and $N_{star}(\lambda)$ before using Eq. (1).

3.1. Dark frame correction

For every observation of flashes and stars, we recorded a hundred frames of dark field (no light input) with the same gains and exposure times just before or just after the observations. We averaged a hundred frames and obtained the dark frame for each observation. We subtracted the dark frame from each frame in raw SER movie files before any other processing.

3.2. Background subtraction and counting of pixel values

We averaged about two hundred frames before and after a flash. The averaged image was subtracted from a frame where the flash was recognized. We thus obtained a background-subtracted-image (Fig. 2a). In the averaging process, we also calculated the temporal standard deviation of count values for each pixel. The average of the standard deviations in a counting area of the background-subtracted-image was used to calculate the error bars in Fig. 2b.

In both System1 and System2, the spectral dispersion direction is

[2] Virtual moon Atlas: https://www.ap-i.net/avl/en/start/, last access on 4th March. 2020.

[3] SIMBAD: http://simbad.u-strasbg.fr/simbad/, last access on 4th March. 2020.

horizontal in images. We summed pixel values of the background-subtracted-image over some pixels along a column. The vertical range of the columns is determined visually. We thus obtained the summed count as a function of horizontal position (Fig. 2b).

In the analyses of movie frames of a star, we averaged about a hundred frames. Then, we summed pixel values of the averaged image over some pixels along each column. We obtained a background count for each column using pixel values in the upper and lower portion of the column, where the pixel values were not affected by the star. After the correction of the background, the summed counts as is shown in Fig. 2b are obtained.

3.3. Corrections for the atmospheric dispersion

Light rays from a star bend due to the atmospheric refraction, and the star appears higher above the horizon than it actually is. Wavelength dependence of the refraction angle makes blue image up and red image down relatively and leads to a vertically elongated image of the star. If it were not for the atmosphere, spectral dispersion by the grating would make a zero-order point image of a star and a 1st order line image (spectral image). The wavelength dependence distorts both the zero-order and the 1st order images. If the dispersion direction by the grating is parallel to the local horizon, blue components of a stellar image shift up and red components shift down due to the atmospheric dispersion. Then, the zero-order image slightly elongates vertically, and the spectral image bends a little. The dependence is well formulated as a function of wavelength and zenith angle (Schubert and Walterscheid 1999). We considered the atmospheric dispersion and converted the x-coordinate in Fig. 2b to wavelengths for each of the flashes and comparison stars (see Yanagisawa and Kakinuma, in prep. for details).

3.4. Corrections for the 2nd order image

In the images of flashes and stars observed by our spectral cameras, the 1st order image of, for example, 800 nm, is contaminated by the 2nd order image of 400 nm. We must, therefore, remove the contribution from the 2nd order image. We measured the ratios of the brightness intensities between the 2nd and the 1st order images of a monochromatic artificial star in laboratory experiments for wavelengths between 400 nm and 800 nm. The relationship between the ratio and wavelengths was expressed by a polynomial function of wavelengths and used for subtracting the counts of the 2nd order images from the 1st order counts. The function is obtained independently for System1 and System2. In the laboratory experiments with the spectral camera in System2, we substituted a commercial camera lens for the 280 mm telescope. The substitution may lead to some errors in the coefficients of the polynomial function.

3.5. Comparison stars

We approximated that the spectrum of a comparison star was expressed by the Planck function at its effective temperature multiplied by some value related to its brightness, that is, $k \cdot \pi B_{T\_star}(\lambda)$ in Eq. (1). The value k was calculated from its V-magnitude. The spectral flux density of a flash is then derived from the temperature, the magnitude, and the count ratios between the flash and the star, according to Eq. (1). We used Pollux (β Gem) observed on March 26, 2019 as the comparison star for System1 because the stars observed on the night of the Geminids flashes were faint or M in spectral type whose spectra were not approximated well by the Planck function. The weather was fine on both nights despite the three months difference in time. We derived the spectrum of a faint G type main-sequence star, HD222799, observed on the night of the Geminids flashes according to the procedures described in this Chapter (Supplementary Fig. S in the online version), where the comparison star was Pollux. The spectrum is well approximated by a blackbody spectrum of 5400 K, and its V-magnitude, calculated by Eq. (3) in Section 4.2, is 8.4. On the other hand, the B- and V-magnitudes of the star in SIMBAD[3] are respectively 9.59 and 8.82. Its effective temperature is 5359 K, according to $B - V = 0.77$ and Table 3 in Flower (1996). Despite the 0.4 difference in V-magnitude, the agreement of the temperatures validates the use of Pollux as the comparison star for studying the spectral features of the impact flashes. For System2, we used HD222465 observed on the night of Geminids flashes. This star is an F6 type main-sequence star of 7.2 in V-magnitude (SIMBAD[3]). The spectrum of HD222799 mentioned above observed on the same night by System2, obtained with the comparison star HD222465, shows 5600 K and 8.9 in V-magnitude. Both values approximately agree to the temperature and the magnitude based on SIMBAD[3] and Flower (1996). The agreement validates the use of HD222465 as a comparison star for System2.

3.6. Corrections for the atmospheric absorption

A flash and a comparison star are not necessarily recorded in the same movie frames. They are usually observed independently at different times and in different directions. We made corrections for the atmospheric absorption with the assumption that there was no difference in atmospheric conditions, such as water vapor and aerosol contents, among observations. The atmospheric transmittance depends on zenith angles as well as wavelengths. We obtained the zenithal atmospheric transmittance as a function of wavelengths between 400 nm and 1000 nm with the following three parameters using a free web application of MODTRAN[4]; summer, mid-latitude, and urban. The temperature in Tokyo, Japan in between December and March is not so cold as typical mid-latitude countries. We adopted “summer” therefore instead of “winter” as a parameter. The transmittance between 300 nm and 400 nm was obtained from Table 11.25 in Schubert and Walterscheid (1999).

3.7. Spectral flat-field correction

One of the drawbacks of our spectral cameras is that the count profiles as shown in Fig. 2b depends on where the spectral image (Fig. 2a) appears in a frame (Yanagisawa and Kakinuma, in prep.). For example, the profiles derived from images observed in the left-side area in frames are different from those in the right-side area. To avoid the problem, we recorded the comparison star Pollux along twenty horizontal lines in movie frames by System1. The frames where the star is located nearest to the flash coordinate on a frame were used to obtain the count profile of the comparison star.

On the other hand, a star, HD166, was observed on November 15, 2018 at 25 points distributed uniformly in the field of view of System2. We compared a profile obtained from a movie where HD166 appeared nearest to the flash coordinate with the other profile obtained from a movie where HD166 appeared nearest to the comparison star (HD222465). The results of the comparisons were used in the spectral flat-field corrections. HD166 is a variable star, so we did not use it as a comparison star as we did for System1.

The correction is almost complete in System1 but not in System2. The correction for the 2nd order image described in Section 3.4 is also more accurate for System1 than for System2. Furthermore, the aperture of the telescope is larger, and the framing rate of the camera is higher for System1 than for System2. Therefore, in the following chapter, we show the results obtained by System1 unless the observations were interrupted in the system.

4. Results

4.1. Spectra

The spectral flux densities $\overline{F}_{flash}(\lambda)$, observed outside the terrestrial atmosphere, of bright flashes are shown in Figs. 3–7. These spectra are

[4] MODTRAN: http://modtran.spectral.com/, last access on 4th Mar. 2020.

reliable between 400 nm and 870 nm in wavelengths except Flash H (Fig. 5), which was observed by System2. Spectra of the other flashes are shown in the Supplementary figures (online version only). The analyses of the subsequent frames are possible for these bright flashes, and we also show their spectra. Flash A is also bright, but a probable mechanical twitch of the telescope in System1 blurred an image in the 1st frame where the flash abruptly appeared. Therefore, the reliable spectrum was not obtained for the frame. The twitch would also have occurred in System1 at Flash M, and the blurred image prohibited the derivation of the reliable spectrum.

Error bars in the figures are based on the temporal variation of the background described in Section 3.2. They include photon shot noise and electric noises. The same kinds of noise for the comparison stars are not considered because the averages of about a hundred frames reduce the noises. The effect of the atmospheric scintillation discussed later is not included in the error bars. Error bars are not shown for the 2nd and the 3rd frames, but they are almost the same as for the 1st frame at the same wavelength.

Spectral flux densities in the wavelength range between 300 nm and 400 nm might be overestimated because of the following reasons. There could be some non-negligible absorptions in the stellar atmosphere in this range. The blackbody approximations for the comparison stars, Pollux and HD222465, could then overestimate the real flux. That is to say, $k \cdot \pi B_{T\_star}(\lambda)$ in Eq. (1) could overestimate the real flux from the stars, then $\overline{F}_{flash}(\lambda)$ could also be overestimated. Besides, terrestrial atmospheric absorptions are 55% at 400 nm and 100% at 300 nm in the zenithal direction (Schubert and Walterscheid 1999) and more significant in the non-zenithal directions. The absorption in this wavelength range is more variable than in the longer wavelengths. It may have been deeper on the nights of the comparison stars' observations in Japanese spring and autumn than on the night of the Geminids flashes in winter. $N_{star}(\lambda)$ in Eq. (1) could be larger if we had observed the stars on 15th December. These two possibilities could cause the overestimations at these wavelengths.

The uncertainties, which are related to the correction for the 2nd order image and not included in the error bars in the figures, should be considered at long wavelengths. Corrections are relatively small for the flashes but not negligible for the comparison stars because the stars are bluer than the recorded flashes (dominated by latter stages of the process) and the contribution of a 400 nm light to an 800 nm image is for

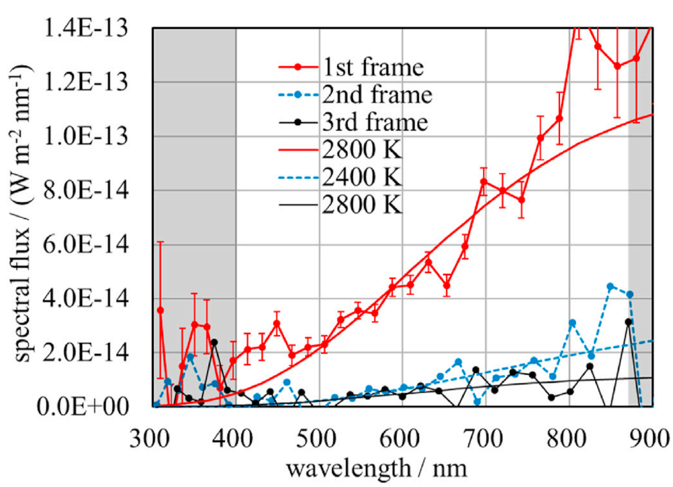

Fig. 3. Spectra of Flash B, observed outside the terrestrial atmosphere, at the 1st (red solid polygonal line), the 2nd (blue broken polygonal line), and the 3rd (black thin polygonal line) frames observed by System1. Error bars represent one standard deviation of the background fluctuation. We do not show error bars for the 2nd and the 3rd frames, but they are almost the same as for the 1st frame at the same wavelength. The fluxes are reliable between 400 nm and 870 nm in wavelengths (the non-shaded area). Blackbody spectra were best-fitted to the plots in the non-shaded area and are shown by smooth curves. We show the blackbody temperatures in the plot area. Both the exposure time and the frame interval of the camera were 16 ms. (For interpretation of the references to color in this figure legend, the reader is referred to the Web version of this article.)

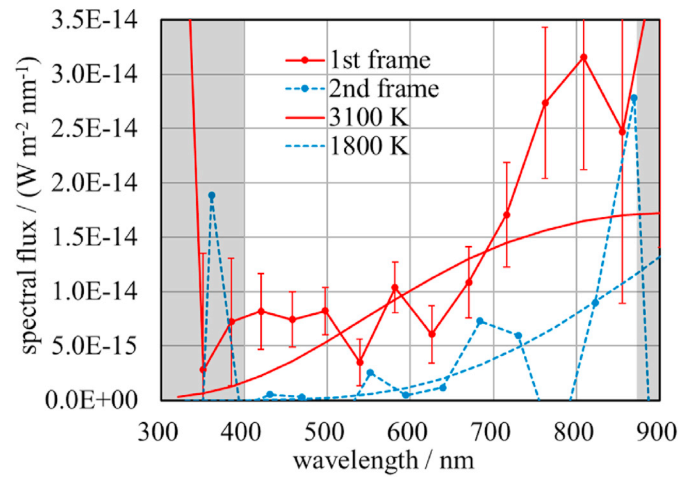

Fig. 4. Spectra of Flash G observed by System1.

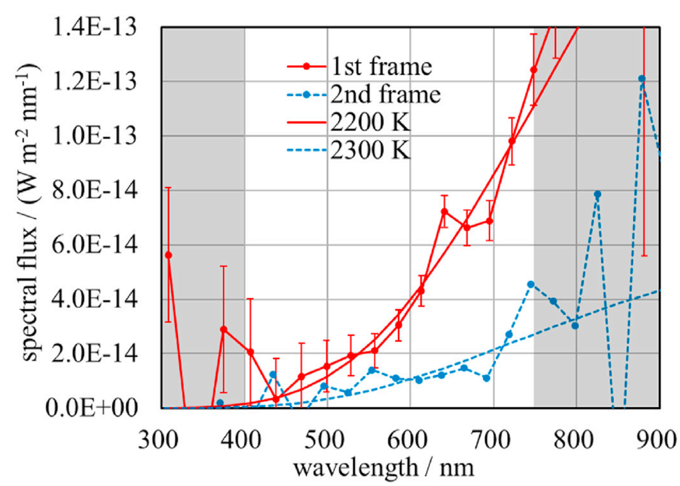

Fig. 5. Spectra of Flash H observed by System2. The observation was interrupted in System1. Both the exposure time and the frame interval are 25 ms.

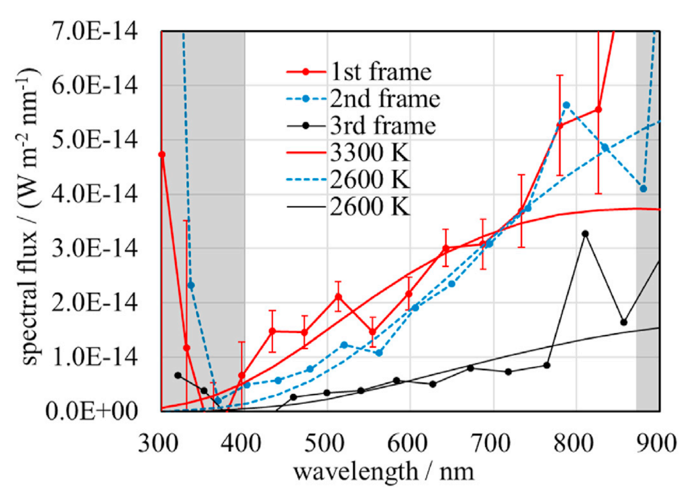

Fig. 6. Spectra of Flash I observed by System1.

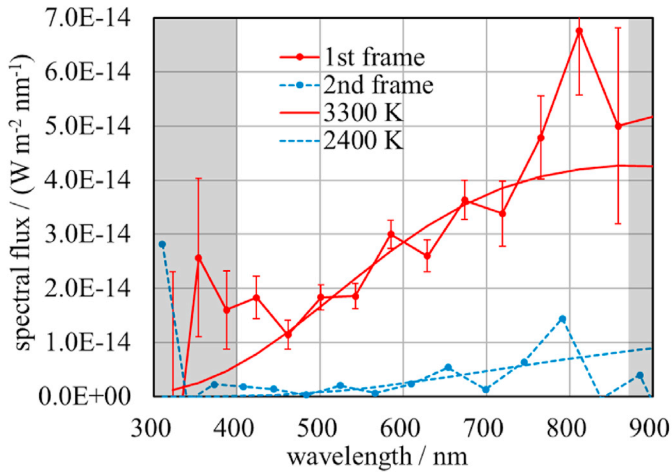

Fig. 7. Spectra of Flash L observed by System1.

example more significant for the stars. For the comparison star, Pollux, observed by System1, the contribution of $\lambda/2$ light exceeds 10% at about $\lambda = 870$ nm. The contribution exceeds 10% at about $\lambda = 750$ nm in the case of System2. The coefficients of the polynomials used for the correction of the 2nd order light could be associated with non-negligible errors, especially for System2. The errors in $N_{star}(\lambda)$ lead to the errors in $\overline{F}_{flash}(\lambda)$ plotted in Figs. 3–7.

To examine the temporal variation of spectral features due to atmospheric scintillations, we obtained count profiles as Fig. 2b for each of the frames of a bright star, HD4128 (β Cet), observed at 54° in zenith angle on November 9, 2017 by System1. The count profile fluctuates with time with the amplitude (standard deviation) of about 15%. Though the scintillation varies day by day, we expect it would not make the spectra unreliable. However, detailed discussions on a single spectrum could lead to incorrect conclusions. We should discuss with a broad view of all the spectra. We did not examine the temporal variation in the same way by using System2. The observed spectra may be affected more significantly by the atmospheric scintillations in System2 than System1 because of the smaller aperture of the telescope.

The amplitudes of the spectral flux densities and brightness magnitudes for the 1st frame described in the next section importantly depend on the time lag between the beginnings of a flash and a camera exposure, as illustrated in Fig. 8. The lightcurve of a typical lunar impact flash is characterized by a sudden brightening and a decrease in brightness with a time constant of about a few of the exposure time of the movie camera (e.g., Yanagisawa and Kisaichi 2002). When the exposure starts around the beginning of a flash, its image in the 1st frame appears bright. On the other hand, when the exposure starts earlier, the flash appears less bright. As Eq. (2) shows, the spectral flux densities $\overline{F}_{flash}(\lambda)$ in Figs. 3–7 show averages over the camera exposure, and their amplitude at the 1st frame depends on the time lag, which we do not know. Longer exposure duration of System2 could statistically lead to lower flux densities and darker magnitudes for the 1st frames than those derived from System1 observations. The blackbody temperatures described below would also depend on the time lag and the exposure time to some extent if the temperature changes quickly.

A blackbody spectrum was best-fitted to each spectrum. It is drawn as a smooth line, and we show the blackbody temperature in each figure. The plots in the reliable wavelength ranges were used in the best-fittings. We tried to fit Planck functions of different temperatures to the observed spectra and estimated the error in the temperatures to be about 300 K. We show the temporal variations of the temperatures in Fig. 9. The temperatures and their decreases with time roughly agree to the previous results (Avdellidou and Vaubaillon 2019; Liakos et al., 2020).

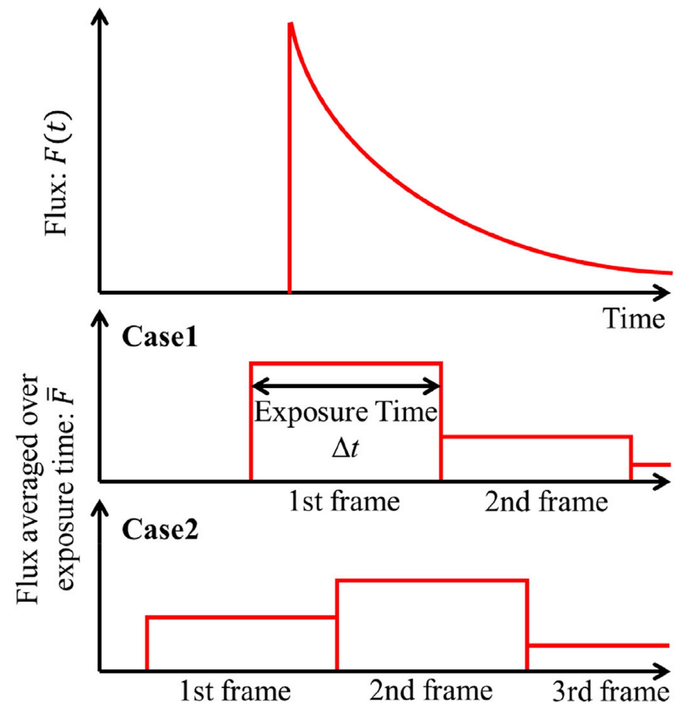

Fig. 8. Effect of the time lag between the beginnings of a flash and exposure of a camera on observed fluxes. The exposure of the 1st frame started just before the beginning of the flash in Case1; then, the averaged flux is relatively large. The exposure started much before the beginning of the flash in Case2; then, the averaged flux is relatively small.

4.2. Magnitudes and meteoroid masses

The magnitudes m_{flash} were calculated according to the following formula for the V-, R-, and I-bands independently;

$$m_{flash} - m_{sun} = -2.5 \ \log_{10}\left[\int \overline{F}_{flash}(\lambda)R(\lambda)\mathrm{d}\lambda \Big/ \int F_{sun}(\lambda)R(\lambda)\mathrm{d}\lambda\right] \tag{3}$$

where m_{sun} is the solar magnitude and $R(\lambda)$ is the response function for a band (Bessell 2005). The integrals were calculated numerically, where we used the plot intervals in the spectral figures as dλ. We truncated the integration at 870 nm and 750 nm for the flashes observed by System1 and System2 respectively, while there was no truncation for the sun. For the System2, this makes the R-magnitude a little dimmer and prohibits the derivation of the I-magnitude because its effective wavelength is 800 nm (Bessell 2005). The magnitudes at the 1st frames are listed in Table 2. It should be noted that there are uncertainties in these magnitudes due to an unknown parameter, the time lag.

Luminous energy $\mathscr{E}_{flash}$, observed outside the terrestrial atmosphere, were calculated as

$$\mathscr{E}_{flash} = \sum\left[\int \overline{F}_{flash}(\lambda)R_{video}(\lambda)\mathrm{d}\lambda\right]\Delta t \tag{4}$$

where $R_{video}(\lambda)$ is the response function of the video camera, WAT-100 N, manufactured by WATEC company. We call this “video-band” from now on. $R_{video}(\lambda)$ is non-zero between 310 nm and 1000 nm in wavelength and has a peak value of 1.0 at 615 nm. The integrals were calculated numerically over the reliable wavelength ranges. We used the plot intervals in the spectral figures as dλ. Δt is the exposure time for each frame and the summation in Eq. (4) is calculated over the frames for which we obtained spectra.

The luminous energy at the moon was obtained as

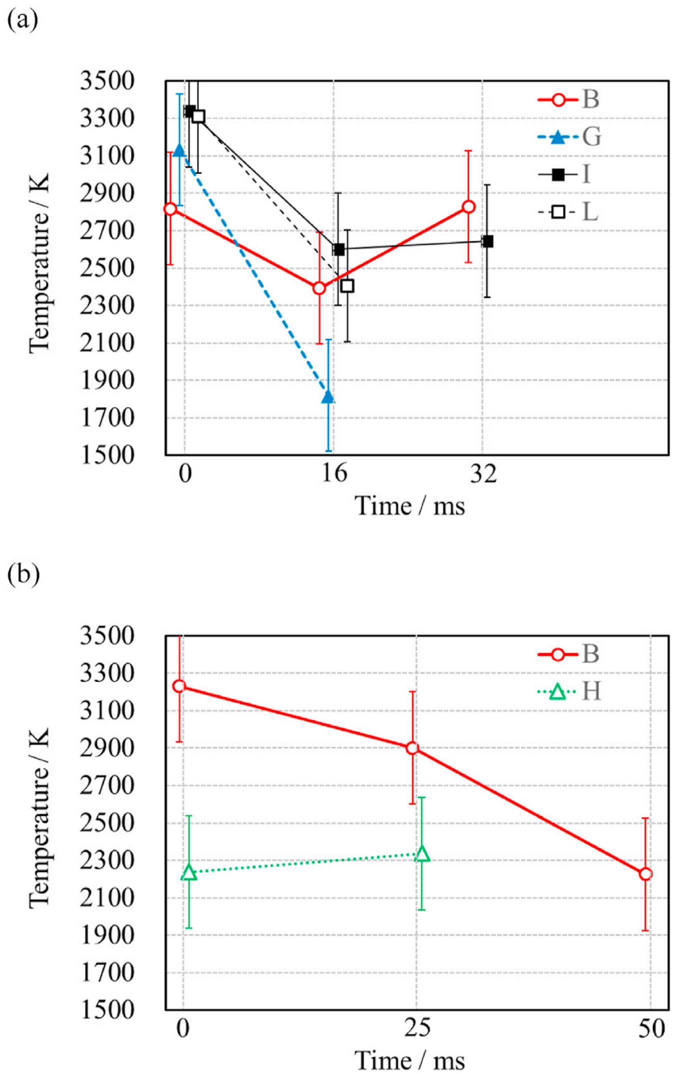

Fig. 9. Temporal variations of the blackbody temperatures of the bright flashes observed by System1 (a) and System2 (b). The temperature for a frame in which a flash appears first is plotted at zero in the horizontal axis. That for the 2nd frame is plotted at 16 ms and 25 ms (frame intervals) for System1 and System2, respectively. The abscissa does not necessarily represent the time after the beginning of a flash. There is an uncertainty of 16 ms or 25 ms. The error of the temperatures is estimated to be about 300 K.

$$E_{flash} = \mathscr{E}_{flash} \cdot 4\pi r^2 \tag{5}$$

where r is the distance between the moon and the observatory (4.0×10^5 km), and we assume the flashes were radiated uniformly into 4π steradians.

The impact energy, that is, the kinetic energy of the meteoroid is obtained as

$$E_{imp} = \eta E_{flash} \tag{6}$$

where η is the luminous efficiency. Some studies (Bellot Rubio et al. 2000a, 2000b; Moser et al., 2010) show its value to be between 0.1% and 0.2%. We adopted 0.2% in our calculations. The meteoroids that hit the lunar surface must be Geminids; therefore, we calculated their masses in Table 2 with their impact velocity of 35 km s^{-1}. There is no problem with the time lag because of the multiplication by Δt and the summation in Eq. (4). The real masses would be a little bit larger than the ones listed in the table due to the truncations of the integration range in Eq. (4).

Table 2
Summary of the magnitudes of the flashes at the 1st frames of their movie sequences.

Flash	magnitude by System1			magnitude by System2		mass/g
	V	R	I	V	R	
A				8.7	7.7	130[a]
B	7.5	6.2	5.1	8.4	7.4	600
C	11.4	8.7	7.6			35
D	9.4	8.5	8.8			48
E				9.8	9.6	-[b]
F	10.6	9.9	-[b]			11
G	9.3	7.9	6.6			130
H				7.9	6.2	660[a]
I	8.1	7.0	6.1	8.9	7.6	490
J	10.0	9.0	-[b]			26
K	9.4	8.3	6.9			82
L	8.0	6.8	5.8	8.5	7.3	290
M				8.8	9.1	100[a]

[a] The meteoroid masses were derived from the observations by System2. The masses for the others were derived from the observations by System1.
[b] Integrals of fluxes over the I-band or the video-band wavelengths are negative.

5. Discussion

Before discussing the spectra of the lunar impact flashes, we examine the brightness magnitudes at the 1st frames in Table 2. The magnitudes were obtained by both System1 and System2 for the Flashes B, I, and L (Table 2). Those by System2 is larger (dimmer) by about 0.7 on average than those by System1 for both V- and R-magnitude. The most probable cause of this disagreement could be the difference in the exposure time between System1 (16 ms) and System2 (25 ms). If the duration of the bright phase at the beginning of a flash is much shorter than the exposure time, $N_{flash}(\lambda)$ in Eq. (1) does not depend importantly on the exposure time, while $N_{star}(\lambda)$ increases linearly with the exposure time. With the increase of the exposure time, the spectral flux density $\overline{F}_{flash}(\lambda)$ reduces, and the magnitude increases. The difference in the exposure time, 16 ms vs. 25 ms, leads to a difference of 0.5 in magnitude in this case. Because of the dependence of the magnitudes on the exposure time, we must be careful when we compare the magnitude distribution between, for example, Suggs et al. (2014) and Liakos et al. (2020), where their exposure times are 16 ms and 23 ms respectively.

The spectra of the bright flashes shown in Figs. 3–7 are continuous and increase almost monotonically with wavelengths. Those of the other flashes are much noisier but show the same tendency. Despite the uncertainty of the magnitudes discussed above, the color indices that are the differences in the magnitudes between the two wavelength bands do not depend on the exposure time at all. The average and the standard deviation of the color index, V - R, calculated from the magnitudes listed in Table 2 for both System1 and System2 are 1.1 $\pm$ 0.6, and those of R–I are 0.9 $\pm$ 0.6. Besides, the average and the standard deviation of R–I calculated for the 1st frame in Table 1 in Bonanos et al. (2018) is 1.2 $\pm$ 0.4 and almost agrees to our result. Our smaller value in R–I may be due to the truncation of the integration at 870 nm in calculating the I-magnitudes by Eq. (3). The truncation makes the I-magnitude a little bit larger (dimmer), then makes R–I smaller. It is interesting to note that the impact flashes by Geminids and other ones observed by Bonanos et al. (2018) show similar R–I on average. Both V - R and R–I of the sun are 0.35 (Ramírez et al., 2012) and smaller than the indices of the flashes. One can say that lunar impact flashes are redder than the sun in the visible and near-infrared wavelengths, though they may appear bluer at the very beginnings if we observe them with higher time resolution.

As a first approximation, the blackbody spectra of single temperatures fit the observed spectra of the lunar impact flashes in the visible and near-infrared wavelengths (Figs. 3–7). However, the fittings for the 1st frames seem to be less satisfactory than for the 2nd and the 3rd frames. There may be excess fluxes in the short wavelengths less than around 600 nm for the 1st frames. This is not unnatural because each part of a plume or ejecta must radiate at different temperatures at a time, and the radiation from some part could not necessarily dominate the total radiation. Furthermore, the temperature distribution in the plume or ejecta must vary with time during an exposure time for a movie frame, e.g., 16 ms. The nonuniformity and the time variation have been observed in laboratory experiments in the initial stages (within several tens of microseconds) of impact phenomena (Schultz and Eberhardy 2015). As the second approximation, we fitted the composite of two blackbody spectra to the plots in each of the 1st frame spectra (Fig. 10). We made the fittings visually while changing the two temperatures and the two intensities of the blackbody radiations variously. The composites seem to approximate each of the observed spectra much better than the single blackbody spectra. The composites consist of blackbody radiations, one at about 6000 K and the other at about 2000 K.

The former temperature is close to the maximums observed in laboratory impact experiments. Sugita et al. (1998) and Sugita and Schultz (1999) observed the spectra for the first few microseconds of the flashes at collisions of spherical quartz and copper projectiles of less than 1 cm in diameter with dolomite blocks at about 5 km s^{-1}. They analyzed the ratios among line emission intensities of Ca and Cu and derived the excitation temperatures around 6000 K. They supposed that they observed jets that squirted out from the interface between the projectiles and targets (e.g., Section 4.4 in Melosh 1989).

After the jetting, still in the initial stage of impact phenomena, self-luminous plumes, which consist of gas and dust, and are sometimes called “vapor plume” or “vapor cloud,” are observed in laboratory experiments (Section 5.3 in Melosh 1989, Fig. 19 in Schultz et al., 2007). They are observed for more than several tens of microseconds. The time-integrated light energy would be larger for the plumes than the jets. Furthermore, thin layers of carbon, which would be contained in meteoroids, over dolomite powder targets increase the continuum radiation from the plumes (Schultz et al., 2007; Schultz and Eberhardy 2015). The plumes could be bright enough to appear as the high-temperature components.

Ernst and Schultz (2004) conducted experiments with pumice dust targets and subcentimeter Pyrex projectiles at about 5 km s^{-1}. The blackbody temperatures of the plumes were measured by multi-band photometry. They are about 4000 K for the first 20 μs. Similar experiments with 20 mm thick dolomite plates and polycarbonate projectiles at less than 4.2 km s^{-1} also show about 4000 K (Tang et al., 2015). These temperatures are lower than 6000 K of the high-temperature components. However, the plume temperature could increase with impact velocities as suggested by Ernst and Schultz (2002). Consequently, the expanding, self-luminous vapor plume would be the major contributor to the high-temperature component captured in the lunar impact flash.

We expected the low-temperature components to show the temperatures at the 2nd and the 3rd frames, but 2000 K is a little bit too low. The disagreement may be due to the oversimplification of the two-component model. Despite the possibility of oversimplification, the better fits of the model indicate that the single blackbody model adopted in Figs. 3–7 and previous works (e.g., Avdellidou and Vaubaillon 2019; Liakos et al.,

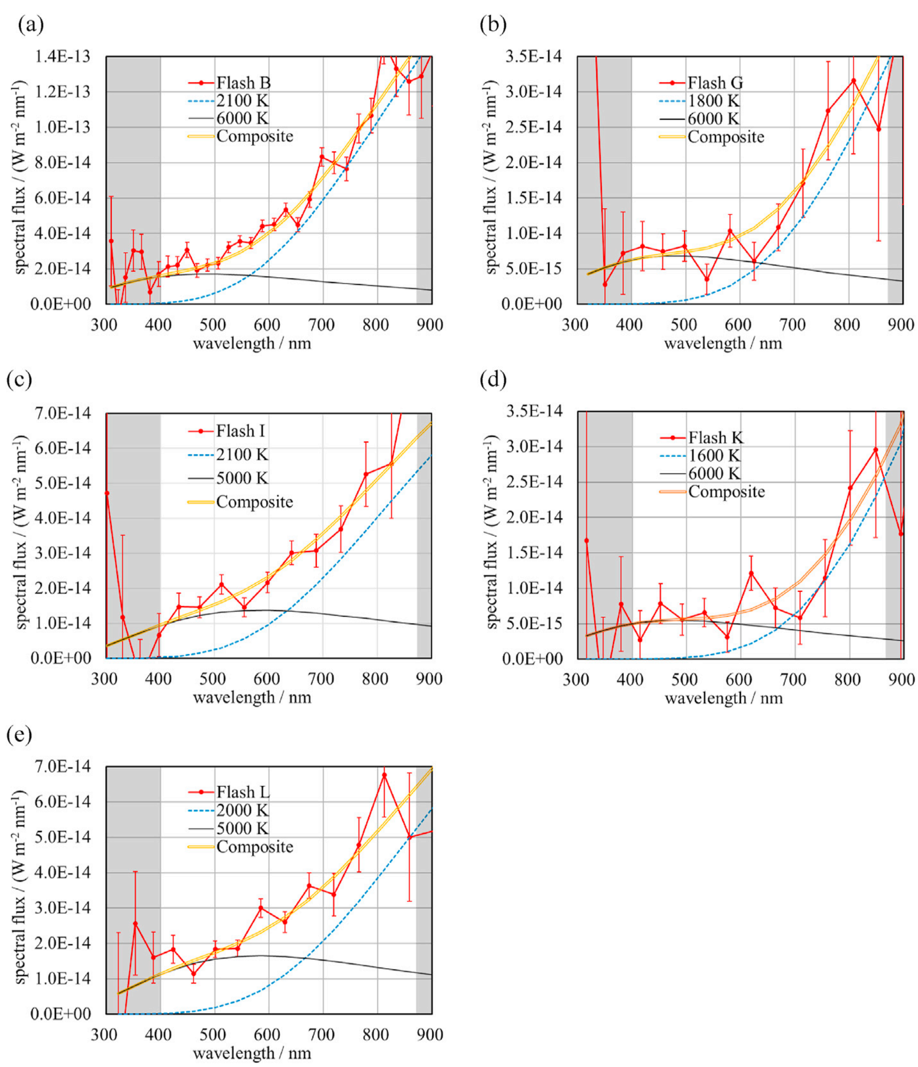

Fig. 10. Spectra at the 1st frames of bright flashes (red solid polygonal lines) except Flash H. These were observed by System1 with 16 ms in the exposure time of the camera. Error bars represent one standard deviation of the background fluctuation. The fluxes are reliable between 400 nm and 870 nm in wavelengths (the non-shaded area). A composite of two blackbody spectra (blue broken and black thin smooth lines) was fitted visually to the plots in each of the spectra and is shown by a smooth double curve. (For interpretation of the references to color in this figure legend, the reader is referred to the Web version of this article.)

2020) may not be appropriate to derive the physically meaningful temperatures for the 1st frames (at the beginning of flashes). It may be better to refer to the 1st frame temperatures as "apparent temperatures."

The apparent temperatures at the 1st frames obtained assuming a single blackbody would depend on the wavelength range used to derive them. The high- and low-temperature components respectively dominate visible and near-infrared wavelengths in the spectra (Fig. 10). Therefore, the temperatures derived from visible wavelengths would tend to be higher than temperatures mainly from near-infrared wavelengths. Temperatures at the 1st frames obtained in the NELIOTA project by Bonanos et al. (2018), Avdellidou and Vaubaillon (2019), and Liakos et al. (2020) from the brightness ratios between the R- and I-bands (red and near-infrared wavelengths) distribute over 1300–5800 K. Whereas, Madiedo et al. (2019b) obtained almost the upper end of this distribution, 5700 K, for a bright flash from the ratios among B-, V-, and R-bands (visible wavelengths). They do not report the temperature for the next frame, probably because the flash became too dark in the frame to be analyzed. This would deny the possibility that the exposure of the first frame ended just after the very beginning of the impact phenomena and only the brief high-temperature phase was recorded in the frame. They might have observed one of the rare high-temperature-events by chance. However, it would be more probable that the time-integrated spectrum of the flash approximately consisted of the high- and low-temperature components and the observation without near-infrared wavelengths led to the high temperature.

The spectrum at the 1st frame of Flash H does not show an apparent excess in the wavelength range of less than 600 nm (Fig. 5). There are four possibilities regarding the lack of excess. First, the impact angle measured from the local horizon is smallest for the flash among the others (Table 1). Schultz (1996) found that shear heating is important in oblique impacts on particulate targets such as lunar regolith, and the amount of impact-generated vapor increases with decreasing angle while vapor temperature decreases. Radiation from a large amount of low-temperature vapor plume, including melts and dust, could have dominated this bright flash. Second, Flash H occurred near the limb of the lunar disk. Pre-existing crater rims or hills might block the radiation from the plume. Third, atmospheric scintillations could accidently change the spectral feature. Fourth, the incomplete spectral flat-field correction for System2 described in Section 3.7 might reduce the spectral flux densities in this wavelength range.

Flash L observed by System2 does not show an apparent excess either (Supplementary figures). The atmospheric scintillation or the incomplete spectral flat-field correction could have hidden the excess. However, on the other hand, all the excesses in the spectra in Fig. 10 might be due to the atmospheric scintillations. Further spectral observations are needed to verify the existence of the excesses.

The temperatures at the 2nd and the 3rd frames (Fig. 9) are below 3000 K that is below the evaporation temperature of all silicates in Table 2 in Ahrens and O'Keefe (1972). Those after the 1st frames obtained in the NELIOTA project (Avdellidou and Vaubaillon 2019; Liakos et al., 2020) are also below 3000 K. Incandescent ejecta consisting of melts and solid particles that follows a vapor plume in a cratering process, or a radiant crater floor could be the sources of a lunar impact flash at the 2nd frame and later. Radiation probably dominated by the thermal radiation from ejecta in the latter stage was observed at the collision of the Centaur rocket with the lunar surface at 2.5 km s^{-1} (Schultz et al., 2010; Hermalyn et al., 2012). The incandescent ejecta and a crater floor observed in laboratory experiments where polycarbonate projectiles of 4.76 mm in diameter hit the quartz sand at about 6.5 km s^{-1} (Fig. 1 in Fuse et al., 2020) may simulate lunar impact flashes after the vapor plume.

Madiedo et al. (2018) reported a flash of about 7 in V-magnitude observed both at video wavelengths (no filter) and in the I-band. They assumed single blackbody radiation and calculated temperature for each set of the video- and I-band frames, and show that temperatures around 3200 K lasted for about 0.1 s after the 1st frame (frame interval of their cameras is 20 ms). However, their two video cameras were not synchronized, and probably the exposure of the no-filter camera would have preceded the exposure of the I-band camera. Because of the decrease of brightness with time, the ratio of video wavelength brightness to I-band brightness could be larger than the real ratio. The overestimated ratios lead to higher temperatures than real temperatures. The temperatures of this flash may have been less than 3000 K as with the other results described in the previous paragraph.

Now, we consider areas radiated on the lunar surface inferred from blackbody spectra fitted to the observed spectra. There is a following relationship between the blackbody spectra $\Phi(\lambda)$ and the Planck function $B_T(\lambda)$ of the flash temperature T,

$$\overline{F}_{flash}(\lambda) \cong \Phi(\lambda) = \overline{A} \Big/ r^2 \cdot B_T(\lambda) \tag{7}$$

where r is the distance to the moon and $\overline{A}$ is the cross-sectional area of a radiating source perpendicular to the observers' line of sight. We substituted the fitted blackbody spectrum for $\Phi(\lambda)$ and obtained $\overline{A}$ for the 2nd and the 3rd frames. They are listed in Table 3 as the diameters of circles that have the same area as radiating sources, $2 \cdot \sqrt{\overline{A}/\pi}$ (effective diameter). We do not obtain the area for the 1st frames because the temperatures could be "apparent" as discussed above, and brightness would vary significantly during the exposure of the cameras. The temporal variation would be more gentle in the 2nd and the 3rd frames.

To compare with the radiating source areas, we calculated the crater diameters according to the formula for lunar craters up to roughly 100 m in diameter in loose soil or regolith developed by Gault (1974) and shown in Section 7.8 in a textbook (Melosh 1989). Impact energies, that is, the kinetic energies of meteoroids, are calculated from the masses in Table 2 and the Geminids' impact velocity of 35 km s^{-1}. The impact angles in Table 1 are used. We used the density of meteoroids 2.9×10^3 kg m^{-3} (Babadzhanov 2002) and of lunar regolith 1.6×10^3 kg m^{-3} (McKay et al., 1991). These parameters result in crater diameters at the level of the pre-existing lunar surface (apparent diameters) listed in Table 3. The sizes at the 2nd frames in the table are comparable to the crater diameters; that is, the radiating source areas are comparable to the areas of crater floors. In a crater floor, only some parts would radiate. Therefore, the crater floors do not necessarily dominantly contribute to the radiation at the 2nd frames. The widespread incandescent ejecta curtain, whose effective radiating area is comparable to a crater floor area, would also be an important source. A thermally radiating spot larger than the crater size produced by the collision of the Centaur rocket with the lunar surface was observed for about 1 s after the impact before the sun illuminates the ejecta (Schultz et al., 2010). This finding also supports the idea that the coincidence of radiating sizes and crater sizes does not necessarily mean the dominance of the crater floor radiation.

6. Conclusions

Two simple spectral cameras at UEC recorded 13 lunar impact flashes between 6.2 and 9.9 in R-magnitude on December 15, 2018 during the Geminids meteor activity. NU and Lulin observatories separated far

Table 3
Radiating source area at the 2nd and the 3rd frames.

Flash	2nd frame		3rd frame		Crater
	T/K	size[a]/m	T/K	size[a]/m	diameter/m
A	2700	3.1			4.2
B	2400	4.4	2800	1.8	7.0
G	1800	9.4			4.2
H[b]	2300	6.4			5.2
I	2600	5.0	2600	2.6	6.5
L	2400	2.6			5.8

[a] : The size (diameter) of a circle that has the same area as a radiating source.
[b] : Flash H was observed by System2, where the frame interval was 25 ms. The interval for the other flashes is 16 ms.

enough from UEC to discriminate lunar flashes from satellites' glints confirmed 11 of them. We derived their spectra with a time resolution of 16 ms through sophisticated procedures, such as corrections for the atmospheric dispersions and the spectral flat field. Their spectra at wavelengths between 400 nm and 870 nm are continuous and red. Best-fitted single blackbody spectra show the temperatures of about 2000–4000 K. These temperatures are almost concordant with the results obtained from multi-wavelength-band observations.

However, the composite of high (about 6000 K) and low (about 2000 K) temperature blackbody spectra could fit the observed spectra in the initial stage of a flash much better. An impact-generated optically thick vapor plume could contribute to the high-temperature component. Each part of a plume must radiate at different temperatures at a time. Furthermore, the temperature distribution in the plume must vary quickly during an exposure time for a movie frame. Nevertheless, the radiation from a part for a period may dominate the total radiation from the plume, and appears as the high-temperature component. The radiation from hot ejecta or crater floors may represent the low-temperature components. Further spectral observations are necessary to confirm the high-temperature component probably due to hot plumes.

The temperatures decrease with time, and those at the 2nd and the 3rd frames are less than 3000 K, certainly less than the evaporation temperatures of silicates. The radiating source areas at the 2nd frames are comparable to the areas of the crater floor generated by the Geminid impacts. The rough agreement does not necessarily mean that the radiant crater floors are the sources in the latter stage of the lunar impact flashes because radiating areas would be only some parts of the floors. The widespread incandescent ejecta curtain, whose effective radiating area is comparable to a crater floor area, would also be an important source.

CRediT authorship contribution statement

Masahisa Yanagisawa: Conceptualization, Methodology, Software, Validation, Investigation, Writing - original draft, Supervision, Project administration. **Yuki Uchida:** Formal analysis, Investigation, Data curation. **Seiya Kurihara:** Formal analysis, Investigation, Data curation. **Shinsuke Abe:** Investigation, Supervision. **Ryota Fuse:** Investigation. **Satoshi Tanaka:** Supervision, Project administration. **Keisuke Onodera:** Formal analysis, Investigation, Data curation. **Fumi Yoshida:** Project administration. **Hsin-Chang Chi:** Investigation, Supervision. **Zhong-Yi Lin:** Investigation, Supervision. **Jim Lee:** Investigation, Supervision. **Taichi Kawamura:** Project administration. **Ryuhei Yamada:** Project administration.

Declaration of competing interest

The authors declare that they have no known competing financial interests or personal relationships that could have appeared to influence the work reported in this paper.

Acknowledgments

We are indebted to the students of the Univ. Electro-Comm., Nihon Univ., and National Dong Hwa Univ. for their efforts in the observations. MY, SA, ST, TK, and RY were supported by the Bilateral Joint Research Program, Japan Society for the Promotion of Science, Japan. SA was supported by the Nihon University College of Science and Technology Leading Research Grant. We are greatly indebted to Prof. J. M. Madiedo and another referee for their very useful comments. MY, SA, and RF appreciate the support and hospitality of the committee members of Meteoroids (2019) held in Bratislava, Slovakia.

Appendix A. Supplementary data

Supplementary data to this article can be found online at https://doi.org/10.1016/j.pss.2020.105131.

References

Abe, S., Ogawa, T., Maeda, K., Arai, T., 2020. Sodium variation in Geminid meteoroids from (3200) Phaethon. Planet. Space Sci. 194, 105040 https://doi.org/10.1016/j.pss.2020.105040.

Ahrens, T.J., O'Keefe, J.D., 1972. Shock melting and vaporization of lunar rocks and minerals. Moon 4, 214–249. https://doi.org/10.1007/BF00562927.

Arai, T., 41 coauthors, 2018. DESTINY+ mission: Flyby of Geminids parent asteroid (3200) Phaethon and in-situ analyses of dust accreting on the earth. In: 49th Lunar and Planetary Science Conference, Abstract No. 2570.

Artemieva, N.A., Shuvalov, V.V., Trubetskaya, I.A., 2000. Lunar leonid meteors - Numerical simulations. 31th Lunar and Planetary Science Conference, Abstract No. 1402.

Avdellidou, C., Vaubaillon, J., 2019. Temperatures of lunar impact flashes: mass and size distribution of small impactors hitting the moon. Mon. Not. Roy. Astron. Soc. 484, 5212–5222. https://doi.org/10.1093/mnras/stz355.

Babadzhanov, P.B., 2002. Fragmentation and densities of meteoroids. Astron. Astrophys. 384, 317–321. https://doi.org/10.1051/0004-6361:20020010.

Beech, M., 2002. The age of the Geminids: a constraint from the spin-up time-scale. Mon. Not. Roy. Astron. Soc. 336, 559–563. https://doi.org/10.1046/j.1365-8711.2002.05778.x.

Bellot Rubio, L.R., Ortiz, J.L., Sada, P.V., 2000a. Luminous efficiency in hypervelocity impacts from the 1999 Lunar Leonids. Astrophys. J. 542, L65–L68. https://doi.org/10.1086/312914.

Bellot Rubio, L.R., Ortiz, J.L., Sada, P.V., 2000b. Observation and interpretation of meteoroid impact flashes on the moon. Earth Moon Planets 82-83, 575–598. https://doi.org/10.1023/A:1017097724416.

Bessell, M.S., 2005. Standard photometric systems. Annu. Rev. Astron. Astrophys. 43, 293–336. https://doi.org/10.1146/annurev.astro.41.082801.100251.

Bonanos, A.Z., Avdellidou, C., Liakos, A., Xilouris, E.M., Dapergolas, A., Koschny, D., Bellas-Velidis, I., Boumis, P., Charmandaris, V., Fytsilis, A., Maroussis, A., 2018. NELIOTA: first temperature measurement of lunar impact flashes. Astron. Astrophys. 612 (A76), 6. https://doi.org/10.1051/0004-6361/201732109.

Cooke, W.J., Suggs, R.M., Suggs, R.J., Swift, W.R., Hollon, N.P., 2007. Rate and distribution of kilogram lunar impactors. 38th Lunar and Planetary Science Conference, Abstract No. 1986.

Ernst, C.M., Schultz, P.H., 2002. Effect of velocity and angle on light intensity generated by hypervelocity impacts. 33th Lunar and Planetary Science Conference, Abstract No. 1782.

Ernst, C.M., Schultz, P.H., 2004. Early-time temperature evolution of the impact flash and beyond. 35th Lunar and Planetary Science Conference, Abstract No. 1721.

Ernst, C.M., Schultz, P.H., 2007. Evolution of the Deep Impact flash: implications for the nucleus surface based on laboratory experiments. Icarus 190, 334–344. https://doi.org/10.1016/j.icarus.2007.03.030.

Flower, P.J., 1996. Transformations from theoretical Hertzsprung-Russell diagrams to color-magnitude diagrams: effective temperatures, B-V colors, and bolometric corrections. Astrophys. J. 469, 355–365. https://doi.org/10.1086/177785.

Fuse, R., Abe, S., Yanagisawa, M., Hasegawa, S., 2020. An experimental study of the impact flash: the relationship between luminous efficiency and vacuum level. Planet. Space Sci. 187, 104921 https://doi.org/10.1016/j.pss.2020.104921.

Gault, D.E., 1974. Impact cratering. In: Greeley, R., Schultz, P.H. (Eds.), A Primer in Lunar Geology. NASA Ames, pp. 137–175.

Hermalyn, B., Schultz, P.H., Shirley, M., Ennico, K., Colaprete, A., 2012. Scouring the surface: ejecta dynamics and the LCROSS impact event. Icarus 218, 654–665. https://doi.org/10.1016/j.icarus.2011.12.025.

Jewitt, D., Hsieh, H., Agarwal, J., 2015. The active asteroids. In: Michel, P., DeMeo, F.E., Bottke, W.F. (Eds.), Asteroids IV. Univ. Arizona Press, Tucson, pp. 221–241. https://doi.org/10.2458/azu_uapress_9780816532131-ch012.

Kasuga, T., Jewitt, D., 2019. Asteroid-Meteoroid Complexes. In: Ryabova, G.O., Asher, D.J., Campbell-Brown, M.D. (Eds.), Meteoroids. Cambridge Univ. Press, pp. 187–209. https://doi.org/10.1017/9781108606462.

Kurosawa, K., Kadono, T., Sugita, S., Shigemori, K., Sakaiya, T., Hironaka, Y., Ozaki, N., Shiroshita, A., Cho, Y., Tachibana, S., Vinci, T., Ohno, S., Kodama, R., Matsui, T., 2012a. Shock-induced silicate vaporization: the role of electrons. J. Geophys. Res. 117 (E4), 14. https://doi.org/10.1029/2011JE004031.

Kurosawa, K., Ohno, S., Sugita, S., Mieno, T., Matsui, T., Hasagawa, S., 2012b. The nature of shock-induced calcite ($CaCO_3$) devolatilization in an open system investigated using a two-stage light gas gun. Earth Planet. Sci. Let. 337–338, 68–76. https://doi.org/10.1016/j.epsl.2012.05.022.

Liakos, A., Bonanos, A., Xilouris, E., Bellas-Velidis, I., Boumis, P., Charmandaris, V., Dapergolas, A., Fytsilis, A., Maroussis, A., Koschny, D., Moissl, R., Navarro, V., January 2019. NELIOTA lunar impact flash detection and event validation. In: Proceedings of the "ESA NEO and Debris Detection Conference - Exploiting Synergies. held in ESA/ESOC, Darmstadt, Germany, pp. 22–24.

Liakos, A., Bonanos, A.Z., Xilouris, E.M., Koschny, D., Bellas-Velidis, I., Boumis, P., Charmandaris, V., Dapergolas, A., Fytsilis, A., Maroussis, A., Moissl, R., 2020. NELIOTA: methods, statistics, and results for meteoroids impacting the moon. Astron. Astrophys. 633 (A112), 29. https://doi.org/10.1051/0004-6361/201936709.

Madiedo, J.M., Ortiz, J.L., Yanagisawa, M., Aceituno, J., Aceituno, F., 2019a. Impact Flashes of Meteoroids on the Moon. In: Ryabova, G.O., Asher, D.J., Campbell-Brown, M.D. (Eds.), Meteoroids. Cambridge Univ. Press, pp. 136–158. https://doi.org/10.1017/9781108606462.

McKay, D.S., Heiken, G., Basu, A., Blanford, G., Simon, S., Reedy, R., French, B.M., Papike, J., 1991. The Lunar Regolith. In: Heiken, G.H., Vaniman, D.T., French, B.M. (Eds.), Lunar Source Book. Cambridge Univ. Press, pp. 285–356.

Madiedo, J.M., Ortiz, J.L., Morales, N., 2018. The first observations to determine the temperature of a lunar impact flash and its evolution. Mon. Not. Roy. Astron. Soc. 480, 5010–5016. https://doi.org/10.1093/mnras/sty1862.
Madiedo, J.M., Ortiz, J.L., Morales, N., Román, A., Alonso, S., 2019c. Lunar impact flashes recorded during the 2018 Geminids: preliminary results. 50th lunar and planetary science conference, abstract No. 1406.
Madiedo, J.M., Ortiz, J.L., Morales, N., Santos-Sanz, P., 2019b. Multiwavelength observations of a bright impact flash during the January 2019 total lunar eclipse. Mon. Not. Roy. Astron. Soc. 486, 3380–3387. https://doi.org/10.1093/mnras/stz932.
Melosh, H.J., 1989. Impact Cratering: A Geologic Process. Oxford Univ. Press, New York. https://doi.org/10.1017/S0016756800007068.
Moser, D.E., Suggs, R.M., Swift, W.R., Suggs, R.J., Cooke, W.J., Diekmann, A.M., Koehler, H.M., 2010. Luminous efficiency of hypervelocity meteoroid impacts on the moon derived from the 2006 Geminids, 2007 Lyrids, and 2008 Taurids. Proceedings of the Meteoroids 2010 Conference. 142–154. In: NASA CP-2011–216469.
Nemtchinov, I.V., Shuvalov, V.V., Artemieva, N.A., Ivanov, B.A., Kosarev, I.B., Trubetskaya, I.A., 1998a. Light flashes caused by meteoroid impacts on the lunar surface. Sol. Syst. Res. 32, 99–114.
Nemtchinov, I.V., Shuvalov, V.V., Artemieva, N.A., Ivanov, B.A., Kosarev, I.B., Trubetskaya, I.A., 1998b. Light impulse created by meteoroids impacting the moon. 29th Lunar and Planetary Science Conference, Abstract No. 1032.
Ortiz, J.L., Madiedo, J.M., Morales, N., Santos-Sanz, P., Aceituno, F.J., 2015. Lunar impact flashes from Geminids: analysis of luminous efficiencies and the flux of large meteoroids on Earth. Mon. Not. Roy. Astron. Soc. 454, 344–352. https://doi.org/10.1093/mnras/stv1921.
Ramírez, I., Michel, R., Sefako, R., Tucci Maia, M., Schuster, W.J., van Wyk, F., Meléndez, J., Casagrande, L., Castilho, B.V., 2012. The $UBV(RI)_C$ colors of the sun. Astrophys. J. 752, 12. https://doi.org/10.1088/0004-637X/752/1/5.
Schubert, G., Walterscheid, R.L., 1999. Earth. In: Cox, A.N. (Ed.), Allen's Astrophysical Quantities, fourth ed. Springer, New York, pp. 239–292.
Schultz, P.H., 1996. Effect of impact angle on vaporization. J. Geophys. Res. 101 (E9), 21117–21136. https://doi.org/10.1029/96JE02266.
Schultz, P.H., Eberhardy, C.A., Ernst, C.M., A'Hearn, M.F., Sunshine, J.M., Lisse, C.M., 2007. The Deep Impact oblique impact cratering experiment. Icarus 190, 295–333. https://doi.org/10.1016/j.icarus.2007.06.006.
Schultz, P.H., Hermalyn, B., Colaprete, A., Ennico, K., Shirley, M., Marshall, W.S., 2010. The LCROSS cratering experiment. Science 330, 468–472. https://doi.org/10.1126/science.1187454.
Schultz, P.H., Eberhardy, C.A., 2015. Spectral probing of impact-generated vapor in laboratory experiments. Icarus 248, 448–462. https://doi.org/10.1016/j.icarus.2014.10.041.
Sugita, S., Schultz, P.H., Adams, M.A., 1998. Spectroscopic measurement of vapor clouds due to oblique impacts. J. Geophys. Res. 103, 19,427–19,441. https://doi.org/10.1029/98JE02026.
Sugita, S., Schultz, P.H., 1999. Spectroscopic characterization of hypervelocity jetting: comparison with a standard theory. J. Geophys. Res. 104, 30,825–30,845. https://doi.org/10.1029/1999JE001061.
Sugita, S., Schultz, P.H., Hasegawa, S., 2003. Intensities of atomic lines and molecular bands observed in impact-induced luminescence. J. Geophys. Res. 108 (E12), 14. https://doi.org/10.1029/2003JE002156.
Suggs, R.M., Moser, D.E., Cooke, W.J., Suggs, R.J., 2014. The flux of kilogram-sized meteoroids from lunar impact monitoring. Icarus 238, 23–26. https://doi.org/10.1016/j.icarus.2014.04.032.
Szalay, J.R., Pokorný, P., Jenniskens, P., Horányi, M., 2018. Activity of the 2013 Geminid meteoroid stream at the moon. Mon. Not. Roy. Astron. Soc. 474, 4225–4231. https://doi.org/10.1093/mnras/stx3007.
Tang, E., Shi, X., Zhang, Q., Wang, M., Wang, D., Xiang, S., Liu, S., Xia, J., He, L., Han, Y., 2015. Characterization of light flash signatures using optical-fiber pyrometer detectors during hypervelocity impact. Int. J. Appl. Electromagn. Mech. 47, 513–521. https://doi.org/10.3233/JAE-140015.
Vaubaillon, J., Neslusan, L., Sekhar, A., Rudawska, R., Ryabova, G.O., 2019. From Parent Body to Meteor Shower: The Dynamics of Meteoroid Streams. In: Ryabova, G.O., Asher, D.J., Campbell-Brown, M.D. (Eds.), Meteoroids. Cambridge Univ. Press, pp. 161–186. https://doi.org/10.1017/9781108606462.
Xilouris, E.M., Bonanos, A.Z., Bellas-Velidis, I., Boumis, P., Dapergolas, A., Maroussis, A., Liakos, A., Alikakos, I., Charmandaris, V., Dimou, G., Fytsilis, A., Kelley, M., Koschny, D., Navarro, V., Tsiganis, K., Tsinganos, K., 2018. NELIOTA: the wide-field, high-cadence, lunar monitoring system at the prime focus of the Kryoneri telescope. Astron. Astrophys. 619 (A141), 14. https://doi.org/10.1051/0004-6361/201833499.
Yamada, R., Garcia, R.F., Lognonné, P., Le Feuvre, M., Calvet, M., Gagnepain-Beyneix, J., 2011. Optimisation of seismic network design: application to a geophysical international lunar network. Planet. Space Sci. 59, 343–354. https://doi.org/10.1016/j.pss.2010.12.007.
Yamada, R., Kawamura, T., Yanagisawa, M., Abe, S., Fukuhara, T., Onodera, K., Uchida, Y., Kurihara, S., Fuse, R., Yoshida, F., Chi, H., Avdellidou, C., Shirai, K., Ishihara, Y., Tanaka, S., Shiraishi, H., Wieczoreck, M., 2019. The international observation of lunar impact flashes and application of the results to future lunar seismic experiments. 50th Lunar and Planetary Science Conference, Abstract No. 1770.
Yanagisawa, M., Kisaichi, N., 2002. Lightcurves of 1999 Leonid impact flashes on the moon. Icarus 159, 31–38. https://doi.org/10.1006/icar.2002.6931.
Yanagisawa, M., Ikegami, H., Ishida, M., Karasaki, H., Takahashi, J., Kinoshita, K., Ohnishi, K., 2008. Lunar impact flashes by Geminid meteoroids. In: 2007. 71st Annual Meteoritical Society Meeting, Meteoritics and Planetary Sciences Supplement 43, Id. 5169.

The Astronomical Journal, 161:116 (15pp), 2021 March https://doi.org/10.3847/1538-3881/abd94b

Initial Characterization of Active Transitioning Centaur, P/2019 LD_2 (ATLAS), Using Hubble, Spitzer, ZTF, Keck, Apache Point Observatory, and GROWTH Visible and Infrared Imaging and Spectroscopy

Bryce T. Bolin[1,2], Yanga R. Fernandez[3], Carey M. Lisse[4], Timothy R. Holt[5,6], Zhong-Yi Lin[7], Josiah N. Purdum[8], Kunal P. Deshmukh[9], James M. Bauer[10], Eric C. Bellm[11], Dennis Bodewits[12], Kevin B. Burdge[1], Sean J. Carey[2], Chris M. Copperwheat[13], George Helou[2], Anna Y. Q. Ho[1], Jonathan Horner[5], Jan van Roestel[1], Varun Bhalerao[14], Chan-Kao Chang[7], Christine Chen[15,16], Chen-Yen Hsu[7], Wing-Huen Ip[7], Mansi M. Kasliwal[1], Frank J. Masci[2], Chow-Choong Ngeow[7], Robert Quimby[8,17], Rick Burruss[18], Michael Coughlin[19], Richard Dekany[18], Alexandre Delacroix[18], Andrew Drake[1], Dmitry A. Duev[1], Matthew Graham[1], David Hale[18], Thomas Kupfer[20], Russ R. Laher[2], Ashish Mahabal[1,21], Przemyslaw J. Mróz[1], James D. Neill[1], Reed Riddle[19], Hector Rodriguez[19], Roger M. Smith[19], Maayane T. Soumagnac[22,23], Richard Walters[1], Lin Yan[24], and Jeffry Zolkower[18]

[1] Division of Physics, Mathematics and Astronomy, California Institute of Technology, Pasadena, CA 91125, USA; bbolin@caltech.edu
[2] IPAC, Mail Code 100-22, Caltech, 1200 E. California Blvd., Pasadena, CA 91125, USA
[3] Department of Physics, University of Central Florida, Orlando, FL 32816, USA
[4] Johns Hopkins University Applied Physics Laboratory, Laurel, MD 20723, USA
[5] Centre for Astrophysics, University of Southern Queensland, West St., Toowoomba, QLD 4350, Australia
[6] Southwest Research Institute, Department of Space Studies, Boulder, CO 80302, USA
[7] Graduate Institute of Astronomy, National Central University, 32001, Taiwan
[8] Department of Astronomy, San Diego State University, 5500 Campanile Dr., San Diego, CA 92182, USA
[9] Department of Metallurgical Engineering and Materials Science, Indian Institute of Technology Bombay, Powai, Mumbai-400076, India
[10] Department of Astronomy, University of Maryland, College Park, MD 20742-0001, USA
[11] DIRAC Institute, Department of Astronomy, University of Washington, 3910 15th Ave. NE, Seattle, WA 98195, USA
[12] Physics Department, Leach Science Center, Auburn University, Auburn, AL 36832, USA
[13] Astrophysics Research Institute Liverpool John Moores University, 146 Brownlow Hill, Liverpool L3 5RF, UK
[14] Department of Physics, Indian Institute of Technology Bombay, Powai, Mumbai-400076, India
[15] Space Telescope Science Institute (STScI), 3700 San Martin Dr., Baltimore, MD 21218, USA
[16] Department of Physics and Astronomy, The Johns Hopkins University, 3701 San Martin Dr., Baltimore, MD 21218, USA
[17] Kavli Institute for the Physics and Mathematics of the Universe (WPI), The University of Tokyo Institutes for Advanced Study, The University of Tokyo, Kashiwa, Chiba 277-8583, Japan
[18] Caltech Optical Observatories, California Institute of Technology, Pasadena, CA 91125, USA
[19] School of Physics and Astronomy, University of Minnesota, Minneapolis, MN 55455, USA
[20] Kavli Institute for Theoretical Physics, University of California, Santa Barbara, CA 93106, USA
[21] Center for Data Driven Discovery, California Institute of Technology, Pasadena, CA 91125, USA
[22] Lawrence Berkeley National Laboratory, 1 Cyclotron Rd., Berkeley, CA 94720, USA
[23] Department of Particle Physics and Astrophysics, Weizmann Institute of Science, Rehovot 76100, Israel
[24] The Caltech Optical Observatories, California Institute of Technology, Pasadena, CA 91125, USA
Received 2020 November 6; revised 2020 December 21; accepted 2021 January 5; published 2021 February 11

Abstract

We present visible and mid-infrared imagery and photometry of temporary Jovian co-orbital comet P/2019 LD_2 taken with Hubble Space Telescope/Wide Field Camera 3 (HST/WFC3), Spitzer Space Telescope/Infrared Array Camera (Spitzer/IRAC), and the GROWTH telescope network, visible spectroscopy from Keck/Low-Resolution Imaging Spectrometer (LRIS), and archival Zwicky Transient Facility observations taken between 2019 April and 2020 August. Our observations indicate that the nucleus of LD_2 has a radius between 0.2 and 1.8 km assuming a 0.08 albedo and a coma dominated by $\sim$100 μm-scale dust ejected at $\sim$1 m s^{-1} speeds with a $\sim$1′ jet pointing in the southwest direction. LD_2 experienced a total dust mass loss of $\sim 10^8$ kg at a loss rate of $\sim$6 kg s^{-1} with Afρ/cross section varying between $\sim$85 cm/125 km^2 and $\sim$200 cm/310 km^2 from 2019 April 9 to 2019 November 8. If the increase in Afρ/cross section remained constant, it implies LD_2's activity began $\sim$2018 November when within 4.8 au of the Sun, implying the onset of H_2O sublimation. We measure CO/CO_2 gas production of $\lesssim 10^{27}$ mol s^{-1}/$\lesssim 10^{26}$ mol s^{-1} from our 4.5 μm Spitzer observations; g–$r = 0.59 \pm 0.03$, r–$i = 0.18 \pm 0.05$, and i–$z = 0.01 \pm 0.07$ from GROWTH observations; and H_2O gas production of $\lesssim$80 kg s^{-1} scaling from our estimated C_2 production of $Q_{C_2} \lesssim 7.5 \times 10^{24}$ mol s^{-1} from Keck/LRIS spectroscopy. We determine that the long-term orbit of LD_2 is similar to Jupiter-family comets having close encounters with Jupiter within $\sim$0.5 Hill radius in the last $\sim$3 y and within 0.8 Hill radius in $\sim$9 y. Additionally, 78.8% of our orbital clones are ejected from the solar system within 1×10^6 yr, having a dynamical half-life of 3.4×10^5 yr.

Unified Astronomy Thesaurus concepts: Celestial mechanics (211); Centaurs (215); Short period comets (1452)

1. Introduction

The gas giant Jupiter is the dominant gravitational perturbing body affecting the dynamical transfer of solar system comets from the outer solar system's trans-Neptunian disk beyond the orbit of Neptune into the inner reaches of the solar system (recently described in Dones et al. 2015). The vast majority of comets transfer from the outer solar system regions such as the Oort Cloud in the case of long-period comets (recently described in Vokrouhlický et al. 2019) or the trans-Neptunian region in the case of short-period comets (recently described in Nesvorný et al. 2017). Once the comets originating from the trans-Neptunian region randomly walk their way through the outer solar system and become strongly influenced by close encounters with Neptune and Uranus, a significant portion are transformed in their orbital configuration into the Centaur group of small bodies. The Centaur class is defined as having semimajor axes, a, and perihelion, q, between 5.2 au, the semimajor axis a_J of Jupiter, and 30 au, the semimajor axis of Neptune, a_N (Jewitt 2009). An additional quantity used to define the small bodies in the inner solar system is the Tisserand parameter with respect to Jupiter, T_J, defined as

$$T_J = \frac{a_J}{a} + 2\sqrt{(1 - e^2)\frac{a}{a_J}}\cos i \tag{1}$$

where e is the eccentricity of the body and i is the inclination. The parameter T_J can be used as a rough indication of how much an object is influenced by the gravitational perturbations of Jupiter (Murray & Dermott 1999). Centaurs are objects that generally have $T_j > 3.05$ (Gladman et al. 2008), whereas Jupiter-family comets have $3 > T_J > 2$ (Duncan et al. 2004). However, we note that the $T_j > 3.05$ boundary does not strictly define objects as Centaurs as there can be non-Centaur objects with $T_j > 3.05$.

The mean dynamical half-life of Centaurs is ∼2.7 Myr, with the vast majority of Centaurs eventually being ejected from the solar system (Horner et al. 2004b), while the Jupiter-family comets have a bit shorter lifetimes of ∼0.5 Myr (Levison & Duncan 1994). The chaotic evolution of the Centaurs causes a significant number (around one-third) to become Jupiter-family comets at some point in their lifetimes, prior to their eventual ejection from the solar system (Horner et al. 2004a). The Centaur 2014 OG_{392}, recently discovered to be active (Chandler et al. 2020), may be an example of an object transitioning between the Centaur and Jupiter-family comet groups. Some can even be temporarily captured as satellites of the giant planets, or by the Jovian and Neptunian Trojan populations (e.g., Horner & Evans 2006; Horner & Lykawka 2012). Another example of a Centaur recently in the stage of becoming a Jupiter-family comet is 29P/Schwassmann-Wachmann. Centaur 29P is located in a region of orbital parameter space with $5.5\ \mathrm{au} < q < 8.0\ \mathrm{au}$ and aphelion $5\ \mathrm{au} < Q < 7\ \mathrm{au}$ that acts as a "gateway" that the Centaurs preferentially inhabit while in the process of dynamically transferring to become Jupiter-family comets (Sarid et al. 2019).

The recently discovered, briefly Jovian co-orbital comet P/2019 LD_2 (Sato et al. 2020), with a semimajor axis of 5.30 au, a perihelion of 4.57 au, and aphelion of 6.02 au, may be another example of an object in the transition region between Centaur objects and Jupiter-family comets. The comet will only spend about one orbit in the dynamical configuration where it has a Jupiter-similar semimajor axis (Hsieh et al. 2021; Kareta et al. 2020a). Initially reported as an inactive object by the ATLAS survey (Tonry 2011) in 2019 June and designated by the Minor Planet Center as 2019 LD_2,[25] it was discovered to be active by amateur astronomers.[26] Prediscovery images and follow-up images of the comet taken by ATLAS and other ground-based telescopes resulted in it being given the cometary designation P/2019 LD_2 (Fitzsimmons et al. 2020). While technically some of the orbital elements of P/2019 LD_2, such as its semimajor axis, resemble those of a Jovian co-orbital, it is inherently unstable, in stark contrast to the stable orbits of Jovian Trojans, which are stable on timescales comparable to the age of the solar system and are located at $\sim\pm 60°$ mean longitude with respect to Jupiter (e.g., Marzari et al. 2002). In addition, the Jovian Trojans have a different origin, having most likely been captured as a result of Jupiter's migration during the solar system's formation, 4.5 Gyr ago (e.g., Morbidelli et al. 2005; Roig & Nesvorný 2015).

One proposed origin for P/2019 LD_2 is that it is a Jupiter-family comet in the transition region in orbital parameter space inhabited by objects that are in transition between Centaurs and Jupiter-family comets (Steckloff et al. 2020). As comets transfer from their origins in the outer solar system beyond the orbit of Neptune and become denizens of the inner solar system, they will experience a dramatic shift in thermal environment, due to increased thermal insolation from the Sun (De Sanctis et al. 2000; Sarid & Prialnik 2009). The consequence of the increased solar insolation as the comet nears the Sun is the increased heating and sublimation of volatiles such as CO and H_2O near the comet's surface (Meech & Svoren 2004). Another consequence of the increased heating from closer proximity to the Sun is that large-scale ablation of the comet's structure due to thermal stress can occur, resulting in it becoming partially or completely disrupted (Fernández 2009). Since P/2019 LD_2 is now in transition between the Centaur and Jupiter-family comet populations, it seems likely that it has become active for the first time, and as such, its activity will be rapidly evolving in response to the new epoch of increased solar heating.

We therefore present in this paper an analysis of visible-light, high-resolution Hubble Space Telescope/Wide Field Camera 3 (HST/WFC3; Dressel 2012) observations of P/2019 LD_2 using the approach of Jewitt et al. (2014) and Bolin & Lisse (2020) to understand the dust coma and nucleus properties, and to constrain the cause of P/2019 LD_2's activity. We will also use mid-infrared (MIR) P/2019 LD_2 observations taken with the Spitzer Space Telescope/Infrared Array Camera (Spitzer/IRAC; Werner et al. 2004) combined with the analysis techniques of Reach et al. (2013) and Lisse et al. (2020) to place upper limits on the comet's $CO+CO_2$ gas production. We also use multiwavelength observations covering the visible and MIR by building on the techniques of Bolin et al. (2020b) by using a network of ground-based observatories to characterize the physical properties of this transitioning Centaur. In addition, we will examine the long-term orbital properties of P/2019 LD_2 using its latest orbital solution in order to better understand its possible origins and future dynamical evolution.

2. Observations

Observations of P/2019 LD_2 were obtained before the official announcement of its activity in 2020 May both by targeted observations by ground- and space-based observatories and serendipitously in the survey observations by the Zwicky Transient Facility (ZTF; Graham et al. 2019). The time span of our targeted observations is 2019 September 7 UTC to 2020 August 19 UTC, including observations by the Astrophysical Research Consortium 3.5 m telescope (ARC 3.5 m),

[25] https://minorplanetcenter.net/db_search/show_object?utf8=%E2%9C%93&object_id=P%2F2019+LD2
[26] http://aerith.net/comet/catalog/2019LD2/2019LD2.html

Table 1
Summary of P/2019 LD_2 Target Observations Viewing Geometry

Date[1] UTC	Facility[2]	Filter[3]	θ_s^4 (″)	χ_{am}^5	r_H^6 (au)	Δ^7 (au)	α^8 (°)	δ_E^9 (°)	$T - T_p^{10}$ (days)
2019 Apr 26	ZTF[a]	r	2.17	1.76	4.693	4.147	10.99	−1.56	−343.97
2019 Sep 07	ARC	g,r	1.4	1.81	4.622	4.279	12.23	−0.74	−216.58
2020 Jan 25–26	Spitzer	4.5 μm	⋯	⋯	4.584	4.256[b]	12.61[b]	0.23[b]	−76.58
2020 Apr 01	HST	F350LP	⋯	⋯	4.578	5.023	10.71	−0.44	−9.58
2020 May 27	MLO 1.0-m	B,V,R	1.92	1.49	4.580	4.221	12.38	−2.50	46.42
2020 May 29	LT	g,r,i,z	1.21	1.75	4.580	4.193	12.27	−2.56	48.42
2020 June 23–27	LOT	B,V,R	1.47	1.14	4.583	3.848	9.59	−3.00	75.42
2020 July 10	LOT	B,V,R	1.45	1.15	4.586	3.707	7.11	−2.97	90.42
2020 Aug 19	Keck I	Sp.[c]	0.85	1.80	4.594	3.608	3.20	−1.76	130.42

Notes. Columns: (1) observation date; (2) observational facility; (3) filter (for the Keck I observations, the B600/4000 grism and R600/7500 grating are used with the Low-Resolution Imaging Spectrometer instrument[c]); (4) in-image seeing of observations; (5) air mass of observations; (6) heliocentric distance; (7) topocentric distance; (8) phase angle; (9) topocentric and target orbital plane angle; (10) difference between time of observation T and time of perihelion T_p.
[a] Serendipitous observation of P/2019 LD_2 with ZTF, but included in this table because of its inclusion in the top left panel of Figure 1.
[b] *Spitzer*-centric.
[c] https://www2.keck.hawaii.edu/inst/lris/dispersive_elements.html

Spitzer, HST, Keck I, and members of the GROWTH network (Kasliwal et al. 2019), such as the Mount Laguna Observatory 40 inch Telescope (MLO 1.0 m), Liverpool Telescope (LT), and Lulin Optical Telescope (LOT). A list of our targeted observations and their viewing geometry are provided in Table 1. The time span of our serendipitous observations of P/2019 LD_2 made with the ZTF survey is between 2019 April 9 UTC and 2019 November 8 UTC, and the photometry data are listed with the viewing geometry in Table 2.

2.1. Zwicky Transient Facility

We searched for serendipitous observations of P/2019 LD_2 made with the Zwicky Transient Facility survey mounted on the Palomar Observatory's 48 inch telescope (Bellm et al. 2019) in the ZTF archive (Masci et al. 2019). The ZTF archive possessed observations of P/2019 LD_2 made as far back as 2019 April 9 UTC, which we include up to 2019 November 8 UTC. The observations were made in the g and r bands in images consisting of 30 s exposures. Seeing conditions were typically between 1.″5 and 2.″5 and at air masses ranging from 1.4 to 2.6. A full list of observations of P/2019 LD_2 made by ZTF containing the viewing geometry and observing conditions is presented in Table 2.

2.2. Apache Point Astrophysical Research Consortium 3.5 m

Following the announcement of the appearance of activity of P/2019 LD_2^2 (then called 2019 LD_2), we triggered target-of-opportunity observations with the ARC 3.5 m telescope at Apache Point Observatory (APO) on 2019 September 7 UTC using the ARCTIC large-format optical CCD camera (Huehnerhoff et al. 2016). The camera was used in full-frame, quad amplifier readout, 2 × 2 binning mode, resulting in a pixel scale of 0.″228, and it was used with the g and r filters. In total, 14 g and r exposures were obtained, each 120 s long and in alternating order between the g and r filters. The telescope was tracked at the sky-motion rate of the comet of 8.″6 hr^{-1}. The seeing was 1.″4 and the air mass was 1.8 during the observations.

2.3. Spitzer Space Telescope

Observations of P/2019 LD_2 were made with the Spitzer Space Telescope (Spitzer) using the IRAC instrument (Fazio et al. 2004) on 2020 January 25–26 UTC (DDT program 14331, PI Bolin et al. 2019). The observations consisted of 11 Astronomical Observing Requests (AORs), each consisting of 80 × 12 s dithered frames and having a ∼0.44 hr duration for a total of 4.8 hr clock time. The frames where dithered in groups of 10, with each using a large cycling pattern. The sky at the location of P/2019 LD_2 during the Spitzer observations possessed a high density of stars due to its low −18° galactic latitude, so shadow observations were used to improve the sensitivity of the observations. Out of a total of 11 AORs, eight were focused on the observed P/2019 LD_2, for a total of 2.13 hr of on-source time. The remaining three AORs were shadow observations that were evenly spaced in the sky location covering the trajectory of P/2019 LD_2 during 2020 January 02:23:32–23:10:44 that P/2019 LD_2 was being observed. The target was centered in the 4.5 μm channel because this channel is sensitive to CO/CO_2 emission and also because the object was expected to be the brightest at this wavelength. The 4.5 μm IRAC channel has a spatial resolution of 1.″2 $pixel^{-1}$. The data were reduced in a method as described in Fernández et al. (2013).

2.4. Hubble Space Telescope

The *Hubble Space Telescope* was used to observe P/2019 LD_2 with General Observer's (GO) time on 2020 April 1 UTC (HST GO 16077, PI Bolin et al. 2020a). During the one orbit visit, five 380 s F350LP filter exposures were obtained with the UVIS2 array of the WFC3/UVIS camera (Dressel 2012) for a total of 1900 s of integration time over a single orbit. The F350LP filter has a central wavelength of 582 nm with an FWHM bandpass of 490 nm (Deustua et al. 2017). The instrument and filter combination of WFC3 and the F350LP filter provides a per-pixel resolution of 0.″04 corresponding to 145 km at the topocentric distance of the comet. The comet was tracked nonsidereally according to its sky-plane rate of motion of 40″ hr^{-1}.

Table 2
Summary of ZTF P/2019 LD_2 Photometry

Date[1] UTC	r_H^2 (au)	Δ^3 (au)	α^4 (°)	$T - T_p^5$ (days)	Filter[6]	mag[7]	σ_{mag}^8	θ_s^9 (″)	χ_{am}^{10}	A(0°)$f\rho$[11] (cm)	C[12] (km^2)
2019 Apr 09-10:32	4.704	4.391	12.0	−360.20	*r*	19.33	0.15	2.36	1.72	85.28	127.69
2019 Apr 12-10:32	4.702	4.345	11.9	−357.32	*r*	19.27	0.16	2.83	1.66	87.90	131.53
2019 Apr 15-09:59	4.700	4.300	11.7	−354.47	*r*	19.13	0.15	1.82	2.02	97.23	145.35
2019 Apr 20-09:33	4.697	4.227	11.4	−349.70	*r*	18.97	0.23	1.87	1.83	107.69	160.77
2019 Apr 20-10:04	4.697	4.226	11.4	−349.68	*r*	18.83	0.23	2.44	1.51	122.45	182.81
2019 Apr 26-09:00	4.693	4.142	11.0	−343.97	*g*	19.69	0.14	2.14	1.91	83.20	124.00
2019 Apr 26-09:07	4.693	4.142	11.0	−343.96	*g*	19.38	0.13	2.18	2.12	110.69	164.97
2019 Apr 26-11:26	4.693	4.141	11.0	−343.87	*r*	18.89	0.07	1.90	1.41	109.63	163.38
2019 Apr 26-11:36	4.693	4.141	11.0	−343.86	*r*	19.18	0.07	1.68	1.37	83.93	125.08
2019 May 02-10:03	4.689	4.061	10.4	−338.17	*r*	18.95	0.11	2.47	1.56	97.64	145.18
2019 May 02-10:32	4.689	4.061	10.4	−338.15	*r*	18.99	0.09	1.82	1.41	94.11	139.93
2019 May 31-08:22	4.672	3.763	6.1	−310.33	*r*	18.76	0.07	1.60	1.44	85.34	125.82
2019 May 31-10:34	4.672	3.762	6.1	−310.24	*g*	18.96	0.07	1.79	1.44	112.44	165.78
2019 Jun 01-09:04	4.671	3.755	6.0	−309.33	*r*	18.57	0.05	1.78	1.38	100.81	148.64
2019 Jun 02-09:34	4.671	3.748	5.8	−308.35	*r*	18.49	0.07	2.53	1.37	107.32	158.24
2019 Jun 02-10:57	4.671	3.748	5.8	−308.29	*g*	18.95	0.08	1.93	1.52	111.35	164.18
2019 Jun 03-11:33	4.670	3.741	5.6	−307.30	*g*	18.52	0.18	1.99	1.71	163.56	241.16
2019 Jun 04-07:01	4.670	3.736	5.5	−306.52	*r*	18.06	0.06	2.07	1.67	156.64	230.96
2019 Jun 04-08:31	4.670	3.736	5.5	−306.46	*g*	18.68	0.09	2.55	1.40	140.25	206.79
2019 Jun 06-06:37	4.668	3.725	5.1	−304.60	*r*	18.36	0.08	1.99	1.77	116.28	171.48
2019 Jun 06-08:33	4.668	3.724	5.1	−304.53	*g*	18.63	0.09	2.11	1.39	143.63	211.82
2019 Jun 07-09:33	4.668	3.719	4.9	−303.52	*r*	18.14	0.06	1.87	1.39	140.87	207.78
2019 Jun 08-06:36	4.667	3.714	4.8	−302.67	*r*	18.57	0.09	1.90	1.73	94.15	138.88
2019 Jun 08-09:12	4.667	3.713	4.8	−302.57	*g*	18.56	0.08	2.07	1.37	150.52	222.03
2019 Jun 09-06:36	4.667	3.709	4.6	−301.71	*r*	18.38	0.06	1.89	1.70	111.02	163.79
2019 Jun 10-07:02	4.666	3.704	4.5	−300.72	*r*	18.34	0.06	1.90	1.56	114.39	168.78
2019 Jun 10-08:03	4.666	3.704	4.5	−300.68	*g*	18.70	0.10	2.27	1.40	130.13	192.01
2019 Jun 11-09:43	4.666	3.699	4.3	−299.65	*g*	18.90	0.10	1.93	1.42	107.13	158.11
2019 Jun 14-08:02	4.664	3.688	3.9	−296.81	*g*	18.74	0.22	2.03	1.38	121.43	179.30
2019 Jun 20-07:50	4.661	3.673	3.3	−291.02	*g*	18.61	0.22	2.51	1.38	132.47	195.84
2019 Jun 20-08:17	4.661	3.673	3.3	−291.00	*r*	18.15	0.10	1.97	1.37	127.68	188.75
2019 Jun 23-09:02	4.659	3.669	3.2	−288.07	*r*	18.23	0.08	2.41	1.43	117.79	174.17
2019 Jun 23-10:34	4.659	3.669	3.2	−288.00	*g*	18.77	0.18	2.57	1.84	113.53	167.87
2019 Jun 26-07:37	4.657	3.667	3.2	−285.22	*r*	18.21	0.05	1.87	1.37	119.75	177.06
2019 Jun 26-08:02	4.657	3.667	3.2	−285.20	*g*	18.80	0.08	2.19	1.38	110.22	162.98
2019 Jul 01-06:45	4.655	3.671	3.5	−280.41	*r*	18.33	0.05	1.84	1.40	108.62	160.51
2019 Jul 01-06:46	4.655	3.671	3.5	−280.41	*r*	18.33	0.05	1.77	1.39	108.62	160.51
2019 Jul 01-07:44	4.655	3.671	3.5	−280.37	*r*	18.34	0.06	2.37	1.38	107.63	159.04
2019 Jul 01-07:44	4.655	3.671	3.5	−280.37	*r*	18.34	0.06	2.18	1.38	107.63	159.04
2019 Jul 03-07:10	4.654	3.674	3.8	−278.45	*r*	18.17	0.05	2.31	1.37	127.49	188.29
2019 Jul 03-07:32	4.654	3.674	3.8	−278.44	*g*	18.58	0.07	2.14	1.37	138.51	204.56
2019 Jul 04-07:36	4.653	3.676	3.9	−277.46	*r*	18.09	0.05	2.04	1.38	137.86	203.57
2019 Jul 06-06:43	4.652	3.681	4.2	−275.56	*g*	18.74	0.09	1.92	1.38	121.73	179.68
2019 Jul 08-07:32	4.651	3.687	4.5	−273.59	*g*	18.48	0.07	1.92	1.39	156.89	231.49
2019 Jul 09-05:29	4.651	3.690	4.6	−272.70	*r*	18.13	0.04	1.58	1.48	137.39	202.69
2019 Jul 09-07:36	4.651	3.690	4.6	−272.61	*g*	18.61	0.07	1.84	1.40	139.94	206.46
2019 Jul 10-06:01	4.650	3.694	4.8	−271.71	*r*	18.21	0.06	2.02	1.41	128.82	190.02
2019 Jul 10-06:02	4.650	3.694	4.8	−271.71	*r*	18.06	0.06	2.30	1.41	147.90	218.17
2019 Jul 10-06:13	4.650	3.694	4.8	−271.70	*r*	18.27	0.06	1.96	1.39	121.89	179.80
2019 Jul 10-06:31	4.650	3.694	4.8	−271.69	*r*	18.20	0.07	2.44	1.38	130.01	191.77
2019 Jul 10-06:41	4.650	3.694	4.8	−271.68	*r*	18.15	0.05	2.04	1.37	136.14	200.81
2019 Jul 10-06:42	4.650	3.694	4.8	−271.68	*r*	18.18	0.06	2.14	1.37	132.43	195.34
2019 Jul 11-07:29	4.649	3.698	4.9	−270.68	*g*	18.70	0.13	1.90	1.40	130.73	192.82
2019 Jul 12-06:32	4.649	3.702	5.1	−269.74	*r*	18.23	0.11	2.46	1.37	128.40	189.36
2019 Jul 12-06:33	4.649	3.702	5.1	−269.74	*r*	18.25	0.10	2.35	1.37	126.06	185.90
2019 Jul 12-07:24	4.649	3.702	5.1	−269.71	*g*	18.53	0.15	2.01	1.40	154.37	227.66
2019 Jul 13-06:03	4.648	3.706	5.3	−268.79	*r*	18.12	0.10	2.49	1.39	143.40	211.46
2019 Jul 13-07:51	4.648	3.707	5.3	−268.72	*g*	18.80	0.24	1.69	1.45	121.56	179.25
2019 Jul 16-05:21	4.647	3.721	5.8	−265.91	*g*	18.57	0.28	2.10	1.39	154.15	227.28
2019 Jul 16-06:32	4.647	3.721	5.8	−265.86	*r*	18.26	0.16	1.92	1.39	129.40	190.79
2019 Jul 20-06:54	4.645	3.745	6.5	−261.96	*g*	18.65	0.16	2.67	1.45	148.69	219.26
2019 Jul 21-05:12	4.645	3.751	6.6	−261.05	*r*	18.22	0.04	1.52	1.38	140.36	206.99
2019 Jul 21-05:13	4.645	3.751	6.6	−261.05	*r*	18.18	0.04	1.58	1.38	145.63	214.76

Table 2
(Continued)

Date[1] UTC	r_H^2 (au)	Δ^3 (au)	α^4 (°)	$T - T_p^5$ (days)	Filter[6]	mag[7]	σ_{mag}^8	θ_s^9 (″)	χ_{am}^{10}	A(0°)$f\rho$[11] (cm)	C[12] (km^2)
2019 Jul 21-05:43	4.644	3.751	6.6	−261.03	*r*	18.17	0.05	1.44	1.37	146.91	216.66
2019 Jul 21-06:07	4.644	3.751	6.7	−261.01	*r*	18.34	0.05	1.46	1.38	126.07	185.94
2019 Jul 21-06:44	4.644	3.752	6.7	−260.99	*r*	18.35	0.09	2.67	1.43	124.98	184.33
2019 Jul 21-06:44	4.644	3.752	6.7	−260.99	*r*	18.31	0.08	2.71	1.44	129.68	191.25
2019 Jul 30-06:02	4.640	3.820	8.2	−252.26	*r*	18.21	0.05	1.85	1.42	155.19	229.33
2019 Jul 30-06:03	4.640	3.820	8.2	−252.26	*r*	18.20	0.04	1.70	1.42	156.63	231.45
2019 Jul 30-06:29	4.640	3.820	8.2	−252.24	*r*	18.27	0.05	1.92	1.49	146.85	217.00
2019 Jul 30-06:30	4.640	3.820	8.2	−252.24	*r*	18.30	0.05	1.82	1.49	142.85	211.08
2019 Aug 03-04:02	4.638	3.856	8.8	−248.45	*r*	18.31	0.10	1.65	1.40	147.13	217.68
2019 Aug 12-03:38	4.634	3.949	10.0	−239.69	*r*	18.11	0.16	3.23	1.39	192.88	286.40
2019 Aug 16-07:30	4.632	3.996	10.5	−235.63	*r*	18.34	0.16	1.83	1.78	162.34	241.48
2019 Aug 19-03:27	4.631	4.030	10.8	−232.87	*r*	18.33	0.09	1.41	1.38	168.23	250.52
2019 Aug 23-04:03	4.629	4.080	11.2	−228.94	*g*	18.73	0.09	1.80	1.39	191.39	285.49
2019 Aug 28-04:52	4.627	4.145	11.6	−224.02	*r*	18.34	0.06	1.73	1.54	180.68	269.98
2019 Aug 28-04:53	4.627	4.145	11.6	−224.02	*r*	18.37	0.06	1.78	1.54	175.75	262.63
2019 Aug 28-05:28	4.627	4.146	11.6	−223.99	*r*	18.43	0.06	1.56	1.71	166.38	248.63
2019 Aug 28-05:29	4.627	4.146	11.6	−223.99	*r*	18.51	0.06	1.68	1.72	154.56	230.97
2019 Aug 29-04:45	4.627	4.159	11.7	−223.05	*r*	18.37	0.06	2.22	1.53	177.51	265.38
2019 Aug 29-04:46	4.627	4.159	11.7	−223.05	*r*	18.43	0.07	2.42	1.53	167.97	251.11
2019 Aug 29-05:46	4.627	4.159	11.7	−223.00	*r*	18.37	0.06	1.60	1.86	177.51	265.38
2019 Aug 29-05:46	4.627	4.159	11.7	−223.00	*r*	18.38	0.06	1.62	1.87	175.88	262.95
2019 Aug 29-06:13	4.627	4.159	11.7	−222.99	*g*	18.85	0.14	1.96	2.13	180.81	270.31
2019 Sep 02-03:50	4.625	4.212	12.0	−219.17	*g*	18.94	0.11	1.84	1.43	172.19	257.81
2019 Sep 02-05:06	4.625	4.213	12.0	−219.12	*r*	18.56	0.09	2.20	1.70	154.25	230.94
2019 Sep 03-03:40	4.624	4.226	12.0	−218.20	*g*	18.73	0.14	1.85	1.41	210.23	314.76
2019 Sep 09-03:04	4.622	4.309	12.3	−212.35	*g*	18.97	0.26	1.95	1.40	176.75	265.04
2019 Sep 09-05:38	4.622	4.311	12.3	−212.25	*r*	18.65	0.22	2.84	2.23	149.88	224.75
2019 Sep 25-03:09	4.616	4.540	12.5	−196.68	*r*	18.61	0.12	4.13	1.57	173.11	259.86
2019 Sep 25-04:55	4.616	4.542	12.5	−196.61	*g*	19.11	0.23	2.74	2.55	173.26	260.09
2019 Oct 01-03:35	4.614	4.628	12.4	−190.78	*g*	18.95	0.12	2.15	1.67	207.61	311.48
2019 Oct 09-02:21	4.611	4.742	12.2	−182.98	*g*	19.16	0.25	1.78	1.49	178.27	267.18
2019 Oct 12-02:42	4.610	4.785	12.0	−180.02	*r*	18.50	0.12	2.11	1.62	208.92	312.79
2019 Oct 16-02:42	4.608	4.840	11.8	−176.09	*g*	19.09	0.17	2.40	1.70	195.32	292.15
2019 Oct 19-02:09	4.607	4.881	11.6	−173.17	*r*	18.71	0.12	1.47	1.59	176.65	263.96
2019 Oct 19-02:36	4.607	4.882	11.6	−173.15	*g*	19.10	0.14	1.94	1.74	195.56	292.23
2019 Oct 22-02:40	4.606	4.922	11.4	−170.20	*g*	19.14	0.15	2.32	1.852	190.28	284.07
2019 Oct 26-02:30	4.605	4.975	11.1	−166.27	*g*	19.42	0.22	3.93	1.891	148.68	221.69
2019 Oct 26-02:35	4.605	4.975	11.1	−166.27	*r*	18.57	0.12	2.23	1.935	205.24	306.01
2019 Nov 08-01:48	4.601	5.135	9.9	−153.51	*r*	18.60	0.19	2.13	1.755	204.05	302.88

Note. Columns: (1) observation date; (2) heliocentric distance; (3) topocentric distance; (4) phase angle; (5) difference between time of observation T and time of perihelion T_p; (6) filter; (7) 2×10^4 km aperture mag; (8) 1σ mag uncertainty; (9) in-image seeing of observations; (10) air mass of observations; (11) A(0°)$f\rho$ of observations; (12) cross section of observations.

2.5. Mount Laguna Observatory 40 inch Telescope

Multiband optical images of P/2019 LD_2 were obtained with the 1.0 m Telescope at the Mount Laguna Observatory (Smith & Nelson 1969) on 2020 May 17 UTC. Johnson–Cousins *B*, *V*, and *R* filters were used in combination with the E2V 42–40 CCD camera to obtain seven to nine 120 s exposures in each filter. The seeing conditions were 1″.92, the air mass was 1.49, and sidereal tracking was used. This facility is a member of the GROWTH collaboration.

2.6. Liverpool Telescope

Observations of P/2019 LD_2 were made in *g*, *r*, *i*, and *z* filters by the 2 m Liverpool Telescope located at the Observatorio del Roque de los Muchachos on 2020 May 29 UTC. The IO:O wide-field camera was used with a 2 × 2 binning, providing a pixel scale of 0″.3 (Steele et al. 2004). Two 30 s exposures were made per filter with the telescope tracking at the sidereal rate. The seeing conditions were 1″.21, and the air mass was 1.75. Detrending of data was performed using the automated IO:O pipeline software (Steele et al. 2004). This facility is a member of the GROWTH collaboration.

2.7. Lulin Optical Telescope

Multiband *B*, *V*, and *R* imaging of P/2019 LD_2 was made by the 1 m Lulin Optical Telescope on 2020 June 23–27 UTC and 2020 July 10 UTC. The observations were made using the 2K × 2K SOPHIA camera with a pixel scale of 0″.52 (Kinoshita et al. 2005). Exposure times of 90 s were where the telescope was tracked at the nonsidereal rate determined by the ephemeris of the comet. The seeing conditions of the observations were ∼1″.5, and the air mass was ∼1.15.

2.8. Keck I Telescope

A spectrum of P/2019 LD_2 was obtained using the Low-Resolution Imaging Spectrometer (LRIS; Oke et al. 1995) on the Keck I telescope on 2020 August 19 UTC (PI J. von Roestel, C272). The blue camera consisting of a 2 × 2K × 4K Marconi CCD array was used with the red camera consisting of a science-grade Lawrence Berkeley National Laboratory 2K × 4K CCD array. Both cameras have a spatial resolution of 0.″135 pixel^{-1}. We used the 560 nm dichroic with ∼50% transmission efficiency in combination with the 600/4000 grism for the blue camera, rebinned twice in both the spectral and spatial directions, and the 600/7500 grating for the red camera, rebinned once in the spectral direction and twice in the spatial direction, providing a spectral resolution of 0.8 nm and 0.5 nm, respectively, and a spatial resolution of 0.″27. A total integration time of 300 s was used for the exposure and was obtained at air mass 1.″8 in 0.″85 seeing conditions. Both telluric correction and solar-analog stars were observed at air masses similar to that of P/2019 LD_2. Wavelength calibration was completed using the HgCdZn lamps for the blue camera and the ArNeXe lamps for the red camera. We used a local solar-analog star to remove the solar component from the spectrum of P/2019 LD_2. The LPipe spectroscopy reduction package was used to reduce the data (Perley 2019).

3. Results

3.1. Morphology and Nucleus

Serendipitous prediscovery observations of P/2019 LD_2 were obtained with ZTF on 2019 April 26 UTC consisting of three 30 s exposures in the r band. These prediscovery data of P/2019 LD_2 have been coadded into a composite image with an equivalent 90 s integration time presented in the top left panel of Figure 1. The comet has an extended appearance with a ∼20″ long tail with a position angle of ∼260° in the antisolar direction. ZTF obtained prediscovery detections of P/2019 LD_2 on 2019 April 9, 15, and 20, but the comet did not have a discernible extended appearance in these data.

On 2019 September 7 UTC, the ARC 3.5 m was used to obtain 20 × 120 s exposures of P/2019 LD_2 in the r band. A composite median stack with an equivalent exposure time of 2400 s is presented in the top right panel of Figure 1. In the ARC 3.5 m images, the comet has a diffuse, nonstellar appearance. The tail is not easily defined in the ARC 3.5 m median stack, though the comet's extended appearance is enhanced in the opposite direction of the comet's orbital motion with a position angle of ∼230° and length of 5″.

The center panel of Figure 1 presents the appearance of P/2019 LD_2 in a median stack of five 380 s F350LP images with an equivalent integration time of 1900 s taken with HST/WFC3 on 2020 April 01 UTC. Cosmic rays have been removed from the composite image stack, with median interpolation of the surrounding pixels. The high-resolution composite HST stack was taken when the comet was at an orbit-plane angle of ∼−0.°44 and had a tail with a length of ∼32″ limited by background structure caused by galaxies and sky noise opposite to the solar direction with a position angle of ∼250°. The ∼32″-long tail translates into a length of 6.2×10^8 m given its topocentric distance of 5.02 au and a phase angle of 10.°7. An enhanced version of the HST median composite stack normalized by the distance from the optocenter reveals a possible jet structure ∼1″ long, as seen in the bottom panel of Figure 1. We will discuss the implications of the comet's morphology from these observations for its dust properties in Section 3.3.

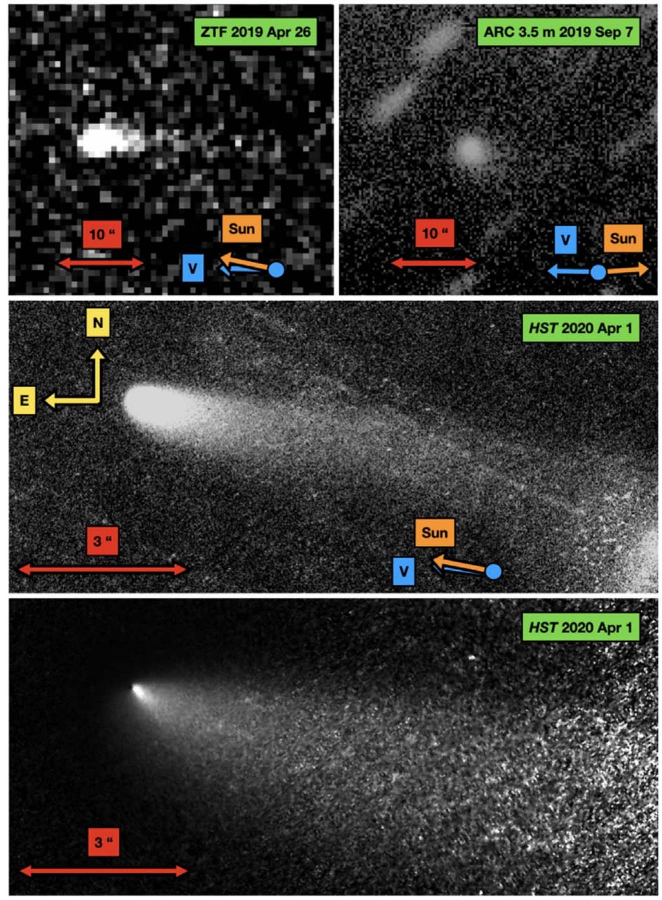

Figure 1. Top left panel: a 90 s equivalent exposure time stack of 3 × 30 s r-filter images of P/2019 LD_2 taken by ZTF on 2019 April 26 UTC. The image stack was compiled using the ZChecker software (Kelley et al. 2019). The pixel scale is 1″/pixel, and the seeing was ∼2.″2. An arrow indicating a width of 10″ is shown for scale, equivalent to ∼30,000 km at the geocentric distance of 4.15 au of the comet on 2020 April 26 UTC. The solar, orbital velocity, and cardinal directions are indicated. Top right panel: a 2400 s equivalent exposure time robust mean stack of 20 × 120 s r-filter images of P/2019 LD_2 taken with the ARC 3.5 m telescope on 2019 September 7 UTC. The telescope was tracked at the comet's motion. The pixel scale is 0.″228 pixel^{-1} and the seeing was ∼1.″4. An arrow indicating a width of 10″ is shown for scale, equivalent to ∼31,000 km at the geocentric distance of 4.28 au of the comet on 2020 September 7 UTC. Center panel: a 1900 s equivalent exposure time robust mean stack of 5 × 380 s F350LP filter images of P/2019 LD_2 taken with HST/WFC3 on 2020 April 1 UTC. The pixel scale is 0.″04/pixel. An arrow indicating a width of 3″ is shown for scale, equivalent to ∼11,000 km at the geocentric distance of 5.02 au of the comet on 2020 April 1 UTC. Bottom panel: the same as the center panel but normalized according to the radial profile of the comet. A ∼1″ jet-like structure is seen with a position angle of ∼210°.

We compare the surface-brightness profile of P/2019 LD_2 to the simulated surface-brightness profile of a G2 field star WFC3 point-spread function (PSF) assuming the use of the F350LP filter using the TinyTim software (Krist et al. 2011), as seen in Figure 2. The radial profiles of both P/2019 LD_2 and the simulated stellar G2V source are computed by azimuthally averaging concentric apertures centered on the optocenter separated by the pixel scale allowed by WFC3 using the F350LP filter. The normalized surface-brightness profile of P/2019 LD_2 between 0.″24 and 1.″2 was fit to the functional form of $\Sigma \propto \theta^m$, where Σ is the surface brightness and θ is the

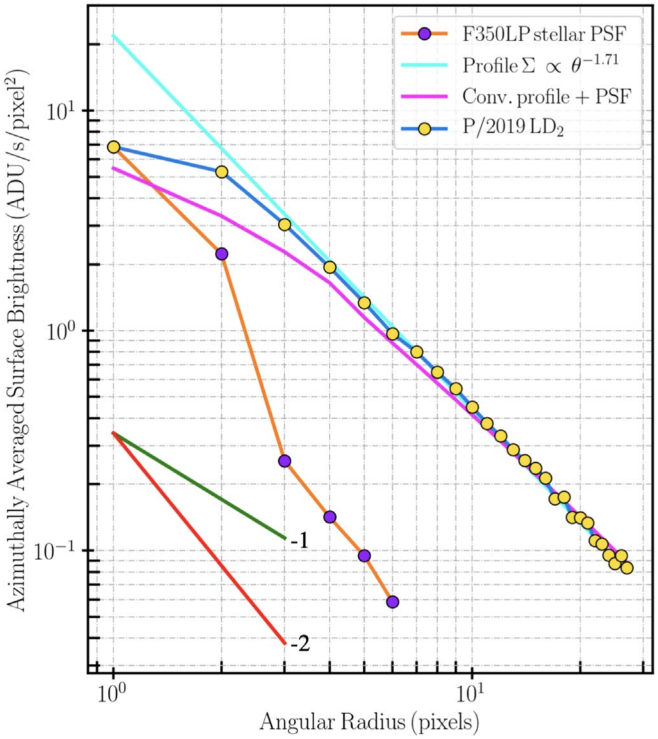

Figure 2. Normalized surface-brightness profile of P/2019 LD$_2$ taken with HST/WFC3 on 2020 April 1 UTC presented as yellow circles with a connecting blue line. A surface-brightness profile of $\Sigma \propto \theta^{-1.71}$ fitted to the profile of P/2019 LD$_2$ between 0.″24 and 1.″20 is plotted as the cyan line using the same vertical scale as the the normalized surface-brightness profile of P/2019 LD$_2$. The normalized surface-brightness profile of a F350LP stellar PSF assuming a G2V-like source generated using TinyTim (Krist et al. 2011) is plotted as purple circles with a connecting orange line. The surface-brightness profile resulting from the convolution of the F350LP stellar PSF and the fitted $\Sigma \propto \theta^{-1.71}$ surface-brightness profile of P/2019 LD$_2$ is plotted as a pink line using the same vertical scale as the the normalized surface-brightness profile of P/2019 LD$_2$. Logarithmic surface-brightness gradients with $m = -1$ and $m = -2$ are plotted as green and red lines, respectively, for comparison. Statistical error bars on the surface brightness computed assuming Poissonian statistics at each radius element are smaller than the plot symbols used for both P/2019 LD$_2$ and the synthetic stellar PSF.

distance from the optocenter in pixels, resulting in a radial profile slope of m ~ -1.71. We note that the radial profile slope is steeper than the typical -1 to -1.5 radial profile slope of comets with an isotopic coma in a steady state. The steeper radial profile slope of P/2019 LD$_2$ compared to comets with isotopic coma may be an independent indication of the comet's evolving dust production rate (Jewitt & Meech 1987).

The fitted 0.″24–1.″2 radial profile of P/2019 LD$_2$ was convolved with the synthetic G2V PSF and subtracted from the measured radial profile of P/2019 LD$_2$ to calculate a equivalent nucleus brightness of $V = 22.6 \pm 0.04$ assuming a m_V-$m_{F350LP} \sim 0.1$ (Bolin et al. 2020b). We assume the following phase function for determining the absolute magnitude of the nucleus, H:

$$H = V - 5\log_{10}(r_h\Delta) - \Phi(\alpha) \tag{2}$$

where r_h, Δ, and α are the heliocentric distance, topocentric distance, and phase angle of the comet as listed in Table 1 for the 2020 April 1 UTC observation. Here, $\Phi(\alpha) = 0.04\alpha$, where we assume a phase coefficient of 0.04 in magnitudes/degree, resulting in $H = 15.53 \pm 0.05$. The true phase coefficient of P/2019 LD$_2$ is unknown, so our uncertainty on the measured value of H is considered a lower limit.

From our measured value of H, we calculate the light-scattering cross section, C, of P/2019 LD$_2$ in km^2 using the following function:

$$C = 1.5 \times 10^6\, p_v^{-1}\, 10^{-0.4H} \tag{3}$$

where p_v is the albedo of the nucleus, assumed to be $\sim$0.08, the typical albedo measured for Centaurs (Bauer et al. 2013), resulting in $C = 11.15 \pm 0.42$ km^2. Converting our measured cross section to a radius using $r = (C/\pi)^2$, we obtain a radius of $\sim$1.8 km, comparable to the radius estimates of P/2019 LD$_2$ based on unresolved photometry and the nondetection of P/2019 LD$_2$ from ground-based observations (Schambeau et al. 2020). We note that this is a radius estimate based on a single observation and represents a size assuming a spheroidal shape. Significant deviations from a spheroidal shape, such as a bilobal (Nesvorný et al. 2018) or elongated shape (Bolin et al. 2018; Hanuš et al. 2018) as has been observed for other comet-like bodies, may require additional observations to be made of P/2019 LD$_2$ to accurately determine its size.

3.2. Photometry and Lightcurve

Using the combination of our ground-based observations with the ARC 3.5 m taken on 2019 September 7 UTC, the MLO 1.0 m on 2020 May 27 UTC, the LT on 2020 May 29 UTC, and the Lulin Optical Observatory on 2020 July 10 UTC, we have calculated the mean colors of P/2019 LD$_2$ using 10,000 km photometric apertures of g–$r = 0.60 \pm 0.03$, r–$i = 0.18 \pm 0.05$, and i–$z = 0.01 \pm 0.07$. The filter configuration and viewing geometry of our observations are presented in Table 1. The equivalent angular size of the 10,000 km used in our photometric calculations ranged from 3.″2 to 3.″7, with the seeing during observations ranging from 1.″2 to 1.″9. We used the color transformations from Jordi et al. (2006) to convert the *BVR* Johnson–Cousins photometry of P/2019 LD$_2$ from the MLO 1.0 m and LT to the Sloan Digital Sky Survey (SDSS) system.

Our visible measured colors of P/2019 LD$_2$ are reddish to neutral in the $\sim$480 nm to $\sim$910 nm wavelength range covered by our filters, which is consistent with the measured colors of other active solar system comets as presented in Figure 3. For comparison purposes only, we have included the colors of inactive objects in Figure 3. We note that the measured colors of P/2019 LD$_2$ from our observations are somewhat bluer than the colors of active and inactive Centaurs measured by Jewitt (2015), though this may be due to the longer wavelength coverage of our observations, which go as far as $\sim$910 nm, compared to the shorter visible-wavelength observations of Jewitt (2015).

Images from each of the Spitzer DDT program 14331 AORs 1, 4, 6, 9, and 10 that were used to take images of P/2019 LD$_2$ from 2020 January 25 2:23 to 23:11 UTC were reduced using the reduction methods described in Fernández et al. (2013). Images obtained during each of these five AORs using the 4.5 μm channel were coadded to form a single composite image with an equivalent exposure time of 948 s for each AOR.

P/2019 LD$_2$ was located in a crowded star field at a galactic latitude of $\sim -18°$. Therefore, due to the imperfections in the shadowing technique, we used an aperture size with an angular

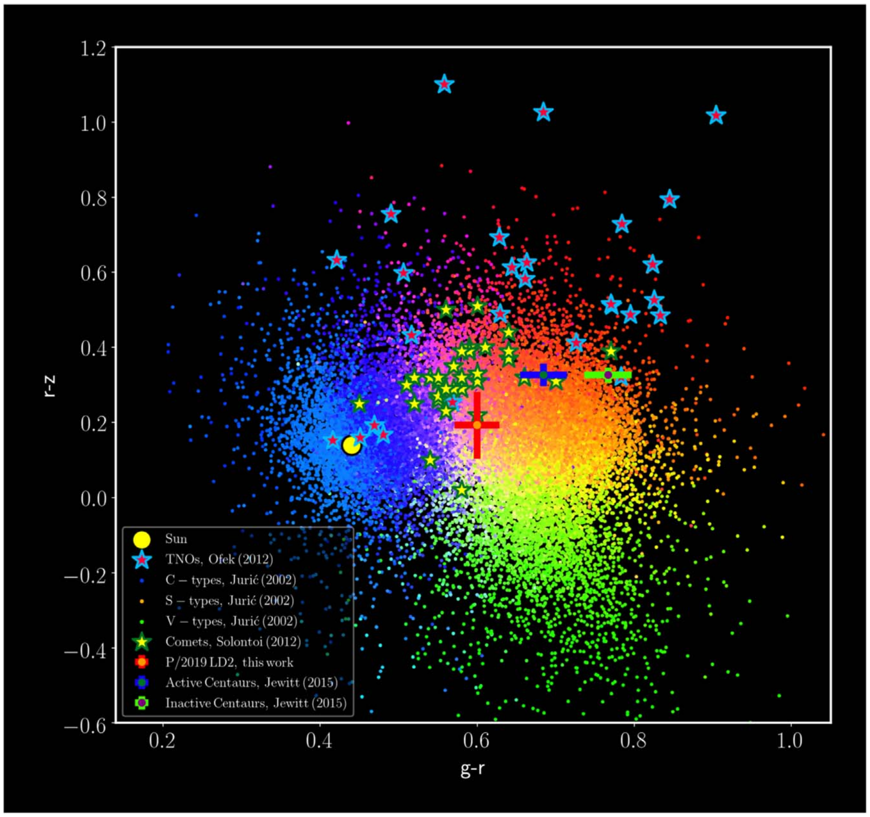

Figure 3. $g-r$ vs. $r-z$ colors of P/2019 LD_2 plotted with $g-r$ and $r-z$ colors of inactive solar system C-, S-, and V-type asteroids (Ivezić et al. 2001; Jurić et al. 2002; DeMeo & Carry 2013), active comets (Solontoi et al. 2012), and Kuiper Belt objects (Ofek 2012). The colorization scheme of data points for asteroids by their *griz* colors is adapted from Ivezić et al. (2002). The colors of active and inactive Centaurs from Jewitt (2015) are also included. The most appropriate color comparison between the color of P/2019 LD_2 and other solar system bodies is between the active comets in Solontoi et al. (2012) and the active Centaurs from Jewitt (2015) because the colors of P/2019 LD_2 are most representative of its dust rather than bare nucleus. The colors of inactive bodies are included for comparison purposes only.

width of 3.″24, equivalent to 10,000 km at the topocentric distance of 4.26 au of the comet from Spitzer. We obtain an on-source flux density for P/2019 LD_2 of 35.6 ± 2.8 μJy at 4.5 μm using the average of the five photometry measurements from the composite images made from each of the AORs 1, 4, 6, 9, and 10. The comet has a slightly extended appearance of more than ∼2.″4 as seen in Figure 4, and an aperture correction was applied to the flux density measurement. The flux from the nucleus assuming a kilometer-scale nucleus radius as measured in Section 3.1 is ∼0.1 μJy, less than 1% of the total flux.

We present the A$f\rho$ based on the Spitzer/IRAC photometry of P/2019 LD_2 using the A$f\rho$ definition of A'Hearn et al. (1984), which is a quantity in units of length, in this case centimeters, that corrects the comet's brightness with respect to heliocentric distance, geocentric distance, aperture size, solar spectrum, and filter wavelength. The values A$f\rho$ are normalized to 0° phase angle, $A(0°)f\rho$, using the Halley–Marcus cometary phase function defined by Schleicher & Bair (2011). Assuming that the entirety of the flux in the 4.5 μm Spitzer/IRAC observations is from dust in local thermal equilibrium, we calculate $A(0°)f\rho = 334$ cm. This is strictly an upper limit on $A(0°)f\rho$, due to the possible contribution of gas in the measured flux of the comet.

If we assume that the entirety of the flux from the comet is from CO emission and that the gas speed is 0.5 km s^{-1}, we measure a gas production rate of $1.6 \pm 0.1 \times 10^{27}$ mol s^{-1}, which is similar to the results of Kareta et al. (2020b). For CO_2, assuming that the entirety of the flux is due to gas emission, we

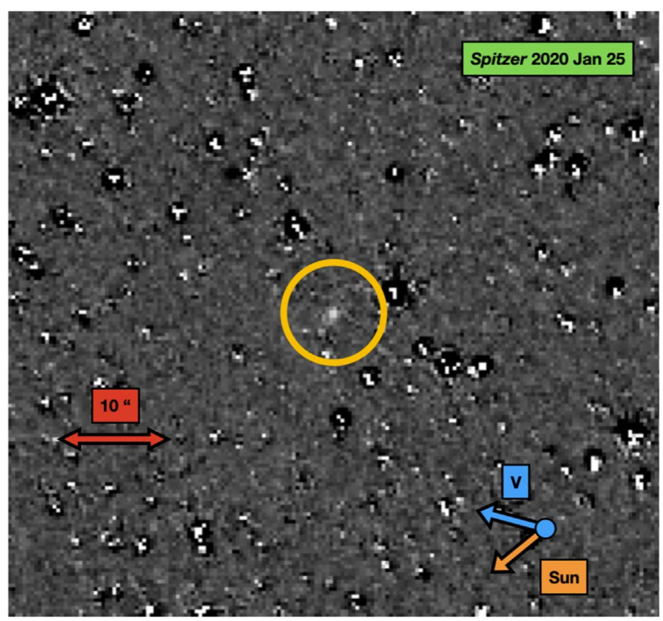

Figure 4. A 948 s equivalent integration time composite image stack made from Spitzer/IRAC observations of P/2019 LD_2 taken during Spitzer DDT program 14331 AOR 1 on 2020 January 25 02:23:32 UTC. The detection of P/2019 LD_2 has been encircled in yellow. The pixel scale is 1.″2 pixel^{-1}. An arrow indicating the width of 10″ is shown for scale, equivalent to ∼31,000 km at the topocentric distance of 4.256 au of the comet on 2020 January 25 UTC. The solar, orbital velocity, and cardinal directions are indicated.

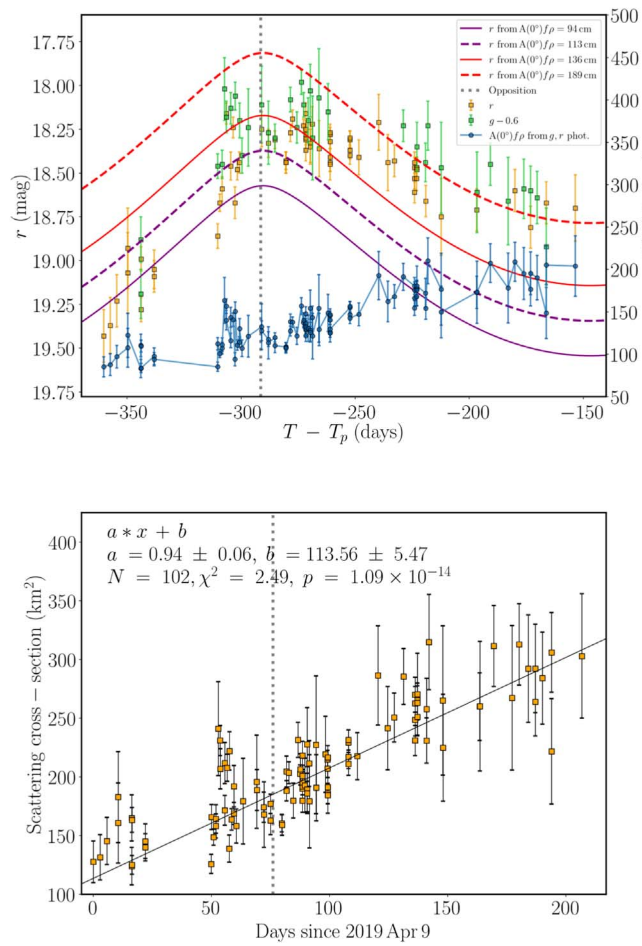

Figure 5. Top panel: g- and r-band photometric lightcurve of P/2019 LD_2 versus time from perihelion $(T - T_p)$ measured using a fixed 20,000 km aperture between 2019 April 9 UTC and 2019 November 8 UTC using the data from Table 2. Multiple lines of $A(0°)f\rho$ = 94 cm, 113 cm, 136 cm, 189 cm are shown as purple and red solid and dashed lines to reflect the change in the comet's brightness as the comet moved through opposition at $(T - T_p) = -291.5$ days on 2019 June 24 UTC, which is shown as a vertical gray dotted line. In addition, values of $A(0°)f\rho$ calculated using the brightness values and viewing geometry in Table 2 are presented as dark blue data points connected by a light blue solid line. Bottom panel: scattering cross section of P/2019 LD_2 calculated using Equation (3) as a function of days since 2019 April 09 UTC from the photometric data presented in Table 2. The black line shows the minimized χ^2 fit to the cross-sectional measurements, and the vertical dashed–dotted line corresponds to the date when P/2019 LD_2 was at opposition on 2019 June 24 UTC.

obtain a gas production rate of $1.4 \pm 0.1 \times 10^{26}$ mol s^{-1}, which is comparable to the CO_2 measured for comets observed in the MIR at similar heliocentric distances (Reach et al. 2013; Bauer et al. 2015).

Using our archival observations of P/2019 LD_2 from ZTF taken between 2019 April 9 UTC and 2019 November 8 UTC, we have plotted the equivalent r magnitudes of P/2019 LD_2 as a function of time since the perihelion date of 2020 April 10 UTC, $(T - T_p)$, measured with equivalent 20,000 km apertures and presented in the top panel of Figure 5 with observational details in Table 2. These observations include data taken in the g band, which have been corrected to an equivalent r-band magnitude using our g–r color estimate for P/2019 LD_2 of ∼0.6. The 20,000 km aperture was equivalent to an angular size of 5.″4 on 2019 November 8 UTC, when the comet had a geocentric distance of 5.14 au and an angular size of 7.52″, and when the comet had a geocentric distance of 3.67 au on 2019 July 1 UTC. The measured local seeing in the ZTF images at the time of observation ranged between 1.″6 and 3.″9 with a median seeing value of 2.″0. Using only the r-band photometry, the data show a secular brightening trend of the comet as the comet approached opposition on 2019 June 24.42 UTC and was increasing in brightness by $1.6 \pm 0.2 \times 10^{-2}$ mags/day. After leaving opposition, the comet showed an asymmetrical secular fading trend of $0.4 \pm 0.1 \times 10^{-2}$ mags/day compared to the preopposition brightening trend.

In addition to photometry, we present the $Af\rho$ based on the ZTF photometry of P/2019 LD_2 as implemented by Mommert et al. (2019). The values $Af\rho$ are normalized to 0° phase angle, $A(0°)f\rho$, and are plotted against the second Y-axis in the top panel of Figure 5 and presented in Table 2. Values of constant $A(0°)f\rho$ are plotted for reference in the top panel of Figure 5. The value of $A(0°)f\rho$ rises consistently over the span of our observations, resulting in asymmetry in the brightness of P/2019 LD_2 as it passed through opposition on 2019 June 24 UTC $(T - T_p = -291$ days). Before opposition, between $T - T_p = -370$ and -312, the error-weighted mean of $A(0°)f\rho = 93.9 \pm 11.8$ cm, and between $T - T_p = -312$ and -291, $A(0°)f\rho = 113.1 \pm 8.57$ cm. After opposition, the error-weighted mean of $A(0°)f\rho$ between $T - T_p = -291$ and -211 equaled 136.2 ± 9.7 cm, and from $T - T_p = -211$ and -50, $A(0°)f\rho = 188.8 \pm 25.8$ cm. The range of $A(0°)f\rho$ from 85 cm to 200 cm is consistent with the observed $Af\rho$ range of comets, which ranges from 1 to 10,000 cm (A'Hearn et al. 1995).

3.3. Dust Properties and Mass Loss

In addition to calculating the $A(0°)f\rho$ of P/2019 LD_2, we calculate the value of C for each of the equivalent r-band magnitudes in Table 2 using Equation (3), which are plotted in the bottom panel of Figure 5. A linear function is fit to these data, resulting in a fitted slope parameter value of $dC/dt = 0.94 \pm 0.06$ km^2/day. The change in phase angle over the time of our observations is modest, as seen in Table 2, so variations in the phase function used to calculate C should have a minimal effect on the estimate of the uncertainty of our measured slope parameter. Extrapolating backward in time beyond the range of our data results in $C = 0$ km^2 at ∼135 days before 2019 April 9 UTC, the date of our first photometry data point, or on 2018 November 24 UTC, during which P/2019 LD_2 had a heliocentric distance of ∼4.8 au, when water ice begins to sublimate (Lisse et al. 2019).

The dimensionless ratio of solar radiation and gravitational forces is defined by β (Burns et al. 1979):

$$\beta = \frac{2L_0 r_H^2}{g_{\odot}(1\text{au})t^2} \tag{4}$$

where L_0 is the length of dust travel, in this case, the observed length of the tail of P/2019 LD_2 of 6.2×10^8 m; r_H is the heliocentric distance; $g_{\odot}(1\text{au})$ is the gravitational acceleration toward the Sun at 1 au equal to 6.0×10^{-3} m/s^2; and t is the time of particle release. Assuming a mean value of $r_H \sim 4.6$ au, $L_0 = 6.2 \times 10^8$ m, the length of the tail estimated from the 2020 April 1 UTC HST/WFC3 images, and $t = 4.3 \times 10^7$ s, the time between the 2020 April 1 UTC HST/WFC3 observations and the estimated start of the activity, we calculate a value of

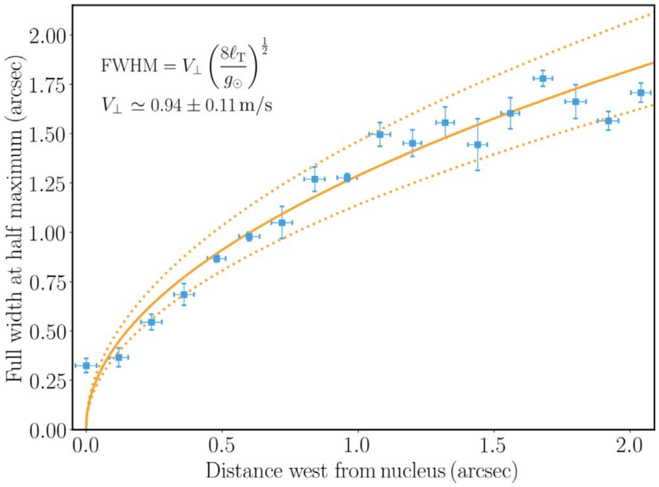

Figure 6. FWHM of the dust tail of P/2019 LD_2 versus the westward angular distance, ℓ_T, from the nucleus optocenter of P/2019 LD_2 plotted as blue data points when the comet was observed at a $-0\overset{\circ}{.}44$ topocentric and target orbital plane angle with HST/WFC3 on 2020 April 1 UTC. The best-fit line in ℓ_T versus FWHM space according to Equation (5) with $V_\perp = 0.94 \pm 0.11$ m s^{-1} is plotted as an orange line.

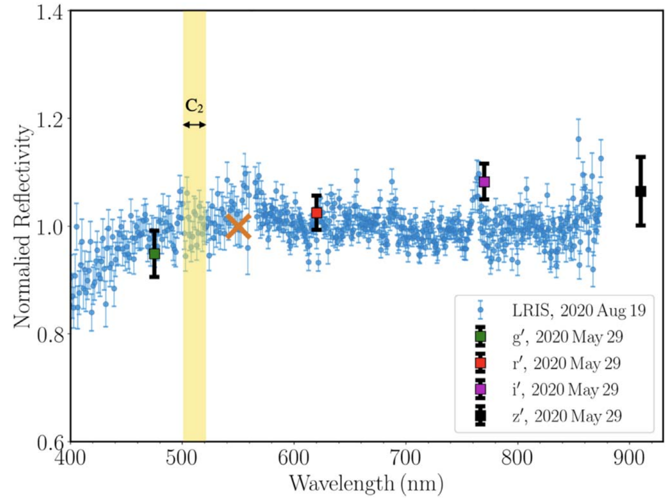

Figure 7. Visible-wavelength reflectance spectrum taken of P/2019 LD_2 with the LRIS instrument on Keck I on 2020 August 19 plotted as blue dots. The error bars on the spectrum data points correspond to 1σ uncertainty. The spectrum has been normalized to unity at 550 nm, indicated by the orange cross. The spectrum presented was obtained by combining two spectra from the blue camera using the 600/4000 grism and the red camera using the 600/7500 grating with a 560 nm dichroic (Oke et al. 1995; McCarthy et al. 1998). The data have been rebinned and smoothed by a factor of 10 using an error-weighted mean. The spectral range of the cometary C_2 emission line has been indicated by the yellow shaded area (Farnham et al. 2000). The spike in the spectrum at ~560 nm is due to an artifact caused by the dichroic solution, and the spike at ~760 nm is caused by the telluric H_2O absorption feature in both the comet and solar-analog spectra. The data to reproduce our plot of the reflectivity spectrum of P/2019 LD_2 are available at the following link: [link].

$\beta = 2.4 \times 10^3$. Making the assumption that the dust particles are dielectric spheres (Bohren & Huffman 1983), we find that the reciprocal of our estimated value of β translates into a particle size, $\bar{a}$, of ~400 μm. However, we caution that this may be an upper limit on the dust size because of the limitations of our tail length measurement by the contamination of background galaxies in the HST/WFC3 images due to variations in the activity of P/2019 LD_2 affecting our estimate of t based on the backward extrapolation of the photometric data.

Assuming our estimated particle size of ~400 μm, we estimate the total mass loss over the duration of our ZTF observations between 2019 April 9 UTC and 2019 November 8 UTC as $M = 4/3\ \rho\bar{a}\Delta C$, where ΔC is the difference between the cross sections at the start and end of our observations and is equal to 220 km^2. Assuming a dust density of 1 kg m^{-3} (McDonnell et al. 1986), we obtain a total mass loss over the time span of our observations of $\sim 10^8$ kg. Adopting our estimated value of $dC/dt \sim 1\ km^2$/day, we obtain a mass-loss rate using $\dot{M} = 4/3\rho\bar{a}\ dC/dt \sim 5 \times 10^5$ kg/day.

To estimate the fraction of active area of P/2019 LD_2, A, we take the ratio between the mass-loss rate and the equilibrium mass sublimation flux at 4.6 au, $f_s = 1.4 \times 10^{-5}$ kg m^{-2} (Jewitt et al. 2015), where $A \sim 0.4\ km^2$. Thus, ~10% of P/2019 LD_2's surface is active assuming our inferred size radius of 1.8 km from Section 3.1, comparable to the active surface area measured for Jupiter-family comets (Fernández et al. 1999). An alternative assumption is that P/2019 LD_2 has a 100% active area, setting a lower limit to its radius of 0.2 km.

In addition, we use the perpendicular profile of P/2019 LD_2 taken with the high-resolution images from HST/WFC3 to estimate the out-of-plane distribution of dust with a minimum of projection effects as the Earth passed through the projected orbital plane of P/2019 LD_2 with a projected orbital plane angle of only $0\overset{\circ}{.}4$ on 2020 April 1 UTC. We measured the FWHM along the direction perpendicular to the tail's profile as a function of distance from the optocenter, ℓ_T, between 0 and $\sim 2''$ in increments of $0\overset{''}{.}12$ slices, as plotted in Figure 6.

Neglecting projection effects, the FWHM of the tail gradually widened with ℓ_T and was fit to the function

$$\mathrm{FWHM} = V_\perp \left(\frac{8\ell_T}{g_\odot}\right)^{\frac{1}{2}} \quad (5)$$

from Jewitt et al. (2014), where $V_\perp$ is the component of the ejection velocity perpendicular to the orbital plane, equal to ~1 m s^{-1}. We estimate that the perpendicular component of the ejection velocity scales with $V_\perp \sim 1$ m s^{-1} $(\bar{a}/\bar{a}_0)^{-1/2}$ where $\bar{a}_0 = 400\ \mu$m (Jewitt et al. 2014).

3.4. Spectrum

The spectrum of P/2019 LD_2 was extracted using a $7\overset{''}{.}4$-wide region centered on the peak of the continuum's brightness. We compute the normalized reflectance spectrum of P/2019 LD_2 taken with Keck/LRIS on 2020 August 19 UTC in the wavelength range between 400 nm and 1000 nm by dividing the P/2019 LD_2 spectrum by our solar-analog spectrum and normalizing to unity at 550 nm. The resulting spectrum indicates a reddish to neutral coma color for P/2019 LD_2, as seen in Figure 7. We measured a slope of ~16%/100 nm between 480 and 760 nm and a flatter spectrum between 760 nm and 900 nm consistent with the photometric colors taken by LT on 2020 May 29 plotted over the LRIS spectra in Figure 7 for reference. Our spectrum shows no sign of C_2 emission in the 505 nm to 522 nm range (Farnham et al. 2000) in the highlighted range in Figure 7.

We set an upper limit on the C_2 gas production of P/2019 LD_2 using the mean V-band continuum flux density of P/2019 LD_2 using its measured 550 nm flux, $\mathrm{flux}_V = 1.52 \times 10^{-15}$

$\mathrm{erg\,cm^{-2}\,s^{-1}\,nm^{-1}}$. The fractional 1σ continuum statistical uncertainty of our P/2019 LD_2 spectrum in the range spanning 505 nm to 522 nm is 0.01, corresponding to a 3σ flux $\mathrm{density}_{C_2} = 2.13 \times 10^{-17}\,\mathrm{erg\,cm^{-2}\,s^{-1}\,nm^{-1}}$ including a correction of 0.6 for slit losses. The 3σ upper limit to the flux in the 17 nm width of the C_2 band is $F_{C_2} \leqslant 3.62 \times 10^{-16}\,\mathrm{erg\,cm^{-2}\,s^{-1}}$. The 3σ upper limit on the number of C_2 molecules projected within the $7\farcs4 \times 1\farcs0$ spectroscopic slit assuming that the coma is optically thin is

$$N_{mol} = \frac{4\pi\Delta^2 F_{C_2}}{g(r_h)} \tag{6}$$

where $g(r_h)$ is the fluorescence efficiency factor of the C_2 spectral band at r_h where $g(1\,\mathrm{au}) = 2.2 \times 10^{-14}\,\mathrm{erg\,s^{-1}\,radical^{-1}}$ (A'Hearn 1982), which results in $N_{mol} \leqslant 1.27 \times 10^{27}$ molecules.

We apply the assumptions of the Haser model (Haser 1957) to determine a coarse 3σ upper limit on the production rate of C_2. The Haser model uses two length scales, the "parent" molecule species length scale, L_P, and the "daughter" molecule species length scale, L_D, to describe the distribution of the radicals. For C_2 at an r_h of 4.594 au, $L_P = 5.3 \times 10^5$ km and $L_D = 2.5 \times 10^6$ km (Cochran 1985). In addition, we assume the speed of the molecular gas is 0.5 km $\mathrm{s^{-1}}$, which is used to determine the residence time of the molecules in the projected slit (Combi et al. 2004). Using these assumptions with the Haser model, we find the 3σ upper limit to the gas production rate $Q_{C_2} \lesssim 7.5 \times 10^{24}\,\mathrm{mol\,s^{-1}}$, which is a similar limit to the measured Q_{C_2} of other solar system comets at similar heliocentric distances (Feldman et al. 2004) and to the results of Licandro et al. (2020). Scaling our measured spectroscopic upper limit on the Q_{C_2} gas production rate to a OH gas production rate using the median ratio of C_2 to hydroxyl production rate for solar system comets (A'Hearn et al. 1995) results in an estimated spectroscopic upper limit of $Q_{OH} \lesssim 2.4 \times 10^{27}\,\mathrm{mol\,s^{-1}}$ and a mass-loss rate in water of $dM_{H_2O}/dt \lesssim 80\,\mathrm{kg\,s^{-1}}$.

3.5. Orbital Evolution

In order to investigate the long-term dynamics of 2019 LD_2, we simulated 27,000 clones of its orbit. The clone set is created by using 1000 three-dimensional locations using the positional uncertainties. The velocity uncertainties are accounted for by creating 27 clones in the three-dimensional velocity space at each positional location for a total of 27,000 clones. Orbital six-vectors were generated with uncertainties from the JPL Horizons Orbit Solution dated 2020 May 20 at 00:43:28 and set for the 2019 September 15 00:00 UTC epoch. In addition, we use the major gravitational components of the solar system (Sun, Venus, Earth, Mars, Jupiter, Saturn, Uranus, and Neptune). The simulations were conducted using `REBOUND` (Rein & Liu 2012) with the hybrid `MERCURIUS` integrator (Rein et al. 2019). We ran two sets of integrations, a short-term set, integrated for 100 yr, and a long-term set for 1×10^7 yr. For each simulation set, we use a time-step size of 0.025 yr. For the long-term integrations, we output every 1000 yr and analyze the time at which the clones escape the solar system (distance from the Sun larger than 1000 au).

The short-term integrations replicate the previous work of Steckloff et al. (2020) and Hsieh et al. (2021). In the simulations, we find that the clones entered the Jovian region approximately 2.37 yr ago and are ejected from the region 8.70 yr in the future (see the top left panel of Figure 8 for a clone example). As was found previously, 2019 LD_2 transitions from a Centaur, with an approximate semimajor axis of 8.6 au, to a Jupiter-family comet with a semimajor axis of 6.2 au, spending 11.0712 yr in the Jovian region (semimajor axis 5.2 au). In the long-term simulations (1×10^7 yr), we find that one-half of the clones escape the solar system in 3.4×10^5 yr and 78.8% of the clones escape the solar system within the first 1×10^6 yr, as seen in the bottom right panel of Figure 8. After ~3.8 Myrs, 95% of the P/2019 LD_2 clones have escaped.

4. Discussion and Conclusions

From our observations spanning multiple observatories, transitioning comet P/2019 LD_2 exhibits interesting features in comparison with other short-period solar system comets. P/2019 LD_2 has a higher value of $Af\rho$ of 85–200 cm (A'Hearn et al. 1995) at a heliocentric distance between 4.7 and 4.6 au compared to other short-period comets at a similar heliocentric distance (Kelley et al. 2013; Ivanova et al. 2014; Bauer et al. 2015) and a kilometer-scale nucleus (Fernández et al. 2013), as well as reddish to neutral color properties (Jewitt 2015). The comet's morphology when observed over multiple epochs since 2019 April exhibits the presence of a tail, suggesting sustained activity versus an impulsive event. In addition, P/2019 LD_2 has a moderate upper limit for the production of CO and CO_2 of $\sim 10^{27}\,\mathrm{mol\,s^{-1}}$ and $\sim 10^{26}\,\mathrm{mol\,s^{-1}}$, respectively, based on our Spitzer observations taken in 2020 January. It is also very active when compared to 29P (although 29P is located at a slightly farther heliocentric distance of ~6 au) on a per unit surface area basis ($Af\rho \sim 150\,\mathrm{cm}/(1.8\,\mathrm{km})^2 \sim 50\,\mathrm{cm\,km^{-2}}$ for P/2019 LD_2 versus $Af\rho \sim 1000\,\mathrm{cm}/(30.5\,\mathrm{km})^2 \sim 1\,\mathrm{cm\,km^{-2}}$ for 29P; Ivanova et al. 2011), using the latest value for SW1's size from Schambeau et al. (2019). But this activity seems to produce quite large (~100 μm), reddish dust particles containing copious amounts of water ice according to our work and that of Kareta et al. (2020b).

In addition to the morphology of the comet indicating sustained activity, the photometry of the comet observed between 2019 April and 2019 November by ZTF is consistent with the activity steadily increasing since late 2018 up through the end of 2019 and into 2020 as the comet nears its perihelion on 2020 April 10 UTC. The length of the tail in deep HST imaging as well as our inferred start date of activity of late 2018 implies that the coma consists of ~100 μm-scale dust ejected at a relatively low velocity of ~1 m $\mathrm{s^{-1}}$. Although this is roughly consistent with the escape speed of a nonrotating comet nucleus of radius ~1.8 km as inferred by our observations, it is unlikely that the dust is being ejected exclusively by the rotational mass shedding suggested by the low ejection velocity (e.g., Ye et al. 2019; Lin et al. 2020). Rather, the increased activity of the comet as it nears perihelion suggests that dust is being transported by the sublimation, or that the activity is a product of both the sublimation of volatiles and rotational mass shedding.

The size of the active region on P/2019 LD_2 of ~0.4 $\mathrm{km^2}$ is too large to explain the low ejection velocity of the dust as for other comets with low dust ejection velocities whose activity is driven by the sublimation of volatiles (Jewitt et al. 2014). Subsequent observations of P/2019 LD_2 to determine the rotation state of the comet will be necessary to understand if it is rotating near its critical rotation limit, indicating the role of

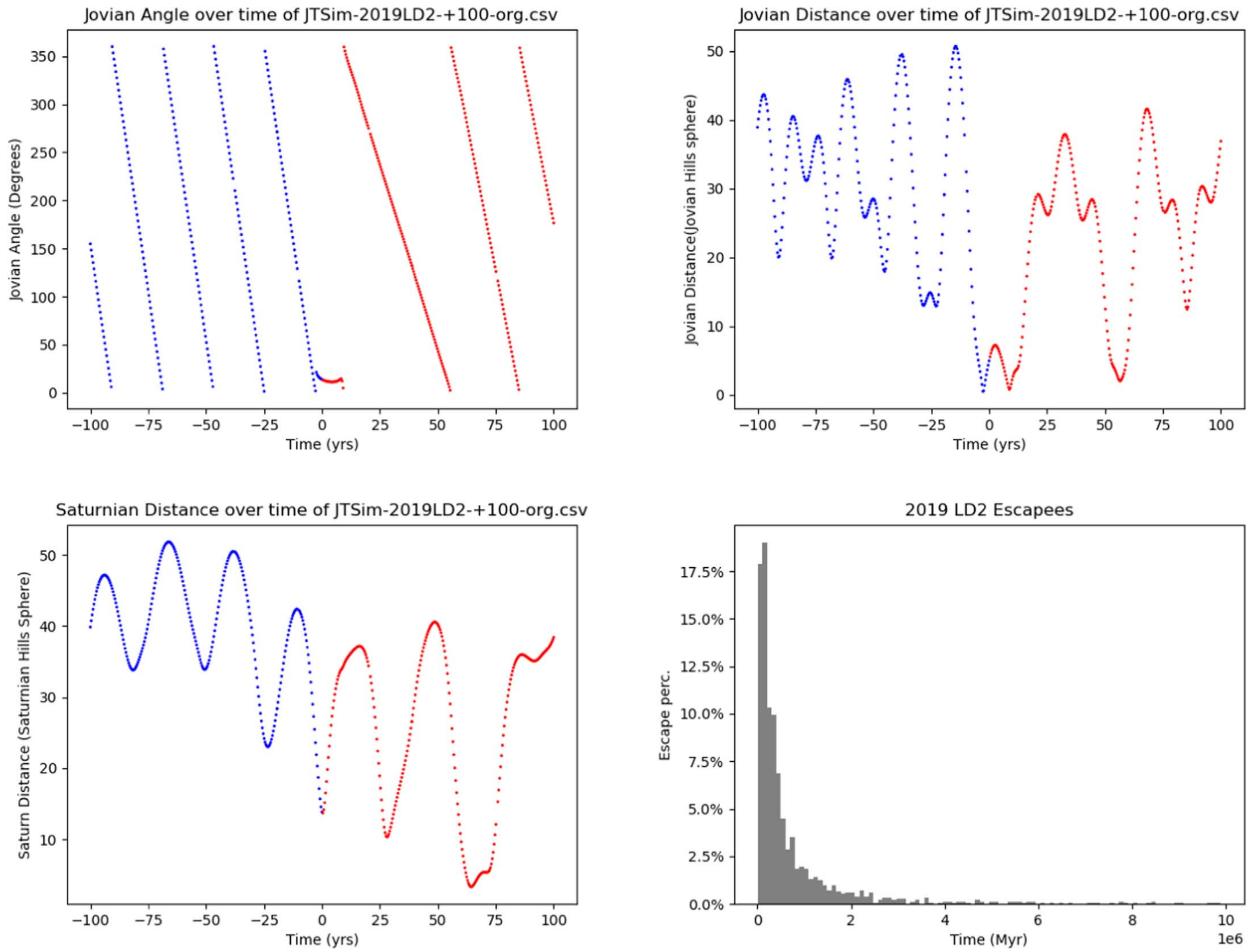

Figure 8. Top left panel: Jovian angle defined as the relative longitude between Jupiter and P/2019 LD_2 as a function of time between −100 and 100 yr centered on 2019 September 15 UTC. Except for a brief period of time between −3 and 8 yr where the Jovian angle was ~20°, the Jovian angle cycled between 0° and 360°. Top right panel: same as the top left panel except for the Jovian distance defined as the distance between P/2019 LD_2 and Jupiter in Jovian Hill spheres (~0.35 au) as a function of time. The local minimum in the Jovian distance occurred ~2.77 yr ago with a distance of ~0.50 Jovian Hill radius, or 0.17 au. Bottom left panel: same as the top right panel except for the Saturn distance defined as the distance between P/2019 LD_2 and Saturn in Saturn Hill spheres (0.43 au). The local minimum occurs in ~60 yr when P/2019 LD_2 comes within ~3.3 Hill radii or 1.42 au of Saturn. Bottom right panel: percentage of orbital P/2019 LD_2 clones that have escaped the solar system (reached >1000 au from the Sun) per bin in duration of time. Each bin is ~100,000 yr wide. Within the first million years of the simulation, ~78.8% have escaped the solar system. By 10 million years, ~95% have escaped the solar system.

rotational mass shedding in its activity or if the comet has the possibility of becoming rotationally disrupted in the near future or if it was disrupted in the recent past (Moreno et al. 2017; Vokrouhlický et al. 2017). Given the 4–5 au location of the comet during its recent epoch of activity, the distance at which water ice begins to sublimate (Meech & Svoren 2004), it is likely that the activity is being driven primarily by the sublimation of water ice. An additional possible mechanism may be the transformation of amorphous water ice into crystalline water, as has been suggested as an activity-driving mechanism for Centaurs (Jewitt 2009). It is possible for other volatiles such as CO to partially drive the activity of P/2019 LD_2, as seen in other distant comets (e.g., Bolin et al. 2020b) and 29P (Gunnarsson et al. 2008), but the lack of detection of the activity at large heliocentric distances (Schambeau et al. 2020) seems to suggest that hypervolatiles are not the dominant drivers of the activity of P/2019 LD_2. If the lack of hypervolatiles driving the activity of P/2019 LD_2 is confirmed, it may suggest that P/2019 LD_2 has spent a significant amount of time as a Centaur within 15 au of the Sun (Horner et al. 2004b), where these hypervolatiles may have had a greater chance to become depleted compared to water ice, which is nonvolatile at that distance.

Additionally, some comets show evidence of a strong transition between H_2O-driven and CO-driven activity at heliocentric distances past ~3.5 au, such as for comets 67P (Läuter et al. 2019) and Hale-Bopp (Biver et al. 1997). Our observation of the activity of P/2019 LD_2 and its inferred H_2O-driven activity at its heliocentric distance of ~4.6 au at the time of our observations is seemingly at odds with the transition to CO-driven activity at larger heliocentric distances as observed for other comets. However, it has been shown that the shape and rotation pole orientation of comets can have a strong effect on the distance at which comet activity is driven by H_2O. H_2O-driven activity can increase at larger heliocentric distances for comet shapes and orientations deviating from a spherically shaped comet rotating perpendicular to its orbital plane (Marshall et al. 2019). Therefore, the inferred H_2O-driven activity of P/2019 LD_2 at its large heliocentric distance of 4.6 au could be explained by it having a nonspherical shape and significant obliquity, which has been shown to sustain H_2O activity at these heliocentric distances in comet-activity models.

P/2019 LD_2 is beginning to enter the region where water ice begins to appreciably sublimate at rates high enough that a patch of pure water ice in the surface would disappear on year-long timescales. The beginnings of mobilization of water ice for a weakly structured surface such as found on 67P (O'Rourke et al. 2020) could lead to the slow flaking off of large chunks of the loosest, weakest material that had never felt such stresses before. In this scenario, gas will evolve at low levels in order to drive dust off the object. The material driven off should be rich in water ice, as this ice is the last, most refractory ice expected in a cometary body before it is totally depleted of volatile ice. We then may expect to see P/2019 LD_2's activity modulated by its motion toward or away from the Sun over an orbit similar to how the activity of Main Belt Comets are modulated as they travel inside or outside the 2.5 au water "ice line," where water ice boils furiously into vacuum (Hsieh et al. 2015a, 2015b); P/2019 LD_2's activity could be modulated by its traversing the water ice turn-on line of activity. Future monitoring observations over the next years will determine if this is the case, as is suggested by the smoothly increasing $Af\rho$ toward perihelion values we find for P/2019 LD_2; they do not appear to be describing an impulsive outburst.

In our long-term simulations (1×10^7 yr), we show the temporary nature of 2019 LD_2. Up to 78.8% of our orbital clones escape in the first 1×10^6 yr. The half-life of the clones is approximately 3.4×10^5 yr. This is an order of magnitude smaller than the mean half-life of Centaurs (2.7×10^6 yr; Horner et al. 2004b) and more comparable to the lifetimes of Jupiter-family group comets of $\sim 5 \times 10^5$ yr (Levison & Duncan 1994).

Without a robust assessment of survey selection effects (e.g., Jedicke et al. 2016; Boe et al. 2019), it is difficult to assess the true population of comets in a temporary co-orbital configuration with Jupiter and transitioning between the Centaur and Jupiter-family comet populations (Sarid et al. 2019). However, we can use our estimated size of P/2019 LD_2 in comparison with the population estimates of Centaurs in the transition region (Steckloff et al. 2020). Steckloff et al. (2020) predict that there are $\sim$40–1000 objects in the transition region with radius >1–3 km, and fewer if cometary fading is considered in the population estimate (Brasser & Wang 2015). Using these transition-object population estimates and our estimate of the radius of P/2019 LD_2 of $\sim$1.8 km suggests that there are $\sim$100 objects the size of P/2019 LD_2 in the transition region at any given time. Additional monitoring of P/2019 LD_2 and objects like it in the gateway region will be required to understand their activity drivers and population.

The authors wish to thank the two anonymous reviewers for their help in revising this manuscript, which greatly improved its text.

This work is based on observations with the NASA/ESA *Hubble Space Telescope* obtained from the Data Archive at the Space Telescope Science Institute, which is operated by the Association of Universities for Research in Astronomy, Incorporated, under NASA contract NAS5-26555. Support for program GO 16077 was provided through a grant from the STScI under NASA contract NAS5-26555.

This work is based on observations made with the Spitzer Space Telescope, which was operated by the Jet Propulsion Laboratory, California Institute of Technology, under a contract with NASA.

This work is based on observations obtained with the Samuel Oschin Telescope 48 inch and the 60 inch Telescope at the Palomar Observatory as part of the Zwicky Transient Facility project. ZTF is supported by the National Science Foundation under grant No. AST-1440341 and a collaboration including Caltech, IPAC, the Weizmann Institute for Science, the Oskar Klein Center at Stockholm University, the University of Maryland, the University of Washington, Deutsches Elektronen-Synchrotron and Humboldt University, Los Alamos National Laboratories, the TANGO Consortium of Taiwan, the University of Wisconsin at Milwaukee, and Lawrence Berkeley National Laboratories. Operations are conducted by COO, IPAC, and UW.

The Liverpool Telescope is operated on the island of La Palma by Liverpool John Moores University in the Spanish Observatorio del Roque de los Muchachos of the Instituto de Astrofisica de Canarias with financial support from the UK Science and Technology Facilities Council.

This work was supported by the GROWTH project funded by the National Science Foundation under PIRE Grant No. 1545949.

Some of the data presented herein were obtained at the W. M. Keck Observatory, which is operated as a scientific partnership among the California Institute of Technology, the University of California, and the National Aeronautics and Space Administration. The observatory was made possible by the generous financial support of the W. M. Keck Foundation.

The authors wish to recognize and acknowledge the very significant cultural role and reverence that the summit of Maunakea has always had within the indigenous Hawaiian community. We are most fortunate to have the opportunity to conduct observations from this mountain.

B.T.B., G.H., and F.J.M. acknowledge support from NASA with grant No. 80NSSC19K0780.

C.F. gratefully acknowledges the support of his research by the Heising-Simons Foundation (2018-0907).

M.W.C. acknowledges support from the National Science Foundation with grant No. PHY-2010970.

This publication has made use of data collected at Lulin Observatory, partly supported by MoST grant 108-2112-M-008-001.

C.C.N. gratefully acknowledges the funding from MOST grant 104-2923-M-008-004-MY5.

The authors would like to acknowledge the helpful discussion of P/2019 LD_2 with L. Woodney and Q.-Z. Ye.

This work has made use of data from the European Space Agency (ESA) mission Gaia (https://www.cosmos.esa.int/gaia), processed by the Gaia Data Processing and Analysis Consortium (DPAC; https://www.cosmos.esa.int/web/gaia/dpac/consortium). Funding for the DPAC has been provided by national institutions, in particular the institutions participating in the Gaia Multilateral Agreement.

Facilities: Hubble Space Telescope, Spitzer Space Telescope, Keck I Telescope, P48 Oschin Schmidt telescope/Zwicky Transient Facility, Apache Point Astrophysical Research Consortium 3.5 m telescope, Liverpool Telescope, Lulin Optical Telescope, Mount Laguna Observatory 40 inch Telescope.

Software: Small Body Python, ZChecker, LPipe, REBOUND.

ORCID iDs

Bryce T. Bolin https://orcid.org/0000-0002-4950-6323
Yanga R. Fernandez https://orcid.org/0000-0003-1156-9721
Carey M. Lisse https://orcid.org/0000-0002-9548-1526
Timothy R. Holt https://orcid.org/0000-0003-0437-3296
Zhong-Yi Lin https://orcid.org/0000-0003-3827-8991
Kunal P. Deshmukh https://orcid.org/0000-0001-5253-3480
James M. Bauer https://orcid.org/0000-0001-9542-0953
Eric C. Bellm https://orcid.org/0000-0001-8018-5348
Dennis Bodewits https://orcid.org/0000-0002-2668-7248
Kevin B. Burdge https://orcid.org/0000-0002-7226-836X
Sean J. Carey https://orcid.org/0000-0002-0221-6871
Chris M. Copperwheat https://orcid.org/0000-0001-7983-8698
George Helou https://orcid.org/0000-0003-3367-3415
Jonathan Horner https://orcid.org/0000-0002-1160-7970
Varun Bhalerao https://orcid.org/0000-0002-6112-7609
Chan-Kao Chang https://orcid.org/0000-0003-1656-4540
Christine Chen https://orcid.org/0000-0002-8382-0447
Mansi M. Kasliwal https://orcid.org/0000-0002-5619-4938
Frank J. Masci https://orcid.org/0000-0002-8532-9395
Chow-Choong Ngeow https://orcid.org/0000-0001-8771-7554
Robert Quimby https://orcid.org/0000-0001-9171-5236
Michael Coughlin https://orcid.org/0000-0002-8262-2924
Richard Dekany https://orcid.org/0000-0002-5884-7867
Dmitry A. Duev https://orcid.org/0000-0001-5060-8733
Matthew Graham https://orcid.org/0000-0002-3168-0139
Thomas Kupfer https://orcid.org/0000-0002-6540-1484
Russ R. Laher https://orcid.org/0000-0003-2451-5482
Ashish Mahabal https://orcid.org/0000-0003-2242-0244
Przemyslaw J. Mróz https://orcid.org/0000-0001-7016-1692
Reed Riddle https://orcid.org/0000-0002-0387-370X
Roger M. Smith https://orcid.org/0000-0001-7062-9726
Maayane T. Soumagnac https://orcid.org/0000-0001-6753-1488
Lin Yan https://orcid.org/0000-0003-1710-9339

References

A'Hearn, M. F. 1982, in Comets, ed. L. L. Wilkening (Tucson, AZ: Univ. Arizona Press), 433
A'Hearn, M. F., Millis, R. C., Schleicher, D. O., Osip, D. J., & Birch, P. V. 1995, Icar, 118, 223
A'Hearn, M. F., Schleicher, D. G., Millis, R. L., Feldman, P. D., & Thompson, D. T. 1984, AJ, 89, 579
Bauer, J. M., Grav, T., Blauvelt, E., et al. 2013, ApJ, 773, 22
Bauer, J. M., Stevenson, R., Kramer, E., et al. 2015, ApJ, 814, 85
Bellm, E. C., Kulkarni, S. R., Graham, M. J., et al. 2019, PASP, 131, 018002
Biver, N., Bockelée-Morvan, D., Colom, P., et al. 1997, EM&P, 78, 5
Boe, B., Jedicke, R., Meech, K. J., et al. 2019, Icar, 333, 252
Bohren, C. F., & Huffman, D. R. 1983, Absorption and Scattering of Light by Small Particles (New York: Wiley)
Bolin, B., Fernandez, Y., Bauer, J., Helou, G., & Lisse, C. 2019, Spitzer investigation of the first known active Trojan, 2019 LD2, Spitzer Proposal 14331
Bolin, B. T., Bodewits, D., Fernandez, Y., & Lisse, C. M. 2020a, Determining the cause of activity of the first active Trojan, 2019 LD2, HST Proposal 16077
Bolin, B. T., & Lisse, C. M. 2020, MNRAS, 497, 4031
Bolin, B. T., Lisse, C. M., Kasliwal, M. M., et al. 2020b, AJ, 160, 26
Bolin, B. T., Weaver, H. A., Fernandez, Y. R., et al. 2018, ApJL, 852, L2
Brasser, R., & Wang, J. H. 2015, A&A, 573, A102
Burns, J. A., Lamy, P. L., & Soter, S. 1979, Icar, 40, 1
Chandler, C. O., Kueny, J. K., Trujillo, C. A., Trilling, D. E., & Oldroyd, W. J. 2020, ApJL, 892, L38
Cochran, A. L. 1985, AJ, 90, 2609
Combi, M. R., Harris, W. M., & Smyth, W. H. 2004, in Comets II, ed. M. C. Festou, H. U. Keller, & H. A. Weaver (Tucson, AZ: Univ. Arizona Press), 523
De Sanctis, M. C., Capria, M. T., Coradini, A., & Orosei, R. 2000, AJ, 120, 1571
DeMeo, F. E., & Carry, B. 2013, Icar, 226, 723
Deustua, S. E., Mack, J., Bajaj, V., & Khandrika, H. 2017, WFC3/UVIS Updated 2017 Chip-Dependent Inverse Sensitivity Values, Instrument Science Rep. WFC3 2017-14
Dones, L., Brasser, R., Kaib, N., & Rickman, H. 2015, SSRv, 197, 191
Dressel, L. 2012, Wide Field Camera 3 Instrument Handbook for Cycle 21 v. 5.0 (Baltimore, MD: STScI)
Duncan, M., Levison, H., & Dones, L. 2004, in Comets II, ed. M. C. Festou, H. U. Keller, & H. A. Weaver (Tucson, AZ: Univ. Arizona Press), 193
Farnham, T. L., Schleicher, D. G., & A'Hearn, M. F. 2000, Icar, 147, 180
Fazio, G. G., Hora, J. L., Allen, L. E., et al. 2004, ApJS, 154, 10
Feldman, P. D., Cochran, A. L., & Combi, M. R. 2004, in Comets II, ed. M. C. Festou, H. U. Keller, & H. A. Weaver (Tucson, AZ: Univ. Arizona Press), 425
Fernández, J. A., Tancredi, G., Rickman, H., & Licandro, J. 1999, A&A, 352, 327
Fernández, Y. R. 2009, P&SS, 57, 1218
Fernández, Y. R., Kelley, M. S., Lamy, P. L., et al. 2013, Icar, 226, 1138
Fitzsimmons, A., Young, D., Armstrong, J., Moss, S., & Sato, H. 2020, COMET P/2019 LD2 (ATLAS), Minor Planet Electronic Circulars MPEC 2020-K134, https://www.minorplanetcenter.net/mpec/K20/K20KD4.html
Gladman, B., Marsden, B. G., & Vanlaerhoven, C. 2008, in The Solar System Beyond Neptune, ed. M. A. Barucci et al. (Tucson, AZ: Univ. Arizona Press), 43
Graham, M. J., Kulkarni, S. R., Bellm, E. C., et al. 2019, PASP, 131, 078001
Gunnarsson, M., Bockelée-Morvan, D., Biver, N., Crovisier, J., & Rickman, H. 2008, A&A, 484, 537
Hanuš, J., Delbo, M., Alí-Lagoa, V., et al. 2018, Icar, 299, 84
Haser, L. 1957, BSRSL, 43, 740
Horner, J., & Evans, N. W. 2006, MNRAS, 367, L20
Horner, J., Evans, N. W., & Bailey, M. E. 2004a, MNRAS, 355, 321
Horner, J., Evans, N. W., & Bailey, M. E. 2004b, Mon. Not.R. Astron. Soc., 354, 798
Horner, J., & Lykawka, P. S. 2012, MNRAS, 426, 159
Hsieh, H. H., Denneau, L., Wainscoat, R. J., et al. 2015a, Icar, 248, 289
Hsieh, H. H., Fitzsimmons, A., Novaković, B., Denneau, L., & Heinze, A. N. 2021, Icar, 354, 114019
Hsieh, H. H., Hainaut, O., Novaković, B., et al. 2015b, ApJL, 800, L16
Huehnerhoff, J., Ketzeback, W., Bradley, A., et al. 2016, Proc. SPIE, 9908, 99085H
Ivanova, O., Borysenko, S., & Golovin, A. 2014, Icar, 227, 202
Ivanova, O. V., Skorov, Y. V., Korsun, P. P., Afanasiev, V. L., & Blum, J. 2011, Icar, 211, 559
Ivezić, Ž., Tabachnik, S., Rafikov, R., et al. 2001, AJ, 122, 2749
Jedicke, R., Bolin, B., Granvik, M., & Beshore, E. 2016, Icar, 266, 173
Jewitt, D. 2015, AJ, 150, 201
Jewitt, D., Hsieh, H., & Agarwal, J. 2015, in Asteroids IV, ed. P. Michel, F. E. DeMeo, & W. F. Bottke (Tucson, AZ: Univ. Arizona Press), 221
Jewitt, D., Ishiguro, M., Weaver, H., et al. 2014, AJ, 147, 117
Jewitt, D. C. 2009, AJ, 137, 4296
Jewitt, D. C., & Meech, K. J. 1987, ApJ, 317, 992
Jordi, K., Grebel, E. K., & Ammon, K. 2006, A&A, 460, 339
Jurić, M., Ivezić, Ž., Lupton, R. H., et al. 2002, AJ, 124, 1776
Kareta, T., Volk, K., Noonan, J. W., et al. 2020a, RNAAS, 4, 74
Kareta, T., Woodney, L. M., Schambeau, C., et al. 2020b, arXiv:2011.09993

Kasliwal, M. M., Cannella, C., Bagdasaryan, A., et al. 2019, PASP, 131, 038003
Kelley, M. S., Fernández, Y. R., Licandro, J., et al. 2013, Icar, 225, 475
Kelley, M. S. P., Bodewits, D., Ye, Q., et al. 2019, in ASP Conf. Ser., 523, Astronomical Data Analysis Software and Systems XXVII, ed. P. J. Teuben et al. (San Francisco, CA: ASP), 471
Kinoshita, D., Chen, C.-W., Lin, H.-C., et al. 2005, ChJAA, 5, 315
Krist, J. E., Hook, R. N., & Stoehr, F. 2011, Proc. SPIE, 8127, 81270J
Läuter, M., Kramer, T., Rubin, M., & Altwegg, K. 2019, MNRAS, 483, 852
Levison, H. F., & Duncan, M. J. 1994, Icar, 108, 18
Licandro, J., Pinilla-Alonso, N., de Leon, J., et al. 2020, AAS/DPS Meeting, 52, 404.06
Lin, Z.-Y., Cheng, Y.-L., Vincent, J.-B., et al. 2020, PASJ, 72, 79
Lisse, C., Bauer, J., Cruikshank, D., et al. 2020, NatAs, 4, 930
Lisse, C. M., Young, L. A., Cruikshank, D., Sandford, S., & Schmitt, B. 2019, Icar, submitted
Ivezić, Ž, Lupton, R. H., Jurić, M., et al. 2002, AJ, 124, 2943
Marshall, D., Rezac, L., Hartogh, P., Zhao, Y., & Attree, N. 2019, A&A, 623, A120
Marzari, F., Scholl, H., Murray, C., & Lagerkvist, C. 2002, in Asteroids III, ed. W. F. Bottke, Jr. et al. (Tucson, AZ: Univ. Arizona Press), 725
Masci, F. J., Laher, R. R., Rusholme, B., et al. 2019, PASP, 131, 018003
McCarthy, J. K., Cohen, J. G., Butcher, B., et al. 1998, Proc. SPIE, 3355, 81
McDonnell, J. A. M., Alexander, W. M., Burton, W. M., et al. 1986, Natur, 321, 338
Meech, K. J., & Svoren, J. 2004, in Comets II, ed. M. C. Festou, H. U. Keller, & H. A. Weaver (Tucson, AZ: Univ. Arizona Press), 317
Mommert, M., Kelley, M., de Val-Borro, M., et al. 2019, JOSS, 4, 1426
Morbidelli, A., Levison, H. F., Tsiganis, K., & Gomes, R. 2005, Natur, 435, 462
Moreno, F., Pozuelos, F. J., Novaković, B., et al. 2017, ApJL, 837, L3
Murray, C. D., & Dermott, S. F. 1999, Solar System Dynamics (Cambridge: Cambridge Univ. Press)
Nesvorný, D., Parker, J., & Vokrouhlický, D. 2018, AJ, 155, 246
Nesvorný, D., Vokrouhlický, D., Dones, L., et al. 2017, ApJ, 845, 27
Ofek, E. O. 2012, ApJ, 749, 10
Oke, J. B., Cohen, J. G., Carr, M., et al. 1995, PASP, 107, 375
O'Rourke, L., Heinisch, P., Blum, J., et al. 2020, Natur, 586, 697
Perley, D. A. 2019, PASP, 131, 084503
Reach, W. T., Kelley, M. S., & Vaubaillon, J. 2013, Icar, 226, 777
Rein, H., Hernandez, D. M., Tamayo, D., et al. 2019, MNRAS, 485, 5490
Rein, H., & Liu, S.-F. 2012, A&A, 537, A128
Roig, F., & Nesvorný, D. 2015, AJ, 150, 186
Sarid, G., & Prialnik, D. 2009, M&PS, 44, 1905
Sarid, G., Volk, K., Steckloff, J. K., et al. 2019, ApJL, 883, L25
Sato, H., Heinze, A., & Nakano, S. 2020, CBET, 4780, 1
Schambeau, C., Fernandez, Y., Belton, R., et al. 2020, CBET, 4821, 1
Schambeau, C. A., Fernández, Y. R., Samarasinha, N. H., Woodney, L. M., & Kundu, A. 2019, AJ, 158, 259
Schleicher, D. G., & Bair, A. N. 2011, AJ, 141, 177
Smith, C. E., & Nelson, B. 1969, PASP, 81, 74
Solontoi, M., Ivezić, Ž, Jurić, M., et al. 2012, Icar, 218, 571
Steckloff, J. K., Sarid, G., Volk, K., et al. 2020, ApJL, 904, L20
Steele, I. A., Smith, R. J., Rees, P. C. T., et al. 2004, Proc. SPIE, 5489, 679
Tonry, J. L. 2011, PASP, 123, 58
Vokrouhlický, D., Nesvorný, D., & Dones, L. 2019, AJ, 157, 181
Vokrouhlický, D., Pravec, P., Durech, J., et al. 2017, A&A, 598, A91
Werner, M. W., Roellig, T. L., Low, F. J., et al. 2004, ApJS, 154, 1
Ye, Q., Kelley, M. S. P., Bodewits, D., et al. 2019, ApJL, 874, L16

A&A 633, A98 (2020)
https://doi.org/10.1051/0004-6361/201935097

Astronomy & Astrophysics

Full orbital solution for the binary system in the northern Galactic disc microlensing event Gaia16aye★

Ł. Wyrzykowski[1], P. Mróz[1], K. A. Rybicki[1], M. Gromadzki[1], Z. Kołaczkowski[44,78,†], M. Zieliński[1], P. Zieliński[1], N. Britavskiy[4,5], A. Gomboc[34], K. Sokolovsky[18,3,65], S. T. Hodgkin[6], L. Abe[88], G. F. Aldi[19,79], A. AlMannaei[61,99], G. Altavilla[71,7], A. Al Qasim[61,99], G. C. Anupama[8], S. Awiphan[9], E. Bachelet[62], V. Bakış[10], S. Baker[99], S. Bartlett[49], P. Bendjoya[11], K. Benson[99], I. F. Bikmaev[75,86], G. Birenbaum[12], N. Blagorodnova[23], S. Blanco-Cuaresma[14,73], S. Boeva[15], A. Z. Bonanos[18], V. Bozza[19,79], D. M. Bramich[61], I. Bruni[24], R. A. Burenin[83,84], U. Burgaz[20], T. Butterley[21], H. E. Caines[33], D. B. Caton[92], S. Calchi Novati[82], J. M. Carrasco[22], A. Cassan[28], V. Čepas[55], M. Cropper[99], M. Chruślińska[1,23], G. Clementini[24], A. Clerici[34], D. Conti[90], M. Conti[47], S. Cross[62], F. Cusano[24], G. Damljanovic[25], A. Dapergolas[18], G. D'Ago[80], J. H. J. de Bruijne[26], M. Dennefeld[28], V. S. Dhillon[29,4], M. Dominik[30], J. Dziedzic[1], O. Erece[31], M. V. Eselevich[85], H. Esenoglu[32], L. Eyer[73], R. Figuera Jaimes[30,52], S. J. Fossey[33], A. I. Galeev[75,86], S. A. Grebenev[83], A. C. Gupta[98], A. G. Gutaev[75], N. Hallakoun[12], A. Hamanowicz[1,35], C. Han[2], B. Handzlik[36], J. B. Haislip[93], L. Hanlon[101], L. K. Hardy[29], D. L. Harrison[6,87], H. J. van Heerden[102], V. L. Hoette[94], K. Horne[30], R. Hudec[38,75,39], M. Hundertmark[40], N. Ihanec[34], E. N. Irtuganov[75,86], R. Itoh[42], P. Iwanek[1], M. D. Jovanovic[25], R. Janulis[55], M. Jelínek[38], E. Jensen[91], Z. Kaczmarek[1], D. Katz[100], I. M. Khamitov[43,75], Y. Kilic[31], J. Klencki[1,23], U. Kolb[46], G. Kopacki[44], V. V. Kouprianov[93], K. Kruszyńska[1], S. Kurowski[36], G. Latev[15], C.-H. Lee[16,17], S. Leonini[47], G. Leto[48], F. Lewis[49,58], Z. Li[62], A. Liakos[18], S. P. Littlefair[29], J. Lu[50], C. J. Manser[51], S. Mao[52], D. Maoz[12], A. Martin-Carrillo[101], J. P. Marais[102], M. Maskoliūnas[55], J. R. Maund[29], P. J. Meintjes[102], S. S. Melnikov[75,86], K. Ment[40], P. Mikołajczyk[44], M. Morrell[46], N. Mowlavi[73], D. Moździerski[44], D. Murphy[101], S. Nazarov[89], H. Netzel[1,78], R. Nesci[66], C.-C. Ngeow[53], A. J. Norton[46], E. O. Ofek[54], E. Pakštienė[55], L. Palaversa[6,73], A. Pandey[98], E. Paraskeva[18,77], M. Pawlak[1,64], M. T. Penny[56], B. E. Penprase[57], A. Piascik[58], J. L. Prieto [95,96], J. K. T. Qvam[97], C. Ranc[69], A. Rebassa-Mansergas[59,70], D. E. Reichart[93], P. Reig[60,74], L. Rhodes[29], J.-P. Rivet[88], G. Rixon[6], D. Roberts[46], P. Rosi[47], D. M. Russell[61], R. Zanmar Sanchez[48], G. Scarpetta[19,81], G. Seabroke[99], B. J. Shappee[68], R. Schmidt[40], Y. Shvartzvald[13,★★], M. Sitek[1], J. Skowron[1], M. Śniegowska[1,76,78], C. Snodgrass[45], P. S. Soares[33], B. van Soelen[102], Z. T. Spetsieri[18,77], A. Stankevičiūtė[1], I. A. Steele[58], R. A. Street[62], J. Strobl[38], E. Strubble[94], H. Szegedi[102], L. M. Tinjaca Ramirez[47], L. Tomasella[63], Y. Tsapras[40], D. Vernet[11], S. Villanueva Jr.[56], O. Vince[25], J. Wambsganss[40,41], I. P. van der Westhuizen[102], K. Wiersema[51,67], D. Wium[102], R. W. Wilson[21], A. Yoldas[6], R. Ya. Zhuchkov[75,86], D. G. Zhukov[75], J. Zdanavičius[55], S. Zoła[36,37], and A. Zubareva[72,3]

(Affiliations can be found after the references)

Received 22 January 2019 / Accepted 10 October 2019

ABSTRACT

Gaia16aye was a binary microlensing event discovered in the direction towards the northern Galactic disc and was one of the first microlensing events detected and alerted to by the *Gaia* space mission. Its light curve exhibited five distinct brightening episodes, reaching up to $I = 12$ mag, and it was covered in great detail with almost 25 000 data points gathered by a network of telescopes. We present the photometric and spectroscopic follow-up covering 500 days of the event evolution. We employed a full Keplerian binary orbit microlensing model combined with the motion of Earth and *Gaia* around the Sun to reproduce the complex light curve. The photometric data allowed us to solve the microlensing event entirely and to derive the complete and unique set of orbital parameters of the binary lensing system. We also report on the detection of the first-ever microlensing space-parallax between the Earth and *Gaia* located at L2. The properties of the binary system were derived from microlensing parameters, and we found that the system is composed of two main-sequence stars with masses $0.57 \pm 0.05\,M_{\odot}$ and $0.36 \pm 0.03\,M_{\odot}$ at 780 pc, with an orbital period of 2.88 years and an eccentricity of 0.30. We also predict the astrometric microlensing signal for this binary lens as it will be seen by *Gaia* as well as the radial velocity curve for the binary system. Events such as Gaia16aye indicate the potential for the microlensing method of probing the mass function of dark objects, including black holes, in directions other than that of the Galactic bulge. This case also emphasises the importance of long-term time-domain coordinated observations that can be made with a network of heterogeneous telescopes.

Key words. gravitational lensing: micro – techniques: photometric – binaries: general – stars: individual: Gaia16aye-L

1. Introduction

Measuring the masses of stars or stellar remnants is one of the most challenging tasks in modern astronomy. Binary systems were the first to facilitate mass measurement through the Doppler effect in radial velocity measurements (e.g. Popper 1967), leading to the mass-luminosity relation and an advancement in the understanding of stellar evolution (e.g. Paczyński 1971; Pietrzyński et al. 2010). However, these techniques require the binary components to emit detectable amounts of light, often demanding large-aperture telescopes and sensitive instruments. In order to study the invisible objects, in particular stellar remnants such as neutron stars or black holes, other means of mass measurement are necessary. Recently, the masses of black holes

★ Full Tables B.1–D.1 are only available at the CDS via anonymous ftp to cdsarc.u-strasbg.fr (130.79.128.5) or via http://cdsarc.u-strasbg.fr/viz-bin/cat/J/A+A/633/A98

★★ NASA Postdoctoral Program Fellow.

† Deceased.

were measured when a close binary system tightened its orbit and emitted gravitational waves (e.g. Abbott et al. 2016), yielding unexpectedly high masses that were not observed before (e.g. Abbott et al. 2017; Belczynski et al. 2016; Bird et al. 2016). Because of the low merger rates, gravitational wave experiment detections are limited to very distant galaxies. Other means of mass measurement are therefore required to probe the faint and invisible populations in the Milky Way and its vicinity.

Gravitational microlensing allows for detection and study of binary systems regardless of the amount of light they emit and regardless of the radial velocities of the components, as long as the binary crosses the line of sight to a star that is bright enough to be observed. Therefore, this method offers an opportunity to detect binary systems that contain planets (e.g. Gould & Loeb 1992; Albrow et al. 1998; Bond et al. 2004; Udalski et al. 2005), planets orbiting a binary system of stars (e.g. Poleski et al. 2014; Bennett et al. 2016), and black holes or other dark stellar remnants (e.g. Shvartzvald et al. 2015).

Typically, searches for microlensing events are conducted in the direction of the Galactic bulge because of the high stellar density, potential sources and lenses, and the high microlensing optical depth (e.g. Kiraga & Paczynski 1994; Udalski et al. 1994a, 2015a; Paczynski 1996; Wozniak et al. 2001; Sumi et al. 2013; Wyrzykowski et al. 2015; Mróz et al. 2017). The regions of the Galactic plane outside of the bulge have occasionally also been monitored in the past for microlensing events, however, even though the predicted rates of events were orders of magnitude lower (e.g. Han 2008; Gaudi et al. 2008). Derue et al. (2001) first published microlensing events that were detected during the long-term monitoring of the selected disc fields. Two serendipitous discoveries of bright microlensing events outside of the bulge were reported by amateur observers, the Tago event (Fukui et al. 2007; Gaudi et al. 2008), and the Kojima-1 event (Nucita et al. 2018; Dong et al. 2019; Fukui et al. 2019), which has a signature of a planet next to the lens. The first binary microlensing event in the Galactic disc was reported in Rahal et al. (2009) (GSA14), but its light curve was too poorly sampled in order to conclude on the parameters of the binary lens.

The best-sampled light curves come from bulge surveys, such as MACHO (Alcock et al. 1997; Popowski et al. 2000), the Expérience pour la Recherche d'Objets Sombres (EROS; Hamadache et al. 2006), the Optical Gravitational Lensing Experiment (OGLE; Udalski et al. 1994a, 2000, 2015a), the Microlensing Observations in Astrophysics (MOA; Yock 1998; Sumi et al. 2013), and the Korean Microlensing Telescope Network (KMNet; Kim et al. 2016). In particular, the OGLE project has been monitoring the Galactic bulge regularly since 1992 and was the first to report on a binary microlensing event in 1993 (Udalski et al. 1994b). Binary microlensing events constitute about 10% of all events reported by the microlensing surveys of the bulge. The binary lens differs from a single lens when the component separation on the sky is of order of their Einstein radius Paczynski (1996) and Gould (2000), which is computed as

$$\theta_{\rm E} = \sqrt{\kappa M_L(\pi_{\rm l} - \pi_{\rm s})}, \ \kappa \equiv \frac{4G}{c^2} \approx 8.144 \,{\rm mas}\, M_\odot^{-1}, \quad (1)$$

where M_L is the total mass of the binary and $\pi_{\rm l}$ and $\pi_{\rm s}$ are parallaxes of the lens and the source, respectively. For the conditions in the Galaxy and a typical mass of the lens, the size of the Einstein ring is about 1 milliarcsecond (1 mas). Instead of a circular Einstein ring as in the case of a single lens (or very tight binary system), two (or more) lensing objects produce a complex curve on the sky, shaped by the mass ratio and projected separation of the components. This is called the critical curve. In the source plane this curve turns into a caustic curve (as opposed to a point in the case of a single lens), which denotes the places where the source is infinitely amplificated (e.g. Bozza 2001; Rattenbury 2009). As the source and the binary lens move, their relative proper motion changes the position of the source with respect to the caustics. Depending on this position, there are three (when the source is outside of the caustic) or five (inside the caustic) images of the source. Images also change their location as well as their size, therefore the combined light of the images we observe changes the observed amplification, with the most dramatic changes at the caustic crossings. In a typical binary lensing event the source–lens trajectory can be approximated with a straight line (e.g. Jaroszynski et al. 2004; Skowron et al. 2007). If the line crosses the caustic, it produces a characteristic U-shaped light curve because the amplification increases steeply as the source approaches the caustic and remains high inside the caustic (e.g. Witt & Mao 1995). If the source approaches one of the caustic cusps, the light curve shows a smooth increase, similar to a single lensing event. Identifying all these features in the light curve helps constrain the shape of the caustic and hence the parameters of the binary. An additional annual parallax effect causes the trajectory of the source to curve, which probes the caustic shape at multiple locations (e.g. An & Gould 2001; Skowron et al. 2009; Udalski et al. 2018) and thus helps constrain the solution of the binary system better.

The situation becomes more complex when a binary system rotates while lensing, which causes the binary configuration on the sky to change. This in turn changes the shape and size of the caustic (Albrow et al. 2000). In the case of most binary microlensing events the effect of the orbital motion can be neglected because the orbital periods are often much longer (typically years) than the duration of the event (typically weeks). However, in longer events the orbital motion has to be taken into account in the model. Together with the source–lens relative motion and the parallax effect, this causes the observed amplification to vary significantly during the event and may generate multiple crossings of the caustic and amplification due to cusp approach (e.g. Skowron et al. 2009). However, in rare cases, such a complex event allows us not only to measure the mass and distance of the lens, but also to derive all orbital parameters of the binary. The first such case was found by the OGLE survey in the event OGLE-2009-BLG-020 (Skowron et al. 2011), and its orbital parameters found in the model were verified with radial velocity measurement (Yee et al. 2016). The orbital motion was also modelled in the MOA-2011-BLG-090 and OGLE-2011-BLG-0417 events (Shin et al. 2012), but the former was too faint and the latter was not confirmed with radial velocity data (Boisse et al. 2015; Bachelet et al. 2018).

Additional information that helps constrain the parameters of the system may also come from space parallax (e.g. Refsdal 1966; Gould 1992; Gould et al. 2009). This is now being routinely done by observing microlensing events from the Earth and *Spitzer* or *Kepler*, separated by more than 1 au (e.g. Udalski et al. 2015b; Yee et al. 2015; Calchi Novati & Scarpetta 2016; Shvartzvald et al. 2016; Zhu et al. 2016; Poleski et al. 2016).

The most difficult parameter to measure, however, is the size of the Einstein radius. It can be found when the finite source effects are detected, when the angular source size is large enough to experience a significant gradient in the magnification near the centre of the Einstein ring or the binary lens caustic (e.g. Yoo et al. 2004; Zub et al. 2011). The measurement of the angular separation between the luminous lens and the source years or decades after the event also directly leads to calculation of

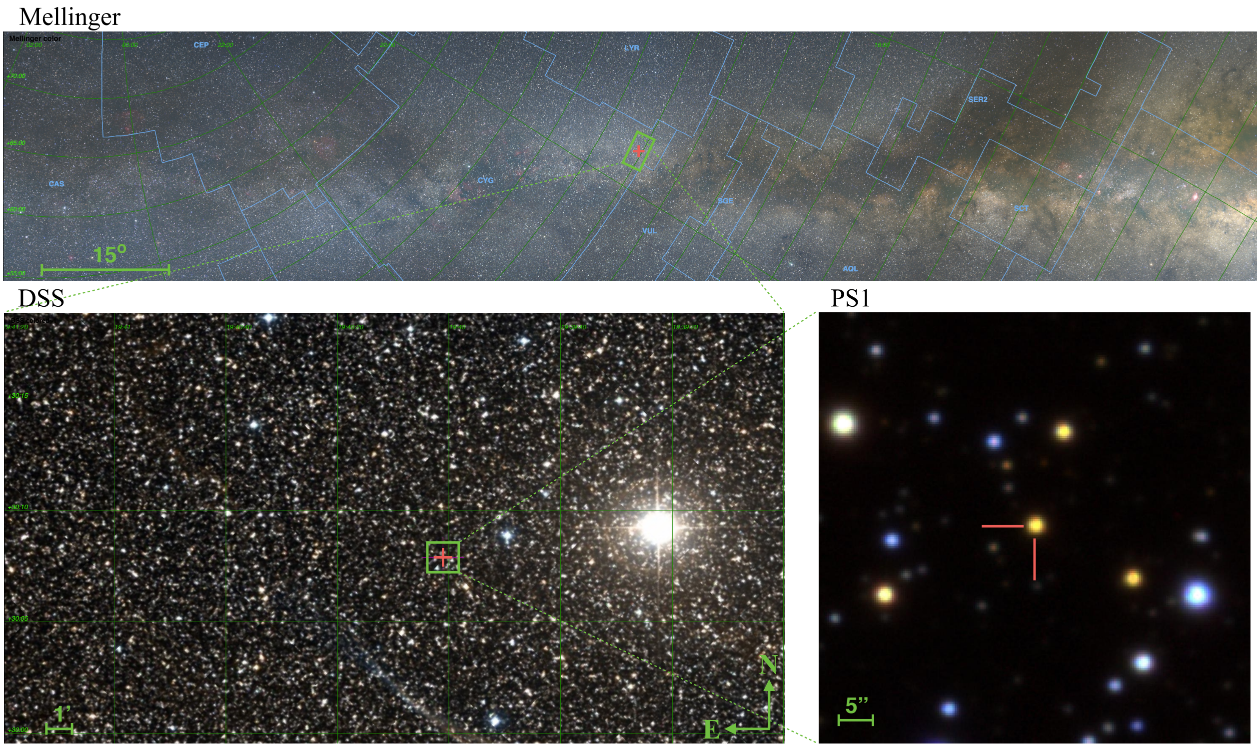

Fig. 1. Location of Gaia16aye on the sky. Images from Mellinger and DSS were obtained using the Aladin tool.

θ_E (e.g. Kozłowski et al. 2007). Otherwise, for dark lenses, the measurement of θ_E can only come from astrometric microlensing (Dominik & Sahu 2000; Belokurov & Evans 2002; Lu et al. 2016; Kains et al. 2017; Sahu et al. 2017). As shown in Rybicki et al. (2018), *Gaia* will soon provide precise astrometric observations for microlensing events, which will allow us to measure θ_E, but only for events brighter than about $V < 15$ mag.

Here we present Gaia16aye, a unique event from the Galactic disc, far from the Galactic bulge, which lasted almost two years and exhibited effects of binary lens rotation, an annual and space parallax, and a finite source. The very densely sampled light curve was obtained solely thanks to an early alert from *Gaia* and a dedicated ground-based follow-up of tens of observers, including amateurs and school pupils. The wealth of photometric data allowed us to find the unique solution for the binary system parameters.

The paper is organised as follows. Sections 2 and 3 describe the history of the detection and the photometric and spectroscopic data collected during the follow-up of Gaia16aye. In Sect. 4 we describe the microlensing model we used to reproduce the data. We then discuss the results in Sect. 5.

2. Discovery and follow-up of Gaia16aye

Gaia16aye was found during the regular examination of the photometric data collected by the *Gaia* mission. *Gaia* is a space mission of the European Space Agency (ESA) in science operation since 2014. Its main goal is to collect high-precision astrometric data, that is, positions, proper motions, and parallaxes, of all stars on the sky down to about 20.7 mag in *Gaia G* band (Gaia Collaboration 2016; Evans et al. 2018). While *Gaia* scans the sky multiple times, it provides near-real-time photometric data, which can be used to detect unexpected changes in the brightness or appearance of new objects from all over the sky. This is dealt with by the *Gaia* Science Alerts system (Wyrzykowski & Hodgkin 2012; Hodgkin et al. 2013; Wyrzykowski et al. 2014), which processes daily portions of the spacecraft data and produces alerts on potentially interesting transients. The main purpose of the publication of the alerts from *Gaia* is to enable the astronomical community to study the unexpected and temporary events. Photometric follow-up is necessary in particular in the case of microlensing events in order to fill the gaps between *Gaia* observations and subsequently construct a densely sampled light curve, sensitive to short-lived anomalies and deviations to the standard microlensing evolution (e.g. Wyrzykowski et al. 2012).

Gaia16aye was identified as an alert in the data chunk from 5 August 2016, processed on 8 August by the *Gaia* Science Alerts pipeline (*AlertPipe*), and published on *Gaia* Science Alerts webpages[1] on 9 August 2016, 10:45 GMT. The full *Gaia* photometry of Gaia16aye is listed in Table B.1.

The alert was triggered by a significant change in brightness of an otherwise constant-brightness star with $G = 15.51$ mag. The star has a counterpart in the 2MASS catalogue as 2MASS19400112+3007533 at RA, Dec (J2000.0) = 19:40:01.14, 30:07:53.36, and its source Id in *Gaia* DR2 is 2032454944878107008 (Gaia Collaboration 2018). Its Galactic coordinates are l,b = 64.999872, 3.839052 deg, which locates Gaia16aye well in the northern part of the Galactic Plane towards the Cygnus constellation (see Fig. 1).

Gaia collected its first observation of this star in October 2014, and until the alert in August 2016, there were no significant brightness variation in its light curve. Additionally, this part of the sky was observed prior to *Gaia* in 2011–2013 as part of a Nova Patrol (Sokolovsky et al. 2014), and no previous brightenings were detected at a limiting magnitude of $V \approx 14.2$.

In the case of Gaia16aye the follow-up was initiated because the source at its baseline was relatively bright and easily

[1] http://gsaweb.ast.cam.ac.uk/alerts/alert/Gaia16aye

accessible for a broad range of telescopes with smaller apertures. Moreover, microlensing events brighter than about $G = 16$ mag will have *Gaia* astrometric data of sufficient accuracy in order to detect the astrometric microlensing signal (Rybicki et al. 2018). For this purpose, we have organised a network of volunteering telescopes and observers who respond to *Gaia* alerts, in particular to microlensing event candidates, and invest their observing time to provide dense coverage of the light curve. The network is arranged under the Time-Domain work package of the European Commission's Optical Infrared Coordination Network for Astronomy (OPTICON) grant[2].

The follow-up observations started immediately after the announcement of the alert (the list of telescopes and their acronyms is provided in Table 1), with the first data points taken on the night 9/10 Aug. 2016 with the 0.6 m Akdeniz Univ. UBT60 telescope in the TUBITAK National Observatory, Antalya, the SAI Southern Station in Crimea, the pt5m telescope at the Roque de los Muchachos Observatory on La Palma (Hardy et al. 2015), the 0.8m Telescopi *Joan Oró* (TJO) at l'Observatori Astronomic del Montsec, and the 0.8 m robotic APT2 telescope in Serra La Nave (Catania). The data showed a curious evolution and a gradual rise (0.1 mag day^{-1}) in the light curve without change in colour, which is atypical for many known types of variable and cataclysmic variable stars. On the night 13/14 Aug. 2016 (HJD′ ≡ HJD-2450000.0 ~ 7614.5) the object reached a peak $V = 13.8$ mag ($B-V = 1.6$ mag, $I = 12.2$ mag), as detected by ATP2 and TJO, which was followed by a sudden drop by about 2 mag. Alerted by the unusual shape of the light curve, we obtained spectra of Gaia16aye with the 1.22 m Asiago telescope on 11 August and with the 2.0 m Liverpool Telescope (LT, La Palma) on 12 August, which were consistent with a normal K8-M2 type star (Bakis et al. 2016). The stellar spectra along with the shape of the light curve implied that Gaia16aye was a binary microlensing event, which was detected by *Gaia* at its plateau between the two caustic crossings, and we have observed the caustic exit with clear signatures of the finite source effects.

The continued follow-up after the first caustic exit revealed a very slow gradual rise in brightness (around 0.1 mag in a month). On 17 September 2016, it increased sharply by 2 mag (first spotted by the APT2 telescope), indicating the second caustic entry. The caustic crossing again showed a broad and long-lasting effect of finite source size (flattened peak), lasting for nearly 48 h between HJD′ = 7649.4 and 7651.4 and reaching about $V = 13.6$ mag and $I = 12$ mag. The caustic crossing was densely covered by the Liverpool Telescope and the 0.6 m Ostrowik Observatory near Warsaw, Poland.

Following the second caustic entry, the object remained very bright ($I \sim 12-14$ mag) and was observed by multiple telescopes from around the globe, both photometrically and spectroscopically. The complete list of telescopes and instruments involved in the follow-up observations of Gaia16aye is shown in Table 1, and their parameters are gathered in Table A.1. In total, more than 25 000 photometric and more than 20 spectroscopic observations were taken over the period of about two years. In early November 2016, the brightness trend changed from falling to rising, as expected for binary events during the caustic crossing (Nesci 2016; Khamitov et al. 2016a). A simple preliminary model for the binary microlensing event predicted the caustic exit to occur around November 20.8 UT (HJD′ = 7713.3) and the caustic crossing to last about seven hours (Mroz et al. 2016). In order to catch and cover the caustic exit well, an intensive observing campaign was begun, involving also amateur astronomical associations (including the British Astronomical Association and the German Haus der Astronomie) and school pupils. The observations were also reported live on Twitter (hashtag #Gaia16aye). A DDT observing time was allocated at the *William Herschel* Telescope (WHT/ACAM) and the Telescopio Nazionale *Galileo* (TNG/DOLORES) to provide low- and high-resolution spectroscopy at times close to the peak. However, the actual peak occurred about 20 h later than expected, on 21 November 16 UT (7714.17), and was followed by TRT-GAO, Aries130, CrAO, AUT25, T60, T100, RTT150 (detection of the fourth caustic was reported in Khamitov et al. 2016b), Montarrenti, Bialkow, Ostrowik, Krakow50, OndrejovD50, LT, pt5m, Salerno, and UCLO, spanning the whole globe, which provided 24-h coverage of the caustic exit. The sequence of spectroscopic observations before and at the very peak was taken with the IDS instrument on the *Isaac Newton* Telescope (INT). After the peak at 11.85 mag in I band, the event brightness smoothly declined, as caught by Swarthmore24, DEMONEXT, and AAVSO. The first datapoint taken on the next night from India (Aries130 telescope) showed $I = 14.33$ mag, indicating the complete exit from the caustic. The event then again began to rise very slowly, with a rate of 1 mag over four months, and it exhibited a smooth peak on 5 May 2017 (HJD′ = 7878), reaching $I = 13.3$ mag ($G \sim 14$ mag) (Wyrzykowski et al. 2017). After this, the light curve declined slowly and reached the pre-alert level in November 2017, at $G = 15.5$ mag. We continued our photometric follow-up for another year to confirm that there was no further re-brightening. Throughout the event, the All-Sky Automated Survey for SuperNovae (ASAS-SN; Shappee et al. 2014; Kochanek et al. 2017) observed Gaia16aye serendipitously with a typical cadence of between two and five days. Its data cover various parts of the light curve of the event, including the part before the *Gaia* alert, where a smooth rise and the first caustic entry occurred.

2.1. Ground-based photometry calibrations

Each observatory processed the raw data with their own standard data reduction procedures to create bias, dark-subtracted, and flat-fielded images. Then, the images were solved astrometrically, most often with the use of `Astrometry.net` code (Hogg et al. 2008; Lang et al. 2010), and the instrumental photometry for all objects within the field of view was derived with a variety of tools, including Source EXtractor (Bertin & Arnouts 1996) and Daophot (Stetson 1987). The lists of detected sources with their measured instrumental magnitudes were uploaded to the Cambridge Photometric Calibration Server (CPCS)[3], designed and maintained by Sergey Koposov and Lukasz Wyrzykowski. The CPCS matches the field stars to a reference catalogue, identifies the target source, and determines which filter was used for observations. This tool acted as a central repository for all the data, but primarily, it standardised the data into a homogenous photometric system. It relied on available archival catalogues of this patch of the sky (primarily the AAVSO Photometric All-Sky Survey, APASS, and the Pan-STARRS1 Surveys, PS1) and derived zero-points for each of the observations. The use of a common repository allowed for near-real-time tracking of the evolution of the event, which is particularly important near the caustic entry and exit. Photometric data were uploaded by the observers within minutes of the

[2] https://www.astro-opticon.org/h2020/network/na4.html

[3] http://gsaweb.ast.cam.ac.uk/followup

Table 1. Telescopes used in the photometric follow-up observations of Gaia16aye.

Telescope code	Telescope/observatory name	Location	Longitude [deg]	Latitude [deg]	Reference
AAVSO	American Association of Variable Star Observers	world-wide network, MA, USA	–	–	–
Akeno50	50-cm telescope, Akeno Observatory	Asao, Akeno-mura, Japan	138.30	35.47	–
APT2	Automatic Photometric Telescope 2, Catania Astrophysical Observatory	Serra La Nave, Mt. Etna, Italy	14.97	37.69	–
Aries130	1.30-m telescope, Aryabhatta Research Institute of Observational Sciences	Manora Peak, Nainital, India	79.45	29.37	–
Aristarchos	Aristarchos Telescope, Helmos Observatory	Mt. Helmos, Peloponnese	22.20	37.99	Goudis et al. (2010)
ASASSN	All-Sky Automated Survey for Supernovae	world-wide network of 20 telescopes	–	–	Kochanek et al. (2017)
ASV1	Astronomical Station Vidojevica 0.6 m	Vidojevica, near Prokuplje, Serbia	21.56	43.14	–
ASV2	Astronomical Station Vidojevica 1.4 m	Vidojevica, near Prokuplje, Serbia	21.56	43.14	–
AUT25	25-cm telescope, Akdeniz University	Antalya, Turkey	30.66	36.90	–
BAS2	Rozhen 2 m, National Astronomical Observatory, Bulgarian Academy of Sciences	Rozhen, Bulgaria	24.74	41.70	–
BAS50/70	Schmidt-camera 50/70 cm, National Astronomical Observatory, Bulgarian Academy of Sciences	Rozhen, Bulgaria	24.74	41.70	–
Bialkow	Białków Observatory, Astronomical Institute of the University of Wrocław	Białków, Poland	16.66	51.48	–
C2PU	C2PU-Omicron, Center for Pedagogy in Planet and Universe sciences	OCA, Calern Plateau, France	6.92	43.75	–
Conti	Conti Private Observatory	MD, USA	−76.49	38.93	–
CrAO	Crimean Astrophysical Observatory	Nauchnyi, Crimea	34.01	44.73	–
DEMONEXT	DEdicated MONitor of EXotransits and Transients, Winer Observatory	AZ, USA	−110.60	31.67	Villanueva et al. (2018)
Foligno	Foligno Observatory	Perugia Province, Italy	12.70	42.96	–
HAO50	Horten Astronomical Telescope	Nykirke, Horten, Norway	10.39	59.43	–
Krakow50	50-cm Cassegrain telescope, Astronomical Observatory of Jagiellonian University	Kraków, Poland	19.82	50.05	–
Kryoneri	1.2-m Kryoneri telescope, Kryoneri Observatory	Mt. Kyllini, Peloponnese, Greece	22.63	38.07	Xilouris et al. (2018)
LCO-Texas	Las Cumbres Observatory	McDonald Observatory, TX, USA	−104.02	30.67	Brown et al. (2013)
LCO-Hawaii	Las Cumbres Observatory	Haleakala, HI, USA	−156.26	20.71	Brown et al. (2013)
Leicester	University of Leicester Observatory	Oadby, UK	−1.07	52.61	–
Loiano	1.52 m Cassini Telescope, INAF – Bologna Observatory of Astrophysics and Space Science	INAF-Bologna, Loiano, Italy	11.33	44.26	–
LOT1m	Lulin One-meter Telescope	Lulin Observatory, Taiwan	120.87	23.47	–
LT	Liverpool Telescope, Roque de Los Muchachos Observatory	La Palma, Spain	−17.88	28.76	Steele et al. (2004)
MAO165	1.65-m Ritchey-Chretien telescope, Molėtai Astronomical Observatory	Molėtai, Kulionys, Lithuania	25.56	55.32	–
Mercator	*Mercator* Telescope, Roque de Los Muchachos Observatory	La Palma, Spain	–17.88	28.76	–
Montarrenti	Montarrenti Observatory	Siena, Italy	11.18	43.23	–
OHP	T120, L'Observatoire de Haute-Provence	St. Michel, France	5.71	43.93	–
OndrejovD50	D50 telescope, Astronomical Institute of Academy of Sciences of the Czech Republic	Ondrejov, Czech Rep.	14.78	49.91	–
Ostrowik	Cassegrain telescope, Warsaw University Astronomical Observatory	Ostrowik, Poland	21.42	52.09	–
PIRATE	Physics Innovations Robotic Astronomical Telescope Explorer Mark-III, Teide Observatory	Tenerife, Spain	−16.51	28.30	Kolb et al. (2018)
pt5m	0.5m robotic telescope, Roque de Los Muchachos Observatory	La Palma, Spain	−17.88	28.76	Hardy et al. (2015)
RTT150	1.5-m Russian-Turkish Telescope, TUBITAK National Observatory	Mt. Bakirlitepe, Antalya, Turkey	30.33	36.83	–
SAI	60-cm Zeiss-2 telescope, Moscow State Univercity	Nauchnyi, Crimea	34.01	44.73	–

Table 1. continued.

Telescope code	Telescope/observatory name	Location	Longitude [deg]	Latitude [deg]	Reference
	observational station of Sternberg Astronomical Institute				
Salerno	Salerno University Observatory	Fisciano, Italy	14.79	40.78	–
SKAS-KFU28	C28 CGEM-1100 telescope, Zelenchukskaya Station of Kazan Federal University	Zelenchukskaya, Caucasus, Russia	41.43	43.65	–
Skinakas	1.3-m telescope, Skinakas Observatory	Skinakas, Crete, Greece	24.90	35.21	–
SKYNET	Skynet Robotic Telescope Network, 41-inch telescope, Yerkes Observatory	WI, USA	−88.56	42.57	–
Swarthmore24	24-inch telescope, Peter van de Kamp Observatory	Swarthmore College, PA, USA	−75.36	39.91	–
T60	60-cm telescope, TUBITAK National Observatory	Mt. Bakirlitepe, Antalya, Turkey	30.33	36.83	–
T100	1.0-m telescope, TUBITAK National Observatory	Mt. Bakirlitepe, Antalya, Turkey	30.33	36.83	–
TJO	*Joan Oró* Telescope, Montsec Observatory	Sant Esteve de la Sarga, Lleida, Spain	0.73	42.03	–
TRT-GAO	Thai Robotic Telescope GAO, Yunnan Observatory	Phoenix Mountain, Kunming, China	105.03	26.70	–
TRT-TNO	Thai Robotic Telescope TNO, Thai National Observatory	Doi Inthanon, Chiang Mai, Thailand	98.48	18.57	–
UCLO-C14E	University College London Observatory, C14 East	Mill Hill, London, UK	−0.24	51.61	–
UCLO-C14W	University College London Observatory, C14 West	Mill Hill, London, UK	−0.24	51.61	–
UBT60	Akdeniz University Telescope, TUBITAK National Observatory	Mt. Bakirlitepe, Antalya, Turkey	30.33	36.83	–
Watcher	40-cm telescope, Boyden Observatory	Orange Free State, South Africa	26.40	–29.04	French et al. (2004)
WHT-ACAM	*William Herschel* Telescope, Roque de Los Muchachos Observatory	La Palma, Spain	−17.88	28.76	–
Wise1m	1.0-m telescope, Wise Observatory	Mitzpe Ramon, Israel	34.76	30.60	–
WiseC28	C28 Jay Baum Rich telescope, Wise Observatory	Mitzpe Ramon, Israel	34.76	30.60	–

observation, which facilitated detailed planning of the spectroscopic follow-up.

The list of all the ground-based photometric observations is summarised in Table 2 and the photometric observations are listed in Table C.1. The full table contains 23 730 entries and is available at the CDS. Figure 2 shows all follow-up measurements collected for Gaia16aye over a period of about one and a half years.

2.2. Gaia data

Since October 2014 *Gaia* collected 27 observations before the alert on the 5 August 2016. In total, *Gaia* observed Gaia16aye 84 times as of November 2018. The *G*-band photometric data points collected by *Gaia* are listed in Table B.1. Photometric uncertainties are not provided for *Gaia* alerts, and for this event we assumed 0.01 mag (Gaia Collaboration 2016), but as we show below, these were scaled to about 0.015 mag by requiring the microlensing model χ^2 per degree of freedom to be 1.0. Details of the *Gaia* photometric system and its calibrations can be found in Evans et al. (2018).

The on-board Radial Velocity Spectrometer (RVS) of *Gaia*, collects medium-resolution ($R \sim 11\,700$) spectra over the wavelength range 845–872 nm centred on the Calcium II triplet region of objects brighter than $V \sim 17$ mag (Gaia Collaboration 2016; Cropper et al. 2018). However, individual spectra for selected observations are made available already for brighter *Gaia* alerts using parts of the RVS data processing pipeline (Sartoretti et al. 2018). For Gaia16aye the RVS collected a spectrum on 21 November 2016, 17:05:47 UT (HJD = 2457714.21), see Fig. 3, the moment is caught by *Gaia* at very high magnification, when Gaia16aye reached G = 12.91 mag. The exposure time for the combined three RVS CCDs was 3×4.4 s.

2.3. Spectroscopy

Spectroscopic measurements of the event were obtained at various stages of its evolution. The list of spectroscopic observations is presented in Table 3. The very first set of spectra was taken with the Asiago 1.22 m telescope equipped with the DU440A-BU2 instrument, the Asiago 1.82 m telescope with AFOSC, and the SPRAT instrument on the 2 m Liverpool Telescope (LT), which showed no obvious features seen in outbursting Galactic variables. Other spectra gathered by the 5 m P200 Palomar Hale Telescope and by ACAM on the 4.2 m WHT confirmed this behaviour. This therefore led us to conclude that this is a microlensing event.

We did not find significant differences between spectra taken at various consecutive stages of the event evolution. The features and general shape of the spectra were the same, regardless of whether the spectrum was recorded during amplification or in the baseline. This allows us to conclude that the spectra were dominated by radiation from the source, and contribution from the lens was negligible.

Most of the spectra were obtained in low-resolution mode ($R \leq 1000$) and relatively poor weather conditions, which were useful for an early classification of the transient as a microlensing event. A more detailed analysis of the low-resolution spectra will be presented elsewhere (Zielinski et al., in prep.).

Table 2. Summary of observations taken by the observatories involved in the photometric follow-up of Gaia16aye.

Telescope code	First epoch [HJD-2450000]	Last epoch [HJD-2450000]	Npoints (filter), Npoints (filter2), etc.
AAVSO	7653.283	7714.561	288(V) 151(i) 95(r)
Akeno50	7711.012	7715.301	169(r)*
APT2	7612.294	8055.256	285(B) 467(V) 439(i) 452(r)
Aries130	7714.070	7718.030	6(B) 6(V) 6(R) 6(I)
Aristarchos	8035.219	8039.086	2(B) 2(V) 1(g) 6(i) 44(r)
ASASSN	7547.097	7907.897	68(V)*
ASV1	7929.570	8079.302	11(B) 34(V) 36(i) 28(r)
ASV2	7628.483	7924.511	42(B) 64(V) 1(g) 69(i) 73(r)
AUT25	7712.258	7715.274	136(i) 142(r)
BAS2+BAS50/70	7687.225	7933.497	8(B) 23(V) 9(g) 28(i) 31(r)
Bialkow	7619.340	8028.296	218(B) 499(V) 657(i) 641(r)
C2PU	7637.331	7878.619	8(V) 41(r)
Conti	7714.470	7714.510	38(V)
CrAO	7710.306	7871.562	639(r)
DEMONEXT	7690.672	8162.029	476(V) 483(i) 427(r)
Foligno	7654.361	7719.251	11(V)
HAO50	7818.318	8056.320	22(V)*, 10(R)*
Krakow50	7659.243	7919.552	17(B) 44(V) 49(i) 60(r)
Kryoneri	7652.327	8039.210	92(i) 96(r)
LCO-Texas	7663.570	7904.530	63(B) 70(V) 30(g) 29(i) 94(r)
LCO-Hawaii	6792.778	7708.778	197(gp)*, 318(rp)*, 518(ip)*, 294(V)*, 146(B)*, 24(R)*, 12(I)*
Leicester	7645.461	8063.274	10(B) 9(V) 3(i) 1(r)
Loiano	7660.301	7709.269	77(B) 66(V) 108(g) 119(i) 164(r)
LOT1m	7711.936	7888.223	54(g) 59(i) 55(r)
LT	7647.327	7976.490	2(V) 362(g) 415(i) 488(r)
MAO165	7680.350	7997.400	6(B)* 31(V)* 34(R)* 27(I)*
Mercator	7651.332	7657.397	7(g) 5(r)
Montarrenti	7654.280	7929.545	92(r)
OHP	7665.329	8019.350	6(V) 3(g) 11(i) 13(r)
OndrejovD50	7614.564	8095.253	397(B) 410(V) 413(i) 423(r)
Ostrowik	7619.303	7735.192	3(B) 42(V) 1(g) 185(i) 193(r)
PIRATE	7650.498	7849.748	1473(r) 713(V)
pt5m	7610.408	8094.350	205(B) 2452(V) 243(i) 266(r)
RTT150	7657.696	7937.559	114(B) 112(V) 1(g) 1(i) 1(r)
SAI	7610.282	7613.265	16(B) 16(V) 18(r)
Salerno	7651.308	7765.244	610(R)*
SKAS-KFU28	7662.357	7846.548	124(B)* 158(G)* 170(R)*
Skinakas	7668.246	7993.770	5(B) 1(G) 5(V) 2(g) 6(i) 5(r)
SKYNET	7670.521	7729.487	6(g) 64(i) 38(r)
Swarthmore24	7714.444	7954.598	287(i)
T60	7670.862	8436.268	1(B) 9(V) 8(r) 8(i)
T100	7637.476	7963.499	27(B) 34(V) 24(g) 21(i) 21(r)
TJO	7610.503	8090.273	485(B) 563(V) 1(g) 494(i) 524(r) 2(z)
TRT-GAO	7712.986	7886.388	3(V) 1016(r)
TRT-TNO	7833.368	7843.437	41(i) 48(r)
UCLO-C14E	7678.287	7711.319	5(V) 28(r)
UCLO-C14W	7666.399	7955.577	122(i) 44(r)
UBT60	7610.246	7715.274	279(B) 349(V) 440(i) 448(r)
Watcher	7617.004	8017.002	258(V) 264(i) 261(r)
WHT-ACAM	7701.314	7701.375	26(g) 30(i) 30(r)
Wise1m	7654.236	7749.173	305(i)
WiseC28	7652.396	7660.294	25(i)

Notes. In brackets we list the best-matching filters as found by the Calibration Server. Asterisks mark data that were not uploaded to the CPCS.

We also obtained spectra of higher resolution ($R \sim 6500$) with the 2.5 m INT, La Palma, Canary Islands, during three consecutive nights on 19−21 November 2016. The INT spectra were obtained using the Intermediate Dispersion Spectrograph (IDS, Cassegrain Focal Station, 235 mm focal length camera RED+2) with the grating set to R1200Y, and a dispersion of 0.53 Å pixel^{-1} with a slit width projected onto the sky equal to 1.298″ (see Table 3, spectrum INT 3–5). The exposure time was 400 s for each spectrum centred at wavelength 8100 Å.

The spectra were processed by the observers with their own pipelines or in a standard way using IRAF[4] tasks and scripts. The reduction procedure consisted of the usual bias- and dark-subtraction, flat-field correction, and wavelength calibration.

[4] IRAF is distributed by the National Optical Astronomy Observatories, which are operated by the Association of Universities for Research in Astronomy, Inc., under cooperative agreement with the National Science Foundation.

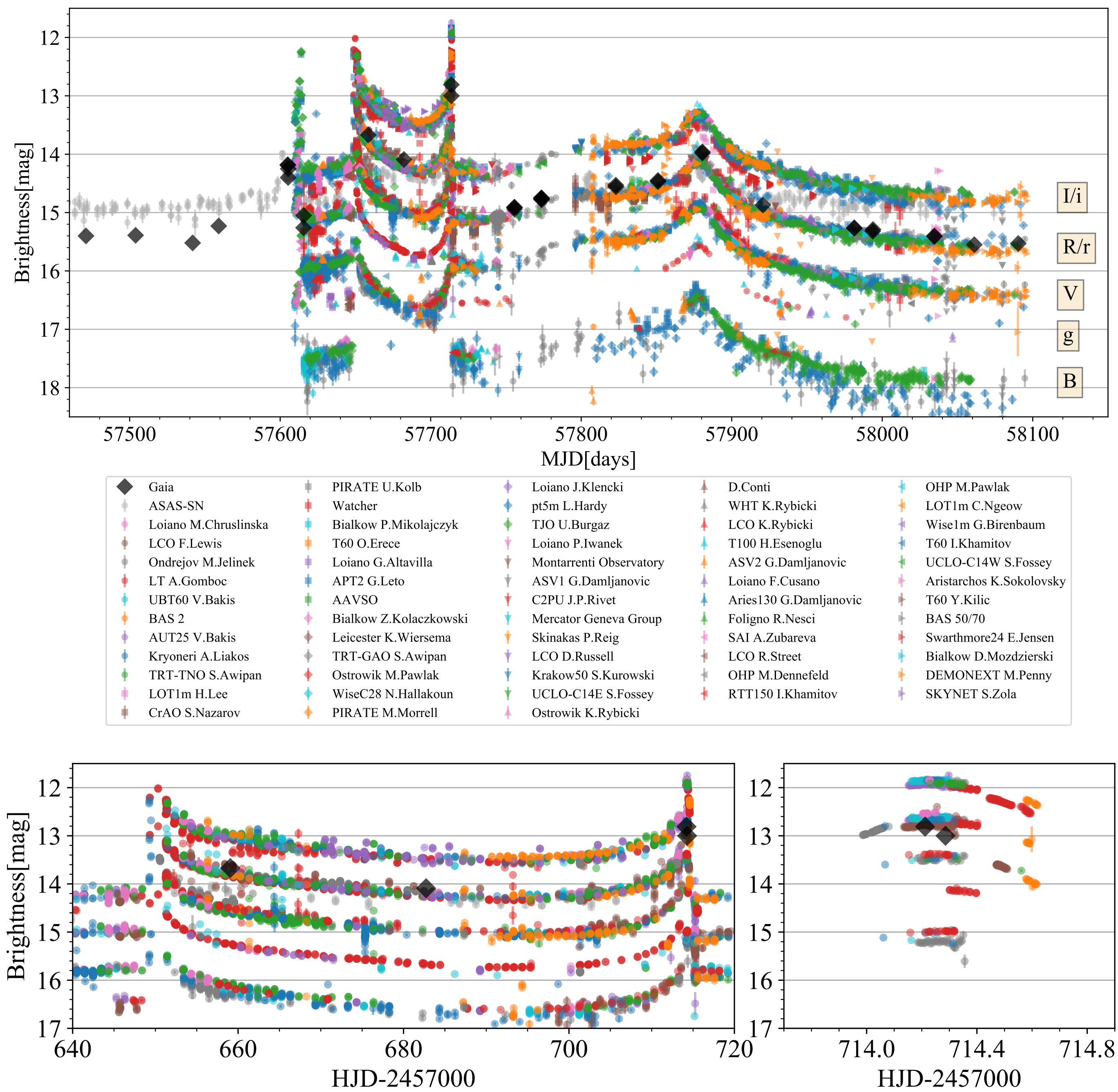

Fig. 2. *Gaia*, ASAS-SN, and follow-up photometric observations of Gaia16aye. Each observatory and observer is marked with a different colour. The marker is explained in the legend. The figure shows only the follow-up data, which were automatically calibrated using the Cambridge Photometric Calibration Server. *Upper panel*: entire event, and *bottom panels*: zoom on the second pair of caustic crossings (*left*) and a detail of the fourth caustic crossing (*right*).

2.4. Swift observations

In order to rule out the possibility that Gaia16aye is some type of cataclysmic variable star outburst, we requested X-ray and ultraviolet *Swift* observations. *Swift* observed Gaia16aye for 1.5 ks on 18 August 2016. *Swift*/XRT detected no X-ray source at the position of the transient with an upper limit of 0.0007 ± 0.0007 cts s^{-1} (a single background photon appeared in the source region during the exposure). Assuming a power-law emission with a photon index of 2 and HI column density of 43.10×10^{20} cm^{-2} (corresponding to the total Galactic column density in this direction; Kalberla et al. 2005), this translates into an unabsorbed 0.3–10 keV flux limit of 5.4×10^{-14} ergs cm^{-2} s^{-1}.

No ultraviolet source was detected by the UVOT instrument at the position of the transient. The upper limit at epoch HJD′ = 7618.86 was derived as >20.28 mag for UVM2-band (Vega system).

2.5. Keck adaptive optics imaging

The event was observed with Keck adaptive optics (AO) imaging on 8 October 2016 (HJD′ = 7669.7). Figure 4 shows the

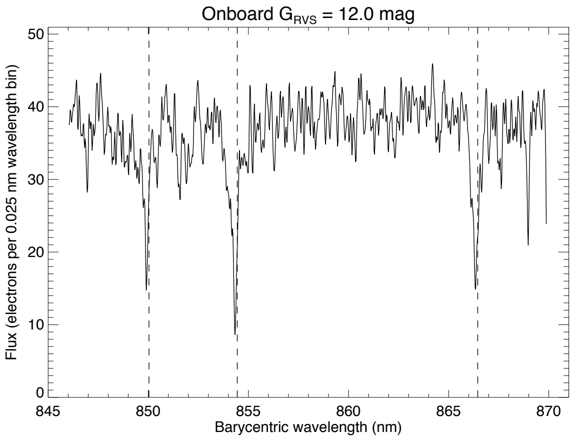

Fig. 3. Medium-resolution spectrum of the Gaia16aye event obtained with the *Gaia* RVS at the brightest moment of the event as seen by *Gaia* at the fourth caustic crossing. The Ca II lines of the lensed source are clearly visible.

10 arcsec field of view obtained with the Keck AO instrument. The full width at half-maximum (FWHM) of the star is about 52 mas. The image shows a single object with no additional light sources in its neighbourhood. This indicates that no additional luminous components contributed to the observed light.

3. Spectroscopy of the source star

During a microlensing event, the variation in the amplification changes the ratio of the flux from the source, while the blend or lens light remains at the same level. Therefore, the spectroscopic data obtained at different amplifications can be used to de-blend the light of the source from any additional constant components and to derive the source properties.

In order to obtain the spectral type and stellar parameters of the Gaia16aye source, we used three spectra gathered by the 2.5 m INT. Based on these spectra we were able to determine the atmospheric parameters of the microlensing source. We used a dedicated spectral analysis framework, iSpec[5], which integrates several radiative transfer codes (Blanco-Cuaresma et al. 2014). In our case, the SPECTRUM code was used (Gray & Corbally 1994), together with well-known Kurucz model atmospheres (Kurucz 1993) and solar abundances of chemical elements taken from Asplund et al. (2009). The list of absorption lines with atomic data was taken from the VALD database (Kupka & Dubernet 2011). We modelled synthetic spectra for the whole wavelength region between 7200 and 8800 Å. The spectrum that was synthesized to the observational data with the lowest χ^2 value constituted the final fit generated for specific atmospheric parameters: effective temperature ($T_{\rm eff}$), surface gravity (log g), and metallicity ([M/H]). For simplification purposes, we adopted solar values of micro– and macroturbulence velocities and also neglected stellar rotation. The resolution of the synthetic spectra was fixed as $R = 10\,000$. We applied this method to all three INT spectra independently and then averaged the results. The mean values for the source parameter in Gaia16aye were as follows: $T_{\rm eff} = 3933 \pm 135$ K, $\log g = 2.20 \pm 1.44$, and [M/H] = 0.08 ± 0.41 dex. Figure 5 presents the best fit of the synthetic to observational INT spectrum in the same spectral region as was covered by the RVS spectrum of Gaia16aye, that is, 8400–8800 Å (Ca II triplet), generated for averaged parameter results. These parameters imply that the microlensing source is a K5-type giant or a super-giant with solar metallicity. We discuss the estimate for the source distance in the next section because it is first necessary to de-blend the light of the lens and the source, which is possible in the microlensing model. We note that the asymmetry of the *Gaia* RVS lines is not visible in the same-resolution INT/IDS spectrum, and we suspect that the broadening visible in the *Gaia* spectrum is a result of a stack of spectra from separate RVS CCDs.

[5] https://www.blancocuaresma.com/s/iSpec

4. Microlensing model

4.1. Data preparation

The data sets we used in the modelling are listed in Table D.1. Because the microlensing model is complex, we had to restrict the number of data points that were used. We chose data sets that cover large parts of the light curve or important features (such as caustics). Some of the available data sets were also disregarded because they showed strong systematic variations in residuals from the best-fit model, which are not supported by other data sets. We used observations collected in the Cousins I or Sloan i band because the signal-to-noise ratio in these filters is highest. The only exceptions were *Gaia* (G-band filter) and ASAS-SN data (V band), which cover large portions of the light curve, especially before the transient alert.

Calculating microlensing magnifications (especially during caustic crossings) requires much computational time. We thus binned the data to speed up the modelling. We commonly used one-day bins, except for caustic crossings (when brightness variations during one night are substantial), for which we used 0.5 h or 1 h bins. *Gaia* and ASAS-SN data were not binned.

We rescaled the error bars, so that χ^2/d.o.f. ~ 1 for each data set. The error bars were corrected using the formula $\sigma_{i,\rm new} = \sqrt{(\gamma\sigma_i)^2 + \epsilon^2}$. Coefficients γ and ϵ for each data set are shown in Table 4. The final light curve is presented in Fig. 6.

4.2. Binary lens model

The simplest model describing a microlensing event caused by a binary system needs seven parameters: the time of the closest approach between the source and the centre of mass of the lens t_0, the projected separation between source and barycenter of the lens at that time u_0 (in Einstein radius units), the Einstein crossing time $t_{\rm E}$, the mass ratio of the lens components q, the projected separation between two binary components s, the angle between the source–lens relative trajectory and the binary axis α, and the angular radius of the source ρ normalised to the Einstein radius (Eq. (1)).

This simple model is insufficient to explain all features in the light curve. We therefore included additional parameters that describe second-order effects: the orbital motion of the Earth (microlensing parallax) and the orbital motion of the lens. The microlensing parallax $\boldsymbol{\pi}_{\rm E} = (\pi_{\rm E,N}, \pi_{\rm E,E})$ is a vector quantity: $\boldsymbol{\pi}_{\rm E} = \frac{\pi_{\rm rel}}{\theta_{\rm E}} \frac{\boldsymbol{\mu}_{\rm rel}}{\mu_{\rm rel}}$, where $\boldsymbol{\mu}_{\rm rel}$ is the relative lens-source proper motion (Gould 2000). It describes the shape of the relative lens-source trajectory (Fig. 7). The microlensing parallax can also be measured using simultaneous observations from two separated observatories, for exmaple, from the ground and a distant satellite (Refsdal 1966; Gould 1994). Because *Gaia* is located at the L_2 Lagrange point (about 0.01 au from the Earth) and the Einstein radius projected onto the observer's plane is au/$\pi_{\rm E} \approx 2.5$ au, the magnification gradient changes by less than the data precision throughout most of the light curve (see

Table 3. Summary of the spectroscopic observations of Gaia16aye.

Spectrum ID	Observation date HJD	Wavelength range (Å)	Telescope – Instrument
LT 1	2457612.900668	4200–7994	Liverpool Telescope – SPRAT
LT 2	2457617.940097	4200–7994	Liverpool Telescope – SPRAT
LT 3	2457643.845837	4200–7994	Liverpool Telescope – SPRAT
WHT 1	2457701.3045827	4303–9500	*William Herschel* Telescope – ACAM
Palomar 1	2457662.1047682	3100–10200	Palomar Hale Telescope – DBSP
Palomar 2	2457932.6881373	3800–10000	Palomar Hale Telescope – DBSP
INT 1	2457703.4230518	7550–9000	*Isaac Newton* Telescope – IDS; R831R grating
INT 2	2457706.3547417	7550–9000	*Isaac Newton* Telescope – IDS; R831R grating
INT 3	2457712.2970278	7500–8795	*Isaac Newton* Telescope – IDS; R1200Y grating
INT 4	2457713.2967616	7500–8795	*Isaac Newton* Telescope – IDS; R1200Y grating
INT 5	2457714.2949097	7500–8795	*Isaac Newton* Telescope – IDS; R1200Y grating
Asiago 1	2457612.430953	3320–7880	1.22 m Reflector – DU440A-BU2
Asiago 2	2457623.364186	4160–6530	1.82 m Reflector – AFOSC; GR07 grating
Asiago 3a	2457700.264730	8200–9210	1.82 m Reflector – AFOSC; VPH5 grating
Asiago 3b	2457700.275567	5000–9280	1.82 m Reflector – AFOSC; VPH6 grating
Asiago 4a	2457700.260113	8200–9210	1.82 m Reflector – AFOSC; VPH5 grating
Asiago 4b	2457700.270951	5000–9280	1.82 m Reflector – AFOSC; VPH6 grating
Asiago 5a	2457722.263836	8200–9210	1.82 m Reflector – AFOSC; VPH5 grating
Asiago 5b	2457722.235417	5000–9280	1.82 m Reflector – AFOSC; VPH6 grating
Asiago 6a	2457723.246689	8200–9210	1.82 m Reflector – AFOSC; VPH5 grating
Asiago 6b	2457723.204078	5000–9280	1.82 m Reflector – AFOSC; VPH6 grating

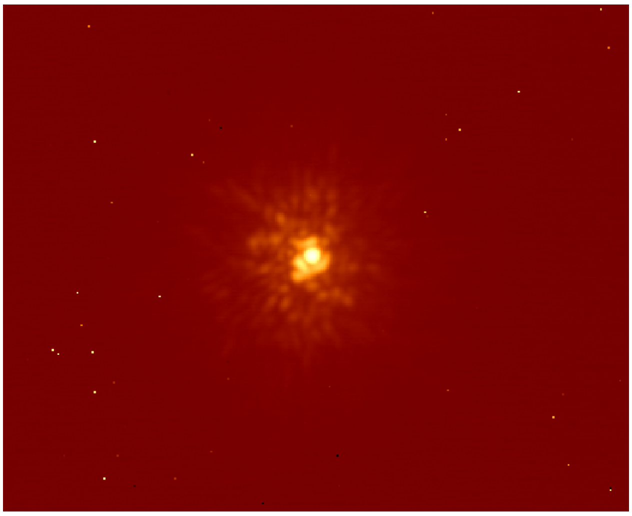

Fig. 4. Keck Adaptive Optics image of Gaia16aye taken between the third and fourth caustic crossing. The single star has an FWHM of about 52 mas. No other light sources contribute significantly to the blending in the event.

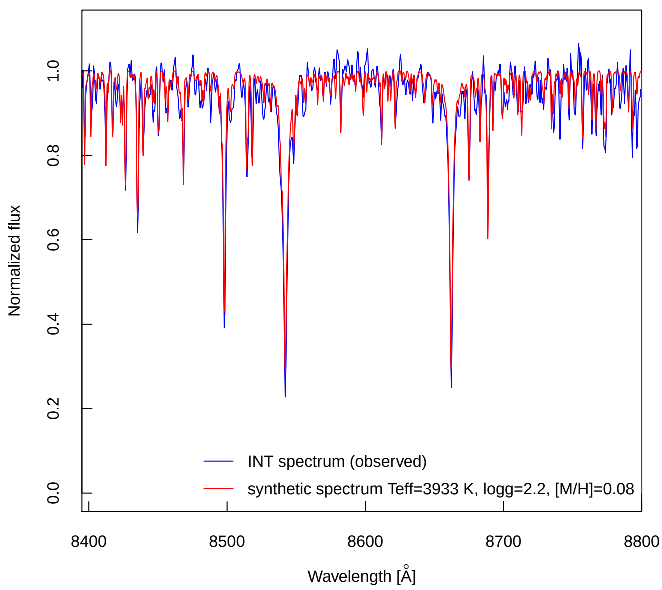

Fig. 5. Spectrum of the source of the Gaia16aye event (blue) taken using the 2.5 m INT/IDS on 19 November 2016 in comparison with a synthetic spectrum (red) calculated for the best-fit atmospheric parameters. The plot shows the Ca II triplet region, 8400–8800 Å.

Fig. 8). Fortunately, two *Gaia* measurements were collected near HJD′ ∼ 7714, when the space-parallax signal is strongest due to rapid change in magnification near the caustic. Therefore, we included the space-parallax and *Gaia* observations in the final modelling.

The orbital motion of the lens can in the simplest scenario be approximated as linear changes of separation $s(t) = s_0 + \dot{s}(t - t_{0,\rm kep})$ and angle $\alpha(t) = \alpha_0 + \dot{\alpha}(t - t_{0,\rm kep})$, $t_{0,\rm kep}$ can be any arbitrary moment of time and is not a fit parameter (Albrow et al. 2000). This approximation, which works well for the majority of binary microlensing events, is insufficient in this case.

We have to describe the orbital motion of the lens using a full Keplerian approach (Skowron et al. 2011). This model is parameterised by the physical relative 3D position and velocity of the secondary component relative to the primary, $\Delta\boldsymbol{r} = D_{\rm l}\theta_{\rm E}(s_0, 0, s_z)$, $\Delta\boldsymbol{v} = D_{\rm l}\theta_{\rm E}s_0(\gamma_x, \gamma_y, \gamma_z)$ at time $t_{0,\rm kep}$. For a given angular radius of the source star θ_* and source distance $D_{\rm s}$, we can calculate the angular Einstein radius $\theta_{\rm E} = \theta_*/\rho$ and distance to the lens $D_{\rm l} = {\rm au}/(\theta_{\rm E}\pi_{\rm E} + {\rm au}/D_{\rm s})$. Subsequently, positions and

Table 4. Data sets used in the modelling.

Observatory	Filter	Number	γ	ϵ
Gaia	G	53	1.4	0.0
Bialkow	I	72	1.15	0.005
APT2	I	156	1.70	0.01
LT	i	94	1.15	0.005
DEMONEXT	I	110	1.35	0.005
Swarthmore	I	19	1.00	0.00
UBT60	I	18	1.00	0.005
ASAS-SN	V	68	1.45	0.01

velocities can be transformed to orbital elements of the binary (semi-major axis a, orbital period P, eccentricity e, inclination i, longitude of the ascending node Ω, argument of periapsis ω, and time of periastron $t_{\rm peri}$). These can be used to calculate the projected position of both components on the sky at any moment in time.

In all previous cases of binary events with significant binary motion, Keplerian orbital motion provided only a small improvement relative to the linear approximation (Skowron et al. 2011; Shin et al. 2012). This is not the case here, because, as we show below, the orbital period of the lens is similar to the duration of the event (e.g. Penny et al. 2011). Modelling of this event is an iterative process: for given microlensing parameters, we estimated the angular radius and distance to the source, we calculated best-fit microlensing parameters, and we repeated the procedure until all parameters converged.

The best-fit microlensing parameters are presented in Table 5. Uncertainties were calculated using the Markov chain Monte Carlo approach (MCMC; Foreman-Mackey et al. 2013) and represent 68% confidence intervals of marginalized posterior distributions. We note that another degenerate solution exists for the microlensing model that differs only by the signs of s_z and γ_z ($(s_z, \gamma_z) \to -(s_z, \gamma_z)$). The second solution has the same physical parameters (except for $\Omega \to \pi - \Omega$ and $\omega \to \omega - \pi$) and differs by the sign of the radial velocity. Thus, the degeneracy can be broken with additional radial velocity measurements of the lens (Skowron et al. 2011).

4.3. Source star

Spectroscopic observations of the event indicate that the source is a K5-type giant or a super-giant. If the effective temperature of the source were higher than 4250 K, TiO absorption features would be invisible. If the temperature were lower than 3800 K, these features would be stronger than those in the observed spectra. Spectral modelling indicates that the effective temperature of the source is 3933 ± 135 K. According to Houdashelt et al. (2000), the intrinsic Johnson–Cousins colours of a star of this spectral type and solar metallicity should be $(V-R)_0 = 0.83^{+0.03}_{-0.12}$, $(V-I)_0 = 1.60^{+0.03}_{-0.12}$ and $(V-K)_0 = 3.64^{+0.11}_{-0.37}$ (error bars correspond to the source of K4- and M0-type, respectively).

We used a model-independent regression to calculate the observed colours of the source (we used observations collected in the Bialkow Observatory, which were calibrated to the standard system): $V-R = 0.99 \pm 0.01$ and $V-I = 1.91 \pm 0.01$. Thus, the colour excess is $E(V-I) = 0.31$ and $E(V-R) = 0.16$, consistent with the standard reddening law (Cardelli et al. 1989) and $A_V = 0.62$.

According to the best-fitting microlensing model, the amount of light coming from the magnified source is $V_{\rm s} = 16.61 \pm 0.02$ and $I_{\rm s} = 14.70 \pm 0.02$. The V-band brightness of the source after correcting for extinction is therefore $V_0 = 15.99$ mag. Subsequently, we used the colour–surface brightness relations for giants from Adams et al. (2018) to estimate the angular radius of the source: $\theta_* = 9.2 \pm 0.7\,\mu$as. Because the linear radius of giants of this spectral type is about $31 \pm 6\,R_\odot$ (Dyck et al. 1996), the source is located about 15.7 ± 3.0 kpc from the Sun, but the uncertainties are large. For the modelling we assumed $D_{\rm s} = 15$ kpc. We note that the exact value of the distance has in practice a very small effect on the final models because $\pi_{\rm s} \ll \theta_{\rm E}\pi_{\rm E}$.

4.4. Physical parameters of the binary lens

The Gaia16aye microlensing model allows us to convert microlensing quantities into physical properties of the lensing binary system. Finite source effects over the caustics enabled us to measure the angular Einstein radius,

$$\theta_{\rm E} = \frac{\theta_*}{\rho} = 3.04 \pm 0.24\ \text{mas}$$

and the relative lens-source proper motion,

$$\mu_{\rm rel} = \frac{\theta_{\rm E}}{t_{\rm E}} = 10.1 \pm 0.8\ \text{mas yr}^{-1}.$$

Because the microlensing parallax was precisely measured from the light curve (Table 5), we were able to measure the total mass of the lens,

$$M = \frac{\theta_{\rm E}}{\kappa\pi_{\rm E}} = 0.93 \pm 0.09\,M_\odot$$

and its distance,

$$D_{\rm l} = \frac{\text{au}}{\theta_{\rm E}\pi_{\rm E} + \text{au}/D_{\rm s}} = 780 \pm 60\ \text{pc}.$$

The orbital parameters of the lens were calculated using the prescriptions from Skowron et al. (2011) based on the full information about the relative 3D position and velocity of the secondary star relative to the primary. All physical parameters of the lens are given in Table 6. Figure 9 shows the orbital parameters and their confidence ranges as derived from the MCMC sampling of the microlensing model. Our microlensing model also allowed us to separate the flux from the source and the unmagnified blended flux (that comes from the lens, as we show below): $V_{\rm blend} = 17.98 \pm 0.02$, $R_{\rm blend} = 17.05 \pm 0.02$, and $I_{\rm blend} = 16.09 \pm 0.02$ (Table 5).

5. Discussion

A massive follow-up campaign allowed us to collect a very detailed light curve for *Gaia* 16aye and hence to cover the evolution of the event exhaustively. Photometric data were obtained over a period of more than two years by a network of observers scattered around the world. It should be emphasised that the vast majority of the observations were taken by enthusiastic individuals, including both professional astronomers and amateurs, who devoted their telescope time to this task.

The case of Gaia16aye illustrates the power of coordinated long-term time-domain observations, which lead to a scientific discovery. The field of microlensing has particularly well benefit in the past from such follow-up observations, which resulted, for example, in the first microlensing planetary discoveries (e.g. Udalski et al. 2005; Beaulieu et al. 2006). This event also

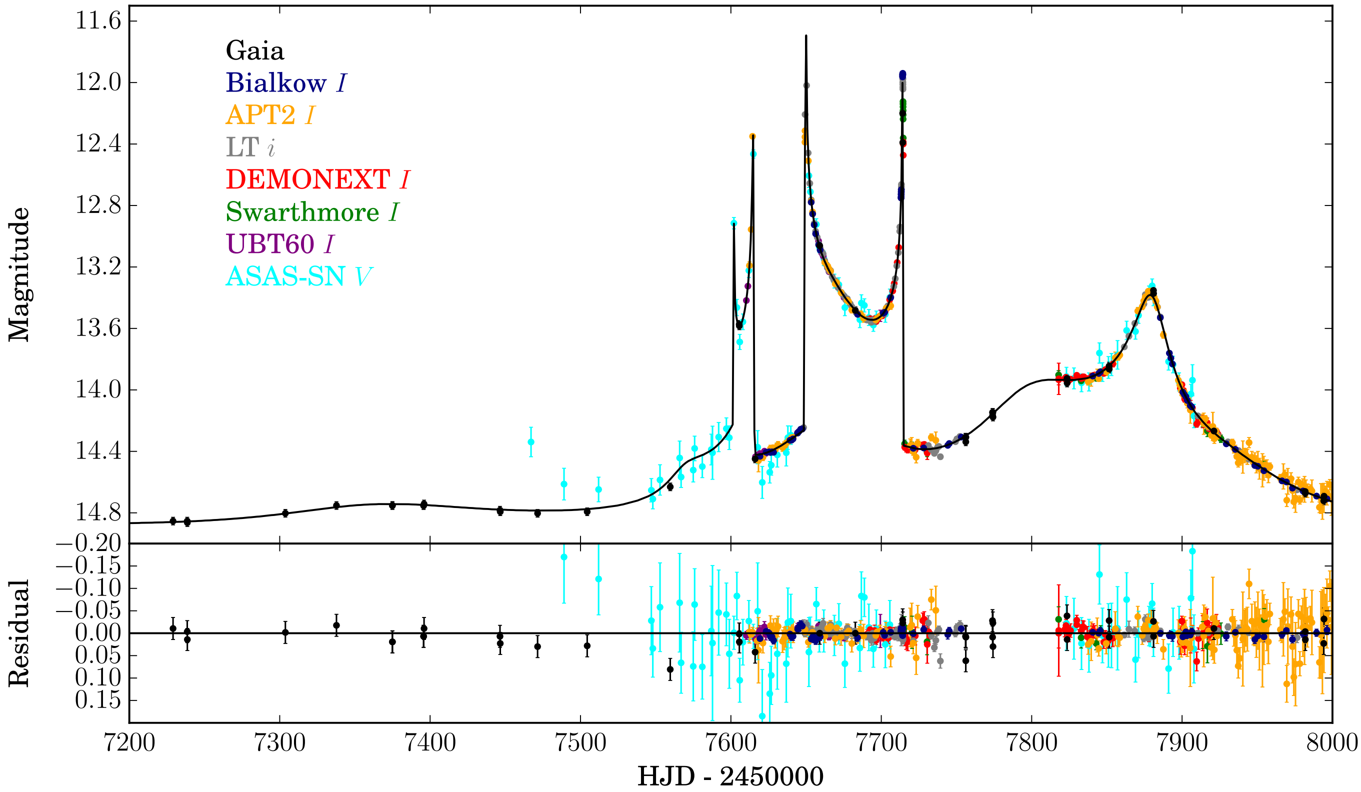

Fig. 6. Light curve of the microlensing event Gaia16aye, showing only the data used in the microlensing model. All measurements are transformed into the LT i-band magnitude scale.

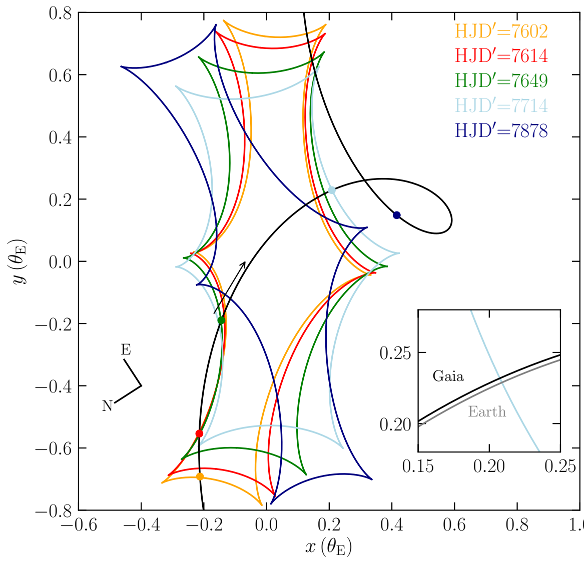

Fig. 7. Caustic curves corresponding to the best-fitting model of Gaia16aye. The lens-source relative trajectory is shown by a black curve. The barycenter of the lens is at (0, 0) and the lens components are located along the x-axis at time $t_{0,\mathrm{kep}}$ = 7675. Caustics are plotted at the times of caustic crossings; the large points are marked with respective colours. The inset shows a zoom on the trajectory of the Earth and *Gaia* at the moment of the caustic crossing around HJD′ ∼ 7714.

offered excitement with its multiple, rapid, and often dramatic changes in brightness. Therefore it was also essential to use tools that facilitated the observations and data processing. Of particular importance was the Cambridge Photometric Calibration Server (CPCS, Zieliński et al. 2019), which performed the standardisation of the photometric observations collected by a large variety of different instruments. Moreover, the operation of the CPCS can be scripted, hence the observations could be automatically uploaded and processed without any human intervention. This solution helped track the evolution of the light curve, especially at times when the event changed dramatically. The processed observations and photometric measurements were immediately available for everyone to view, and appropriate actions were undertaken, such as an increase of the observing cadence when the peak at the fourth caustic crossing was approached. We note that no archival catalogues are available in I and R filters for the part of the sky with the Gaia16aye event. All the observations carried out in these filters were automatically adjusted by the CPCS to the nearest Sloan i and r bands. This does not affect the microlensing modelling, but the standardised light curve in i and r filters is systematically offset. On the other hand, the B-, g- and V-band observations processed by the CPCS are calibrated correctly to the 1% level.

In the case of Gaia16aye, the light curve contains multiple features, which allowed us to constrain the microlensing model uniquely, despite its complexity. In addition to the four caustic crossings and a cusp approach, the microlensing model also predicted a smooth low-amplitude long-term bump about a year before the first caustic crossing, at about HJD′ = 7350. This feature was indeed found in the *Gaia* data, see Fig. 6. The amplitude of this rise was about 0.1 mag, which is close to the level of *Gaia*'s photometric error bars, and the signal was far too faint to trigger an alert.

Additional confirmation of the correctness of the microlensing model comes from the detection of the microlensing space-parallax effect, see Fig. 8. The offset in the timing of the fourth

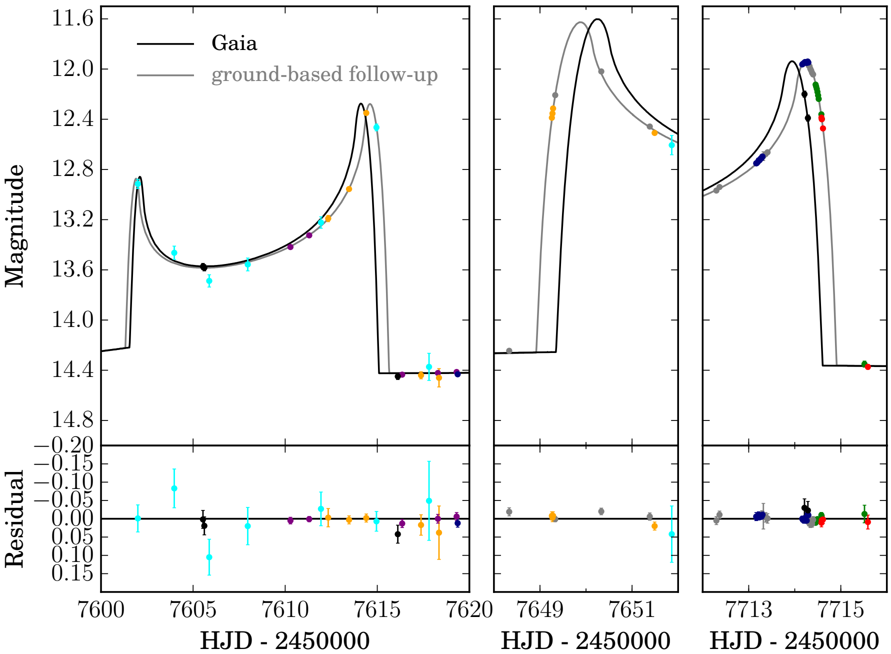

Fig. 8. Space-based parallax in Gaia16aye. As *Gaia* is separated by 0.01 au from the Earth, the *Gaia* light curve (black) differs slightly from Earth-based observations (grey curve). Space parallax can be measured through two fortuitous *Gaia* data points collected near HJD′ ~ 7714. All measurements are transformed into the LT *i*-band magnitude scale.

Table 5. Best-fit microlensing model parameters of the Gaia16aye binary event.

Parameter	Value
t_0 (HJD′)	7674.738 ± 0.057
u_0	0.0400 ± 0.0014
t_E (d)	111.09 ± 0.41
$\pi_{E,N}$	−0.373 ± 0.002
$\pi_{E,E}$	−0.145 ± 0.001
$\log \rho$	−2.519 ± 0.003
q	0.639 ± 0.004
s_0	1.007 ± 0.002
α (rad)	5.339 ± 0.002
s_z	0.404 ± 0.028
γ_x (yr^{-1})	0.384 ± 0.009
γ_y (yr^{-1})	0.591 ± 0.012
γ_z (yr^{-1})	−1.121 ± 0.032
I_s (mag)	14.70 ± 0.02
I_{blend} (mag)	16.09 ± 0.02
R_s (mag)	15.62 ± 0.02
R_{blend} (mag)	17.05 ± 0.02
V_s (mag)	16.61 ± 0.02
V_{blend} (mag)	17.98 ± 0.02

Notes. HJD′ = HJD-2450000. We adopt $t_{0,par} = t_{0,kep} = 7675$.

Table 6. Physical parameters of the binary lens system.

Parameter	Value
θ_E (mas)	3.04 ± 0.24
μ_{rel} (mas yr^{-1})	10.1 ± 0.8
M_1 ($M_\odot$)	0.57 ± 0.05
M_2 ($M_\odot$)	0.36 ± 0.03
D_l (pc)	780 ± 60
a (au)	1.98 ± 0.03
P (yr)	2.88 ± 0.05
e	0.30 ± 0.03
i (deg)	65.5 ± 0.7
Ω (deg)	−169.4 ± 0.9
ω (deg)	−30.5 ± 3.8
t_{peri} (HJD′)	8170 ± 14

Notes. Uncertainties of orbital parameters do not include the uncertainty in θ_* and D_s. We adopt $\theta_* = 9.2\,\mu$as and $D_s = 15$ kpc.

caustic crossing as seen by *Gaia* and ground-based telescopes is due to the distance of *Gaia* of 1.5 million km away from Earth. The offset in time was 6.63 h (i.e. the caustic crossing by the source occurred first at *Gaia*'s location) and the amplification difference was −0.007 mag, that is, it was brighter at *Gaia*. The model from ground-based data only predicted these offsets to within 3 min and 0.003 mag, respectively. This indicates our model is unique and robust.

From the microlensing light curve analysis, we can derive an upper limit on the amount of light emitted by the lensing object, or constraints on the dark nature of the lens can be obtained (e.g. Yee 2015; Wyrzykowski et al. 2016). We find that the masses of the lens components are 0.57 ± 0.05 $M_\odot$ and 0.36 ± 0.03 $M_\odot$ and that the lens is located about $D_l = 780 \pm 60$ pc from the Sun. Because the V-band absolute magnitudes of main-sequence stars of these masses are 8.62 and 11.14 (Pecaut & Mamajek 2013), respectively, the total brightness of the binary is $V = 17.97$ and $I = 16.26$, assuming conservatively $A_V = 0.1$ towards the lens. This is consistent with the brightness and colour of the blend ($V_{blend} = 17.98$ and $I_{blend} = 16.09$). The blended light therefore comes from the lens, which is also consistent with the lack of any additional sources of light on the Keck AO image. This is an additional check that our model is correct.

The largest uncertainty in our lens mass determination comes from the θ_E parameter, which we derived from the finite source effects. Through the multiple caustic crossings, but particularly through very detailed coverage of the fourth crossing with multiple observatories, we were able to constrain the size of the source stellar disc in units of the Einstein radius ($\log \rho$) with an uncertainty smaller than 1%. However, in order to derive θ_E, we relied on the colour-angular size relation and theoretical predictions for the de-reddened colour of the source based on its spectral type. These may have introduced systematic errors

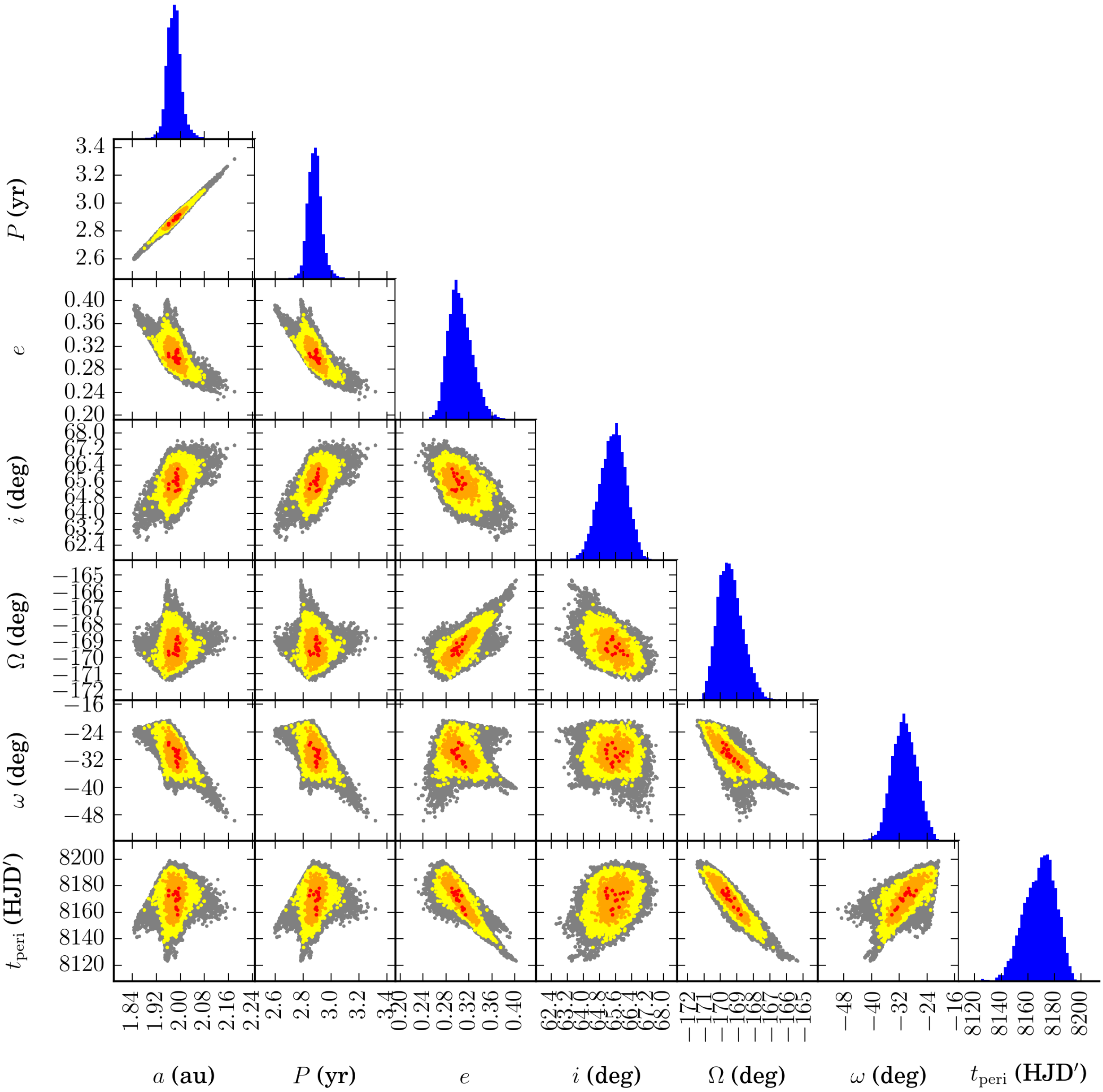

Fig. 9. Orbital elements of Gaia16aye. The panels show 2D and 1D projections of posterior distributions in the space of Kepler parameters. Red, orange, and yellow points mark 1σ, 2σ, and 3σ confidence regions, respectively.

to the angular size and hence to the lens mass measurement. We also note that the amount of the extinction derived based on our photometry ($A_V = 0.62$ mag) is significantly smaller than that measured by Schlafly & Finkbeiner (2011) in this direction ($A_V = 1.6$ mag). This and the uncertainty in the physical size of giant stars affects the estimate of the source distance, but because the lens is very nearby at less than 1 kpc, the source distance does not affect the overall result of this s study.

Nevertheless, an independent measurement of the Einstein radius, and thus the final confirmation of the nature of the lens in Gaia16aye, can be obtained in the near future from *Gaia* astrometric time-domain data. Using our photometry-based model, we computed the positions and amplifications of the images throughout the evolution of the event. Figure 10 shows the expected position of the combined light of all the images shown in the frame of the centre of mass of the binary and in units of the Einstein radius. The figure shows only the centroid motion due to microlensing relative to the unlensed position of the source. The moments of *Gaia* observations are marked with black dots. Because $\theta_{\rm E} = 3.04 \pm 0.24$ mas, the expected amplitude of the astrometric variation is about 3 mas. This should be detectable in *Gaia* astrometric time-series because *Gaia* is expected to have error bars in the along-scan direction of about 0.1 mas (Rybicki et al. 2018). The estimate of $\theta_{\rm E}$ from *Gaia* will be free of our assumptions about the intrinsic colours of the source and the interstellar extinction. The actual *Gaia* astrometry will also include the effects of parallax and proper motion of the source as well as the blended light from both components of the binary lens. The contribution of the lens brightness to the total light is about 25%, therefore the astrometric data might also be affected by the orbital motion of the binary. It is worth emphasising that without the microlensing model presented above, obtained from photometric *Gaia* and follow-up data alone, the interpretation of the *Gaia* astrometry will not be possible due to the high complexity of the centroid motion.

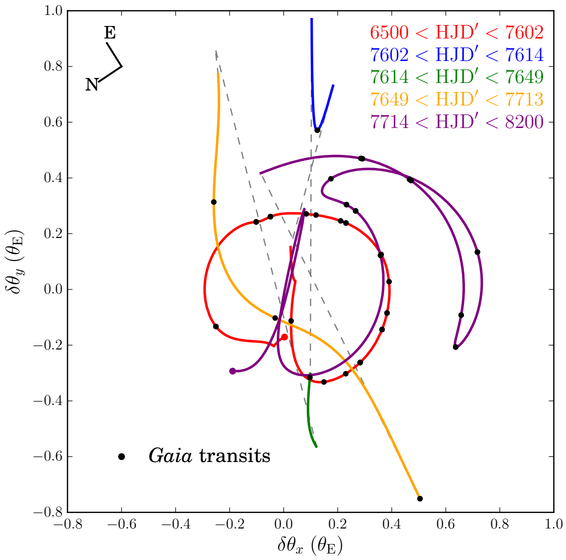

Fig. 10. As the source star moves across the caustics, new images of the source can be created while others may disappear, resulting in changes of the image centroid. Colour curves show the path of the centroid of the source images relative to the unlensed position of the source (additional light from components of the lens is not included). Moments of *Gaia* transits are marked with black points. The coordinate system is the same as in Fig. 7. The shifts are scaled to the angular Einstein radius of the system ($\theta_E = 3.04 \pm 0.24$ mas). Analysis of the *Gaia* astrometric measurements will provide an independent estimate of θ_E.

Radial velocity measurements of nearby binary lenses offer an additional way for post-event verification of the orbital parameters inferred from the microlensing model. So far, such an attempt was successfully achieved only in the case of OGLE-2009-BLG-020, a binary lens event with a clear orbital motion effect (Skowron et al. 2011). Follow-up observations from the Keck and Magellan telescopes measured the radial velocity of the binary to agree with the one predicted based on the microlensing event full binary lens orbit solution (Yee et al. 2016). The binary system presented in this work (to be denoted Gaia16aye-L, with its components Gaia16aye-La and Gaia16aye-Lb) is nearby (780 ± 60 pc) and fairly bright ($I \sim 16.5$ mag without the source star), hence such observations are obtainable. The expected amplitude of the radial velocity curve of the primary is about $K \approx 7.6\,\mathrm{km\,s^{-1}}$. We strongly encourage such observations to be carried out in order to verify the binary solution found in microlensing.

Yet another possibility to verify the model might come from AO or other high-resolution imaging techniques (e.g. Scott 2019) in some years when the source and the lens separate (e.g. Jung et al. 2018). With the relative proper motion of $10.1 \pm 0.8\,\mathrm{mas\,yr^{-1}}$, the binary lens should become visible at a separation of about 50 mas even in 2021.

6. Conclusions

We analysed the long-lasting event Gaia16aye, which exhibited four caustic crossings and a cusp approach, as well as space-parallax between the Earth and the *Gaia* spacecraft. The very well-sampled light curve allowed us to determine the masses of the binary system ($0.57 \pm 0.05\,M_\odot$ and $0.36 \pm 0.03\,M_\odot$) and all its orbital components. We derived the period (2.88 ± 0.05 years) and semi-major axis (1.98 ± 0.03 au), as well as the eccentricity of the orbit (0.30 ± 0.03). Gaia16aye is one of only a few microlensing binary systems with a full orbital solution, which offers an opportunity for confirming the binary parameters with radial velocity measurements and high-resolution imaging after some years. This event will also be detectable as an astrometric microlensing event in the forthcoming *Gaia* astrometric time-series data.

Increasingly more such events will be detectable in the current era of large-scale photometric surveys (e.g. *Gaia*, OGLE, ZTF). With the forthcoming thousands of alerts from all over the sky with the Large Synoptic Survey Telescope (LSST), it will become a necessity to use automated tools for transients discovery, their follow-up and follow-up data processing in order to fully identify and characterise the most interesting events. Robotic observations of selected alerts, automated analysis of the follow-up data, and light curve generation will soon become new standards in transient time-domain astronomy. The case of Gaia16aye shows that microlensing can be a useful tool for studying also binary systems where the lensing is caused by dark objects. A detection of a microlensing binary system composed of black holes and neutron stars would provide information about this elusive population of remnants that is complementary to other studies.

Acknowledgements. This work relies on the results from the European Space Agency (ESA) space mission *Gaia*. *Gaia* data are being processed by the *Gaia* Data Processing and Analysis Consortium (DPAC). Funding for the DPAC is provided by national institutions, in particular the institutions participating in the *Gaia* Multi-Lateral Agreement (MLA). The *Gaia* mission website is `https://www.cosmos.esa.int/gaia`. In particular we acknowledge *Gaia* Photometric Science Alerts Team, website `http://gsaweb.ast.cam.ac.uk/alerts`. We thank the members of the OGLE team for discussions and support. We also would like to thank the Polish Children Fund (KFnRD) for support of an internship of their pupils in Ostrowik Observatory of the Warsaw University, during which some of the data were collected, in particular we thank: Robert Nowicki, Michał Porębski and Karol Niczyj. The work presented here has been supported by the following grants from the Polish National Science Centre (NCN): HARMONIA NCN grant 2015/18/M/ST9/00544, OPUS NCN grant 2015/17/B/ST9/03167, DAINA NCN grant 2017/27/L/ST9/03221, as well as European Commission's FP7 and H2020 OPTICON grants (312430 and 730890), Polish Ministry of Higher Education support for OPTICON FP7, 3040/7.PR/2014/2, MNiSW grant DIR/WK/2018/12. PMr and JS acknowledge support from MAESTRO NCN grant 2014/14/A/ST9/00121 to Andrzej Udalski. We would like to thank the following members of the AAVSO for their amazing work with collecting vast amounts of data: Teofilo Arranz, James Boardman, Stephen Brincat, Geoff Chaplin, Emery Erdelyi, Rafael Farfan, William Goff, Franklin Guenther, Kevin Hills, Jens Jacobsen, Raymond Kneip, David Lane, Fernando Limon Martinez, Gianpiero Locatelli, Andrea Mantero, Attila Madai, Peter Meadows, Otmar Nickel, Arto Oksanen, Luis Perez, Roger Pieri, Ulisse Quadri, Diego Rodriguez Perez, Frank Schorr, George Sjoberg, Andras Timar, Ray Tomlin, Tonny Vanmunster, Klaus Wenzel, Thomas Wikander. We also thank the amateur observers from around the world, in particular, Pietro Capuozzo, Leone Trascianelli, Igor Zharkov from Ardingly College and Angelo Tomassini, Karl-Ludwig Bath. We also thank Roger Pickard from the British Astronomical Association and Matthias Penselin from the German Haus der Astronomie association for their contributions. KS thanks Dr. Dmitry Chulkov and Dr. Panagiotis Gavras for the interesting discussion of stellar multiplicity. We acknowledge support of DDT programmes SW2016b12 (WHT) and A34DDT3 (TNG). The INT, TNG and WHT are operated on the island of La Palma by the Isaac Newton Group of Telescopes in the Spanish Observatorio del Roque de los Muchachos of the Instituto de Astrofisica de Canarias. The Liverpool Telescope is operated on the island of La Palma by Liverpool John Moores University in the Spanish Observatorio del Roque de los Muchachos of the Instituto de Astrofisica de Canarias with financial support from the UK Science and Technology Facilities Council. SJF would like to thank the UCL students who assisted with the collection and checking of UCLO data for the observing campaign: Martina Aghopian, Ashleigh Arendt, Artem Barinov, Luke Barrett, Jasper Berry-Gair, Arjun Bhogal, Charles Bowesman, William Boyd, Andrei Cuceu, Michael Davies, Max Freedman, Gabriel Fu, Abirami Govindaraju, Iandeep Hothi, Clara Matthews Torres, Darius Modirrousta-Galian, Petru Neague, George Pattinson, Xiaoxi Song, and Brian Yu. P.Mr. acknowledges support from the Foundation for Polish Science (Program START) and the National Science Center, Poland (grant ETIUDA 2018/28/T/ST9/00096). AC, AG and NI acknowledge the financial support from the Slovenian Research Agency (research core funding No. P1-0031 and project grant No. J1-8136) and networking support by the COST Action GWverse CA16104. Skinakas Observatory is a collaborative project of the University of Crete and the Foundation for Research and Technology-Hellas. Work by C.H. was supported by the grant (2017R1A4A1015178) of National Research Foundation of Korea. KW acknowledges funding from STFC, and thanks the University of Leicester for the investment in instrumentation. We gratefully acknowledge financial support by the European Space Agency under the NELIOTA program, contract No. 4000112943. This work has made use of data obtained with the Kryoneri Prime Focus Instrument, developed by the European Space Agency NELIOTA project on the 1.2 m Kryoneri telescope, which is operated by IAASARS, National Observatory of Athens, Greece. The Aristarchos telescope is operated on Helmos Observatory by the IAASARS of the National Observatory of Athens. This work was supported by the GROWTH project funded by the National Science Foundation under Grant No 1545949. This work was supported by the MINECO (Spanish Ministry of Economy) through grant ESP2016-80079-C2-1-R (MINECO/FEDER, UE) and ESP2014-55996-C2-1-R (MINECO/FEDER, UE) and MDM-2014-0369 of ICCUB (Unidad de Excelencia a María de Maeztu). This work was supported by the MINECO (Spanish Ministry of Economy) through grant ESP2016-80079-C2-1-R and RTI2018-095076-B-C21 (MINECO/FEDER, UE), and MDM-2014-0369 of ICCUB (Unidad de Excelencia 'María de Maeztu'). The *Joan Oró* Telescope (TJO) of the Montsec Astronomical Observatory (OAdM) is owned by the Catalan Government and is operated by the Institute for Space Studies of Catalonia (IEEC). Support to this study has been provided by Agenzia Spaziale Italiana (ASI) through grants ASI I/058/10/0 and ASI 2014-025-R.1.2015. KW thanks Dipali Thanki and Ray McErlean for their technical support of the scientific programme of the University of Leicester observatory. This work was supported by Royal Society Research Grant RG170230. CCN thanks the funding from Ministry of Science and Technology (Taiwan) under the contracts 104-2112-M-008-012-MY3 and 104-2923-M-008-004-MY5. The research leading to these results has received funding from the European Research Council under the European Union's Seventh Framework Programme (FP/2007-2013) / ERC Grant Agreement n. 320964 (WDTracer). We thank the Las Cumbres Observatory and its staff for its continuing support of the project. ASAS-SN is supported by the Gordon and Betty Moore Foundation through grant GBMF5490 to the Ohio State University and NSF grant AST-1515927. Development of ASAS-SN has been supported by NSF grant AST-0908816, the Mt. Cuba Astronomical Foundation, the Center for Cosmology and AstroParticle Physics at the Ohio State University, the Chinese Academy of Sciences South America Center for Astronomy (CAS- SACA), the Villum Foundation, and George Skestos. ARM acknowledges support from the MINECO under the Ramón y Cajal programme (RYC-2016-20254) and the AYA2017-86274-P grant, and the AGAUR grant SGR-661/2017. We acknowledge support from the Science and Technology Facilities Council (TB and RWW; ST/P000541/1). K.Horne acknowledges support from STFC consolidated grant ST/M001296/1. This work was partly supported by the Research Council of Lithuania, grant No. S-LL-19-2 Authors thank to TÜBİTAK, IKI, KFU, and AST for partial supports in using RTT150 (Russian-Turkish 1.5-m telescope in Antalya). This work was partially funded by the subsidy 3.6714.2017/8.9 allocated to Kazan Federal University for the state assignment in the sphere of scientific activities. This research was partially supported by contract DN 18/13-12.12.2017 with the National Science Fund (Bulgaria). Work by YS was supported by an appointment to the NASA Postdoctoral Program at the Jet Propulsion Laboratory, California Institute of Technology, administered by Universities Space Research Association through a contract with NASA. GD gratefully acknowledges the observing grant support from the Institute of Astronomy and NAO Rozhen, BAS, via bilateral joint research project "Study of ICRF radio-sources and fast variable astronomical objects" (PI:G.Damljanovic). This work is a part of the Projects no. 176011 "Dynamics and kinematics of celestial bodies and systems", no. 176004 "Stellar physics" and no. 176021 "Visible and invisible matter in nearby galaxies: theory and observations" supported by the Ministry of Education, Science and Technological Development of the Republic of Serbia. YT acknowledges the support of DFG priority program SPP 1992 "Exploring the diversity of Extrasolar Planets" (WA 1074/11-1). This work of PMi, DM and ZK was supported by the NCN grant no. 2016/21/B/ST9/01126. ARM acknowledges support from the MINECO Ramón y Cajal programme RYJ-2016-20254 and grant AYA2017-86274-P and from the AGAUR grant SGR-661/2017. The work by C. R. was supported by an appointment to the NASA Postdoctoral Program at the Goddard Space Flight Center, administered by USRA through a contract with NASA. The Faulkes Telescope Project is an education partner of Las Cumbres Observatory (LCO). The Faulkes Telescopes are maintained and operated by LCO. This research was made possible through the use of the AAVSO Photometric All-Sky Survey (APASS), funded by the Robert Martin Ayers Sciences Fund and NSF AST-1412587. The Pan-STARRS1 Surveys (PS1) and the PS1 public science archive have been made possible through contributions by the Institute for Astronomy, the University of Hawaii, the Pan-STARRS Project Office, the Max-Planck Society and its participating institutes, the Max Planck Institute for Astronomy, Heidelberg and the Max Planck Institute for Extraterrestrial Physics, Garching, The Johns Hopkins University, Durham University, the University of Edinburgh, the Queen's University Belfast, the Harvard-Smithsonian Center for Astrophysics, the Las Cumbres Observatory Global Telescope Network Incorporated, the National Central University of Taiwan, the Space Telescope Science Institute, the National Aeronautics and Space Administration under Grant No. NNX08AR22G issued through the Planetary Science Division of the NASA Science Mission Directorate, the National Science Foundation Grant No. AST-1238877, the University of Maryland, Eotvos Lorand University (ELTE), the Los Alamos National Laboratory, and the Gordon and Betty Moore Foundation. Some of the data presented herein were obtained at the W. M. Keck Observatory, which is operated as a scientific partnership among the California Institute of Technology, the University of California and the National Aeronautics and Space Administration. The Observatory was made possible by the generous financial support of the W. M. Keck Foundation.

References

Abbott, B. P., Abbott, R., Abbott, T. D., et al. 2016, Phys. Rev. X, 6, 041015
Abbott, B. P., Abbott, R., Abbott, T. D., et al. 2017, Phys. Rev. Lett., 118, 221101
Adams, A. D., Boyajian, T. S., & von Braun, K. 2018, MNRAS, 473, 3608
Albrow, M., Beaulieu, J.-P., Birch, P., et al. 1998, ApJ, 509, 687
Albrow, M. D., Beaulieu, J.-P., Caldwell, J. A. R., et al. 2000, ApJ, 534, 894
Alcock, C., Allsman, R. A., Alves, D., et al. 1997, ApJ, 479, 119
An, J. H., & Gould, A. 2001, ApJ, 563, L111
Asplund, M., Grevesse, N., Sauval, A. J., & Scott, P. 2009, ARA&A, 47, 481
Bachelet, E., Beaulieu, J.-P., Boisse, I., Santerne, A., & Street, R. A. 2018, ApJ, 865, 162
Bakis, V., Burgaz, U., Butterley, T., et al. 2016, ATel, 9376
Beaulieu, J.-P., Bennett, D. P., Fouqué, P., et al. 2006, Nature, 439, 437
Belczynski, K., Holz, D. E., Bulik, T., & O'Shaughnessy, R. 2016, Nature, 534, 512
Belokurov, V. A., & Evans, N. W. 2002, MNRAS, 331, 649
Bennett, D. P., Rhie, S. H., Udalski, A., et al. 2016, AJ, 152, 125
Bertin, E., & Arnouts, S. 1996, A&AS, 117, 393
Bird, S., Cholis, I., Muñoz, J. B., et al. 2016, Phys. Rev. Lett., 116, 201301
Blanco-Cuaresma, S., Soubiran, C., Jofré, P., & Heiter, U. 2014, A&A, 566, A98
Boisse, I., Santerne, A., Beaulieu, J.-P., et al. 2015, A&A, 582, L11
Bond, I. A., Udalski, A., Jaroszyński, M., et al. 2004, ApJ, 606, L155
Bozza, V. 2001, A&A, 374, 13
Brown, T. M., Baliber, N., Bianco, F. B., et al. 2013, PASP, 125, 1031
Calchi Novati, S., & Scarpetta, G. 2016, ApJ, 824, 109
Cardelli, J. A., Clayton, G. C., & Mathis, J. S. 1989, ApJ, 345, 245
Cropper, M., Katz, D., Sartoretti, P., et al. 2018, A&A, 616, A5
Derue, F., Afonso, C., Alard, C., et al. 2001, A&A, 373, 126
Dominik, M., & Sahu, K. C. 2000, ApJ, 534, 213
Dong, S., Mérand, A., Delplancke-Ströbele, F., et al. 2019, ApJ, 871, 70
Dyck, H. M., Benson, J. A., van Belle, G. T., & Ridgway, S. T. 1996, AJ, 111, 1705
Evans, D. W., Riello, M., De Angeli, F., et al. 2018, A&A, 616, A4
Foreman-Mackey, D., Hogg, D. W., Lang, D., & Goodman, J. 2013, PASP, 125, 306
French, J., Hanlon, L., McBreen, B., et al. 2004, AIP Conf. Ser., 727, 741
Fukui, A., Abe, F., Ayani, K., et al. 2007, ApJ, 670, 423
Fukui, A., Suzuki, D., Koshimoto, N., et al. 2019, AJ, 158, 206
Gaia Collaboration (Prusti, T., et al.) 2016, A&A, 595, A1
Gaia Collaboration (Brown, A. G. A., et al.) 2018, A&A, 616, A1
Gaudi, B. S., Patterson, J., Spiegel, D. S., et al. 2008, ApJ, 677, 1268
Goudis, C., Hantzios, P., Boumis, P., et al. 2010, ASP Conf. Ser., 424, 422
Gould, A. 1992, ApJ, 392, 442
Gould, A. 1994, ApJ, 421, L75
Gould, A. 2000, ApJ, 542, 785
Gould, A., & Loeb, A. 1992, ApJ, 396, 104
Gould, A., Udalski, A., Monard, B., et al. 2009, ApJ, 698, L147
Gray, R. O., & Corbally, C. J. 1994, AJ, 107, 742
Hamadache, C., Le Guillou, L., Tisserand, P., et al. 2006, A&A, 454, 185
Han, C. 2008, ApJ, 681, 806
Hardy, L. K., Butterley, T., Dhillon, V. S., Littlefair, S. P., & Wilson, R. W. 2015, MNRAS, 454, 4316
Hodgkin, S. T., Wyrzykowski, Ł., Blagorodnova, N., & Koposov, S. 2013, Phil. Trans. R. Soc. London Ser. A, 371, 20120239
Hogg, D. W., Blanton, M., Lang, D., Mierle, K., & Roweis, S. 2008, ASP Conf. Ser., 394, 27
Houdashelt, M. L., Bell, R. A., Sweigart, A. V., & Wing, R. F. 2000, AJ, 119, 1424
Jaroszynski, M., Udalski, A., Kubiak, M., et al. 2004, Acta Astron., 54, 103
Jung, Y. K., Han, C., Udalski, A., et al. 2018, ApJ, 863, 22
Kains, N., Calamida, A., Sahu, K. C., et al. 2017, ApJ, 843, 145

Kalberla, P. M. W., Burton, W. B., Hartmann, D., et al. 2005, A&A, 440, 775
Khamitov, I., Bikmaev, I., Burenin, R., et al. 2016a, ATel, 9753
Khamitov, I., Bikmaev, I., Burenin, R., et al. 2016b, ATel, 9780
Kim, S.-L., Lee, C.-U., Park, B.-G., et al. 2016, J. Korean Astron. Soc., 49, 37
Kiraga, M., & Paczynski, B. 1994, ApJ, 430, L101
Kochanek, C. S., Shappee, B. J., Stanek, K. Z., et al. 2017, PASP, 129, 104502
Kolb, U., Brodeur, M., Braithwaite, N., & Minocha, S. 2018, Robot. Telesc. Stud. Res. Edu. Proc., 1, 127
Kozłowski, S., Woźniak, P. R., Mao, S., & Wood, A. 2007, ApJ, 671, 420
Kupka, F., Dubernet, M. L., & VAMDC Collaboration 2011, Baltic Astron., 20, 503
Kurucz, R. 1993, ATLAS9 Stellar Atmosphere Programs and 2 km/s grid. Kurucz CD-ROM No. 13 (Cambridge, MA: Smithsonian Astrophysical Observatory)
Lang, D., Hogg, D. W., Mierle, K., Blanton, M., & Roweis, S. 2010, AJ, 139, 1782
Lu, J. R., Sinukoff, E., Ofek, E. O., Udalski, A., & Kozlowski, S. 2016, ApJ, 830, 41
Mróz, P., Wyrzykowski, Ł., Rybicki, K., et al. 2016, ATel, 9770
Mróz, P., Udalski, A., Skowron, J., et al. 2017, Nature, 548, 183
Nesci, R. 2016, ATel, 9533
Nucita, A. A., Licchelli, D., De Paolis, F., et al. 2018, MNRAS, 476, 2962
Paczyński, B. 1971, ARA&A, 9, 183
Paczynski, B. 1996, ARA&A, 34, 419
Pecaut, M. J., & Mamajek, E. E. 2013, ApJS, 208, 9
Penny, M. T., Kerins, E., & Mao, S. 2011, MNRAS, 417, 2216
Pietrzyński, G., Thompson, I. B., Gieren, W., et al. 2010, Nature, 468, 542
Poleski, R., Skowron, J., Udalski, A., et al. 2014, ApJ, 795, 42
Poleski, R., Zhu, W., Christie, G. W., et al. 2016, ApJ, 823, 63
Popowski, P., Alcock, C., Allsman, R. A., et al. 2001, ASP Conf. Ser., 239, 244
Popper, D. M. 1967, ARA&A, 5, 85
Rahal, Y. R., Afonso, C., Albert, J. N., et al. 2009, A&A, 500, 1027
Rattenbury, N. J. 2009, MNRAS, 392, 439
Refsdal, S. 1966, MNRAS, 134, 315
Rybicki, K. A., Wyrzykowski, Ł., Klencki, J., et al. 2018, MNRAS, 476, 2013
Sahu, K. C., Anderson, J., Casertano, S., et al. 2017, Am. Astron. Soc. Meet. Abstr., 230, 315.13
Sartoretti, P., Katz, D., Cropper, M., et al. 2018, A&A, 616, A6
Schlafly, E. F., & Finkbeiner, D. P. 2011, ApJ, 737, 103
Scott, N. J. 2019, AAS/Division Extreme Sol. Syst. Abstr., 51, 330.15
Shappee, B. J., Prieto, J. L., Grupe, D., et al. 2014, ApJ, 788, 48
Shin, I.-G., Han, C., Choi, J.-Y., et al. 2012, ApJ, 755, 91
Shvartzvald, Y., Udalski, A., Gould, A., et al. 2015, ApJ, 814, 111
Shvartzvald, Y., Li, Z., Udalski, A., et al. 2016, ApJ, 831, 183
Skowron, J., Jaroszynski, M., Udalski, A., et al. 2007, Acta Astron., 57, 281
Skowron, J., Wyrzykowski, Ł., Mao, S., & Jaroszyński, M. 2009, MNRAS, 393, 999
Skowron, J., Udalski, A., Gould, A., et al. 2011, ApJ, 738, 87
Sokolovsky, K., Korotkiy, S., & Lebedev, A. 2014, ASP Conf. Ser., 490, 395
Steele, I. A., Smith, R. J., Rees, P. C., et al. 2004, Proc. SPIE, 5489, 679
Stetson, P. B. 1987, PASP, 99, 191
Sumi, T., Bennett, D. P., Bond, I. A., et al. 2013, ApJ, 778, 150
Udalski, A., Szymanski, M., Stanek, K. Z., et al. 1994a, Acta Astron., 44, 165
Udalski, A., Szymanski, M., Mao, S., et al. 1994b, ApJ, 436, L103
Udalski, A., Zebrun, K., Szymanski, M., et al. 2000, Acta Astron., 50, 1
Udalski, A., Jaroszyński, M., Paczyński, B., et al. 2005, ApJ, 628, L109
Udalski, A., Szymański, M. K., & Szymański, G. 2015a, Acta Astron., 65, 1
Udalski, A., Yee, J. C., Gould, A., et al. 2015b, ApJ, 799, 237
Udalski, A., Han, C., Bozza, V., et al. 2018, ApJ, 853, 70
Villanueva, Jr., S., Gaudi, B. S., Pogge, R. W., et al. 2018, PASP, 130, 015001
Witt, H. J., & Mao, S. 1995, ApJ, 447, L105
Wozniak, P. R., Udalski, A., Szymanski, M., et al. 2001, Acta Astron., 51, 175
Wyrzykowski, Ł., & Hodgkin, S. 2012, IAU Symp., 285, 425
Wyrzykowski, Ł., Hodgkin, S., Blogorodnova, N., Koposov, S., & Burgon, R. 2012, 2nd Gaia Follow-up Network for Solar System Objects, 21
Wyrzykowski, Ł., Hodgkin, S., & Blagorodnova, N. 2014, Gaia-FUN-SSO-3, 31
Wyrzykowski, Ł., Rynkiewicz, A. E., Skowron, J., et al. 2015, ApJS, 216, 12
Wyrzykowski, Ł., Kostrzewa-Rutkowska, Z., Skowron, J., et al. 2016, MNRAS, 458, 3012
Wyrzykowski, Ł., Mroz, P., Rybicki, K., et al. 2017, ATel, 10341
Xilouris, E. M., Bonanos, A. Z., Bellas-Velidis, I., et al. 2018, A&A, 619, A141
Yee, J. C. 2015, ApJ, 814, L11
Yee, J. C., Udalski, A., Calchi Novati, S., et al. 2015, ApJ, 802, 76
Yee, J. C., Johnson, J. A., Skowron, J., et al. 2016, ApJ, 821, 121
Yock, P. C. M. 1998, in Frontiers Science Series 23: Black Holes and High Energy Astrophysics, eds. H. Sato, & N. Sugiyama, 375
Yoo, J., DePoy, D. L., Gal-Yam, A., et al. 2004, ApJ, 603, 139
Zhu, W., Calchi Novati, S., Gould, A., et al. 2016, ApJ, 825, 60
Zieliński, P., Wyrzykowski, Ł., Rybicki, K., et al. 2019, Contrib. Astron. Obs. Skalnate Pleso, 49, 125
Zub, M., Cassan, A., Heyrovský, D., et al. 2011, A&A, 525, A15

---

[1] Warsaw University Astronomical Observatory, Al. Ujazdowskie 4, 00-478 Warszawa, Poland
e-mail: `wyrzykow@astrouw.edu.pl`
[2] Department of Physics, Chungbuk National University, Cheongju 28644, Republic of Korea
[3] Sternberg Astronomical Institute, Moscow State University, Universitetskii pr. 13, 119992 Moscow, Russia
[4] Instituto de Astrofisica de Canarias (IAC), 38205 La Laguna, Tenerife, Spain
[5] Universidad de La Laguna, Dpto. Astrofísica, 38206 La Laguna, Tenerife, Spain
[6] Institute of Astronomy, University of Cambridge, Madingley Road, CB3 0HA Cambridge, UK
[7] INAF – Osservatorio Astronomico di Roma, Via di Frascati 33, 00078 Monte Porzio Catone, Roma, Italy
[8] Indian Institute of Astrophysics, II Block Koramangala, Bengaluru 560034, India
[9] National Astronomical Research Institute of Thailand, 260, Moo 4, T. Donkaew, A. Mae Rim, Chiang Mai 50180, Thailand
[10] Department of Space Sciences and Technologies, Faculty of Science, Akdeniz University, 07058, Antalya, Turkey
[11] Université Côte d'Azur, Observatoire de la Côte d'Azur, CNRS, Laboratoire Lagrange, France
[12] School of Physics and Astronomy, Tel-Aviv University, Tel-Aviv 6997801, Israel
[13] Jet Propulsion Laboratory, California Institute of Technology, 4800 Oak Grove Drive, Pasadena, CA 91109, USA
[14] Harvard-Smithsonian Center for Astrophysics, 60 Garden Street, Cambridge, MA 02138, USA
[15] Institute of Astronomy and NAO Rozhen, BAS, 72 Tsarighradsko Shousse Blvd., 1784 Sofia, Bulgaria
[16] National Optical Astronomy Observatory, 950 N Cherry Avenue, Tucson, AZ 85719, USA
[17] Subaru Telescope, National Astronomical Observatory of Japan, 650 N Aohoku Place, Hilo, HI 96720, USA
[18] IAASARS, National Observatory of Athens, Vas. Pavlou & I. Metaxa, 15236 Penteli, Greece
[19] Dipartimento di Fisica E.R. Caianiello, Università di Salerno, Via Giovanni Paolo II 132, 84084 Fisciano, SA, Italy
[20] Department of Astronomy and Space Sciences, Ege University, 35100 Izmir, Turkey
[21] Centre for Advanced Instrumentation, University of Durham, South Road, Durham DH1 3LE, UK
[22] Institut del Ciències del Cosmos (ICC), Universitat de Barcelona (IEEC-UB), c/ Martí i Franquès, 1, 08028 Barcelona, Spain
[23] Department of Astrophysics/IMAPP, Radboud University Nijmegen, PO Box 9010, 6500 Nijmegen, The Netherlands
[24] INAF – Osservatorio di Astrofisica e Scienza dello Spazio di Bologna, Via Gobetti 93/3, 40129 Bologna, Italy
[25] Astronomical Observatory, Volgina 7, 11060 Belgrade, Serbia
[26] Science Support Office, Directorate of Science, European Space Research and Technology Centre (ESA/ESTEC), Keplerlaan 1, 2201 Noordwijk, The Netherlands
[27] Qatar Environment and Energy Research Institute(QEERI), HBKU, Qatar Foundation, Doha, Qatar
[28] Institut d'Astrophysique de Paris, Sorbonne Université, CNRS, UMR 7095, 98 bis bd Arago, 75014 Paris, France
[29] Department of Physics and Astronomy, University of Sheffield, Sheffield S3 7RH, UK
[30] Centre for Exoplanet Science, SUPA School of Physics & Astronomy, University of St Andrews, North Haugh, St Andrews KY16 9SS, UK
[31] Akdeniz University, Dumlupinar Blv., Campus, 07058 Antalya, Turkey
[32] Istanbul University, Department of Astronomy and Space Sciences, 34119, Beyazit Istanbul, Turkey

[33] Dept. of Physics & Astronomy, UCL, Gower St., London WC1E 6BT, UK
[34] Center for Astrophysics and Cosmology, University of Nova Gorica, Vipavska cesta 11c, 5270 Ajdovščina, Slovenia
[35] European Southern Observatory, Karl Schwarzschild Str 2, 85748 Garching, Germany
[36] Astronomical Observatory, Jagiellonian University, Kraków, Poland
[37] Mt. Suhora Observatory, Pedagogical University, ul. Podchor ażych 2, 30-084 Kraków, Poland
[38] Astronomical Institute of the Academy of Sciences of the Czech Republic, Ondřejov, Czech Republic
[39] Czech Technical University, Faculty of Electrical Engineering, Technická 2. 166 27, Praha 6, Czech Republic
[40] Zentrum für Astronomie der Universität Heidelberg, Astronomisches Rechen-Institut, Mönchhofstr. 12-14, 69120 Heidelberg, Germany
[41] International Space Science Institute, Hallerstrasse 6, 3012 Bern, Switzerland
[42] Department of Physics, School of Science, Tokyo Institute of Technology, 2-12-1 Ohokayama, Meguro, Tokyo 152-8551, Japan
[43] TÜBİTAK National Observatory, Akdeniz University Campus, 07058 Antalya, Turkey
[44] Instytut Astronomiczny Uniwersytetu Wrocławskiego, ul. Kopernika 11, 51-622 Wrocław, Poland
[45] Institute for Astronomy, University of Edinburgh, Royal Observatory, Edinburgh EH9 3HJ, UK
[46] School of Physical Sciences, The Open University, Walton Hall, Milton Keynes MK7 6AA, UK
[47] Osservatorio Astronomico Provinciale di Montarrenti, S. S. 73 Ponente, 53018, Sovicille Siena, Italy
[48] INAF – Osservatorio Astrofisico di Catania, Via Santa Sofia 78, 95123 Catania, Italy
[49] Faulkes Telescope Project, School of Physics, and Astronomy, Cardiff University, The Parade, Cardiff CF24 3AA, UK
[50] Astronomy Department, University of California, Berkeley, CA 94720, USA
[51] Department of Physics, University of Warwick, Coventry CV4 7AL, UK
[52] National Astronomical Observatories, Chinese Academy of Sciences, 100012 Beijing, PR China
[53] Graduate Institute of Astronomy, National Central University, Jhongli 32001, Taiwan
[54] Department of particle physics and astrophysics, Weizmann Institute of Science, Revovot, Israel
[55] Institute of Theoretical Physics and Astronomy, Vilnius University, Saulėtekio Av. 3, 10257 Vilnius, Lithuania
[56] Department of Astronomy, Ohio State University, 140 W. 18th Ave., Columbus, OH 43210, USA
[57] Soka University of America, 1 University Drive, Aliso Viejo, CA 92656, USA
[58] Astrophysics Research Institute, Liverpool John Moores University, 146 Brownlow Hill, Liverpool L3 5RF, UK
[59] Universitat Politècnica de Catalunya, Departament de Física, c/Esteve Terrades 5, 08860 Castelldefels, Spain
[60] Institute of Astrophysics, Foundation for Research and Technology-Hellas, 71110 Heraklion, Crete, Greece
[61] New York University Abu Dhabi, Saadiyat Island, PO Box 129188, Abu Dhabi, UAE
[62] Las Cumbres Observatory Global Telescope Network, 6740 Cortona Drive, Suite 102, Goleta, CA 93117, USA
[63] INAF Osservatorio Astronomico di Padova, Vicolo dell'Osservatorio 5, 35122 Padova, Italy
[64] Institute of Theoretical Physics, Faculty of Mathematics and Physics, Charles University, Prague, Czech Republic
[65] Astro Space Center of Lebedev Physical Institute, Profsoyuznaya St. 84/32, 117997 Moscow, Russia
[66] INAF – Istituto di Astrofisica e Planetologia Spaziali, Roma, Italy
[67] Department of Physics and Astronomy, University of Leicester, University Road, Leicester LE1 7RH, UK
[68] Institute for Astronomy, University of Hawai'i, 2680 Woodlawn Drive, Honolulu, HI 96822, USA
[69] Astrophysics Science Division, NASA/Goddard Space Flight Center, Greenbelt, MD 20771, USA
[70] Institute for Space Studies of Catalonia, c/Gran Capitá 2–4, Edif. Nexus 104, 08034 Barcelona, Spain
[71] Space Science Data Center – ASI, Via del Politecnico SNC, 00133 Roma, Italy
[72] Institute of Astronomy, Russian Academy of Sciences, Pyatnitskaya str. 48, 119017 Moscow, Russia
[73] Observatoire de Genève, Université de Genève, 1290 Versoix, Switzerland
[74] University of Crete, Physics Department & Institute of Theoretical & Computational Physics, 71003 Heraklion, Crete, Greece
[75] Kazan Federal University, ul. Kremlevskaya 18, 420008 Kazan, Russia
[76] Center for Theoretical Physics, Polish Academy of Sciences, Al. Lotników 32/46, 02-668 Warsaw, Poland
[77] Department of Astrophysics, Astronomy & Mechanics, Faculty of Physics, University of Athens, 15783 Athens, Greece
[78] Nicolaus Copernicus Astronomical Center, Polish Academy of Sciences, ul. Bartycka 18, 00-716 Warsaw, Poland
[79] Istituto Nazionale di Fisica Nucleare, Sezione di Napoli, Italy
[80] Instituto de Astrofísica, Facultad de Física, Pontificia Universidad Católica de Chile, Av. Vicuña Mackenna 4860, 7820436, Macul Santiago, Chile
[81] Istituto Internazionale per gli Alti Studi Scientifici (IIASS), Via G. Pellegrino 19, 84019 Vietri sul Mare, SA, Italy
[82] IPAC, Mail Code 100-22, California Institute of Technology, 1200 East California Boulevard, Pasadena, CA 91125, USA
[83] Space Research Institute of Russian Academy of Sciences (IKI), 84/32 Profsoyuznaya, Moscow, Russia
[84] National Research University Higher School of Economics, Myasnitskaya ul. 20, 101000 Moscow, Russia
[85] Institute of Solar-Terrestrial Physics SB RAS, Irkutsk, Russia
[86] Academy of Sciences of Tatarstan, Kazan, Russia
[87] Kavli Institute for Cosmology, Madingley Road, Cambridge CB3 0HA, UK
[88] Université Côte d'Azur, OCA, CNRS, Laboratoire Lagrange, Nice, France
[89] Crimean Astrophysical Observatory, Nauchnyi, Crimea
[90] American Association of Variable Star Observers (AAVSO), 49 Bay State Road, Cambridge, MA 02138, USA
[91] Swarthmore College, 500 College Avenue, Swarthmore, PA 19081, USA
[92] Dark Sky Observatory, Department of Physics and Astronomy, Appalachian State University, Boone, NC 28608, USA
[93] University of North Carolina, Chapel Hill, North Carolina, NC 27599, USA
[94] Yerkes Observatory, Department of Astronomy and Astrophysics, University of Chicago, 373 W. Geneva St., Williams Bay, WI 53191, USA
[95] Núcleo de Astronomía de la Facultad de Ingeniería, Universidad Diego Portales, Av. Ejército 441, Santiago, Chile
[96] Millenium Institute of Astrophysics, Santiago, Chile
[97] Horten Upper Secondary School, Bekkegata 2, 3181 Horten, Norway
[98] Aryabhatta Research Institute of Observational Sciences (ARIES), Manora Peak, Nainital 263002, India
[99] Mullard Space Science Laboratory, University College London, Holmbury St Mary, Dorking RH5 6NT, UK
[100] GEPI, Observatoire de Paris, Université PSL, CNRS, 5 Place Jules Janssen, 92190 Meudon, France
[101] School of Physics, University College Dublin, Belfield, Dublin 4, Ireland
[102] Department of Physics, Faculty of Natural and Agricultural Sciences, University of the Free State, Bloemfontein 9300, Republic of South Africa

Appendix A: Parameters of the telescopes taking part in the follow-up

Table A.1 lists the instruments that were used in all telescopes that took part in the photometric follow-up of the Gaia16aye binary microlensing event.

Table A.1. Photometric instruments used in the follow-up observations of Gaia16aye.

Telescope code	Mirror size [m]	Instrument	Pixel scale [arcsec]
AAVSO	–	–	–
Akeno50	0.5	3 × Apogee Alta U6	1.64
APT2	0.8	e2v CCD230-42	0.93
Aries130	1.30	CCD Andor DZ436	0.54
Aristarchos	2.3	VersArray 2048B	0.16
ASASSN	0.14	FLI ProLine230	7.80
ASV1	0.6	SBIG ST10 XME	0.23
		Apogee Alta E47	0.45
ASV2	1.4	Apogee Alta U42	0.24
AUT25	0.25	QSI532swg	0.71
BAS2	2.0	CCD VersArray 1300B	0.74
		Photometrics for FoReRo2 system	0.88
BAS50/70	0.5/0.7	FLI ProLine16803	1.08
Bialkow	0.6	Andor iKon DW432-BV	0.61
C2PU	1.04	SBIG ST16803	0.56
Conti	0.28	SX694 mono CCD	0.56
CrAO	0.2	SBIG ST8300M	1.10
DEMONEXT	0.5	Fairchild CCD3041 $2k \times 2k$ array	0.90
Foligno	0.3	Nikon D90	0.76
HAO50	0.5	ATIK314+	0.67
Krakow50	0.5	Apogee Alta U42	0.42
Kryoneri	1.2	Andor Zyla 5.5	0.40
LCO-Texas	1.0	Sinistro $4k \times 4k$	0.39
LCO-Hawaii	0.4	SBIG STL-6303 $3k \times 2k$	1.14
	2.0	Spectral $4k \times 4k$	0.30
Leicester	0.5	SBIG ST2000XM (before 2017 Nov.)	0.89
		Moravian G3-11000 (after 2017 Nov.)	1.08
Loiano	1.52	BFOSC	0.58
LOT1m	1.0	Apogee Alta U42	0.35
LT	2.0	IO:O e2v CCD231	0.27
MAO165	1.65	Apogee Alta U47	0.51
Mercator	1.2	Merope	0.19
Montarrenti	0.53	Apogee Alta U47	1.16
OHP	1.2	$1k \times 1k$ CCD	0.67
OndrejovD50	0.5	CCD FLI IMG 4710	1.18
Ostrowik	0.6	CCD 512 × 512 Tektronix	0.76
PIRATE	0.42	FLI ProLine16803	0.63
pt5m	0.5	QSI532 CCD	0.28
RTT150	1.5	TFOSC	0.39
SAI	0.6	Apogee Aspen CG42	0.76
Salerno	0.6	FLI ProLine230	0.60
SKAS-KFU28	0.28	QSI 583wsg	0.40
Skinakas	1.3	Andor DZ436	0.28
SKYNET	1.0	512 × 512 CCD 48um	1.21
Swarthmore24	0.6	Apogee Alta U16M	0.38
T60	0.6	FLI ProLine3041	0.51
T100	1.0	$4k \times 4k$ CCD	0.31
TJO	0.8	MEIA e2V CCD42-40	0.36
TRT-GAO	0.7	Andor iKon-L 936	0.61
TRT-TNO	0.5	Andor iKon-L 936	0.68
UCLO-C14E	0.35	SBIG STL6303E	0.86
UCLO-C14W	0.35	SBIG STL6303E	0.86
UBT60	0.6	Apogee Alta U47	0.68
Watcher	0.4	Andor iXon EM+	0.60
WHT-ACAM	4.2	ACAM	0.25
Wise1m	1.0	PI camera	0.58
WiseC28	0.71	FLI ProLine16801	0.83

Appendix B: *Gaia* photometry

Table B.1 contains all *Gaia* mean G-band photometry for the Gaia16aye event that was collected and calibrated by the *Gaia* Science Alerts system, available online[6]. The typical error bar is about 0.1 mag.

Table B.1. *Gaia* photometric measurements of the Gaia16aye microlensing event.

Observation date TCB	JD	Average G mag
2014-10-30 20:50:59	2456961.369	15.48
2014-10-30 22:37:33	2456961.443	15.48
2015-02-15 09:54:03	2457068.913	15.44
2015-02-15 14:07:43	2457069.089	15.44
2015-02-15 15:54:18	2457069.163	15.45
2015-03-09 08:16:20	2457090.845	15.45
2015-03-09 10:02:55	2457090.919	15.43
2015-03-09 14:16:35	2457091.095	15.45
2015-03-09 16:03:10	2457091.169	15.45
2015-05-20 19:20:37	2457163.306	15.45
2015-06-10 03:08:39	2457183.631	15.47
2015-07-25 13:45:22	2457229.073	15.45
2015-08-04 00:05:24	2457238.504	15.45
2015-08-04 01:51:58	2457238.578	15.46
2015-10-08 06:23:08	2457303.766	15.40
2015-11-11 05:44:30	2457337.739	15.35
2015-12-18 09:29:34	2457374.896	15.35
2015-12-18 11:16:08	2457374.970	15.35
2016-01-08 03:37:06	2457395.651	15.35
2016-01-08 05:23:40	2457395.725	15.35
2016-01-08 09:37:20	2457395.901	15.39
2016-01-08 11:23:54	2457395.975	15.34
2016-02-27 21:18:55	2457446.388	15.48
2016-02-27 23:05:29	2457446.462	15.38
2016-02-28 03:19:09	2457446.638	15.39
2016-03-23 23:08:54	2457471.465	15.40
2016-04-25 22:50:35	2457504.452	15.39
2016-06-02 20:18:57	2457542.346	15.52
2016-06-20 04:10:13	2457559.674	15.23
2016-08-05 00:53:51	2457605.537	14.18
2016-08-05 02:40:25	2457605.611	14.19
2016-08-05 06:54:05	2457605.788	14.40
2016-08-05 08:40:39	2457605.862	14.25
2016-08-15 13:00:28	2457616.042	15.26
2016-08-15 14:47:02	2457616.116	15.05
2016-09-27 13:28:36	2457659.062	13.67
2016-10-21 05:33:20	2457682.731	14.09
2016-11-21 17:05:46	2457714.212	12.81
2016-11-21 18:52:20	2457714.286	13.00
2017-01-02 12:24:22	2457756.017	14.91
2017-01-02 16:38:01	2457756.193	14.94
2017-01-02 18:24:35	2457756.267	14.91
2017-01-20 10:48:21	2457773.950	14.75
2017-01-20 12:34:55	2457774.024	14.77
2017-01-20 16:48:35	2457774.200	14.75
2017-01-20 18:35:09	2457774.274	14.78
2017-03-10 23:52:28	2457823.495	14.53

Table B.1. continued.

Observation date TCB	JD	Average G mag
2017-03-11 01:39:02	2457823.569	14.56
2017-04-07 23:48:22	2457851.492	14.45
2017-04-08 01:34:57	2457851.566	14.47
2017-05-07 11:34:44	2457880.982	13.96
2017-05-07 13:21:19	2457881.056	13.98
2017-06-16 16:39:01	2457921.194	14.87
2017-08-16 09:12:15	2457981.884	15.26
2017-08-16 10:58:49	2457981.958	15.27
2017-08-28 17:04:45	2457994.212	15.32
2017-08-28 21:18:24	2457994.388	15.29
2017-10-08 14:08:21	2458035.089	15.4
2017-10-08 15:54:55	2458035.163	15.41
2017-11-04 03:39:50	2458061.653	15.55
2017-12-03 09:23:18	2458090.891	15.53
2018-01-18 19:12:05	2458137.300	15.53
2018-01-18 20:58:40	2458137.374	15.53
2018-01-19 01:12:20	2458137.550	15.52
2018-01-19 07:12:33	2458137.800	15.54
2018-02-04 19:23:34	2458154.308	15.52
2018-02-04 21:10:08	2458154.382	15.51
2018-02-05 01:23:49	2458154.558	15.51
2018-02-05 03:10:23	2458154.632	15.51
2018-03-23 01:03:21	2458200.544	15.54
2018-04-22 12:49:53	2458231.035	15.54
2018-04-22 14:36:27	2458231.109	15.56
2018-05-19 00:41:48	2458257.529	15.53
2018-06-30 07:22:25	2458299.807	15.56
2018-07-12 01:29:24	2458311.562	15.58
...	...	

Notes. TCB is the barycentric coordinate time. The full table is available at the CDS.

[6] http://gsaweb.ast.cam.ac.uk/alerts/alert/Gaia16aye

Appendix C: Photometric follow-up data

Photometric follow-up observations calibrated with the Cambridge Photometric Calibration Server are gathered in Table C.1. The complete table is available at the CDS.

Table C.1. Photometric follow-up observations of Gaia16aye.

ID	MJD [d]	Magnitude [mag]	Error [mag]	Filter	Observatory/Observer
41329	57609.74664	16.635	0.052	*B*	UBT60 V.Bakis
41348	57609.74742	14.914	0.012	*V*	UBT60 V.Bakis
41367	57609.74819	14.108	0.006	*r*	UBT60 V.Bakis
41386	57609.74897	13.375	0.005	*i*	UBT60 V.Bakis
41330	57609.74978	16.548	0.037	*B*	UBT60 V.Bakis
41349	57609.75055	14.907	0.010	*V*	UBT60 V.Bakis
41368	57609.75133	14.102	0.005	*r*	UBT60 V.Bakis
41387	57609.75210	13.378	0.005	*i*	UBT60 V.Bakis
41331	57609.75281	16.600	0.037	*B*	UBT60 V.Bakis
41350	57609.75359	14.897	0.010	*V*	UBT60 V.Bakis
41369	57609.75436	14.117	0.005	*r*	UBT60 V.Bakis
41388	57609.75514	13.374	0.005	*i*	UBT60 V.Bakis
41332	57609.75588	16.504	0.035	*B*	UBT60 V.Bakis
41351	57609.75665	14.902	0.010	*V*	UBT60 V.Bakis
41370	57609.75743	14.105	0.005	*r*	UBT60 V.Bakis
41389	57609.75820	13.399	0.005	*i*	UBT60 V.Bakis
41333	57609.75896	16.538	0.035	*B*	UBT60 V.Bakis
41352	57609.75973	14.904	0.010	*V*	UBT60 V.Bakis
41371	57609.76051	14.117	0.006	*r*	UBT60 V.Bakis
41390	57609.76128	13.403	0.005	*i*	UBT60 V.Bakis
54690	57609.78240	14.202	0.009	*r*	SAI A.Zubareva
54689	57609.78569	16.528	0.024	*B*	SAI A.Zubareva
54680	57609.78902	16.544	0.016	*B*	SAI A.Zubareva
54663	57609.79078	14.974	0.007	*V*	SAI A.Zubareva
54681	57609.79218	14.148	0.005	*r*	SAI A.Zubareva
54682	57609.79395	16.539	0.019	*B*	SAI A.Zubareva
41334	57609.79522	16.599	0.024	*B*	UBT60 V.Bakis
54664	57609.79569	14.971	0.008	*V*	SAI A.Zubareva
41353	57609.79600	14.884	0.008	*V*	UBT60 V.Bakis
41372	57609.79677	14.082	0.005	*r*	UBT60 V.Bakis
54683	57609.79711	14.167	0.005	*r*	SAI A.Zubareva
41391	57609.79755	13.355	0.005	*i*	UBT60 V.Bakis
54684	57609.79888	16.583	0.020	*B*	SAI A.Zubareva
54665	57609.80063	15.014	0.009	*V*	SAI A.Zubareva
54685	57609.80202	14.168	0.005	*r*	SAI A.Zubareva
54686	57609.80373	14.178	0.005	*r*	SAI A.Zubareva
41335	57609.80477	16.605	0.026	*B*	UBT60 V.Bakis
41354	57609.80554	14.876	0.008	*V*	UBT60 V.Bakis
41373	57609.80632	14.102	0.005	*r*	UBT60 V.Bakis
41392	57609.80709	13.374	0.005	*i*	UBT60 V.Bakis
41336	57609.80787	16.549	0.025	*B*	UBT60 V.Bakis
41355	57609.80864	14.864	0.008	*V*	UBT60 V.Bakis
41374	57609.80942	14.106	0.005	*r*	UBT60 V.Bakis
41393	57609.81019	13.380	0.005	*i*	UBT60 V.Bakis
41337	57609.81094	16.488	0.025	*B*	UBT60 V.Bakis
41356	57609.81171	14.884	0.008	*V*	UBT60 V.Bakis
41375	57609.81249	14.102	0.005	*r*	UBT60 V.Bakis
41394	57609.81326	13.382	0.005	*i*	UBT60 V.Bakis
41338	57609.81405	16.492	0.027	*B*	UBT60 V.Bakis
41357	57609.81483	14.879	0.008	*V*	UBT60 V.Bakis
41376	57609.81560	14.101	0.005	*r*	UBT60 V.Bakis
41395	57609.81638	13.374	0.005	*i*	UBT60 V.Bakis
40186	57609.90821	17.158	0.134	*B*	pt5m L.Hardy
40187	57609.90927	16.939	0.116	*B*	pt5m L.Hardy
40188	57609.91009	16.548	0.098	*B*	pt5m L.Hardy
40189	57609.91092	14.917	0.022	*V*	pt5m L.Hardy
40190	57609.91181	14.964	0.021	*V*	pt5m L.Hardy
40191	57609.91263	14.958	0.022	*V*	pt5m L.Hardy
40192	57609.91346	14.132	0.009	*r*	pt5m L.Hardy
40193	57609.91457	14.188	0.011	*r*	pt5m L.Hardy
40194	57609.91540	14.106	0.010	*r*	pt5m L.Hardy
40195	57609.91640	13.439	0.010	*i*	pt5m L.Hardy
40196	57609.91751	13.448	0.009	*i*	pt5m L.Hardy
40197	57609.91834	13.453	0.010	*i*	pt5m L.Hardy
40268	57610.00399	16.522	0.014	*B*	TJO U.Burgaz

Table C.1. continued.

ID	MJD [d]	Magnitude [mag]	Error [mag]	Filter	Observatory/Observer
40271	57610.01489	15.002	0.006	*V*	TJO U.Burgaz
40272	57610.01842	14.956	0.020	*V*	TJO U.Burgaz
40274	57610.03669	13.107	0.055	*i*	TJO U.Burgaz
40275	57610.04022	13.293	0.011	*i*	TJO U.Burgaz
40276	57610.04375	13.388	0.004	*i*	TJO U.Burgaz
54687	57610.05719	16.491	0.057	*B*	SAI A.Zubareva
54666	57610.05894	14.977	0.018	*V*	SAI A.Zubareva
54688	57610.06035	14.192	0.009	*r*	SAI A.Zubareva
41339	57610.76348	16.499	0.029	*B*	UBT60 V.Bakis
41358	57610.76424	14.805	0.009	*V*	UBT60 V.Bakis
41377	57610.76499	14.009	0.005	*r*	UBT60 V.Bakis
41396	57610.76576	13.285	0.005	*i*	UBT60 V.Bakis
...	...	...	...	.	...

Notes. ID denotes the unique id of the observation in the Calibration Server. The full table is available at the CDS.

Appendix D: Photometric data used in the microlensing modelling

Photometric observations that were used in the microlensing model are shown in Table D.1. The complete table is available at the CDS.

Table D.1. Photometric follow-up observations of Gaia16aye used in the model.

HJD [d]	Magnitude [mag]	Error [mag]	Observatory code
2456961.36775	15.480	0.010	1
2456961.44175	15.480	0.010	1
2457068.91154	15.440	0.010	1
...	...	...	...
2457619.36442	14.350	0.009	2
2457623.42542	14.323	0.006	2
2457625.43582	14.320	0.006	2
...	...	...	...
2457612.33545	13.127	0.013	3
2457613.46778	12.894	0.003	3
2457614.40174	12.293	0.003	3
...	...	...	...
2457647.43662	14.256	0.007	4
2457648.33147	14.245	0.009	4
2457649.33125	12.208	0.004	4
...	...	...	...
2457690.67443	13.433	0.007	5
2457691.65978	13.433	0.006	5
2457692.59705	13.428	0.006	5
...	...	...	...
2457714.45266	12.246	0.003	6
2457714.46433	12.261	0.004	6
2457714.47873	12.280	0.005	6
...	...	...	...
2457610.28565	13.379	0.007	7
2457611.30428	13.286	0.005	7
2457616.35217	14.400	0.010	7
...	...	...	...
2457467.10912	17.020	0.170	8
2457489.03978	17.940	0.330	8
2457512.02932	18.110	0.290	8
...	...	...	...

Notes. Observatory codes: 1 *Gaia* (*G*), 2 Bialkow (*I*), 3 APT2 (*I*), 4 LT (*i*), 5 DEMONEXT (*I*), 6 Swarthmore (*I*), 7 UBT60 (*I*), and 8 ASAS-SN (*V*). The full data set is available at the CDS.

A&A 638, A108 (2020)
https://doi.org/10.1051/0004-6361/201937172

Astronomy & Astrophysics

The EXOTIME project: signals in the O–C diagrams of the rapidly pulsating subdwarfs DW Lyn, V1636 Ori, QQ Vir, and V541 Hya*,**

F. Mackebrandt[1,2], S. Schuh[1], R. Silvotti[3], S.-L. Kim[4], D. Kilkenny[5], E. M. Green[6], R. Lutz[7], T. Nagel[8], J. L. Provencal[9,10], T. Otani[11,12], T. D. Oswalt[11,12], S. Benatti[13], L. Lanteri[3], A. Bonanno[14], A. Frasca[14], R. Janulis[15], M. Paparó[16], L. Molnár[16,17], R. Claudi[13], and R. H. Østensen[18]

[1] Max-Planck-Institut für Sonnensystemforschung, Justus-von-Liebig-Weg 3, 37077 Göttingen, Germany
e-mail: mackebrandt@mps.mpg.de
[2] Institut für Astrophysik, Georg-August-Universität Göttingen, Friedrich-Hund-Platz 1, 37077 Göttingen, Germany
[3] INAF – Osservatorio Astrofisico di Torino, strada dell'Osservatorio 20, 10025 Pino Torinese, Italy
[4] Korea Astronomy and Space Science Institute, Daejeon 34055, South Korea
[5] Department of Physics and Astronomy, University of the Western Cape, Private Bag X17, Bellville 7535, South Africa
[6] Steward Observatory, University of Arizona, 933 N. Cherry Avenue, Tucson, AZ 85721, USA
[7] German Aerospace Center (DLR), Remote Sensing Technology Institute, Münchener Str. 20, 82234 Weßling, Germany
[8] Institute for Astronomy and Astrophysics, Kepler Center for Astro and Particle Physics, University of Tübingen, 72076 Tübingen, Germany
[9] University of Delaware, Department of Physics and Astronomy Newark, DE 19716, USA
[10] Delaware Asteroseismic Research Center, Mt. Cuba Observatory, Greenville, DE 19807, USA
[11] Embry-Riddle Aeronautical University, Department of Physical Science and SARA, Daytona Beach, FL 32114, USA
[12] Florida Institute of Technology, Department of Physics & Space Sciences, Melbourne, FL 32901, USA
[13] INAF – Osservatorio Astronomico di Padova, Vicolo dell'Osservatorio 5, 35122 Padova, Italy
[14] INAF – Osservatorio Astrofisico di Catania, Via S. Sofia 78, 95123 Catania, Italy
[15] Institute of Theoretical Physics and Astronomy, Vilnius University, Gostauto 12, Vilnius 01108, Lithuania
[16] Konkoly Observatory, Research Centre for Astronomy and Earth Sciences, Konkoly-Thege M. út 15-17, 1121 Budapest, Hungary
[17] MTA CSFK Lendület Near-Field Cosmology Research Group, Konkoly Observatory, Budapest, Hungary
[18] Department of Physics, Astronomy, and Materials Science, Missouri State University, Springfield, MO 65897, USA

Received 22 November 2019 / Accepted 12 March 2020

ABSTRACT

Aims. We aim to investigate variations in the arrival time of coherent stellar pulsations due to the light-travel time effect to test for the presence of sub-stellar companions. Those companions are the key to one possible formation scenario of apparently single sub-dwarf B stars.

Methods. We made use of an extensive set of ground-based observations of the four large amplitude p-mode pulsators DW Lyn, V1636 Ori, QQ Vir, and V541 Hya. Observations of the TESS space telescope are available on two of the targets. The timing method compares the phase of sinusoidal fits to the full multi-epoch light curves with phases from the fit of a number of subsets of the original time series.

Results. Observations of the TESS mission do not sample the pulsations well enough to be useful due to the (currently) fixed two-minute cadence. From the ground-based observations, we infer evolutionary parameters from the arrival times. The residual signals show many statistically significant periodic signals, but no clear evidence for changes in arrival time induced by sub-stellar companions. The signals can be explained partly by mode beating effects. We derive upper limits on companion masses set by the observational campaign.

Key words. stars: horizontal-branch – planets and satellites: detection – subdwarfs – asteroseismology – techniques: photometric

1. Introduction

Subdwarf B stars (sdBs) are sub-luminous stars with a mass of about $0.5\,M_\odot$ located at the blue end of the horizontal branch, which is the so-called extreme horizontal branch (EHB, Heber 1986). They maintain a helium burning core, but their thin hydrogen envelope ($M_{\rm env} < 0.01\,M_\odot$) cannot sustain hydrogen shell burning, which identifies sdBs with stripped cores of red giants (Heber 2016). Binary evolution with a common envelope (CE) is the favoured formation scenario for most sdBs. The sdB progenitor fills its Roche lobe near the tip of the RGB. A CE is formed when the mass transfer rate is sufficiently high and the companion star cannot accrete all the matter. For close binary systems with small initial mass ratios $q < 1.2$–1.5, two phases

* Photometric data of Fig. 1, results in Figs. 8, 10, 12, and 14, and figures in the appendix are only available at the CDS via anonymous ftp to cdsarc.u-strasbg.fr (130.79.128.5) or via http://cdsarc.u-strasbg.fr/viz-bin/cat/J/A+A/638/A108

** Based on observations obtained at the 0.9 m SARA-KP telescope, which is operated by the Southeastern Association for Research in Astronomy (saraobservatory.org).

of mass transfer occur. The first Roche-lobe overflow is stable, whereas the second one is unstable, leading to the ejection of the CE. The resulting binary consists of an sdB star and a white dwarf in a short-period orbit. For initial mass ratios $q > 1.2$–1.5, the first mass-transfer phase is unstable and the CE is ejected, producing an sdB star with a non-degenerate (e.g. main sequence star) companion. A more detailed review of formation and evolution of compact binary systems can be found in Podsiadlowski (2008) and Postnov & Yungelson (2014). These formation scenarios cannot explain the observed additional occurrence of apparently single sdBs (Maxted et al. 2001). Among the proposed formation scenarios is the proposal by Webbink (1984) that they could be formed by a merger of two helium white dwarfs. But such mergers are problematic, as they are expected to retain very little hydrogen (Han et al. 2002) and be left with higher rotation rates than what has been observed (Charpinet et al. 2018). Moreover, the overall observed mass distribution of single sdB stars is not consistent with that expected from the proposed formation scenario. Sub-stellar companions could resolve this disagreement between theory and observations. Planetary-mass companions like the candidates V391 Peg b (Silvotti et al. 2007), KIC 05807616 b,c (Charpinet et al. 2011), KIC 10001893 b,c,d (Silvotti et al. 2014), or brown dwarf companions like V2008-1753 B (Schaffenroth et al. 2015) or CS 1246 (Barlow et al. 2011b) indicate the existence of a previously undiscovered population of companions to apparently single sdBs.

Due to the high surface gravity and effective temperature (leading to few, strongly broadened spectral lines in the optical) and the small radii of sdBs, the detection efficiency for companions via methods like radial velocity variations or transits is small. The timing of stellar pulsations offers a complementary detection method, sensitive to large orbital separations.

A small fraction of sdB stars shows pulsational variations in the *p*- (pressure-) and *g*- (gravity-) mode regimes. Rapid *p*-mode pulsators (sdBV$_r$), discovered by Kilkenny et al. (1997), show periods of the order of minutes and amplitudes of a few tens of mmag. Such pulsations were predicted by Charpinet et al. (1997, et seq.) to be driven by the κ-mechanism due to a *Z*-opacity bump. For slow pulsators (sdBV$_s$) the periods range from 30 to 80 min with small amplitudes of a few mmag. This class was discovered by Green et al. (2003) and the pulsations are explained by the ϰ-mechanism as well (Fontaine et al. 2003). Some sdB stars show both types of pulsation modes simultaneously (sdBV$_{rs}$). These hybrid pulsators lie at the temperature boundary near 28 000 K between the two classes of pulsating stars, for example, the prototype for this class DW Lyn (Schuh et al. 2006), which is also addressed in this work, or Balloon 090100001 (Baran et al. 2005).

Pulsations driven by the κ-mechanism are coherent, which qualifies these objects for the timing method to search for sub-stellar companions. This method is based on the light-travel time effect, with the host star acting as a stable "clock" spatial movements of the star around the barycentre induced by a companion result in time delays of the stellar light measured by the observer. Examples of detections using this method are "pulsar planets" (e.g. Wolszczan & Frail 1992), planets detected by transit timing variations (e.g. Kepler 19 c, Ballard et al. 2011), planets orbiting δ Scuti stars (Murphy et al. 2016), or eclipsing binaries (e.g. V2051 Oph (AB) b, Qian et al. 2015). In particular, the detection of a late-type main sequence star companion to the sdB CS 1246 by Barlow et al. (2011b), subsequently confirmed with radial velocity data (Barlow et al. 2011a), or other studies like Otani et al. (2018), demonstrate the viability of this method in sdB systems. On the other hand, the particular example of V391 Peg b is currently under discussion (Silvotti et al. 2018) because of possible non-linear interactions between different pulsation modes that change arrival times (see Zong et al. 2018 for a detailed study of amplitude/frequency variations related to non-linear effects). Stochastically driven pulsations, are suspected by Reed et al. (2007a); Kilkenny (2010) and their nature confirmed by Østensen et al. (2014). Also, the candidate detections of KIC 05807616 and KIC 10001893 are uncertain, since other sdBs observed within the *Kepler* K2 mission exhibit *g*-modes with long periods up to a few hours. They question the interpretation of the low-frequency variations for KIC 05807616 and KIC 10001893 (e.g. Krzesinski 2015; Blokesz et al. 2019).

In order to detect sub-stellar companions orbiting rapidly pulsating sdB stars, the EXOTIME observational programme (EXOplanet search with the TIming MEthod) has been taking long-term data since 1999. EXOTIME conducted a long-term monitoring programme of five rapidly pulsating sdB stars. V391 Peg has been discussed by Silvotti et al. (2007, 2018). In this paper, we present the observations of DW Lyn and V1636 Ori, previously discussed in Lutz et al. (2008a, 2011); Schuh et al. (2010); Lutz (2011), and re-evaluate their findings using an extended set of observations. In addition, the observations of QQ Vir and V541 Hya are presented and analysed. In the beginning of the programme, the mode stability was tested for all targets over a timespan of months in order to ensure the pulsation modes were coherent.

For the DW Lyn observations, Lutz et al. (2011) found no significant signals in a periodogram of the O–C data of the two analysed pulsation frequencies, which would indicate sub-stellar companions. A tentative signal in the second frequency (in this work labelled f_2, as well), formally corresponding to an 80-day companion orbit, is concluded to arise from mode beating of an unresolved frequency doublet. The analysis of V1636 Ori revealed a signal at 160 d in the periodogram of the main frequency O–C data (Lutz et al. 2011). Although this periodicity showed a significance of only 1σ, Lutz et al. (2011) predicted an increase of significance with follow-up observations. We are using this extended data set in our work, now incorporating observations up to 2015.

This paper is organised as follows. Section 2 describes the observational aspects within the EXOTIME programme and the data reduction, followed by a description of our analysis in Sect. 3. Our results are presented in Sect. 4, together with a discussion.

2. Observations and data reduction

The observational data necessary for the analysis are comprised of many individual data sets gathered over the course of up to two decades. The detection method demands the observation of a target for a total time base at least as long as one orbit of a potential companion, which can span several years. This requires coordinated campaigns with observatories using ~1–4 m telescopes. In order to derive sufficient accuracy for the analysis, observations with at least three to four consecutive nights, each with a minimum of two to three hours per target are required. To resolve the short-period p-modes the cadence must be shorter than about 30 s but still with a sufficient signal-to-noise ratio (S/N). All observations used the Johnson–Bessel *B* band. The correct time stamps for each observation are of most importance for the timing analysis. Most observatories of this study already successfully contributed to the work of Silvotti et al. (2007); Silvotti (2008, Table 2). The following list features some

Table 1. Atmospheric parameters of the targets.

Target	$T_{\rm eff}$/ K	$\log\left(g/\frac{\rm cm}{\rm s}\right)$	$\log\left(\frac{N({\rm He})}{N({\rm H})}\right)$	Ref.
DW Lyn	$28\,400 \pm 600$	5.35 ± 0.1	-2.7 ± 0.1	1
V1636 Ori	$33\,800 \pm 1000$	5.60 ± 0.15	-1.85 ± 0.20	2
QQ Vir	$34\,800 \pm 610$	5.81 ± 0.05	-1.65 ± 0.05	3
V541 Hya	$34\,806 \pm 230$	5.794 ± 0.044	-1.680 ± 0.056	4

References. (1) Dreizler et al. (2002); (2) Østensen et al. (2001); (3) Telting & Østensen (2004); (4) Randall et al. (2009).

references where telescopes used for this study contributed successfully to other timing-relevant observations. Konkoly RCC 1.0 m Telescope: Provencal et al. (2009); Stello et al. (2006); Mt. Lemmon Optical Astronomy Observatory: Bischoff-Kim et al. (2019); Lee et al. (2014); Serra la Nave 0.9 m: Bonanno et al. (2003a,b); SARA-KP 0.9 m telescope: Kilkenny (2014); Baran et al. (2018).

Table 1 lists the atmospheric parameters of the stars, and Table 2 summarises the photometric observations obtained at multiple medium-class telescopes. Figure 1 summarises the observational coverage.

2.1. DW Lyn

Dreizler et al. (2002) identified DW Lyn (HS 0702+6043) as a p-mode pulsator. Schuh et al. (2006) discovered additional g-mode pulsations making this star the prototype of hybrid sdB pulsators.

There are photometric data available from 1999. Large gaps make a consistent O–C analysis difficult. Regular monitoring within the EXOTIME programme ran from 2007 until the beginning of 2010. Further observations cover a period up to the end of 2010. These multi-site observations are described in Lutz et al. (2008a,b, 2011). Here, we add observations made with the SARA-KP 0.9 m telescope at Kitt Peak National Observatory in Arizona, that used exposure times of 30 s.

2.2. V1636 Ori

Østensen et al. (2001) discovered V1636 Ori (HS 0444+0458) as a pulsating sdB star. Reed et al. (2007b) conducted a frequency analysis, reporting one small and two large amplitude p-modes.

V1636 Ori was observed between August 2008 and January 2015 for the EXOTIME project. About a third of the data was obtained using the 1 m South African Astronomical Observatory (SAAO) with the UCT and STE3 CCD instruments. Observations at the 1.2 m MONET/North telescope, equipped with an Apogee 1k × 1k E2V CCD camera, were taken in 2 × 2 binnings, using 20 s exposure times. Observations at the 2.2 m Calar Alto Observatory (CAHA) used the CAFOS instrument with 10 s exposure time. Two nights were obtained at the 1.5 m telescope at Loiano observatory, using the BFOSC (Bologna Faint Object Spectrograph & Camera) instrument and 15 s exposure times. Between October 2008 and December 2009, observations at the 1 m Mt. Lemmon Optical Astronomy Observatory (LOAO) were conducted with a 2k × 2k CCD camera with exposure times of 12 s and 20 s. The observations at the 3.6 m Telescopio Nazionale *Galileo* (TNG) in August 2008 and 2010 were performed with the DOLORES instrument and 5 s exposure times.

2.3. QQ Vir

The discovery of QQ Vir (PG 1325+101) as a multi-period pulsator was reported in Silvotti et al. (2002), followed by a frequency analysis and asteroseismological modelling by Silvotti et al. (2006) and Charpinet et al. (2006), respectively.

Observations of QQ Vir in 2001 and 2003 are described in Silvotti et al. (2002) and Silvotti et al. (2006), respectively. Between March 2008 and April 2010, the object was observed as part of the EXOTIME project (Benatti et al. 2010). Additionally, one observation run in February 2005 was performed at the 1.5 m telescope at Loiano observatory, using the BFOSC instrument. Most of the observations were obtained in 2009, 2010, 2011, and 2012 at the LOAO, using an exposure time of 10 s. The CAHA and MONET/North observations were conducted with 10 s and 20 s exposure times, respectively. The Loiano observatory performed additional observations in 2009, 2010 and 2011 with the 1.5 m telescope, using BFOSC and an exposure times of 12 s, 15 s, and 20 s. Observations at the Molėtai Astronomical Observatory (Mol) in 2008 were performed using the 1.6 m telescope and an Apogee 1k × 1k E2V CCD camera using 17.5 s of exposure time. Observations at the SAAO used the same instrumental setup as described in Sect. 2.2. The TNG observed in 2010 and 2011. A DARC-WET campaign on QQ Vir was performed in May 2010.

2.4. V541 Hya

V541 Hya (EC 09582-1137) was discovered by Kilkenny et al. (2006). Randall et al. (2009) conducted an asteroseismological analysis of this target.

Between 2005 and 2015, a large number of observations were obtained at the SAAO, using the same instrumentation noted in Sect. 2.2 and exposure times of 10 s. The LOAO conducted observations in 2009, 2012, and 2013 with exposure times of 20 s. During March 2009 and February and March 2010, V541 Hya was observed at the CAHA, using an exposure time of 10 s.

2.5. TESS observations

The primary goal of the NASA Transiting Exoplanet Survey Satellite (TESS) space telescope is to detect exoplanets transiting bright nearby stars (Ricker et al. 2015). However, the extensive time series photometry is valuable for asteroseimology and the TESS Asteroseismic Science Consortium (TASC) coordinates short cadence observations of pulsating evolved stars. TESS observed V1636 Ori and V541 Hya with a cadence of 120 s between November 15, 2018 and December 11, 2018, and February 2, 2019 and February 27, 2019, respectively. We used the light curves provided by the MAST archive[1] that had common instrumental trends removed by the Pre-Search Data Conditioning Pipeline (PDC, Stumpe et al. 2012). Light curves and amplitude spectra are presented in Figs. A.1 and A.2. The two-minute ("shor"') cadence undersamples the p-modes at about 140 s. In combination with the large photometric scatter, the amplitude spectra show no evidence of the p-modes. Thus, we did not make use of the TESS observations in our study.

2.6. Data reduction

For the EXOTIME observations, the data reduction was carried out using the IDL software TRIPP (Time Resolved Imaging Photometry Package, see Schuh et al. 2000). TRIPP performs bias-, dark-, flat-field corrections, and differential aperture photometry to calculate the relative flux of a target with respect to one or more comparison stars and extinction corrections (second order polynomial in time). In the presence of sub-stellar

[1] https://archive.stsci.edu/

Table 2. Summary of the observing time per target, per site in hours.

Site	DW Lyn	V1636 Ori	QQ Vir	V541 Hya
Asiago 1.8 m Copernico Telescope (Asi)	20.25			
Calar Alto Observatory 2.2 m (CAHA)	52.38	32.49	48.73	10.19
Baker 0.4 m			41.10	
BAO 0.85 m			47.70	
BOAO 1.8 m			25.60	
Göttingen IAG 0.5 m Telescope (Goe)	52.53			
Konkoly RCC 1.0 m Telescope (Kon)	14.27		4.76	
La Palma 0.6 m			37.30	
Mt. Lemmon Optical Astronomy Observatory 1.0 m (LOAO)	167.76	40.12	126.11	24.15
Loiano 1.5 m Telescope (Loi)		2.66	78.40	
Lulin Observatory 1 m Telescope (Lul)	9.30			
Moletai 1.6 m Telescope (Mol)	13.47		2.95	
MONET/North Telescope 1.2 m (M/N)	138.90	41.29	34.24	
Mt. Bigelow Kuiper Telescope 1.5 m (MtB)	440.85			
Nordic Optical Telescope 2.5 m (NOT)			3.86	
SARA-KP 0.9 m telescope	66.26		1.80	
Serra la Nave 0.9 m			26.40	
South African Astronomical Observatory 1 m (SAAO)		64.04	36.93	166.31
Steward Observatory Bok Telescope 2.2 m (StB)	12.00			
Telescopio Nazionale *Galileo* 3.6 m (TNG)		7.00	3.37	
Tübingen 0.8 m Telescope (Tue)	23.05			
Whole Earth Telescope (WET)			40.00	
Wise 1 m			9.00	
Σ	998.21	187.80	568.25	200.67

Notes. Detailed tables, including observing dates and times per observatory are available online at the CDS, as are tables listing the allocation into the epochs. Observations at Baker Observatory, Mt. Bigelow Kuiper Telescope, Nordic Optical Telescope, Steward Observatory Bok Telescope were initially collected for other project(s) but also used for this work.

companions, we might expect variations in the arrival times of stellar pulsations on the order of seconds to tens of seconds. The corresponding uncertainties are expected to be about one second. These uncertainties rise from observational constraints, such as smearing and sampling effects due to the integration time. The accuracy of individual time stamps is better than ±0.5 s. All time stamps were converted from GJD(UTC) to BJD(TDB), according to Eastman et al. (2010), with an accuracy well below the expected observational uncertainty.

Typical S/N for our ground-based observations range from 60 for large amplitude pulsations, to 3 for the smallest pulsation amplitudes we investigate in this work. The amplitude spectra in Sect. 4 also show pulsations with smaller S/N, but these are not suitable for timing analysis because the uncertainties are too large (see Table B.1).

3. Analysis

In order to detect variations in the arrival time of stellar pulsations, we developed a pipeline to process the reduced data. A schematic flowchart of our pipeline is presented in Fig. 2. The input consists of the light curve (time series) and the dates of the observational epochs. In a light curve, typically spanning several years at a very low duty cycle of 0.2 to 1.7 per cent, an epoch consists of a few roughly consecutive nights of observation.

Outlier removal. In case no uncertainty in the flux measurement F is provided, the root-mean-square of each observation is used as an approximate photometric error for the later analysis. We have used a running median filter to exclude 5σ flux-outliers. The length of the window size depends on the cadence of the observations. We constrained it to be not longer than half of the period of the main frequency. The analysis is performed for each frequency individually before all frequencies were analysed simultaneously.

Full data fit. For the individual fitting of pulsations, we first determined the frequency of the main signal. For this, we used the `astropy` package to calculate the Lomb–Scargle periodogram (Astropy Collaboration 2013, 2018). From this periodogram, we selected the frequency with the largest amplitude to continue. In the next step, we performed the fit of a sinusoidal function to the light curve, using

$$F(t) = A \sin(ft + \phi) + o \tag{1}$$

with amplitude A, frequency f, phase ϕ and offset o. The minimisation problem is solved using the *scipy* implementation of the Trust Region Reflective algorithm (Jones et al. 2011). The selected frequency from the amplitude spectrum serves as initial value, the full width at half maximum of the corresponding peak in the periodogram is used as a boundary. The amplitude-guess is taken from the amplitude spectrum. In case of highly varying amplitudes, the initial value can be set manually. The fitting routine returns the parameters and their variance.

Epoch fit. Frequency and offset are all kept fixed for the following analysis of the individual observational epochs. The starting value of the current phase fit is determined by the average of the previous j phase values (or the global fit value from

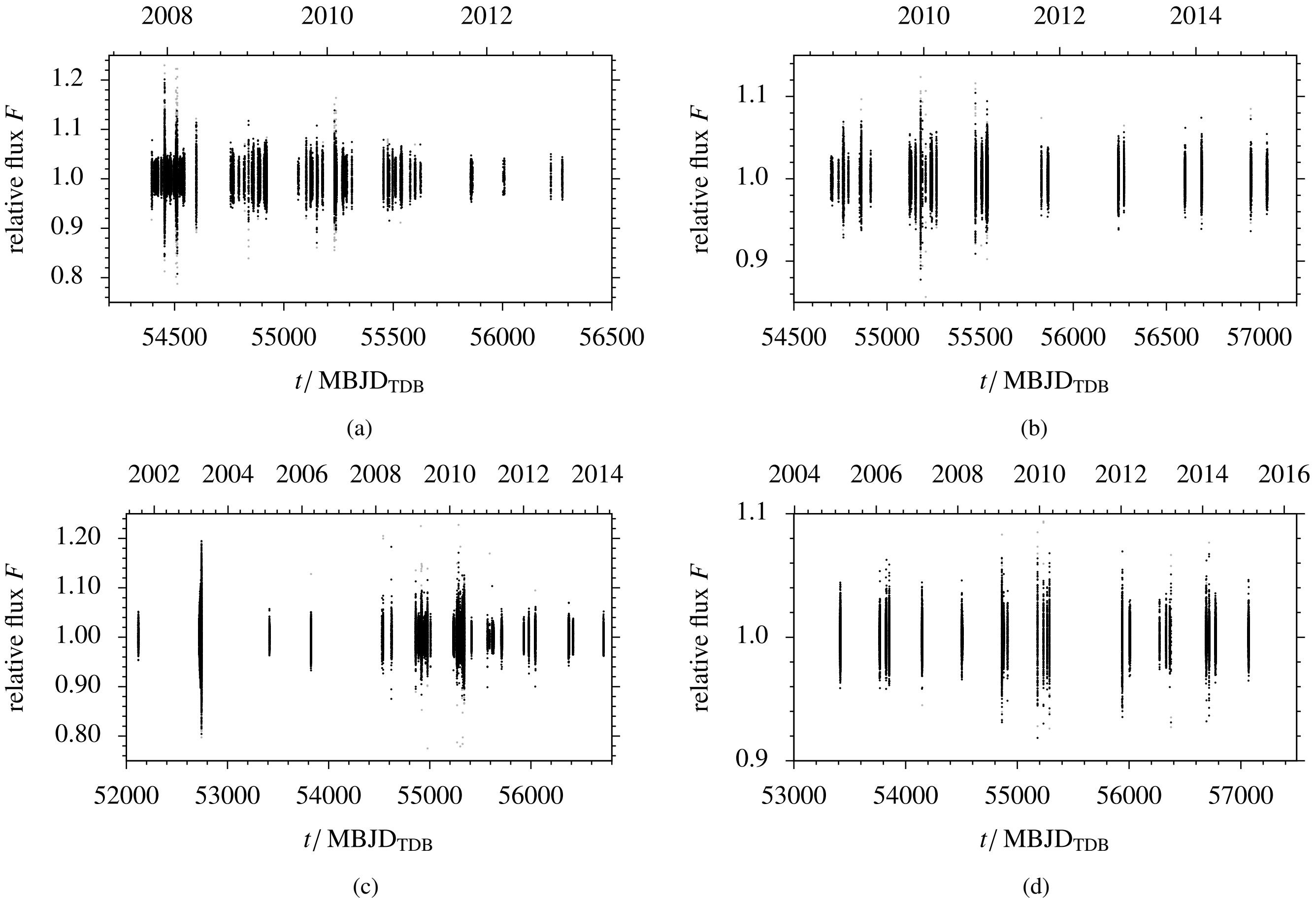

Fig. 1. Light curves. Grey points are considered outliers and partially exceed the plotting range. (*a*) DW Lyn. (*b*) V1636 Ori. (*c*) QQ Vir. (*d*) V541 Hya.

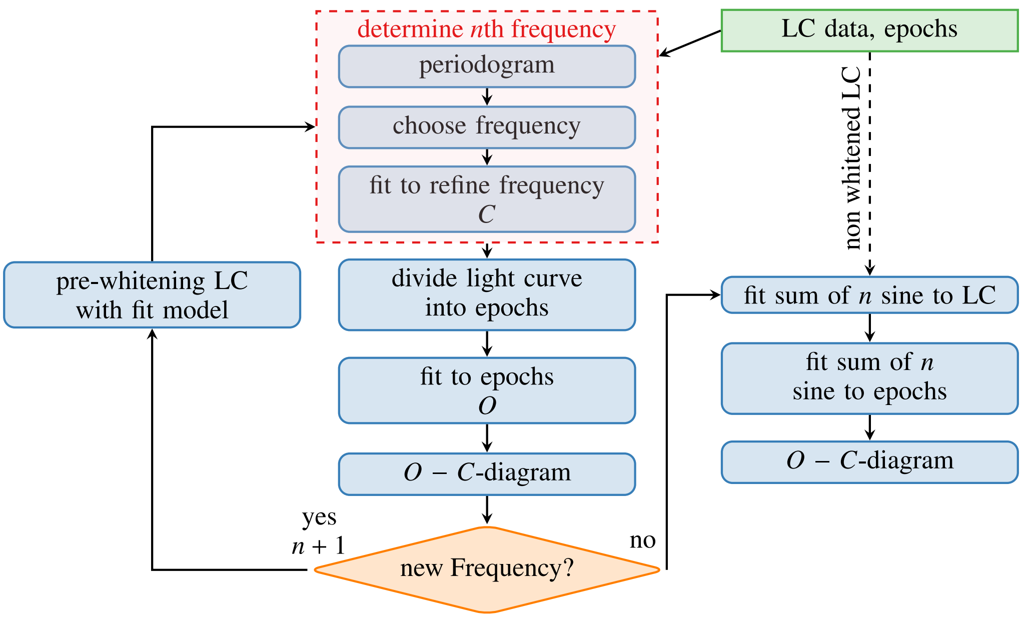

Fig. 2. Flow chart representing time of arrival analysis. Light curve (LC) and start/ end time of each observational epoch are provided as input. Each frequency is analysed, leading to an intermediate O–C-diagram, and subtracted from the LC by itself before the sum of all sinusoidal functions is fitted simultaneously to the LC, resulting in the final O–C-diagram.

Table 3. Parameters of the simultaneously fitted pulsations per target over their full observational time span and the pulsation period P.

Target		f/d^{-1}	P/s	$A/\%$	ϕ/d
DW Lyn	f_1	237.941160 (8)	363.114982(12)	2.19 (9)	54 394.741 (5)
	f_2	225.15898 (5)	383.72887(9)	0.35 (9)	54 394.74 (3)
V1636 Ori	f_1	631.7346 (2)	136.76629(5)	0.54 (3)	54 698.72 (3)
	f_2	509.780 (3)	169.4191(1)	0.24 (3)	54 698.72 (7)
QQ Vir	f_1	626.877627 (3)	137.8259429(7)	2.6 (1)	52 117.924 (6)
	f_2	552.00714 (9)	156.51971(3)	0.10 (9)	52 117.9 (1)
	f_3	642.0515 (1)	134.56864(3)	0. 07 (1)	52 117.9 (2)
V541 Hya	f_1	635.32218 (5)	135.993993(11)	0.31 (8)	53 413.88 (3)
	f_2	571.28556 (3)	151.237850(8)	0.21 (7)	53 413.88 (3)

Notes. The phase ϕ refers to the time corresponding to the first zero-crossing of the function after the first measurement t_0 in MBJD.

above in case there are no j previous values yet) in order to keep the fitting process stable and avoid "phase-jumps". For our target sample, a value of $j = 3$ has proven to be reasonable, except when observational gaps span over several years.

The uncertainty in the phase measurement scales inverse with the length of the epochs. Thus, this length is chosen in a way to minimize the uncertainties of the fit but at the same time keep the epochs as short as possible to maximize the temporal resolution of the final O–C diagram. Often, the observations themselves constrain the length of the epochs (e.g. three consecutive nights of observations and a gap of several weeks before the next block of observations). If possible, we aimed for an epoch length such that the timing uncertainties are of the order of one second. The phase information of the global and the epoch fit result in a intermediate O–C diagram.

As a last step in the single-frequency analysis, the fitted model is subtracted from the light curve. We noticed significant amplitude variations for some of our targets. Thus, we subtracted the model using the amplitude of the individual epochs. This pre-whitening procedure is repeated for every relevant pulsation in the data.

Multi frequency fit. Close frequencies are likely to introduce artificial trends in the arrival times in such a step-by-step analysis. Thus, the sum of all sinusoidal functions,

$$F(t) = A_n \sin(f_n t + \phi_n) + o, \tag{2}$$

is fitted to the non-whitened light curve, where n is the number of investigated frequencies. The previously retrieved values for amplitude, frequency, phase and offset are used as initial values. We used the phase information ϕ_n of the light curve as reference phase, namely calculated phase C in the final O–C diagram. Similar to the single-frequency analysis, the observational epochs are fitted individually using the sum of sinusoidal functions to yield the observed phase information O.

The results of the simultaneous fit for each target in this paper are summarised in Table 3. We list pulsation modes not used for the timing analysis in Table B.1. Figures 3–6 show example light curves of the targets for one epoch each, including their multi frequency fit and the respective amplitude spectrum.

4. Results and discussion

In the following, we discuss the implications of the obtained amplitude spectra and O–C measurements on the evolutionary state and presence of sub-stellar companions to the targets.

4.1. DW Lyn

The amplitude spectrum of DW Lyn in Fig. B.1 reveals two strong pulsation modes at $f_1 = 237.941160\,\mathrm{d}^{-1}$ and $f_2 = 225.15898\,\mathrm{d}^{-1}$. A closer look to the amplitude spectrum in Fig. 7 reveals small asymmetries compared to the window function. The pre-whitening of both frequencies leaves residuals well above noise level in the amplitude spectrum, indicating unresolved multiplets or mode splitting, especially for f_2.

The S/N of modes at higher frequencies, for example, at about $320\,\mathrm{d}^{-1}$ and $480\,\mathrm{d}^{-1}$, are too small for a stable O–C analysis (see Table B.1). Therefore, the O–C diagram in Fig. 8 shows the analysis of the two main pulsation modes, with the time-dependent variation of the pulsation amplitudes.

In order to determine evolutionary timescales of the pulsations, we investigated the long-term evolution in the O–C data. A constant change in period results in a second-order term as a function of time (Sterken 2005), which allows us to derive a value for the secular change of the period $\dot{P}$, and hence the evolutionary timescale. Results of the fits of the second order polynomial are included in Fig. 8, which are $\dot{P}/P_{f1} = (5.8 \pm 0.2) \times 10^{-5}\,\mathrm{d}^{-1}$ and $\dot{P}/P_{f2} = (-29.3 \pm 0.8) \times 10^{-5}\,\mathrm{d}^{-1}$. Assuming $\dot{P}$ is based on stellar evolution, stellar model calculations show that the sign of the rate of period change indicates the phase of the sdB after the zero-age extreme horizontal branch (ZAEHB; Charpinet et al. 2002). For p-modes, a positive $\dot{P}$ relates to the first evolutionary phase of the ZAEHB, in which the surface gravity decreases due to He burning in the core. A negative $\dot{P}$ would correspond to the second evolutionary phase, in which the sdB contracts because the depletion of He in its core, and this happens before the post-EHB evolution. The turning point between these two states occurs between 87 and 91 Myr after the ZAEHB. According to our measurement of a positive $\dot{P}$ for f_1, DW Lyn would still be in its first evolutionary phase. With the lack of a mode identification from an asteroseismic model for DW Lyn, we can not directly compare the measured $\dot{P}$ with theoretical predictions from Charpinet et al. (2002). However, stellar models with pulsation periods of around 360 s show values for $\dot{P}$ with a comparable order of magnitude to our measurement $\dot{P} = (4.3 \pm 0.15) \times 10^{-1}\,\mathrm{s\,Myr}^{-1}$, for example, $\dot{P} = 1.62\,\mathrm{s\,Myr}^{-1}$ for a model with a mode of $l = 0, k = 0$ at the age of 67.83 Myr (Charpinet et al. 2002, Appendix C). The large $\dot{P}$ of f_2 is consistent with the apparent mode splitting seen in the amplitude spectra in Fig. 7, and thus does not reflect the evolutionary phase of DW Lyn.

After subtracting the long-term trend, small timescale features are evident. For example, the O–C data for f_2 show an

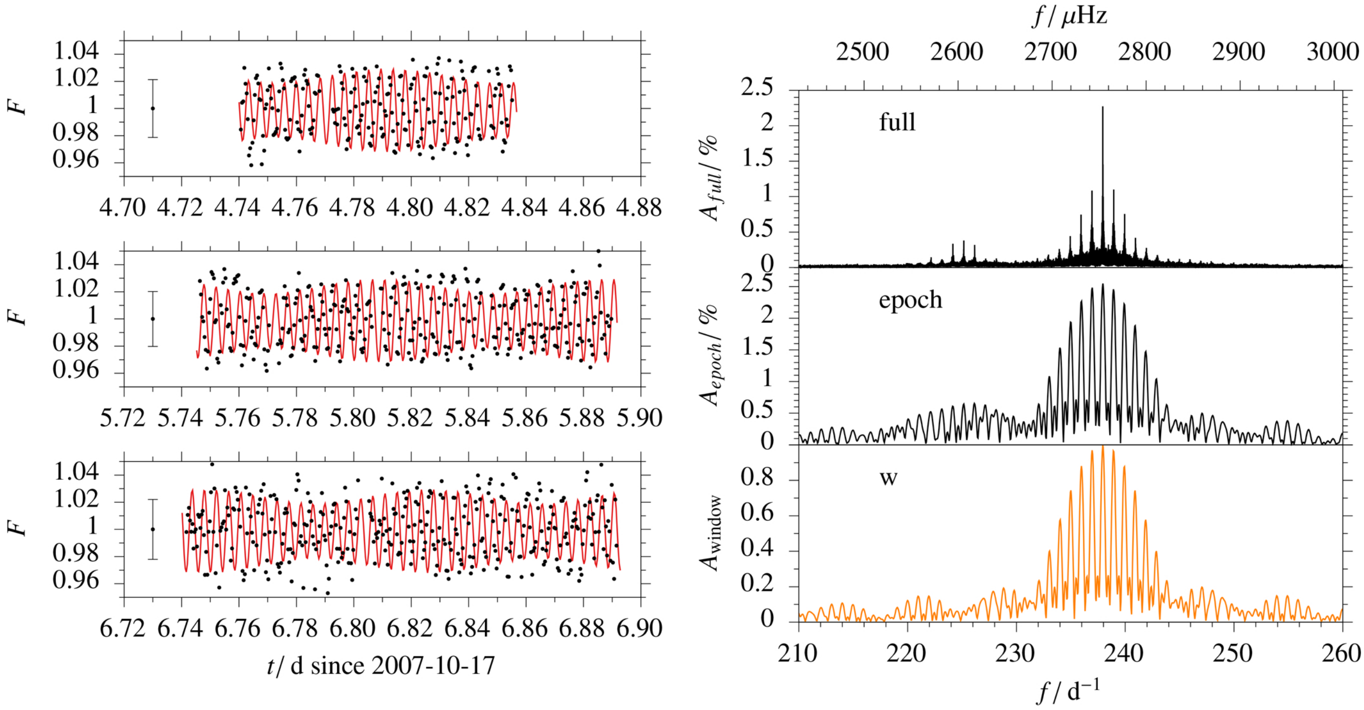

Fig. 3. Example observations of DW Lyn from October 21, 22, and 23, 2010 at the Lulin observatory (*left, from top to bottom*), combined used as one O–C measurement. The error bar on the left of each plot represents the photometric al uncertainty. The red line shows the simultaneous two frequency fits to the epoch data. The amplitude spectra on the right hand side show the spectrum of the full data set (*top*), the spectrum of this epoch (*middle*) and the respective window function computed at f_1.

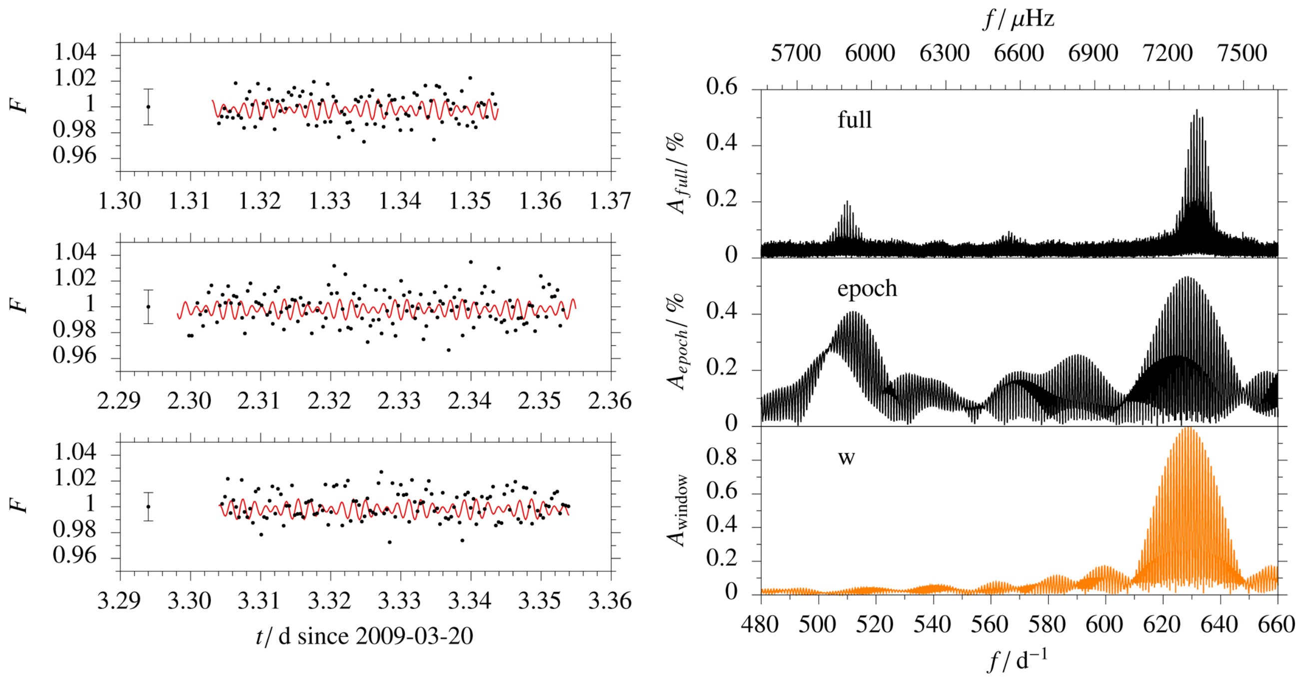

Fig. 4. Example observations of V1636 Ori from March 20, 21, and 22, 2009 at the CAHA (*left, from top to bottom*), combined used as one O–C measurement. The error bar on the left of each plot represents the photometric uncertainty. The red line shows the simultaneous two frequency fit to the epoch data. The amplitude spectra on the right hand side show the spectrum of the full data set (*top*), the spectrum of this epoch (*middle*) and the respective window function computed at f_1.

oscillating behaviour with a significance of 3σ within the first 200 days, while the arrival times for f_1 remain constant during the same period of time. In later epochs, the O–C data for both frequencies agree mostly within 2σ. During the second half of the observations, the phase of f_2 jumps by about 100 s. This behavior lacks an explanation.

Additionally, the evolution of the pulsation-amplitudes in Fig. 8 shows a comparable oscillating behaviour for f_2 within

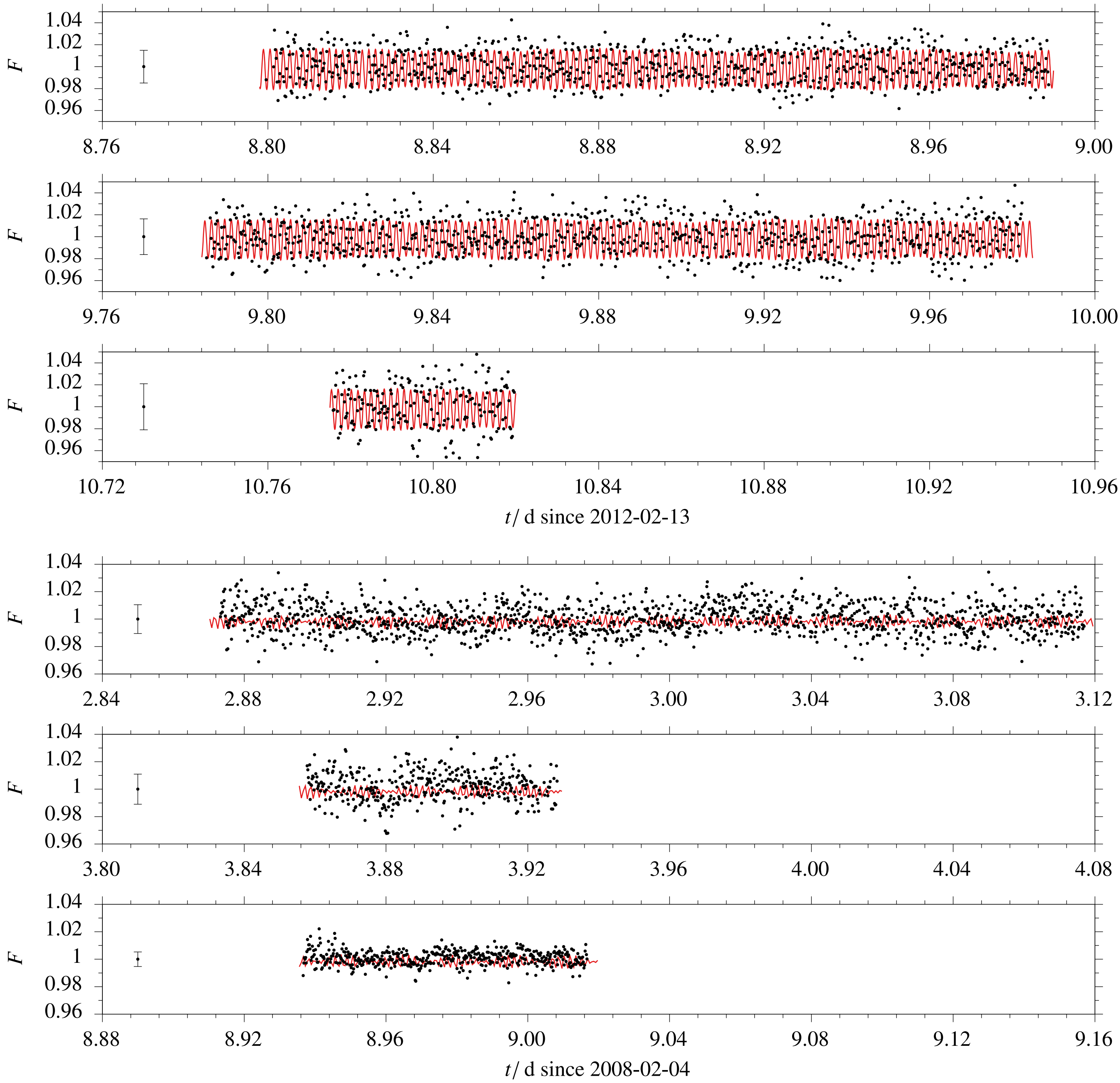

Fig. 5. Example observations of QQ Vir from February 20, 21, and 22, 2012 at the Monet telescope (*top three panels*), and V541 Hya from February 6, 7, and 12, 2008 at the SAAO (*bottom three panels*), combined used as one O–C measurement each. The error bar on the left of each plot represents the photometric uncertainty. The red line shows the simultaneous three and two frequency fit to the epoch data, repsectively.

the first epochs similar to the change in arrival times. Although the periodic variations in amplitude are not as significant as for the phase, the occurrence of simultaneous phase- and amplitude-modulations indicate a mode beating of two close, unresolved frequencies. The residuals in the amplitude spectrum support this explanation. In later observations, the amplitude remains almost constant within the uncertainties. The beating mode might lose energy or shift frequency over time. The amplitude for the f_1 pulsation drops by about 1 per cent (amplitude), or about 35 per cent (relative) to the second half of the observation campaign with a similar quasi-periodic variation as the phase. The residuals in the amplitude spectrum show no indication of an unresolved frequency leading to mode-beating. Besides stochastically driven pulsation modes, Kilkenny (2010) suggested energy transfer between modes as possible explanation for amplitude variations. For both frequencies, a possible interaction between amplitude and phase of pulsations is not well understood.

4.2. V1636 Ori

The amplitude spectrum of V1636 Ori in Fig. B.2 shows two main pulsation modes with frequencies at $f_1 = 631.7346\,\mathrm{d}^{-1}$ and $f_2 = 509.9780\,\mathrm{d}^{-1}$. The S/N is not sufficient to use a third

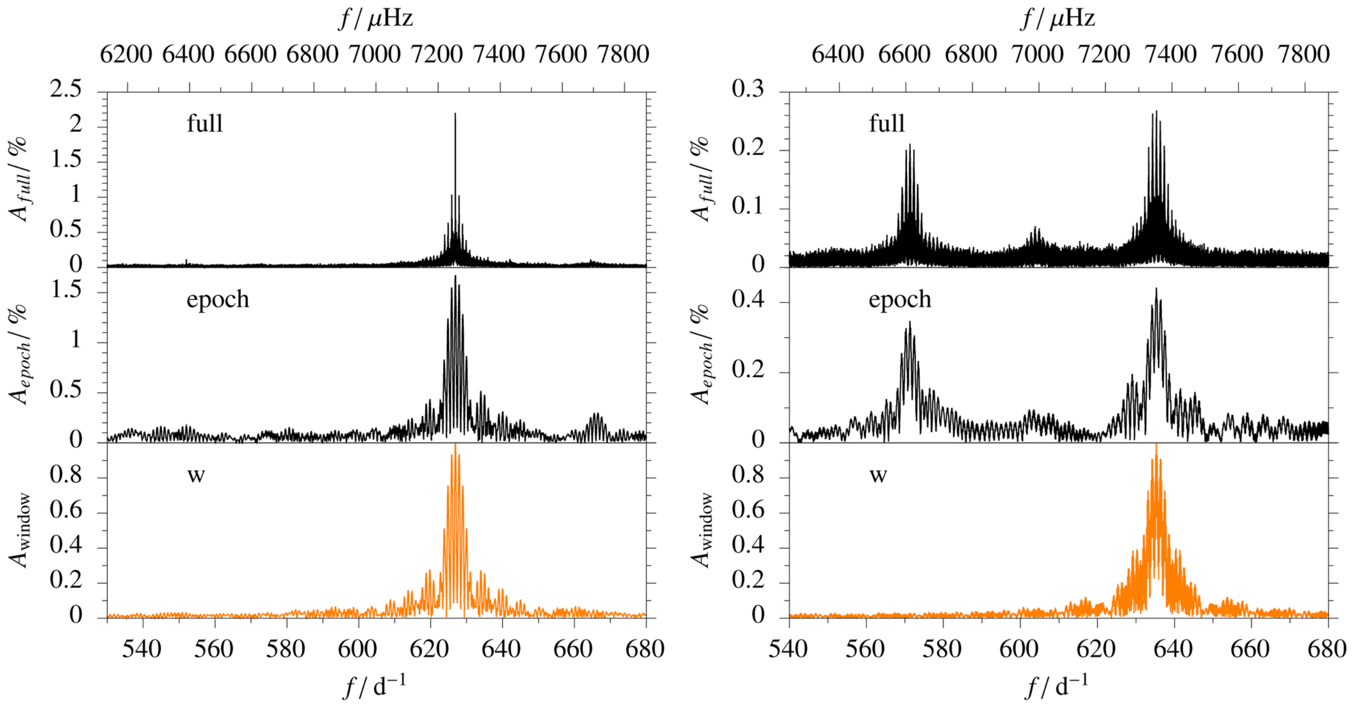

Fig. 6. Amplitude spectra for epoch data in Fig. 5 of QQ Vir (*left*) and V541 Hya (*right*) show the spectrum of the full data set (*top*), the spectrum of this epoch (*middle*), and the respective window function computed at f_1.

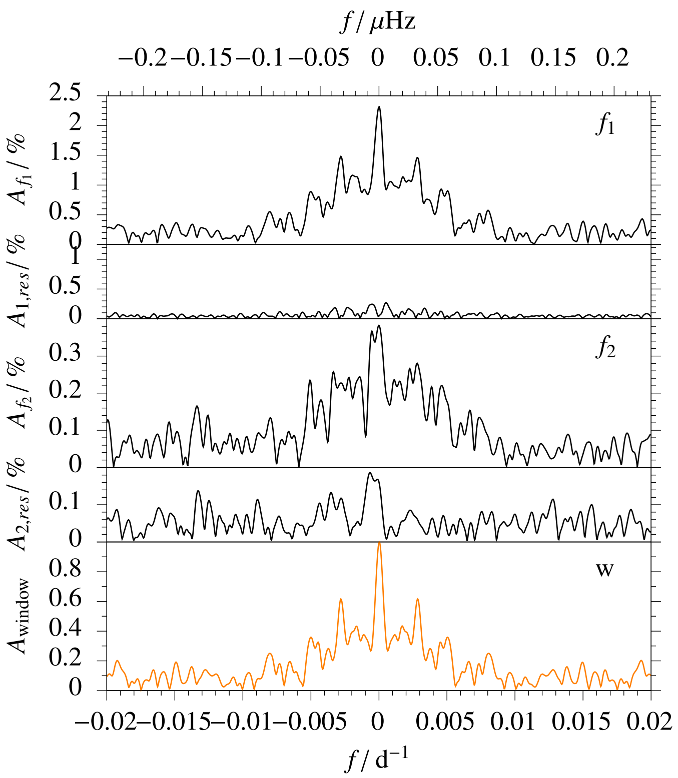

Fig. 7. Amplitude spectrum of DW Lyn of the main pulsation frequency $f_1 = 237.941160\,\mathrm{d}^{-1}$ (*top*), $f_2 = 225.15898\,\mathrm{d}^{-1}$ (*middle*) with the respective residuals after the pre-whitening below, and the normalised window function (*bottom*).

pulsation mode at $566.2\,\mathrm{d}^{-1}$ ($6553\,\mu$Hz, Reed et al. 2007b). The amplitude spectrum of TESS data in Fig. A.2 shows no evidence for *g*-mode pulsations with amplitudes greater than 0.4 per cent.

A detailed look at the spectra of the two main frequencies in Fig. 9 shows mode splitting, likely due to a change in frequency over the long observation time.

The O–C diagram in Fig. 10 shows the two main pulsation modes and the variation of the pulsation amplitudes.

From the second order fit in time, we derive the changes in period $\dot{P}/P_{f1} = (-8.54 \pm 0.14) \times 10^{-5}\,\mathrm{d}^{-1}$ and $\dot{P}/P_{f2} = (-2.5 \pm 0.5) \times 10^{-5}\,\mathrm{d}^{-1}$. We caution the interpretation of these values as evolutionary timescales since the apparent mode splitting seen in Fig. 9 could explain these trends as well.

The residuals after subtracting the long term trend show a large variation. They change by up to about ± 50 s for f_1 ($\sim 14\sigma$ significance) and up to about ± 30 s for f_2 ($\sim 3\sigma$ significance). The amplitude for f_1 drops by about 0.25 per cent (amplitude) or about 33 per cent (relative) in the time between MBJD = 55 100 *d* and 55 300 *d*, and returns to its previous level afterwards, while the amplitude for f_2 remains constant within the uncertainties. This decrease in amplitude coincides with earlier arrival times in the O–C diagram. As already discussed in the previous section, a possible amplitude- and phase-interaction is not well understood. The f_1 pulsation mode may not be coherent on such long timescales but of a short-term stochastic nature not resolvable by our data set (e.g. KIC 2991276, Østensen et al. 2014).

4.3. QQ Vir

Figure B.3 shows the amplitude spectrum for the QQ Vir observations. The main frequency at about $f_1 = 626.877628\,\mathrm{d}^{-1}$ is presented in Fig. 11 in detail and shows asymmetries compared to the window function. After the pre-whitening process, a close frequency at about $626.881270\,\mathrm{d}^{-1}$ remains but attempts to model this pulsation fail with uncertainties too large for the timing analysis. There appear two more frequencies suitable for our study. The amplitude spectra around $f_2 = 552.00713\,\mathrm{d}^{-1}$ and

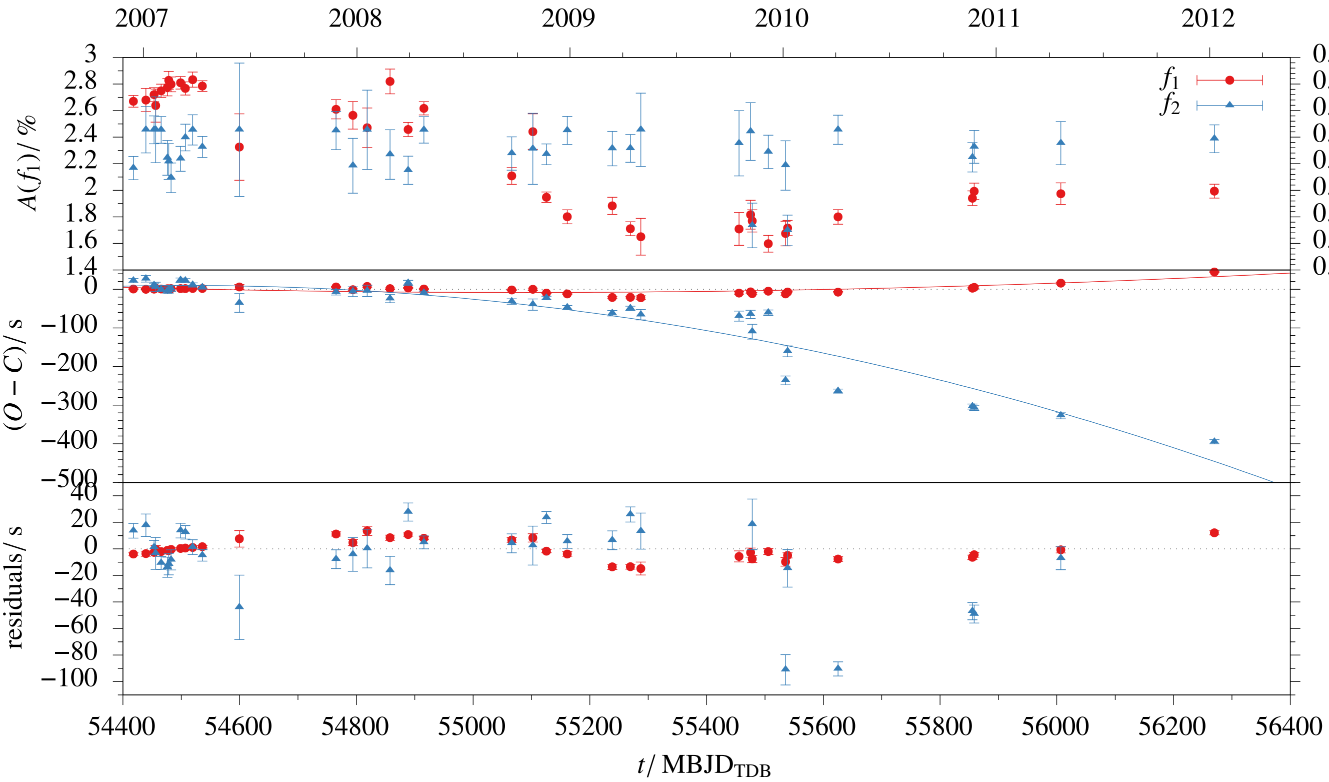

Fig. 8. Results for the two main pulsations of DW Lyn. *Top panel*: amplitudes. *Middle panel*: fits of the O–C data with second order polynomials in time. *Lower panel*: residuals.

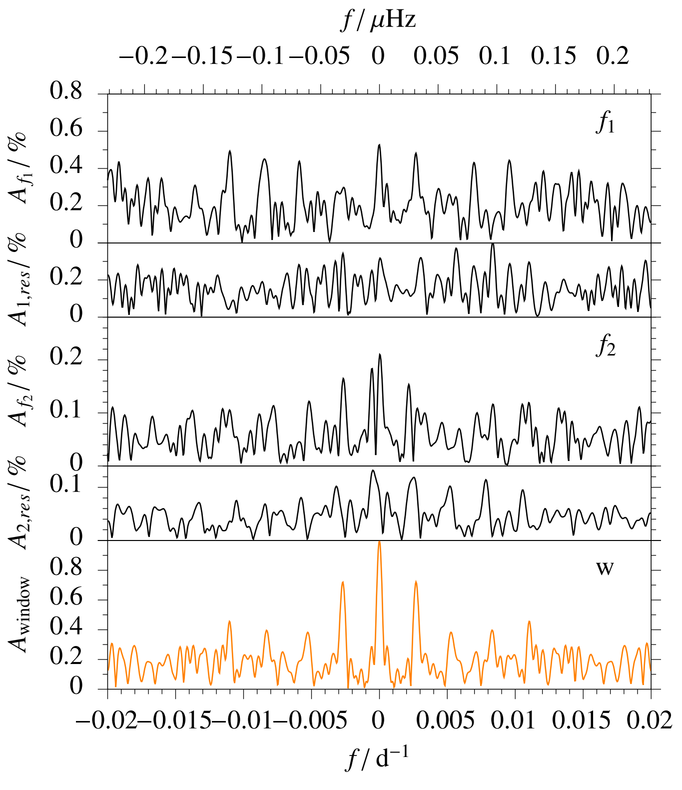

Fig. 9. Amplitude spectrum of V1636 Ori of the main pulsation frequency $f_1 = 631.7346\,\mathrm{d}^{-1}$ (*top*), $f_2 = 509.9780\,\mathrm{d}^{-1}$ (*middle*) with the respective residuals after the pre-whitening below and the normalised window-function (*bottom*).

$f_3 = 642.0516\,\mathrm{d}^{-1}$ are presented next to f_1 in Fig. 11. Another peak at about $665\,\mathrm{d}^{-1}$ consists of at least two frequencies at $664.488549\,\mathrm{d}^{-1}$ and $665.478133\,\mathrm{d}^{-1}$, but they are not sufficiently resolvable within the individual epochs, and lead to uncertainties in the O–C analysis that are too large.

Figure 12 shows the resulting O–C diagram and the amplitudes at different epochs. Due to the large observational gap from 2003 to 2008 with only one block of observations in between, we had difficulties avoiding errors in cycle count. In order to avoid a phase jump, we increased the averaging window for initial phase values to $q = 6$. With this set up, the changes in pulsation frequencies read as follows: $\dot{P}/P_{f1} = (1.7 \pm 1.6) \times 10^{-7}\,\mathrm{d}^{-1}$, $\dot{P}/P_{f2} = (2.4 \pm 0.4) \times 10^{-5}\,\mathrm{d}^{-1}$ and $\dot{P}/P_{f3} = (4.0 \pm 0.5) \times 10^{-6}\,\mathrm{d}^{-1}$. While f_2 and f_3 show no significant variation of pulsation amplitude, f_1 varies by 1.5 per cent (amplitude) or 50 per cent (relative). Thus, the corresponding phase changes should be interpreted with caution. Charpinet et al. (2006) identified the radial order k and degree l from asteroseismic modelling to be f_1: $l = 2, k = 2$; f_2: $l = 4, k = 1$; f_3: $l = 3, k = 2$. These combinations do not allow a direct comparison of our $\dot{P}$ measurements to the model calculations from Charpinet et al. (2002), but the sign of $\dot{P}$ indicates QQ Vir to be in the stage of He burning.

4.4. V541 Hya

The amplitude spectrum in Fig. B.4 shows two pulsation modes with frequencies at $f_1 = 635.32218\,\mathrm{d}^{-1}$ and at $f_2 = 571.28556\,\mathrm{d}^{-1}$. Both of them show a complex behaviour (Fig. 13), indicating unresolved multiplets and/or frequency changes that we see also in the O–C diagrams (Fig. 14). The

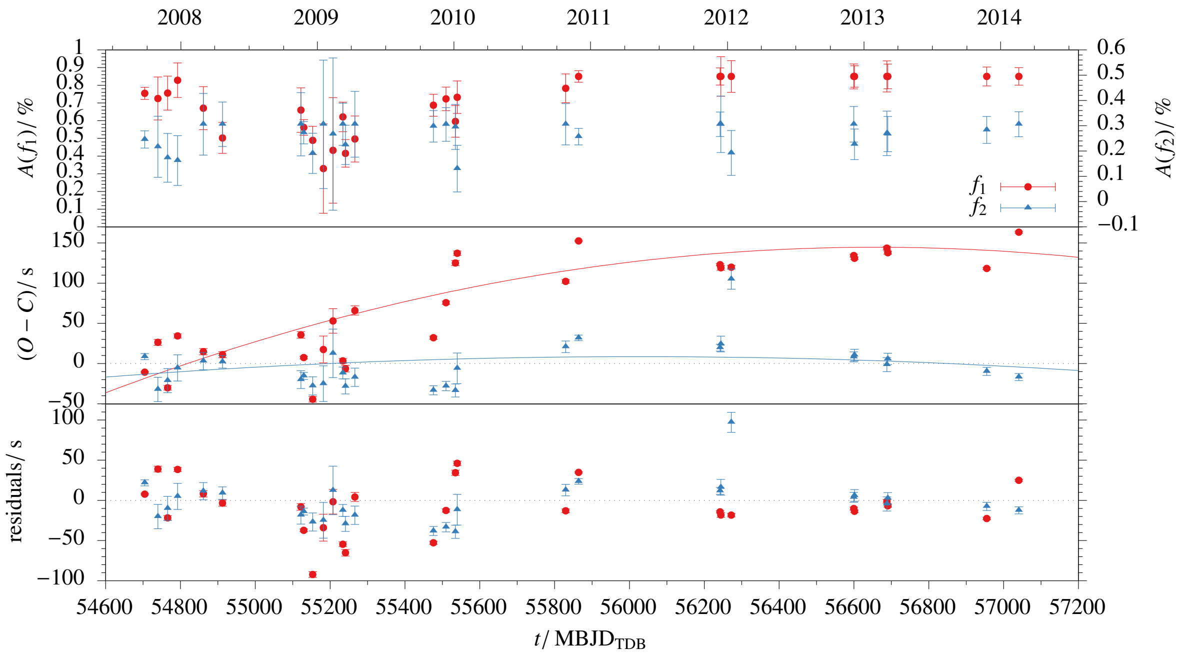

Fig. 10. Results for the two main pulsations of V1636 Ori. *Top panel*: amplitudes. *Middle panel*: fits of the O–C data with second order polynomials in time. *Lower panel*: residuals.

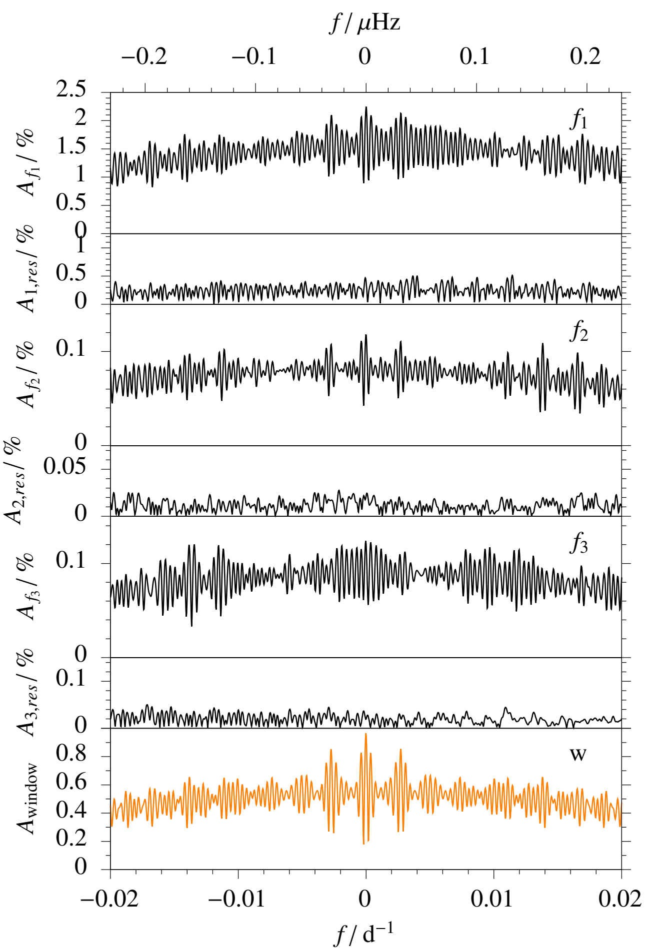

Fig. 11. Amplitude spectrum of QQ Vir of the main pulsation frequency $f_1 = 626.877628\,\mathrm{d}^{-1}$ (*top*), $f_2 = 552.00713\,\mathrm{d}^{-1}$ (*top middle*), $f_3 = 642.0516\,\mathrm{d}^{-1}$ (*bottom middle*) with the respective residuals after the pre-whitening below and the normalised window-function (*bottom*).

S/N for a third frequency at $603.88741\,\mathrm{d}^{-1}$ is not sufficient for the O–C analysis. Similar to V1636 Ori, the amplitude spectrum obtained from the TESS light curve in Fig. A.2 shows no evidence for *g*-mode pulsations with amplitudes greater than 0.4 per cent.

Randall et al. (2009) speculated about rotational mode splitting for f_3 with $\Delta f_{3,-} = 5.12\,\mu\mathrm{Hz}$ and $\Delta f_{3,+} = 3.68\,\mu\mathrm{Hz}$. The asteroseismic modelling associates f_1 with a $l = 0$ mode and f_2 with $l = 0$ or 1 mode (depending on the favoured model). f_3 corresponds to a $l = 2$ mode. They caution this interpretation due to their limited resolution in frequency space, the mode splitting could be an unresolved quintuplet. Our data set shows no clear evidence for a mode splitting with $\Delta f_{3,-} = 5.12\,\mu\mathrm{Hz}$ or $\Delta f_{3,+} = 3.68\,\mu\mathrm{Hz}$ (see Fig. 15) but rather a mode splitting for f_1 and f_2 with about $\Delta f = 0.08\,\mu\mathrm{Hz}$ (Fig. 13). Assuming these modes are of degree $l = 1$, this could be interpreted as a triplet. But Randall et al. (2009) model these modes with a degree of $l = 0$, which does not support a mode splitting into triplets.

The O–C diagram in Fig. 14 shows the analysis of the two main pulsation modes and the variation of the pulsation amplitudes. The second order fits in time correspond to changes in period of $\dot{P}/P_{f1} = (-1.49 \pm 0.11) \times 10^{-5}\,\mathrm{d}^{-1}$ and $\dot{P}/P_{f2} = (-0.7 \pm 1.5) \times 10^{-5}\,\mathrm{d}^{-1}$. For f_2, the change in period does not significantly differ from the null hypothesis. Assuming these changes origin from stellar evolution, V541 Hya might just have passed the point of sign change in $\dot{P}$ and at the beginning of the contraction phase. While the arrival times scatter widely, the amplitudes of both pulsations remain almost constant within the uncertainties. If V541 Hya is in its evolution close to starting the contraction phase, as indicated by a $\dot{P}$ close to zero, the changes in stellar structure may cancel the strict phase coherence.

4.5. Testing the sub-stellar companion hypothesis

In order to set upper limits to the mass of a companion, we computed a series of synthetic O–C curves for different orbital

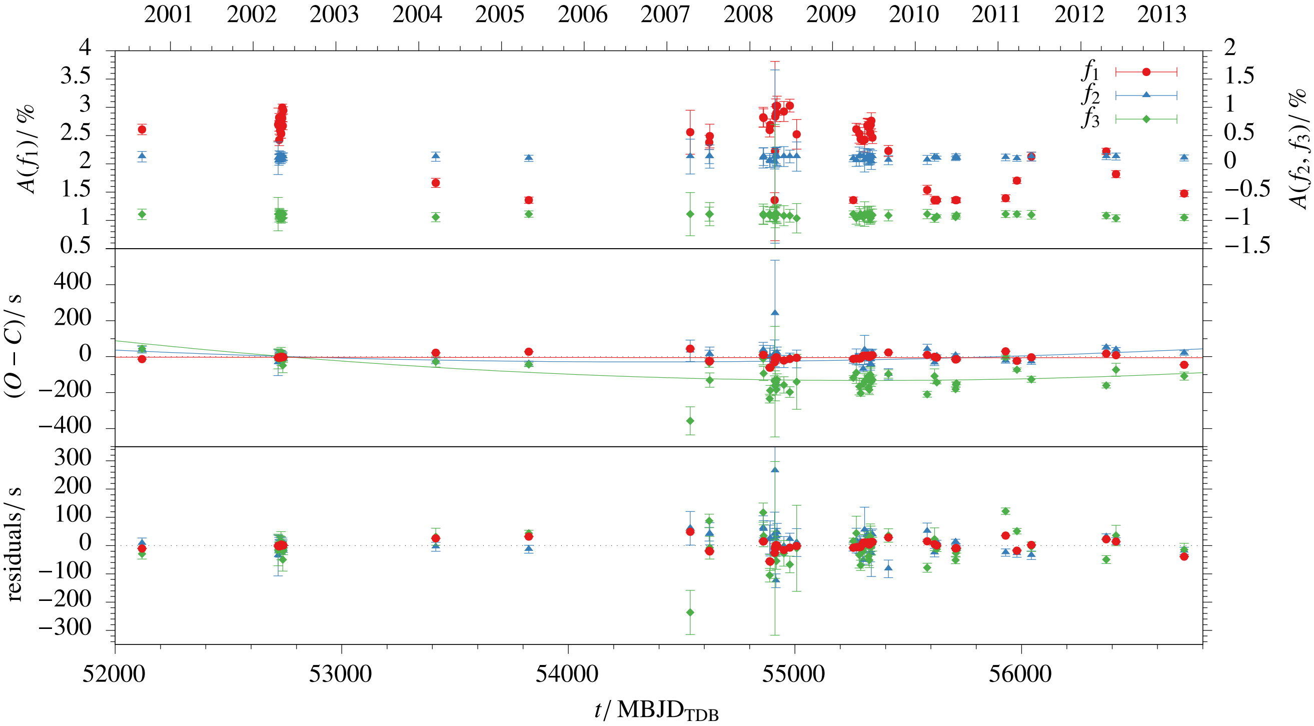

Fig. 12. Results for the three main pulsations of QQ Vir. *Top panel*: amplitudes. f_3 has a vertical offset of −1 for clarity. *Middle panel*: fits of the O–C data with second order polynomials in time. *Lower panel*: residuals.

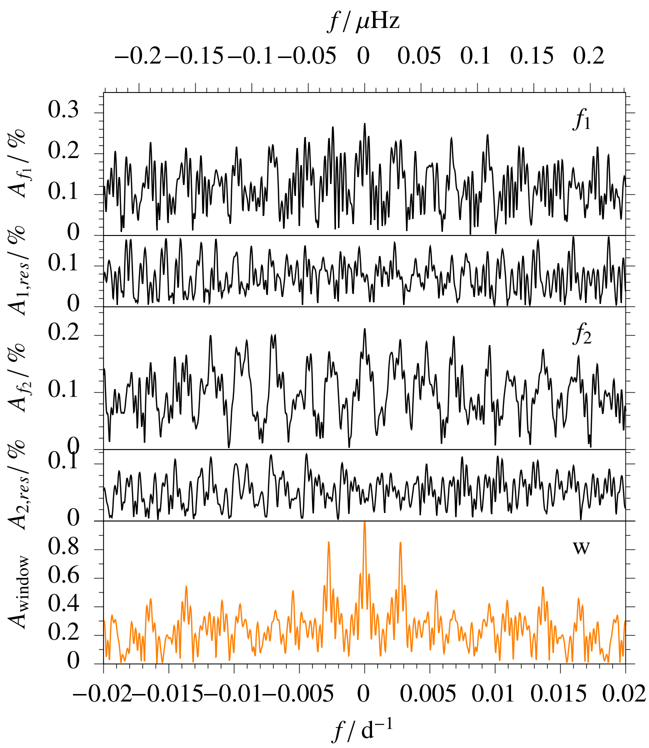

Fig. 13. Amplitude spectrum of V541 Hya of the main pulsation frequency $f_1 = 635.32218\,\mathrm{d}^{-1}$ (*top*), $f_2 = 571.28556\,\mathrm{d}^{-1}$ (*middle*) with the respective residuals after the pre-whitening below and the normalised window-function (*bottom*).

periods and companion masses, assuming circular orbits, and compared these curves with the O–C measurements after subtracting the long-term variations.

For each synthetic O–C curve, we selected the phase that gives the best fit to the data using a weighted least squares algorithm. For each observational point, we computed the difference, in absolute value and in σ units (where σ is the O–C error), between O–C and the synthetic value. The greyscale in Figs. 16 and 17 corresponds to the mean value of this difference in σ units, which means that the presence of a companion is indicated by a minimum (bright areas) of this parameter. We see that in V1636 Ori, QQ Vir, and V541 Hya, the mean difference for f_1 is always very high, implying that the data are not compatible with a companion. However, these results are limited by the fact that the O–C diagrams of these stars are "contaminated" by other irregular variations, presumably due to other reasons like non-linear interactions between different pulsation modes, for example, and therefore these constraints to the orbital period and mass of a companion must be taken with some caution. For the f_2 and f_3 measurements, the mean difference to the synthetic data is smaller in sigma units (because of the larger uncertainties) and very uniform. The uncertainties of the O–C measurements are not small enough to favour a set of models in the period-mass parameter space.

For f_1 of DW Lyn, there is a significant minimum at about 1450 d (∼4 yr) and ∼5 $M_{♃}$[2], which is also well visible in the O–C diagram of Fig. 8. This periodicity is not visible in the second frequency f_2 which, however, has much larger error bars due to the much lower amplitude of f_2 with respect to f_1.

Lutz et al. (2011) described a periodicity at 80 days, detected for f_2. We can recover this signal, however, with a low significance. This would correspond to a light-travel time amplitude of 4 s (for $m \sin i \approx 15\,\mathrm{M}_{♃}$), which is smaller than the 15 s measured by Lutz et al. (2011). Nevertheless, this signal is not confirmed by f_1. Thus, we rule out a companion induced signal in the arrival times due to the lack of simultaneous signals in f_1

[2] 1 $M_{♃}$ (Jupiter mass) = 1.899×10^{27} kg.

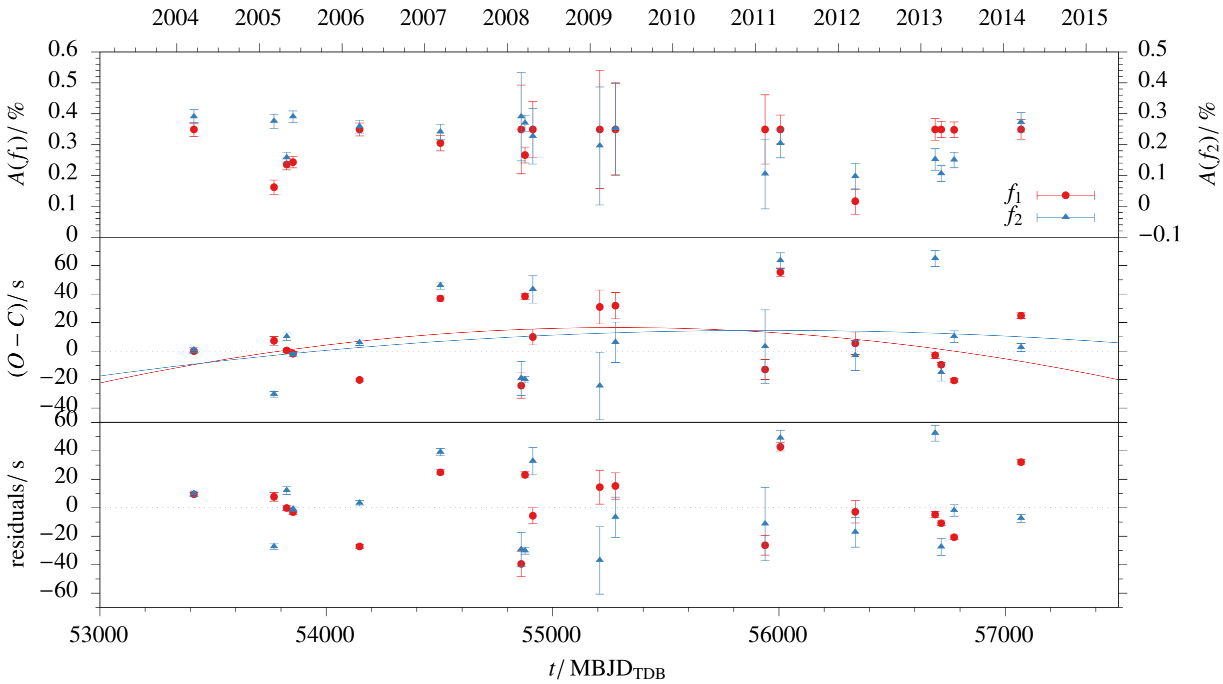

Fig. 14. Results for the two main pulsations of V541 Hya. *Top panel*: amplitudes. *Middle panel*: fits of the O–C data with second order polynomials in time. *Lower panel*: residuals.

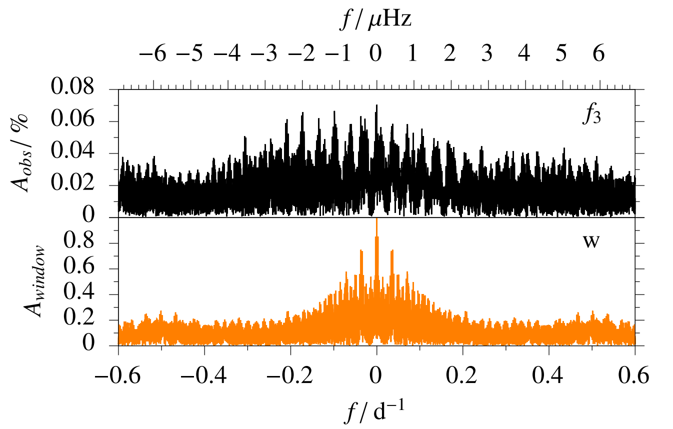

Fig. 15. Amplitude A spectrum with respect to the pulsation frequency f_3 = 603.88741 d^{-1} of V541 Hya (*top*) and the normalised window function (*bottom*).

and f_2 with similar amplitude. The tentative signal in f_2 is better explained by mode beating, as already described in Sect. 4.1. The variations seen in the first 200 days of the O–C diagram in Fig. 8 correspond to a periodicity of about 80 days and are accompanied by variations in the amplitude of the pulsation.

For V1636 Ori, Lutz (2011) predicted a period at 160 d and amplitude of 12 s. This can not be confirmed as a companion-induced signal. A periodic signal with an amplitude of 6.5 s (for $m \sin i \approx 15\,M_{♃}$) is indicated in the analysis of f_1, but at a low significance and accompanied by many other signals of similar significance. This periodicity is not confirmed by a significant signal in the measurements of f_2.

5. Summary and conclusion

In this work, we present ground-based multi-site observations for the four sdBs, DW Lyn, V1636 Ori, QQ Vir, and V541 Hya. We investigated variations in the arrival times of their dominant stellar pulsation modes to draw conclusions about secular period drifts and possible sub-stellar companions. All light curves are analysed homogeneously.

From the O–C measurements, we derive an evolutionary timescale from the change in period $\dot{P}$. Comparing to model calculations from Charpinet et al. (2002), we infer the evolutionary phase of the target. Although some $\dot{P}$ measurements are influenced by mode splitting, we can tell from the sign of $\dot{P}_1$ of DW Lyn that the star is likely still in the stage of central He burning. We can draw a similar conclusion from the sign of $\dot{P}$ of QQ Vir. The $\dot{P}$ measurements of V1636 Ori are likely affected by mode splitting, making it difficult to interpret the results in the context of stellar evolution. V541 Hya shows $\dot{P}$ measurements close to zero, which indicates the star being at the transition phase between He burning and contraction due to the depletion of He in the core.

Comparing the atmospheric properties from Table 1 with the evolutionary tracks for different models from Fig. 1 in Charpinet et al. (2002), we can confirm the hypothesis that DW Lyn and QQ Vir are in their He burning phase. V541 Hya agrees within 2σ of the $\log g$ measurement with one model at the turning point between the two evolutionary stages.

However, we can not exclude frequency and amplitude variations on smaller timescales than resolvable by our data set. Using temporally higher resolved *Kepler*-data of KIC 3527751, Zong et al. (2018) cautioned about long-term frequency or phase evolutions ascribing to non-linear amplitude and frequency modulations in pulsating sdBs. We see such effects already in our data set, even with a low temporal resolution compared to the *Kepler* sampling with a duty cycle of more than 90 per cent.

Observations on DW Lyn and V1636 Ori were published by Lutz et al. (2008a, 2011); Schuh et al. (2010); Lutz (2011). Our analysis of these observations, including extended data sets, do not confirm the tentative companion periods of 80 and 160 days,

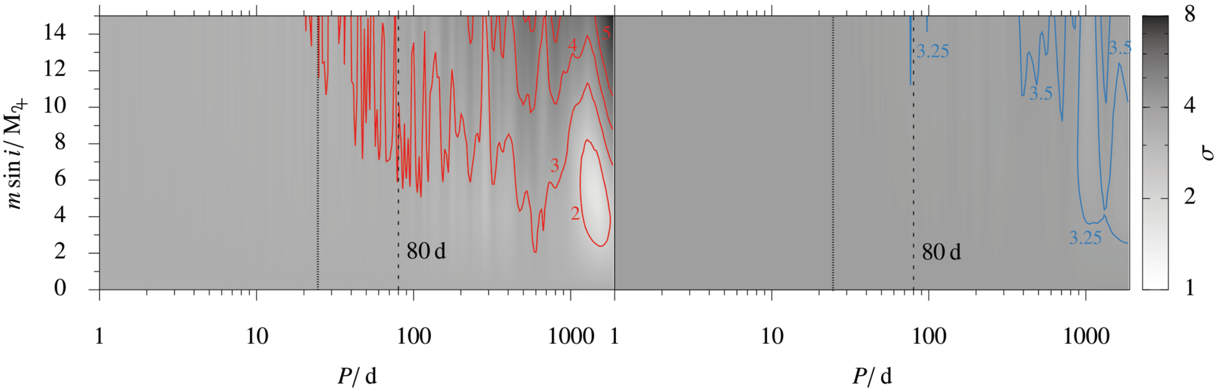

(a)

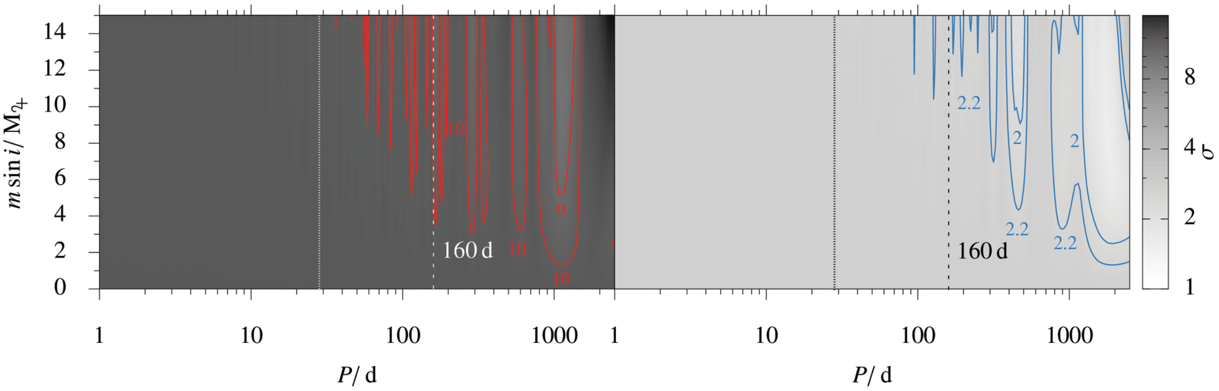

(b)

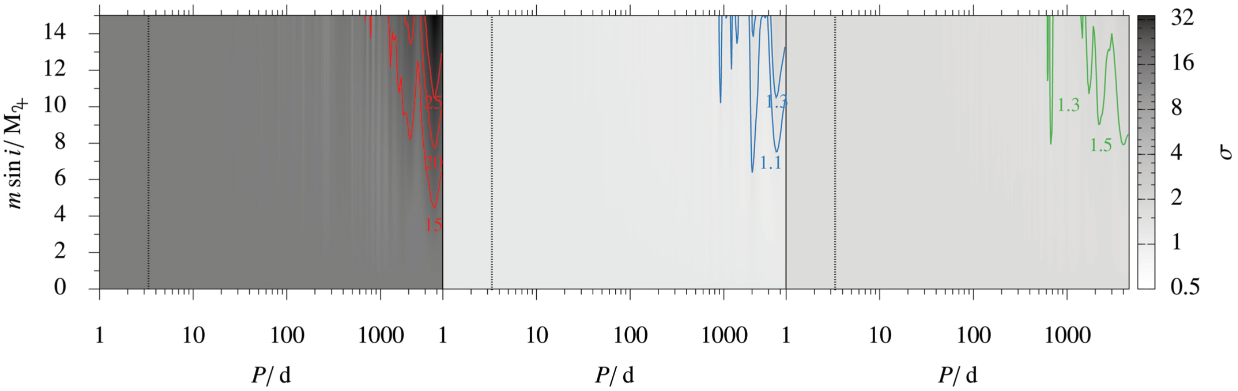

(c)

Fig. 16. Minimum companion mass as a function of orbital period. Greyscale shows the difference between the O–C measurements and artificial O–C data generated for a given combination of companion mass and orbit. We note that at this stage, the phase optimisation of the artificial data is done independently for each pulsation frequency. The median of gaps in between the epochs is indicated by a vertical dotted line. See text for more details. (*a*) DW Lyn. Contour lines for f_1 are placed at 2, 3, 4, and 5 σ (*left panel*), and for f_2 at 3.25 and 3.5 σ (*right panel*), as indicated by their labels. The planetary signal proposed by Lutz et al. (2011) at a period of 80 d is indicated as dashed line. (*b*) V1636 Ori. Contour lines for f_1 are placed at 9 and 10 σ (*left panel*), and for f_2 at 2 and 2.2 σ (*right panel*), as indicated by their labels. The planetary signal proposed by Lutz et al. (2011) at a period of 160 d is indicated as dashed line. (*c*) QQ Vir. Contour lines for f_1 are placed at 15, 20, and 25 σ (*left panel*), for f_2 at 1.1 and 1.3 σ (*middle panel*), and for f_3 at 1.3 and 1.5 σ (*right panel*), as indicated by their labels.

respectively. These signals more likely arise due to mode beating indicated by partly unresolved frequency multiplets and amplitude modulations.

Almost all analysed pulsation modes show formal significant changes in arrival times, but the amplitudes of these periodic signals do not correlate with frequencies, excluding the light-travel time effect due to orbital reflex motions for such variations and thus giving upper limits on companion masses. Only DW Lyn might have a planetary companion on a long orbital period, as indicated by one arrival time measurement. But this can not be confirmed with a second measurement, due to larger uncertainties. Additionally, more studies question the presence of already proposed companions, for example, Krzesinski (2015); Hutchens et al. (2017). Our unique sample of long-term observations shows

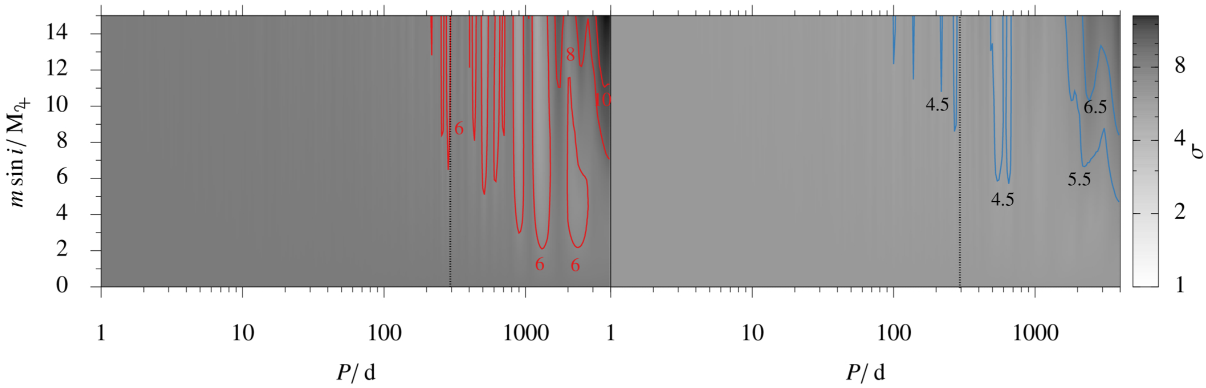

Fig. 17. Continuation of Fig. 16. V541 Hya. Contour lines for f_1 are placed at 6, 8, and 10 σ (*left panel*), and for f_2 at 4.5, 5.5, and 6.5 σ (*right panel*), as indicated by their labels.

a complex behaviour of mode- and amplitude interactions in sdBs which should be addressed in further studies. Until this has been addressed, caution is advised when interpreting O–C pulse arrival times in terms of companions.

Acknowledgements. We thank Wen-Shan Hsiao for observing at the Lulin Observatory and Mike D. Reed for observing at the Baker Observatory and Elia Leibowitz for observing at the WISE observatory. F.M. conducted the work in this paper in the framework of the International Max-Planck Research School (IMPRS) for Solar System Science at the University of Göttingen (Volkswagen Foundation project grant number VWZN3020). D.K. thanks the SAAO for generous allocations of telescope time and the National Research Foundation of South Africa and the University of the Western Cape for financial support. TDO gratefully acknowledges support from the U.S. National Science Foundation grant AST-0807919. L.M. was supported by the Premium Postdoctoral Research Program of the Hungarian Academy of Sciences. This project has been supported by the Lendület Program of the Hungarian Academy of Sciences, project No. LP2018-7/2019. Based on observations made with the Italian Telescopio Nazionale *Galileo* (TNG) operated on the island of La Palma by the Fundación Galileo Galilei of the INAF (Istituto Nazionale di Astrofisica) at the Spanish Observatorio del Roque de los Muchachos of the Instituto de Astrofisica de Canarias. Based on observations collected at the Centro Astronómico Hispánico en Andalucía (CAHA) at Calar Alto, operated jointly by the Andalusian Universities and the Instituto de Astrofísica de Andalucía (CSIC). Based on observations collected at Copernico telescope (Asiago, Italy) of the INAF – Osservatorio Astronomico di Padova. Based on observations made with the Nordic Optical Telescope, operated by the Nordic Optical Telescope Scientific Association at the Observatorio del Roque de los Muchachos, La Palma, Spain, of the Instituto de Astrofisica de Canarias. This paper includes data collected by the TESS mission. Funding for the TESS mission is provided by the NASA Explorer Program.

References

Astropy Collaboration (Robitaille, T. P., et al.) 2013, A&A, 558, A33
Astropy Collaboration (Price-Whelan, A. M., et al.) 2018, AJ, 156, 123
Ballard, S., Fabrycky, D., Fressin, F., et al. 2011, ApJ, 743, 200
Baran, A., Pigulski, A., Kozieł, D., et al. 2005, MNRAS, 360, 737
Baran, A. S., Østensen, R. H., Telting, J. H., et al. 2018, MNRAS, 481, 2721
Barlow, B. N., Dunlap, B. H., & Clemens, J. C. 2011a, ApJ, 737, L2
Barlow, B. N., Dunlap, B. H., Clemens, J. C., et al. 2011b, MNRAS, 414, 3434
Benatti, S., Silvotti, R., Claudi, R. U., et al. 2010, ArXiv e-prints [arXiv:1012.0747]
Bischoff-Kim, A., Provencal, J. L., Bradley, P. A., et al. 2019, ApJ, 871, 13
Blokesz, A., Krzesinski, J., & Kedziora-Chudczer, L. 2019, A&A 627, A86
Bonanno, A., Catalano, S., Frasca, A., Mignemi, G., & Paternò, L. 2003a, A&A, 398, 283
Bonanno, A., Frasca, A., Lanza, A. F., et al. 2003b, Balt. Astron., 12, 287
Charpinet, S., Fontaine, G., Brassard, P., et al. 1997, ApJ, 483, L123
Charpinet, S., Fontaine, G., Brassard, P., & Dorman, B. 2002, ApJS, 140, 469
Charpinet, S., Silvotti, R., Bonanno, A., et al. 2006, A&A, 459, 565
Charpinet, S., Fontaine, G., Brassard, P., et al. 2011, Nature, 480, 496
Charpinet, S., Giammichele, N., Zong, W., et al. 2018, Open Astron., 27, 112
Dreizler, S., Schuh, S. L., Deetjen, J. L., Edelmann, H., & Heber, U. 2002, A&A, 386, 249
Eastman, J., Siverd, R., & Gaudi, B. S. 2010, PASP, 122, 935
Fontaine, G., Brassard, P., Charpinet, S., et al. 2003, ApJ, 597, 518
Green, E. M., Fontaine, G., Reed, M. D., et al. 2003, ApJ, 583, L31
Han, Z., Podsiadlowski, P., Maxted, P. F. L., Marsh, T. R., & Ivanova, N. 2002, MNRAS, 336, 449
Heber, U. 1986, A&A, 155, 33
Heber, U. 2016, PASP, 128, 082001
Hutchens, Z. L., Barlow, B. N., Soto, A. V., et al. 2017, Open Astron., 26, 252
Jones, E., Oliphant, T., & Peterson, P. 2011, SciPy: Open Source Scientific Tools for Python, https://www.scipy.org/
Kilkenny, D. 2010, Ap&SS, 329, 175
Kilkenny, D. 2014, MNRAS, 445, 4247
Kilkenny, D., Koen, C., Stobie, R. S., et al. 1997, Third Conf. Faint Blue Stars (USA: L. David), 77
Kilkenny, D., Stobie, R. S., O'Donoghue, D., et al. 2006, MNRAS, 367, 1603
Krzesinski, J. 2015, A&A, 581, A7
Lee, J. W., Hinse, T. C., Youn, J.-H., & Han, W. 2014, MNRAS, 445, 2331
Lutz, R. 2011, Ph.D. thesis, University of Gottingen, Gottingen, Germany
Lutz, R., Schuh, S., Silvotti, R., et al. 2008a, ASP Conf. Ser., 392, 339
Lutz, R., Schuh, S., Silvotti, R., Kruspe, R., & Dreizler, S. 2008b, Commun. Asteroseismol., 157, 185
Lutz, R., Schuh, S., & Silvotti, R. 2011, AIP Conf. Ser., 1331, 155
Maxted, P. F. L., Heber, U., Marsh, T. R., & North, R. C. 2001, MNRAS, 326, 1391
Murphy, S. J., Bedding, T. R., & Shibahashi, H. 2016, ApJ, 827, L17
Østensen, R., Heber, U., Silvotti, R., et al. 2001, A&A, 378, 466
Østensen, R. H., Reed, M. D., Baran, A. S., & Telting, J. H. 2014, A&A, 564, L14
Otani, T., Oswalt, T. D., Lynas-Gray, A. E., et al. 2018, ApJ, 859, 145
Podsiadlowski, P. 2008, ASP Conf Ser., 401, 63
Postnov, K. A., & Yungelson, L. R. 2014, Liv. Rev. Rel., 17, 60
Provencal, J. L., Montgomery, M. H., Kanaan, A., et al. 2009, ApJ, 693, 564
Qian, S. B., Han, Z. T., Lajús, E. F., et al. 2015, ApJS, 221, 17
Randall, S. K., Van Grootel, V., Fontaine, G., Charpinet, S., & Brassard, P. 2009, A&A, 507, 911
Reed, M. D., O'Toole, S. J., Terndrup, D. M., et al. 2007a, ApJ, 664, 518
Reed, M. D., Terndrup, D. M., Zhou, A.-Y., et al. 2007b, MNRAS, 378, 1049
Ricker, G. R., Winn, J. N., Vanderspek, R., et al. 2015, J. Astron. Teles. Instrum. Sys., 1, 014003
Schaffenroth, V., Barlow, B. N., Drechsel, H., & Dunlap, B. H. 2015, A&A, 576, A123
Schuh, S., Dreizler, S., Deetjen, J. L., Heber, U., & Geckeler, R. D. 2000, Balt. Astron., 9, 395
Schuh, S., Huber, J., Dreizler, S., et al. 2006, A&A, 445, L31
Schuh, S., Silvotti, R., Lutz, R., et al. 2010, Ap&SS, 329, 231
Silvotti, R. 2008, ASP Conf. Ser., 392, 215
Silvotti, R., Østensen, R., Heber, U., et al. 2002, A&A, 383, 239
Silvotti, R., Bonanno, A., Bernabei, S., et al. 2006, A&A, 459, 557
Silvotti, R., Schuh, S., Janulis, R., et al. 2007, Nature, 449, 189
Silvotti, R., Charpinet, S., Green, E., et al. 2014, A&A, 570, A130
Silvotti, R., Schuh, S., Kim, S.-L., et al. 2018, A&A, 611, A85
Stello, D., Arentoft, T., Bedding, T. R., et al. 2006, MNRAS, 373, 1141
Sterken, C. 2005, ASP Conf. Ser., 335, 3
Stumpe, M. C., Smith, J. C., Van Cleve, J. E., et al. 2012, PASP, 124, 985
Telting, J. H., & Østensen, R. H. 2004, A&A, 419, 685
Webbink, R. F. 1984, ApJ, 277, 355
Wolszczan, A., & Frail, D. A. 1992, Nature, 355, 145
Zong, W., Charpinet, S., Fu, J.-N., et al. 2018, ApJ, 853, 98

Appendix A: TESS data

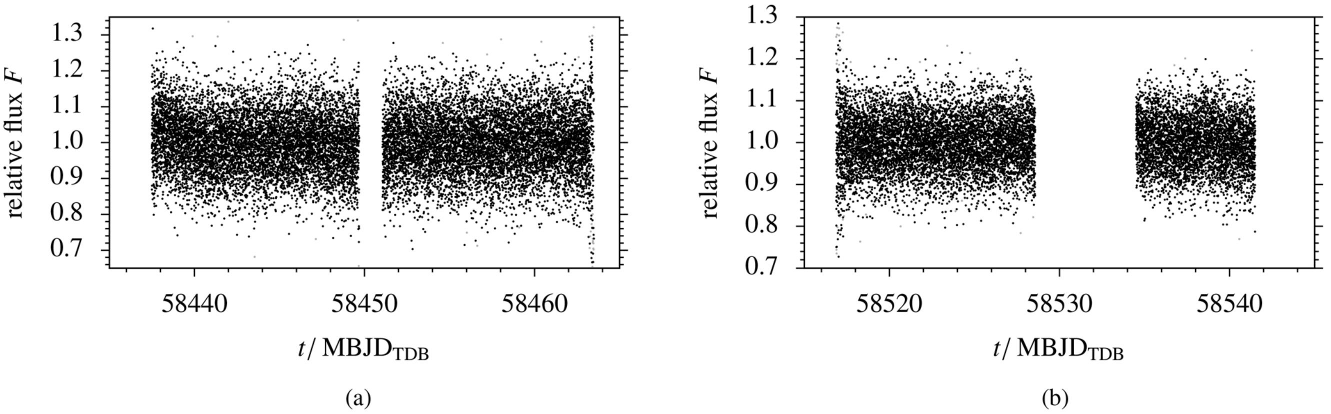

Fig. A.1. Light curves of the TESS observations. Grey points are considered outliers and partially exceeding the plotting range. (*a*) V1636 Ori. (*b*) V541 Hya.

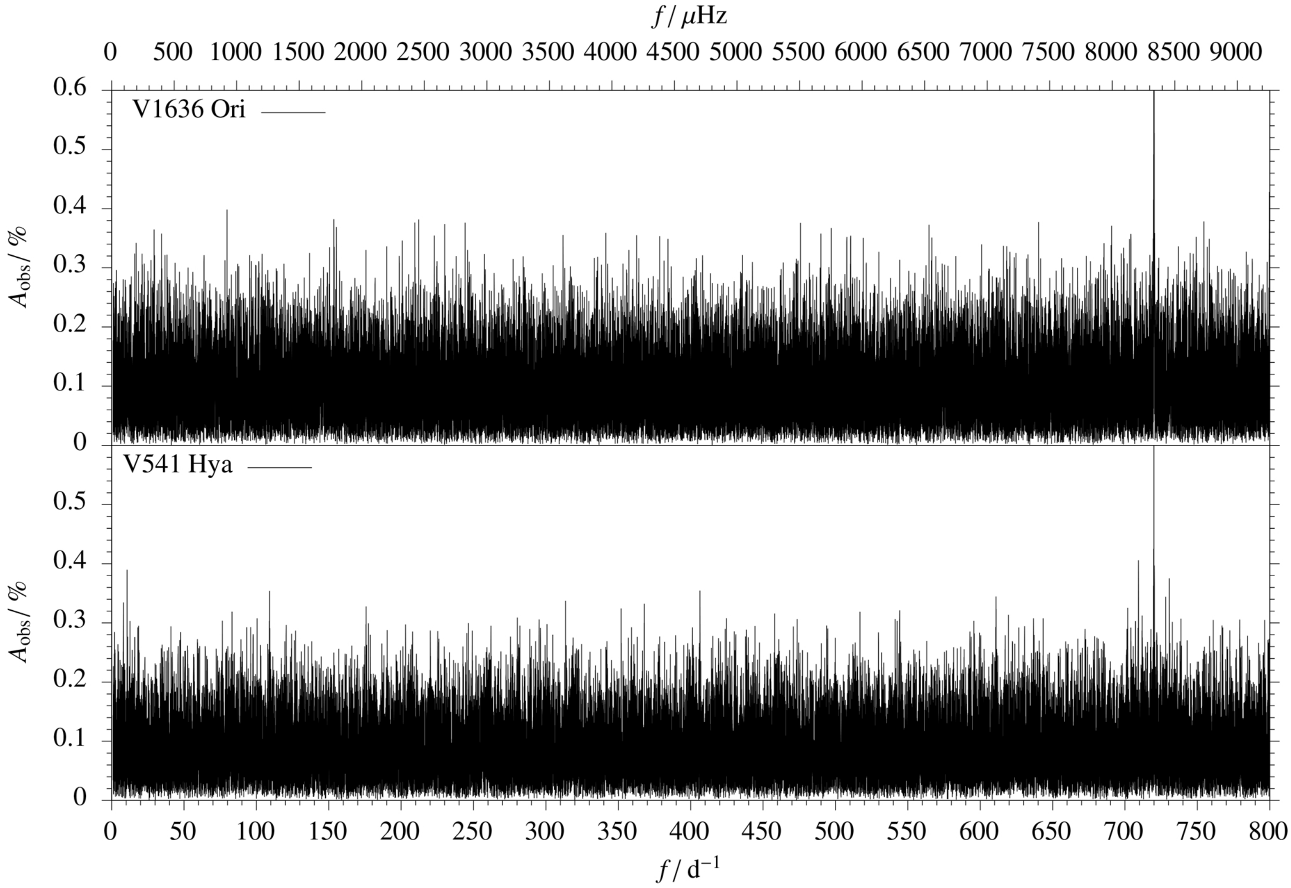

Fig. A.2. Amplitude A spectrum of the TESS observations. *Upper panel*: spectrum of V1636 Ori. *Lower panel*: spectrum of V541 Hya. The only peak above the noise level is the 120 s alias due to the cadence of the observations.

Appendix B: Amplitude spectra

Table B.1. Additional pulsation modes identified for our targets not used in the O–C analysis due to their low S/N.

Target	f/d^{-1}	$A/\%$
DW Lyn	475.8231(2)	0.09(18)
	319.4042(3)	0.06(12)
	463.0100(6)	0.03(18)
V1636 Ori	566.24031(3)	0.6(3)
QQ Vir	733.0704(1)	0.3(1)
	664.4886(1)	0.2(1)
	572.73611(5)	0.19(9)
	664.7122(1)	0.1(1)
	434.1522(6)	0.01(7)
	502.410(2)	0.01(9)
V541 Hya	531.16759(16)	0.03(7)
	603.88741(6)	0.03(8)

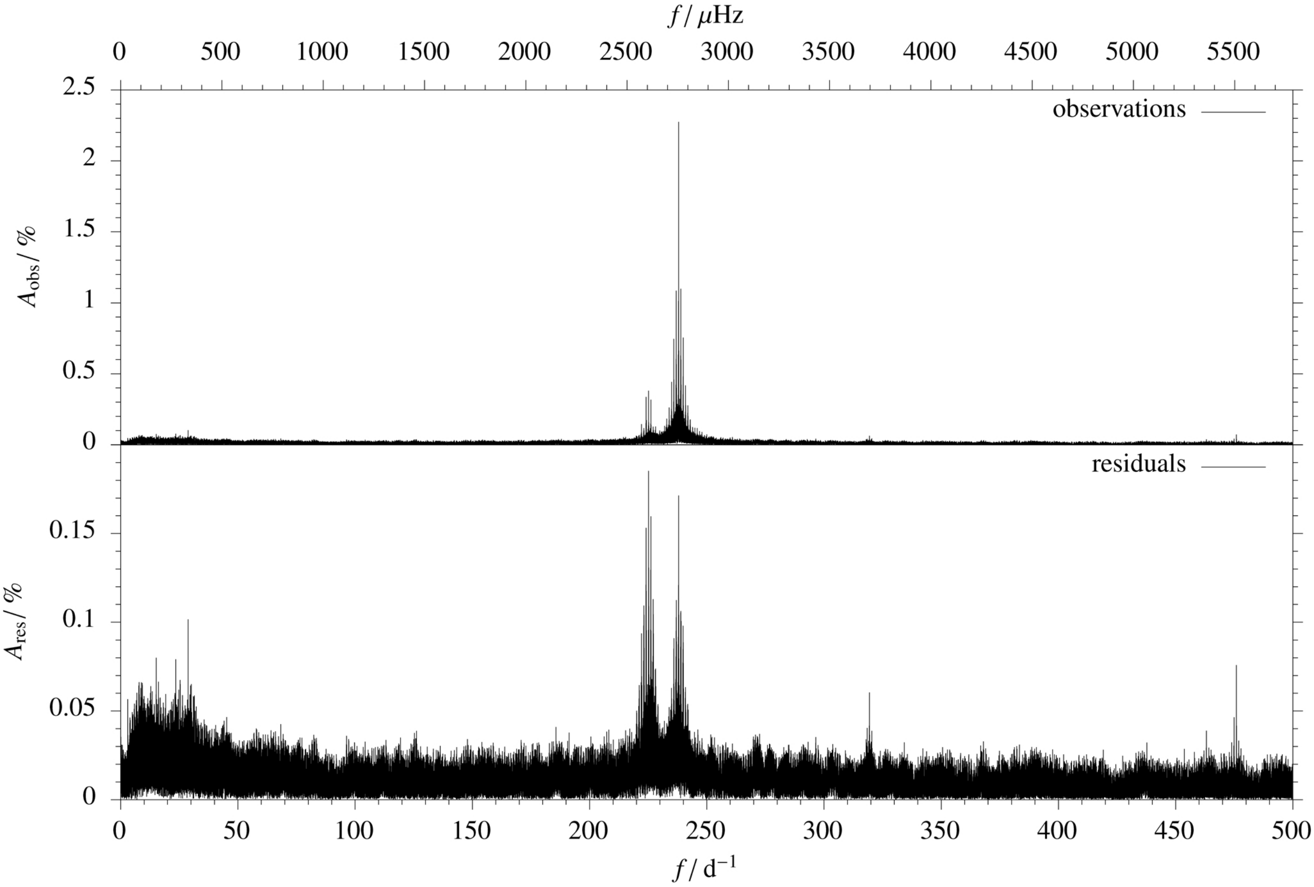

Fig. B.1. Amplitude spectrum of DW Lyn. *Upper panel*: observations $A_{\rm obs}$. *Lower panel*: residuals $A_{\rm res}$ after subtracting the light curve models from the observations.

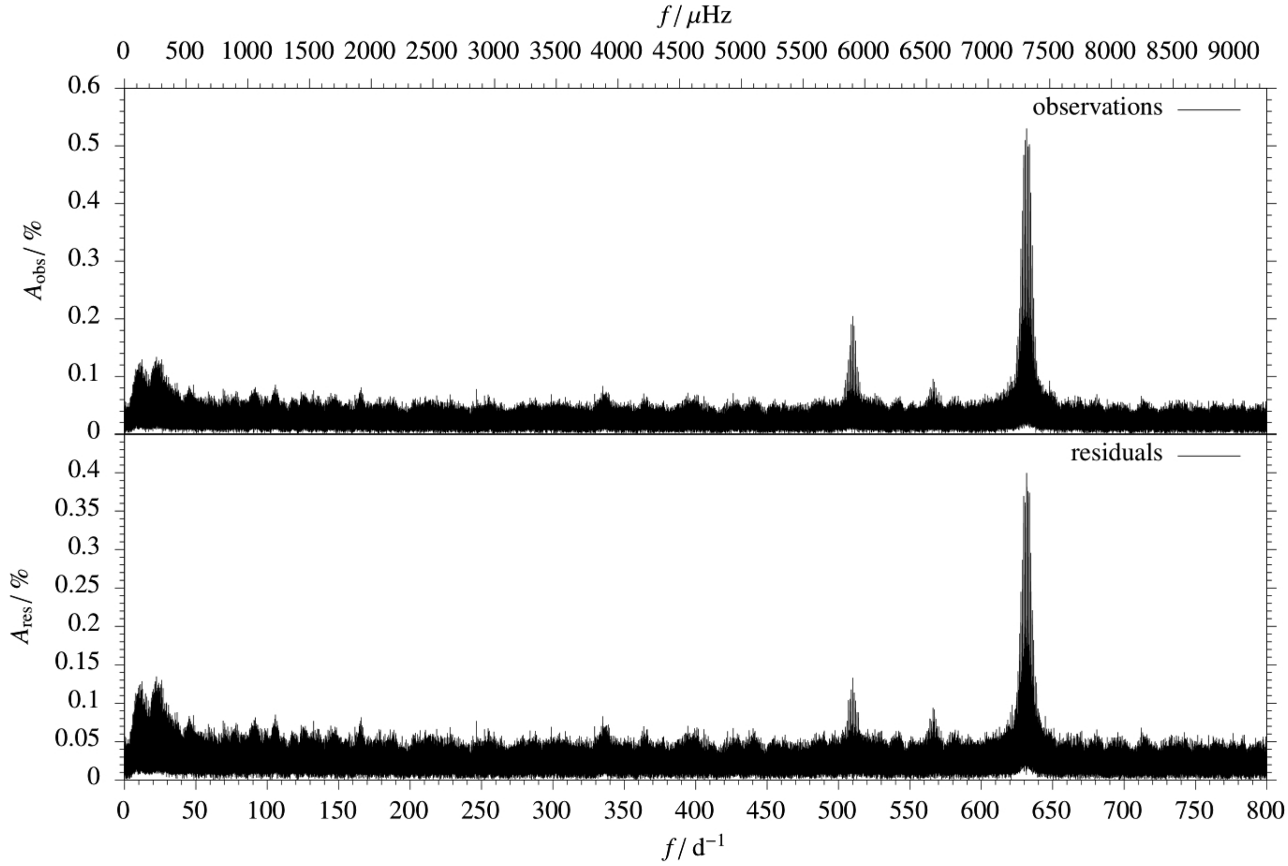

Fig. B.2. Same as Fig. B.1 but for V1636 Ori.

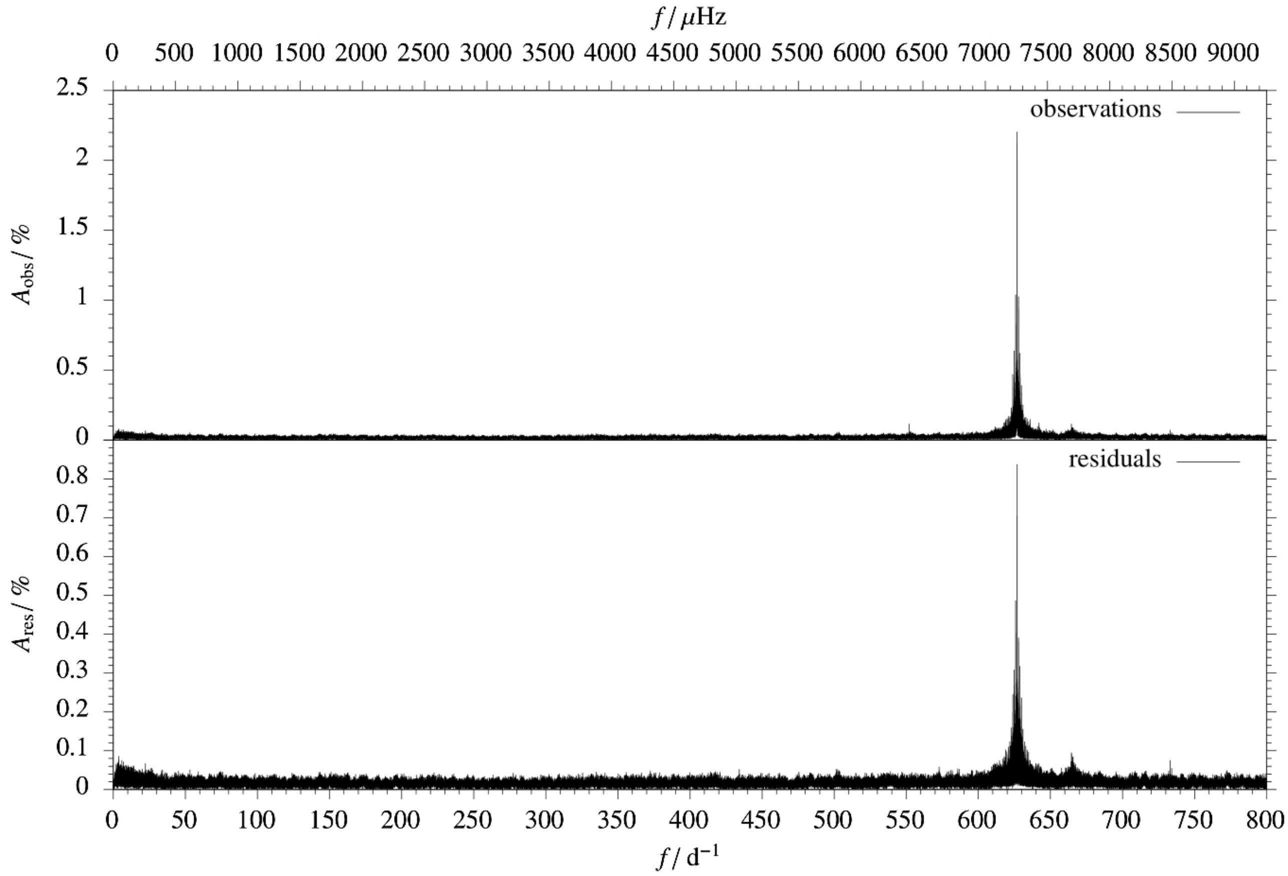

Fig. B.3. Same as Fig. B.1 but for QQ Vir.

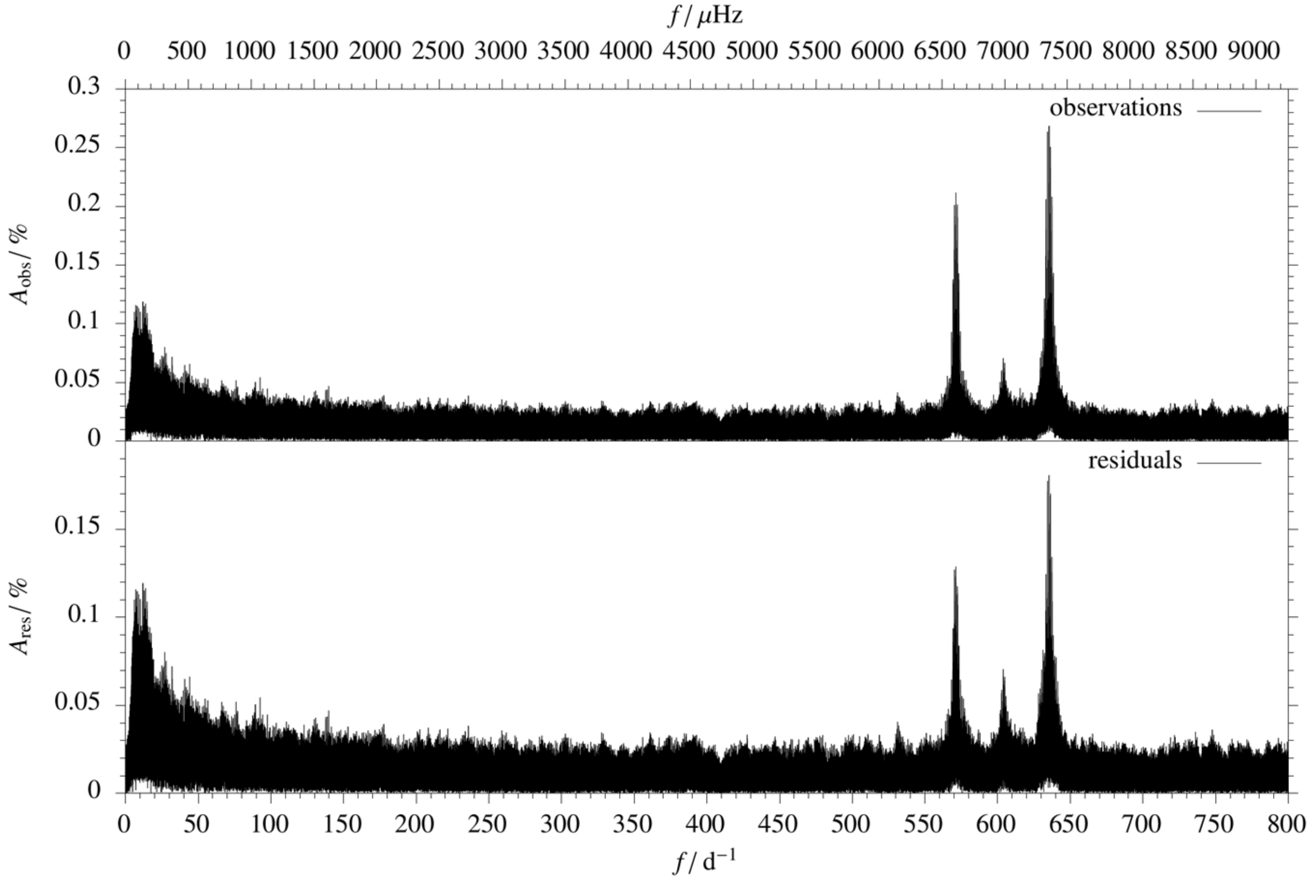

Fig. B.4. Same as Fig. B.1 but for V541 Hya.

Research in Astronomy and Astrophysics

PAPER

Discovery of extended structures around two evolved planetary nebulae M2–55 and Abell 2

To cite this article: Chih-Hao Hsia *et al* 2020 *Res. Astron. Astrophys.* **20** 107

RAA 2020 Vol. **20** No. **7**, 107(12pp) doi: 10.1088/1674–4527/20/7/107

http://www.raa-journal.org *http://iopscience.iop.org/raa*

Research in Astronomy and Astrophysics

Discovery of extended structures around two evolved planetary nebulae M 2–55 and Abell 2

Chih-Hao Hsia (夏志浩)[1], Yong Zhang (张泳)[2], Xi-Liang Zhang (张西亮)[3] and Tao Luo (骆韬)[1]

[1] State Key Laboratory of Lunar and Planetary Sciences, Macau University of Science and Technology, Taipa, Macau, China; *chhsia@must.edu.mo*

[2] School of Physics and Astronomy, Sun Yat-Sen University Zhuhai Campus, Tangjia, Zhuhai 519082, China; *zhangyong5@mail.sysu.edu.cn*

[3] Yunnan Observatories, Chinese Academy of Sciences, Kunming 650216, China

Received 2019 December 11; accepted 2020 March 4

Abstract We report a multi-wavelength study of two evolved planetary nebulae (PNs) M 2–55 and Abell 2. Deep optical narrow-band images ([O III], Hα, and [N II]) of M 2–55 reveal two pairs of bipolar lobes and a new faint arc-like structure. This arc-shaped filament around M 2–55 appears as a well-defined boundary from southwest to southeast, strongly suggesting that this nebula is in interaction with its surrounding interstellar medium. From the imaging data of *Wide-field Infrared Survey Explorer* (WISE) all-sky survey, we discovered extensive mid-infrared halos around these PNs, which are approximately twice the size of their main nebulae seen in the visible. We also present a mid-resolution optical spectrum of M 2–55, which shows that it is a high-excitation evolved PN with a low electron density of 250 cm^{-3}. Furthermore, we investigate the properties of these nebulae from their spectral energy distributions (SEDs) by means of archival data.

Key words: infrared: ISM — ISM: structure — planetary nebulae: individual (M 2–55 and Abell 2) — stars: AGB and post-AGB

1 INTRODUCTION

As descendants of asymptotic giant branch (AGB) stars, planetary nebulae (PNs) are important objects to understand galactic abundance distribution and the ending of stellar evolution of low- and intermediate-mass stars. When the infrared (IR) technique was first developed, the PN NGC 7027 was found to have a strong excess in the IR, far above the continuum level expected from thermal free-free emission (Gillett et al. 1967). This excess was soon identified as due to thermal dust emission. From the fact that PNs are descendants of AGB stars, Kwok (1982) predicted that the remaining circumstellar dust envelope from AGB stars should be commonly detectable in PNs. The predictions were confirmed by the *Infrared Astronomical Satellite* (IRAS) observations, where over 1000 PNs were detected (Pottasch et al. 1984). The relative contributions from the stellar, nebular free-bound (f-b) and free-free (f-f) components, and dust continuum emissions in PNs have been analyzed by many researchers such as Zhang & Kwok (1991) and Hsia et al. (2014).

The faint structures around PNs in the visible have been studied in several surveys (e.g., Stanghellini et al. 1993; Corradi et al. 2003; Cohen et al. 2011). Comparing with the observations at optical wavelengths, IR observations are less likely to be affected by the interstellar extinction. Thus it is highly desirable to observe faint structures around PNs in the IR. Moreover, unlike IR emissions, optical emissions are dominated by ionized gas. Therefore, a comparison study between IR and optical images allow us to better understand the processes of dust and gas components. Recent IR surveys have revealed new structures surrounding PNs (Ramos-Larios & Phillips 2009; Zhang et al. 2012a,b), these results suggest that PNs may reveal different morphologies in the optical and IR. The *Wide-field Infrared Survey Explorer* (WISE) survey covers entire sky area and its sensitivity is 100 times higher than IRAS (Wright et al. 2010). Thus, this survey provides a useful tool for us to resolve PNs with higher sensitivities

(Benjamin et al. 2003; Churchwell et al. 2009) and detect weak emissions from extended structures of known PNs.

Evolved PNs represent the last stage of the dispersion of stellar material into the interstellar medium (ISM). Gurzadyan (1969) first suggested that the interaction between PN and the ISM can decelerate the nebula. The observational evidence of PN-ISM interaction was later reported by Jacoby (1981). The signs of PN-ISM interactions have been found to be common among evolved PNs (Borkowski et al. 1990). To search and investigate the nebula/ISM boundary of evolved PNs can provide significant clue to study the mass-loss history of these objects and the matter enhancement in the galaxy.

The PNs M 2–55 (PN G116.2+08.5, IRAS 23296+7005) and Abell 2 (PN G122.1–04.9, IRAS 00426+5741) were first discovered and identified as evolved PNs by R. Minkowski in 1947 and Abell (1955) according to their low surface brightnesses and large angular diameters (Abell 1966). Based on early imaging studies, these objects have been classified as an irregular PN (Felli & Perinotto 1979) for M 2–55 and an elliptical nebula (Hua 1988) for Abell 2, respectively. Although their angular sizes ($\sim 60''$) are relatively larger than most PNs ($\sim 10''$–$30''$), they have rarely been paid attention in the past thirty years. After a keyword search in the astrophysics data system (ADS) for these objects, only four records were found in the literature. The distance determination of PNs has long been a difficult problem. Recently, trigonometric parallex data release (DR) of Gaia mission has induced an investigation of reliable distances for many PNs (Bailer-Jones et al. 2018), allowing us to evaluate the distances of these two PNs with a higher accuracy.

In this paper, we present the results of a multi-wavelength investigation for PNs M 2–55 and Abell 2 based on optical and mid-infrared (MIR) images taken from *Lulin One-meter Telescope* and *WISE* all-sky survey, respectively, aiming to investigate the natures of the two PNs and their PN-ISM interactions. In Section 2, we describe the observations and data reductions. The results of imaging and spectroscopic observations in the optical and MIR are presented in Section 3. An analysis of the properties of the sources by analyzing their spectral energy distributions (SEDs) are presented in Section 4. A discussion and conclusions are summarized in Section 5 and Section 6, respectively.

2 OBSERVATIONS AND DATA REDUCTION

2.1 LOT Narrow-band Imaging

Narrow-band Images of these nebulae were obtained from the *Lulin One-meter Telescope* (LOT) on the Lulin Observatory of National Central University (NCU) on the nights of 2018 November 4 – 2019 November 16. The Lulin Compact Imager (LCI) Sophia 2048B camera with a 2048×2048 CCD was used. The CCD camera has a field of view (FOV) of $13.2' \times 13.2'$ with an angular resolution of $0.39''$. These PNs were observed with three narrow-band filters: [O III] ($\lambda_c = 5009$ Å, $\Delta\lambda = 30$ Å), Hα ($\lambda_c = 6563$ Å, $\Delta\lambda = 30$ Å), and [N II] ($\lambda_c = 6584$ Å, $\Delta\lambda = 10$ Å). The total exposures ranged from 7200 to 31 800 s for each filter of the deep observations. We process all imaging data using the IRAF software package. Dark-current correction, bias subtraction, and flat-field calibration were performed. A summary of these observations is given in Table 1. The reduced [OIII], Hα, and [NII] images of these nebulae are shown in Figures 1 and 2, respectively.

2.2 YFOSC Optical Spectra

The spectra of M 2–55 were obtained on the nights of 2018 December 02 – 03, with the *Lijiang 2.4 m* telescope of the Yunnan Astronomy Observatories of China. The *Yunnan Faint Object Spectrograph and Camera* (YFOSC) instrument and an E2V 2048×4608 CCD were used. The spectral dispersion of the spectra is $\sim$1.7 Å pixel^{-1}. The seeing conditions varied from $1.7''$ and $2.3''$ during the observing runs. The wavelength coverage of spectroscopic observations is between 3600 and 7700 Å. The aperture size of a slit is $5' \times 1.8''$ and it was set through the central region of this nebula oriented toward the N-S direction. The exposures ranged from 1800 to 11 700 s and then the signal-to-noise (S/N) ratios of > 75 for main nebula were produced.

The data were reduced by a standard procedure using the NOAO IRAF V2.16 software package, including background subtraction, flat-fielding, and debiasing. For flux calibration, three KPNO standard stars each night were observed. To improve the S/N ratio, the final spectrum of this nebula was produced using the spectra with individual exposures. The journal of spectroscopic observations is given in Table 2.

Gaussian line profile fitting is used for measuring the fluxes of line emissions of this object. The uncertainties of line fluxes are derived from the continuum noise level. If we consider the flux errors of the measurements, the characteristic uncertainties of line emissions are about $\sim$5% – 37%.

2.3 WISE Infrared Observations

MIR images of these PNs were taken from the *WISE* all-sky survey. The WISE mission has imaged all sky with four bands at 3.4, 4.6, 12, and 22 μm (W1–W4). The angular resolutions of the images for these four bands are $6.1''$,

Table 1 Summary of Narrow-band Imaging Observations

Object	Observation Date	Filter	λ_c (Å)	$\triangle\lambda$ (Å)	Seeing (arcsec)	Exposure (s)
M 2–55	2018 Nov. 04	Hα	6563	30	2.1	600$\times$20
	2018 Nov. 05	Hα	6563	30	1.7	1800$\times$11
	2018 Nov. 07	[O III]	5007	30	2.3	1800$\times$4
	2018 Nov. 07	[N II]	6584	10	2.6	1800$\times$7
Abell 2	2018 Nov. 05	Hα	6563	30	1.8	1800$\times$7
	2018 Nov. 06	Hα	6563	30	1.9	1800$\times$5
	2018 Nov. 06	[O III]	5007	30	2.2	1800$\times$5
	2019 Oct. 13	[O III]	5007	30	1.8	1800$\times$5
	2019 Oct. 16	[N II]	6584	10	1.4	1800$\times$4
	2019 Nov. 16	[N II]	6584	10	1.3	1800$\times$6

Table 2 Summary of *YFOSC* Spectroscopic Observations

Object	Observation Date	Wavelength (Å)	Dispersion (Å pix^{-1})	Width of Slit (arcsec)	Integration Time (s)
M 2–55	2018 Dec. 02	3600 – 7400	1.7	1.8	1800$\times$2
	2018 Dec. 03	3600 – 7400	1.7	1.8	2700$\times$3

6.4$''$, 6.5$''$, and 12$''$, respectively. The data used in this paper were retrieved from the NASA/IPAC Infrared Science Archive (IRSA)[1].

We performed the aperture photometric measurements for these nebulae using the method described in Hsia & Zhang (2014). The fluxes measured from the WISE images of these PNs have been calibrated using the color correction presented in Wright et al. (2010). To estimate the flux uncertainties, the standard deviations of systematic errors and all flux measurements are adopted. The estimated flux errors of the measurements in four bands for all objects are about 8% for W1, 9% for W2, 7% for W3, and 8% for W4 channels, respectively.

3 RESULTS

3.1 Optical Morphology

3.1.1 *Multipolar planetary nebula – M 2–55*

The PN of M 2–55 is originally classified as a B-class nebula with symmetrical structures (Sabbadin & Perinotto 1981). Our *LOT* narrow-band images (Hα, [O III], and [N II]) of the nebula (Fig. 1) clearly show that this object is a multipolar PN with a size of $\sim$67.6$''$, which is larger than the size of 39$''$ measured from the optical image reported by Acker et al. (1992). The appearance of M 2–55 is similar to that of the young PN M 1-30 (see fig. 1 of Hsia et al. 2014) and can be related to the quadrupolar PN (Manchado et al. 1996). The main structure of this PN consists two bipolar lobes (labeled as $a - a'$ and $b - b'$) and they are intersecting approximately at the central region of this object as shown in the Hα and [N II] images (Fig. 1).

[1] `http://irsa.ipac.caltech.edu/frontpage/`

From Figure 1, we can see that the edges of two bipolar lobes are sharp and they are prominent in the Hα and [N II] images. The central region of this nebula is mainly dominated by [O III] emission, while the lobes are more obscure in the [O III] image compared to those seen in the Hα and [N II] images. Several clumpy regions can be seen within the main nebula. These regions may be due to the projection of two interlaced lobes. We note that some ray-shaped structures and radial filaments pointing toward the outer regions can be seen in the deep Hα image. They may be the result of shadows of the clumpy region in the main nebula. These features can also be seen in other nebulae such as NGC 40, NGC 3242, NGC 3918, NGC 7009, NGC 7026, and NGC 7662 (Corradi et al. 2004). The position angles (PAs) of two pairs of lobes ($a - a'$ and $b - b'$) are measured to be PA $= 146^\circ \pm 3^\circ$ and $42^\circ \pm 3^\circ$. We measured the sizes of two lobes by fitting the shapes of these features to deep Hα image. Two pairs of bipolar lobes have approximately the same extent. The angular sizes of two bipolar lobes are measured to be 67.2$''\times$36.6$''$ and 65.5$''\times$34.3$''$ for lobes $a - a'$ and $b - b'$, respectively.

Adopting a distance of 691 pc for M 2–55 (Bailer-Jones et al. 2018), the extent size is 0.23 $\sec\theta$ pc for lobe $a - a'$, where θ is the inclination angle. The expansion velocity is assumed to be 20.3 km s^{-1} with [O III] emission (Weinberger 1989), the derived kinematic age of this nebula is about 5500 $\sec\theta$ yr. This estimation is in good agreement with the earlier suggestion that M 2–55 is an evolved PN (Sati$\bar{\text{o}}$ et al. 1999).

3.1.2 *Arc-like structure discovered around M 2–55*

The filamentary appearance of the halo as observational evidence can provide that the nebula interacts with high-

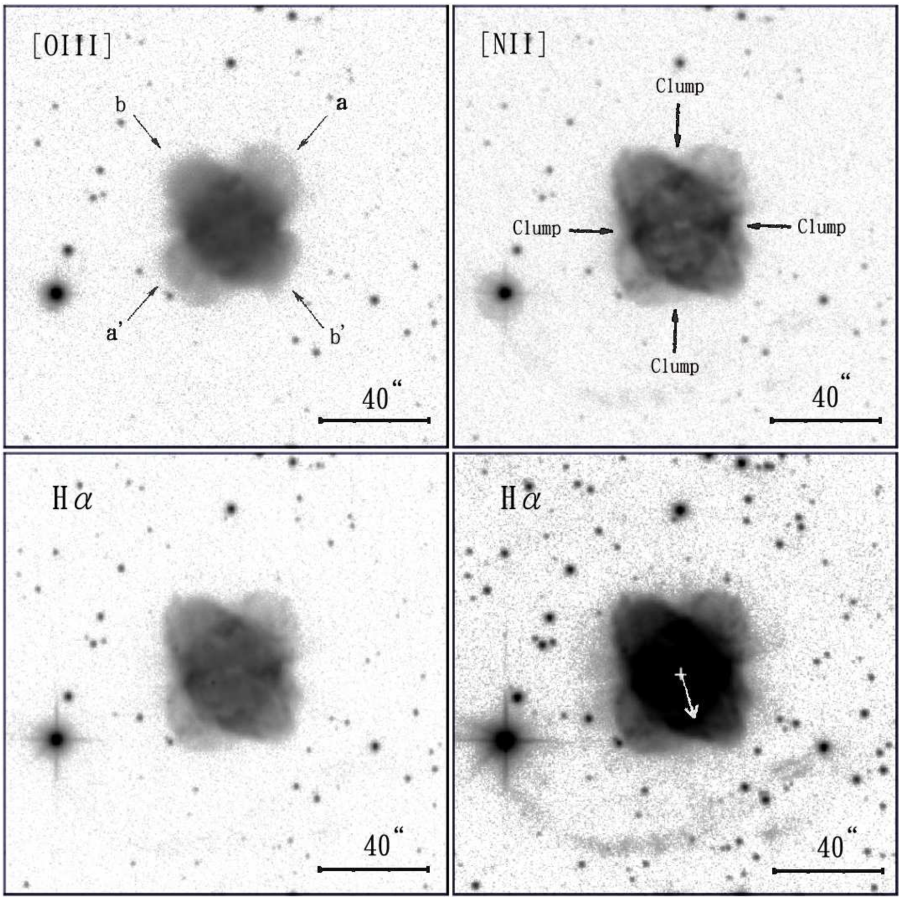

Fig. 1 Narrow-band images of M 2–55 in [O III] (*upper left*), [N II] (*upper right*), and Hα (*lower left and lower right*) displayed with a logarithmic intensity scale. East is to the left and north is up. In the main nebula, two bipolar lobes (labeled as $a - a'$ and $b - b'$) and several clumps can be seen. Lower right panel: Same as on the lower-left panel but shown at different intensity levels. Outer extended filaments around this PN can be detected in the deep Hα image. The position of the central star is marked with a *cross*. The *white line* denotes the direction of proper motion of this nebula.

density ISM (Dgani & Soker 1998; Ali et al. 2012). As a PN with low density moving through its surrounding ISM, the leading region of the halo is compressed and then the arc-like/bow-shock structure forms (Ali et al. 2012).

A new arc-like filament extending to $\sim$61″ from the central star of this nebula can be seen in our deep Hα image (see Fig. 1). The filamentary feature has not been detected in previous optical images. This arc shows a well-defined boundary from SW to SE, indicating that it may be a bow-shocked structure. The existence of this arc-shaped structure may suggest the PN-ISM interaction (Ramos-Larios et al. 2018; Wareing et al. 2007), which is supported by the proper motion direction of M 2–55 with PA $= 192^\circ$ (Roeser et al. 2010). The surface brightness (SB) profile of this filamentary feature with Hα emission is shown in Figure 3. We made this profile from the average of the intervals between PA $= 155^\circ$ and PA $= 185^\circ$, after removing all field stars. From Figure 3, the peak surface brightness of the arc-shaped structure (at the distance of 61″ from the central star) is $\sim 6\times10^{-2}$ times fainter than that of main nebula, and the feature is significantly brighter than the normal AGB halo (with a SB 10^{-3} times fainter than main shell; Corradi et al. 2003). Adopting a distance of 691 pc (Bailer-Jones et al. 2018) and assuming a typical expansion velocity of 13.7 km s^{-1} for this faint structure (Gussie & Taylor 1994), the observed size of this extended structure leads to a dynamical age of $\sim$15 000 yr. This suggests that the arc-like feature can be an important event of its AGB mass-loss history.

3.1.3 Double-shell planetary nebula – Abell 2

As can be seen in our narrow-band imaging, some structural features of PN Abell 2 show slightly different appearances which depends on the observed bands (Fig. 2). A close inspection of Figure 2 shows that two concentric elliptical shells (a brighter inner shell and a diffuse outer shell) are located in the main nebula. The limb-brightening

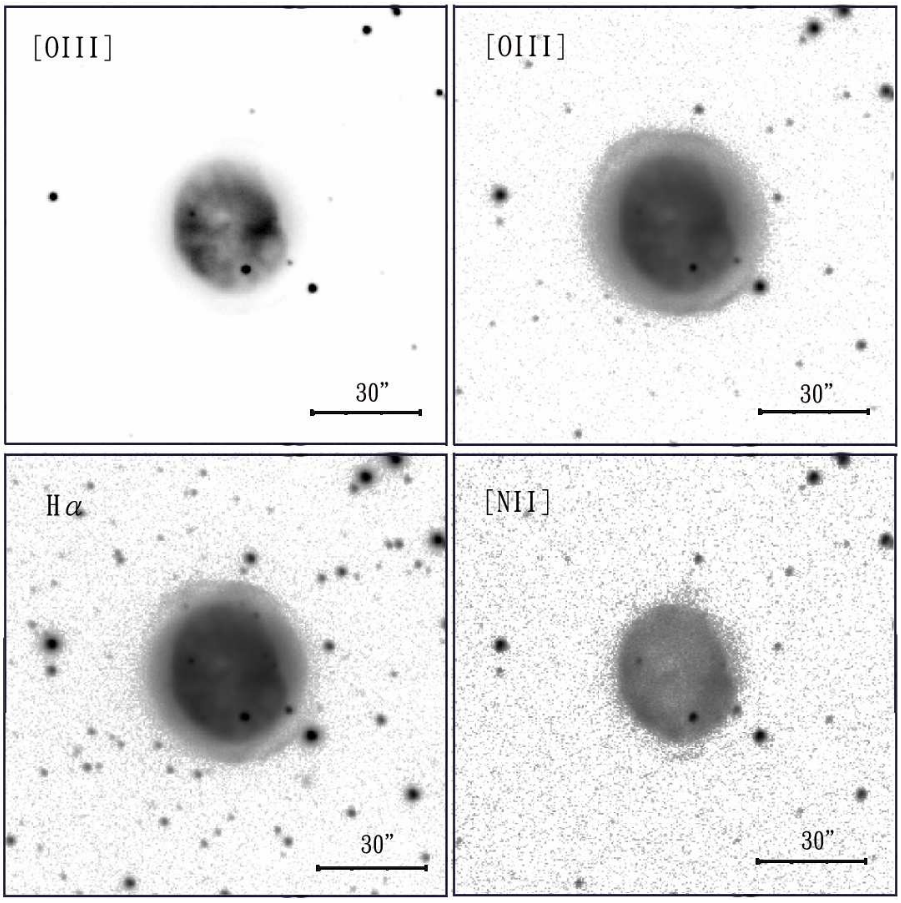

Fig. 2 (*Upper left*) Image of Abell 2 in [O III] displayed with a linear scale, where few clumpy structures can be seen in the inner shell. The [O III] (*upper right*), Hα (*lower left*), and [N II] (*lower right*) images of this object are displayed on a logarithmic intensity scale to show the outer shell of the nebula. North is up and east is to the left.

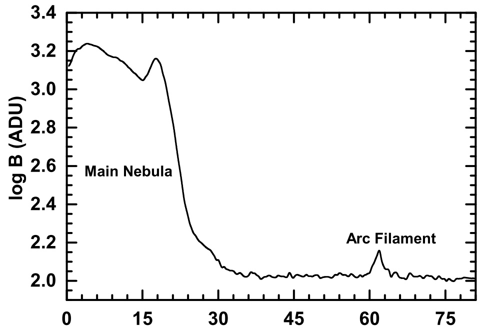

Fig. 3 Hα surface brightness profile in M 2–55 averaged over the angles between PA $= 155°$ and PA $= 185°$. The horizontal axis is the distance from the central star in units of arcsec. The position of the arc-shaped structure is marked.

inner shell has a size of $\sim$37.4$''\times$31.2$''$ and it is surrounded by a diffuse outer shell with a diameter of $\sim$52.3$''\times$47.6$''$, which is larger than previously reported size of 35$''\times$35$''$ (Hua 1988). The major axes of these shells are oriented along PA $= 33°$. From Figure 2, we can see that the inner elliptical shell with a clear boundary is prominent in Hα, [O III], and [N II] emissions, whereas the outer shell is undetectable in [N II]. These results suggest that the inner shell of this nebula is relatively lower excitation and outer diffuse shell farther away is relatively higher excitation, which is unusual among common PNs (Guerrero et al. 2018). Inside the inner shell of this nebula, a few small structural components can be seen in the [O III] and Hα images. The origin and formation of these structures are still unclear. It is possible that these features are produced from ionized non-uniform dense clumps. For this PN, the averaged value of nebular minor and major axial lengths as its size was adopted. At a distance of 2.82 kpc (Bailer-Jones et al. 2018), the average nebular size of this source is 0.68 pc, we obtained the dynamical age of $\sim$9 800 yr. Assuming an expansion velocity of the nebula is 34 km s^{-1} (Acker et al. 1992). This suggests that this nebula is indeed an old PN (Abell 1966; Hua 1988).

3.2 Extended Dust Halos around M 2–55 and Abell 2

To study the dust distributions and their properties of PNs M 2–55 and Abell 2, we have analyzed the MIR images of these nebulae retrieved from the *WISE* all-sky survey archive. The extended halos with IR emission surrounding the objects can clearly be seen in Figure 4. The MIR images show that the colors of the field stars are bluer than those of the nebulae, which suggests that they are dusty. The halos are detectable at *WISE* 12 and 22 μm bands, and they are brighter in the 22 μm images compared to the 12 μm images for these nebulae. Assuming that their emission peaks at 22 μm, we infer that IR fluxes emitted from the halos of these PNs are mainly dominated by dust components with a temperature of ∼130 K. From Figure 4, we also note that PN M 2–55 shows lower IR surface brightness compared to PN Abell 2. In the *WISE* 12 and 22 μm images, the central parts of these nebulae show prominent IR emissions, probably suggesting a large amount of dust located in the central regions of these PNs although the emissions of [Ne V] λ24.3 μm and [O IV] λ25.89 μm may partly contribute to the fluxes of 22 μm band emissions (Chu et al. 2009).

The *WISE* color composite image of M 2–55 (left panel of Fig. 4) clearly shows that this PN has a slightly elliptical central nebula and an extended outer halo. The morphology of this nebula in the IR is different from that observed in the *LOT* optical narrow-band images. In this image, the central nebula is the brightest feature of this object, whereas the outer halo is 2×10^{-2} fainter. The southern part of the halo exhibits a well-defined boundary (with a size of ∼166″), in contrast to a diffuse structure seen in the northern part of the halo. Such morphology gives an indication that this source is moving roughly toward the south and probably shows the PN-ISM interaction (Ramos-Larios & Phillips 2009; Zhang et al. 2012b). For Abell 2, the optical and MIR morphologies of this object are similar. Our MIR image (right panel of Fig. 4) shows an almost round halo with an angular diameter of ∼92″. The central elliptical-shaped nebula is prominent in all *WISE* IR images. No evidence of related extended structure is found outside the halo of this object.

3.3 Spectral Properties of M 2–55

In order to understand the spatial distributions of extended arc-shaped structures with Hα emission around PN M 2–55 (see Fig. 1), we have carried out spectroscopic observations. However, the faint filamentary feature is undetectable in our spectroscopic observations due to its low surface brightness compared to main shells of this PN (see Sect. 3.1.2). Nevertheless, the properties of the main nebula can still be studied from our spectra.

Table 3 Characteristic Lines in M 2–55

$\lambda_{\rm obs}$ (Å) (1)	Identification $\lambda_{\rm lab}$ (Å) (2)	Ion (3)	Observed Flux[a] (4)	Dereddened Flux[a] (5)
4685.54	4685.68	He II	4.41 (16.5)	11.39 (16.5)
4860.74	4861.33	Hβ	16.81 (5.4)	37.78 (5.4)
4958.45	4958.91	[O III]	44.45 (13.8)	96.30 (13.8)
5006.31	5006.84	[O III]	137.91 (7.8)	289.80 (7.9)
5874.36	5875.66	He I	2.35 (13.6)	3.10 (13.7)
6300.03	6300.34	[O I]	2.20 (18.5)	2.43 (18.5)
6364.57	6363.78	[O I]	1.11 (36.7)	1.19 (36.7)
6547.04	6548.10	[N II]	17.24 (13.9)	17.34 (13.9)
6562.34	6562.77	Hα	100.00 (3.2)	100.00 (3.2)
6582.81	6583.50	[N II]	56.56 (4.7)	56.12 (4.7)
6679.13	6678.16	He I	2.76 (5.4)	2.64 (5.4)
6716.07	6716.44	[S II]	4.60 (3.7)	4.35 (3.7)
6730.39	6730.82	[S II]	3.73 (7.6)	3.51 (7.6)
7178.15	7177.50	He II	6.39 (5.0)	5.17 (5.0)
7280.68	7281.35	He I	1.22 (11.1)	0.96 (11.1)
7299.17	7298.04	He I	1.59 (8.9)	1.24 (8.9)
7321.46	7319.99	[O II]	3.07 (7.1)	2.38 (7.1)

[a] The normalized emission fluxes (H$\alpha = 100$). The brackets represent the flux uncertainty errors with percentage.

The YFOSC spectrum of PN M 2–55 is shown in Figure 5. From Figure 5, we can see that a number of emission lines are typical in PN spectra. Among the prominent emission lines detected are Hβ at 4861 Å, Hα at 6563 Å, [O III] at 4959, 5007 Å, [N II] at 6548, 6584 Å, and [S II] at 6717, 6731 Å. Some weak emission features such as He I $\lambda\lambda$5876, 6678, 7281, 7298, He II $\lambda\lambda$4686, 7178, [O I] $\lambda\lambda$6300, 6364, and [O II] $\lambda\lambda$ 7320 can also be seen. The N(He)/N(H) and $\log$ N/O ratios (Peimbert & Torres-Peimbert 1983) suggest that the nebula is a type I PN (Peimbert & Torres-Peimbert 1983, 1987), which is believed to originate from a massive progenitor star (Calvet & Peimbert 1983; Kingsburgh & Barlow 1994). The Hα/Hβ flux ratio measured from M 2–55 is 5.95±0.48. Given the theoretical values at $T_e = 10^4$ K and $n_e = 10^2$ cm^{-3} (Hummer & Storey 1987), the extinction value of $c = 1.13\pm0.13$ is derived by comparing the observed Hα/Hβ ratio and using the reddening law with a $R_V = 3.1$ (Howarth 1983). This extinction is in good agreement with the earlier reported value of $c = 1.24$ (Kaler et al. 1990).

The measured emission fluxes are given in Table 3. Columns (1)–(3) list the observed emission wavelengths and line identifications. The normalized measured and dereddened fluxes (Hα = 100) of this object are listed in Columns (4) and (5). The observed integrated Hβ flux measured from this PN is 3.73×10^{-14} erg cm^{-2} s^{-1}. From Table 3, the line ratios of [O III] λ5007/λ4959 and [N II] λ6584/λ6548 of this nebula are 3.0 and 3.2, respectively, which are consistent with the theoretical values suggested

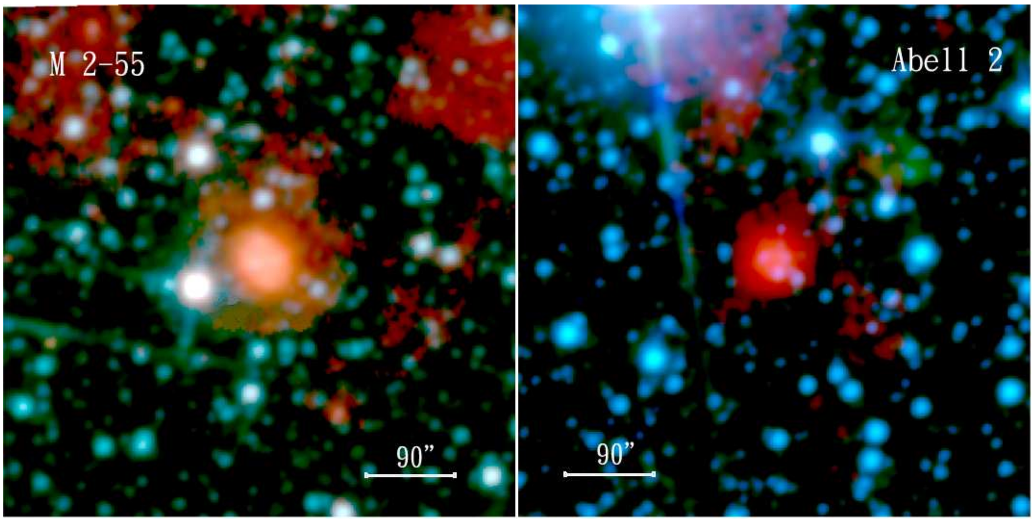

Fig. 4 Color composite *WISE* images of M 2–55 and Abell 2. The infrared images are shown on a logarithmic scale. These PNs are made from three bands: 3.4 µm (shown as *blue*), 4.6 µm (*green*), and 22 µm (*red*). North is up and east is to left. The extended halos around these PNs can be seen in the images.

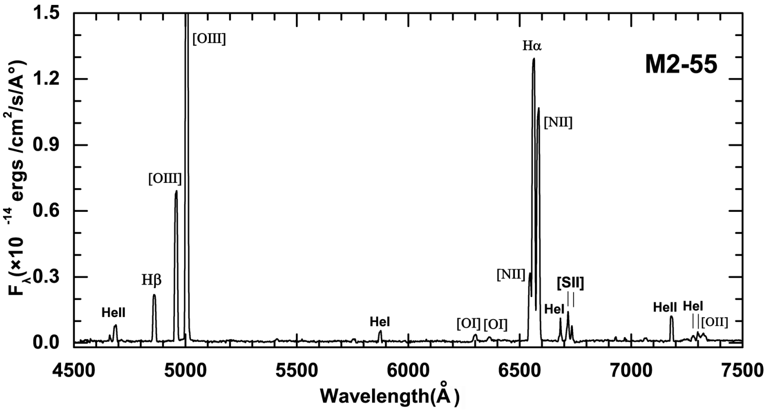

Fig. 5 Optical spectrum of M 2–55 in the wavelength range of 4500 Å to 7500 Å. The prominent emission features are marked.

by Storey & Zeippen (2000). Adopting an electron temperature of $T_e = 10\,200$ K (Peimbert & Torres-Peimbert 1987) for this nebula and using the [S II] λ6731/λ6717 line ratio, the electron density $n_e = 250^{+210}_{-190}$ cm^{-3} was derived. This value is in good agreement with the earlier results of 460 cm^{-3} (Peimbert & Torres-Peimbert 1987) and 512 cm^{-3} (Phillips 1998). The slight difference stems from different diaphragm sizes and slit positions. The emission ratio of log([O III] λ5007+λ4959/HeII λ4686) is a useful probe to determine the excitation class of a PN (Gurzadyan 1988). For this object, the value of log([O III] λ5007+λ4959/HeII λ4686) ratio is about 1.53, which indicates that this nebula is a high-excitation class PN. Moreover, the Hα/[O III] λ5007 flux ratio of M 2–55 is 0.35, which is smaller than that of normal young PNs ($>$1.5; Sahai & Trauger 1998), suggesting that this object is evolved.

4 SPECTRAL ENERGY DISTRIBUTION

To understand the properties of the ionized gas, photospheric, and dust components of these objects, the SEDs for PNs M 2–55 and Abell 2 were constructed (Figs. 6 and 7). In the IR, the Infrared Space Observatory (ISO) Long Wavelength Spectrometer (LWS) spectrum was used. For photometric measurements, the near-ultraviolet (NUV) and optical B, V, i, z, and y photometry of these objects are obtained from Shaw & Kaler (1985), Martin et al. (2005), Zacharias et al. (2005), and Chambers et al. (2016). J, H, and Ks band photometric data are taken from *Two Micron All Sky Survey* (2MASS) database. In the MIR, we used the data from *AKARI* and *IRAS* Source catalogs. In addition, the photometric data of these PNs measured form *WISE* MIR images are also added. A summary of these data used is given in Table 4.

Table 4 Photometric Measurements of M 2–55 and Abell 2

Filters	M 2–55 Flux/Flux density	M 2–55 Reference	Abell 2 Flux/Flux density	Abell 2 Reference
Central star and nebula				
Galex NUV (mag)	...	...	17.59±0.04	Martin et al. (2005)
B (mag)	17.43	Zacharias et al. (2005)	16.07±0.30	Shaw & Kaler (1985)
V (mag)	...	...	15.85±0.20	Shaw & Kaler (1985)
Pan-Starrs i (mag)	16.36±0.01	Chambers et al. (2016)	...	...
Pan-Starrs z (mag)	16.01±0.01	Chambers et al. (2016)	...	...
Pan-Starrs y (mag)	15.75±0.01	Chambers et al. (2016)	...	...
Dust[a]				
2MASS J (mag)	14.57±0.04	Cutri et al. (2003)	...	...
2MASS H (mag)	13.75±0.05	Cutri et al. (2003)	...	...
2MASS Ks (mag)	13.56±0.05	Cutri et al. (2003)	...	...
WISE 3.4 μm (mag)	11.43±0.03	this study	12.92±0.02	this study
WISE 4.6 μm (mag)	10.13±0.02	this study	12.34±0.03	this study
WISE 12 μm (mag)	6.83±0.02	this study	8.35±0.04	this study
WISE 22 μm (mag)	3.75±0.03	this study	5.05±0.03	this study
IRAS 12 μm[b] (Jy)	0.49:	Tajitsu & Tamura (1998)	0.11:	Tajitsu & Tamura (1998)
IRAS 25 μm (Jy)	0.80±0.07	Tajitsu & Tamura (1998)	0.14±0.02	Tajitsu & Tamura (1998)
IRAS 60 μm (Jy)	3.55±0.28	Tajitsu & Tamura (1998)	0.65±0.13	Tajitsu & Tamura (1998)
IRAS 100 μm[b] (Jy)	4.99±0.40	Tajitsu & Tamura (1998)	7.77:	Tajitsu & Tamura (1998)
AKARI 65 μm (Jy)	1.85:	Yamamura et al. (2010)	...	...
AKARI 90 μm (Jy)	3.76±0.16	Yamamura et al. (2010)	0.67±0.08	Yamamura et al. (2010)
AKARI 140 μm (Jy)	3.58±0.63	Yamamura et al. (2010)	0.01:	Yamamura et al. (2010)
AKARI 160 μm (Jy)	1.76:	Yamamura et al. (2010)	0.33:	Yamamura et al. (2010)
Free-free emission				
5 GHz (mJy)	19	Siódmiak & Tylenda (2001)	2.3	Stanghellini et al. (2008)
4.85 GHz (mJy)	28±4	Gregory et al. (1996)	...	...
1.4 GHz (mJy)	26.6	Siódmiak & Tylenda (2001)	7.6±0.6	Condon et al. (1998)
1.4 GHz (mJy)	...	...	9.4±1.1	Condon & Kaplan (1998)

[a] The colons represent the uncertain flux measurement. [b] Some IRAS 12 and 100 μm fluxes are upper limit detections.

The preliminary impression of the SEDs (Figs. 6 and 7) is that most of the fluxes from these PNs are mainly dominated in the IR. Assuming that the dust emission can be represented by a single blackbody (BB), the peak fluxes of these SEDs are 8.5×10^{-10} erg cm^{-2} s^{-1} and 1×10^{-10} erg cm^{-2} s^{-1} for M 2–55 and Abell 2, and the total fluxes emitted from the objects are approximately 1.2×10^{-9} erg cm^{-2} s^{-1} for M 2–55 and 1.4×10^{-10} erg cm^{-2} s^{-1} for Abell 2. Adopting their distances of 691 pc and 2.82 kpc for M 2–55 and Abell 2 (Bailer-Jones et al. 2018), the total luminosity of these nebulae are about 18 and 35 $L_\odot$ for M 2–55 and Abell 2, respectively. From Figures 6 and 7, we note that the IR SED of each PN cannot be fitted by a single BB, thus these derived values are just the minima.

We fitted the emerging fluxes of these objects by a two-component model including the reddened photospheric emission (emitted from the central star and gaseous emission) and dust continuum using the same expressions described in Hsia et al. (2019). The mid- to far-infrared component of the SED is not fitted by a single dust component. We have tried to fit the observed SED by a radiation transfer model using the software code DUSTY (Ivezic et al. 1999). For the fitting, we assumed the standard MRN distribution of grain sizes (Mathis et al. 1977) with a dust temperature on the inner shell boundary of 90 K and a density distribution of R^{-2} for each object, where R is the distance to the central star. In order to arrive at the best fitting, the optical thicknesses of the shells at 0.55 μm were adopted to be $\tau = 3$ and $\tau = 0.6$ for M 2–55 and Abell 2. The dust grains are assumed to be the mixings of silicates and graphite, which can give the approximations to the dust continua. The separated contributions from different components of these PNs can be clearly seen in Figures 6 and 7. For the SED fittings, our best estimates for the central star temperatures are 80 000 K for M 2–55 and 78 000 K for Abell 2, which are in good agreement with previously results of 85 000 K (Kaler & Jacoby 1989) and 75 000±4000 K (Shaw & Kaler 1985) for M 2–55 and Abell 2. With the adopted distances of 691 pc for M 2–55 and 2.82 kpc for Abell 2 (Bailer-Jones et al. 2018), the derived total luminosity of the objects are about 35 and 50 $L_\odot$ for M 2–55 and Abell 2, respectively, which are higher than our earlier estimates because parts of UV radiation emitted from the central stars are not counted in the total observed fluxes. The higher central star temperatures and low luminosities of these PNs indicate that they are on the cooling paths of their evolutions

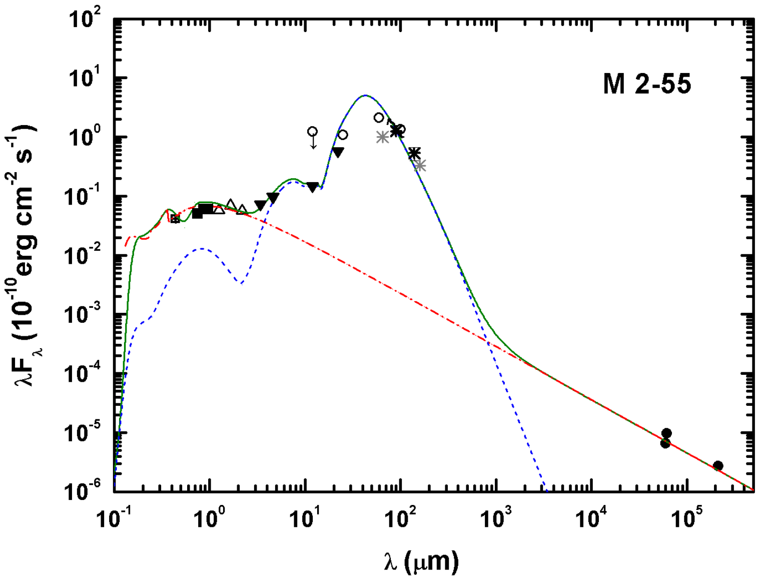

Fig. 6 The SED of M 2–55 with wavelength range from UV to radio. The Pan-Starrs measurements are shown as *filled squares*, the NUV, B, and V measurements as *open squares*, the 2MASS results as *open triangles*, WISE measurements as *filled triangles*, IRAS as *open circles*, AKARI photometry as *asterisks*, and radio measurements as *filled circles*. The uncertain AKARI detections are marked as the *light asterisks*. Note that the measured IRAS 12 and 100 μm fluxes are upper limit detections. The ISO LWS spectrum for M 2–55 is also plotted. The nebular emissions are plotted as the *red curve*. The *blue curve* represents a dust continuum fitting by using the radiation transfer model. The total fluxes derived from all components are plotted as the *green curve*.

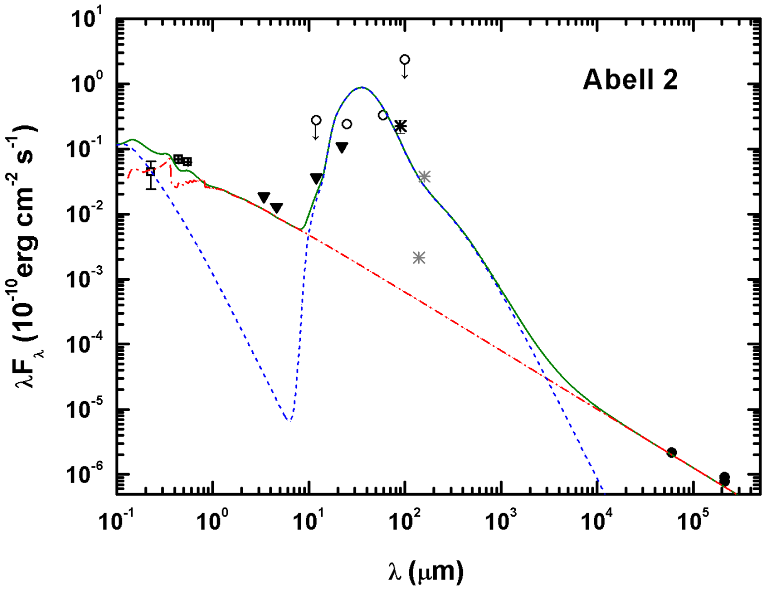

Fig. 7 The SED of Abell 2 with the spectral range from 1000 Å to 50 cm. The notations of data points and fitting curves are the same as Fig. 6.

in the Hertzsprung-Russell (H-R) diagram. Using the formulas presented in Hsia et al. (2010), we can derive the mass of dust component (M_d) and the mass of ionized gas (M_i) of PN M 2–55. Assuming the emissivity of dust particles of $Q_\lambda = Q_0(\lambda/\lambda_0)^{-\alpha}$, where $Q_0 = 0.1$, $\alpha = 1$, and $\lambda_0 = 1$ μm. The assumed density of dust grains of $\rho_s = 1$ g cm^{-3} and the adopted distance of 691 pc, we obtain $4.01\times10^{-4}\ M_\odot$ and $1.1\times10^{-2}\ M_\odot$ for the masses of the dust component (M_d) and ionized gas (M_i), respectively. The M_d/M_i ratio of M 2–55 is ∼0.04, significantly higher than the dust-to-gas ratios of typical PNs ($10^{-2} - 10^{-3}$, Stasińska & Szczerba 1999). This probably suggests that a mass of gas in this evolved PN is in neutral form.

5 DISCUSSION

5.1 M 2–55

According to Tweedy & Kwitter (1996) and Dgani & Soker (1998), the interacting PNs show three distinct features of the interactions with their surrounding ISM; (i) the outer regions around the PNs are asymmetric; (ii) brightness enhancements seen in the outer regions of these PNs accompanied by the drops in the ionization levels; (iii) the presences of fragments in the halos and/or arc-shaped filaments. Dgani & Soker (1998) suggested that the striped appearances of interacting PNs may be the result of Rayleigh-Taylor (RT) instabilities, resulting in fragmentations at the halos of the PNs. The optical-infrared morphology of PN M 2–55 as seen in Figures 1 and 4 is composed of an arc-like structure with brightness enhancement on its edge from SW to SE (see Sect. 3.1.2) and an asymmetric infrared halo (see Sect. 3.2). Such features have been detected in other nebulae such as NGC 6751 (Clark et al. 2010), NGC 6894 (Soker & Zucker 1997), NGC 7293 (Zhang et al. 2012b), HW 4, S176, and S188 (Tweedy & Kwitter 1996), and have been attributed to the interactions between the AGB winds and the ISM. No evidence of the other two distinct characteristics of PN-ISM interactions can be seen in this object. We conclude that the presence of the arc-shaped structure seen around PN M 2–55 is caused by the compression from the motion of this nebula through its surrounding ISM.

Wilkin (1996) found that the arc-shaped structure depends on relative velocities and densities between slow AGB wind and the surrounding ISM, the presence of the feature can be used to determine the properties of AGB wind of the PN and its surrounding ISM. We note that the appearance of this newly discovered arc filament is similar to that of brightening structure as the first stage of PN-ISM interaction in the simulations of Wareing et al. (2007), probably suggesting that the PN is not affected by the ISM interaction. If the central star of the planetary nebula (CSPN) moves slowly through the ISM (i.e., <50 km s^{-1}; Burton 1988), this interaction can remain for the entire lifetime of the nebula and other PN-ISM interactions will never be observed (Wareing et al. 2007). In the case of PN M 2–55, the radial velocity of this object is 22.6 km s^{-1} (Acker et al. 1992), hence we infer that the arc-shaped structure around this PN may be observed for a long time.

Although M 2–55 has been known to present two pairs of bipolar lobes (Sabbadin & Perinotto 1981), previous images did not reveal internal details of this nebula. Figure 1 shows that the nebular structures are point symmetric about the center, and the two pairs of lobes have approximately the same extent, indicating that they were ejected during a short period. This PN also reveals a large central cavity, differing from young bipolar PNs which usually exhibit a narrow waist (see, e.g., Manchado et al. 1996; Kwok & Su 2005). Presumably, the central cavity was created by the increasing thermal pressure with PN evolution. The clumpy structures in Figure 1 might be the debris of the torus that have collimated the outflows. A hypothesis of PN evolutionary transition from bipolar (lobe-dominant) to elliptical (cavity-dominant) has been suggested by Huarte-Espinosa et al. (2012) and Hsia et al. (2014). The appearance of PN M 2–55 suggests that it is in an evolutionary stage between the lobe-dominant phase and the cavity-dominant phase.

5.2 Abell 2

According to the evolutionary tracks presented in Blöcker (1995), the temperature and luminosity of the central star of Abell 2 indicate that it has a mass of $\sim$0.605 $M_{\odot}$. This is normal among PNs (Stasińska et al. 1997). Soker (1997) classified Abell 2 as an elliptical PN, which might result from axisymmetric mass loss of its progenitor interacted with a substellar companion during the common envelope phase. This scenario also predicts the existence of a spherical halo surrounding elliptical nebula (Soker 1997), which is confirmed by our observation of Abell 2 (see Sect. 3.2).

The hydrodynamical models presented by Gawryszczak et al. (2002) suggest that PNs with binary cores will evolve from bipolar to elliptical shapes. Therefore, elliptical PNs can be produced in wide binary systems and most evolved PNs appear spherical or elliptical morphologies. This results from the possibility that there is a companion in the nucleus of Abell 2. Although our observations could not identify whether a companion exists in this PN, new spectroscopic observation is required to reveal the nature of the nucleus in Abell 2.

The double-shell structure of Abell 2 can be explained in terms of radiation-hydrodynamics simulations (Schönberner et al. 2014). Similar to the PN double-shell HuBi 1 (Guerrero et al. 2018), the inner and outer shells of Abell 2 appears to have an opposite ionization structure to those of typical PNs. Guerrero et al. (2018) suggested that the anomalous excitations are related the Wolf-Rayet central star of the PN. In this case, the nucleus of the nebula may experience a born-again event produced by a thermal pulsation at the ending of AGB stage, during the post-AGB phase (Blöcker 2001), or on the cooling stage of white dwarf evolution (Schönberner 1979). The shocks produced by the ejecta excite the inner shell, resulting in an inverted ionization structure as seen in Abell 2.

It is instructive to investigate the evolution of SEDs from young to old PNs. The SED of a young PN IRAS 21282+5050 (hereafter referred to as IRAS 21282) has been presented by Hsia et al. (2019), whether a strong IR excess due to thermal emission of dust components has been revealed. In IRAS 21282, the dust envelope is optically thick with an optical depth of $\tau = 5.5$ at 0.55 μm, and has a high temperature of ∼250 K. It is clear that the evolved PN Abell 2 exhibits a lower optical depth and a lower temperature. Therefore, the infrared colors can reflect the evolutionary stage of PNs.

6 CONCLUSIONS

Recent narrow-band imaging studies have provided an effective tool for us to understand the ionized gaseous environments around evolved PNs. Although more than one hundred extended, faint PNs have been studied via these advanced observational tools (Tweedy & Kwitter 1996; Corradi et al. 2003; Ali et al. 2012), the nature and properties of these nebulae are still unclear. In this paper, we present a visible and MIR study of two evolved PNs (M 2–55 and Abell 2). Our deep optical narrow-band images of PN M 2–55 reveal two pairs of bipolar lobes and a new arc-like structure. The arc-shaped structure seen around this object appears as a well-defined boundary from SW to SE, furnishing strong evidence for an interaction of the expanding nebula of this PN with its surrounding ISM. The [O III] and Hα images of PN Abell 2 reveal inner and outer elliptical shells in the main nebula, whereas the inner shell of this PN can only be seen in the [N II] image. This suggests that the nucleus of this PN experienced a born-again event. We have studied the nebular properties of PN M 2–55 by the mid-resolution spectrum. The spectral analysis of this object shows that the nebula is an evolved PN with a high excitation class and a low electron density of 250 cm^{-3}.

From the MIR images of *WISE* all-sky survey data release, these PNs presented in our study are found to show prominent infrared features. Obvious MIR emissions detected in the central parts of these objects suggest that a mass of dust is located in their central regions. The SEDs of these PNs are constructed from extensive archival data. We successfully fitted the observed fluxes by a two-component model including the reddened photospheric emission and dust continuum. These PNs might have thick dusty envelopes because most of the fluxes from the objects are emitted by dust components.

Interacting PN is thought to be the result of dynamical interaction between slow AGB wind (halo) and its surrounding ISM. The presence of arc-shaped/bow-shock structure suggests that PN-ISM interaction may be very common. M 2–55 and Abell 2 can serve as an astrophysical laboratory to study the dynamical processes of the interactions between PNs and ISM in the space.

Acknowledgements We would like to thank the anonymous referee for his/her helpful comments that improved the manuscript. This publication has made use of data collected at the Lulin Observatory, partly supported by MoST grant (108-2112-M-008-001). We acknowledge the support of the staff of the Lijiang 2.4m telescope. Funding for the telescope has been provided by Chinese Academy of Sciences and the People's Government of Yunnan Province. Financial support for this work is supported by the grants from The Science and Technology Development Fund, Macau SAR (file no: 061/2017/A2 and 0007/2019/A) and the Faculty Research Grants of Macau University of Science and Technology (project code: FRG-19-004-SSI). X.L. is supported by the National Natural Science Foundation of China (NSFC, Grant No. U1731122). Y.Z. thanks NSFC (Grant No. 11973099) for financial support.

References

Abell, G. O. 1955, PASP, 67, 258
Abell, G. O. 1966, ApJ, 144, 259
Acker, A., Ochsenbein, F., Stenholm, B., et al. 1992, Strasbourg-ESO Catalog of Galactic Planetary Nebulae, Parts I and II (Garching: European Southern Observatory)
Ali, A., Sabin, L., Snaid, S., & Basurah, H. M. 2012, A&A, 541, A98
Bailer-Jones, C. A. L., Rybizki, J., Fouesneau, M., et al. 2018, AJ, 156, 58
Benjamin, R. A., Churchwell, E., Babler, B. L., et al. 2003, PASP, 115, 953
Blöcker, T., 1995, A&A, 299, 755
Blöcker, T., 2001, Ap&SS, 275, 1
Borkowski, K. J., Sarazin, C. L., & Soker, N. 1990, ApJ, 360, 173
Burton, W. B., 1988, in Galactic and Extragalactic Radio Astronomy, eds. K. Kellermann, & G. L. Verschuur (New York: Springer), 295
Calvet, N., & Peimbert, M. 1983, Rev. Mexicana Astron. Astrofis., 5, 319
Chambers, K. C., Magnier, E. A., Metcalfe, N., et al. 2016, arXiv e-prints, arXiv:1612.05560
Chu, Y. -H., Gruendl, R. A., Guerrero, M. A., et al. 2009, AJ, 138, 691
Churchwell, E., Babler, B. L., Meade, M. R., et al. 2009, PASP, 121, 213
Clark, D. M., García-Díaz, Ma. T., López, J. A., et al. 2010, ApJ, 722, 1260

Condon, J. J., Cotton, W. D., Greisen, E. W., et al. 1998, AJ, 115, 1693
Condon, J. J., & Kaplan, D. L. 1998, ApJS, 117, 361
Cohen, M., Parker, Q. A., Green, A. J., et al. 2011, MNRAS, 413, 514
Corradi, R. L. M., Schönberner, D., Steffen, M., et al. 2003, MNRAS, 340, 417
Corradi, R. L. M., Sánchez-Blázquez, P., Mellema, G., et al. 2004, A&A, 417, 637
Cutri, R. M., Skrutskie, M. F., van DyK, S., et al. 2003, VizieR Online Data Catalog, II/246
Dgani, R., & Soker, N. 1998, ApJ, 495, 337
Felli, M., & Perinotto, M. 1979, A&A, 76, 69
Gawryszczak, A. J., Mikołajewska, J., & Różyczka, M. 2002, A&A, 385, 205
Gillett, F. C., Low, F. J., & Stein, W. A. 1967, ApJ, 149, L97
Gregory, P. C., Scott, W. K., Douglas, K., et al. 1996, ApJS, 103, 427
Guerrero, M. A., Fang, X., Miller Bertolami, M. M., et al. 2018, Nature Astronomy, 2, 784
Gurzadyan, G. A. 1969, Planetary Nebulae (New York: Gordon & Breach)
Gurzadyan, G. A. 1988, Ap&SS, 149, 343
Gussie, G. T., & Taylor, A. R. 1994, PASP, 106, 500
Howarth, I. D. 1983, MNRAS, 203, 301
Hsia, C. -H., Kwok, S., Zhang, Y., et al. 2010, ApJ, 725, 173
Hsia, C. -H., Chau, W., Zhang, Y., et al. 2014, ApJ, 787, 25
Hsia, C. -H., & Zhang, Y. 2014, A&A, 563A, 63
Hsia, C. -H., Zhang, Y., Kwok, S., et al. 2019, Ap&SS, 364, 32
Hua, C. T. 1988, A&A, 193, 273
Huarte-Espinosa, M., Frank, A., Balick, B., et al. 2012, MNRAS, 424, 2055
Hummer, D. G., & Storey, P. J. 1987, MNRAS, 224, 801
Ivezic , Z., Nenkova, M., & Elitzur, M. 1999, User Manual for Dusty (University of Kentucky) eprint arXiv:astro-ph/9910475
Jacoby, G. H. 1981, AJ, 244, 903
Kaler, J. B., & Jacoby, G. H. 1989, ApJ, 345, 871
Kaler, J. B., Shaw, R. A., & Kwitter, K. B. 1990, ApJ, 359, 392
Kingsburgh R. L., & Barlow M. J. 1994, MNRAS, 271, 257
Kwok, S. 1982, ApJ, 258, 280
Kwok, S., & Su, K. Y. L. 2005, ApJ, 635, 49
Manchado, A., Stanghellini, L., & Guerrero, M. A. 1996, ApJ, 466, 95
Martin, D. C., Fanson, J., Schiminovich, D., et al. 2005, ApJ, 619, L1
Mathis, J. S., Rumpl, W., & Nordsieck, K. H. 1977, ApJ, 217, 425
Peimbert M. & Torres-Peimbert S. 1983, IAU Symp. 103, Reidel, Dordrecht, 233
Peimbert M. & Torres-Peimbert S. 1987, Rev. Mexicana Astron. Astrofis., 14, 540
Phillips, J. P. 1998, A&A, 340, 527
Pottasch, S. R., Baud, B., Beintema, D., et al. 1984, A&A, 138, 10
Ramos-Larios, G., & Phillips, J. P. 2009, MNRAS, 400, 575
Ramos-Larios, G., Guerrero, M. A., Nigoche-Netro, A., et al. 2018, MNRAS, 475, 932
Roeser, S., Demleitner, M., & Schilback, E. 2010, AJ, 139, 2440
Sabbadin, F., & Perinotto, M. 1981, A&A, 94, 25
Sahai, R., & Trauger, J. T. 1998, AJ, 116, 1357
Sati̅o, M., Iwata, I., Okumura, S., Mori, A., & Yamashita, T. 1999, PASJ, 51, 673
Schönberner, D., 1979, A&A, 79, 108
Schönberner, D., Jacob, R., Lehmann, H., et al. 2014, Astron. Nachr., 335, 378
Shaw, R. A., & Kaler, J. B. 1985, ApJ, 295, 537
Siódmiak, N., & Tylenda, R. 2001, A&A, 373, 1032
Soker, N., 1997, ApJS, 112, 487
Soker, N., & Zucker, D. B. 1997, MNRAS, 289, 665
Stanghellini, L., Corradi, R. L. M., & Schwarz, H. E. 1993, A&A, 279, 521
Stanghellini, L., Shaw, R. A., & Villaver, E. 2008, ApJ, 689, 194
Stasińska, G., Górny, S. K. & Tylenda, R., 1997, A&A, 327, 736
Stasińska, G., & Szczerba, R. 1999, A&A, 352, 297
Storey, P. J. & Zeippen, C. J. 2000, MNRAS, 312, 813
Tajitsu, A., & Tamura, S. 1998, AJ, 115, 1989
Tweedy, R. W., & Kwitter, K. B. 1996, ApJS, 107, 255
Wareing, C. J., Zijlstra, A. A., & O'brien, T. J. 2007, MNRAS, 382, 1233
Weinberger, R. 1989, A&AS, 78, 301
Wilkin, F. P. 1996, ApJ, 459, L31
Wright, E. L., Eisenhardt, P. R. M., Mainzer, A. K., et al. 2010, AJ, 140, 1868
Yamamura, I., Makiuti, S., Ikeda, N., et al. 2010, VizieR Online Data Catalog, 2298, 0
Zacharias, N., Monet, D. G., Levine, S. E., et al. 2005, VizieR Online Data Catalog, 1297, 0
Zhang, C. Y., & Kwok, S. 1991, A&A, 250, 179
Zhang, Y., Hsia, C. -H., & Kwok, S. 2012a, ApJ, 745, 59
Zhang, Y., Hsia, C. -H., & Kwok, S. 2012b, ApJ, 755, 53

The Astrophysical Journal Letters, 894:L1 (6pp), 2020 May 1 https://doi.org/10.3847/2041-8213/ab79a4

Spitzer Observations of the Predicted Eddington Flare from Blazar OJ 287

Seppo Laine[1], Lankeswar Dey[2], Mauri Valtonen[3], A. Gopakumar[2], Stanislaw Zola[4,5], S. Komossa[6], Mark Kidger[7], Pauli Pihajoki[8], José L. Gómez[9], Daniel Caton[10], Stefano Ciprini[11,12], Marek Drozdz[13], Kosmas Gazeas[14], Vira Godunova[15], Shirin Haque[16], Felix Hildebrandt[17], Rene Hudec[18,19], Helen Jermak[20], Albert K. H. Kong[21], Harry Lehto[22], Alexios Liakos[23], Katsura Matsumoto[24], Markus Mugrauer[17], Tapio Pursimo[25], Daniel E. Reichart[26], Andrii Simon[27], Michal Siwak[13], and Eda Sonbas[28]

[1] IPAC, Mail Code 314-6, Caltech, 1200 E. California Blvd., Pasadena, CA 91125, USA
[2] Department of Astronomy and Astrophysics, Tata Institute of Fundamental Research, Mumbai 400005, India; lankeswar.dey@tifr.res.in
[3] Finnish Centre for Astronomy with ESO, University of Turku, FI-20014 Turku, Finland
[4] Astronomical Observatory, Jagiellonian University, ul. Orla 171, Cracow PL-30-244, Poland
[5] Mt. Suhora Astronomical Observatory, Pedagogical University, ul. Podchorazych 2, PL30-084 Cracow, Poland
[6] Max-Planck-Institut für Radioastronomie, Auf dem Hügel 69, D-53121 Bonn, Germany
[7] PLATO Science Operations Centre, ESAC, European Space Agency, E-28691 Villanueva de la Cañada, Madrid, Spain
[8] Department of Physics, University of Helsinki, Gustaf Hällströmin katu 2a, FI-00560, Helsinki, Finland
[9] Instituto de Astrofísica de Andalucía-CSIC, Glorieta de la Astronomía s/n, E-18008 Granada, Spain
[10] Dark Sky Observatory, Dept. of Physics and Astronomy, Appalachian State University, Boone, NC 28608, USA
[11] Space Science Data Center—Agenzia Spaziale Italiana, via del Politecnico, snc, I-00133, Roma, Italy
[12] Instituto Nazionale di Fisica Nucleare, Sezione di Perugia, Perugia I-06123, Italy
[13] Pedagogical University of Cracow, Mt. Suhora Astronomical Observatory, ul. Podchorazych 2, PL30-084 Cracow, Poland
[14] Department of Astrophysics, Astronomy and Mechanics, National and Kapodistrian University of Athens, Zografos GR-15784, Athens, Greece
[15] ICAMER Observatory of NASU, 27 Acad. Zabolotnoho Str., 03143 Kyiv, Ukraine
[16] Department of Physics, University of the West Indies, St. Augustine, Trinidad and Tobago
[17] Astrophysikalisches Institut und Universitäts-Sternwarte, Schillergäßchen 2, D-07745 Jena, Germany
[18] Czech Technical University in Prague, Faculty of Electrical Engineering, Technicka 2, Prague 166 27, Czech Republic
[19] 27 Kazan Federal University, Kremlyovskaya 18, 420000 Kazan, Russia
[20] Astrophysics Research Institute, Liverpool John Moores University, IC2, Liverpool Science Park, Brownlow Hill, L3 5RF, UK
[21] Institute of Astronomy, National Tsing Hua University, Hsinchu 30013, Taiwan
[22] Department of Physics and Astronomy, Tuorla Observatory, University of Turku, FI-20014, Finland
[23] Institute for Astronomy, Astrophysics, Space Applications and Remote Sensing, National Observatory of Athens, Metaxa and Vas. Pavlou St., Penteli, Athens GR-15236, Greece
[24] Astronomical Institute, Osaka Kyoiku University, 4-698 Asahigaoka, Kashiwara, Osaka 582-8582, Japan
[25] Nordic Optical Telescope, Apartado 474, E-38700, Santa Cruz de la Palma, Spain
[26] University of North Carolina at Chapel Hill, Chapel Hill, North Carolina NC 27599, USA
[27] Astronomy and Space Physics Department, Taras Shevchenko National University of Kyiv, 64/13, Volodymyrska St., Kyiv, 01601 Ukraine
[28] University of Adiyaman, Department of Physics, 02040 Adiyaman, Turkey

Received 2020 February 7; accepted 2020 February 25; published 2020 April 28

Abstract

Binary black hole (BH) central engine description for the unique blazar OJ 287 predicted that the next secondary BH impact-induced bremsstrahlung flare should peak on 2019 July 31. This prediction was based on detailed general relativistic modeling of the secondary BH trajectory around the primary BH and its accretion disk. The expected flare was termed the Eddington flare to commemorate the centennial celebrations of now-famous solar eclipse observations to test general relativity by Sir Arthur Eddington. We analyze the multi-epoch Spitzer observations of the expected flare between 2019 July 31 and 2019 September 6, as well as baseline observations during 2019 February–March. Observed Spitzer flux density variations during the predicted outburst time display a strong similarity with the observed optical pericenter flare from OJ 287 during 2007 September. The predicted flare appears comparable to the 2007 flare after subtracting the expected higher base-level Spitzer flux densities at 3.55 and 4.49 μm compared to the optical *R*-band. Comparing the 2019 and 2007 outburst lightcurves and the previously calculated predictions, we find that the Eddington flare arrived within 4 hr of the predicted time. Our Spitzer observations are well consistent with the presence of a nano-Hertz gravitational-wave emitting spinning massive binary BH that inspirals along a general relativistic eccentric orbit in OJ 287. These multi-epoch Spitzer observations provide a parametric constraint on the celebrated BH no-hair theorem.

Unified Astronomy Thesaurus concepts: Gravitation (661); Black hole physics (159); BL Lacertae objects (158)

1. Introduction

The International Pulsar Timing Array (IPTA) consortium aims to inaugurate the era of nano-Hertz (Hz) gravitational-wave (GW) astronomy during the next decade (Perera et al. 2019). This is expected to augment the already established hecto-Hz GW astronomy by the LIGO–Virgo collaboration (Abbott et al. 2019) and the milli-Hz GW astronomy to be established by space-based observatories in the 2030s (Baker et al. 2019). Massive black hole (BH) binaries, emitting nano-Hz GWs, are the most prominent IPTA sources (Burke-Spolaor et al. 2019). Therefore, observational evidence for the existence of such binaries has important IPTA implications (Goulding et al. 2019).

The binary black hole (BBH) central engine description for the bright blazar OJ 287 provides the most promising scenario for the existence of a nano-Hz GW emitting massive BH binary (Dey et al. 2019). The model naturally explains the observed double-peaked high brightness flares (outbursts) from OJ 287 and predicts the arrival time of future outbursts. These flares arise due to the impact of an orbiting secondary BH onto the accretion disk of the primary. In the resulting thermal flares, flux densities (hereafter "flux") in the UV–infrared wavelengths increase sharply within just a day or so and then fall off more slowly in the following days (Valtonen et al. 2019). Accurate timing of these flares allows us to track the general relativistic trajectory of the secondary BH and to determine BBH central engine parameters (Dey et al. 2018, hereafter D18).

The nature of such flares and the method of predicting future flares were detailed by Lehto & Valtonen (1996) and Sundelius et al. (1997). In their model, the secondary BH plunges through the accretion disk twice per orbit, which ensures two flares per period. This model also predicted that impact flares should be thermal, with a nearly flat bremsstrahlung spectrum, rather than the ubiquitous synchrotron flares with a power-law spectrum. It was not a trivial prediction, as no bremsstrahlung flares had been observed in any blazar up to that time. The observations of the 2005 November flare confirmed this prediction (Valtonen et al. 2006, 2008a, 2012). This was followed by a successful observational campaign, launched to monitor the predicted pericenter flare of 2007 (Valtonen et al. 2008b). These observations demonstrated the importance of incorporating the effects of quadrupolar order GW emission while predicting the impact flare epochs from the blazar. Further, the successful observation of OJ 287's 2015 apocenter impact flare, predicted by Valtonen et al. (2011), provided an estimate for the spin of its primary BH (Valtonen et al. 2016). The present BBH model, extracted from the accurate timing of 10 flares between 1913 and 2015 (D18), is specified by the following parameters: primary with mass $1.835 \times 10^{10} M_{\odot}$ and Kerr parameter $a = 0.38$, and a $1.5 \times 10^{8} M_{\odot}$ secondary in an eccentric ($e \sim 0.65$) orbit with a redshifted orbital period of 12 yr.

D18 predicted that the next impact flare from OJ 287 should peak in the early hours of 2019 July 31, UT, within a specified time interval of ± 4.4 hr (Eddington flare). This prediction is fairly unique as there are no free parameters whose value can be constrained from the actual observations of the flare, in contrast to the earlier flares. Ideally, we would have launched a ground-based optical observational campaign to monitor the predicted Eddington flare. However, OJ 287 was at a solar elongation $<5°$ during the peak of the flare. Therefore, there was no option to confirm it by means of a ground-based observing campaign. The Spitzer Space Telescope, operating at infrared wavelengths, turned out to be the best substitute for optical monitoring. An earlier optical/infrared campaign was organized for flux normalization. In what follows, we explain why we are confident about the presence of the predicted Eddington flare in our Spitzer data and state its implications.

2. BBH Central Engine of OJ 287 and Its 2019 Prediction

The 130 yr long optical lightcurve of OJ 287 reveals two prominent outbursts every 12 yr (Dey et al. 2019). The outburst timings are consistent with a scenario in which biorbital secondary BH impacts generate a hot bubble of plasma on each side of the primary BH accretion disk. These bubbles expand and eventually become optically thin. At this epoch, the radiation from the entire bubble volume is released and we observe a big thermal flare. In the model, the observed steeply rising flux during a flare arises from an increase in the visible radiating volume, while the declining flux comes with the decreasing temperature from the associated adiabatic expansion. Both processes should produce radiation that is wavelength independent while timing various epochs of the flare.

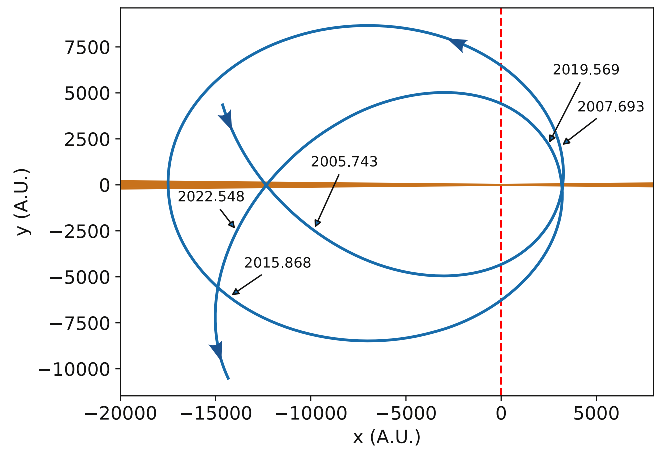

Figure 1. General relativistic orbit of the secondary BH in OJ 287 during the 2005–2023 window (D18). The primary BH is situated at the origin with its accretion disk in the $y = 0$ plane. The impacts that caused the 2007 and 2019 outbursts happen to originate roughly from the same location of the disk near the pericenter, and the secondary BH follows similar trajectories, leading to fairly identical lightcurves. In contrast, the 2005 and 2022 impact flare lightcurves are expected to be different. The orbit is calculated using our PN accurate binary BH description.

In general, the points of impact are located at different distances from the primary due to the general relativity (GR) induced pericenter advance (Lehto & Valtonen 1996). However, there are occasions during which two impacts happen close to the pericenter of such a relativistic orbit. We expect that the astrophysical conditions are fairly similar at such impacts, leading to essentially similar flares. The orbit solution of D18 shows a pair of pericenter flares during 2007 September 14 and 2019 July 31 (Figure 1). This allowed us to use the observed optical lightcurve of the 2007 outburst as a template to analyze our Spitzer observations of OJ 287 during late July and early August of 2019.

A post-Newtonian (PN) approximation to GR is employed to track the secondary BH orbit around the primary BH (Will & Maitra 2017). We incorporate higher-order corrections to both the conservative and reactive contributions to the relative acceleration $\ddot{\boldsymbol{x}}$ (see Equation (1) in D18). Crucially, these corrections involve certain GW-emission-induced $\ddot{\boldsymbol{x}}_{4PN(tail)}$ contributions due to the scattering of quadrupolar GWs from the spacetime curvature created by the total mass (monopole) of the system (Blanchet & Schafer 1993; D18). Additionally, we incorporate various spin-induced contributions to $\ddot{\boldsymbol{x}}$ that arise from general relativistic spin–orbit and the classical spin–orbit interactions. The latter contributions depend on the quadrupole moment of the primary BH and affect the expected outburst time of the Eddington flare. Therefore, the accurate determination of the epoch of this flare has the potential to constrain the celebrated BH no-hair theorem (Valtonen et al. 2011; D18). This is because the theorem allows us to connect the scaled quadrupole moment q_2 and the Kerr parameter χ of the primary BH by

$$q_2 = -q\,\chi^2, \tag{1}$$

where q should be unity in GR (Thorne 1980) and therefore testable with present observations.

Table 1
Multi-epoch Spitzer Observations in 3.6 μm (Ch-1) and 4.5 μm (Ch-2) Wavelength Bands and the Ground-based Observations in the Optical *R*-band

Epoch (UT)	Ch-1 Flux (mJy)	Ch-2 Flux (mJy)	*R*-band Flux (mJy)
2019 Feb 25 23:23:06.905	17.8 ± 0.1	21.8 ± 0.1	2.836 ± 0.005
2019 Feb 26 22:02:51.370	17.7 ± 0.1	21.6 ± 0.1	2.825 ± 0.005
2019 Feb 28 01:21:52.252	18.2 ± 0.1	22.6 ± 0.1	2.881 ± 0.003
2019 Mar 1 01:01:21.123	17.3 ± 0.1	21.2 ± 0.1	2.875 ± 0.011
2019 Mar 2 01:39:00.677	17.0 ± 0.1	20.8 ± 0.1	2.825 ± 0.013
2019 Jul 31 15:25:33.651	26.3 ± 0.1	32.3 ± 0.1	…
2019 Aug 1 07:53:36.630	26.0 ± 0.1	31.7 ± 0.1	…
2019 Aug 1 16:04:46.053	26.5 ± 0.2	32.0 ± 0.1	…
2019 Aug 2 02:03:48.230	25.5 ± 0.1	31.0 ± 0.1	…
2019 Aug 2 18:44:48.833	24.7 ± 0.1	30.0 ± 0.1	…
2019 Aug 3 15:41:47.976	25.7 ± 0.1	31.3 ± 0.1	…
2019 Aug 4 15:15:32.277	24.5 ± 0.1	29.9 ± 0.1	…
2019 Aug 5 14:21:42.642	23.8 ± 0.2	28.9 ± 0.1	…
2019 Aug 6 12:09:24.649	23.5 ± 0.2	28.9 ± 0.1	…
2019 Aug 7 13:10:27.952	23.6 ± 0.1	29.0 ± 0.1	…
2019 Aug 8 19:12:35.339	24.0 ± 0.1	29.2 ± 0.1	…
2019 Aug 9 12:52:32.488	24.0 ± 0.1	29.6 ± 0.1	…
2019 Aug 10 19:13:55.542	24.3 ± 0.1	29.8 ± 0.1	…
2019 Aug 13 07:03:26.024	23.5 ± 0.1	28.8 ± 0.1	…
2019 Aug 16 21:11:01.225	23.0 ± 0.1	28.5 ± 0.1	…
2019 Aug 20 18:12:49.690	24.3 ± 0.1	29.7 ± 0.1	…
2019 Aug 22 19:27:51.842	23.9 ± 0.1	29.3 ± 0.1	…
2019 Aug 25 01:46:53.100	25.0 ± 0.2	30.6 ± 0.1	…
2019 Aug 28 02:42:37.747	22.9 ± 0.1	28.4 ± 0.2	…
2019 Sep 2 21:10:17.922	22.3 ± 0.1	27.7 ± 0.1	…
2019 Sep 4 05:44:12.19	…	…	2.918 ± 0.007
2019 Sep 5 02:44:00.96	…	…	3.179 ± 0.092
2019 Sep 5 02:52:00.48	…	…	3.138 ± 0.080
2019 Sep 6 01:47:09.46	…	…	3.313 ± 0.060
2019 Sep 6 17:43:11.593	23.7 ± 0.1	29.8 ± 0.2	…

Note. Times are in UT and reflect the start of the observation in Ch-2. The Ch-1 observations started after the Ch-2 observations were done, about 2 minutes and 10 s after the start of the Ch-2 observations typically. The *R*-band flux observations are not exactly simultaneous with the Spitzer observations but at very close epochs (within 2 hr).

3. Observations and Implications of the 2019 Outburst

3.1. Spitzer Observations and Data Reduction

Visibility and scheduling constraints did not permit Spitzer (Werner et al. 2004) to observe OJ 287 until 2019 July 31, 15 UT, several hours after the predicted time window for the occurrence of the impact flare peak. Therefore, we focused on the declining part of the expected flare where the radiating bubbles are optically thin in all relevant wavebands (Valtonen et al. 2019). This part lies between the first brightness peak and the first major minimum, predicted to occur during 2019 August 7. The Spitzer scheduling permitted dense monitoring during this critical period. Altogether OJ 287 was observed with Spitzer's Infrared Array Camera (Fazio et al. 2004) on 21 epochs between 2019 July 31 and 2019 September 6. The cadence was approximately 12 hr for the first five epochs, then once per day for the next eight epochs, and thereafter approximately twice a week for the last eight epochs. Additionally, OJ 287 was monitored on five epochs between 2019 February 25 and 2019 March 2 with daily cadence for normalization purposes with simultaneous optical observations. February–March observations permitted us to convert the infrared Spitzer/IRAC channel-1 (3.6 μm) and channel-2 (4.5 μm) flux densities, observed during the flare, to equivalent *R*-band flux densities. These observations were taken as part of the Spitzer DDT program pid 14206. The observing log and reduced flux densities are given in Table 1.

All of the observations were taken both in the 3.6 and 4.5 μm channels (corresponding approximately to the conventional photometric *L*- and *M*-bands) using the 2 s frame time with a 10-position medium-scale dither (typical dither amplitudes of less than an arcminute). The same dither starting point was used in every observation so that OJ 287 landed roughly on the same pixel position in each observation and dither offset.

The corrected basic calibrated data frames were inspected by eye, and remaining artifacts, such as column pulldown, were removed with the imclean tool.[29] Frames with a cosmic-ray detection within a 10-pixel (approximately 12″) radius of OJ 287 were not included in the analysis (in general there were zero to one such frames per observation). The centroid of the image of OJ 287 was found with the first moment centroiding method.[30] We performed aperture photometry with the IDL procedure *aper* using a source aperture radius of six pixels and a background annulus between 12 and 20 pixel radial distance from the centroid position. We corrected the flux densities with

[29] https://irsa.ipac.caltech.edu/data/SPITZER/docs/dataanalysistools/tools/contributed/irac/imclean/

[30] https://irsa.ipac.caltech.edu/data/SPITZER/docs/irac/calibrationfiles/pixelphase/box_centroider.pro

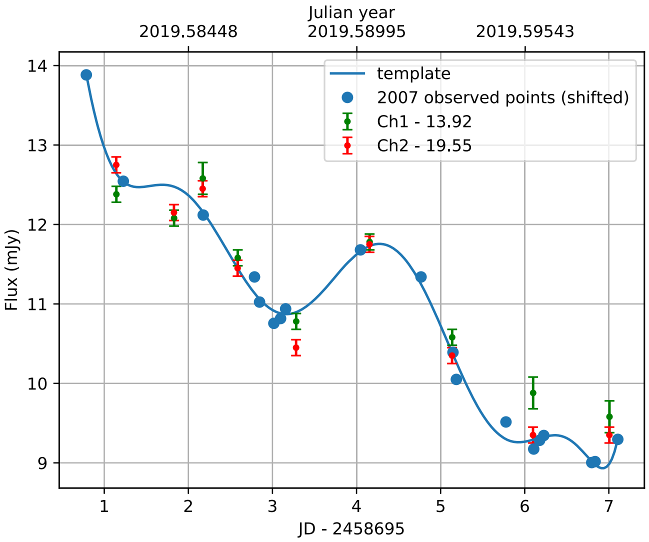

Figure 2. Observed Spitzer flux variations of OJ 287 during 2019 July 31 to 2019 August 6 (green and red points with the error bars provide the base-level corrected fluxes in the two near-infrared Spitzer channels). Solid line connects the multi-epoch optical observations (blue filled circles) of the 2007 impact flare, shifted by the predicted $11.8752 + (0.06/365.25) \approx 11.8754$ yr time interval. The temporal shift of our 2007 template does incorporate the fact that the observed flare came 0.06 days later than our prediction. The template is given by a ninth-order polynomial that minimally and smoothly fits the 2007 optical data. An apparent agreement does exist between our prediction and observations.

the irac_aphot_corr.pro procedure,[31] for the pixel phase and array location-dependent response functions. In addition, we performed an aperture correction as tabulated in the IRAC Instrument Handbook.[32] For each channel, at each epoch, we finally calculated the mean flux density and the uncertainty from the standard error of the mean, as presented in Table 1.

3.2. Extracting the Presence of the Impact Flare and Its Implications

Recall that we predicted the optical R-band lightcurve for the 2019 impact flare from the corresponding observations in 2007. However, our observations of the Eddington flare are in the two near-infrared Spitzer channels. Therefore, it is crucial to estimate how the predicted flare lightcurve should look in the Spitzer bands. In the quiescent state, the infrared–optical wavelength emission comes from synchrotron radiation, and the spectrum follows a power law with a spectral index $\alpha \sim -0.95$ (Kidger et al. 2018). In contrast, BH impact flares are dominated by bremsstrahlung radiation, which has a nearly flat spectrum in the near-infrared–optical wavelengths superposed on the usual synchrotron emission. Therefore, we expect that the impact-induced fluxes in the Spitzer bands will be similar to those in the optical bands. However, the base levels of the fluxes in the Spitzer and optical wavelengths should be different during such outbursts due to the steep power-law spectrum of the synchrotron background. Therefore, we subtract the base-level fluxes from the observed Spitzer band fluxes during the outburst to compare with the predicted R-band flux curve. We expect the 2019 impact flare to be coincident in time in the optical and the near-infrared as multiwavelength observations of the 2015 impact flare show no time delay across the relevant wavebands (Valtonen et al. 2016; Kushwaha et al. 2018).

We now examine if our observed Spitzer lightcurve does contain the predicted impact flare. This requires us to create a template of the expected flare, as given in Figure 2, and we focus on the declining part after the first peak which lasts around 7 days. The template is obtained by fitting a polynomial to the observed R-band lightcurve of the 2007 flare (Valtonen & Sillanpää 2011), shifted forward by 11.8752 yr. This time shift between the 2007 and 2019 flares, with ± 4 hr uncertainty, was previously found in the orbit solution (D18). We introduce the three parameters Δt, ΔF_1, and ΔF_2 for fitting the Spitzer data with the outburst template. The parameters ΔF_1 and ΔF_2 are used to correct for the expected base-level differences between R-band and Spitzer's Ch-1 and Ch-2 fluxes, respectively. The Δt parameter allows us to find the difference between the predicted and actual arrival times of the 2019 outburst. Note that it shifts the time variable in our polynomial fit for the 2007 lightcurve. We employ only a single Δt parameter for both channels as we expect the impact flare to produce simultaneous flux variations in both channels. The best-fit values with 1σ uncertainties read $\Delta t = -0.06 \pm 0.05$ days, $\Delta F_1 = 13.92 \pm 0.11$ mJy, and $\Delta F_2 = 19.55 \pm 0.09$ mJy. This implies that the Eddington flare arrived 1.4 ± 1.2 hr *late* of the predicted epoch but well within the expected time interval. Therefore, we shift our flux templates forward in time by 0.06 days to obtain Figure 2 where we compare the base-level corrected flux variations in Spitzer channels with the template of 2007. We also performed a self-consistency test by fitting the Ch-1 and Ch-2 fluxes separately, and the resulting values of Δt's for the two channels agree with each other within their uncertainties, as required. Qualitatively, the predicted lightcurve template for the 2019 impact outburst matches fairly well with the base-level corrected fluxes of both Spitzer channels. To quantify these similarities, we computed Pearson's r between the observed Spitzer data sets and the time-corrected template of Figure 2 and found high correlations (Pearson's $r \sim 0.98$). We repeated this analysis using 20,000 random 1 week long OJ 287 lightcurves to rule out the occurrence of high Pearson's r values due to chance coincidences.

It turns out that the possible template choices introduce $\sim$1 hr uncertainty in the flare timing. The template curve of Figure 2 should actually be a Gaussian band instead of a single line, since there is always some background noise in the source, and because the 2007 observations have associated error bars. Instead of a single template curve there could be any number of alternative ones that fit inside the band of ± 0.3 mJy vertical half-width. Repeating the above processes with this band instead of a single line widens the error bars in ΔF but has no effect on Δt beyond the 1 hr additional error. Further, the radiating bubble that emits bremsstrahlung with a Maxwellian velocity distribution can give the spectral index $\alpha \sim -0.2$, rather than 0.0, the exactly flat spectrum (intensity $\sim \nu^{\alpha}$) if the source has a constant temperature T (Karzas & Latter 1961). However, when we are looking at an expanding bubble, the light travel time is different from different parts of the source, and therefore the spectrum is composed of contributions from different temperatures T within some range ΔT. The intensity depends essentially only on the parameter $u = h\nu/kT$. If we employ a reasonable assumption that temperatures T are uniformly distributed over this range, then the intensity is

[31] https://irsa.ipac.caltech.edu/data/SPITZER/docs/dataanalysistools/tools/contributed/irac/iracaphotcorr/
[32] https://irsa.ipac.caltech.edu/data/SPITZER/docs/irac/iracinstrumenthandbook/

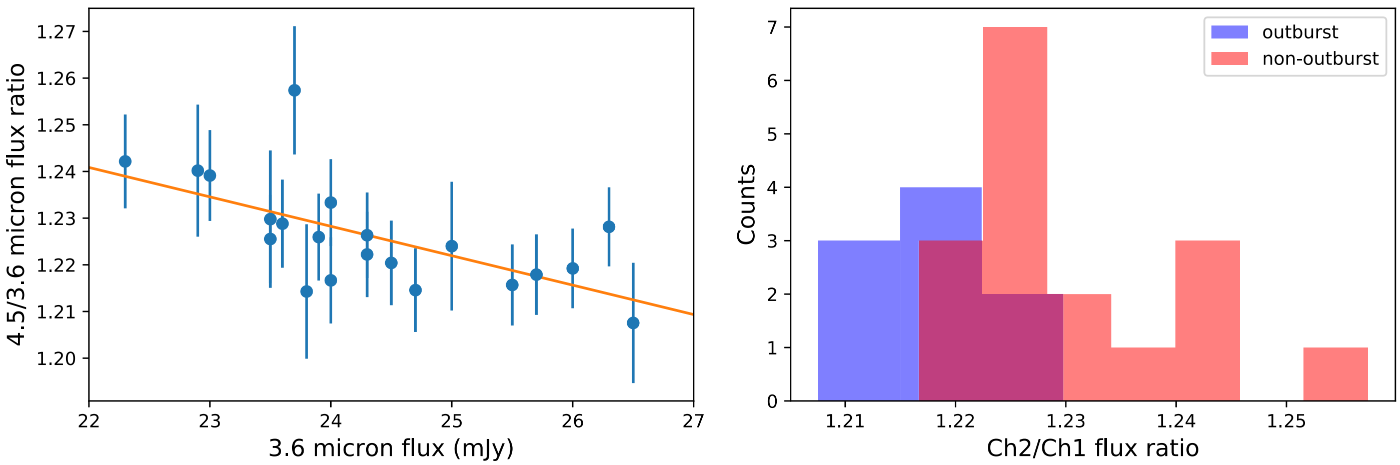

Figure 3. Left panel: we display the flux ratio between the 4.5 and 3.6 μm Spitzer channels against the 3.6 μm flux, which shows the expected decrease in the ratio when the flux is high. Right panel: distribution of the above flux ratio during outburst and non-outburst stretches of data. The bremsstrahlung nature of the flare is responsible for the small flux ratio during flare epochs.

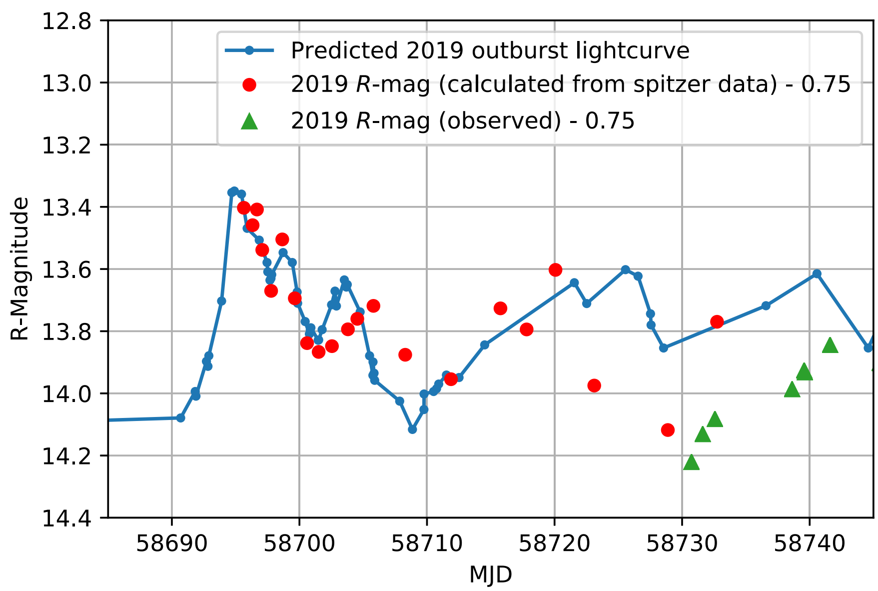

Figure 4. Reconstructed R-band lightcurve (red points) and actual R-band observation (green triangles) along with the prediction (blue line with dots; D18). The red R-band points are constructed from the associated Spitzer fluxes after subtracting the measured 2019 August 16 fluxes as the synchrotron base level and adding our estimated R-band base-level flux of $\sim$3.73 mJy. Also, we consider $\alpha = -0.2$ while converting the Spitzer fluxes to R-band fluxes.

constant over the corresponding range in frequency $\Delta\nu$ and we get a flat emission spectrum. Naturally, details depend on the models of the emitting bubble (Pihajoki 2016). It is likely that the spectral index α lies between -0.2 and 0.0. For $\alpha = -0.2$, we get $\Delta t = 0.10 \pm 0.05$ implying that the flare arrived 2.5 ± 1.2 hr *early*. Thus, considering these uncertainties, the Eddington flare came within $\sim$4 hr of the predicted time.

The nearly flat spectrum of the impact flare should cause an overall decrease in the ratio of 4.5 and 3.6 μm fluxes in the neighborhood of flare peak in Spitzer data. Plots in Figure 3 confirm this expectation. The flux ratios during the outburst window from 2019 July 31 to August 6 have a significantly different distribution with smaller values compared to their counterparts during the non-outburst phases. Further, we got a Kolmogorov–Smirnov (K-S) statistic of 0.66 with a p-value $= 0.0053$ while doing the K-S test between the two set flux ratios. At this significance level, the flux ratios during the outburst and non-outburst epochs come from two distinct distributions.

It is also possible to construct a fiducial R-band magnitude flare lightcurve from Spitzer data using the calibration measurements that involved both optical R-band and the Spitzer channels during 2019 February 25–2019 March 2. We find that the Ch-1 flux can be converted to an equivalent optical R-band value by dividing the former by $\sim$6.2 and for Ch-2 the factor is $\sim$7.6. Therefore, using the previously obtained base-level contributions to the infrared flux, the R-band base flux during the 2019 impact flare should be $\sim$3.73 mJy. Thereafter, this R-band flux is added to the excess flux above the base level in the two Spitzer bands. The resulting two fluxes are averaged at every epoch and converted to R magnitudes (using the Gemini observatory converter). This is plotted in Figure 4, together with the actual ground-based R-band observations. Indeed, the fiducial R-band magnitudes join smoothly with the direct R-band observations in early September where both Spitzer and optical observations overlap. These plots endorse the similar nature of 2007 and 2019 flares both in their total sizes and general lightcurve shapes.

4. Discussion

We presented observational evidence and astrophysical arguments for the occurrence of an impact flare during 2019 July 31 in OJ 287 that was predicted using the BBH central engine model. These efforts confirm OJ 287 as a source of nano-Hz GWs, which should provide additional motivation for probing the IPTA data sets for GWs from massive BH binaries in general relativistic eccentric orbits (Susobhanan et al. 2020). The present analysis underlines the importance of incorporating the effects of higher-order GW emission in the model. Interestingly, we would have predicted the flare to occur 1.5 days earlier than it did if we included only the dominant quadrupolar order GW emission in the BBH dynamics. Observational evidence for the flare arrival within 4 hr of the actual prediction supports the prominent role of including 2PN-accurate GW emission effects while tracking the orbit of the secondary BH. More importantly, our Spitzer observations constrain the celebrated no-hair theorem by bounding the parameter q in Equation (1). The above-mentioned timing accuracy corresponds to $q = 1.0 \pm 0.15$ (D18), in agreement with the GR value $q = 1.0$, provided identical impacts generate identical flares, and that the higher-order GW emission is calculated accurately enough. Such accuracy is possible as our Spitzer observations cover the crucial epoch of fast decline in the flux where the shape of the lightcurve is essentially wavelength independent, which allowed us to tie the variability timescale to the 130 yr long record at optical wavelengths. These observations are setting the stage for observational campaigns that employ the unprecedented high-resolution imaging capabilities of the Event Horizon Telescope, in combination with the Global Millimeter VLBI Array and the space VLBI mission RadioAstron, to spatially resolve the BBH system in OJ 287.

We thank Sean Carey for useful discussions on Spitzer data. This work is based in part on observations made with the Spitzer Space Telescope, which is operated by the Jet Propulsion Laboratory, California Institute of Technology under a contract with NASA. L.D. and A.G. acknowledge support of the Department of Atomic Energy, Government of India, under project No. 12-R&D-TFR-5.02-0200. S.Z. acknowledges grant No. NCN 2018/29/B/ST9/01793.

ORCID iDs

Seppo Laine https://orcid.org/0000-0003-1250-8314
Lankeswar Dey https://orcid.org/0000-0002-2554-0674
Mauri Valtonen https://orcid.org/0000-0001-8580-8874
A. Gopakumar https://orcid.org/0000-0003-4274-4369
Stanislaw Zola https://orcid.org/0000-0003-3609-382X
S. Komossa https://orcid.org/0000-0002-9214-4428
Pauli Pihajoki https://orcid.org/0000-0003-1758-1908
José L. Gómez https://orcid.org/0000-0003-4190-7613
Stefano Ciprini https://orcid.org/0000-0002-0712-2479
Kosmas Gazeas https://orcid.org/0000-0002-8855-3923
Vira Godunova https://orcid.org/0000-0001-7668-7994
Rene Hudec https://orcid.org/0000-0002-7273-7349
Albert K. H. Kong https://orcid.org/0000-0002-5105-344X
Alexios Liakos https://orcid.org/0000-0002-0490-1469
Daniel E. Reichart https://orcid.org/0000-0002-5060-3673
Andrii Simon https://orcid.org/0000-0003-0404-5559
Eda Sonbas https://orcid.org/0000-0002-6909-192X

References

Abbott, B. P., Abbott, R., Abbott, T. D., et al. 2019, PhRvX, 9, 031040
Baker, J., Bellovary, J., Bender, P. L., et al. 2019, arXiv:1907.06482
Blanchet, L., & Schafer, G. 1993, CQGra, 10, 2699
Burke-Spolaor, S., Taylor, S. R., Charisi, M., et al. 2019, A&ARv, 27, 5
Dey, L., Gopakumar, A., Valtonen, M., et al. 2019, Univ, 5, 108
Dey, L., Valtonen, M. J., Gopakumar, A., et al. 2018, ApJ, 866, 11
Fazio, G. G., Hora, J. L., Allen, L. E., et al. 2004, ApJS, 154, 10
Goulding, A. D., Pardo, K., Greene, J. E., et al. 2019, ApJL, 879, L21
Karzas, W. J., & Latter, R. 1961, ApJS, 6, 167
Kidger, M., Zola, S., Valtonen, M., et al. 2018, A&A, 610, 74
Kushwaha, P., Gupta, A. C., Wiita, P. J., et al. 2018, MNRAS, 473, 1145
Lehto, H. J., & Valtonen, M. J. 1996, ApJ, 460, 207
Perera, B. B. P., DeCesar, M. E., Demorest, P. B., et al. 2019, MNRAS, 490, 4666
Pihajoki, P. 2016, MNRAS, 457, 1145
Sundelius, B., Wahde, M., Lehto, H., et al. 1997, ApJ, 484, 180
Susobhanan, A., Gopakumar, A., Hobbs, G., & Taylor, S. 2020, PhRvD, 101, 043022
Thorne, K. S. 1980, RvMP, 52, 299
Valtonen, M., & Sillanpää, A. 2011, AcPol, 51, 76
Valtonen, M. J., Ciprini, S., & Lehto, H. J. 2012, MNRAS, 427, 77
Valtonen, M. J., Kidger, M., Lehto, H. J., et al. 2008a, A&A, 477, 407
Valtonen, M. J., Lehto, H. J., Nilsson, K., et al. 2008b, Natur, 452, 851
Valtonen, M. J., Mikkola, S., Lehto, H. J., et al. 2011, ApJ, 742, 22
Valtonen, M. J., Nilsson, K., Sillanpää, A., et al. 2006, ApJL, 643, L9
Valtonen, M. J., Zola, S., Ciprini, S., et al. 2016, ApJL, 819, L39
Valtonen, M. J., Zola, S., Pihajoki, P., et al. 2019, ApJ, 882, 88
Werner, M. W., Roellig, T. L., Low, F. J., et al. 2004, ApJS, 154, 1
Will, C. M., & Maitra, M. 2017, PhRvD, 95, 064003

The Astrophysical Journal, 905:145 (31pp), 2020 December 20 https://doi.org/10.3847/1538-4357/abc335

Kilonova Luminosity Function Constraints Based on Zwicky Transient Facility Searches for 13 Neutron Star Merger Triggers during O3

Mansi M. Kasliwal[1], Shreya Anand[1], Tomás Ahumada[2], Robert Stein[3,4], Ana Sagués Carracedo[5], Igor Andreoni[1], Michael W. Coughlin[1,6], Leo P. Singer[7,8], Erik C. Kool[9], Kishalay De[1], Harsh Kumar[10], Mouza AlMualla[11], Yuhan Yao[1], Mattia Bulla[12], Dougal Dobie[13,14,15], Simeon Reusch[3,4], Daniel A. Perley[16], S. Bradley Cenko[7,8], Varun Bhalerao[10], David L. Kaplan[17], Jesper Sollerman[9], Ariel Goobar[5], Christopher M. Copperwheat[16], Eric C. Bellm[18], G. C. Anupama[19], Alessandra Corsi[20], Samaya Nissanke[21], Iván Agudo[22], Ashot Bagdasaryan[1], Sudhanshu Barway[19], Justin Belicki[23], Joshua S. Bloom[24,25], Bryce Bolin[1], David A. H. Buckley[26], Kevin B. Burdge[1], Rick Burruss[23], Maria D. Caballero-García[27], Chris Cannella[1], Alberto J. Castro-Tirado[22,28], David O. Cook[29], Jeff Cooke[15,30], Virginia Cunningham[2], Aishwarya Dahiwale[1], Kunal Deshmukh[10], Simone Dichiara[2,7], Dmitry A. Duev[1], Anirban Dutta[19], Michael Feeney[23], Anna Franckowiak[3], Sara Frederick[2], Christoffer Fremling[1], Avishay Gal-Yam[31], Pradip Gatkine[2], Shaon Ghosh[32], Daniel A. Goldstein[1,54], V. Zach Golkhou[18,33,55], Matthew J. Graham[1], Melissa L. Graham[1], Matthew J. Hankins[1], George Helou[34], Youdong Hu[22,35], Wing-Huen Ip[36], Amruta Jaodand[1], Viraj Karambelkar[1], Albert K. H. Kong[37], Marek Kowalski[38,39], Maitreya Khandagale[10], S. R. Kulkarni[1], Brajesh Kumar[19], Russ R. Laher[34], K. L. Li[37], Ashish Mahabal[1,40], Frank J. Masci[34], Adam A. Miller[41,42], Moses Mogotsi[26,43], Siddharth Mohite[17,56], Kunal Mooley[1], Przemek Mroz[1], Jeffrey A. Newman[44], Chow-Choong Ngeow[36], Samantha R. Oates[45], Atharva Sunil Patil[36], Shashi B. Pandey[46], M. Pavana[19], Elena Pian[47], Reed Riddle[23], Rubén Sánchez-Ramírez[48], Yashvi Sharma[1], Avinash Singh[19], Roger Smith[23], Maayane T. Soumagnac[49,50], Kirsty Taggart[16], Hanjie Tan[36], Anastasios Tzanidakis[1], Eleonora Troja[2,7], Azamat F. Valeev[51], Richard Walters[23], Gaurav Waratkar[10], Sara Webb[15,30], Po-Chieh Yu[36], Bin-Bin Zhang[52,53], Rongpu Zhou[49], and Jeffry Zolkower[23]

[1] Division of Physics, Mathematics, and Astronomy, California Institute of Technology, Pasadena, CA 91125, USA
[2] Department of Astronomy, University of Maryland, College Park, MD 20742, USA
[3] Deutsches Elektronen Synchrotron DESY, Platanenallee 6, D-15738 Zeuthen, Germany
[4] Institut für Physik, Humboldt-Universität zu Berlin, D-12489 Berlin, Germany
[5] The Oskar Klein Centre, Department of Physics, Stockholm University, AlbaNova, SE-106 91 Stockholm, Sweden
[6] School of Physics and Astronomy, University of Minnesota, Minneapolis, MN 55455, USA
[7] Astrophysics Science Division, NASA Goddard Space Flight Center, MC 661, Greenbelt, MD 20771, USA
[8] Joint Space-Science Institute, University of Maryland, College Park, MD 20742, USA
[9] The Oskar Klein Centre, Department of Astronomy, Stockholm University, AlbaNova, SE-106 91 Stockholm, Sweden
[10] Indian Institute of Technology Bombay, Powai, Mumbai 400076, India
[11] American University of Sharjah, Physics Department, P.O. Box 26666, Sharjah, UAE
[12] Nordita, KTH Royal Institute of Technology and Stockholm University, Roslagstullsbacken 23, SE-106 91 Stockholm, Sweden
[13] Sydney Institute for Astronomy, School of Physics, University of Sydney, NSW 2006, Australia
[14] CSIRO Astronomy and Space Science, P.O. Box 76, Epping, NSW 1710, Australia
[15] Australian Research Council Centre of Excellence for Gravitational Wave Discovery (OzGrav), Swinburne University of Technology, Hawthorn, VIC 3122, Australia
[16] Astrophysics Research Institute, Liverpool John Moores University, IC2, Liverpool Science Park, 146 Brownlow Hill, Liverpool L3 5RF, UK
[17] Center for Gravitation, Cosmology and Astrophysics, Department of Physics, University of Wisconsin–Milwaukee, P.O. Box 413, Milwaukee, WI 53201, USA
[18] DIRAC Institute, Department of Astronomy, University of Washington, 3910 15th Avenue NE, Seattle, WA 98195, USA
[19] Indian Institute of Astrophysics, II Block Koramangala, Bengaluru 560034, India
[20] Department of Physics and Astronomy, Texas Tech University, Box 1051, Lubbock, TX 79409-1051, USA
[21] Center of Excellence in Gravitation and Astroparticle Physics, University of Amsterdam, Netherlands
[22] Instituto de Astrofísica de Andalucía (IAA-CSIC), Glorieta de la Astronomía s/n, E-18008, Granada, Spain
[23] Caltech Optical Observatories, California Institute of Technology, Pasadena, CA 91125, USA
[24] Department of Astronomy, University of California, Berkeley, CA 94720, USA
[25] Physics Division, Lawrence Berkeley National Laboratory, 1 Cyclotron Road, MS 50B-4206, Berkeley, CA 94720, USA
[26] South African Astronomical Observatory, P.O. Box 9, Observatory 7935, Cape Town, South Africa
[27] Astronomical Institute of the Academy of Sciences, Boční II 1401, CZ-14100 Praha 4, Czech Republic
[28] Unidad Asociada Departamento de Ingeniería de Sistemas y Automática, E.T.S. de Ingenieros Industriales, Universidad de Málaga, Spain
[29] Caltech/IPAC, California Institute of Technology, 1200 East California Boulevard, Pasadena, CA 91125, USA
[30] Centre for Astrophysics and Supercomputing, Swinburne University of Technology, Hawthorn, VIC 3122, Australia
[31] Edna and K.B. Weissman Building of Physical Sciences, Weizmann Institute of Science, Rehovot 76100, Israel
[32] Department of Physics and Astronomy, Montclair State University, Montclair, NJ 07043, USA
[33] The eScience Institute, University of Washington, Seattle, WA 98195, USA
[34] IPAC, California Institute of Technology, 1200 East California Boulevard, Pasadena, CA 91125, USA
[35] Universidad de Granada, Facultad de Ciencias Campus Fuentenueva S/N CP E-18071 Granada, Spain
[36] Graduate Institute of Astronomy, National Central University, 32001, Taiwan
[37] Institute of Astronomy, National Tsing Hua University, Hsinchu 30013, Taiwan
[38] Institute of Physics, Humboldt-Universität zu Berlin, Newtonstr. 15, D-124 89 Berlin, Germany
[39] Deutsches Elektronensynchrotron, Platanenallee 6, D-15738, Zeuthen, Germany
[40] Center for Data Driven Discovery, California Institute of Technology, Pasadena, CA 91125, USA
[41] Center for Interdisciplinary Exploration and Research in Astrophysics (CIERA) and Department of Physics and Astronomy, Northwestern University, 1800 Sherman Road, Evanston, IL 60201, USA
[42] The Adler Planetarium, Chicago, IL 60605, USA
[43] Southern African Large Telescope Foundation, P.O. Box 9, Observatory 7935, Cape Town, South Africa
[44] Department of Physics and Astronomy and PITT PACC, University of Pittsburgh, PA 15260, USA

[45] School of Physics and Astronomy & Institute for Gravitational Wave Astronomy, University of Birmingham, Birmingham, B15 2TT, UK
[46] Aryabhatta Research Institute of Observational Sciences, Manora Peak, Nainital 263001, India
[47] INAF, Astrophysics and Space Science Observatory, via P. Gobetti 101, I-40129 Bologna, Italy
[48] INAF, Istituto di Astrofisica e Planetologia Spaziali, Rome, Italy
[49] Lawrence Berkeley National Laboratory, 1 Cyclotron Road, Berkeley, CA 94720, USA
[50] Department of Particle Physics and Astrophysics, Weizmann Institute of Science, Rehovot 76100, Israel
[51] Special Astrophysical Observatory, Russian Academy of Sciences, Nizhnii Arkhyz, 369167, Russia
[52] School of Astronomy and Space Science, Nanjing University, Nanjing 210093, People's Republic of China
[53] Key Laboratory of Modern Astronomy and Astrophysics (Nanjing University), Ministry of Education, People's Republic of China
Received 2020 June 19; revised 2020 October 19; accepted 2020 October 19; published 2020 December 22

Abstract

We present a systematic search for optical counterparts to 13 gravitational wave (GW) triggers involving at least one neutron star during LIGO/Virgo's third observing run (O3). We searched binary neutron star (BNS) and neutron star black hole (NSBH) merger localizations with the Zwicky Transient Facility (ZTF) and undertook follow-up with the Global Relay of Observatories Watching Transients Happen (GROWTH) collaboration. The GW triggers had a median localization area of 4480 deg^2, a median distance of 267 Mpc, and false-alarm rates ranging from 1.5 to 10^{-25} yr^{-1}. The ZTF coverage in the g and r bands had a median enclosed probability of 39%, median depth of 20.8 mag, and median time lag between merger and the start of observations of 1.5 hr. The O3 follow-up by the GROWTH team comprised 340 UltraViolet/Optical/InfraRed (UVOIR) photometric points, 64 OIR spectra, and three radio images using 17 different telescopes. We find no promising kilonovae (radioactivity-powered counterparts), and we show how to convert the upper limits to constrain the underlying kilonova luminosity function. Initially, we assume that all GW triggers are bona fide astrophysical events regardless of false-alarm rate and that kilonovae accompanying BNS and NSBH mergers are drawn from a common population; later, we relax these assumptions. Assuming that all kilonovae are at least as luminous as the discovery magnitude of GW170817 (-16.1 mag), we calculate that our joint probability of detecting zero kilonovae is only 4.2%. If we assume that all kilonovae are brighter than -16.6 mag (the extrapolated peak magnitude of GW170817) and fade at a rate of 1 mag day^{-1} (similar to GW170817), the joint probability of zero detections is 7%. If we separate the NSBH and BNS populations based on the online classifications, the joint probability of zero detections, assuming all kilonovae are brighter than -16.6 mag, is 9.7% for NSBH and 7.9% for BNS mergers. Moreover, no more than $<57\%$ ($<89\%$) of putative kilonovae could be brighter than -16.6 mag assuming flat evolution (fading by 1 mag day^{-1}) at the 90% confidence level. If we further take into account the online terrestrial probability for each GW trigger, we find that no more than $<68\%$ of putative kilonovae could be brighter than -16.6 mag. Comparing to model grids, we find that some kilonovae must have $M_{\rm ej} < 0.03\,M_\odot$, $X_{\rm lan} > 10^{-4}$, or $\phi > 30^\circ$ to be consistent with our limits. We look forward to searches in the fourth GW observing run; even 17 neutron star mergers with only 50% coverage to a depth of -16 mag would constrain the maximum fraction of bright kilonovae to $<25\%$.

Unified Astronomy Thesaurus concepts: Neutron stars (1108); Black holes (162); Gravitational waves (678); Nucleosynthesis (1131); R-process (1324); Compact objects (288); Spectroscopy (1558); Sky surveys (1464); Photometry (1234)

1. Introduction

Gravitational-wave (GW) astrophysics is achieving a new frontier every 2 yr. On 2015 September 14, the Advanced LIGO/Virgo Collaboration (LVC) celebrated the revolutionary discovery of GWs from merging massive stellar black holes (BBHs; Abbott et al. 2016). On 2017 August 17, the physics and astronomy communities jointly celebrated the detection of GWs from the first binary neutron star (BNS) merger that lit up the entire electromagnetic (EM) spectrum (Abbott et al. 2017a, 2017b; Coulter et al. 2017; Evans et al. 2017; Goldstein et al. 2017; Haggard et al. 2017; Hallinan et al. 2017; Margutti et al. 2017; Troja et al. 2017; Kasliwal et al. 2019b). On 2019 April 26, the first candidate neutron star black hole (NSBH) merger was announced by Advanced LIGO/Virgo (Ligo Scientific Collaboration & VIRGO Collaboration 2019a, 2019b), and since then, there have been eight additional candidate NSBH events.

Unlike a BNS system, the very existence of an NSBH binary was observationally unconstrained. No pulsar in the Milky Way is known to have a black hole companion. A compact BNS merger has a viable stellar evolutionary formation channel (Tauris et al. 2015), since a few ultrastripped supernovae (SNe) have been seen (De et al. 2018; Nakaoka et al. 2020; Yao et al. 2020). On the other hand, it has been argued that the supermassive black holes in the nuclei of galaxies assist in the formation of compact NSBH (and BBH) systems by the eccentric Kozai–Lidov (EKL) mechanism (Naoz 2016; Stephan et al. 2019). Unlike a BNS merger, for which GW170817 serves as the Rosetta Stone of what to look for, theoretical predictions of the EM counterparts to NSBH mergers span a wide spectrum, depending on the system parameters (e.g., mass ratio, spin of the black hole, equation of state of the neutron star). While some scenarios predict that the neutron star is swallowed whole by the black hole and there is no EM emission, others predict a luminous kilonova where, compared to the BNS case, more lanthanide-rich material is ejected dynamically while comparable masses are ejected from the disk (e.g., Rosswog 2005; Foucart 2012; Hotokezaka et al. 2013; Kiuchi et al. 2015; Kawaguchi et al. 2016; Kasen et al. 2017; Kruckow et al. 2018; Broekgaarden et al. 2019; Nakar 2020; Fernández et al. 2020).

[54] Hubble Fellow.
[55] Moore-Sloan, WRF, and DIRAC Fellow.
[56] LSSTC Data Science Fellow.

LIGO/Virgo's third observing run (O3; from 2019 April to 2020 March) has yielded real-time alerts on six BNS mergers and nine NSBH mergers. Alerts and localization maps were publicly released within minutes to a few hours after the mergers. Updates to localization maps and false-alarm rates (FARs) were released days to weeks after the mergers. The median localization was 4480 deg^2. The median distance to BNS mergers was 214 Mpc, and that to NSBH mergers was 377 Mpc.

Given that the optical counterpart of GW170817 was first observed only 10.8 hr after merger, there is considerable debate on how the early emission evolves. Different models predict different early evolution (e.g., Drout et al. 2017; Kasliwal et al. 2017; Arcavi 2018; Piro & Kollmeier 2018; Waxman et al. 2018). Thanks to the low latency in the public O3 alerts, prompt follow-up was undertaken. Despite the localizations being coarser and the distances being further than expected (Abbott et al. 2018), the Global Relay of Observatories Watching Transients Happen (GROWTH[57]) collaboration undertook systematic searches and extensive follow-up of every trigger with a worldwide network of telescopes. We used three discovery engines, the Zwicky Transient Facility (ZTF; Bellm et al. 2018; Masci et al. 2018; Graham et al. 2019), Palomar Gattini-IR (PGIR; Moore & Kasliwal 2019; De et al. 2020a), and Dark Energy Camera (DECam; Goldstein et al. 2019), and a suite of 17 follow-up facilities. Candidate counterparts and follow-up results from these searches were promptly announced via Gamma-ray Coordinates Network (GCN) circulars. In addition to GROWTH, several teams undertook wide-field searches for optical counterparts in O3, including Electromagnetic counterparts of Gravitational wave sources at the Very Large Telescope (ENGRAVE; Levan 2020), Global Rapid Advanced Network Devoted to the Multi-messenger Addicts (GRANDMA; Antier et al. 2020), Gravitational-wave Optical Transient Observer (GOTO; Gompertz et al. 2020), All Sky Automated Survey for SuperNovae (ASAS-SN; Shappee et al. 2014), Asteroid Terrestrial Last Alert System (ATLAS; Tonry et al. 2018), Panoramic Survey Telescope and Rapid Response System (PanSTARRS; Chambers et al. 2016), MASTER-Net (Lipunov et al. 2017), Searches after Gravitational Waves Using ARizona Observatories (SAGUARO; Lundquist et al. 2019), Dark Energy Survey Gravitational Wave Collaboration (DES-GW; Soares-Santos et al. 2017), Burst Optical Observer and Transient Exploring System (BOOTES), KM3Net,[58] and VINROUGE[59] (PI: Tanvir). We also undertook a wide-field radio search with the Australian Square Kilometre Array Pathfinder (ASKAP; Dobie et al. 2019).

This paper focuses on events that contain at least one neutron star; see Graham et al. (2020) for our candidate counterpart to a binary black hole merger. The LVC published GW190425 as a confirmed astrophysical BNS with a total system mass of 3.4 $M_{\odot}$ (Abbott et al. 2020a). The LVC also published GW190814 as a confirmed astrophysical merger of a 23 $M_{\odot}$ black hole with a 2.6 $M_{\odot}$ compact object (Abbott et al. 2020b). While we await the final LVC results on the candidature and binary parameters of all other merger candidates from O3, we use the classifications and parameters released via GCN circulars. We refer to GW190814 and GW190425 as "sources" or "confirmed events" and use a "GW" prefix in the name. We refer to all others as "triggers" or "candidate events" with an "S" prefix in the name. We refer to the full set as "events."

We have previously published our search results for the highest-significance mergers: GW190425 (Coughlin et al. 2019d), GW190814 (Dobie et al. 2019; Andreoni et al. 2020b), and S2001015ae and S200115j (Anand et al. 2020). Here we focus on ZTF searches of the full set of O3 triggers and the implications of the joint nondetection of kilonovae from all merger candidates. In Section 2, we summarize the GW trigger selection criteria. In Section 3, we detail the discovery, follow-up, and rejection of candidate optical counterparts. In Section 4, we examine the model-independent implications of the luminosity function of kilonovae. In Section 5, we summarize our key results and look ahead to future GW observing runs.

2. Summary of GW Triggers

During the third LIGO/Virgo observing run, we triggered target-of-opportunity (ToO) searches based on the following criteria: (a) an initial classification with the highest probability of either BNS, NSBH, or MassGap; (b) if MassGap, then a nonzero probability of containing a neutron star; and (c) a visibility and mapping speed allowing us to observe >30% of the initial BAYESTAR sky map (Singer & Price 2016) within 24 hr of merger.

A total of 15 GW events satisfied criteria (a) and (b). In Table 1, we summarize 13 GW triggers during O3 for which we obtained either serendipitous or triggered coverage with the ZTF (we did not get any ZTF data on S190510g, as the sky position was too far south, or S190924h, as the sky position was too close to the Moon). In Figures 1–3, we show the ZTF coverage overlaid on the GW localization contours. Since the public ZTF survey systematically covers the accessible northern sky at an average cadence of 3 days to a median depth of 20.5 mag (Bellm et al. 2018), we "serendipitously" covered several GW sky maps. Serendipitous coverage contributed to more than 30% enclosed probability for the following triggers: GW190814, S190910d, S190910h, S190923y, S190930t, S200105ae, and S200213t. To improve depth/coverage/response time, we triggered ZTF ToO observations for 11 out of 15 events (and undertook DECam searches for three events; see Andreoni et al. 2019c, 2020b; Goldstein et al. 2019). Our triggered ToO observations optimized the trade-off between depth (more exposure time per pointing) and coverage of the localization map (more pointings to enclose more probability) using the `gwemopt` algorithm. A detailed case study of the ToO observations can be found in Coughlin et al. (2019d) and Anand et al. (2020). For S191205ah, our triggered observations were not completed due to bad weather, and only a small fraction was covered serendipitously. For S190910h, given the coarse localization, we relied only on serendipitous coverage as part of regular ZTF operations. For S190923y, given the large time lag between GW alert and first target visibility, we also relied only on serendipitous coverage.

The location of Palomar Observatory relative to LIGO's quadrupolar antenna sensitivity pattern helps minimize the time lag to respond to triggers in real time (see Figure 4); the latency to first observation was between 11 s and 13.7 hr. (The lowest latency of 11 s was enabled by serendipitous coverage.) As predicted by simulations (Nissanke et al. 2013; Kasliwal & Nissanke 2014), all (but one) GW public alerts were accessible from Palomar Observatory, and more than half could be

[57] http://growth.caltech.edu/
[58] https://www.km3net.org/
[59] https://www.star.le.ac.uk/nrt3/VINROUGE/

Table 1
Summary of ZTF Follow-up of 13 GW Triggers in O3

Name	FAR (P_t)	Localization	Distance	Class	P_1	P_2	Time Lag	Depth	$E(B-V)$
GW190425	1 per 69,000 yr (1%)	7461 deg^2	156 ± 41 Mpc	BNS	24.13% (45.92%)	23.90% (44.62%)	0.003 hr	21.5	0.03
S190426c	1 per 1.6 yr (58%)	1131 deg^2	377 ± 100 Mpc	NSBH	52.33% (59.69%)	51.57% (57.40%)	13.06 hr	21.5	0.34
GW190814	1 per 10^{25} yr (1%)	23 deg^2	267 ± 52 Mpc	NSBH	88.57% (87.00%)	78.37% (70.60%)	0.00 hr	21.0	0.02
S190901ap	1 per 4.5 yr (14%)	14,753 deg^2	241 ± 79 Mpc	BNS	56.94% (50.67%)	49.39% (42.76%)	3.61 hr	21.0	0.03
S190910d	1 per 8.5 yr (2%)	2482 deg^2	632 ± 186 Mpc	NSBH	32.99%(42.50%)	31.17% (39.64%)	1.51 hr	20.3	0.04
S190910h	1 per 0.9 yr (39%)	24,264 deg^2	230 ± 88 Mpc	BNS	33.26% (42.95%)	28.92% (38.44%)	0.015 hr	20.4	0.08
S190923y	1 per 0.67 yr (32%)	2107 deg^2	438 ± 133 Mpc	NSBH	NA (38.99%)	NA (19.22%)	13.73 hr	20.1	0.09
S190930t	1 per 2.0 yr (26%)	24,220 deg^2	108 ± 38 Mpc	NSBH	NA (50.63%)	NA (43.42%)	11.91 hr	21.1	0.05
S191205ah	1 per 2.5 yr (7%)	6378 deg^2	385 ± 164 Mpc	NSBH	NA (5.68%)	NA (4.85%)	10.66 hr	17.9	0.04
S191213g	1 per 0.89 yr (23%)	4480 deg^2	201 ± 81 Mpc	BNS	27.50% (0.80%)	25.10% (0.09%)	0.013 hr	20.4	0.30
S200105ae	NA (97%)	7373 deg^2	283 ± 74 Mpc	NSBH	52.39% (56.40%)	43.99% (47.96%)	9.96 hr	20.2	0.05
S200115j	1 per 1513 yr (1%)	765 deg^2	340 ± 79 Mpc	NSBH	22.21% (34.92%)	15.76% (18.17%)	0.24 hr	20.8	0.13
S200213t	1 per 1.8 yr (37%)	2326 deg^2	201 ± 80 Mpc	BNS	72.17% (79.29%)	70.48% (76.08%)	0.40 hr	21.2	0.19

Note. We list the GW FAR and, in parantheses, the probability that the event is terrestrial (P_t). We list the total size of the GW localization region, the GW median distance, and the most probable GW classification. We report the integrated probability within the 90% contour of the LALInference sky map, covered by triggered and serendipitous ZTF searches during the first 3 days after merger observed at least once (P_1) and probability observed at least twice (P_2). In parentheses, we include the coverage based on the BAYESTAR sky map. For some alerts, only BAYESTAR sky maps were made available. All estimates correct for chip gaps and processing failures. We also report the time lag between merger time and the start of ZTF observations (hours), the median depth (AB mag), and the median line-of-sight extinction.

followed up within 4 hr of the merger. Throughout the paper, we only use enclosed probability based on the LALInference sky map, as it is deemed more accurate (Veitch et al. 2015), when available. The LALInference sky maps were mostly released only after our observations were completed. Hence, the enclosed probability estimates were systematically lower than those estimated by the observation plan based on the initial BAYESTAR sky maps (see Table 1).

The process for triggering ToO observations for a survey system like the ZTF differs from traditional telescopes, as it involves halting the ongoing survey observations and scheduling observations of only certain fields as selected by an observation plan. Observation plans are generated by `gwemopt`,[60] a code base for optimizing galaxy-targeted and synoptic searches within GW sky maps (Coughlin et al. 2018, 2019a). Over the course of O3, we implemented several improvements to the existing code framework, including additional features that allow us to strategically handle sky maps spanning thousands of square degrees, slice sky maps by R.A. and schedule slices separately, and balance coverage in multiple filters. These improvements, among others, are described in Almualla et al. (2020). All of our triggered follow-up of GW events, gamma-ray bursts (GRBs; T. Ahumada et al. 2020, in preparation), and high-energy neutrino events (Stein et al. 2020) occurs through a user interface called the GROWTH ToO Marshal,[61] a database designed to ingest GCN circulars, display event properties and sky maps, design plans, trigger observations, query for candidates within the observed region, and retrieve summary statistics for completed observations, including probability covered and median depth (Coughlin et al. 2019a; Kasliwal et al. 2019a).

3. Investigating Candidate Counterparts

Our candidate vetting methodology has continued to improve over the past few years, starting with Fermi afterglow searches (Singer et al. 2015), to BBH searches in O1 (Kasliwal et al. 2016), to BNS and NSBH searches in O3 (Coughlin et al. 2019a; Anand et al. 2020). We graphically summarize the candidate vetting process in Figure 5. Here we first discuss the prompt vetting procedure that quickly led to a GCN circular announcing candidate counterparts (Section 3.1). Next, we discuss follow-up of the candidates to discern their nature (Section 3.2). Finally, we discuss a deeper offline search to look for any missed candidates (Section 3.3).

3.1. Initial Transient Vetting

For each of the 13 GW triggers followed up by ZTF, we systematically identified transient candidates within the localization region and ruled them out using various metrics. Below, we summarize the transient filtering process and results from our candidate vetting.

The GROWTH team has three independent database systems to retrieve interesting objects in real time: the GROWTH Marshal (Kasliwal et al. 2019a), the `Kowalski`[62] system (Duev et al. 2019), and the Alert Management, Photometry and Evaluation of Lightcurves (`AMPEL`) system (Soumagnac & Ofek 2018; Nordin et al. 2019). Each platform retrieves a stream of `AVRO` packet alerts (Patterson et al. 2019) containing significant object detections identified by the ZTF image subtraction pipeline, defined as a $>5\sigma$ change in brightness relative to a reference image (Masci et al. 2018). Each of these objects undergoes a series of filtering steps in order to identify candidates that could be interesting to pursue for follow-up. The following criteria were common for all three queries.

1. Positive subtraction. The object must have brightened relative to the reference image.
2. Astrophysical. The object must have a real bogus (rb) score >0.25 or a deep learning (drb) score >0.8 (Duev et al. 2019; Mahabal et al. 2019) for it to be considered astrophysical.

[60] https://github.com/mcoughlin/gwemopt
[61] https://github.com/growth-astro/growth-too-marshal
[62] https://github.com/dmitryduev/kowalski

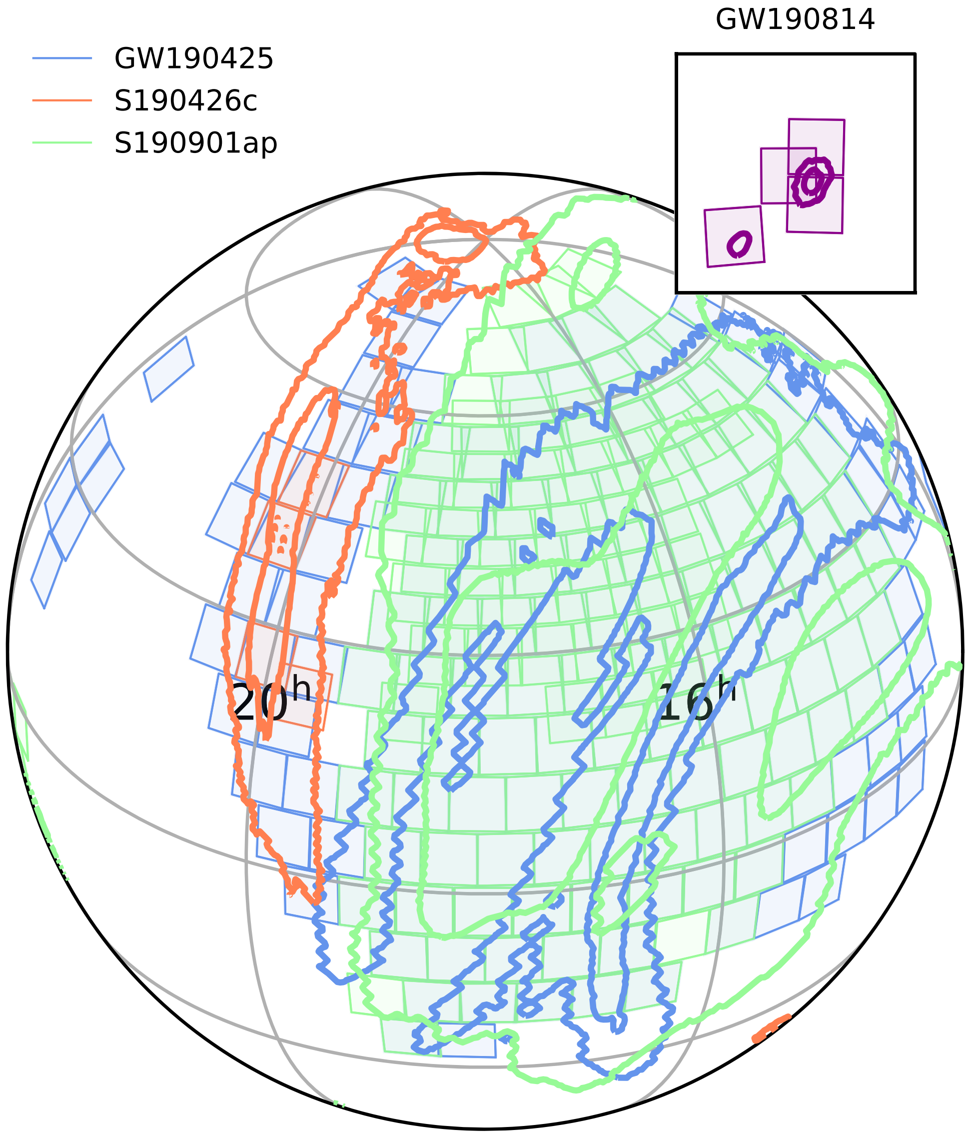

Figure 1. The ZTF coverage maps of two BNS triggers (S190901ap and GW190425) and two NSBH triggers (S190426c and GW190814) during O3 of LIGO/Virgo. Each square represents a ZTF pointing, and the solid line denotes the latest available GW 90% localization contour. Despite both BNS triggers being localized to a π of the sky, the ZTF was able to map the accessible localization area in a few hours.

3. Not stellar. The object must be $>2''$ away from a cataloged point source in the PanSTARRS Point Source Catalog (Tachibana & Miller 2018).
4. Far from a bright source. The object must be at least $20''$ away from a bright ($m_{\rm AB} < 15$ mag) star to avoid blooming artifacts.
5. Not moving. The object must have at least two detections separated by at least 15 minutes to reject asteroids (moves $<4''\,{\rm hr}^{-1}$)
6. No previous history. The object must not have any historical detections in the ZTF alert stream prior to the GW merger time.

While the GROWTH Marshal queried all fields triggered as part of the ToO search, the `Kowalski` and `AMPEL` queries searched for candidates in both serendipitous and triggered data within the 95% contour of the latest sky map that was available. The `AMPEL` query[63] had further image quality cuts performed to reject poor subtractions based on morphology, an additional cut based on proximity to known solar system objects, and another cut based on cross-matching to the Gaia Data Release 2 (DR2) catalog and PS1 to identify likely stellar sources.

All candidates that passed the filtering criteria were saved to the GROWTH Marshal for further vetting in real time by a dedicated team of scanners. If a transient was consistent with the nucleus of a galaxy and the mid-infrared colors (based on the Wide-field Infrared Survey Explorer (WISE) catalog; Wright et al. 2010) of the host galaxy were consistent with active galactic nuclei (AGNs), the candidate was deemed unrelated.

All viable candidates were promptly announced to the worldwide community via GCN circulars, and many teams (not only GROWTH) triggered follow-up observations for many of our candidates.[64] Using the GROWTH Marshal system, we prioritized and triggered follow-up of candidates that exhibited

[63] https://github.com/robertdstein/ampel_followup_pipeline

[64] The GROWTH collaboration posted 82 GCNs during O3. An additional 151 GCNs refer to follow-up of ZTF objects by other teams.

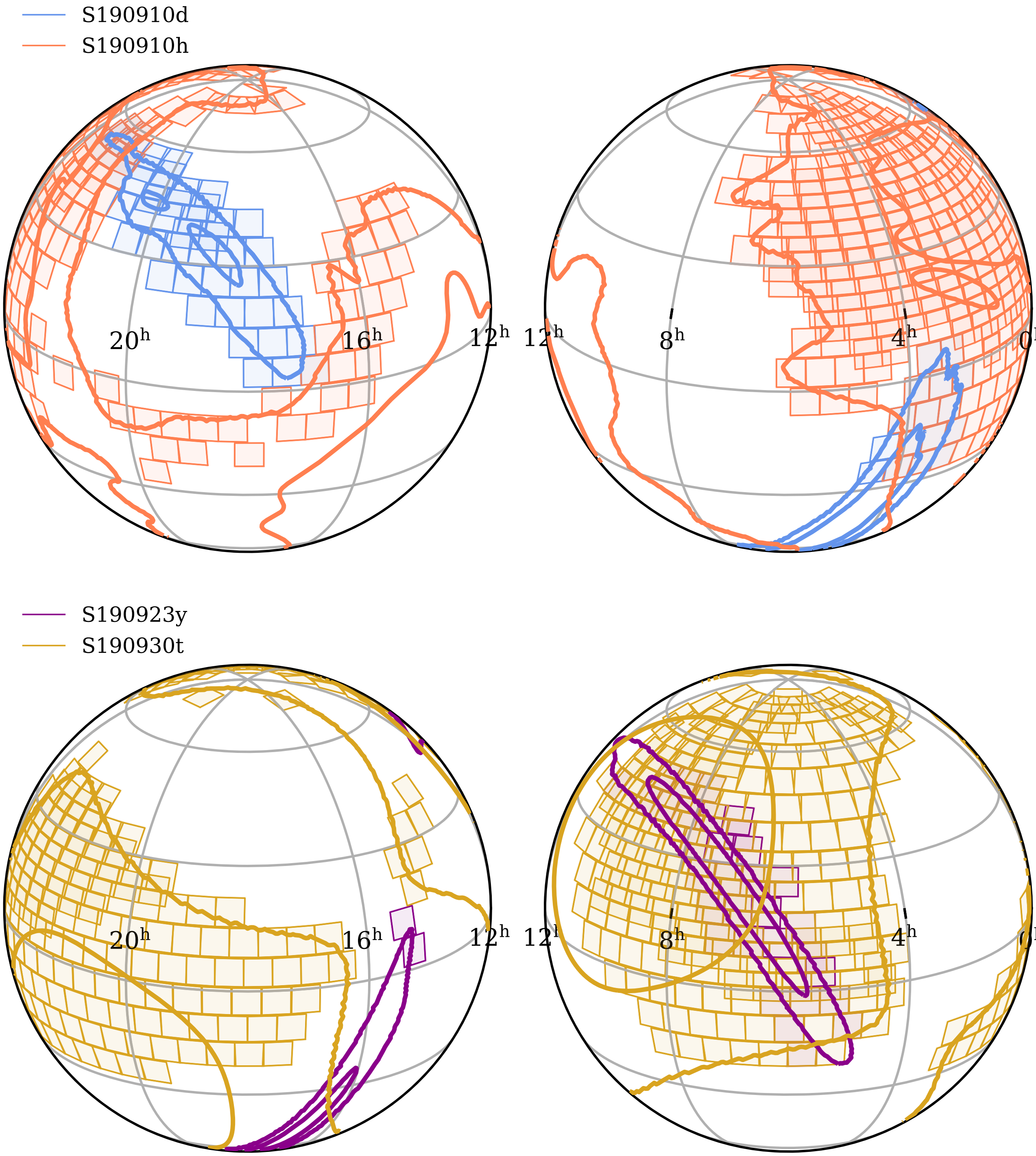

Figure 2. Top: ZTF coverage maps of the two same-day triggers occurring on September 10 (S190910d and S190910h) during O3 of LIGO/Virgo. Given the spatial and temporal overlap of these two GW triggers, some field observations contributed to coverage of both. Bottom: ZTF coverage maps of two NSBH triggers (S190923y and S190930t) during O3. Each square represents a ZTF pointing, and the solid line denotes the latest available GW 90% localization contour.

rapid photometric evolution (faster than 0.3 mag day^{-1}), showed red colors, or were close to a host galaxy with a redshift consistent with the GW distance constraint.

3.2. Examining Promising Candidate Counterparts with Additional Follow-up

We now briefly describe how we ruled out the association between vetted counterpart candidates and the GW event. A detailed account of every candidate announced via GCN is in Appendix B.

The GROWTH team obtained follow-up with the following facilities to characterize the photometric and/or spectroscopic evolution: the Liverpool Telescope (LT; Steele et al. 2004), Lowell Discovery Telescope (LDT,[65] formerly known as the Discovery Channel Telescope), Las Cumbres Observatory (LCO; Brown et al. 2013), Apache Point Observatory (APO; Huehnerhoff et al. 2016), Kitt Peak EMCCD Demonstrator (KPED; Coughlin et al. 2019b), Lulin One-meter Telescope

[65] https://lowell.edu/research/research-facilities/4-3-meter-ldt/

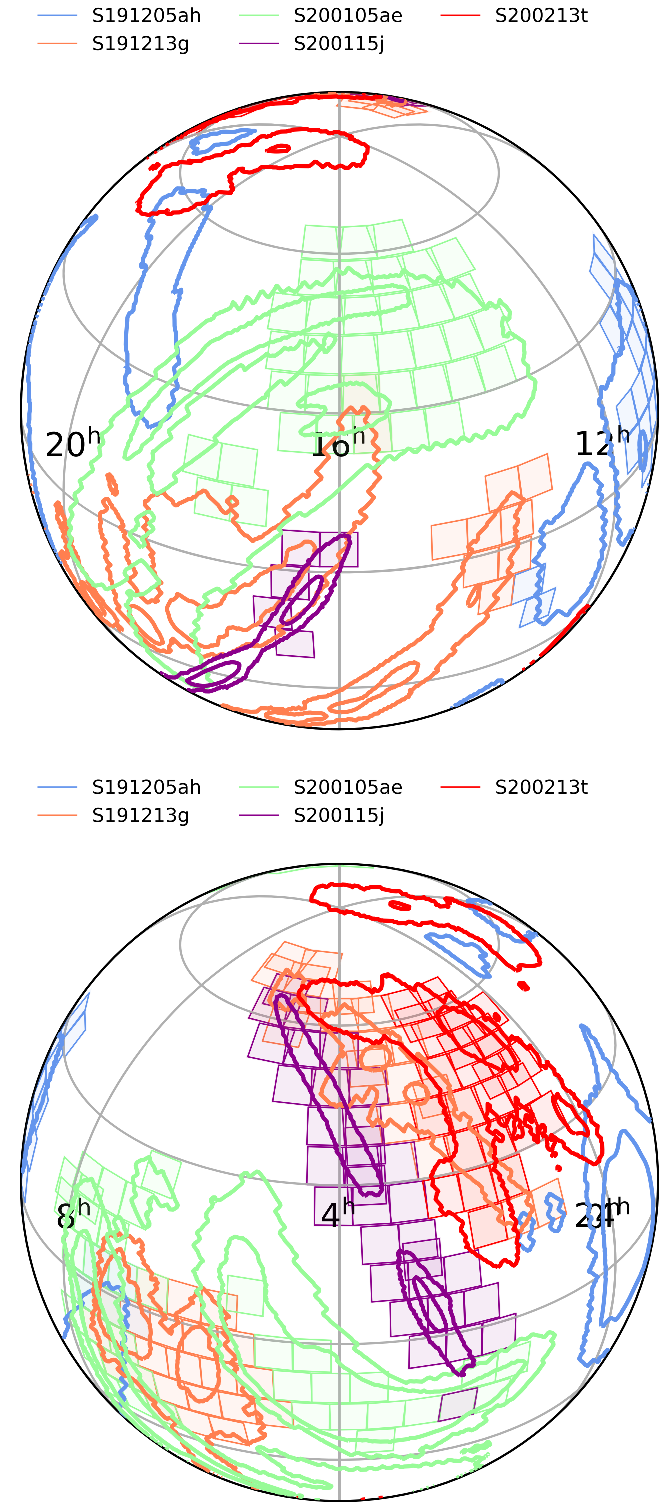

Figure 3. The ZTF coverage maps of the triggers during the second half of O3 of LIGO/Virgo: S191205ah, S191213g, S200105ae, S200115j, and S200213t. The top and bottom panels show opposite sides of the globe. Each square represents a ZTF pointing, and the solid line denotes the latest available GW 90% localization contour.

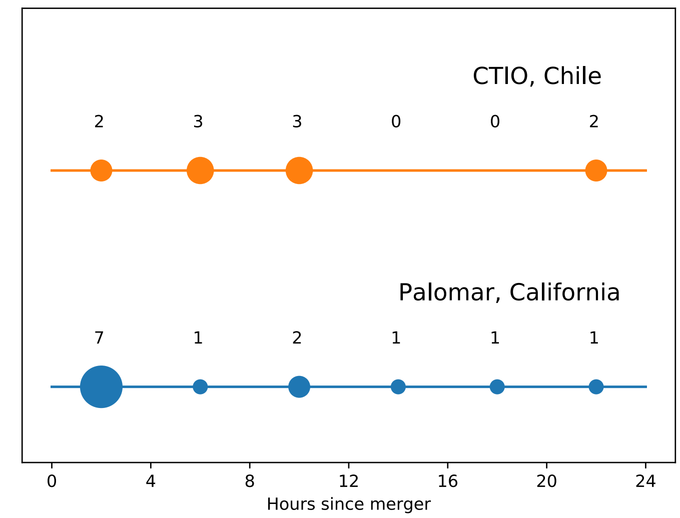

Figure 4. Distribution of response time, defined as the time lag between merger time and earliest possible observation time at a given site, for all 15 BNS/NSBH triggers in O3. We define that observations can begin when at least 30% of the enclosed probability of a GW localization contour is above airmass 2.0 and the Sun is 12° below the horizon at a given site. The size of the filled circles scales with the number of triggers in each time bin. Note that the location of Palomar Observatory enables a response to more triggers than CTIO overall (13 vs. 10 triggers) and a larger number (seven vs. two triggers) within 4 hr after merger.

(LOT; Huang et al. 2005), GROWTH-India telescope (GIT;[66] V. Bhalerao et al. 2020, in preparation), Palomar 60 inch telescope (P60; Cenko et al. 2006), Palomar 200 inch Hale Telescope[67] (P200), Keck Observatory,[68] Gemini Observatory,[69] Southern African Large Telescope[70] (SALT), Himalayan Chandra Telescope[71] (HCT), and Gran Telescopio Canarias[72] (GTC). Figures 6 and 7 illustrate examples of follow-up by the GROWTH team on some ZTF candidates. The specific instrument configurations and data reduction methods are described in Appendix A.

The follow-up observations include both photometric and spectroscopic data. Moreover, the association of a candidate with a GW trigger was rejected if its properties fell into one or more of the categories described as follows.

1. Inconsistent spectroscopic classification. We ruled out candidates that could be spectroscopically classified as SNe, AGNs, cataclysmic variables (CVs), and other flare stars. We used `SNID` (Blondin & Tonry 2007) and `dash` (Muthukrishna et al. 2019) to classify the SNe and AGNs found in our searches. The CVs and variable stars often showed hydrogen features at zero redshift.
2. Inconsistent distance. We ruled out candidates whose spectroscopic redshift was not consistent with the GW distance within 2σ. We cross-matched the transient positions with the Census of the Local Universe (CLU; Cook et al. 2019) galaxy catalog and the NASA Extragalactic Database (NED) to look up host redshifts where available. We also cross-matched the candidates against the Photometric Redshifts Legacy Survey (PRLS; Zhou et al. 2020) catalog and reported the photometric redshifts when the spectroscopic redshift was unavailable.

66 https://sites.google.com/view/growthindia/

67 https://www.astro.caltech.edu/palomar/about/telescopes/hale.html

68 http://www.keckobservatory.org/

69 http://www.gemini.edu/

70 https://www.salt.ac.za/

71 https://www.iiap.res.in/?q=telescope_iao

72 http://www.gtc.iac.es/gtc/gtc.php

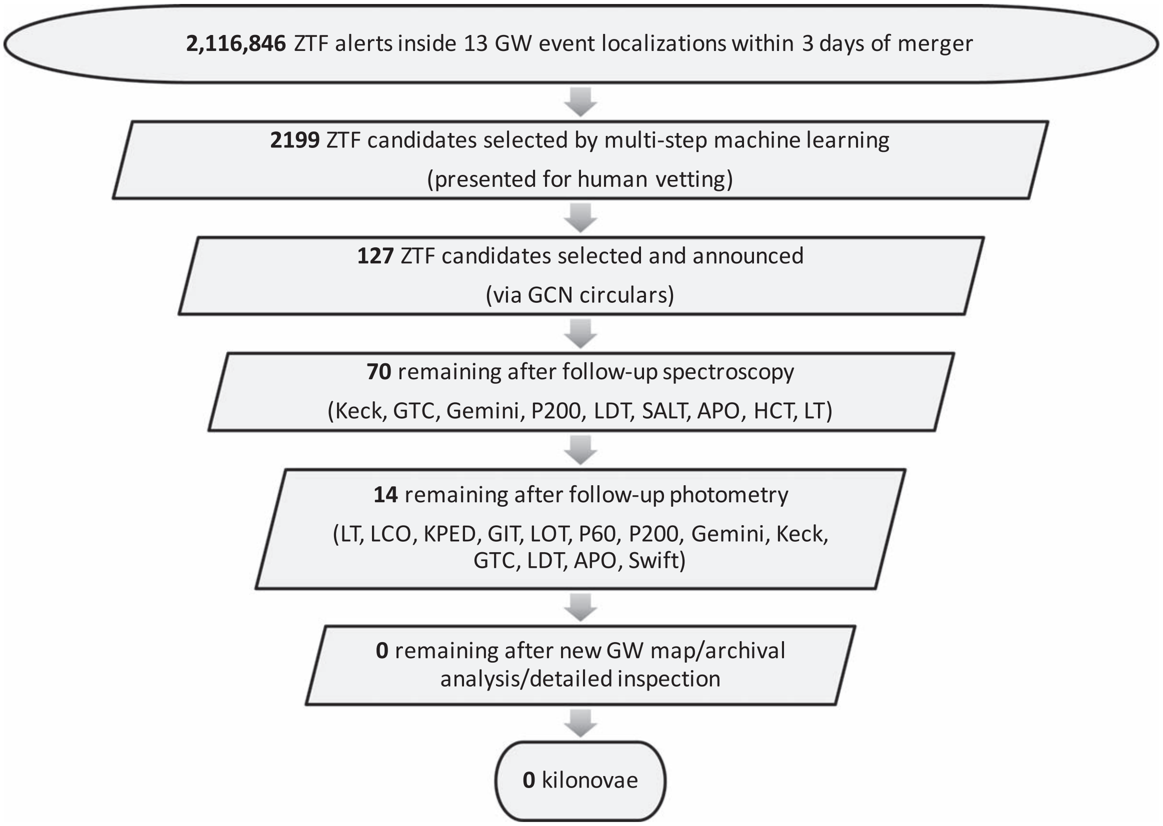

Figure 5. Flowchart to show how our candidate vetting funneled from a large number of spatially and temporally consistent alerts, to a smaller number of candidates that deem human vetting, to an even smaller number of candidates that warrant detailed follow-up characterization over the course of O3.

3. Slow photometric evolution. As kilonovae are expected to evolve faster than SNe, we ruled out candidates that evolved slower than 0.3 mag day^{-1}. We used `ForcePhot`[73] (Yao et al. 2019), a forced photometry package, to examine the transient light curves. To quantify the evolution of a given transient, we define the parameter $\alpha_f = \Delta m/\Delta t$ [mag day^{-1}], where f corresponds to the filter used to determine the variation in magnitude (Δm) over time (Δt). A positive α indicates a fading source, while a negative α describes a rising source. The baseline (Δt) is defined to be the number of days it takes an object to rise from its discovery to its peak magnitude ($\alpha < 0$) or the number of days it takes the transient to fade from peak to undetectable by ZTF ($\alpha > 0$). We used a minimum time baseline of 3 days to compute slopes.
4. Outside of the latest LALInference map. The majority of the candidates were selected and announced via GCN based on the promptly available BAYESTAR map (Singer & Price 2016). When the LALInference map was made available, if a candidate was outside the 90% probability contour, we rejected it.
5. Artifacts. Most of the ZTF ghosts and artifacts are well known (Bellm et al. 2018; Masci et al. 2018)[74] and masked automatically. Additionally, we take further precautions by ignoring transients close to bright stars in our initial vetting. However, for example, our extensive analysis revealed a subtle gain mismatch in the reference images that posed as a faint and fast transient (see discussion related to ZTF19aassfws in Appendix B). All references for ToOs were rebuilt after this artifact was identified.
6. Asteroids. Sometimes slow-moving asteroids, especially near stationary points, can mimic a fast-fading transient (Jedicke et al. 2016). For these objects, either a more careful inspection of the centroids or movement in follow-up imaging served as the reason for rejection.
7. Previous activity. Candidates were rejected if they showed previous detections prior to the GW merger time in other surveys, e.g., the Catalina Real Time Survey (CRTS; Djorgovski et al. 2011), Palomar Transient Factory (PTF; Law et al. 2009), intermediate Palomar Transient Factory (iPTF; Cao et al. 2016; Masci et al. 2017), and PS1 (Tachibana & Miller 2018).

Some candidates prompted panchromatic follow-up. We followed up five candidates in the ultraviolet and X-ray with the Neil Gehrels Swift Observatory (see the Appendix for details). We followed up two candidates in the radio with the Arcminute Microkelvin Imager (AMI) and one with the Karl G. Jansky Very Large Array (VLA; see the Appendix for details). All candidates, grouped by GW trigger, are listed in Tables 2–10, along with their respective rejection criteria.

3.3. Candidates from Deeper Offline Searches

We complemented our real-time analysis described above with a deeper offline search by relaxing the selection criteria (e.g., requiring only one detection instead of two). The following steps describe our offline search.

[73] https://github.com/yaoyuhan/ForcePhotZTF
[74] http://nesssi.cacr.caltech.edu/ZTF/Web/Ghosts.html

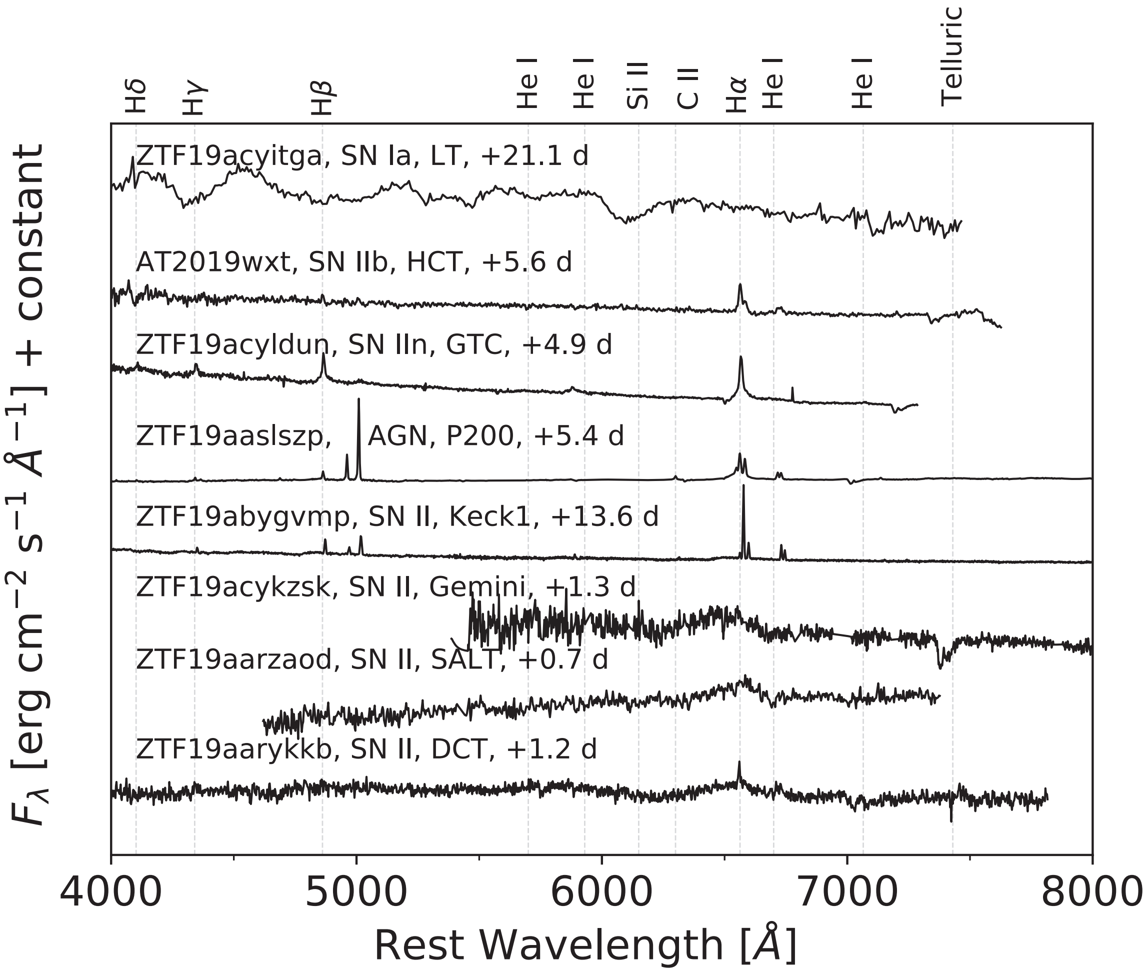

Figure 6. Collage of spectra taken during our GW follow-up in O3, one from each spectroscopic facility. The spectra displayed include six Type II SNe, one AGN, and one Type Ia SN and were taken with LT+SPRAT and GTC+OSIRIS in Roque de los Muchachos, Spain; P200+DBSP on Palomar Mountain, USA; Keck1+LRIS and Gemini+GMOS-N on Maunakea, USA; SALT+RSS in Sutherland, South Africa; HCT+HFOSC in Hanle, India; and LDT+Deveny in Happy Jack, USA.

1. We used `Kowalski` to query the ZTF database looking for any source (i) located within 95% of the most updated sky map, (ii) never detected before the merger time, (iii) with at least one detection within 72 hr of merger, (iv) with the last detection occurring within 10 days of the first detection, and (v) passing real/bogus thresholds of rb > 0.5 and drb > 0.8 (or braai > 0.8; Duev et al. 2019). Further details on the selection criteria will be described in I. Andreoni et al. (2020, in preparation).
2. Forced point-spread function (PSF) photometry was performed at the location of each transient candidate using `ForcePhot`, setting a detection threshold of signal-to-noise ratio (S/N) > 3, where the images were available.
3. The flux measured using forced photometry was stacked nightly in each band, allowing us to become sensitive to fainter sources when multiple images were available on the same night.
4. The rising and fading rates were computed in each band with a linear fit before and after the brightest data point of each light curve. A time baseline of $>$3 hr was required for the fit to be performed.
5. Candidates were selected with a fading rate more rapid than 0.3 mag day^{-1} or rising rate faster than 1 mag day^{-1}. We rejected candidates still detected after 6, 12, and 14 days after the merger time in the g, r, and i bands, respectively. More details are given in I. Andreoni et al. (2020, in preparation).

The `Kowalski` query initially returned 8026 sources for the 13 GW triggers. Applying all of the selection criteria described above, 453 candidates survived the automatic cuts. Of these, 21 had at least two ZTF alerts, and 432 had only one ZTF alert (additional detections were recovered by forced photometry and stacking).

Of the 21 sources with at least two detections in the ZTF alert stream, only five candidates passed visual inspection of the images and light curves: ZTF19acbxacj was an AGN candidate (Assef et al. 2018; Bailer-Jones et al. 2019); ZTF19abwsfsl was a cataloged CV (Gaia Collaboration 2018); ZTF19acbqtue was followed up with the Gemini Multi-Object Spectrograph (GMOS-N), and a quiescent source was found at $g = 24.69 \pm 0.07$ mag with a color $g - i = 1.89$ mag, consistent with an M dwarf (West et al. 2011); ZTF19abyndjf was a fast-evolving transient without an obvious host galaxy; and ZTF19acbwtmt was hostless and had a previous detection in the PS1-DR2 catalog from 2012 (see Figure 8). For the last two candidates, upper limits between the GW merger time and the

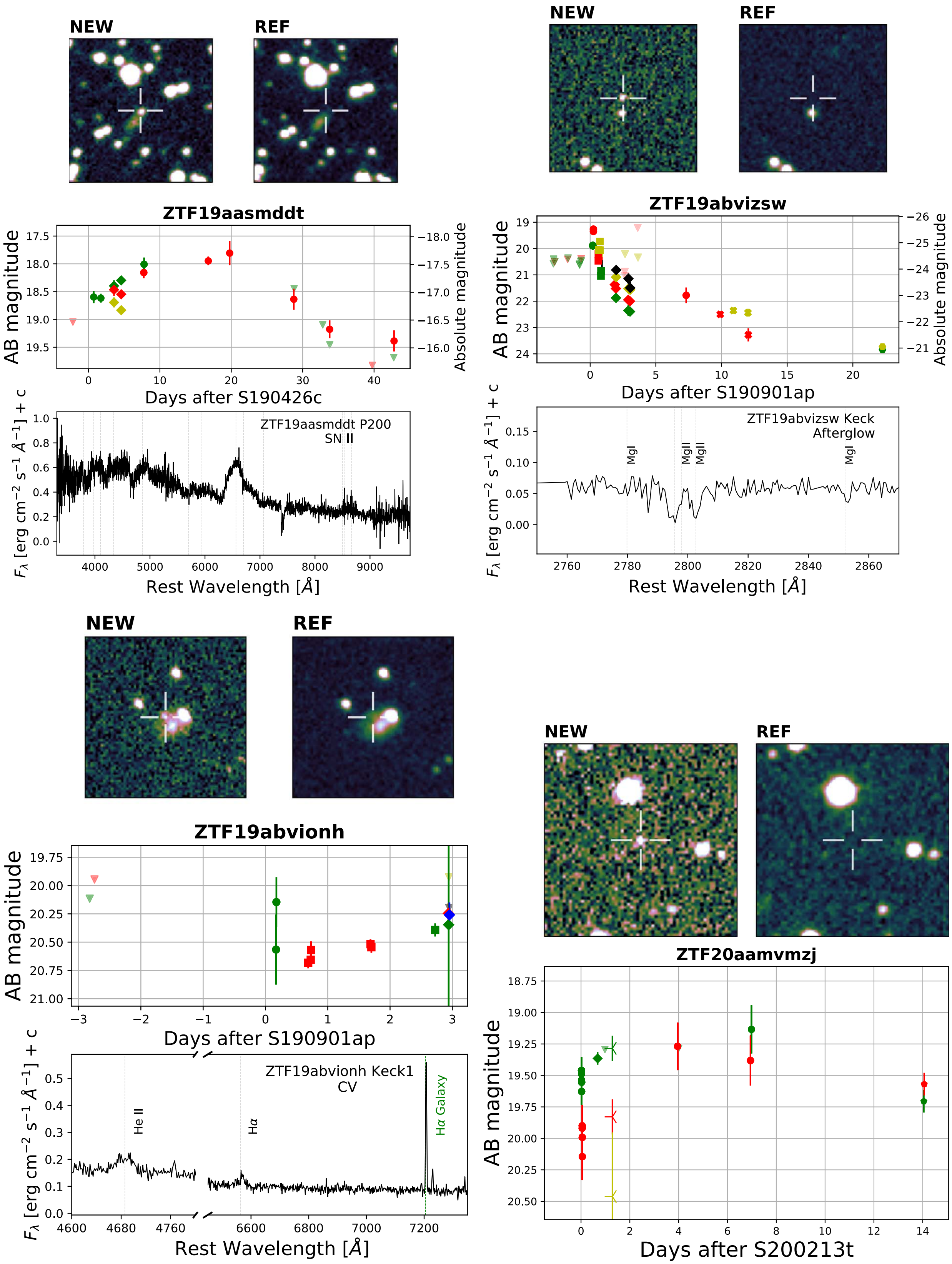

Figure 7. Collage of candidate counterparts found during real-time searches. We show a 7″ × 7″ region with north up and east left for the discovery (NEW) and reference (REF) images. We also show the light curve of the candidate, where the *u*-, *g*-, *r*-, *i*-, and *z*-band data are shown in blue, green, red, yellow, and black respectively. The ZTF data are presented with filled circles, while data from the LT, GIT, Keck, WHT, and LCO are presented as filled diamonds, squares, elongated diamonds, crosses, and pentagons, respectively. Absolute magnitude is shown for the candidates with a known redshift, and upper limits are shown as inverted triangles. We also display the spectra of the transient where available and mark the hydrogen and helium lines for ZTF19aasmddt (SN II), the H and He II features of ZTF19abvionh (CV), and the Mg I and Mg II lines for ZTF19abvizsw (long GRB afterglow).

Table 2
List of Candidate Counterparts to S190426c

Name	TNS	R.A.	Decl.	Host/Redshift	Discov. Mag	Rejection Crit.
ZTF19aasmftm	AT2019sne	325.9004479	77.8315634	0.156 [s]	$g = 18.78 \pm 0.19$	SN Ia
ZTF19aaslzjf	AT2019snh	320.6262982	65.8134516	0.028 [s]	$g = 19.45 \pm 0.14$	SN Ia
ZTF19aasmddt	SN2019fht	299.25055	9.7016748	0.028 [s]	$g = 18.6 \pm 0.11$	SN II
ZTF19aasmekb	AT2019snl	300.6013987	14.2873159	⋯	$g = 17.33 \pm 0.04$	$\alpha_g = 0.24$
ZTF19aassfws	AT2019fuc	298.6678611	61.2400121	⋯	$r = 21.35 \pm 0.21$	Artifact
ZTF19aaslszp	AT2019snj	301.3434628	53.3990477	0.084 [s]	$g = 20.12 \pm 0.15$	$\alpha_r = 0.01$, AGN
ZTF19aaslolf	AT2019snn	288.7838539	79.4357187	⋯	$r = 21.12 \pm 0.18$	$\alpha_r < 0.01$, AGN, PS1
ZTF19aaslozu	AT2019snr	306.3144981	65.1093759	⋯	$r = 20.59 \pm 0.21$	$\alpha_g = 0.06$, AGN, PS1
ZTF19aasshpf	AT2019snt	315.4768651	70.2055771	⋯	$r = 19.99 \pm 0.23$	$\alpha_r < 0.01$
ZTF19aaslphi	AT2019sno	297.3809977	61.9605925	⋯	$r = 21.26 \pm 0.20$	$\alpha_r = -0.08$
ZTF19aaslpds	AT2019snq	306.2625186	61.521461	⋯	$r = 19.9 \pm 0.14$	$\alpha_r = 0.03$
ZTF19aasmzqf	AT2019aaco	353.5204911	78.9577781	⋯	$r = 19.86 \pm 0.09$	$\alpha_r = 0.01$
ZTF19aaslzfk	AT2019snd	308.968271	72.3536353	⋯	$g = 20.0 \pm 0.26$	$\alpha_g = -0.02$
ZTF19aaslvwn	AT2019snf	299.059846	46.463559	⋯	$g = 20.68 \pm 0.17$	$\alpha_r < 0.01$
ZTF19aasmdir	AT2019sng	300.2360007	9.504002	⋯	$g = 20.07 \pm 0.11$	$\alpha_r < 0.01$

Table 3
List of Candidate Counterparts to S190901ap

Name	TNS	R.A.	Decl.	Host/Redshift	Discov. Mag	Rejection Crit.
ZTF19abvizsw	AT2019pim	279.47282	61.497984	1.26 [s]	$r = 19.89 \pm 0.16$	Long GRB afterglow
ZTF19abwvals	AT2019pni	73.250555	12.69303	0.091 [s]	$r = 18.96 \pm 0.30$	SN Ia
ZTF19abvixoy	AT2019pin	279.552972	27.420935	⋯	$r = 18.93 \pm 0.10$	$\alpha_r = 0.23$, CV
ZTF19abvionh	AT2019pip	253.750924	14.05133	0.0985 [s]	$g = 20.57 \pm 0.31$	$\alpha_g = 0.10$, CV
ZTF19abwsmmd	AT2019pnc	22.666409	−19.712405	0.0972 [s]	$g = 19.78 \pm 0.18$	$\alpha_g = 0.03$
ZTF19abvislp	AT2019pnx	220.349708	54.151153	0.10 [s]	$r = 19.98 \pm 0.20$	$\alpha_r = 0.05$
ZTF19abxdvcs	AT2019qev	252.010477	41.920087	⋯	$g = 20.64 \pm 0.28$	$\alpha_g = 0.03$

Table 4
List of Candidate Counterparts to S190910d

Name	TNS	R.A.	Decl.	Host/Redshift	Discov. Mag	Rejection Crit.
ZTF19abyfhov	AT2019pvu	260.693429	11.424436	0.13 [s]	$g = 19.92 \pm 0.22$	SN Ia
ZTF19abyfbii	AT2019pvz	255.44162	11.602254	0.118 [s]	$r = 19.60 \pm 0.16$	SN Ia 91T
ZTF19abyfazm	AT2019pwa	290.535876	48.069162	0.38 [s]	$g = 17.53 \pm 0.03$	CV, $\alpha_r = 0.09$
ZTF19abyfhaq	AT2019pvv	303.148593	49.392607	0 [s]	$g = 18.01 \pm 0.31$	$\alpha_r = 0.15$, Galactic

Table 5
List of Candidate Counterparts to S190910h

Name	TNS	R.A.	Decl.	Host/Redshift	Discov. Mag	Rejection Crit.
ZTF19abyheza	AT2019pxi	332.913391	60.395816	0 [s]	$r = 16.14 \pm 0.13$	CV, $\alpha_r = 0.08$
ZTF19abyhhml	AT2019pxj	339.691635	55.936649	0 [s]	$r = 17.36 \pm 0.12$	CV, $\alpha_r = 0.13$
ZTF19abyirjl	AT2019pxe	30.471176	30.73355	0.1 [s]	$r = 19.45 \pm 0.13$	SN Ia
ZTF19abyjcom	AT2019pxk	32.936353	12.033344	⋯	$r = 19.63 \pm 0.24$	Artifact
ZTF19abyjcon	AT2019pxl	33.252469	12.472604	⋯	$r = 19.87 \pm 0.19$	Artifact
ZTF19abyjcoo	AT2019pxm	33.089712	12.297698	<0.03 [p]	$r = 19.95 \pm 0.24$	$\alpha_r = 0.06$
ZTF19abyjfiw	AT2019pxn	39.186807	34.647299	⋯	$g = 20.13 \pm 0.21$	$\alpha_r < 0.01$
ZTF19abygvmp	AT2019pzg	28.976258	41.090979	0.049 [s]	$r = 20.13 \pm 0.25$	SN II
ZTF19abyiwiw	AT2019pzi	340.521441	55.220244	⋯	$r = 18.58 \pm 0.30$	$\alpha_g = 0.20$
ZTF19abylleu	AT2019pyu	355.338225	−23.450706	⋯	$r = 19.19 \pm 0.24$	$\alpha_g = 0.03$
ZTF19abymhyi	AT2019pzh	340.85572	34.186344	<0.03 [p]	$g = 20.36 \pm 0.23$	$\alpha_g = -0.13$

Table 6
List of Candidate Counterparts to S190923y

Name	TNS	R.A.	Decl.	Host/Redshift	Discov. Mag	Rejection Crit.
ZTF19acbmopl	AT2019rob	114.040207	28.487381	<0.03 [p]	$g = 19.64 \pm 0.27$	$\alpha_g = 0.01$

Table 7
List of Candidate Counterparts to S190930t

Name	TNS	R.A.	Decl.	Host/Redshift	Discov. Mag	Rejection Crit.
ZTF19acbpqlh	AT2019rpn	319.9216636	37.5220721	0.026 [*s*]	$g = 19.47 \pm 0.18$	SN II
ZTF19acbwaah	AT2019rpp	162.3277489	22.9827302	0.031 [*s*]	$r = 17.61 \pm 0.08$	SN Ia
ATLAS19wyn	AT2019rpj	339.8367397	31.4916262	0.0297 [*s*]	$g = 19.32 \pm 0.11$	SN II

Table 8
List of Candidate Counterparts to S191205ah

Name	TNS	R.A.	Decl.	Host/Redshift	Discov. Mag	Rejection Crit.
ZTF19acxpnvd	AT2019wkv	175.361851	8.241201	<0.03 [*p*]	$i = 19.58 \pm 0.20$	$\alpha_g = 0.06$
ZTF19acxoywk	AT2019wix	149.896148	13.915051	0.05 [*s*]	$r = 19.69 \pm 0.21$	$\alpha_g = -0.15$
ZTF19acxoyra	AT2019wid	153.093775	8.609330	0.09 [*s*]	$r = 19.14 \pm 0.19$	$\alpha_g = 0.05$
ZTF19acxpwlh	AT2019wiy	155.712970	23.603273	<0.24 [*p*]	$g = 19.77 \pm 0.19$	$\alpha_r = 0.07$
ZTF19acyiflj	AT2019wmy	152.899874	23.943843	0.081 [*s*]	$r = 20.05 \pm 19.63$	SN Ia
ZTF19acxowrr	AT2019wib	154.871458	27.883738	0.05 [*s*]	$r = 19.00 \pm 0.13$	SN II
ZTF19acyitga	AT2019wmn	159.796830	5.161942	0.071 [*s*]	$r = 19.20 \pm 0.16$	SN Ia

Table 9
List of Candidate Counterparts to S191213g Reported in GCN 26424 and 26437

Name	TNS	R.A.	Decl.	Host/Redshift	Discov. Mag	Rejection Crit.
ZTF19acykzsk	SN2019wqj	32.904547	34.041346	0.021 [*s*]	$g = 19.0 \pm 0.06$	SN II
ZTF19acymaru	AT2019wnh	80.461954	−19.266401	0.167 [*s*]	$r = 19.92 \pm 0.16$	SN Ia
ZTF19acykzsp	AT2019wne	28.359144	31.801012	0.16 [*s*]	$r = 20.08 \pm 0.31$	SN Ia
ZTF19acyfoha	AT2019wkl	85.104365	−18.097630	0.04 [*s*]	$g = 17.31 \pm 0.08$	SN Ia
ZTF19acymcwv	AT2019wni	36.248920	47.497844	0.09 [*s*]	$r = 19.76 \pm 0.24$	SN Ia
ZTF19acykwsd	AT2019wnl	33.088072	41.388708	⋯	$r = 19.3 \pm 0.25$	Artifact
ZTF19acylvus	AT2019wnk	83.631136	−19.420244	0.104 [*s*]	$r = 19.45 \pm 0.24$	SN Ia
ZTF19acymcna	AT2019wnn	33.207899	40.999726	0.138 [*s*]	$r = 20.48 \pm 0.22$	$\alpha_r = -0.01$, AGN
ZTF19acykyqu	AT2019wre	38.819646	38.319851	⋯	$g = 20.94 \pm 0.21$	Stellar—PS1-DR2
ZTF19acykyrz	AT2019wrf	36.064972	38.080388	⋯	$g = 20.83 \pm 0.17$	Stellar—PS1-DR2
ZTF19acykyzj	AT2019wrg	36.056624	51.367126	⋯	$g = 19.75 \pm 0.20$	$\alpha_r = -0.03$
ZTF19acykzfy	AT2019wrh	43.115194	41.660303	⋯	$g = 20.34 \pm 0.20$	Stellar—PS1-DR2
ZTF19acyldum	AT2019wrn	79.681883	−7.185279	⋯	$g = 19.41 \pm 0.13$	PS1-DR2 detection
ZTF19acyldun	AT2019wrt	79.199993	−7.478682	0.057 [*s*]	$g = 19.42 \pm 0.17$	$\alpha_r = 0.09$, LBV
ZTF19acymapa	AT2019wro	78.207321	−5.948936	⋯	$g = 18.54 \pm 0.22$	$\alpha_r^{\ddagger} = -0.06$
ZTF19acymaxu	AT2019wrp	82.952485	−26.694523	<0.13 [*p*]	$r = 18.65 \pm 0.06$	$\alpha_r = 0.03$
ZTF19acymixu	AT2019wrr	90.913936	60.728245	0.14 [*s*]	$r = 19.66 \pm 0.32$	SN Ia
ZTF19acymlhi	AT2019wrs	91.592426	−18.804727	⋯	$r = 17.99 \pm 0.26$	$\alpha_r^{\ddagger} = -0.17$

Note. The candidates for which photometric evolution has been calculated with a baseline (Δt) between 2 and 3 days are marked with ‡.

first transient detection disfavor their multimessenger association with S190930t or S190910d, respectively (see Figure 8).

Of the 432 sources with only one detection in the ZTF alert stream, only nine candidates passed the visual inspection of the images and light curves. Most other candidates were ruled out as stellar flares, image subtraction artifacts, asteroids, or sporadic nuclear variability. Of these nine candidates, six had photometric or spectroscopic redshifts of the host galaxy too far to be consistent with the GW distance. All three remaining candidates were found during follow-up of S190901ap: ZTF19abvpeir, ZTF19abvozxv, and ZTF19abvphxm. All three are likely SNe or AGNs, given that their absolute magnitudes at the distance of their putative hosts are between −18.0 and −18.8 mag and their locations are consistent with the Galaxy nuclei. We show some light curves and host galaxies in Figure 8.

In summary, all candidates were ruled out as possible kilonovae in both the real-time and offline analyses.

4. Discussion

We start by treating all triggers as bona fide astrophysical events regardless of FAR, assuming that kilonovae accompanying BNS and NSBH mergers are drawn from a common population, and analyzing the implications of zero kilonova detections. Later, we relax these assumptions. Since kilonova models have a wide range of estimates depending on several intrinsic and extrinsic parameters (e.g., ejecta mass, ejecta velocity, lanthanide fraction, viewing angle, remnant lifetime), we took a model-independent approach toward constraining the luminosity function.

Serving as our benchmark is GW170817. The ZTF observations were taken as *g*- and *r*-band pairs, and GW170817 was discovered at an *i*-band magnitude of 17.3 mag about 10.8 hr after merger (Coulter et al. 2017). Compiling and fitting all published data in the *g* and *r* bands for GW170817 in the first 3 days after merger (Andreoni et al. 2017; Arcavi et al. 2017; Coulter et al. 2017; Cowperthwaite et al. 2017; Díaz et al. 2017;

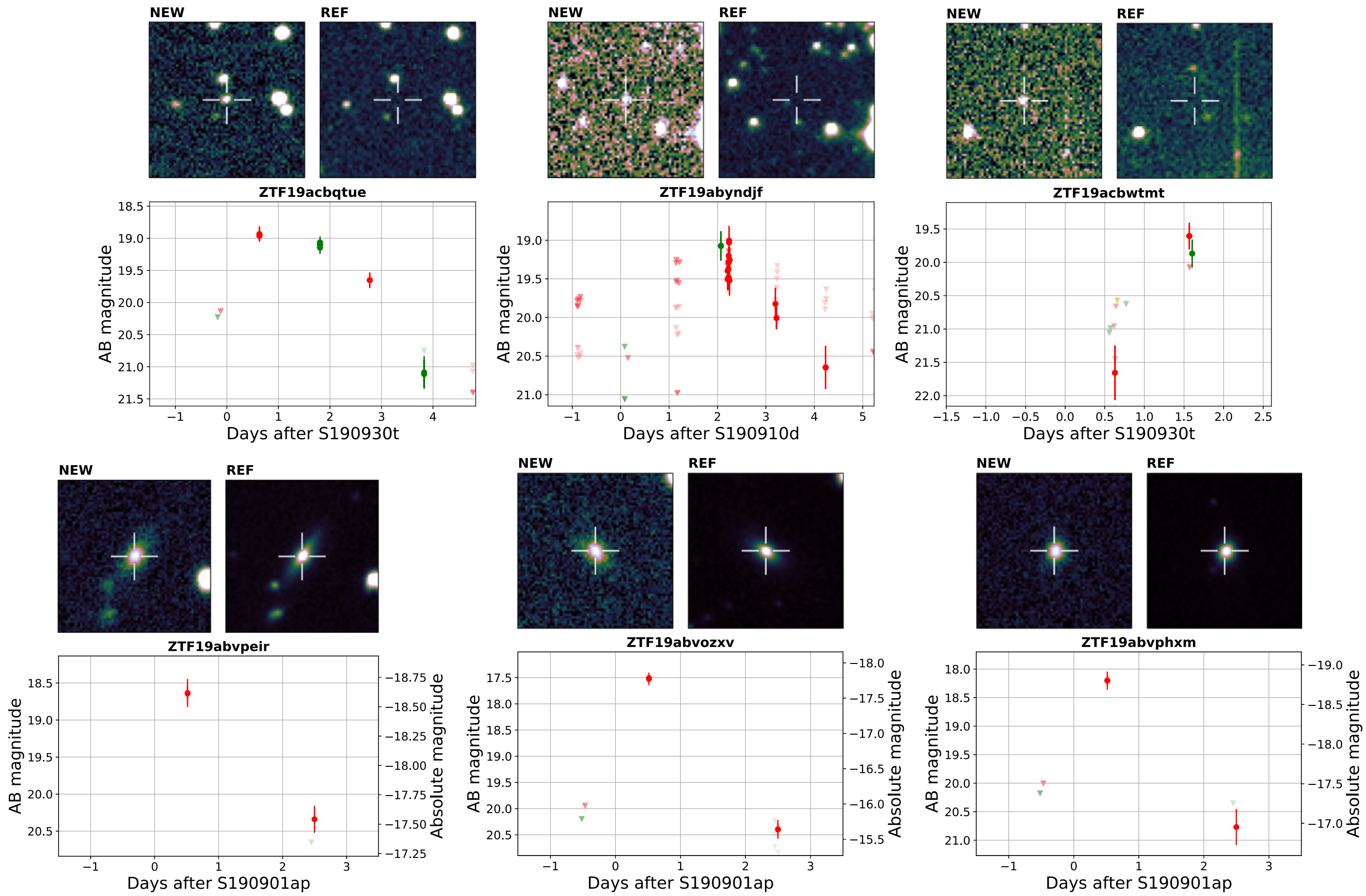

Figure 8. Collage of candidate counterparts found in deeper offline searches. Each candidate in the top row has two or more ZTF alerts: ZTF19acbqtue was ruled out, as we found a quiescent stellar source with GMOS-N; ZTF19abyndjf does not have a galaxy in its vicinity; and ZTF19acbwtmt had archival activity in PS1-DR2. Each candidate in the bottom row had only one ZTF alert but was flagged as interesting after performing forced photometry. These three candidates are nuclear transients that are ruled out, as their absolute magnitudes are brighter than what is expected for kilonovae.

Table 10
List of Candidate Counterparts to S200213t

Name	TNS	R.A.	Decl.	Host/Redshift	Discov. Mag	Rejection Crit.
ZTF20aamvqxl	AT2020ciy	29.237921	53.668882	0.102 [*s*]	$g = 19.44 \pm 0.17$	SN Ia
ZTF20aamvnth	AT2020cjb	18.337721	49.645539	0.061 [*s*]	$g = 19.95 \pm 0.17$	SN II
ZTF20aamvoxx	AT2020cjg	39.399095	26.920616	0.097 [*s*]	$g = 19.47 \pm 0.12$	SN Ia
ZTF20aamvtip	AT2020cje	38.082538	27.810094	0.151 [*s*]	$g = 20.3 \pm 0.16$	SN Ia
ZTF20aamvnat	AT2020ciz	27.239552	56.354579	0.0 [*s*]	$g = 17.42 \pm 0.05$	CV
ZTF20aamvmzj	AT2020cja	27.189195	51.430481	…	$g = 19.46 \pm 0.11$	$\alpha_r = 0.04$
ZTF20aamvoeh	AT2020cjc	33.502011	38.936317	0.14 [*s*]	$g = 20.25 \pm 0.12$	SN Ia
ZTF20aamvodd	AT2020cjf	37.482387	50.319427	0.0 [*s*]	$g = 18.92 \pm 0.11$	Stellar flare
ZTF20aanakwb	AT2020cls	6.5215391	42.7737224	…	$g = 20.75 \pm 0.27$	Stellar
ZTF20aanaltd	AT2020clt	9.7406716	43.4410695	0.2 [*s*]	$g = 20.57 \pm 0.23$	SN Ia
ZTF20aanaksk	AT2020clu	19.4356399	31.1744954	<0.03 [*p*]	$g = 20.27 \pm 0.10$	PS1
ZTF20aanallx	AT2020clv	6.3666608	51.2233877	…	$g = 20.58 \pm 0.28$	Outside the LALInfernce map
ZTF20aanaoyz	AT2020clw	24.5940995	23.3822569	0.276 [*s*]	$g = 21.28 \pm 0.27$	SN Ia
ZTF20aamvpvx	AT2020clx	31.9402981	20.0306147	0.074 [*s*]	$g = 19.95 \pm 0.14$	SN II
ZTF20aanamcs	AT2020crc	13.7433345	43.4980245	0.093 [*s*]	$g = 20.98 \pm 0.28$	SN II
ZTF20aanakge	AT2020crd	12.6306233	41.484178	0.1272 [*s*]	$g = 20.38 \pm 0.33$	SN Ia
ZTF20aanaqhe	AT2020cre	17.0425796	45.5256583	…	$g = 20.63 \pm 0.27$	$\alpha_g = -0.08$
ZTF20aanakes	AT2020cly	2.0985443	38.0441264	…	$g = 20.79 \pm 0.21$	PS1
ZTF20aanakcd	AT2020cmr	8.1571223	41.3156371	0.077 [*s*]	$g = 20.48 \pm 0.17$	SN IIn

Drout et al. 2017; Evans et al. 2017; Pian et al. 2017; Smartt et al. 2017; Utsumi et al. 2017; Valenti et al. 2017; Pozanenko et al. 2018), we find that GW170817 had a decline rate of 0.9 mag day^{-1} in the r band and 1.3 mag day^{-1} in the g band. Extrapolating this decline rate to merger time and correcting for line-of-sight extinction, GW170817 may have peaked at

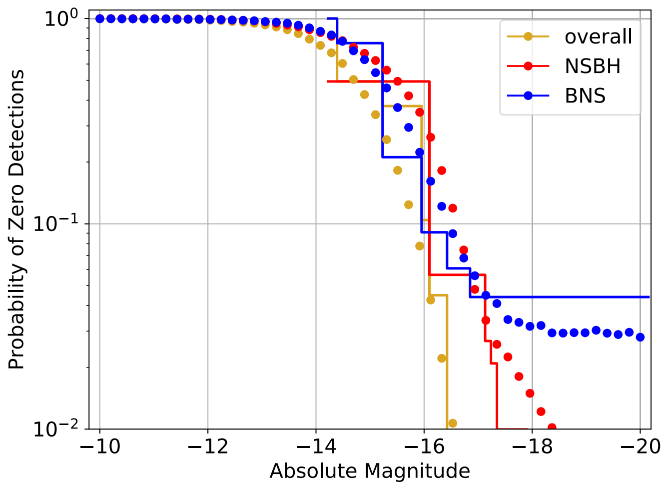

Figure 9. Joint probability of zero detections as a function of absolute magnitude of the kilonova after correcting for line-of-sight extinction. Solid lines represent rough estimates from median estimates. Filled circles represent estimates that take into account the spatial variation in depth, GW distance, and GW probability.

−16.54 mag in the r band and −16.69 mag in the g band (we caution that some kilonova models predict a finite rise time). Here we choose to compare the ZTF limits to an average of these two filters, i.e., −16.6 mag at peak and a decline rate of 1 mag day^{-1}.

4.1. Joint Probability of Zero Detections

We estimate the joint probability of zero kilonova detections as a product of $(1 - q_i)$ terms, where q_i is the enclosed probability for each event as listed in Table 1 (see the sixth column; we used LALInference probability where available). If we were sufficiently sensitive to finding kilonovae in all 13 GW events, the joint probability of zero detections would be only 0.017%. However, each merger had a different observed depth, observed cadence, and GW distance estimate and thus a different sensitivity to detecting kilonovae.

First, we use the median image depth for each trigger and the median GW distance to each trigger to compute a median absolute magnitude sensitivity limit. We correct the median absolute magnitude for the median extinction along the line of sight. In Figure 9, in each luminosity bin, we compute the joint nondetection probability only for the subset of events for which the ZTF observations were sufficiently sensitive. We find that ZTF follow-up of four (six) GW events had a sensitivity deeper than −16.0 mag (−16.6 mag), and the joint nondetection probability is only 4.5% (0.34%). Moreover, three of the four (four of the six) had a preliminary BNS classification, and for all three, the ZTF follow-up began within 4 hr of merger (see Table 1).

Second, we use injection and recovery of fake sources to better quantify both the degree of variation in the depths of individual exposures and the spatial variation in the GW distance estimates. We use an open-source tool called `simsurvey`[75] (Feindt et al. 2019). As input, the tool takes a list of ZTF pointings (observation time, R.A., decl., limiting magnitude, filters, processing success of each CCD quadrant). We inject 10,000 sources distributed according to the 3D GW sky map probability distribution in each luminosity bin (50 bins between −10 and −20 mag). Initially, we assume that each kilonova stays at a constant luminosity between the merger time and 3 days after merger. We require a single observation at the necessary depth for recovery. In addition to losing sources in unobserved fields, we lose sources that land in ZTF chip gaps, chips that failed processing, or chips that were less sensitive due to higher line-of-sight Galactic extinction. This tool does not take into account any detections that would be lost to inefficiency in the software pipeline.

The recovery fraction for each event is shown in Figure 10. We convert this to a joint nondetection probability estimate by multiplying $(1 - {}_{pi})$ in each luminosity bin and overlay this as discrete points on the median estimates above in Figure 9. We find consistent results; the joint probability of zero detections at −16.1 mag (−16.6 mag) is only 4.2% (0.8%). If we separate the NSBH and BNS populations, the joint nondetection probability at −16.6 mag is 9.7% for NSBH and 7.9% for BNS. This is not surprising, as the BNS triggers were, on average, closer than the NSBH triggers. We note that this application of `simsurvey` is different compared to previous applications for SN rates, which were uniform in volume. Taking into account the exact 3D GW sky map is more accurately representative of our success in searching for the counterpart to a GW source on an event-by-event basis.

Third, in addition to spatial variations in depth and distance, we take into account the possible time variations in the light curves of kilonovae (Figure 11). The time window for our observations is limited to within 3 days of merger. We relax the constant luminosity assumption above and inject kilonovae into `simsurvey` that fade linearly between zero and 1 mag day^{-1}. In Figure 11, we color-code the recovery efficiency for a given peak luminosity and photometric decay rate in any filter (g or r band). Any slice of this plot can be converted to a joint probability of zero detections as a function of absolute magnitude. We compare to the GW170817 benchmark of an extrapolated peak of −16.6 mag day^{-1} and a fade rate of 1 mag day^{-1}. We find a joint probability of zero detections of 7%.

Fourth, in addition to spatial and time variations, we inject kilonova models into `simsurvey` and calculate the recovery fraction. We use the best fit to GW170817 from the kilonova model grid in Dietrich et al. (2020) computed using the radiative transfer code `POSSIS` (Bulla 2019). This model fit assumes a rise time, color evolution, and viewing angle of GW170817. The joint nondetection probability is 30%. Even if all kilonova ejecta parameters were similar to GW170817, the viewing angle would be different for different events. Assuming random viewing angles drawn from a distribution uniform in cos(θ), we inject a model grid and find that the joint nondetection probability is 49%. We caution that the model used here underestimates the early g-band flux of GW170817 by 0.3 mag; thus, the recovery fraction estimated here could also be underestimated.

4.2. Constraining the Kilonova Luminosity Function

Next, we consider the implications of the zero-detection probability function on the underlying luminosity function. Let us say the luminosity function dictates that a fraction f_b of kilonovae are brighter than a given absolute magnitude. Then,

$$(1 - \mathrm{CL}) = \prod_{i=1}^{N} (1 - f_b^* p_i),$$

where CL is the confidence level and ${}_{pi}$ is the event-by-event probability of detection. At a given absolute magnitude, we

[75] https://github.com/ZwickyTransientFacility/simsurvey

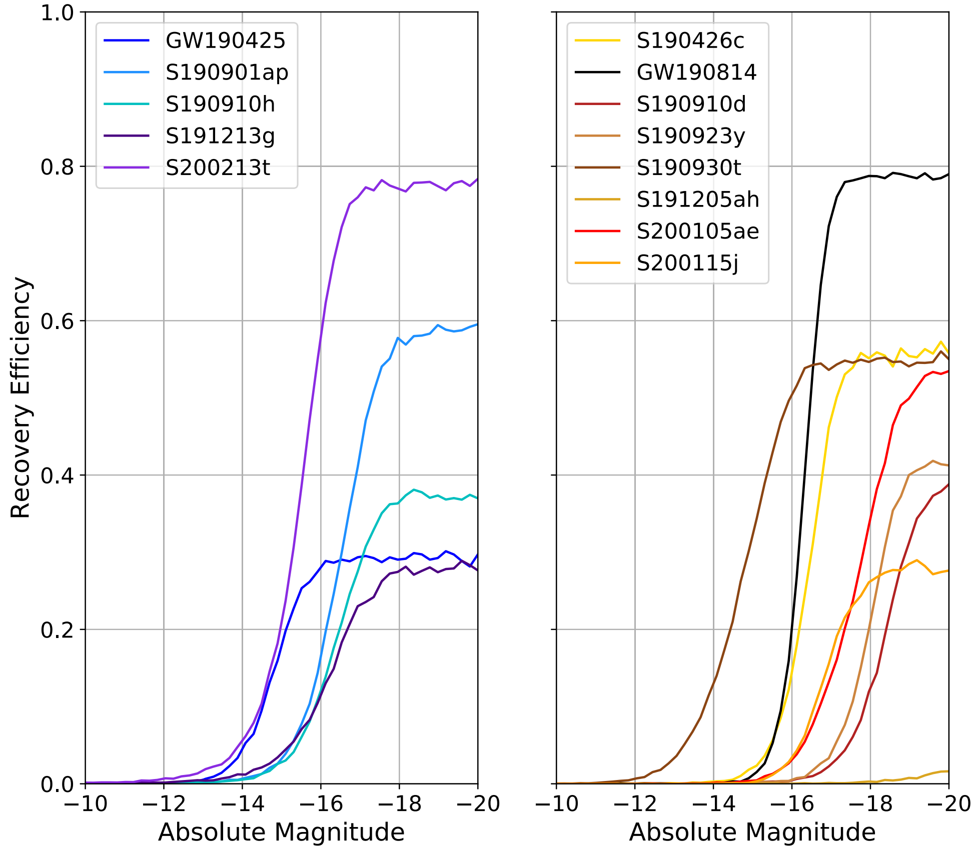

Figure 10. Event-by-event recovery efficiency using `simsurvey` as a function of absolute magnitude for BNS (left panel) and NSBH (right panel) mergers. The recovery efficiency corresponds to the number of kilonovae detected divided by the total number of kilonovae injected. Kilonovae were injected according to the 3D probability distribution of the sky map.

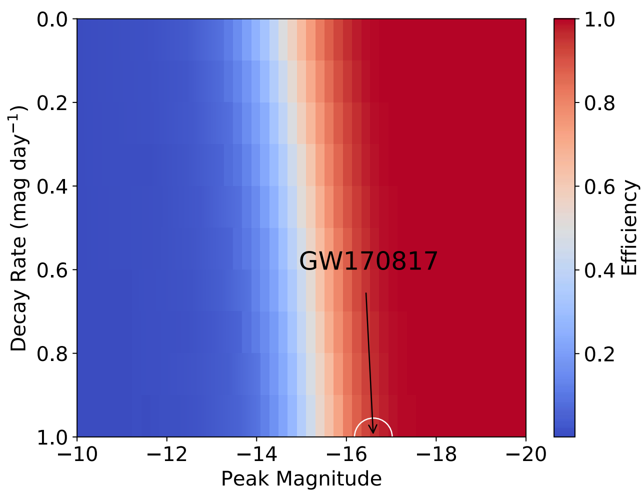

Figure 11. Composite efficiency map using `simsurvey` assuming a linear model for the kilonova with a peak absolute magnitude and fixed decay rate. The color-coding shows the recovery efficiency, or the number of recovered kilonovae within observed regions divided by the total number of kilonovae injected in the sky map. Based on an analysis of a compilation of data from GW170817 (Andreoni et al. 2017; Coulter et al. 2017; Cowperthwaite et al. 2017; Díaz et al. 2017; Drout et al. 2017; Evans et al. 2017; Pian et al. 2017; Smartt et al. 2017; Utsumi et al. 2017; Valenti et al. 2017; Arcavi 2018; Pozanenko et al. 2018), we compute an average extrapolated peak magnitude of ~ -16.6 and a decay rate of ~ 1 mag day^{-1}. If all kilonovae are like GW170817, the joint probability of zero detections is 7%.

compute p_i as the recovery fraction from the `simsurvey` injections for the fading and flat light-curve evolution estimates discussed above that take into account the spatial variation in distance, depth, and enclosed probability. Solving for f_b at a 90% confidence level, we plot our results in Figure 12. At the bright end, we find that no more than $\approx$40% of kilonovae can be brighter than -18 mag. At the faint end, our observations place no constraints on the luminosity function fainter than -15.5 mag. The luminosity of GW170817 at the merger time is unknown, and various models predict diverse rates of evolution in that first day after merger. As discussed above, we use an extrapolated peak of -16.6 mag and a fade rate of 1 mag day^{-1} for GW170817 as a benchmark. We find that no more than $<$57% ($<$89%) of kilonovae could be brighter than -16.6 mag for the flat (fading) light-curve assumptions.

The GW triggers had a very wide range of FARs. Weighting by the available low-latency values for the terrestrial probability (t_i), we fold this into our luminosity function constraint as

$$(1 - \mathrm{CL}) = \prod_{i=1}^{N} (1 - f_b^* p_i^* (1 - t_i)).$$

In Figure 12, we show that the resulting constraints on f_b (red line) are worse only by a difference of $\approx$10%.

Next, we investigate the implications of this constraint on the kilonova parameter space. There are no theoretical luminosity functions available in the literature that we can directly compare to. A model grid is available (Kasen et al. 2017) as a function of three parameters: ejecta mass M_{ej}, ejecta velocity v_{ej}, and

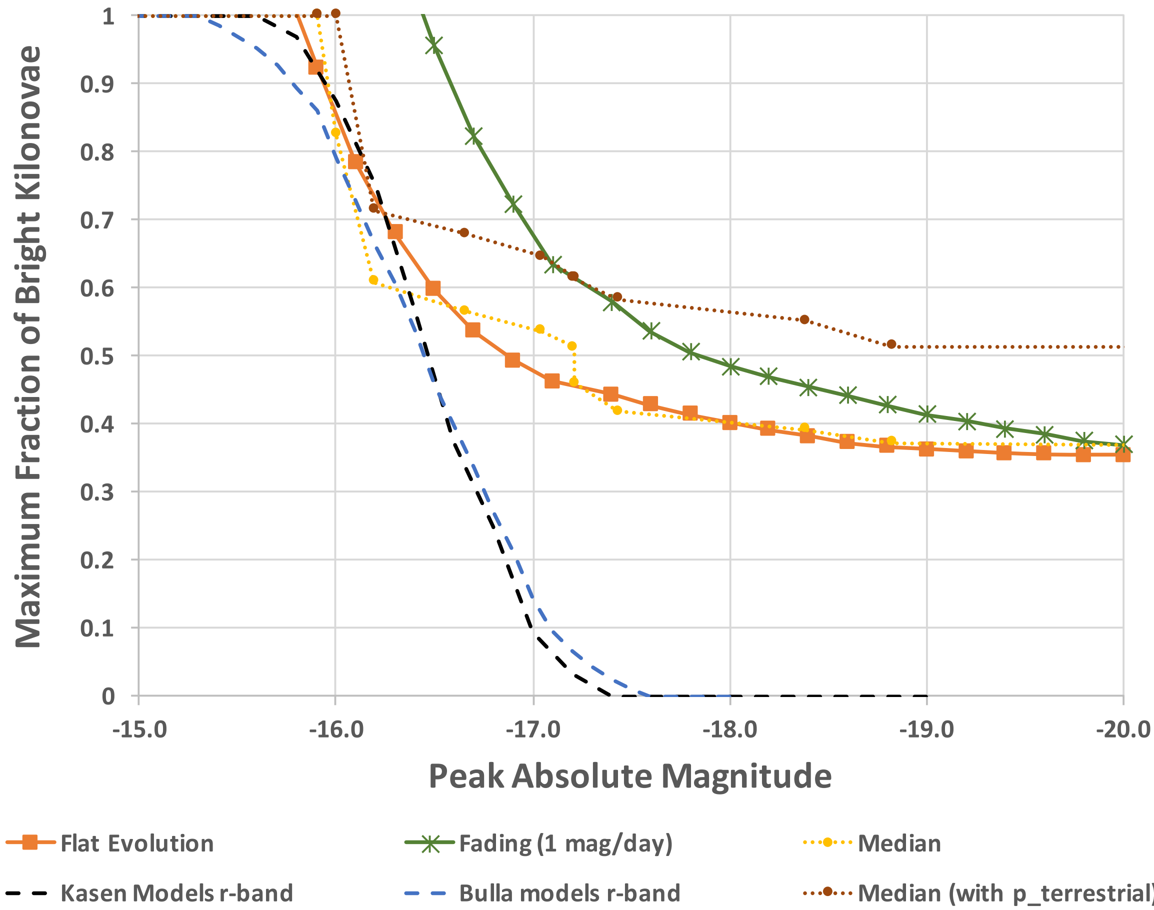

Figure 12. Constraints on the underlying luminosity function of kilonovae represented as the maximum allowed fraction of kilonovae brighter than a given peak absolute magnitude. Constraints are derived at a 90% confidence level. We show constraints assuming flat photometric evolution (orange squares) and fading by 1 mag day^{-1} (green asterisks). We also show the event-by-event constraint based on a median estimate (yellow circles, dotted line). We correct this median estimate by the probability that the GW alert was terrestrial (red circles, dotted line). We compare to a model grid published in Kasen et al. (2017; dashed black line) and find that the limiting line suggests that some kilonovae must either have $M_{ej} < 0.03\,M_\odot$ or $X_{lan} > 10^{-4}$. The limiting line (blue dashed line) for another model grid (Bulla 2019; Dietrich et al. 2020) suggests that some kilonovae must be fainter than GW170817 with $M_{ej,dyn} < 0.005\,M_\odot$, $M_{ej,pm} < 0.05\,M_\odot$, or $\phi > 30°$.

lanthanide fraction X_{lan}. The best-fit model to GW170817 from Kasen et al. (2017) suggested two components: a blue kilonova ($0.025\,M_\odot$, $0.3\,c$, $10^{-4.5}$) and a red kilonova ($0.04\,M_\odot$, $0.1\,c$, 10^{-2}). The blue component dominates at an early time and is more relevant to the ZTF searches described in this paper. Comparing to our luminosity function constraints, we find that our limits suggest that a wide range of parameters are allowed, e.g., $M_{ej} = [0.03, 0.1]\,M_\odot$, $v_{ej} = [0.05, 0.3]\,c$, and $X_{lan} = [10^{-5}, 10^{-4}]$; stricter distributions that yield a brighter kilonova population (e.g., higher ejecta mass or lower lanthanide fraction) are not allowed. Thus, some kilonovae must have $M_{ej} \leqslant 0.03\,M_\odot$ or $X_{lan} > 10^{-4}$ to be consistent with the ZTF constraints.

Similarly, we compare our luminosity function constraints to the kilonova grid from Dietrich et al. (2020) computed using the radiative transfer code POSSIS (Bulla 2019). In addition to the observer viewing angle, this grid depends on three parameters: the dynamical ejecta mass ($M_{ej,dyn}$), the postmerger wind ejecta mass ($M_{ej,pm}$), and the half-opening angle of the lanthanide-rich ejecta component (ϕ). A model with $M_{ej,dyn} = 0.005\,M_\odot$, $M_{ej,pm} = 0.05\,M_\odot$, and $\phi = 30°$ provides a good fit to GW170817 (see Figure 8 of Dietrich et al. 2020). As shown in Figure 12, our constraints suggest that some kilonovae must be fainter than GW170817, i.e., must have either $M_{ej,dyn} < 0.005\,M_\odot$, $M_{ej,pm} < 0.05\,M_\odot$, or $\phi > 30°$.

5. Conclusions and Way Forward

In summary, the ZTF coverage (excluding weather-impacted S191205ah) spanned enclosed probabilities from 22% to 89%, median depths from 20.1 to 21.5 mag, and time lags between merger and the start of observations from 11 s to 13.7 hr. The follow-up by the GROWTH team comprised 340 UltraViolet/Optical/InfraRed (UVOIR) photometric points, 64 OIR spectra, and three radio images. Additionally, many other teams also followed up ZTF candidates. Thanks to the extensive follow-up, all candidate counterparts were ruled out.

The GW triggers had localization areas ranging from 23 to 24,264 deg^2, distances from 108 to 632 Mpc, and FARs from 1.5 to $10^{-25}\,yr^{-1}$. Assuming that all GW alerts were astrophysical, we conclude that the joint probability of zero detections is only 4.2% if all kilonovae are at least as bright as GW170817 at discovery. Furthermore, assuming kilonovae from BNS and NSBH mergers are drawn from a common population, we find that no more than <57% (<89%) of kilonovae could be brighter than −16.6 mag for the flat (fading by 1 mag day^{-1}) assumptions respectively at 90% confidence.

The median time lag of the ZTF observations in O3 was only 1.5 hr after merger. This further constrains the unknown, early-time emission of kilonovae in the g and r bands. Some models predict that the early emission could be very hot and bright in the UV; this can only be addressed once wide-field UV imagers (e.g., Dorado, ULTRASAT, and DUET) are launched.

Given the expected differences in sensitivity between the LIGO and Virgo interferometers, events in O4 are likely to be similarly coarsely localized (until KAGRA or LIGO India come online with high sensitivity). Moreover, given the increased GW sensitivity, we expect more events that are further away. Thus, we plan to implement stricter selection criteria. Specifically, for O4, we plan to only trigger on events with FARs lower than 1 yr^{-1} (i.e., four out of 15 events in O3 would fail this criterion). We plan to only trigger on NSBH events with a nonzero HasRemnant probability (i.e., six out of eight NSBH triggers in O3 would fail this criterion, including GW190814). As we did in O3, we plan to only trigger on MassGap events with a nonzero HasNS probability. In summary, only five out of the 13 events followed up in O3 would pass our new plan for trigger criteria in O4.

The first phase of the ZTF survey ran from 2018 March to 2020 September. The second phase of the ZTF is expected to run from 2020 October to 2023 September. Searches with ZTF Phase II are planned to be up to 2 mag deeper than nominal survey operations, even with 1000 deg^2 localizations, thanks to the availability of deeper stacks as reference images. We plan to require a minimum median image depth of −16.0 mag and minimum enclosed probability of 50% in the first 4 hr of observations. The ZTF mapping speed allows 3600 deg^2 to be mapped in 4 hr to achieve the necessary depth for a median GW distance of 300 Mpc. If the event is more distant, we will increase our exposure time from 180 to 600 s to go deeper. For events that are either too distant or too coarsely localized, we will not undertake triggered searches and will rely only on serendipitous searches of the all-sky public survey at 2 days' cadence to 20.4 mag.

Moreover, redder searches will better constrain the kilonova phase space and probe higher lanthanide fractions. The ZTF II would push to the red, since broader reference coverage is now available in the *i*-band filter (see Sagués Carracedo et al. 2020 for detailed simulations on gain in depth and red sensitivity). New wide-field infrared surveyors are also coming online (e.g., WINTER at Palomar Observatory, USA, and DREAMS at Siding Springs Observatory, Australia)

We look forward to searches in the fourth observing run, as detections will be more likely. For zero detections, about 17 neutron star mergers with only 50% enclosed probability to a depth of −16 mag would constrain the luminosity function fraction brighter than GW170817 to <25% (only 11 events with 75% enclosed probability would place a similarly stringent limit). Thus, as the sample size grows, even with partial coverage of sky maps, the luminosity function of kilonovae will be strongly constrained.

We conclude with some thoughts on what would strengthen the partnership between the GW physics community and the EM astronomy community. First, we encourage efforts that would speed up the release of the more accurate LALInference map (Veitch et al. 2015). Since the LALInference map was often only available after our observations were completed, our net expectation value dropped by 10%, and our net joint nondetection probability dropped by a factor of 2 between the BAYESTAR (Singer & Price 2016) map and the LALInference map. Moreover, three triggers never had an LALInference map released (S190923y, S190930t, and S191205ah).

Second, it is critical that a reliable FAR and terrestrial probability are released as soon as possible. If an event is going to be retracted (or the FAR increases significantly) based on offline analysis, it is essential that the EM community be notified immediately via GCN, so that all pending follow-up can be halted. Third, if the classification of an event changes in offline analysis, the EM community should be promptly notified via GCN. Fourth, since HasNS and HasRemnant are somewhat model-dependent (e.g., Foucart et al. 2018; Chatterjee et al. 2020) but will drive the decision of whether or not some EM teams trigger follow-up, we request the release of rough estimates/ranges for more directly determined parameters (e.g., mass ratio, inclination, and chirp mass) that can help with the EM decision. We strongly encourage any algorithmic or technological development that will enable more accurate 3D skymaps, FARs, HasNS, and HasRemnant at lower latency to better inform the EM community's follow-up decisions.

In summary, the lessons learned from both the single detection in O2 and the dozen nondetections in O3 bode well for an exciting future for multimessenger astrophysics in the coming decade.

This work was supported by the Global Relay of Observatories Watching Transients Happen (GROWTH) project, funded by the National Science Foundation under PIRE grant No. 1545949. GROWTH is a collaborative project among the California Institute of Technology (USA), University of Maryland College Park (USA), University of Wisconsin Milwaukee (USA), Texas Tech University (USA), San Diego State University (USA), University of Washington (USA), Los Alamos National Laboratory (USA), Tokyo Institute of Technology (Japan), National Central University (Taiwan), Indian Institute of Astrophysics (India), Indian Institute of Technology Bombay (India), Weizmann Institute of Science (Israel), The Oskar Klein Centre at Stockholm University (Sweden), Humboldt University (Germany), Liverpool John Moores University (UK), and University of Sydney (Australia). Based on observations obtained with the Samuel Oschin Telescope 48 inch and the 60 inch telescope at the Palomar Observatory as part of the Zwicky Transient Facility project. The ZTF is supported by the National Science Foundation under grant No. AST-1440341 and a collaboration including Caltech, IPAC, the Weizmann Institute for Science, the Oskar Klein Center at Stockholm University, the University of Maryland, the University of Washington, Deutsches Elektronen-Synchrotron and Humboldt University, Los Alamos National Laboratories, the TANGO Consortium of Taiwan, the University of Wisconsin at Milwaukee, and Lawrence Berkeley National Laboratories. Operations are conducted by COO, IPAC, and UW. The ZTF forced photometry service was funded under Heising-Simons Foundation grant No. 12540303 (PI: Graham). The SED Machine is based upon work supported by the National Science Foundation under grant No. 1106171.

The GROWTH-India telescope is a 70 cm telescope with a 0.7° field of view, set up by the Indian Institute of Astrophysics and the Indian Institute of Technology Bombay with support from the Indo-US Science and Technology Forum (IUSSTF) and the Science and Engineering Research Board (SERB) of the Department of Science and Technology (DST), Government of India (https://sites.google.com/view/growthindia/).

It is located at the Indian Astronomical Observatory (Hanle), operated by the Indian Institute of Astrophysics (IIA). The GROWTH-India project is supported by SERB and administered by IUSSTF under grant No. IUSSTF/PIRE Program/GROWTH/2015-16. This research has made use of the VizieR catalog access tool, CDS, Strasbourg, France (doi: 10.26093/cds/vizier). The original description of the VizieR service was published in A&AS 143, 23. These results made use of the Lowell Discovery Telescope (LDT) at Lowell Observatory. Lowell is a private, nonprofit institution dedicated to astrophysical research and public appreciation of astronomy and operates the LDT in partnership with Boston University, the University of Maryland, the University of Toledo, Northern Arizona University, and Yale University. The Large Monolithic Imager was built by Lowell Observatory using funds provided by the National Science Foundation (AST-1005313). The upgrade of the DeVeny optical spectrograph has been funded by a generous grant from John and Ginger Giovale and a grant from the Mt. Cuba Astronomical Foundation. The KPED team thanks the National Science Foundation and the National Optical Astronomical Observatory for making the Kitt Peak 2.1 m telescope available. We thank the observatory staff at Kitt Peak for their efforts to assist Robo-AO KP operations. The KPED team thanks the National Science Foundation, the National Optical Astronomical Observatory, the Caltech Space Innovation Council, and the Murty family for support in the building and operation of KPED. In addition, they thank the CHIMERA project for use of the Electron Multiplying CCD (EMCCD). The Liverpool Telescope is operated on the island of La Palma by Liverpool John Moores University in the Spanish Observatorio del Roque de los Muchachos of the Instituto de Astrofisica de Canarias with financial support from the UK Science and Technology Facilities Council. Some spectroscopic observations were obtained with the Southern African Large Telescope (SALT). The Photometric Redshifts for the Legacy Surveys (PRLS) catalog used in this paper was produced thanks to funding from the U.S. Department of Energy Office of Science, Office of High Energy Physics, via grant DE-SC0007914. This publication has made use of data collected at Lulin Observatory, partly supported by MoST grant 108-2112-M-008-001. Based on observations made with the Gran Telescopio Canarias (GTC), installed at the Spanish Observatorio del Roque de los Muchachos of the Instituto de Astrofísica de Canarias on the island of La Palma.

M.M.K. acknowledges generous support from the David and Lucille Packard Foundation. M.W.C. acknowledges support from the National Science Foundation with grant No. PHY-2010970. A.G. and J.S. acknowledge support from the Knut and Alice Wallenberg Foundation and GREAT research environment grant 2016-06012, funded by the Swedish Research Council. Some of the work by D.A.P. was performed at the Aspen Center for Physics, which is supported by National Science Foundation grant PHY-1607611. D.A.P. was partially supported by a grant from the Simons Foundation. H.K. thanks the LSSTC Data Science Fellowship Program, which is funded by LSSTC, NSF Cybertraining Grant 1829740, the Brinson Foundation, and the Moore Foundation; his participation in the program has benefited this work. This work has been supported by the Spanish Science Ministry Centro de Excelencia Severo Ochoa Program under grant SEV-2017-0709. A.J.C.T. acknowledges support from the Junta de Andalucía (Project P07-TIC-03094) and Spanish Ministry Projects AYA2012-39727-C03-01, AYA2015-71718R, and PID2019-109974RB-I00. V.A.F. was supported by grant RFBR 19-02-00432. I.A. acknowledges support by a Ramón y Cajal grant (RYC-2013-14511) of the Ministerio de Ciencia, Innovación, y Universidades (MICIU) of Spain. He also acknowledges financial support from MCIU through grant AYA2016-80889-P. A.A.M. is funded by the Large Synoptic Survey Telescope Corporation, the Brinson Foundation, and the Moore Foundation in support of the LSSTC Data Science Fellowship Program; he also receives support as a CIERA Fellow by the CIERA Postdoctoral Fellowship Program (Center for Interdisciplinary Exploration and Research in Astrophysics, Northwestern University). A.C. acknowledges support from the National Science Foundation with grant No. 1907975. W.-H.I., A. K., K.-L.L., C.-C.N., A.P., H.T., and P.-C.Y. acknowledge support from Ministry of Science and Technology (MoST) Taiwan grants 104-2923-M-008-004-MY5, 107-2119-M-008-012, 108-2628-M-007-005-RSP, and 108-2112-M-007-025-MY3. D.D. is supported by an Australian Government Research Training Program Scholarship. S.A. is supported by the GROWTH project, funded by the National Science Foundation under PIRE grant No. 1545949. A.S.C. is supported by GREAT research environment grant 2016-06012, funded by the Swedish Research Council. E.C.K. acknowledges support from the G.R.E.A.T. research environment and the Wenner-Gren Foundations. A. J.C.T. is thankful for fruitful discussions with J. Cepa, E. Fernández-García, J. A. Font, S. Jeong, A. Martín-Carrillo, A. M. Sintes, and S. Sokolov. D.A.H.B. acknowledges research support from the National Research Foundation of South Africa. S.B.P. and V.B. acknowledge BRICS grant No. "DST/IMRCD/BRICS/PilotCall1/ProFCheap/2017(G)" for part of the present work. J.S.B. was partially supported by a Gordon and Betty Moore Foundation Data-Driven Discovery grant and a grant from the National Science Foundation, "Conceptualization of a Scalable Cyberinfrastructure Center for Multimessenger Astrophysics."

Appendix A Observing and Data Reduction Details for Follow-up Observations

A.1. Photometric Follow-up

We used the 1 and 2 m telescopes available at the LCO global network to follow up sources discovered with the ZTF. The images were taken with the Sinistro and Spectral cameras (Brown et al. 2013) at the 1 and 2 m, respectively, and scheduled through the LCO Observation Portal.[76] The exposure time varied depending on the brightness of the object, yet our requests would normally involve three sets of 300 s in the *g* and *r* bands. After stacking the reduced images, we extracted sources using the SExtractor package (Bertin & Arnouts 2010), and we calibrated magnitudes against PS1 (Chambers et al. 2016) objects in the vicinity. For nuclear transients located $<8''$ from their potential host, we use the High Order Transform of Psf ANd Template Subtraction code (HOTPANTS; Becker 2015) to subtract a PSF-scaled PS1 template previously aligned using SCAMP (Bertin 2006). The photometry for the nuclear candidates follows the same procedure described before but in the residual image. The images obtained with the LT were acquired using the IO:O camera with the Sloan *griz* filter set. They were reduced using the automated pipeline, which performs bias subtraction,

[76] https://observe.lco.global/

trimming of the overscan regions, and flat-fielding. The image subtraction takes place once a PS1 template is aligned, and the final data come from the analysis of the subtracted image.

We used the Electronic Multiplier CCD camera at KPED to take hour-long exposures in the *r* band to follow up candidates. After stacking the images and following standard reduction techniques, we calibrate the extracted sources using PS1 sources in the field. When the candidate has a host galaxy, we perform image subtraction as described for the LCO.

We obtained data with the GMOS-N (Allington-Smith et al. 2002; Hook et al. 2004; Gimeno et al. 2016), mounted on the Gemini-North 8 m telescope on Maunakea. Data were analyzed after stacking four 200 s exposures in the *g* and *i* bands. The reductions were performed using the python package DRAGONS[77] provided by the Gemini Observatory. We used PS1 sources in the field to calibrate the data.

We used the LOT at the Lulin Observatory in Taiwan to follow up candidates discovered with the ZTF. The standard observations involved 240 s in the g', r', and i' bands. The reduction followed standard methods, and the sources were calibrated against the PS1 catalog. No further image subtraction was applied to the images acquired with the LOT.

We used the 0.7 m robotic GIT equipped with a 4096×4108 pixel back-illuminated Andor camera for LVC event follow-up during O3. The GIT is situated at the IAO (Hanle, Ladakh). We used both tiled and targeted modes for the follow-up for different GW triggers. Tiled observations typically comprise a series of 600 s exposures in the Sloan Digital Sky Survey (SDSS) r' filter. Targeted observations were conducted with varying exposure times in the SDSS u', g', r', and i' filters. All data were downloaded in real time and processed with the automated GIT pipeline. Zero-points for photometry were calculated using the PanSTARRS catalog (Flewelling 2018), downloaded from Vizier. The PSF photometry was performed with PSFEx (Bertin 2011). For sources with significant host background, we performed image subtraction with `pyzogy` (Guevel & Hosseinzadeh 2017), based on the ZOGY algorithm (Zackay et al. 2016).

Additionally, we obtained photometric data with the Spectral Energy Distribution Machine (SEDM; Blagorodnova et al. 2018; Rigault et al. 2019) on the P60 telescope. The processing is automated and can be triggered from the GROWTH Marshal. Standard requests involved *g*-, *r*-, and *i*-band imaging with the Rainbow Camera on the SEDM in 300 s exposures. The data are later reduced using a python-based pipeline that applies standard reduction techniques and a customized version of the Fremling Automated Pipeline (`FPipe`; Fremling et al. 2016) for image subtraction.

We used the imaging capabilities of the OSIRIS (Cepa et al. 2005) camera at the GTC to obtain 60 s exposures in the *r* band. Standard reduction techniques were applied to the data, and we used PS1 sources to calibrate the flux.

We obtained follow-up imaging of candidates with the Wafer Scale Imager for Prime (WASP) and the Wide-field Infrared Camera (WIRC; Wilson et al. 2003), both on the P200 telescope. For WASP data, a python-based pipeline applied standard optical reduction techniques (as described in De et al. 2020a), and the photometric calibration was obtained against PS1 sources in the field. The WIRC data were treated similarly using the same pipeline, but they were additionally stacked using Swarp (Bertin et al. 2002), while the calibration was done using the Two Micron All Sky Survey point-source catalog (Skrutskie et al. 2006).

We obtained imaging of one candidate using the Low Resolution Imaging Spectrometer (LRIS; Oke et al. 1995), mounted at the Keck I telescope. Our data were taken in the *g* and *i* bands reaching $m_{\mathrm{AB}} \approx 24$. The data were reduced following standard methods.

We used the Large Monolithic Imager (LMI; Massey et al. 2013) on the 4.3 m LDT at Happy Jack, Arizona, to follow up the ZTF discoveries. Observations were conducted with the SDSS *r* filter for 90 s each, and the data were reduced using the photopipe[78] pipeline. The magnitudes were calibrated against the SDSS or Gaia catalogs (Ahumada et al. 2020) using the conversion scheme provided in Gaia documentation.[79]

We used the Ultraviolet/Optical Telescope (UVOT; Roming et al. 2005) mounted on the Neil Gehrels Swift Observatory (hereafter referred to as Swift; Gehrels et al. 2004) to follow up interesting sources and track down their UV evolution. The ToO observations were scheduled in the *v*, *b*, *u*, *w*1, *m*2, and *w*2 bands for an average of 320 s exposure^{-1}. We used the products of the Swift pipeline to determine the magnitudes.[80]

We observed candidate counterparts of S200213t using the Astrophysical Research Consortium Telescope Imaging Camera (ARCTIC; Huehnerhoff et al. 2016) at the APO 3.5 m. We obtained dithered 120 s exposures binned 2×2 in the *u*, *g*, *r*, *i*, and *z* bands. Images were bias-corrected, flat-fielded, and combined using standard IRAF packages (noao, imred, and ccdred). SExtractor (Bertin & Arnouts 2010) was used to find and photometer point sources in the images using PSF photometry, and a photometric calibration to PanSTARRS field stars was performed (without filter corrections).

All photometry presented in the light curves and tables in this paper is corrected for galactic extinction using dust maps from Schlafly & Finkbeiner (2011).

We observed the field of ZTF19aassfws with the VLA in its B configuration on 2019 May 10 starting at 07:19:15 UT and 2019 June 4 starting at 08:20:32 UT. Our observations were carried out at a nominal central frequency of 3 GHz. We used 3C 286 as our bandpass and absolute flux calibrator and J1927+6117 as our complex gain calibrator. Data were calibrated using the standard VLA automated calibration pipeline available in the Common Astronomy Software Applications (CASA) package. We then inspected the data for further flagging and imaged interactively using the CLEAN algorithm. The image rms was $\approx 5.2\,\mu$Jy for the first epoch and $\approx 4.6\,\mu$Jy for the second epoch. Within a circular region centered on the optical position of ZTF19aassfws and of radius $\approx 2\farcs1$ (comparable to the nominal half-power beamwidth of the VLA at 3 GHz and for the B configuration), we find no significant radio emission. Thus, we set upper limits on the corresponding 3 GHz flux density of $\lesssim 16$ and $\lesssim 14\,\mu$Jy, respectively, for the first and second epochs.

A.2. Spectroscopic Follow-up

Using the GROWTH Marshal, we regularly triggered the Liverpool Telescope Spectrograph for the Rapid Acquisition of

[77] https://dragons.readthedocs.io/en/stable/

[78] https://github.com/maxperry/photometrypipeline

[79] https://gea.esac.esa.int/archive/documentation/GDR2/Data_processing/chap_cu5pho/sec_cu5pho_calibr/ssec_cu5pho_PhotTransf.html

[80] https://swift.gsfc.nasa.gov/quicklook/

Transients (SPRAT; Piascik et al. 2014). SPRAT uses a 1″.8 slit, which provides a resolution of $R = 350$ at the center of the spectrum. The data were reduced using the automated pipeline, which removes low-level instrumental signatures and then performs source extraction, sky subtraction, and wavelength and flux calibration.

We observed a number of transient candidates during classical observing runs with the P200 Double Spectrograph (DBSP) during O3. For the setup configuration, we used 1″.0, 1″.5, and 2″ slit masks; a D55 dichroic; a blue grating of 600/4000; and a red grating of 316/7500. Using a custom PyRAF DBSP reduction pipeline (Bellm & Sesar 2016),[81] we reduced our data.

We obtained several optical spectra with the 10.4 m GTC telescope (equipped with OSIRIS). We used the R1000B and R500R grisms for our observations, typically using a slit of width of 1″.2. We used standard routines from the Image Reduction and Analysis Facility (IRAF) to perform our data reduction.

We observed ZTF19aarykkb using the DeVeny spectrograph mounted on the 4.3 m LDT. We obtained 22.5 minute exposures at an average airmass of 1.5. We used the DV2 grating (300 g mm^{-1}, 4000 Å blaze) for this observation. Our spectra cover a wavelength range of approximately 3600–8000 Å.

In addition, we obtained a spectrum of ZTF20aarzaod with SALT (Buckley et al. 2003), using the Robert Stobie Spectrograph (RSS; Burgh et al. 2003), covering a wavelength range of 470–760 nm with a spectral resolution of $R = 400$. We triggered special GW follow-up program 2018-2-GWE-002 and reduced the data with a custom pipeline based on PyRAF routines and the PySALT package (Crawford et al. 2010).

Low-resolution spectra using the 2 m HCT were obtained using the HFOSC instrument; ZTF19aarykkb was observed using grisms Gr7 (3500–7800 Å) and Gr8 (5200–9000 Å), while AT2019wxt was observed using Gr7. The spectra were bias-subtracted, cosmic rays were removed, and the 1D spectra were extracted using the optimal extraction method. Wavelength calibration was effected using the arc lamp spectra FeAr (Gr7) and FeNe (Gr8). Instrumental response curves generated using spectrophotometric standards observed during the same night were used to calibrate the spectra onto a relative flux scale. The flux-calibrated spectra of ZTF19aarykkb from the two grisms were combined to a single spectrum covering the wavelength range 4000–9000 Å.

We obtained spectroscopy with the GMOS-N, mounted on the Gemini-North 8 m telescope on Maunakea, by combining six 450 s exposures on the R400 and B600 gratings. We used the GMOS long-slit capability and reduced the data following standard PyRAF techniques.

We obtained near-infrared spectroscopy of candidates using NIRES on the Keck II telescope. The data were acquired using standard ABBA dither patterns on the target source, followed by observations of an A0 telluric standard star close to the science target. The spectral traces were extracted using the `spextool` package (Cushing et al. 2004) for both the science target and standard star. The final spectra presented here were stacked from all individual dithers, followed by flux calibration and telluric correction using the `xtellcor` package (Vacca et al. 2003).

[81] https://github.com/ebellm/pyraf-dbsp

We obtained spectra using the LRIS on the Keck I telescope. The 600/4000 grism was used on the blue side and the 600/7500 grating on the red side, providing wavelength coverage between 3139–5642 Å (blue) and 6236–9516 Å (red). The exposure time was 600 s on both sides. The spectrum was reduced using LPipe (Perley 2019) with BD+28 as a flux calibrator. The red and blue relative fluxes are scaled by matching synthetic photometry to colors inferred from photometry of the transient.

Appendix B
Detailed Candidate Descriptions

Here we provide descriptions of each candidate identified within the sky map of each event followed up with the ZTF. We discuss each object announced via GCN. For candidates with a redshift, we note whether it is spectroscopic [s] or photometric [p]. Some candidates were classified as a part of coordinated spectroscopic follow-up with the Bright Transient Survey (BTS; Fremling et al. 2020) and the ZTF CLU experiment (De et al. 2020b).

B.1. GW190425

For candidates identified within the sky map of GW190425, see Coughlin et al. (2019a). Two candidate counterparts of GW190425z, ZTF19aarykkb and ZTF19aarzoad, were observed with the AMI Large Array at 15 GHz on 2019 April 26 (Rhodes et al. 2019). No radio emission was found to be associated with any of these candidates.

B.2. S190426c

We summarize the candidate counterparts to S190426c in Table 2 and the follow-up photometry in Table 11. Next, we discuss why we conclude that each one is unrelated.

B.2.1. Spectroscopically Classified

ZTF19aasmftm/AT2019sne—The rising light curve of ZTF19aasmftm suggested that it could be a young and faint object with a galaxy host of $m_{\rm AB} = 21.2$ mag in PS1, so we highlighted it in Perley et al. (2019a). A few days later, GTC spectroscopy of this event (Hu et al. 2019b) classified it as a premaximum SN Ia in the outskirts of its host galaxy at z [s] = 0.156.

ZTF19aaslzjf/AT2019snh—Another candidate discovered during our second night of observations, ZTF19aaslzjf, was at low galactic latitude and seemed to be located in a nearby host galaxy. A spectrum from GTC (Hu et al. 2019b) confirmed both that this source was nearby (at z[s] = 0.086) and that it was an SN Ia located in the outskirts of the Galaxy host.

ZTF19aasmddt/SN2019fht—We highlighted this transient because its photometric redshift was consistent with the LVC distance estimate, and the light curve exhibited a rapid rise (Perley et al. 2019a). However, the GTC spectrum taken shortly afterward revealed that this transient was a young SN II prepeak in the outskirts of its galaxy at z[s] = 0.028.

ZTF19aaslszp/AT2019anj—Another candidate whose photo-z was consistent with the LVC distance estimate, ZTF19aaslszp, appeared to be relatively bright and red with a color of $g - r = 0.89$ mag. Subsequent ZTF and LT photometry revealed that the source appeared to have flaring behavior in the light

Table 11
Follow-up Photometry for S190426c Candidates

Name	IAU Name	Date	Telescope	Filter	m (AB)	σ_m	$m_{\rm lim}$
ZTF19aasmftm	AT2019sne	2,458,602.6514	LT	g	21.33	0.15	21.71
ZTF19aasmftm	AT2019sne	2,458,602.6528	LT	r	21.06	0.10	21.51
ZTF19aasmftm	AT2019sne	2,458,602.6542	LT	i	20.90	0.17	21.03
ZTF19aassfws	AT2019fuc	2,458,603.6605	LT	g	99.0	99.0	22.32
ZTF19aassfws	AT2019fuc	2,458,603.6619	LT	r	99.0	99.0	22.04
ZTF19aassfws	AT2019fuc	2,458,603.6633	LT	i	99.0	99.0	21.50
ZTF19aaslszp	AT2019snj	2,458,603.6654	LT	g	20.80	0.07	22.25
ZTF19aaslszp	AT2019snj	2,458,603.6668	LT	r	20.51	0.07	22.12
ZTF19aaslszp	AT2019snj	2,458,603.6682	LT	i	19.19	0.06	22.00
ZTF19aaslzjf	AT2019snh	2,458,603.6703	LT	g	20.94	0.18	21.75
ZTF19aaslzjf	AT2019snh	2,458,603.6717	LT	r	20.40	0.10	22.00
ZTF19aaslzjf	AT2019snh	2,458,603.6731	LT	i	20.30	0.10	22.00
ZTF19aasmddt	SN2019fht	2,458,603.7113	LT	g	19.79	0.10	22.77
ZTF19aasmddt	SN2019fht	2,458,603.7127	LT	r	19.43	0.11	21.54
ZTF19aasmddt	SN2019fht	2,458,603.7141	LT	i	19.41	0.09	21.10
ZTF19aasmddt	SN2019fht	2,458,604.7237	LT	g	19.69	0.06	21.61
ZTF19aasmddt	SN2019fht	2,458,604.7251	LT	r	19.51	0.03	22.29
ZTF19aasmddt	SN2019fht	2,458,604.7265	LT	i	19.55	0.07	20.63

curve. Our P200+DBSP spectrum classified the source as an AGN at $z[s] = 0.084$, as it shows broad hydrogen lines.

B.2.2. Slow Photometric Evolution

ZTF19aaslzfk/AT2019snd—We identified this candidate during our initial search of the imaged region within the BAYESTAR localization of S190426c (Coughlin et al. 2019c). Though the candidate had WISE detections in all four filters, its WISE colors did not definitively place this transient in the AGN class. Continued photometric monitoring of this candidate revealed its slow evolution ($\alpha_g = -0.02$), ruling out its association with S190426c.

ZTF19aaslvwn/AT2019snf —We reported ZTF19aaslvwn in Perley et al. (2019a) as a lower-priority transient, with initially slow photometric evolution at low galactic latitude ($b < 15°$). After monitoring the transient over a period of ∼12 days, the photometry had only risen by 0.4 mag, indicating that it could not be a kilonova and was likely a CV.

ZTF19aasmdir/AT2019sng—Also reported in Perley et al. (2019a), ZTF19aasmdir was a nuclear transient at a low galactic latitude, with WISE colors consistent with an AGN within 1″ of the transient. Several days of monitoring yielded a light curve that was far more consistent with a flaring AGN than a kilonova, with a rate of evolution $\alpha_r < 0.01$.

ZTF19aaslolf/AT2019snn—This nuclear candidate was a low priority in our follow-up list due to its high photometric redshift ($z[p] = 0.42$) and because its WISE colors placed it within the AGN locus. Though we could not spectroscopically confirm this, the slowly evolving "flaring" light curve ($\alpha_r < 0.01$) and archival PS1 detections point to the AGN nature of this candidate.

ZTF19aaslphi/AT2019sno—The candidate ZTF19aaslphi had a photometric redshift that was also nominally inconsistent with the LVC distance. However, we identified it as a candidate of interest due to its relatively quick rise of ∼0.75 mag over the course of 4 days in the g band. Its later-time light curve exhibited a plateau; thus, we consider its evolution too slow to be associated with a GW event.

ZTF19aaslpds/AT2019snq—This candidate, at low galactic latitudes, had multiple detections in the r and g filters; but, as it only evolved by 0.04 mag over a day of monitoring and subsequently was not detected, we ruled it out as a potential counterpart to S190426c.

ZTF19aaslozu/AT2019snr—We included this candidate initially due to its rapid rise and $g - r$ color of 0.3 mag (Perley et al. 2019a). Though ZTF19aaslozu did not clearly fall into the AGN locus, its detections in all four WISE filters, archival detections with PS1, and slow evolution point to it being a strong AGN candidate.

ZTF19aasshpf/AT2019snt—This is a lower-priority candidate on our list discovered at $r = 21.59$ mag in the outskirts of a faint red galaxy. It exhibited a flat evolution (0.06 mag) over a period of 27 days, thus ruling out its association with S190426c.

ZTF19aasmzqf —We could likewise rule out the possibility of ZTF19aasmzqf being a kilonova due to its slow evolution of 0.3 mag over 28 days, despite its initial red color $g - r = 0.22$ mag.

B.2.3. Stellar

ZTF19aasmekb/AT2019snl—Located at low galactic latitude ($b = -8\overset{\circ}{.}64$), ZTF19aasmekb appeared to be hostless and initially exhibited a rapid fade; its later-time light curve is photometrically consistent with a CV, and its slow evolution ($\alpha_g = 0.24$) is inconsistent with a kilonova origin.

B.2.4. Artifacts

ZTF19aassfws/AT2019fuc—We highlighted ZTF19aassfws as a candidate of potential interest because its photometric redshift fell within the LIGO distance uncertainty (Perley et al. 2019a). We also obtained radio follow-up using the VLA and AMI under the Jansky VLA mapping of Gravitational Waves as Afterglows in Radio (JAGWAR; Mooley et al. 2018), and we did not detect any radio emission. However, upon careful inspection of the reference image, we identified a very subtle gain mismatch across the image. Comparing the initial photometry of the transient with the level of the gain mismatch provided a clear indication that our candidate was not astrophysical but rather an artifact. This gain mismatch problem has since been fixed by rebuilding the references.

B.3. GW190814

No candidates were identified in the ZTF follow-up of the small localization of GW190814.

B.4. S190901ap

We summarize the candidate counterparts to S190901ap in Table 3 and the follow-up photometry in Table 12. Next, we discuss why we conclude that each one is unrelated.

B.4.1. Spectroscopically Classified

ZTF19abvizsw/AT2019pim—We discovered a red transient ($g - r \approx 0.5$) that appeared to be hostless and fast-evolving. We had observed the location of this transient every night for the month leading up to 2019 September 1 with no previous detections, therefore indicating strongly that this object was a new transient. Gravitational Wave Inaf Team Collaboration (GRAWITA) spectroscopic observations about 10 hr later seemed to suggest that the object was a galactic K or M dwarf (Salsamo et al. 2019a), but our subsequent LRIS spectroscopic follow-up yielded a featureless continuum with Mg II, Mg I, and Fe II lines at $z[s] = 1.26$ (Burdge et al. 2019). Thus, we posited that the object could be a flaring AGN or a GRB afterglow. Observations with SVOM-GWAC-F60A (Wei et al. 2019) and the LT (Perley et al. 2019b) indicated that the light curve was rapidly decaying, suggesting that the transient was likely an orphan GRB afterglow. More than 10 other GCNs contained reported follow-ups of this transient; the collated evidence posed the coherent picture that we had, remarkably, detected an untriggered long GRB afterglow in temporal and spatial coincidence with the sky map of S190901ap. This candidate will be discussed in more detail in D. A. Perley et al. (2020, in preparation).

ZTF19abvixoy/AT2019pin—We detected this transient with an upper limit from the day before the merger, though it appeared to have a faint counterpart in PS1. GRAWITA spectroscopic observations classified this transient as a CV due to its blue continuum and weak Hα emission surrounded by broad absorption troughs (Salmaso et al. 2019b).

ZTF19abvionh/AT2019pip—The photometric redshift of the putative host of this transient initially made it an interesting candidate for association with S190901ap, even though its first two detections were separated by a short baseline of 7 minutes. About 15 hr later, spectroscopic observations with the Hobby-Eberly observatory suggested that the host galaxy GALEXASC J165500.03+140301.3 was located at a distance of ∼450 Mpc (Rosell et al. 2019); our LRIS spectrum, showing a hot blue continuum and host galaxy lines at $z[s] = 0.0985$, confirmed this conclusion, placing the transient outside of the GW distance error bar by 2.5σ. Upon close inspection of the spectra, we find Hα and He II at zero redshift, suggesting that the transient is a foreground CV and the background host galaxy is unrelated.

ZTF19abwvals/AT2019pni—Another transient detected via the AMPEL alert archive, ZTF19abwvals, appeared to be red ($g - r \sim 0.5$) and had a photometric redshift of 0.13, slightly higher than the GW distance, also with upper limits in the g band the previous day (Stein et al. 2019c). The SNID template matching to the spectra taken with the ALFOSC spectrograph on the Nordic Optical Telescope revealed that ZTF19abwvals was a normal SN Ia, about 4–6 days postpeak (Izzo et al. 2019).

B.4.2. Slow Photometric Evolution

ZTF19abwsmmd/AT2019pnc—Further searches of the data with the AMPEL pipeline yielded two additional candidates, including ZTF19abwsmmd (Stein et al. 2019c). This candidate exhibited a blue color ($g - r \sim 0.25$) and had nondetections in the g band to 20.64 mag a day before the merger. The ZTF survey operations monitored it over a period of about 35 days. The light curve exhibited a change of only 0.2 mag decline over that baseline; therefore, we deemed it too slow to be associated with the GW event.

ZTF19abvislp/AT2019pnx—We performed a second search of the AMPEL alert archive in which we identified this transient, detected on the first night of observations. It was interesting due to its rising light curve and host SDSS galaxy being at a redshift of 0.1, on the upper end of the LIGO distance range. Instead of using our spectroscopic resources, we chose to monitor the transient photometrically, and its evolution over nearly 30 days proved to be too slow ($\alpha_r = 0.05$) to be a kilonova.

ZTF19abxdvcs/AT2019qev—We also discovered ZTF19abxdvcs during a second AMPEL archive search and highlighted it due to its photometric redshift ($z \sim 0.118$) and the fact that it had risen by more than 0.65 mag over the course of 3 days, with its first detection on the first night. Though we did not report this candidate via GCN, our continued photometric monitoring with the ZTF demonstrated that the transient was evolving with $\alpha_g = 0.03$, and its light curve resembled that of an SN, so we could confidently reject it.

B.5. S190910d

We summarize the candidate counterparts to S190910d in Table 4 and the follow-up photometry in Table 13. Next, we discuss why we conclude that each one is unrelated.

B.5.1. Spectroscopically Classified

ZTF19abyfhov/AT2019pvu—We identified this candidate during our follow-up campaign for S190910d with no available photometric redshifts due to cross-matches at its sky position (Anand et al. 2019). Castro-Tirado et al. (2019b) observed it with the 10.4 m GTC telescope equipped with OSIRIS in La Palma, Spain, about 16 hr after initial detection and derived an r-band magnitude of 20.33 mag for the transient. The best match to their spectrum indicated that the candidate was an SN Ia at $z[s] = 0.133 \pm 0.001$. Another spectrum taken with the ACAM instrument on the William Herschel Telesope at the Roque de los Muchachos Observatory in La Palma confirmed the classification (Cannizzaro et al. 2019).

ZTF19abyfhaq/AT2019pvv—Similarly, we detected ZTF19abyfhaq with little other information than the r-band magnitude of its initial detection at 20.3 mag (Anand et al. 2019). The GTC spectrum taken (Castro-Tirado et al. 2019b) about 18 hr after the initial detection had a too-low S/N to merit a classification, but an Hα emission line at $z[s] = 0$ revealed that the transient was galactic and therefore unrelated.

Table 12
Follow-up Photometry for S190901ap Candidates

Name	IAU Name	Date	Telescope	Filter	m (AB)	σ_m	m_{lim}
ZTF19abvizsw	AT2019pim	2,458,729.229	GIT	i	20.14	0.1	20.41
ZTF19abvizsw	AT2019pim	2,458,729.126	GIT	i	20.13	0.09	20.41
ZTF19abvizsw	AT2019pim	2,458,729.303	GIT	g	21.19	0.06	21.43
ZTF19abvizsw	AT2019pim	2,458,729.103	GIT	r	20.57	0.11	20.65
ZTF19abvizsw	AT2019pim	2,458,730.4481	LT	g	22.02	0.10	22.00
ZTF19abvizsw	AT2019pim	2,458,730.4420	LT	r	21.62	0.09	22.0
ZTF19abvizsw	AT2019pim	2,458,730.4541	LT	i	21.16	0.07	22.00
ZTF19abvizsw	AT2019pim	2,458,730.4621	LT	z	20.87	0.12	22.00
ZTF19abvizsw	AT2019pim	2,458,731.14	GIT	i	99.0	99.0	20.29
ZTF19abvizsw	AT2019pim	2,458,731.134	GIT	i	99.0	99.0	20.29
ZTF19abvizsw	AT2019pim	2,458,731.118	GIT	r	99.0	99.0	20.98
ZTF19abvizsw	AT2019pim	2,458,731.125	GIT	r	99.0	99.0	21.14
ZTF19abvizsw	AT2019pim	2,458,731.3862	LT	g	22.50	0.20	22.50
ZTF19abvizsw	AT2019pim	2,458,731.3802	LT	r	22.05	0.10	22.50
ZTF19abvizsw	AT2019pim	2,458,731.3923	LT	i	21.60	0.10	22.50
ZTF19abvizsw	AT2019pim	2,458,731.3983	LT	z	21.20	0.20	22.50
ZTF19abvizsw	AT2019pim	2,458,731.5172	LT	g	22.54	0.16	23.00
ZTF19abvizsw	AT2019pim	2,458,731.5112	LT	r	22.10	0.12	23.00
ZTF19abvizsw	AT2019pim	2,458,731.5232	LT	i	21.64	0.11	23.00
ZTF19abvizsw	AT2019pim	2,458,731.5293	LT	z	21.55	0.22	23.00
ZTF19abvizsw	AT2019pim	2,458,732.102	GIT	r	99.0	99.0	19.32
ZTF19abvizsw	AT2019pim	2,458,732.119	GIT	i	99.0	99.0	20.4
ZTF19abvizsw	AT2019pim	2,458,732.125	GIT	i	99.0	99.0	20.43
ZTF19abvizsw	AT2019pim	2,458,738.3819	WHT	r	22.60	0.12	24.00
ZTF19abvizsw	AT2019pim	2,458,739.3839	WHT	i	22.43	0.12	24.10
ZTF19abvizsw	AT2019pim	2,458,740.4939	WHT	i	22.51	0.15	23.50
ZTF19abvizsw	AT2019pim	2,458,740.5219	WHT	r	23.38	0.25	23.70
ZTF19abvizsw	AT2019pim	2,458,750.7337	Keck1	g	23.99	0.10	26.00
ZTF19abvizsw	AT2019pim	2,458,750.7342	Keck1	i	23.80	0.09	25.00
ZTF19abvionh	AT2019pip	2,458,729.166	GIT	r	20.8	0.05	21.27
ZTF19abvionh	AT2019pip	2,458,729.206	GIT	r	20.77	0.06	21.17
ZTF19abvionh	AT2019pip	2,458,729.213	GIT	r	20.68	0.08	21.15
ZTF19abvionh	AT2019pip	2,458,730.166	GIT	r	20.63	0.04	21.22
ZTF19abvionh	AT2019pip	2,458,730.18	GIT	r	20.66	0.05	21.23
ZTF19abvionh	AT2019pip	2,458,731.204	GIT	g	20.56	0.06	21.16
ZTF19abvionh	AT2019pip	2,458,731.4331	LT	u	20.47	0.11	21.86
ZTF19abvionh	AT2019pip	2,458,731.4208	LT	g	20.51	0.29	22.55
ZTF19abvionh	AT2019pip	2,458,731.4168	LT	r	20.36	0.09	22.35
ZTF19abwsmmd	AT2019pnc	2,458,731.5587	LT	g	19.86	0.16	20.41
ZTF19abwsmmd	AT2019pnc	2,458,731.5641	LT	r	20.02	0.07	22.02
ZTF19abwsmmd	AT2019pnc	2,458,731.5614	LT	i	20.26	0.06	22.47
ZTF19abwvals	AT2019pni	2,458,731.7095	LT	g	20.42	0.07	22.63
ZTF19abwvals	AT2019pni	2,458,731.7149	LT	r	20.04	0.08	22.96
ZTF19abwvals	AT2019pni	2,458,731.7122	LT	i	20.23	0.24	22.30
ZTF19abvixoy	AT2019pin	2,458,729.144	GIT	r	18.97	0.03	21.16
ZTF19abvixoy	AT2019pin	2,458,729.182	GIT	r	18.73	0.02	21.17
ZTF19abvixoy	AT2019pin	2,458,729.238	GIT	i	18.97	0.05	20.35
ZTF19abvixoy	AT2019pin	2,458,729.245	GIT	i	19.06	0.05	20.38
ZTF19abvixoy	AT2019pin	2,458,729.285	GIT	i	19.02	0.1	20.27
ZTF19abvixoy	AT2019pin	2,458,729.292	GIT	i	18.94	0.1	20.23
ZTF19abvislp	AT2019pnx	2,458,734.171	GIT	g	99.0	99.0	20.42
ZTF19abvislp	AT2019pnx	2,458,734.178	GIT	g	99.0	99.0	20.29
ZTF19abvislp	AT2019pnx	2,458,735.113	GIT	g	99.0	99.0	20.34
ZTF19abvislp	AT2019pnx	2,458,735.181	GIT	r	99.0	99.0	19.91
ZTF19abvislp	AT2019pnx	2,458,733.111	GIT	g	99.0	99.0	20.45
ZTF19abvislp	AT2019pnx	2,458,733.118	GIT	g	99.0	99.0	20.36
ZTF19abvislp	AT2019pnx	2,458,735.174	GIT	r	99.0	99.0	19.89
ZTF19abxdvcs	AT2019qev	2,458,733.133	GIT	g	19.93	0.03	20.7
ZTF19abxdvcs	AT2019qev	2,458,733.173	GIT	r	20.18	0.05	20.72
ZTF19abxdvcs	AT2019qev	2,458,733.179	GIT	r	20.28	0.03	20.82

Table 12
(Continued)

Name	IAU Name	Date	Telescope	Filter	m (AB)	σ_m	$m_{\rm lim}$
ZTF19abxdvcs	AT2019qev	2,458,734.242	GIT	g	19.83	0.03	20.55
ZTF19abxdvcs	AT2019qev	2,458,734.249	GIT	g	19.9	0.05	20.38
ZTF19abxdvcs	AT2019qev	2,458,734.258	GIT	r	20.03	0.05	20.31
ZTF19abxdvcs	AT2019qev	2,458,734.264	GIT	r	20.11	0.05	20.32
ZTF19abxdvcs	AT2019qev	2,458,735.206	GIT	r	19.8	0.05	19.94
ZTF19abxdvcs	AT2019qev	2,458,735.213	GIT	r	19.84	0.05	19.89

Table 13
Follow-up Photometry for S190910d Candidates

Name	IAU Name	Date	Telescope	Filter	m (AB)	σ_m	$m_{\rm lim}$
ZTF19abyfazm	AT2019pwa	2,458,736.8848	P60	r	18.17	0.04	20.48
ZTF19abyfazm	AT2019pwa	2,458,737.3704	LT	g	17.95	0.03	21.00
ZTF19abyfazm	AT2019pwa	2,458,737.3704	LT	g	17.96	0.01	21.81
ZTF19abyfazm	AT2019pwa	2,458,737.3715	LT	r	18.30	0.03	21.00
ZTF19abyfazm	AT2019pwa	2,458,737.3715	LT	r	18.30	0.01	22.36
ZTF19abyfazm	AT2019pwa	2,458,737.3725	LT	i	18.65	0.05	21.00
ZTF19abyfazm	AT2019pwa	2,458,737.3725	LT	i	18.62	0.01	22.16

ZTF19abyfazm/AT2019pvz—Among the other candidates identified in Anand et al. (2019), we highlighted this one as being blue ($g - r \sim 0.4$), with its last nondetection 1 day before the merger, and a faint source in PS1 about 2″5 from the transient position. Our imaging and spectroscopy with the LT showed that the transient remained bright and blue, with no obvious emission or absorption lines in the spectrum, suggesting that this was likely a CV (Perley & Copperwheat 2019a); this conclusion was further supported by a GTC spectrum (Castro-Tirado et al. 2019b).

ZTF19abyfbii/AT2019pwa—During the same initial search, we identified ZTF19abyfbii, whose proximity to an SDSS galaxy with a photometric redshift of $z[p] = 0.124$ placed it within the distance uncertainty for S190910d (Anand et al. 2019). Our candidate was classified as an SN Ia at $z[s] = 0.1286 \pm 0.0005$ less than 20 hr later by GTC using the Hα, Hβ, and O II lines in its spectrum (Castro-Tirado et al. 2019b). Further spectroscopy with the William Hershel Telescope provided a detailed classification that this transient was SN Ia 91T–like, 5 days before the peak, at $z[s] = 0.118$ (Cannizzaro et al. 2019).

B.6. S190910h

We summarize the candidate counterparts to S190910h in Table 5 and the follow-up photometry in Table 14. Next, we discuss why we conclude that each one is unrelated.

B.6.1. Spectroscopically Classified

ZTF19abyheza/AT2019pxi—We initially detected ZTF19abyheza at $g = 19.14 \pm 0.13$ with the ZTF with heavy galactic extinction of $\sim$0.8 in the direction of the transient. One day later, Valeev et al. (2019) imaged the transient, reporting that it had brightened to $r = 18.74 \pm 0.05$. The GTC spectroscopy revealed Hα in emission and Hβ in absorption at $z[s] = 0$. Synthesizing this information along with the light-curve shape suggested that this was likely a CV.

ZTF19abyhhml/AT2019pxj—According to our machine-learning algorithms derived from the PS1-DR2 catalog, we could not clearly determine whether this source was of stellar origin. Similar to the previous transient, GTC imaging demonstrated that the light curve had risen to $r = 19.26 \pm 0.04$, and spectra exhibited the He II and He I lines and a double-peaked Hα line, confirming that it was also a galactic CV.

ZTF19abyirjl/AT2019pxe—We highlighted ZTF19abyirjl as being of interest due to its photometric redshift, 0.1 ± 0.017. Having no other information about the transient, we monitored the light curve for several days and determined it was too slow to be associated with the GW event, with an average flat evolution. One month later, we obtained a spectrum using P200+DBSP, which clearly demonstrated through Si II lines that it was an SN Ia.

ZTF19abygvmp/AT2019pzg—This candidate was among those candidates reported in our second set of transients (Stein et al. 2019a). We highlighted ZTF19abygvmp, a transient detected 1 hr after the merger time, in a slightly offset position from the galaxy, as it had appeared to have risen by 0.5 mag since the last nondetection. Cannizzaro et al. acquired a WHT spectrum of the source about 2 days later, but the spectrum, dominated by host galaxy light, yielded only a redshift of $z[s] = 0.049$, exactly consistent with the LVC distance estimate. Two weeks later, we obtained an LRIS spectrum of the source, classifying it as an SN II (also consistent with its slow photometric evolution).

B.6.2. Slow Photometric Evolution

ZTF19abylleu/AT2019pyu—23 hr after the merger, we detected this bright ($r = 19.25$ mag) transient with an upper limit of $r = 20.4$ mag from the day before. Though we could not obtain any spectra, we continued tracking the evolution of the transient over a period of $\sim$25 days; the r-band light curve remained relatively flat, while the g-band light curve exhibited a gradual decline. We concluded that the evolution was too slow ($\alpha_g = 0.03$) to be associated with the GW event.

ZTF19abyjfiw—Valeev et al. (2019) obtained a spectrum with GTC about 2 days later that appeared to be a featureless blue continuum from which they could not derive a conclusive

Table 14
Follow-up Photometry for S190910h Candidates

Name	IAU Name	Date	Telescope	Filter	m (AB)	σ_m	$m_{\rm lim}$
ZTF19abyjcom	AT2019pxk	2,458,737.5558	LT	g	99.0	99.0	20.75
ZTF19abyjcom	AT2019pxk	2,458,737.5569	LT	r	99.0	99.0	20.71
ZTF19abyjcom	AT2019pxk	2,458,737.5579	LT	i	99.0	99.0	20.21
ZTF19abyjcon	AT2019pxl	2,458,737.6142	LT	g	99.0	99.0	21.29
ZTF19abyjcon	AT2019pxl	2,458,737.6152	LT	r	99.0	99.0	21.44
ZTF19abyjcon	AT2019pxl	2,458,737.6163	LT	i	99.0	99.0	21.33
ZTF19abyjcoo	AT2019pxm	2,458,737.6234	LT	g	99.0	99.0	20.84
ZTF19abyjcoo	AT2019pxm	2,458,737.6245	LT	r	99.0	99.0	20.89
ZTF19abyjcoo	AT2019pxm	2,458,737.6255	LT	i	99.0	99.0	21.30

Table 15
Follow-up Photometry for S190930t Candidates

Name	IAU Name	Date	Telescope	Filter	m (AB)	σ_m	$m_{\rm lim}$
ATLAS19wyn	AT2019rpj	2,458,758.0974	LOT	g	19.65	0.08	99.0
ATLAS19wyn	AT2019rpj	2,458,758.0974	LOT	r	19.58	0.09	99.0
ATLAS19wyn	AT2019rpj	2,458,758.0974	LOT	i	19.55	0.12	99.0
ATLAS19wyn	AT2019rpj	2,458,758.8562	LDT	r	19.6	0.1	22.8
ZTF19acbpqlh	AT2019rpn	2,458,758.0937	LOT	g	20.80	0.25	99.0
ZTF19acbpqlh	AT2019rpn	2,458,758.0937	LOT	r	20.67	0.33	99.0
ZTF19acbpqlh	AT2019rpn	2,458,758.0937	LOT	i	20.80	0.39	99.0
ZTF19acbpqlh	AT2019rpn	2,458,758.8548	LDT	r	19.80	0.10	22.8

classification. However, the transient presents a flat evolution, with a coefficient $\alpha < 0.1$. Another detection by the ZTF (4 months after merger) suggests that it could be a CV.

ZTF19abyiwiw/AT2019pzi—We identified this transient in spatial and temporal coincidence with both S190910d and S190910h at 3°.1 galactic latitude and 2.3 mag of extinction in the direction of the transient. It was first discovered at $r = 20.16$ mag, but photometric follow-up determined that its evolution was too slow to be relevant, with $\alpha_g = 0.20$.

ZTF19abymhyi/AT2019pzh—The object ZTF19abymhyi was faint and hostless, with detections in the g band 2 hr after the merger (Stein et al. 2019a) and upper limits of $g = 20.65$ mag from the day before. The transient rose by $\sim$0.3 mag 1 day later. However, it was ruled out because its photometric evolution did not pass our threshold, as it faded slower than expected with $\alpha_g = 0.03$.

ZTF19abyjcoo/AT2019pxm—This orphan transient was discovered at $r = 20.28$ mag, and we rule it out due to its slow evolution ($\alpha_r = 0.06$).

B.6.3. Artifacts

ZTF19abyjcom/AT2019pxk, ZTF19abyjcon/AT2019pxl—On the first night of observations following this GW event, we detected two hostless transients within the same exposure, detected within the same sky region. Imaging with the LT about 1 day later resulted in nondetections of both transients, despite the fact that other transients of a similar magnitude, discovered within the same exposure, were detected. Furthermore, despite clear detections initially in the r and g bands, we could not detect these transients in future serendipitous observations of the sky region with the ZTF. We posit that these three transients are likely cross-talk artifacts that occurred within the same exposure and therefore are unrelated.

B.7. S190923y

We summarize one candidate counterpart to S190923y in Table 6. Despite the small sky localization, the position of S190923y on the sky made it particularly challenging to access. For that reason, we chose to conduct a fully serendipitous search in ZTF data.

ZTF19acbmopl/AT2019rob—We found this transient with a photometric redshift of $\lesssim$0.03, consistent with the LVC distance reported, slightly off the nucleus of its host galaxy. It showed a slow evolution in both the r and g bands: $\alpha_r = 0.03$ and $\alpha_g = 0.03$.

B.8. S190930t

We summarize the candidate counterparts to S190930t in Table 7 and the follow-up photometry in Table 15. Next, we discuss why we conclude that each one is unrelated.

B.8.1. Spectroscopically Classified

ZTF19acbpqlh/AT2019rpn—We first detected this candidate 13.4 hr after the merger using our AMPEL pipeline with a magnitude of $g = 20.36$ mag and upper limits of $g = 20.77$ mag from 3 days before the merger. The transient was at a galactic latitude of $b = -8°.49$. Using its spectroscopic host galaxy redshift, $z[s] = 0.026$, we derived an absolute magnitude of -14.91 mag (Stein et al. 2019b). The same night, we obtained a spectrum with P200+DBSP revealing a mostly featureless blue continuum with a weak broad feature around Hα suggesting that the transient could be a young core-collapse SN. Using the ZTSh 2.6 m telescope at the CrAO observatory, Mazaeva et al. (2019) imaged the SN and found that its $B - R$ color of 0.5 mag was unlike what was expected of any optical transient associated with a GW event.

Table 16
Follow-up Photometry for S191205ah Candidates

Name	IAU Name	Date	Telescope	Filter	m (AB)	σ_m	$m_{\rm lim}$
ZTF19acxowrr	AT2019wib	2,458,850.0554	P60	r	18.91	0.16	99.0
ZTF19acxowrr	AT2019wib	2,458,852.7504	P60	i	99.0	99.0	20.00
ZTF19acyitga	AT2019wmn	2,458,837.8427	P60	r	18.21	0.07	99.0

We followed up by taking a second spectrum with the DBSP on 2019 October 5 and confirmed that the candidate was indeed an SN II.

ZTF19acbwaah/AT2019rpp—22 hr after the merger, we detected this transient, whose slight offset from a potential galaxy host at $z[s] = 0.032$ lends it an absolute magnitude of -18.069 (Stein et al. 2019b). The next night, we conducted observations of this candidate with the DBSP; the spectrum was consistent with an SN Ia a few weeks after maximum light located at $z[s] = 0.03$ (Karambelkar et al. 2019b).

ATLAS19wyn/AT2019rpj—With the ZTF, we independently detected a candidate first reported by ATLAS (Smartt et al. 2019; ZTF19acbpsuf) 13.8 hr after the merger; ATLAS detected it 4 hr later. The transient had a deep upper limit of 20.92 from about 6 days before the merger, and its association with a host at $z[s] = 0.0297$ translated to an absolute magnitude of -15.987. The strong Balmer P Cygni features in our DBSP spectrum, taken the same night as the initial detection, clearly indicated that the transient was an SN (Karambelkar et al. 2019a).

B.9. S191205ah

We summarize the candidate counterparts to S191205ah in Table 8 and follow-up photometry in Table 16. Next, we discuss why we conclude that each one is unrelated.

B.9.1. Spectroscopically Classified

ZTF19acyiflj/AT2019wmy—This transient was discovered at $r = 20.09$ mag and observed by GTC at a magnitude of $r = 19.79$ mag hours after the trigger. A faint host is visible in the PS1 images of the field. However, the GTC spectrum showed an SN Ia at a redshift of $z[s] = 0.081$ (Hu et al. 2019a).

ZTF19acxowrr/AT2019wib—The first detection of this transient was ∼4 days after the GW event at $r = 19.054 \pm 0.13$ mag. It rose over the first ∼15 days, during which several spectra were taken. The first classification came from GTC (Hu et al. 2019c): an SN II at a redshift of $z[s] = 0.05$.

ZTF19acyitga/AT2019wmn—This transient was located in a galaxy at a redshift of $z[s] = 0.071$ and first detected at $r = 19.26$ mag. We obtained an LT spectrum of ZTF19acyitga 14 days after the discovery that showed it was an SN Ia.

B.9.2. Slow Photometric Evolution

ZTF19acxpnvd/AT2019wkv—This transient was reported in Andreoni et al. (2019b) after its discovery at $r = 19.4$ mag. The transient was located in the outskirts of a galaxy located at a photometric SDSS redshift of $z[p] \lesssim 0.03$, and it was ruled out due to the slow evolution shown after peaking, with $\alpha_g = 0.06$.

ZTF19acxoywk/AT2019wix—Similarly, this transient was reported in Andreoni et al. (2019b) with a discovery magnitude of $r = 19.75$ mag. It was located in the outer regions of a galaxy with a spectroscopic redshift of $z[s] = 0.05$; however, the evolution of this transient was only $\alpha_g = -0.15$.

ZTF19acxoyra/AT2019wid—This slow-evolving transient was highlighted in Andreoni et al. (2019b) after being discovered at $r = 19.20$ mag in the nucleus of a galaxy at $z[s] = 0.09$. However, it had an almost flat evolution after reaching its peak ($\alpha_g = 0.05$).

ZTF19acxpwlh/AT2019wiy—This transient was located in a galaxy at an SDSS photometric redshift of $z[p] = 0.12$. Discovered at $g = 19.84$, it showed an almost flat evolution over the days after reaching its peak ($\alpha_r = 0.07$).

B.10. S191213g

We summarize the candidate counterparts to S191213g in Table 9 and the follow-up photometry in Table 17. Next, we discuss why we conclude that each one is unrelated.

B.10.1. Spectroscopically Classified

ZTF19acykzsk/SN2019wqj—This transient was discovered at $g = 19.25$ mag in a galaxy at $z[s] = 0.021$. It was not detected in the ultraviolet by the Swift telescope (Oates et al. 2019). The spectrum taken with the SPRAT on the LT (Perley & Copperwheat 2019b) and the GMOS-N mounted on the Gemini-North 8 m telescope (Fremling et al. 2019) showed prominent hydrogen lines and was classified as an SN II. This was later confirmed by a GTC spectrum that showed similar features (Elias-Rosa et al. 2019). Furthermore, this transient had PS1 detections ∼1 day after the event (Smith et al. 2019). Part of the evolution of this transient was followed up by the LOT (Tan et al. 2019).

ZTF19acymaru/AT2019wnh—This transient was discovered at $r = 20.03$ mag and highlighted in Andreoni et al. (2019a). The ZTF reference image did not show a visible host. Finally, the GTC spectrum revealed an SN Ia at redshift $z[s] = 0.167$ (Castro-Tirado et al. 2019a).

ZTF19acykzsp/AT2019wne—This candidate was first highlighted in Andreoni et al. (2019a), as it was discovered at $r = 20.18$ mag. The LT/SPRAT spectrum showed an SN Ia at maximum light at $z[s] = 0.16$ (Perley & Copperwheat 2019b).

ZTF19acyfoha/AT2019wkl—Similarly, ZTF19acyfoha was reported in Andreoni et al. (2019a) at $g = 17.49$ mag. It was located in one of the arms of a spiral galaxy with a CLU redshift of $z[p] = 0.04$. The candidate was observed with the SEDM at the P60, and its spectra showed clear features of an SN Ia at $z[s] = 0.044$.

ZTF19acymcwv/AT2019wni—This transient was discovered at $r = 20.24$ mag and reported in Andreoni et al. (2019a). The candidate is in the outskirts of an elliptical galaxy, and a spectrum taken with WHT revealed an SN Ia at $z[s] = 0.09$ (Brennan et al. 2019).

ZTF19acymixu/AT2019wrr—This candidate was first reported in Stein et al. (2019d), as it was discovered at $r = 19.87$ mag on top of a faint diffuse source. After

Table 17
Follow-up Photometry for S191213g Candidates

Name	IAU Name	Date	Telescope	Filter	m (AB)	σ_m	$m_{\rm lim}$
ZTF19acykzsk	SN2019wqj	2,458,831.8323	P60	r	19.06	0.08	20.34
ZTF19acykzsk	SN2019wqj	2,458,831.928	LOT	g	19.37	0.10	99.0
ZTF19acykzsk	SN2019wqj	2,458,831.931	LOT	r	19.11	0.16	99.0
ZTF19acykzsk	SN2019wqj	2,458,831.935	LOT	i	19.10	0.11	99.0
ZTF19acykzsk	SN2019wqj	2,458,832.223	LOT	g	19.51	0.11	99.0
ZTF19acykzsk	SN2019wqj	2,458,832.231	LOT	r	19.10	0.14	99.0
ZTF19acykzsk	SN2019wqj	2,458,832.233	LOT	i	19.06	0.24	99.0
ZTF19acykzsk	SN2019wqj	2,458,832.2910	UVOT	v	99.0	99.0	17.2
ZTF19acykzsk	SN2019wqj	2,458,832.2910	UVOT	b	99.0	99.0	17.8
ZTF19acykzsk	SN2019wqj	2,458,832.2910	UVOT	u	99.0	99.0	17.5
ZTF19acykzsk	SN2019wqj	2,458,832.2910	UVOT	$w1$	99.0	99.0	17.5
ZTF19acykzsk	SN2019wqj	2,458,832.2910	UVOT	$m2$	99.0	99.0	18.0
ZTF19acykzsk	SN2019wqj	2,458,832.2910	UVOT	$w2$	99.0	99.0	18.1
ZTF19acymixu	AT2019wrr	2,458,832.2910	UVOT	v	99.0	99.0	19.5
ZTF19acymixu	AT2019wrr	2,458,832.2910	UVOT	b	20.10	0.4	99.0
ZTF19acymixu	AT2019wrr	2,458,832.2910	UVOT	u	99.0	99.0	19.7
ZTF19acymixu	AT2019wrr	2,458,832.2910	UVOT	$w1$	99.0	99.0	19.7
ZTF19acymixu	AT2019wrr	2,458,832.2910	UVOT	$m2$	99.0	99.0	19.7
ZTF19acymixu	AT2019wrr	2,458,832.2910	UVOT	$w2$	99.0	99.0	20.3
ZTF19acymaru	AT2019wnh	2,458,831.9682	LCOGT1m	g	19.83	0.04	21.00
ZTF19acymaru	AT2019wnh	2,458,831.9706	LCOGT1m	i	20.23	0.15	21.00
ZTF19acymaru	AT2019wnh	2,458,831.9755	LCOGT1m	r	20.11	0.05	21.00
ZTF19acyfoha	AT2019wkl	2,458,831.7544	P60	r	17.29	0.05	19.19
ZTF19acyldun	AT2019wrt	2,458,853.7823	P60	i	18.99	0.10	19.87
ZTF19acyldun	AT2019wrt	2,458,832.2910	UVOT	v	99.0	99.0	17.9
ZTF19acyldun	AT2019wrt	2,458,832.2910	UVOT	b	18.83	0.13	99.0
ZTF19acyldun	AT2019wrt	2,458,832.2910	UVOT	u	18.18	0.12	99.0
ZTF19acyldun	AT2019wrt	2,458,832.2910	UVOT	$w1$	17.62	0.11	99.0
ZTF19acyldun	AT2019wrt	2,458,832.2910	UVOT	$m2$	17.71	0.13	99.0
ZTF19acyldun	AT2019wrt	2,458,832.2910	UVOT	$w2$	18.19	0.12	99.0

$\sim$1.6 days, observations with Swift showed a source at $b = 20.1$ mag. However, it was later classified as an SN Ia at $z[s] = 0.14$ with a spectrum taken with the DBSP at the P200.

ZTF19acylvus/AT2019wnk—This transient was discovered at $r = 19.60$ mag, sitting on top of a faint galaxy without a known redshift. It was classified by the GTC as an SN Ia at $z[s] = 0.1$ (Castro-Tirado et al. 2019a).

ZTF19acymcna/AT2019wnn—This transient was detected at $r = 20.74$ mag in the nucleus of an elliptical galaxy. The GTC spectrum showed broad hydrogen features at $z = 0.2$, consistent with an AGN.

ZTF19acyldun/AT2019wrt—This candidate was reported with an initial magnitude of $g = 19.8$. The follow-up with the Swift telescope shown an active source in the ultraviolet (Oates et al. 2019). The observations performed by GTC discovered a source at $z[s] = 0.057$ with narrow Balmer lines consistent with a luminous blue variable (LBV; Castro-Tirado et al. 2019a), as it was also detected in 2012 by PS1. However, the source brightened to a peak absolute magnitude of ≈ -18 mag, and we revise its classification to be an SN IIn. It additionally faded at a rate much slower than our $\alpha = 0.3$ mag evolution threshold, with a coefficient of $\alpha_r = 0.09$.

B.10.2. Slow Photometric Evolution

ZTF19acykyzj/AT2019wrg—This candidate was discovered at $g = 20.55$ and reported in Stein et al. (2019d). It was located in the outskirts of a spiral galaxy at unknown redshift; however, its slow magnitude evolution ($\alpha_r = -0.03$) makes this transient not relevant.

ZTF19acymapa/AT2019wro—This source was detected at $g = 20.31$ and reported in Stein et al. (2019d). To calculate the evolution of this object, we have only used the first 2 nights of data, as there are no more data on this transient. Using this Δt, we obtain a slow-evolving transient with $\alpha_r = -0.06$. Additionally, we note that the first two data points make a color consistent with $g - r = 0$.

ZTF19acymaxu/AT2019wrp—This candidate was highlighted in Stein et al. (2019d) at $r = 18.70$ mag. It is on top of a faint PS1 source, and its slow magnitude evolution of $\alpha_r = 0.03$ allows us to rule it out.

ZTF19acymlhi/AT2019wrs—The first detection of this candidate was of $r = 19.54$ mag, and its initial color was consistent with $g - r = 0$ mag. Similar to ZTF19acymapa, the baseline used in this case was of $\Delta t = 2$ days, and the evolution showed a slow rise of $\alpha_r = -0.17$.

B.10.3. Artifacts

ZTF19acykwsd/AT2019wnl—This transient was highlighted as an orphan source with two detections in different bands: $r = 19.42$ and $g = 19.39$ mag. We proceeded to obtain an LT/SPRAT spectrum; however, the source was not present in the acquisition image. Further investigation showed more sources around ZTF19acykwsd consistent with cross-talk.

B.10.4. Stellar Sources

ZTF19acykyqu/AT2019wre—This transient was detected at $g = 21.13$ mag and has a second detection 3.5 hr later at $r = 20.86$ mag. There are no more ZTF data on this object; however, there is a faint point source underneath the transient and a PS1-DR2 detection ∼1 month before the GW event. We then consider ZTF19acykyqu to be related to a stellar background source.

ZTF19acykyrz/AT2019wrf —Similar to ZTF19acykyqu, this source sits on a PS1 source that has a previous variability history. The first PS1-reported detection was in 2010, while the last PS1-reported detection was in 2014. As the ZTF only detected this source twice, at $g = 20.97$ and $r = 20.16$ mag, we posit that this candidate is related to the PS1 source underneath.

ZTF19acykzfy/AT2019wrh—This orphan transient was first discovered at $g = 20.56$ and detected ∼3.5 hr later at $r = 20.96$ mag. The galactic latitude of ZTF19acykzfy ($b = -15\overset{\circ}{.}73$) and a nearby ($<3''$) detection in the PS1-DR2 catalog back the stellar origin of this transient.

ZTF19acyldum/AT2019wrn—The candidate was first reported by Stein et al. (2019d) with a magnitude of $g = 19.78$ mag. It was later detected twice: 3 hr later at $r = 19.82$ mag and 5 hr later at $g = 19.84$ mag. However, there is a PS1-DR2 detection within $1''$ in 2010 and a faint source in the ZTF reference images. Therefore, we posit this candidate as a stellar variable and thus unrelated.

B.11. S200105ae and S200115j

For candidates identified within the sky map of S200105ae and S200115j, see Anand et al. (2020).

B.12. S200213t

We summarize the candidate counterparts to S200213t in Table 10 and the follow-up photometry in Table 18. Next, we discuss why we conclude that each one is unrelated. All of the transients described for this event (S200213t) were reported in Kasliwal et al. (2020).

B.12.1. Spectroscopically Classified

ZTF20aamvqxl/AT2020ciy—This transient was first reported in Kasliwal et al. (2020), as it was discovered at $g = 20.45$ mag, in the outskirts of a potential host. With the spectra taken with GTC, Valeev et al. (2020) classified the candidate as an SN Ia at $z[s] = 0.1$.

ZTF20aamvnth/AT2020cjb—Similarly, this candidate was first reported in Kasliwal et al. (2020); however, its potential host was a faint and diffuse galaxy visible in the PS1 image of the field. A spectrum from GTC classified this candidate as an SN II at $z[s] = 0.061$ (Castro-Tirado et al. 2020).

ZTF20aamvoxx/AT2020cjg—This transient was first observed at $g = 19.99$ mag, close to the nucleus of an elliptical galaxy. Data taken with GTC classified this candidate as an SN Ia at $z[s] = 0.097$ (Valeev et al. 2020).

ZTF20aamvtip/AT2020cje—The first detection of ZTF20aamvtip was at $g = 20.7$ mag and faded 0.2 mag in the r band after a day. The SDSS photometric redshift of the faint host was $z[p] = 0.225$. The GTC spectra classified it as an SN Ia at $z[s] = 0.15$ (Valeev et al. 2020).

ZTF20aamvnat/AT2020ciz—This transient was discovered at $g = 18.93$ mag, and, while originally thought orphan, a faint red counterpart in the PS1 and ZTF reference image suggested a stellar origin. Additionally, it is located at $b = -5\overset{\circ}{.}62$, backing up the stellar hypothesis. Finally, GTC spectra showed strong hydrogen lines at $z[s] = 0$, consistent with a galactic CV (Castro-Tirado et al. 2020).

ZTF20aamvodd/AT2020cjf —Similarly, this transient sits at $b = -9\overset{\circ}{.}53$ and has a faint red PS1 counterpart. It was later classified as a stellar flare at $z[s] = 0.0$ (Castro-Tirado et al. 2020) due to its Hα features.

ZTF20aamvoeh/AT2020cjc—This transient was discovered at $g = 20.56$ mag on top of an elliptical galaxy. We classified the candidate as an SN Ia at $z[s] = 0.14$ using the spectrum taken with the DBSP at the P200 telescope.

ZTF20aanaltd/AT2020clt—This transient was first reported in Andreoni et al. (2020c), as it was discovered at $g = 20.81$ mag in the outskirts of a faint red galaxy. The spectrum from the LRIS at the Keck observatory revealed an SN Ia at $z[s] = 0.2$ (De 2020).

ZTF20aanaoyz/AT2020clw—This transient was discovered at $g = 21.50$ mag on top of a faint PS1 elongated source. It was classified by GTC as an SN Ia at redshift $z[s] = 0.276$ (Hu et al. 2020).

ZTF20aamvpvx/AT2020clx—The first observation of this transient was at $g = 20.30$ mag in the nucleus of an elliptical galaxy. The GTC spectrum showed an SN II at redshift $z[s] = 0.074$ with prominent hydrogen features (De 2020).

ZTF20aanakcd/AT2020cmr—This candidate was discovered in the outskirts of an elongated, bright elliptical galaxy at $g = 20.70$ mag. The spectrum taken with the DBSP at the P200 classified it as an SN IIn at $z[s] = 0.077$ (Andreoni et al. 2020a).

ZTF20aanamcs/AT2020crc—This object was discovered close to the nucleus of an edge-on galaxy at $g = 21.25$ mag and $z[s] = 0.093$ and subsequently classified as an SN II (De 2020).

ZTF20aanakge/AT2020crd—This candidate was detected as an orphan at $g = 20.64$ mag. The spectrum taken with OSIRIS at the GTC classified it as an SN Ia at $z[s] = 0.1272$ (Hu et al. 2020).

B.12.2. Stellar

ZTF20aanaksk/AT2020clu—This candidate was first reported at $g = 20.48$ mag as an orphan transient. We rule out ZTF20aanaksk, as it has two previous detections in 2010 in the PS1-DR2 catalog, and we posit that it is related to a faint star in the background.

ZTF20aanakes/AT2020cly—This candidate was first detected at $g = 21.11$ mag and with a color consistent with $g - r = 0$. Follow-up with ARCTIC and GTC left only upper limits for this fast transient (Bellm & Graham 2020; Hu et al. 2020). However, there is an archival detection in the PS1-DR2 catalog $1\overset{''}{.}5$ from the ZTF source. Thus, we reject this candidate.

B.12.3. Slow Photometric Evolution

ZTF20aamvmzj/AT2020cja—This transient sits at $b = -10\overset{\circ}{.}43$; however, it does not seem to have a PS1 or ZTF counterpart, as with the previous stellar sources. The spectra taken with Keck I+LRIS and P200 only showed a

Table 18
Follow-up Photometry for S200213t Candidates

Name	IAU Name	Date	Telescope	Filter	m (AB)	σ_m	m_{lim}
ZTF20aamvqxl	AT2020ciy	2,458,893.3371	LT	i	20.17	0.15	21.61
ZTF20aamvqxl	AT2020ciy	2,458,893.3406	LT	g	99.0	99.0	19.54
ZTF20aamvoxx	AT2020cjg	2,458,893.3733	LT	i	20.29	0.21	21.30
ZTF20aamvoxx	AT2020cjg	2,458,893.3751	LT	r	21.47	0.19	22.49
ZTF20aamvoxx	AT2020cjg	2,458,893.3768	LT	g	20.26	0.03	23.36
ZTF20aamvtip	AT2020cje	2,458,893.3457	LT	i	20.68	0.07	22.73
ZTF20aamvtip	AT2020cje	2,458,893.3475	LT	r	20.73	0.11	22.52
ZTF20aamvtip	AT2020cje	2,458,893.3493	LT	g	20.80	0.06	23.14
ZTF20aamvmzj	AT2020cja	2,458,893.3559	LT	g	20.45	0.05	23.10
ZTF20aamvmzj	AT2020cja	2,458,906.7200	LCO2m	g	20.79	0.09	20.91
ZTF20aamvmzj	AT2020cja	2,458,906.7350	LCO2m	r	20.32	0.09	21.30
ZTF20aamvmzj	AT2020cja	2,458,893.9607	LOT	g	20.37	0.10	99.0
ZTF20aamvmzj	AT2020cja	2,458,893.9607	LOT	r	20.58	0.14	99.0
ZTF20aamvmzj	AT2020cja	2,458,893.9607	LOT	i	21.02	0.51	99.0
ZTF20aamvoeh	AT2020cjc	2,458,893.3559	LT	g	20.45	0.05	23.10
ZTF20aamvoeh	AT2020cjc	2,458,906.7200	LCO2m	g	20.79	0.09	20.91
ZTF20aamvoeh	AT2020cjc	2,458,906.7350	LCO2m	r	20.32	0.09	21.30
ZTF20aanakwb	AT2020cls	2,458,893.9607	LOT	g	99.0	99.0	18.9
ZTF20aanakwb	AT2020cls	2,458,893.9607	LOT	r	21.12	0.32	99.0
ZTF20aanakwb	AT2020cls	2,458,893.9607	LOT	i	20.97	0.37	99.0
ZTF20aanaltd	AT2020clt	2,458,893.9607	LOT	g	21.47	0.24	99.0
ZTF20aanaltd	AT2020clt	2,458,893.9607	LOT	r	19.34	0.04	99.0
ZTF20aanaltd	AT2020clt	2,458,893.9607	LOT	i	19.98	0.12	99.0
ZTF20aanaksk	AT2020clu	2,458,893.9607	LOT	g	20.80	0.14	99.0
ZTF20aanaksk	AT2020clu	2,458,893.9607	LOT	r	20.79	0.15	99.0
ZTF20aanaksk	AT2020clu	2,458,893.9607	LOT	i	21.19	0.47	99.0
ZTF20aanaoyz	AT2020clw	2,458,893.9607	LOT	g	21.46	0.42	99.0
ZTF20aanaoyz	AT2020clw	2,458,893.9607	LOT	r	21.09	0.22	99.0
ZTF20aanaoyz	AT2020clw	2,458,893.9607	LOT	i	20.75	0.37	99.0
ZTF20aanakes	AT2020cly	2,458,894.5992	APO	g	99.0	99.0	23.50
ZTF20aanakes	AT2020cly	2,458,894.6012	APO	i	99.0	99.0	21.50
ZTF20aanakes	AT2020cly	2,458,894.6031	APO	r	99.0	99.0	23.00

featureless blue continuum (De 2020). It was first observed (Oates et al. 2020b) by the UVOT (Roming et al. 2005) at Swift 6.7 days after the merger, and it was only detected in the u band at $u = 19.05$ mag. It was later followed up but not detected in any bandpass (Oates et al. 2020a). Nonetheless, the magnitude evolution of the transient was otherwise flat, and it slowly faded over time with $\alpha_r = 0.04$.

ZTF20aanaqhe/AT2020cre—This transient was detected at $g = 20.88$ mag on an elliptical galaxy at a photometric redshift of $z[p] = 0.16$. Its slow rise of $\alpha_g = -0.08$ was inconsistent with the rise of a fast transient.

ZTF20aanakwb/AT2020cls—This transient was first reported in Andreoni et al. (2020c) at $g = 21.03$ mag, offset from a bright Gaia point source ($g = 15.27$ mag). This transient was detected by the LOT 12 hr later at an r-band magnitude consistent with no evolution. The initial color $g - r$ is consistent with 0 mag. In the ZTF reference image, there is a faint point source, which indicates stellar activity.

B.12.4. Outside the GW Map

ZTF20aanallx/AT2020clv—This transient was first reported in Andreoni et al. (2020c) at $g = 21.11$ mag and discovered at a galactic latitude of $b = -11\overset{\circ}{.}43$. It is offset from an elliptical galaxy; however, it falls in a fairly crowded region. The rejection criterion we used for this transient is the fact that it is not within the 95% credible level of the latest LALInference map for S200213t.

ORCID iDs

Mansi M. Kasliwal https://orcid.org/0000-0002-5619-4938
Shreya Anand https://orcid.org/0000-0003-3768-7515
Tomás Ahumada https://orcid.org/0000-0002-2184-6430
Robert Stein https://orcid.org/0000-0003-2434-0387
Igor Andreoni https://orcid.org/0000-0002-8977-1498
Michael W. Coughlin https://orcid.org/0000-0002-8262-2924
Leo P. Singer https://orcid.org/0000-0001-9898-5597
Erik C. Kool https://orcid.org/0000-0002-7252-3877
Yuhan Yao https://orcid.org/0000-0001-6747-8509
Mattia Bulla https://orcid.org/0000-0002-8255-5127
Dougal Dobie https://orcid.org/0000-0003-0699-7019
Daniel A. Perley https://orcid.org/0000-0001-8472-1996
S. Bradley Cenko https://orcid.org/0000-0003-1673-970X
Varun Bhalerao https://orcid.org/0000-0002-6112-7609

David L. Kaplan https://orcid.org/0000-0001-6295-2881
Jesper Sollerman https://orcid.org/0000-0003-1546-6615
Ariel Goobar https://orcid.org/0000-0002-4163-4996
Christopher M. Copperwheat https://orcid.org/0000-0001-7983-8698
Eric C. Bellm https://orcid.org/0000-0001-8018-5348
G. C. Anupama https://orcid.org/0000-0003-3533-7183
Alessandra Corsi https://orcid.org/0000-0001-8104-3536
Samaya Nissanke https://orcid.org/0000-0001-6573-7773
Sudhanshu Barway https://orcid.org/0000-0002-3927-5402
Joshua S. Bloom https://orcid.org/0000-0002-7777-216X
Kevin B. Burdge https://orcid.org/0000-0002-7226-836X
David O. Cook https://orcid.org/0000-0002-6877-7655
Jeff Cooke https://orcid.org/0000-0001-5703-2108
Virginia Cunningham https://orcid.org/0000-0003-2292-0441
Dmitry A. Duev https://orcid.org/0000-0001-5060-8733
Anna Franckowiak https://orcid.org/0000-0002-5605-2219
Sara Frederick https://orcid.org/0000-0001-9676-730X
Christoffer Fremling https://orcid.org/0000-0002-4223-103X
Avishay Gal-Yam https://orcid.org/0000-0002-3653-5598
Pradip Gatkine https://orcid.org/0000-0002-1955-2230
Shaon Ghosh https://orcid.org/0000-0003-4259-8592
Daniel A. Goldstein https://orcid.org/0000-0003-3461-8661
V. Zach Golkhou https://orcid.org/0000-0001-8205-2506
Matthew J. Graham https://orcid.org/0000-0002-3168-0139
Melissa L. Graham https://orcid.org/0000-0002-9154-3136
Matthew J. Hankins https://orcid.org/0000-0001-9315-8437
George Helou https://orcid.org/0000-0003-3367-3415
Youdong Hu https://orcid.org/0000-0002-7400-4608
Amruta Jaodand https://orcid.org/0000-0002-3850-6651
Albert K. H. Kong https://orcid.org/0000-0002-5105-344X
S. R. Kulkarni https://orcid.org/0000-0001-5390-8563
Brajesh Kumar https://orcid.org/0000-0001-7225-2475
Russ R. Laher https://orcid.org/0000-0003-2451-5482
Ashish Mahabal https://orcid.org/0000-0003-2242-0244
Frank J. Masci https://orcid.org/0000-0002-8532-9395
Adam A. Miller https://orcid.org/0000-0001-9515-478X
Kunal Mooley https://orcid.org/0000-0002-2557-5180
Jeffrey A. Newman https://orcid.org/0000-0001-8684-2222
Chow-Choong Ngeow https://orcid.org/0000-0001-8771-7554
Elena Pian https://orcid.org/0000-0001-8646-4858
Reed Riddle https://orcid.org/0000-0002-0387-370X
Maayane T. Soumagnac https://orcid.org/0000-0001-6753-1488
Anastasios Tzanidakis https://orcid.org/0000-0003-0484-3331
Eleonora Troja https://orcid.org/0000-0002-1869-7817
Sara Webb https://orcid.org/0000-0003-2601-1472
Po-Chieh Yu https://orcid.org/0000-0001-8894-0854
Bin-Bin Zhang https://orcid.org/0000-0003-4111-5958
Rongpu Zhou https://orcid.org/0000-0001-5381-4372

References

Abbott, B. P., Abbott, R., Abbott, T. D., et al. 2017a, ApJL, 848, L12
Abbott, B. P., Abbott, R., Abbott, T. D., et al. 2018, LRR, 21, 3
Abbott, B. P., Abbott, R., Abbott, T. D., et al. 2020a, ApJL, 892, L3
Abbott, B. P., Abbott, R., Abbott, T. D., et al. 2016, PhRvL, 116, 061102
Abbott, B. P., Abbott, R., Abbott, T. D., et al. 2017b, PhRvL, 119, 161101
Abbott, B. P., Abbott, T. D., Abraham, S., et al. 2020b, ApJL, 896, L44
Ahumada, R., Allende Prieto, C., Almeida, A., et al. 2020, ApJS, 249, 3
Allington-Smith, J., Murray, G., Content, R., et al. 2002, PASP, 114, 892
Almualla, M., Coughlin, M. W., Anand, S., et al. 2020, MNRAS, 495, 4366
Anand, S., Andreoni, I., Khandagale, M., et al. 2019, GCN, 25706, 1
Anand, S., Coughlin, M. W., Kasliwal, M. M., et al. 2020, NatAs, in press, doi:10.1038/s41550-020-1183-3
Andreoni, I., Ackley, K., Cooke, J., et al. 2017, PASA, 34, e069
Andreoni, I., Anand, S., Bellm, E., et al. 2019a, GCN, 26424, 1
Andreoni, I., Anand, S., Coughlin, M. W., et al. 2019b, GCN, 26416, 1
Andreoni, I., De, K., Kasliwal, M., Huang, Y., & Liu, X. 2020a, GCN, 27075, 1
Andreoni, I., Goldstein, D., Anand, S., et al. 2019c, ApJL, 881, L16
Andreoni, I., Goldstein, D. A., Kasliwal, M. M., et al. 2020b, ApJ, 890, 131
Andreoni, I., Kumar, H., Karambelkar, V., et al. 2020c, GCN, 27065, 1
Antier, S., Agayeva, S., AlMualla, M., et al. 2020, arXiv:2004.04277
Arcavi, I. 2018, ApJL, 855, L23
Arcavi, I., Hosseinzadeh, G., Howell, D. A., et al. 2017, Natur, 551, 64
Assef, R. J., Stern, D., Noirot, G., et al. 2018, ApJS, 234, 23
Bailer-Jones, C. A. L., Fouesneau, M., & Andrae, R. 2019, MNRAS, 490, 5615
Becker, A. 2015, HOTPANTS: High Order Transform of PSF ANd Template Subtraction, Astrophysics Source Code Library, ascl:1504.004
Bellm, E. C., & Graham, M. 2020, GCN, 27118, 1
Bellm, E. C., Kulkarni, S. R., Graham, M. J., et al. 2018, PASP, 131, 018002
Bellm, E. C., & Sesar, B. 2016, pyraf-dbsp: Reduction Pipeline for the Palomar Double Beam Spectrograph, Astrophysics Source Code Library, ascl:1602.002
Bertin, E. 2006, in ASP Conf. Series 351, Astronomical Data Analysis Software and Systems XV, ed. C. Gabriel et al. (San Francisco, CA: ASP), 112
Bertin, E. 2011, in ASP Conf. Ser. 442, Astronomical Data Analysis Software and Systems XX, ed. I. N. Evans et al. (San Francisco, CA: ASP), 435
Bertin, E., & Arnouts, S. 2010, SExtractor: Source Extractor, Astrophysics Source Code Library, ascl:1010.064
Bertin, E., Mellier, Y., Radovich, M., et al. 2002, in ASP Conf. Ser. 281, Astronomical Data Analysis Software and Systems XI, ed. D. A. Bohlender, D. Durand, & T. H. Handley (San Francisco, CA: ASP), 228
Blagorodnova, N., Neill, J. D., Walters, R., et al. 2018, PASP, 130, 035003
Blondin, S., & Tonry, J. L. 2007, ApJ, 666, 1024
Brennan, S., Killestein, T., Fraser, M., et al. 2019, GCN, 26429, 1
Broekgaarden, F. S., Justham, S., de Mink, S. E., et al. 2019, MNRAS, 490, 5228
Brown, T. M., Baliber, N., Bianco, F. B., et al. 2013, PASP, 125, 1031
Buckley, D. A. H., Hearnshaw, J. B., Nordsieck, K. H., & O'Donoghue, D. 2003, Proc. SPIE, 4834, 264
Bulla, M. 2019, MNRAS, 489, 5037
Burdge, K., Perley, D. A., & Kasliwal, M. 2019, GCN, 25639, 1
Burgh, E. B., Nordsieck, K. H., Kobulnicky, H. A., et al. 2003, Proc. SPIE, 4841, 1463
Cannizzaro, G., Pastor-Marazuela, I., Jonker, P., Maguire, K., & Fraser, M. 2019, GCN, 25725, 1
Cao, Y., Nugent, P. E., & Kasliwal, M. M. 2016, PASP, 128, 114502
Castro-Tirado, A., Hu, Y.-D., Valeev, A., et al. 2019a, GCN, 26492, 1
Castro-Tirado, A., Hu, Y.-D., Valeev, A., et al. 2020, GCN, 27063, 1
Castro-Tirado, A., Valeev, A., Sokolov, V., et al. 2019b, GCN, 25721, 1
Cenko, S. B., Fox, D. B., Moon, D.-S., et al. 2006, PASP, 118, 1396
Cepa, J., Aguiar, M., Castañeda, H., et al. 2005, RMxAA, 24, 1
Chambers, K. C., Magnier, E. A., Metcalfe, N., et al. 2016, arXiv:1612.05560
Chatterjee, D., Ghosh, S., Brady, P. R., et al. 2020, ApJ, 896, 54
Cook, D. O., Kasliwal, M. M., Van Sistine, A., et al. 2019, ApJ, 880, 7
Coughlin, M. W., Ahumada, T., Cenko, S. B., et al. 2019a, PASP, 131, 048001
Coughlin, M. W., Dekany, R. G., Duev, D. A., et al. 2019b, MNRAS, 485, 1412
Coughlin, M. W., Kasliwal, M. M., Perley, D. A., et al. 2019c, GCN, 24283, 1
Coughlin, M. W., Ahumada, T., Anand, S., et al. 2019d, ApJL, 885, L19
Coughlin, M. W., Tao, D., Chan, M. L., et al. 2018, MNRAS, 478, 692
Coulter, D. A., Foley, R. J., Kilpatrick, C. D., et al. 2017, Sci, 358, 1556
Cowperthwaite, P. S., Berger, E., Villar, V. A., et al. 2017, ApJL, 848, L17
Crawford, S. M., Still, M., Schellart, P., et al. 2010, Proc. SPIE, 7737, 25
Cushing, M. C., Vacca, W. D., & Rayner, J. T. 2004, PASP, 116, 362
De, K. 2020, GCN, 27140, 1
De, K., Hankins, M. J., Kasliwal, M. M., et al. 2020a, PASP, 132, 025001
De, K., Kasliwal, M. M., Ofek, E. O., et al. 2018, Sci, 362, 201
De, K., Kasliwal, M. M., Tzanidakis, A., et al. 2020b, arXiv:2004.09029
Díaz, M. C., Macri, L. M., Garcia Lambas, D., et al. 2017, ApJL, 848, L29

Dietrich, T., Coughlin, M. W., Pang, P. T. H., et al. 2020, arXiv:2002.11355
Djorgovski, S. G., Drake, A. J., Mahabal, A. A., et al. 2011, arXiv:1102.5004
Dobie, D., Stewart, A., Murphy, T., et al. 2019, ApJL, 887, L13
Drout, M. R., Piro, A. L., Shappee, B. J., et al. 2017, Sci, 358, 1570
Duev, D. A., Mahabal, A., Masci, F. J., et al. 2019, MNRAS, 489, 3582
Elias-Rosa, N., Benetti, S., Piranomonte, S., et al. 2019, GCN, 26428, 1
Evans, P. A., Cenko, S. B., Kennea, J. A., et al. 2017, Sci, 358, 1565
Feindt, U., Nordin, J., Rigault, M., et al. 2019, JCAP, 2019, 005
Fernández, R., Foucart, F., & Lippuner, J. 2020, MNRAS, 497, 3221
Flewelling, H. 2018, AAS Meeting, 231, 436.01
Foucart, F. 2012, PhRvD, 86, 124007
Foucart, F., Hinderer, T., & Nissanke, S. 2018, PhRvD, 98, 081501
Fremling, C., Ahumada, T., Singer, L., De, K., & Kasliwal, M. 2019, GCN, 26427, 1
Fremling, C., Sollerman, J., Taddia, F., et al. 2016, A&A, 593, A68
Fremling, U. C., Miller, A. A., Sharma, Y., et al. 2020, ApJ, 895, 32
Gaia Collaboration 2018, yCat, I/345
Gehrels, N., Chincarini, G., Giommi, P., et al. 2004, ApJ, 611, 1005
Gimeno, G., Roth, K., Chiboucas, K., et al. 2016, Proc. SPIE, 9908, 99082S
Goldstein, A., Veres, P., Burns, E., et al. 2017, ApJL, 848, L14
Goldstein, D. A., Andreoni, I., Nugent, P. E., et al. 2019, ApJ, 881, L7
Gompertz, B., Cutter, R., Steeghs, D., et al. 2020, MNRAS, 497, 726
Graham, M. J., Ford, K. E. S., McKernan, B., et al. 2020, PhRvL, 124, 251102
Graham, M. J., Kulkarni, S. R., Bellm, E. C., et al. 2019, PASP, 131, 078001
Guevel, D., & Hosseinzadeh, G. 2017, Dguevel/Pyzogy: Initial Release, v0.0.1, Zenodo, doi:10.5281/zenodo.1043973
Haggard, D., Nynka, M., Ruan, J. J., et al. 2017, ApJL, 848, L25
Hallinan, G., Corsi, A., Mooley, K. P., et al. 2017, Sci, 358, 1579
Hook, I. M., Jørgensen, I., Allington-Smith, J. R., et al. 2004, PASP, 116, 425
Hotokezaka, K., Kyutoku, K., Tanaka, M., et al. 2013, ApJL, 778, L16
Hu, Y., Valeev, A., Castro-Tirado, A., et al. 2019a, GCN, 26502, 1
Hu, Y.-D., Castro-Tirado, A., Valeev, A., et al. 2020, GCN, 27154, 1
Hu, Y. D., Castro-Tirado, A. J., Valeev, A. F., et al. 2019b, GCN, 24359, 1
Hu, Y.-D., Valeev, A., Castro-Tirado, A., et al. 2019c, GCN, 26422, 1
Huang, K., Urata, Y., Ip, W., et al. 2005, NCimC, 28, 731
Huehnerhoff, J., Ketzeback, W., Bradley, A., et al. 2016, Proc. SPIE, 9908, 99085H
Izzo, L., Leloudas, G., Bruun, S., et al. 2019, GCN, 25675, 1
Jedicke, R., Bolin, B., Granvik, M., & Beshore, E. 2016, Icar, 266, 173
Karambelkar, V., De, K., Van Roestel, J., & Kasliwal, M. 2019a, GCN, 25921, 1
Karambelkar, V., De, K., van Roestel, J., & Kasliwal, M. M. 2019b, GCN, 25931, 1
Kasen, D., Metzger, B., Barnes, J., Quataert, E., & Ramirez-Ruiz, E. 2017, Natur, 551, 80
Kasliwal, M. M., Cannella, C., Bagdasaryan, A., et al. 2019a, PASP, 131, 038003
Kasliwal, M. M., Cenko, S. B., Singer, L. P., et al. 2016, ApJL, 824, L24
Kasliwal, M. M., Kasen, D., Lau, R. M., et al. 2019b, MNRAS, in press, doi:10.1093/mnrasl/slz007
Kasliwal, M. M., Nakar, E., Singer, L. P., et al. 2017, Sci, 358, 1559
Kasliwal, M. M., & Nissanke, S. 2014, ApJL, 789, L5
Kasliwal, M. M., Perley, D., Kumar, H., et al. 2020, GCN, 27051, 1
Kawaguchi, K., Kyutoku, K., Shibata, M., & Tanaka, M. 2016, ApJ, 825, 52
Kiuchi, K., Sekiguchi, Y., Kyutoku, K., et al. 2015, PhRvD, 92, 064034
Kruckow, M. U., Tauris, T. M., Langer, N., Kramer, M., & Izzard, R. G. 2018, MNRAS, 481, 1908
Law, N. M., Kulkarni, S. R., Dekany, R. G., et al. 2009, PASP, 121, 1395
Levan, A. 2020, PoS, Asterics2019, 044
Ligo Scientific Collaboration, & VIRGO Collaboration 2019a, GCN, 24237, 1
Ligo Scientific Collaboration, & VIRGO Collaboration 2019b, GCN, 24411, 1
Lipunov, V. M., Gorbovskoy, E., Kornilov, V. G., et al. 2017, ApJL, 850, L1
Lundquist, M. J., Paterson, K., Fong, W., et al. 2019, ApJL, 881, L26
Mahabal, A., Rebbapragada, U., Walters, R., et al. 2019, PASP, 131, 038002
Margutti, R., Berger, E., Fong, W., et al. 2017, ApJL, 848, L20
Masci, F. J., Laher, R. R., Rebbapragada, U. D., et al. 2017, PASP, 129, 014002
Masci, F. J., Laher, R. R., Rusholme, B., et al. 2018, PASP, 131, 018003
Massey, P., Dunham, E., Bida, T., et al. 2013, AAS Meeting, 221, 345.02
Mazaeva, E., Pozanenko, A., Rumyantsev, V., Belkin, S., & Volnova, A. 2019, GCN, 25943, 1
Mooley, K. P., Frail, D. A., Dobie, D., et al. 2018, ApJL, 868, L11
Moore, A. M., & Kasliwal, M. M. 2019, NatAs, 3, 109
Muthukrishna, D., Parkinson, D., & Tucker, B. E. 2019, ApJ, 885, 85
Nakaoka, T., Maeda, K., Yamanaka, M., et al. 2020, arXiv:2005.02992
Nakar, E. 2020, PhR, 886, 1
Naoz, S. 2016, ARA&A, 54, 441
Nissanke, S., Kasliwal, M., & Georgieva, A. 2013, ApJ, 767, 124
Nordin, J., Brinnel, V., van Santen, J., et al. 2019, A&A, 631, A147
Oates, S., Klingler, N., Page, K., et al. 2020a, GCN, 27400, 1
Oates, S., Page, K., Breeveld, A., et al. 2020b, GCN, 27153, 1
Oates, S., Page, K., De Pasquale, M., et al. 2019, GCN, 26471, 1
Oke, J. B., Cohen, J. G., Carr, M., et al. 1995, PASP, 107, 375
Patterson, M. T., Bellm, E. C., Rusholme, B., et al. 2019, PASP, 131, 018001
Perley, D., & Copperwheat, C. 2019a, GCN, 25720, 1
Perley, D., & Copperwheat, C. 2019b, GCN, 26426, 1
Perley, D. A. 2019, PASP, 131, 084503
Perley, D. A., Goobar, A., Kasliwal, M. M., et al. 2019a, GCN, 24331, 1
Perley, D. A., Ho, A. Y. Q., & Copperwheat, C. M. 2019b, GCN, 25643, 1
Pian, E., D'Avanzo, P., Benetti, S., et al. 2017, Natur, 551, 67
Piascik, A. S., Steele, I. A., Bates, S. D., et al. 2014, Proc. SPIE, 9147, 91478H
Piro, A. L., & Kollmeier, J. A. 2018, ApJ, 855, 103
Pozanenko, A. S., Barkov, M. V., Minaev, P. Y., et al. 2018, ApJL, 852, L30
Rhodes, L., Fender, R., Williams, D., et al. 2019, GCN, 24226, 1
Rigault, M., Neill, J. D., Blagorodnova, N., et al. 2019, A&A, 627, A115
Roming, P. W. A., Kennedy, T. E., Mason, K. O., et al. 2005, SSRv, 120, 95
Rosell, M. J. B., Rostopchin, S., Zimmerman, A., et al. 2019, GCN, 25622, 1
Rosswog, S. 2005, ApJ, 634, 1202
Sagués Carracedo, A., Bulla, M., Feindt, U., & Goobar, A. 2020, arXiv:2004.06137
Salsamo, I., Tomasella, L., Benetti, S., D'Avanzo, P., & Cappellaro, E. 2019a, GCN, 25618, 1
Salmaso, I., Tomasella, L., Benetti, S., et al. 2019b, GCN, 25619, 1
Schlafly, E. F., & Finkbeiner, D. P. 2011, ApJ, 737, 103
Shappee, B. J., Prieto, J. L., Grupe, D., et al. 2014, ApJ, 788, 48
Singer, L. P., Kasliwal, M. M., Cenko, S. B., et al. 2015, ApJ, 806, 52
Singer, L. P., & Price, L. R. 2016, PhRvD, 93, 024013
Skrutskie, M. F., Cutri, R. M., Stiening, R., et al. 2006, AJ, 131, 1163
Smartt, S., Srivastav, S., Smith, K., et al. 2019, GCN, 25922, 1
Smartt, S. J., Chen, T. W., Jerkstrand, A., et al. 2017, Natur, 551, 75
Smith, K., Smartt, S., Young, D., et al. 2019, GCN, 26430, 1
Soares-Santos, M., Holz, D. E., Annis, J., Chornock, R., & Herner, K. 2017, ApJL, 848, L16
Soumagnac, M. T., & Ofek, E. O. 2018, PASP, 130, 075002
Steele, I. A., Smith, R. J., Rees, P. C., et al. 2004, Proc. SPIE, 5489, 679
Stein, R., Andreoni, I., Coughlin, M., et al. 2019a, GCN, 25727, 1
Stein, R., Kasliwal, M. M., Kool, E., et al. 2019b, GCN, 25899, 1
Stein, R., Kool, E., Kumar, H., et al. 2019c, GCN, 25656, 1
Stein, R., Reusch, S., Perley, D., Andreoni, I., & Coughlin, M. 2019d, GCN, 26437, 1
Stein, R., van Velzen, S., Kowalski, M., et al. 2020, arXiv:2005.05340
Stephan, A. P., Naoz, S., Ghez, A. M., et al. 2019, ApJ, 878, 58
Tachibana, Y., & Miller, A. A. 2018, PASP, 130, 128001
Tan, H.-J., Kong, A., Ngeow, C.-C., & Ip, W.-H. 2019, GCN, 26431, 1
Tauris, T. M., Langer, N., & Podsiadlowski, P. 2015, MNRAS, 451, 2123
Tonry, J. L., Denneau, L., Heinze, A. N., et al. 2018, PASP, 130, 064505
Troja, E., Piro, L., van Eerten, H., et al. 2017, Natur, 551, 71
Utsumi, Y., Tanaka, M., Tominaga, N., et al. 2017, PASJ, 69, 101
Vacca, W. D., Cushing, M. C., & Rayner, J. T. 2003, PASP, 115, 389
Valeev, A., Hu, Y., Castro-Tirado, A., et al. 2020, GCN, 27060, 1
Valeev, A., Hu, Y.-D., Castro-Tirado, A., et al. 2019, GCN, 25731, 1
Valenti, S., David, J. S., Yang, S., et al. 2017, ApJL, 848, L24
Veitch, J., Raymond, V., Farr, B., et al. 2015, PhRvD, 91, 042003
Waxman, E., Ofek, E. O., Kushnir, D., & Gal-Yam, A. 2018, MNRAS, 481, 3423
Wei, J., Xin, L., Antier, S., et al. 2019, GCN, 25640, 1
West, A. A., Morgan, D. P., Bochanski, J. J., et al. 2011, AJ, 141, 97
Wilson, J. C., Eikenberry, S. S., Henderson, C. P., et al. 2003, Proc. SPIE, 4841, 451
Wright, E. L., Eisenhardt, P. R. M., Mainzer, A. K., et al. 2010, AJ, 140, 1868
Yao, Y., De, K., Kasliwal, M. M., et al. 2020, arXiv:2005.12922
Yao, Y., Miller, A. A., Kulkarni, S. R., et al. 2019, ApJ, 886, 152
Zackay, B., Ofek, E. O., & Gal-Yam, A. 2016, ApJ, 830, 27
Zhou, R., Newman, J. A., Mao, Y.-Y., et al. 2020, arXiv:2001.06018

REVEALING A NEW BLACK WIDOW BINARY 4FGL J0336.0+7502

Kwan-Lok Li[1], Y. X. Jane Yap[2], Chung Yue Hui[3], and Albert K. H. Kong[2]

Draft version January 28, 2021

ABSTRACT

We report on a discovery of a promising candidate as a black widow millisecond pulsar binary, 4FGL J0336.0+7502, which shows many pulsar-like properties in the 4FGL-DR2 catalog. Within the 95% error region of the LAT source, we identified an optical counterpart with a clear periodicity at $P_{\rm orb} = 3.718178(9)$ hours using the *Bohyunsan 1.8-m Telescope*, *Lulin One-meter Telescope*, *Canada–France–Hawaii Telescope*, and *Gemini*-North. At the optical position, an X-ray source was marginally detected in the *Swift*/XRT archival data, and the detection was confirmed by our *Chandra*/ACIS DDT observation. The spectrum of the X-ray source can be described by a power-law model of $\Gamma_x = 1.6 \pm 0.7$ and $F_{0.3-7\rm keV} = 3.5^{+1.2}_{-1.0} \times 10^{-14}\,\rm erg\,cm^{-2}\,s^{-1}$. The hard X-ray photon index and the low X-ray-to-γ-ray flux ratio (i.e., $< 1\%$) are both consistent with that of many known black widow pulsars. There is also a hint of an X-ray orbital modulation in the *Chandra* data, although the significance is very low (1.3σ). If the pulsar identity and the X-ray modulation are confirmed, it would be the fifth black widow millisecond pulsar binary that showed an orbitally-modulated emission in X-rays.

Subject headings: binaries: close — gamma rays: stars — pulsars: general — X-rays: binaries

1. INTRODUCTION

The *Fermi Large Area Telescope* (LAT) has been observing the MeV/GeV γ-ray sky since June 2008. With the ten years of data taken between 2008 and 2018, 5064 sources are detected in the *Fermi* LAT 10-Year Point Source Catalog (4FGL; Abdollahi et al. 2020; Ballet et al. 2020). While a major portion of the cataloged sources are known systems (e.g., active galaxies, pulsars, etc.), about one-fourth of them are unidentified at other wavelengths. Other than active galaxies, many of these unidentified γ-ray sources are believed to be pulsar systems.

There have been multi-wavelength searching campaigns conducted for new candidates of γ-ray pulsars from the list of the unidentified *Fermi*-LAT sources (e.g., Hui et al. 2015; Braglia et al. 2020). Machine learning techniques were also applied on the classification for pulsars based on only the γ-ray properties recently (e.g., Saz Parkinson et al. 2016; Luo et al. 2020; Hui et al. 2020). These efforts have led to at least a dozen candidates for further radio/γ-ray pulsation searches. Many of these candidates could be associated with two special pulsar classes, black widow (BW) and redback (RB), which are millisecond pulsars in compact binaries (the orbital periods are often less than a day). Besides the compact orbits, the two classes are characterised by the very low-mass companions (i.e., 0.1–0.4 $M_\odot$ for RBs and $< 0.1 M_\odot$ for BWs; Roberts 2013; Chen et al. 2013) ablated by the strong radiations that originate from the primary pulsars. The radiation would also heat up the tidally-locked companion one-sided, and this so-called pulsar heating effect can result in orbital modulations in the optical bands (see, e.g., Romani & Sanchez 2016; Yap et al. 2019 for the details), although exceptions exist (e.g., 3FGL J0212.1+5320 that does not show any observable pulsar heating effect; Li et al. 2016). Some recently discovered BW/RB candidates include 3FGL J0954.8−3948 (Li et al. 2018), 4FGL J2333.1−5527 (Swihart et al. 2020), 4FGL J0935.3+0901 (Wang et al. 2020), 4FGL J0407.7−5702 (Miller et al. 2020), and 4FGL J0940.3−7610 (Swihart et al. 2021; see the Table 3 of Hui & Li 2019 and the references therein for more candidates).

In this paper, we present a multi-wavelength study for 4FGL J0336.0+7502, which is a new BW MSP candidate identified by our unidentified *Fermi*-LAT sources observing campaign. The study includes (i) the *Fermi*-LAT γ-ray properties of 4FGL J0336.0+7502 (§2); (ii) optical photometric observations taken by the *Bohyunsan 1.8-m Telescope*, *Lulin One-meter Telescope* (LOT), *Canada–France–Hawaii Telescope* (CFHT), and *Gemini*-North (§3); (iii) *Swift*/XRT and *Chandra*/ACIS-S X-ray observations (§4); and (iv) a discussion for 4FGL J0336.0+7502 based on its multi-wavelength properties (§5).

2. GAMMA-RAY PROPERTIES

4FGL J0336.0+7502 is a bright γ-ray source (detection significance of 31.1σ) located at a relatively high Galactic latitude of $b = 15.5°$ (Ballet et al. 2020). It was first discovered in γ-rays by *Fermi*-LAT as 1FGL J0334.2+7501 in the 1FGL catalog (Abdo et al. 2010), and was subsequently cataloged in 2FGL, 3FGL, and 4FGL(-DR2) (Nolan et al. 2012; Acero et al. 2015; Abdollahi et al. 2020; Ballet et al. 2020). In 4FGL-DR2 (using data taken from August 2008 to August 2018), 4FGL J0336.0+7502 was classified as a steady source on a yearly time-scale with a variability index[4] of 9.8. The average γ-ray flux in 100 MeV–100 GeV is

[1] Department of Physics, National Cheng Kung University, 70101 Tainan, Taiwan; lilirayhk@phys.ncku.edu.tw (KLL)
[2] Department of Astronomy and Space Science, Chungnam National University, Daejeon, Republic of Korea
[3] Institute of Astronomy, National Tsing Hua University, Hsinchu 30013, Taiwan

[4] A source with a variability index greater than 18.48 has less than 1% chance to be stable

$F_\gamma = (7.4 \pm 0.5) \times 10^{-12}\,\mathrm{erg\,cm^{-2}\,s^{-1}}$ that is among the top 30% of all 4FGL-DR2 sources. According to 4FGL-DR2, the γ-ray spectrum in the LAT energy domain is significantly curved with $> 8\sigma$, and can be described by a `LogParabola` model,

$$\frac{dN}{dE} \propto \left(\frac{E}{E_b}\right)^{-(\Gamma_\gamma+\beta\log(E/E_b))},$$

where Γ_γ is the photon index, β defines the degree of curvature, and E_b is a fixed scale parameter. The best-fit spectral parameters are $\Gamma_\gamma = 1.78 \pm 0.10$ and $\beta = 0.39 \pm 0.07$ (for comparison, $\Gamma_\gamma = 2.04 \pm 0.02$ and $\beta = 0.20 \pm 0.01$ for the black widow PSR J1311−3430).

The γ-ray properties of 4FGL J0336.0+7502, including the high Galactic latitude, the low long-term variability, and the significant spectral curvature, are exactly the characteristics that are commonly seen in γ-ray pulsars (see, e.g., Hui et al. 2015). In fact, 4FGL J0336.0+7502 has been suggested by Saz Parkinson et al. (2016) as a good MSP candidate using machine learning techniques. This motivated us to investigate the system further in multi-wavelength. With the high quality of the LAT data, the 95% positional accuracy of 4FGL J0336.0+7502 is around $1'.5$, which is fine enough to allow a feasible search for the counterpart in optical and X-rays (see Figure 1).

3. OPTICAL PHOTOMETRIC LIGHT CURVES

3.1. *Bohyunsan 1.8-m Telescope*

On 2019 March 31, we observed 4FGL J0336.0+7502 with the 1.8-m telescope at *Bohyunsan Optical Astronomy Observatory* (BOAO) as part of our multi-wavelength observing campaign for unidentified *Fermi*-LAT sources. The idea is to blind search for compact binaries in the field and carry out further multi-wavelength observations for them, if any.

4FGL J0336.0+7502 was observed 19 times in the R band with the BOAO 4k CCD camera. The exposure time is 200 seconds for each image. `IRAF` was used for standard data reduction processes, including bias, dark, and flat calibrations. Aperture photometry was employed to extract light curves, and differential technique was applied to eliminate the variations due to the changing weather condition. We then calibrated the obtained magnitudes using the Fifth USNO CCD Astrograph Catalog (UCAC5; Zacharias et al. 2017).

Within the *Fermi*-LAT 95% error circle, we spotted a variable star that was undetected in the first 9 frames, and then became observable with the magnitude raising from $R \approx 23$ mag to ≈ 21 mag in just 40 minutes. We stacked the first 9 images, and the variable was marginally detected with $R \approx 24$ mag (Figure 3). The variable source is also cataloged in the *Gaia* DR3 with $\alpha(\mathrm{J2000}) = 03^{\mathrm{h}}36^{\mathrm{m}}10^{\mathrm{s}}.1811(1)$, $\delta(\mathrm{J2000}) = +75^\circ03'17''.268(1)$ (54.0424214(5), 75.0547967(3); Gaia Collaboration et al. 2020), at which an X-ray source was marginally detected in archival *Swift*/XRT observations (see §4.1).

3.2. *Lulin One-meter Telescope*

We followed-up the variable source using LOT at *Lulin Observatory*. The observing dates are 2019 October 17/18, 2019 November 10, and 2020 January 8/9. As the source is faint for a 1-m class telescope, the data were taken unfiltered with 600 seconds per frame. 174 frames were taken in total in the 5 days. Standard data reduction and analysis processes were carried out using `IRAF` as described in the previous section. Flux calibration was done using the Pan-STARRS catalog (PS1 DR2; Flewelling et al. 2016), although the observations are unfiltered.

The target's brightness was varying in the LOT light curve as we have seen in the BOAO data. About half of the LOT observations therefore result in non-detections when the source was in the faint phase. Despite the incompleteness, the LOT light curve shows a clear periodic modulation on a time-scale of about 4 hours. We computed a Lomb-Scargle periodogram for the LOT data (the non-detections were all rejected) and a strong signal was found at 3.7182 hours, albeit with aliases due to the non-detection gaps (Figure 2). This periodicity is likely the orbital period of the system. We fitted the LOT light curve with a sinusoidal function to fine tune the orbital period (P_{orb}). The tuned timing parameters are $P_{\mathrm{orb,lot}} = 3.71817$ hours and $T_{0,\mathrm{lot}} = 2458858.016$ (BJD; converted by the method presented in Eastman et al. 2010). The latter is the epoch of phase zero, which is defined as the time when the phased light curve peaks. This should refer to the superior conjunction of the companion (i.e., observer-pulsar-companion along the line of sight), if it is a pulsar binary. In this convention, the ascending node of the pulsar and the inferior conjunction of the companion (i.e., observer-companion-pulsar) are at phases 0.25 and 0.5, respectively, for a circular orbit. The phased LOT light curve and the best-fit sinusoid are shown in Figure 2.

We also combined the LOT data with the BOAO, CFHT, and *Gemini-North* R/r'-band light curves (which will be presented in the following sections) to make a further improvement on the solution. For the R/r'-band light curves, only data points brighter than 22 mag were selected as the fainter parts are not consistent with a sinusoid. The finalised timing solution of 4FGL J0336.0+7502 is $P_{\mathrm{orb}} = 3.718178(9)$ hours and $T_0 = 2458858.0150(2)$, of which the uncertainties are 10 times smaller than that of the LOT solution. Figure 3 shows the LOT, BOAO, CFHT, and *Gemini-North* light curves folded with the improved orbital solution.

3.3. *Canada–France–Hawaii Telescope*

On 2017 January 25 and February 2, we used CFHT/MegaCam on Mauna Kea to observe 4FGL J0336.0+7502 under our snapshot observing program. Two g'-band and two r'-band images were taken on the first night, and four g'-band and two r'-band images were taken in the second run. Except for the first two g'-band observations on the second night that were exposed 30 seconds each, every image has an exposure time of 860 seconds. Pre-processed CFHT observations by the standard `Elixir` pipeline (Magnier & Cuillandre 2004) were directly used. Flux calibration and data analysis methods were the same as the ones for the LOT data.

The optical counterpart was clearly detected in all ten CFHT observations and the faintest measurements are around 25 mag in both bands. Folded with the global

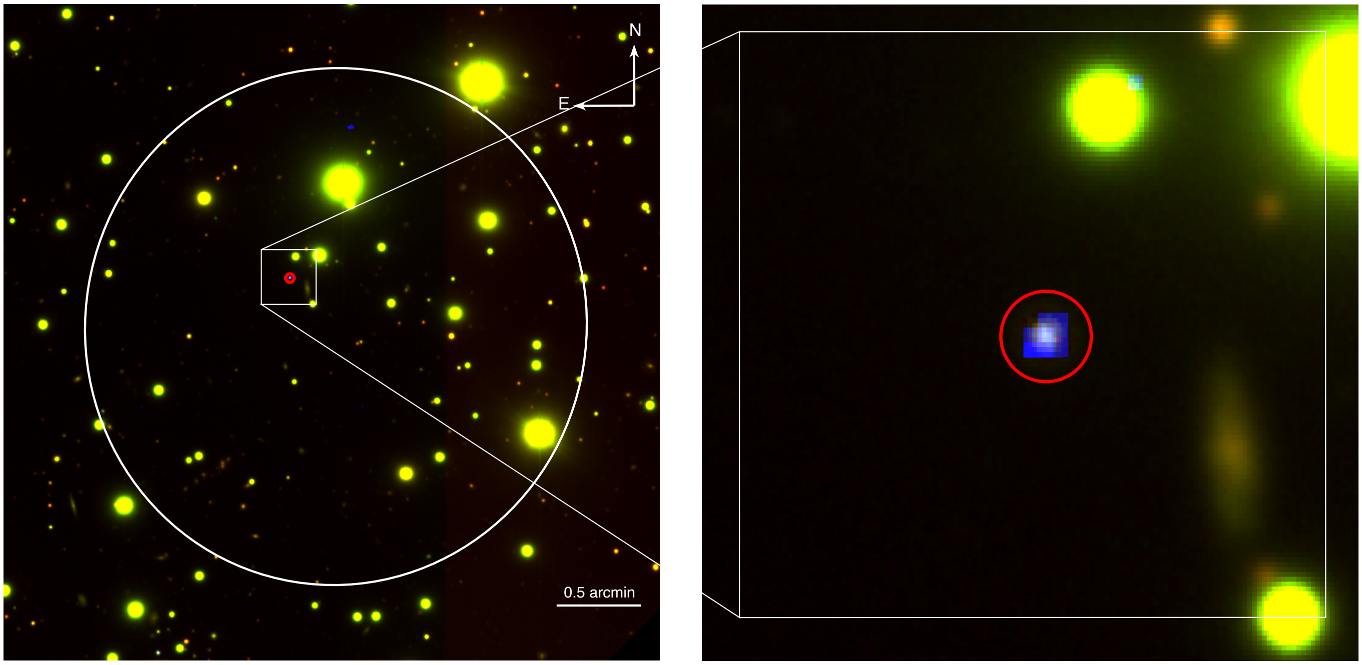

FIG. 1.— False-color image (red: *Gemini-North i'* band; green: *Gemini-North r'* band; and blue: *Chandra*/ACIS 0.3–7 keV) of the field of 4FGL J0336.0+7502. The large white ellipse shows the *Fermi*-LAT 95% error ellipse of 4FGL J0336.0+7502 (about 1.′5 in radius), and the small red circle indicates the proposed optical/X-ray counterpart to the γ-ray source.

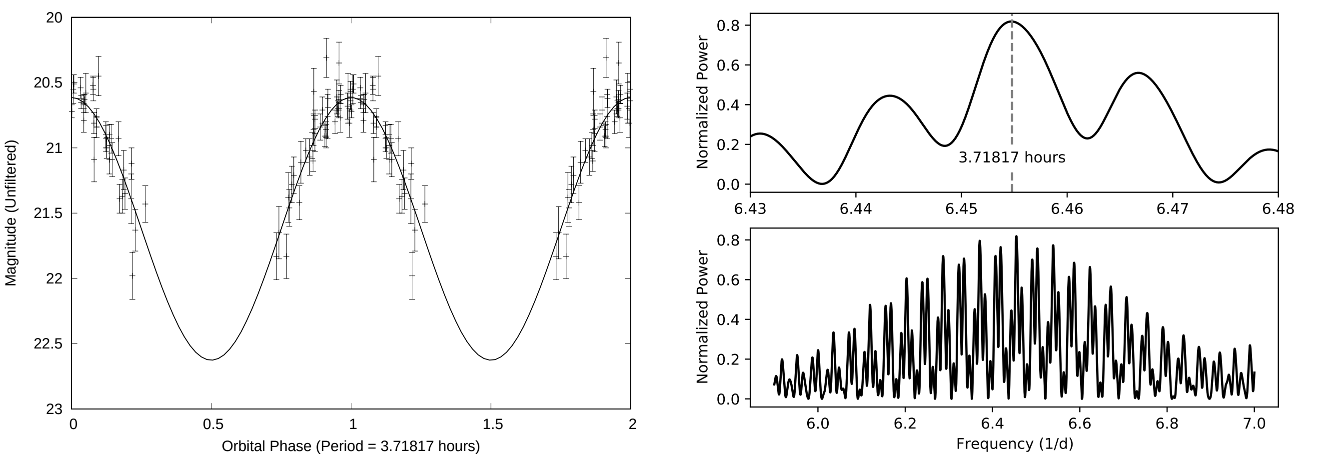

FIG. 2.— Left: The phased optical LOT light curve of 4FGL J0336.0+7502. Phase zero corresponds to the peak of the phased optical light curve (i.e., the superior conjunction of the companion, if it is a pulsar system). The solid line shows the best-fit sinusoidal function of the data. Two identical cycles are shown for clarity. Right: The Lomb-Scargle periodogram of the LOT data (bottom) and a close-up of the global peak (top).

timing solution, both g'- and r'-band light curves show clear modulations that are in phase with the BOAO and LOT light curves (the green and the purple data points in Figure 3). This shows that the binary has been stable over the last 3 years.

3.4. *The Frederick C. Gillett Gemini Telescope*

We also proposed a 4-hour series of *Gemini-North* photometric observations (PI: Kwan-Lok Li) to study the complete modulation profile of 4FGL J0336.0+7502. The observations were all taken using GMOS-N on 2019 November 28. Two filters, r' and i', were used with 150 seconds for each exposure. We set four observations as a turn to alternate between the filters. We intended to combine the observations taken in the same turn when the source became too faint to be detected in a single image, but it turns out that the source was clearly seen in all the individual images. Standard data reduction was done using `DRAGONS` (Labrie et al. 2019). Differential photometry was used to extract the light curves, and the magnitudes were calibrated against the PS1 DR2 catalog.

The light curves were also folded with the orbital solution and the orbital modulations are clearly shown in both bands (Figure 3). The GMOS-r' light curve is well consistent with the ones observed with CFHT-r' and BOAO-R. While the peak-to-peak amplitude is around 5 mag in the r' band, the i'-band amplitude is only 3 mag,

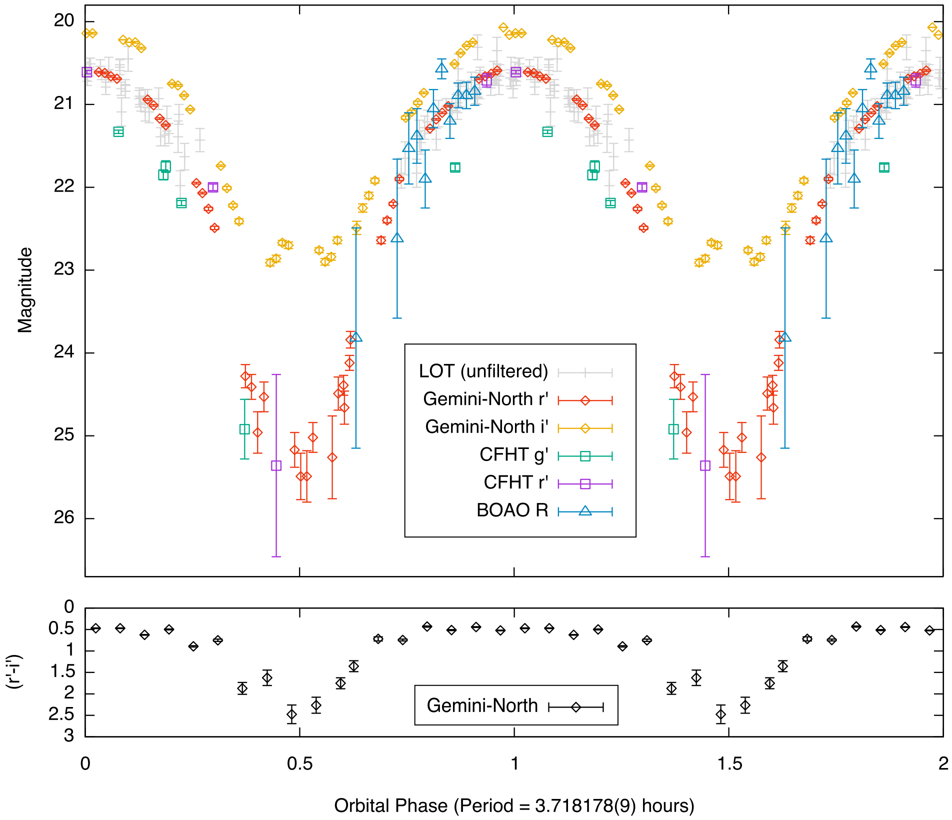

FIG. 3.— The phased optical light curves (top) and color index curve (bottom) of 4FGL J0336.0+7502. Phase zero corresponds to the peak of the phased optical light curve (i.e., the superior conjunction of the companion, if it is a pulsar system). Two identical cycles are shown for clarity.

indicating a significant orbital color variation (i.e., the source becomes redder as it is fainter), which is likely caused by pulsar heating. The modulation profiles are mostly smooth, but the i'-band emission was significantly varying in the order of 0.1 mag around phase 0.5. In the r' band, the variation can also be seen around phase 0.5, although it is less significant. The variations, taken as a whole, look like mini-flares on time-scales of 300–900 seconds.

4. X-RAY OBSERVATIONS

4.1. *Neil Gehrels Swift/XRT*

In the *Swift*'s public data archive, there are four archival *X-Ray Telescope* (XRT) observations taken for 4FGL J0336.0+7502 between 2012 April 14 and 18. The total effective exposure of the XRT data is 9 ksec. In the 0.3–10 keV XRT image, a weak X-ray source was seen at the position of the proposed optical counterpart. 9 photons were detected within a 15″ radius circular source region centred at the optical source. Using a 120″ source-free circular background region, we computed the average background counts within the source region to be 0.9 counts. This gives a net count rate of $\sim 9\times10^{-4}$ counts/s with a detection significance of $> 9\,\sigma$. Despite the low photon statistics, we adopted the *online XRT product generator*[5] to extract the X-ray spectra (binned to at least one count per bin) and used XSPEC (v12.11.1) to estimate the spectra parameters using an absorbed power-law model. The column density ($N_{\rm H}$) was fixed at the Galactic value of $1.47\times10^{21}\,{\rm cm}^{-2}$ (HI4PI Collaboration et al. 2016) and the *Cash statistic* (Cash 1979) was employed as the fitting statistic. The best-fit photon index is $\Gamma_x = 0.9^{+3.3}_{-2.5}$ with a corrected X-ray flux of $F_{0.3-10{\rm keV}} = 5.1^{+4.9}_{-3.9}\times10^{-14}\,{\rm erg\,cm^{-2}\,s^{-1}}$ (all the uncertainties are in 90% confidence interval).

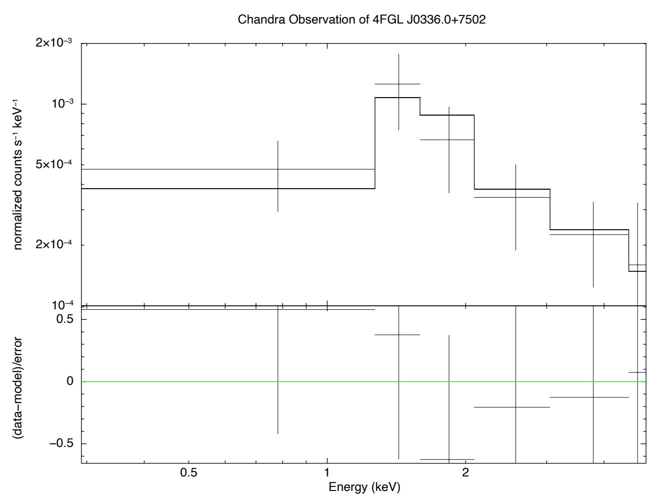

FIG. 4.— The *Chandra*/ACIS X-ray spectrum with its best-fit absorbed power-law model ($N_{\rm H}$=1.47×10^{21} cm^{-2}, $\Gamma_x = 1.6\pm0.7$, and $F_{0.3-7{\rm keV}} = 3.5^{+1.2}_{-1.0}\times10^{-14}\,{\rm erg\,cm^{-2}\,s^{-1}}$). While we used at least one count per bin for the model fitting, the displayed spectrum was binned to 5 counts per bin (except the last bin) for better visualization.

[5] https://www.swift.ac.uk/user_objects/index.php

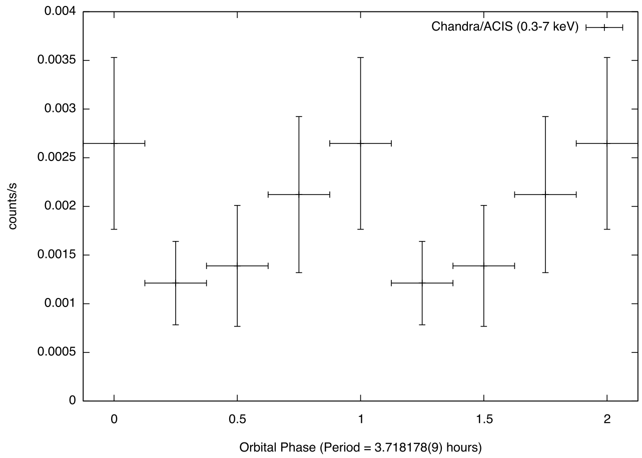

FIG. 5.— The phased *Chandra*/ACIS X-ray light curve of 4FGL J0336.0+7502. Phase zero corresponds to the peak of the phased optical light curve (i.e., the superior conjunction of the companion, if it is a pulsar system). Two identical cycles are shown for clarity.

4.2. *Chandra/ACIS*

We requested and obtained a 15-ksec *Chandra* Director's Discretionary Time (DDT) observation for 4FGL J0336.0+7502 to confirm the XRT detection, study the full-orbit X-ray modulation, and constrain the spectral parameters better. The observation was taken on 2020 January 25 with the Advanced CCD Imaging Spectrometer S-array (ACIS-S; Garmire et al. 2003) operated in the full frame mode.

`CIAO` (v4.12) with `CALDB` (v4.9.0) was used to reduce and analyse the data. After reprocessing the data using the `CIAO` script `chandra_repro`, the proposed X-ray counterpart to 4FGL J0336.0+7502 was clearly detected in the 0.3–7 keV band. We employed `specextract` and `dmextract` with a $1\farcs5$ radius source region and a source-free annulus background region centered at the target (inner/outer radii: $5''/10''$) to extract the X-ray spectrum and light curve of the source, respectively. We also applied a barycentric correction on the X-ray light curve using `axbary`.

A total of 29 photons were extracted in the 0.3–7 keV band, and about 1% of them are from the background. This gives an average net count rate of $\sim 2 \times 10^{-3}$ counts/s. Given the insufficient number of source counts for a detailed spectral analysis, we simply binned the *Chandra* spectrum to at least one count per bin using `grppha` and fitted an absorbed power-law model ($N_{\rm H}$ was fixed to $1.47 \times 10^{21}\,{\rm cm}^{-2}$) to it with *Cash statistic* using `XSPEC` (Figure 4). The best-fit parameters are $\Gamma_x = 1.6 \pm 0.7$ and $F_{0.3-7{\rm keV}} = 3.5^{+1.2}_{-1.0} \times 10^{-14}\,{\rm erg\,cm^{-2}\,s^{-1}}$ (90% confidence interval), which are consistent with the values obtained from the *Swift*/XRT observations.

We folded the X-ray light curve using the optical timing solution. Since the number of counts is low, the phased light curve has only 4 data bins per cycle and each bin has about 7 counts on average. While the signal-to-noise ratios of the light curve are low, it shows a possible X-ray modulation that seemingly peaks at phase zero. However, the light curve is also consistent with a flat count rate of $\sim 2 \times 10^{-3}$ counts/s (Figure 5). Assuming a flat light curve, the χ^2 value is 4.7 with 3 degrees of freedom, equivalent to a chance probability of 19% or 1.3σ. Except the epoch folding, the light curve quality does not allow any further investigations, such as X-ray hardness studies.

5. DISCUSSION AND CONCLUSION

We have identified a likely optical and X-ray counterpart to 4FGL J0336.0+7502, which is an X-ray binary with an orbital period of 3.718178(9) hours. Together with the γ-ray properties (see §2) and the low X-ray-to-γ-ray flux ratio (i.e., $\lesssim 1\%$; see Table 1) that are all consistent with a BW/RB MSP binary, we propose that 4FGL J0336.0+7502 is a new system of the class.

While the optical counterpart to 4FGL J0336.0+7502 has been cataloged in *Gaia* DR3, the source is faint for *Gaia* (i.e., $G = 20.6$ mag), and hence, no distance information can be extracted through the parallax measurement. We estimated the distance to 4FGL J0336.0+7502 by assuming $L_x \lesssim 10^{32}\,{\rm erg\,s^{-1}}$ that is a typical limit for BW/RB pulsars in a rotation-powered state (Lee et al. 2018). The inferred distance is $d \lesssim 5$ kpc, which results in a very faint absolute magnitude of $M_{r'} \gtrsim 11.5$ mag (with no pulsar heating). Therefore, 4FGL J0336.0+7502 would highly likely be a BW (instead of RB) MSP binary. Indeed, the optical orbital modulation of 4FGL J0336.0+7502 is very much close to that of other BW systems (e.g., PSR J1311−3430; Romani et al. 2012).

Besides the optical brightness, the $(r' - i')$ color index changes over the orbit. In general, the color is much redder around the inferior conjunction, and this is a signature of pulsar heating. In addition to the periodic variations, there were a few mini-flares detected around the inferior conjunction. It is unclear whether the flares actually concentrate at the inferior conjunction as they might distribute evenly and just became prominent when the optical brightness of the companion was lowest. It is worth noting that flaring activities have been recently shown common in BW/RB systems in both the rotation/accretion-powered states (e.g., An et al. 2017; Papitto et al. 2018; Kennedy et al. 2018; Yap et al. 2019; Li et al. 2020), although the physical origin is still under debate.

An insignificant orbital modulation (1.3σ) is also seen in X-rays. If confirmed, it would be the fifth BW MSP system that exhibits an orbital modulation in X-rays (Table 1). The X-ray orbital modulation could be caused by the Doppler boosting along the intrabinary shock flow (Takata et al. 2014; Li et al. 2014), and thus the profile strongly depends on the wind momentum ratio between the stellar wind of the companion and the pulsar wind, β. For BWs, $\beta < 1$ (i.e., a much weaker stellar wind) is expected (Romani & Sanchez 2016), and the X-ray emission should peak around the inferior conjunction (i.e., phase 0.5 for the definition used in Figure 5). However, the X-ray orbital modulation profile of 4FGL J0336.0+7502 is different than expected–the X-ray peak is at the superior conjunction–and this might imply a stronger stellar wind (i.e., $\beta > 1$). According to Hui et al. (2020), there are three BW MSPs (one of them is the original BW system, PSR J1959+2048) that possibly have orbitally-modulated X-ray emission (Huang et al. 2012; Gentile et al. 2014). Including PSR J1653−0158 that was identified as a candidate pulsar system by Kong et al. (2014)

TABLE 1
X/γ-ray properties of 4FGL J0336.0+7502 and the BW MSPs with X-ray orbital modulation known in the field.

Name	Variability Index[a] (γ-ray)	Spectral Curvature[b] (γ-ray; σ)	Photon Index (X-ray)	L_x/L_γ[c] (%)	References
4FGL J0336.0+7502[d]	9.8	8.6	1.6	0.5	(this work)
PSR J1124−3653[d]	8.1	11.0	1.3	0.5	Gentile et al. (2014)
PSR J1653−0158[d]	9.2	14.5	1.6	0.5	Kong et al. (2014); Nieder et al. (2020)
PSR J1959+2048	11.5	10.8	2.0	0.4	Huang et al. (2012)
PSR J2256−1024	18.7	7.4	1.8	0.5	Gentile et al. (2014)

[a] A source with a variability index greater than 18.48 has less than 1% chance to be stable.
[b] The fit improvement over a simple power-law (PL) model when a power law with exponential cut-off (PLEC) is assumed.
[c] The energy ranges of the X-ray and γ-ray luminosities are 0.1–100 GeV and 0.3–8 keV, respectively.
[d] The X-ray modulation is just marginally seen.

and recently confirmed as a BW by the GPU-accelerated Einstein@Home (Nieder et al. 2020), four BW systems are known to have (possible) X-ray orbital modulations (Table 1). Surprisingly, PSR J1959+2048 is the only one with a phased X-ray light curve consistent with the case of $\beta < 1$. All three others, as we have seen in 4FGL J0336.0+7502, are more consistent with $\beta > 1$. This might subvert our general impression on the BWs' companions that their winds are not strong. Alternatively, the X-ray modulation could be caused by occultation, if the shock region is small and very close to the companion instead of forming a bow shock which wraps around the star. In this case, $\beta < 1$ is still possible. However, shape dips as the light curve minima would be expected because of the very tiny size of the companion star in a black widow system. This does not match very well with the X-ray observations that show broad minima in the light curves (e.g., Figure 5). Future deep X-ray observations of these systems could confirm/deny these "abnormal" X-ray modulations and/or provide helpful hints to solve the problem.

KLL is supported by the Ministry of Science and Technology of the Republic of China (Taiwan) through grant 109-2636-M-006-017, and he is a Yushan (Young) Scholar of the Ministry of Education of the Republic of China (Taiwan). YXJY and AKHK are supported by the Ministry of Science and Technology of the Republic of China (Taiwan) through grant 109-2628-M-007-005-RSP. C.Y.H. is supported by the National Research Foundation of Korea through grants 2016R1A5A1013277 and 2019R1F1A1062071.

This publication has made use of data collected at Lulin Observatory, partly supported by MoST grant 108-2112-M-008-001.

Based on observations obtained with MegaPrime/MegaCam, a joint project of CFHT and CEA/DAPNIA, at the Canada-France-Hawaii Telescope (CFHT) which is operated by the National Research Council (NRC) of Canada, the Institut National des Science de l'Univers of the Centre National de la Recherche Scientifique (CNRS) of France, and the University of Hawaii. The observations at the Canada-France-Hawaii Telescope were performed with care and respect from the summit of Maunakea which is a significant cultural and historic site.

Based on observations obtained at the international Gemini Observatory, a program of NSF's NOIRLab, which is managed by the Association of Universities for Research in Astronomy (AURA) under a cooperative agreement with the National Science Foundation. on behalf of the Gemini Observatory partnership: the National Science Foundation (United States), National Research Council (Canada), Agencia Nacional de Investigación y Desarrollo (Chile), Ministerio de Ciencia, Tecnología e Innovación (Argentina), Ministério da Ciência, Tecnologia, Inovações e Comunicações (Brazil), and Korea Astronomy and Space Science Institute (Republic of Korea).

This work made use of data supplied by the UK Swift Science Data Centre at the University of Leicester.

The scientific results reported in this article are based on observations made by the Chandra X-ray Observatory. This research has made use of software provided by the Chandra X-ray Center (CXC) in the application packages CIAO, ChIPS, and Sherpa.

Facilities: BOAO:1.8m, LO:1m, Gemini:Gillett, CFHT, CXO, and Swift

REFERENCES

Abdo, A. A., Ackermann, M., Ajello, M., et al. 2010, ApJS, 188, 405
Abdollahi, S., Acero, F., Ackermann, M., et al. 2020, ApJS, 247, 33
Acero, F., Ackermann, M., Ajello, M., et al. 2015, ApJS, 218, 23
An, H., Romani, R. W., Johnson, T., Kerr, M., & Clark, C. J. 2017, ApJ, 850, 100
Ballet, J., Burnett, T. H., Digel, S. W., & Lott, B. 2020, arXiv e-prints, arXiv:2005.11208
Braglia, C., Mignani, R. P., Belfiore, A., et al. 2020, MNRAS, 497, 5364
Cash, W. 1979, ApJ, 228, 939
Chen, H.-L., Chen, X., Tauris, T. M., & Han, Z. 2013, ApJ, 775, 27
Eastman, J., Siverd, R., & Gaudi, B. S. 2010, PASP, 122, 935
Flewelling, H. A., Magnier, E. A., Chambers, K. C., et al. 2016, arXiv e-prints, arXiv:1612.05243
Gaia Collaboration, Brown, A. G. A., Vallenari, A., et al. 2020, Gaia Early Data Release 3: Summary of the contents and survey properties
Garmire, G. P., Bautz, M. W., Ford, P. G., Nousek, J. A., & Ricker, George R., J. 2003, in Society of Photo-Optical Instrumentation Engineers (SPIE) Conference Series, Vol. 4851, X-Ray and Gamma-Ray Telescopes and Instruments for Astronomy., ed. J. E. Truemper & H. D. Tananbaum, 28–44
Gentile, P. A., Roberts, M. S. E., McLaughlin, M. A., et al. 2014, ApJ, 783, 69
HI4PI Collaboration, Ben Bekhti, N., Flöer, L., et al. 2016, A&A, 594, A116

Huang, R. H. H., Kong, A. K. H., Takata, J., et al. 2012, ApJ, 760, 92
Hui, C. Y., & Li, K. L. 2019, Galaxies, 7, 93
Hui, C. Y., Park, S. M., Hu, C. P., et al. 2015, ApJ, 809, 68
Hui, C. Y., Lee, J., Li, K. L., et al. 2020, MNRAS, 495, 1093
Kennedy, M. R., Clark, C. J., Voisin, G., & Breton, R. P. 2018, MNRAS, 477, 1120
Kong, A. K. H., Jin, R., Yen, T. C., et al. 2014, ApJ, 794, L22
Labrie, K., Anderson, K., Cárdenes, R., Simpson, C., & Turner, J. E. H. 2019, in Astronomical Society of the Pacific Conference Series, Vol. 523, Astronomical Data Analysis Software and Systems XXVII, ed. P. J. Teuben, M. W. Pound, B. A. Thomas, & E. M. Warner, 321
Lee, J., Hui, C. Y., Takata, J., et al. 2018, ApJ, 864, 23
Li, K.-L., Kong, A. K. H., Hou, X., et al. 2016, ApJ, 833, 143
Li, K. L., Kong, A. K. H., Takata, J., et al. 2014, ApJ, 797, 111
Li, K.-L., Strader, J., Miller-Jones, J. C. A., Heinke, C. O., & Chomiuk, L. 2020, ApJ, 895, 89
Li, K.-L., Hou, X., Strader, J., et al. 2018, ApJ, 863, 194
Luo, S., Leung, A. P., Hui, C. Y., & Li, K. L. 2020, MNRAS, 492, 5377
Magnier, E. A., & Cuillandre, J. C. 2004, PASP, 116, 449
Miller, J. M., Swihart, S. J., Strader, J., et al. 2020, ApJ, 904, 49
Nieder, L., Clark, C. J., Kandel, D., et al. 2020, ApJ, 902, L46
Nolan, P. L., Abdo, A. A., Ackermann, M., et al. 2012, ApJS, 199, 31
Papitto, A., Rea, N., Coti Zelati, F., et al. 2018, ApJ, 858, L12
Roberts, M. S. E. 2013, in IAU Symposium, Vol. 291, Neutron Stars and Pulsars: Challenges and Opportunities after 80 years, ed. J. van Leeuwen, 127–132
Romani, R. W., Filippenko, A. V., Silverman, J. M., et al. 2012, ApJ, 760, L36
Romani, R. W., & Sanchez, N. 2016, ApJ, 828, 7
Saz Parkinson, P. M., Xu, H., Yu, P. L. H., et al. 2016, ApJ, 820, 8
Swihart, S. J., Strader, J., Aydi, E., et al. 2021, arXiv e-prints, arXiv:2101.08776
Swihart, S. J., Strader, J., Urquhart, R., et al. 2020, ApJ, 892, 21
Takata, J., Li, K. L., Leung, G. C. K., et al. 2014, ApJ, 785, 131
Wang, Z., Xing, Y., Zhang, J., et al. 2020, MNRAS, 493, 4845
Yap, Y. X., Li, K. L., Kong, A. K. H., et al. 2019, A&A, 621, L9
Zacharias, N., Finch, C., & Frouard, J. 2017, AJ, 153, 166

The Astronomical Journal, 159:169 (18pp), 2020 April https://doi.org/10.3847/1538-3881/ab7926

EDEN: Sensitivity Analysis and Transiting Planet Detection Limits for Nearby Late Red Dwarfs

Aidan Gibbs[1,2], Alex Bixel[1,3], Benjamin V. Rackham[4,13], Dániel Apai[1,3,5], Martin Schlecker[6], Néstor Espinoza[7,14], Luigi Mancini[6,8,9,10], Wen-Ping Chen[11], Thomas Henning[6], Paul Gabor[12], Richard Boyle[12], Jose Perez Chavez[1], Allie Mousseau[1], Jeremy Dietrich[1], Quentin Jay Socia[1], Wing Ip[11], Chow-Choong Ngeow[11], An-Li Tsai[11], Asmita Bhandare[6], Victor Marian[6], Hans Baehr[6], Samantha Brown[6], Maximilian Häberle[6], Miriam Keppler[6], Karan Molaverdikhani[6], and Paula Sarkis[6]

[1] Steward Observatory, The University of Arizona, 933 N. Cherry Avenue, Tucson, AZ 85721, USA
[2] Department of Physics & Astronomy, University of California, Los Angeles, Los Angeles, CA 90095, USA
[3] NASA Nexus For Exoplanetary System Science: Earths in Other Solar Systems Team, USA
[4] Department of Earth, Atmospheric, and Planetary Sciences and Kavli Institute for Astrophysics and Space Research, Massachusetts Institute of Technology, 77 Massachusetts Avenue, Cambridge, MA 02139, USA
[5] Lunar and Planetary Laboratory, The University of Arizona, 1640 E. University Boulevard, Tucson, AZ 85718, USA
[6] Max Planck Institute for Astronomy, Konigstuhl 17, D-69117 Heidelberg, Germany
[7] Space Telescope Science Institute, 3700 San Martin Drive, Baltimore, MD 21218, USA
[8] Department of Physics, University of Rome Tor Vergata, Via della Ricerca Scientifica 1, I-00133 Rome, Italy
[9] INAF Osservatorio Astrofisico di Torino, via Osservatorio 20, I-10025 Pino Torinese, Italy
[10] International Institute for Advanced Scientific Studies (IIASS), Via G. Pellegrino 19, I-84019 Vietri sul Mare (SA), Italy
[11] Graduate Institute of Astronomy, National Central University, 300 Jhongda Road, Zhongli, Taoyuan 32001, Taiwan
[12] Vatican Observatory Research Group, University of Arizona, 933 N Cherry Avenue, Tucson AZ, 85721-0065, USA
Received 2019 December 17; revised 2020 February 19; accepted 2020 February 20; published 2020 March 23

Abstract

Small planets are common around late-M dwarfs and can be detected through highly precise photometry by the transit method. Planets orbiting nearby stars are particularly important as they are often the best-suited for future follow-up studies. We present observations of three nearby M dwarfs referred to as EIC-1, EIC-2, and EIC-3, and use them to search for transits and set limits on the presence of planets. On most nights our observations are sensitive to Earth-sized transiting planets, and photometric precision is similar to or better than *TESS* for faint late-M dwarfs of the same magnitude ($I \approx 15$ mag). We present our photometry and transit search pipeline, which utilizes simple median detrending in combination with transit least-squares-based transit detection. For these targets, and transiting planets between one and two Earth radii, we achieve an average transit detection probability of ~60% between periods of 0.5 and 2 days, ~30% between 2 and 5 days, and ~10% between 5 and 10 days. These sensitivities are conservative compared to visual searches.

Unified Astronomy Thesaurus concepts: Exoplanet astronomy (486); Exoplanets (498); Habitable planets (695); Transit photometry (1709)

1. Introduction

Planetary systems around nearby stars are set to play a particularly important role in the future of exoplanet characterization studies, yet only a very small fraction of these planets have been identified to date. Reconnaissance spectroscopy of nearby, small (Earth-sized) transiting planets is possible now with the *Hubble Space Telescope* (e.g., as in the TRAPPIST-1 system; see de Wit et al. 2016, 2018; Zhang et al. 2018; Wakeford et al. 2019) and in-depth spectroscopic studies of these systems will be possible in the near future with the *James Webb Space Telescope* (e.g., Greene et al. 2016; Morley et al. 2017; Lustig-Yaeger et al. 2019) and with the *ARIEL* mission (e.g., Tinetti et al. 2018). Transiting, habitable-zone, Earth-sized planets around nearby stars are likely to be the only type of habitable planets that can be characterized in detail in the next two decades.

Although only a fraction of planets happen to transit as observed from Earth, fortunately, the high frequency of M dwarfs in the solar neighborhood, the most favorable host stars for detecting Earth-sized planets, improves the chances of a positive detection. Based on results from the RECONS group (Henry et al. 2018), there are 283 currently known M-type stars within 10 pc, and that number continues to grow. In addition, small (1–4 $R_{\oplus}$) planets are found to be very common around M dwarfs (Dressing & Charbonneau 2015; Mulders et al. 2015a, 2015b; Hardegree-Ullman et al. 2019). However, M dwarfs in the solar neighborhood are located isotropically in the sky, requiring targeted, star-by-star monitoring (e.g., Nutzman & Charbonneau 2008; Jehin et al. 2011; Delrez et al. 2018). Worldwide networks of ground-based telescopes that can obtain continuous targeted coverage are therefore well-suited to search for these planets (Blake et al. 2008).

The Exoearth Discovery & Exploration Network (EDEN, PIs: D. Apai, P. Gabor, Th. Henning, W-P. Chen) is a multi-continental research network that searches for habitable-zone planets within 50 lt-yr.[15] EDEN's transit survey component began in spring 2018 and currently uses eight telescopes to search for transiting planets around nearby late-M-dwarf stars, which are the easiest stars to find Earth-sized planets around. EDEN differs from other ongoing surveys in that it uses several large pre-existing telescopes (>1 m diameter) and that its

[13] 51 Pegasi b Postdoctoral Fellow.
[14] IAU-Gruber Fellow.
[15] http://project-eden.space

longitudinally distributed stations are capable of providing continuous coverage. When no planet is found in a system, EDEN also aims to place stringent upper limits on the probability that short-period planets are present. The interpretation of such non-detections requires a robust and consistent observing strategy, thorough understanding and modeling of systematics, efficient photometric pipeline and trend removal (detrending), and a well-characterized planet-detection algorithm. With this photometric and detection pipeline, EDEN also provides an excellent telescope network for photometric follow-up of planet candidates identified by NASA's *TESS* (Ricker et al. 2015) transit search mission.

We review here these components of our sensitivity analysis, and present example results for the first three EDEN targets searched in depth. We do not detect any convincing transit candidates for follow-up, but show that there is a high probability we would have detected Earth-sized planets with periods less than 5 days if their orbital planes were aligned with our line of sight. In Section 2 we briefly describe the EDEN telescopes and our observational methods. Section 3 details our data reduction pipeline before lightcurve detrending and transit search described in Section 4. In Section 5, we provide background on the selected EDEN targets for which we perform a sensitivity analysis in Section 6. Finally, in Section 7 we discuss our planet detection limits in the context of M-dwarf planetary occurrence rates, known systems, and NASA's *TESS* mission.

2. Observations

We briefly describe the EDEN telescopes, survey target selection, and photometric data collection procedures in order to provide context for our data reduction, transit search, and sensitivity analysis methods. A nuanced discussion of our strategy for selecting and observing targets, and a comparison with other surveys, will be reserved for a future paper (D. Apai et al. 2020, in preparation), and only necessary details are included here.

2.1. Observatories

EDEN observations are currently conducted with eight unique telescopes at seven observatories in North America, Europe, and Asia. The telescopes are the Kuiper 1.55 m (Mount Bigelow, Arizona), Bok 2.3 m (Kitt Peak, Arizona), Vatican Advanced Technology Telescope 1.8 m (VATT; Mount Graham, Arizona), Phillips 0.6 m and Schulman 0.8 m (Mount Lemmon, Arizona), Calar Alto 1.23 m (Calar Alto, Spain), Cassini 1.52 m (Mount Orzale, Italy), and Lulin 1 m (Mount Lulin, Taiwan). Table 1 details the location, design, and CCD imager of each telescope. With the exception of the robotic Schulman and Phillips telescopes, each of them is manually controlled by an observer, who actively monitors weather conditions and instrument performance during the course of a night. While the telescope designs are varied, each of the telescopes has been carefully evaluated for photometric performance before its inclusion in EDEN and, when necessary, changes have been made in the telescope's operation and setup, which will be detailed in D. Apai et al. (2020, in preparation). Systematic differences between telescopes therefore have very minor effects on the final lightcurves and transit search. These differences can be compensated for during the data reduction and detrending steps, discussed in Sections 3 and 4.

The majority of the EDEN telescopes are not solely dedicated to EDEN, so observations are scheduled at each facility individually in blocks usually from two to 10 days per month, depending on availability. Observing science targets at these sites has been ongoing since 2018 June (following a six month long EDEN pilot program), with observations of the targets discussed in this paper occurring between 2018 June and 2019 February.

2.2. Target Selection

EDEN's primary focus is to search for potentially habitable planets within 15 pc (∼50 lt-yr). Correspondingly, for the EDEN Transit Survey, our target selection prioritizes M4 and later-spectral-type host stars, which offer favorable planet-to-star projected areal ratios, making broadly Earth-sized planets detectable in our data. We eliminate known close binary stars that may reduce the stability of putative planets and would complicate the interpretation of the lightcurve. We then prioritize sources that are too faint ($I > 15$ mag) to be efficiently searched by TESS or are outside TESS's sky coverage. In addition to these high-priority EDEN targets we also include separately targets of particular interest in our source catalog. Such targets may be exoplanet candidate host stars (from radial velocity (RV) or transit searches), for which EDEN data can prove valuable for candidate verification. Such follow-up targets (where prior knowledge about a planet's presence exists) will not be used in future exoplanet occurrence rate studies.

2.3. Science Observations

EDEN targets, including those discussed in this paper, are late-M dwarfs scattered throughout the Northern Hemisphere sky and thus must be observed one at a time. For planets orbiting within the habitable zone of these stars or closer (e.g., Kasting et al. 1993; Kopparapu et al. 2014), expected transit durations range from 0.5 to 3 hr at periods of roughly 0.5–10 days.

To maximize the probability of observing transits with these parameters and to take advantage of the longitudinal coverage of EDEN telescopes, we designed our observing strategy around two pillars. First, we observe each target for as long as possible on a given night. This typically means that on a clear night we observe a primary target for >6 hr, and then a secondary target for 2–3 hr when the primary is not observable. This also increases the chance of observing a full transit, which is easier to detrend and detect than fractional transits. Second, whenever possible, we schedule simultaneous observing campaigns in Arizona, Europe, and Taiwan to allow the potential for continuous 24 hr monitoring of one target for multiple days. On such longer, coordinated runs—given good weather at all sites—we can obtain roughly week-long continuous sequences, limited only by our allocated time on these facilities.

These pillars allow us to quickly get good phase coverage of a target for shorter-period planets. Practically, continuous observation has been difficult to fully exploit because of the rarity of getting good weather on three continents during the entire run. The number of nights dedicated to any target is based on the probability that we would have observed two

Table 1
EDEN Telescopes

Telescope	Location	Operation	Mount	CCD Imager	Det. Size	FOV	Px. Scale	Q_e at 700 nm
Phillips 0.6 m	Mount Lemmon, Arizona	Robotic	EQ	SBIG STX (KAF-16803)	4096 × 4096	22′ × 22′	0″.35	40%
Schulman 0.8 m	Mount Lemmon, Arizona	Robotic	EQ	SBIG STX (KAF-16803)	4096 × 4096	22′ × 22′	0″.35	40%
Lulin 1.0 m	Mount Lulin, Taiwan	Classical	EQ	Sophia 2048B CCD	2048 × 2048	13′.08 × 13′.08	0″.39	60%
Calar Alto 1.23 m	Calar Alto, Spain	Remote	EQ	DLR-MKIII camera with e2v CCD231-84-NIMO-BI-DD sensor	4k×4k	21′.5 × 21′.5	0″.31	93%
Cassini 1.52 m	Mount Orzale, Italy	Classical	EQ	Bologna Faint Object Spectrograph and Camera	1300 × 1340	13′ × 12′.6	0″.34	75%
Kuiper 1.55 m	Mount Bigelow, Arizona	Classical	EQ	Mont4K SN3088 (Weiner et al. 2018)	4096 × 4097	9′.7 × 9′.7	0″.14	62%
VATT 1.8 m	Mount Graham, Arizona	Classical	Alt-Az	VATT4K STA0500A CCD	4064 × 4064	12′.5 × 12′.5	0″.188	80%
Bok 2.3 m	Kitt Peak, Arizona	Classical	EQ	90 Prime Focus Wide-Field Imager (Grant Williams et al. 2004)	4 × 4032 × 4096	1°.16 × 1°.16	0″.4	80%

transits of a planet with an orbital period of less than 10 days. As this probability increases, we deprioritize a given target so that more targets can be adequately sampled. While it is not practically possible to reach 100% detection probability for planets throughout the entire habitable zone (from inner to outer edge; Kopparapu et al. 2014), we aim to reach high sensitivity for transiting planets that orbit at the inner edge of the habitable zone (i.e., ∼50% successful detection of Earth-size transiting planets), which typically translates to some sensitivity ($\gtrsim$10%) throughout the habitable zone.

2.3.1. Observational Procedures

Although each of our telescopes has somewhat different capabilities and performance, we adopt the same observational procedures at each telescope to minimize systematic differences.

Filter. For each telescope we use a near-infrared (NIR) (or blue-blocking) filter, such as Harris-I or similar. This filter choice maximizes the collected photons from our targets, which are brightest in the NIR, while blocking unwanted sky background from the Moon and skyglow. Since spring 2019, the filter has been standardized at all telescopes to an uncoated GG 495[16] glass long-pass filter (transparent at >500 nm). Redder filters such as I or z' have been occasionally used for bright targets if the sky background is very high, for example, during a full Moon. The z' is otherwise generally avoided because of the low quantum efficiency of most CCD detectors at those wavelengths and the greater presence of telluric absorption bands from water vapor (Bailer-Jones & Lamm 2003; Blake et al. 2008).

Exposure Time. The exposure time is chosen to balance competing signal-to-noise and cadence considerations. We never allow the peak target flux to go above ∼60% the detector's full well, where the detector begins to exhibit non-linear behavior. In a given period of time, such as a transit duration, the total Poisson-noise-driven signal-to-noise ratio follows the relationship

$$\mathrm{S/N_{tot}} \propto \sqrt{\frac{R}{1+R}},$$

where R is the ratio of the exposure time to readout time (Howell & Tavackolimehr 2019). This relationship levels off at $R \sim 3.5$, and we thus aim for an exposure time of ∼3.5× the readout time. For our telescopes with a diameter larger than 1 m and targets with magnitude $I \sim 14$, this gives a cadence <60 s.

Focus. Previous work (e.g., Southworth et al. 2009) has shown that defocusing can result in more precise lightcurves as the point-spread function (PSF) is spread across more pixels. We aim for a slight-to-moderate defocus of 2″–3″, so that pixel-to-pixel variations are reduced, but the PSF maintains a Gaussian shape. Since defocusing also reduces the peak of the PSF, it has the additional benefit of allowing longer exposures.

2.4. Calibration Frames

We follow standard calibration procedures for flat, bias, and dark corrections to reduce systematic effects on our lightcurves. Detailed tests (complete re-reduction and analysis of selected data sets) show that the details of the basic calibration do not affect the resulting lightcurve precision significantly.

For our calibration procedure, before or after every night of observation, we collect ∼10 twilight flat-fields with exposure times chosen to maintain a sky flux approximately at 50% the detector's full well, the same as our desired peak target flux. In some cases of inclement weather during twilight, we may use dome flats, but these are not preferred since they have less uniform illumination. The minimum flat exposure time is always long enough so that the shutter time has <1% effect on the precision of the flat.

Generally, at least once per observing run, we collect a set of bias and dark frames. The dark current for our exposure times is nearly zero at all telescopes and is usually not subtracted. At some telescopes darks are not collected for this reason. There is no evidence for persistence on any of our detectors.

3. Data Reduction

EDEN data reduction is performed with a custom Python-based automatic pipeline, `edenAP`, which is based on a precursor pipeline for reducing Las Cumbres Observatory Global Telescope lightcurves (Brown et al. 2013). `edenAP` is designed to accommodate the particularities of the individual telescopes in the EDEN telescope network and reduce the data in a consistent manner. Differences that must be accounted for include number and configuration of chip amplifiers, and pixel scale. `edenAP` is called locally when new raw data arrive, and produces a comparison-star-detrended (Section 3.4) lightcurve for each observation as its final output, which can be further detrended and used for a transit search. The pipeline is highly automated and, in the event of improvements to the algorithm, `edenAP` can be re-run on all previous data with minimal effort. All raw data are stored at the University of Arizona, as well as through a cloud storage provider (Amazon Web Services).

3.1. Science Calibration

The first step in `edenAP` is to calibrate the raw science frames using the calibration frames discussed in Section 2.4. In the event that calibration frames are not available or are of poor quality, this step can be skipped with the rest of the pipeline remaining the same. To create master calibration frames, we collect all bias frames within one month of the observation, and all dark and flat frames within the observation run. Monitoring of flat fields has indicated that these stay mostly constant over the course of a run, with the exception of minor localized dust accumulation and chance occurrences such as insects getting trapped in the optical path. In cases where many hundreds of calibration frames are available in the above time periods, we narrow the period and only collect calibration frames within two to three days of the observation.

3.2. Astrometry

We then derive the astrometric solution for every science frame by using a local installation of the `astrometry.net` software package (Lang et al. 2010). While this solution provides accurate astrometric calibration for most frames, it can fail in case of partial cloud cover or poor seeing. If no astrometric solution can be found for a particular image, the solution from the preceding image is used, despite these data typically being very poor. The astrometric solution derived is used as a first guess for placing photometric apertures; however,

[16] www.us.schott.com

we always refine the centroid using the photutils[17] DAOStarFinder method (Bradley et al. 2019), based on the DAOFIND algorithm (Stetson 1987). Position refinement is key to getting sub-pixel centroid precision, especially for our high proper motion target stars.

3.3. Photometry

Aperture photometry is performed using the photutils package (Bradley et al. 2019). For every star in the field of view, we measure the intensity in apertures ranging from 5 to 50 pixels in steps of 1 pixel. The aperture size that minimizes the rms scatter of the target star lightcurve is selected as the best aperture for all sources. The optimal size depends on detector and seeing, but typical sizes are roughly a few arcseconds. Sky background is calculated as the median of a 60×60 pixel sub-image around the star with other sources clipped. Photometry is saved into a Python pickle file with other important information for each star, such as centroid positions, stellar magnitudes, background, FWHM, airmass, etc., which can later be used for detrending steps and vetting transit-like signals.

3.4. Comparison Star Detrending

The final step in edenAP is to detrend the target lightcurve on the basis of comparison star lightcurves. Trends are long- or short-term photometric variations in the lightcurve that decrease transit detection sensitivity, and can arise from instrumental, atmospheric, and stellar variability. We select the best comparison stars by first filtering out stars that are saturated, are too faint (several magnitudes dimmer than the target), or have too many failed photometric measurements. Next, we divide the flux-normalized target lightcurve by the normalized lightcurves of every comparison star, and rank them based on the average standard deviation in windows of 20 data points. The six with the lowest average deviation (i.e., those with the most similar data trends) are median-combined into a "super comparison" lightcurve, which the target lightcurve is then divided by. For crowded fields with many available comparison stars, it is conceivable that this selection method could weaken or remove transit signals. We believe this is highly unlikely, however, due to the improbability that comparison lightcurves would have the necessary shape to remove a transit, and because the duration of the window is shorter than any expected non-grazing transit. Nevertheless, we account for this in our sensitivity analysis (Section 6.2) by re-selecting comparison stars after injecting transits.

4. Transit Search

In the subsequent steps we identify and remove residual systematic trends (i.e., those not shared fully by comparison stars) and search for lightcurve features that are candidate transit events. Our approach is a modular, automatic, step-by-step process that is robust and easily repeatable, allowing for detailed test runs and process optimization. As detailed in the following subsections, we use a simple median-detrending method and base our vetting methods on instrumental parameters, such as airmass and centroid position, to attempt to explain observed trends and transit-like features. The end result is either a promising candidate, triggering follow-up observations, or sensitivity limits if no convincing candidate is found. A discussion of transit candidate follow-up is reserved for a future paper (D. Apai et al. 2020, in preparation).

4.1. Interactive Data Viewer

We visually inspect every lightcurve on a single EDEN target to ensure that lightcurve anomalies are recognized and managed correctly. We select high-quality data for further analysis without relying on automatic algorithms. To streamline this process, we have implemented an interactive data viewer that displays each lightcurve along with systematic trends, allowing the user to flag large sections of problematic data (e.g., stellar flares, passing clouds) for removal and points of interest (a transit-like feature) for further analysis. Excluding poor-quality data is exceedingly important because strong systematic trends can be fit as transits, and they can throw off the correct period determination if one transit of an otherwise detectable period happened to occur within it. Individual outlier data points are ignored in this step, but are efficiently removed by our automatic filtering in the next step.

4.2. Median Detrending

After visual inspection, lightcurves undergo automated data cleaning and detrending. We fit a long-term trend with a median filter of two hours and 2σ-clip upper outlying data before dividing out the trend. We do not clip below the median because of the risk of clipping deep transits. Median filtering will reduce the depth of all transits slightly, though our use of a two-hour filter window minimizes this effect for transits with durations of less than one hour, which comprises most of our discovery space. An example of median detrending applied to a real EDEN lightcurve with an injected transit of $\sim$1% depth and TRAPPIST-1 b parameters is shown in Figure 1.

While median detrending is a simple method, its effects are predictable and robust. Although the median filtering will not remove short-period, transit-like trends, it will not remove real transits either, if they are deeper than a few tenths of a percent (a danger of more complicated detrending techniques). Other trend-fitting methods with which we have experimented when performing transit injection tests include Savitzky–Golay (Savitzky & Golay 1964), biweight, and multivariate polynomials constructed from external parameters such as airmass, and centroid positions. Savitzky–Golay and biweight filtering have very similar results to median detrending, and while multivariate polynomials can outperform median filters, they are also more likely to accidentally remove a real transit feature. Despite their relative simplicity, median filters are reliable (Hippke et al. 2019).

4.3. Transit Least Squares

To search for transits in our detrended lightcurves, we utilize the package transit least squares (TLS; Hippke & Heller 2019). The primary improvement over box least squares (BLS; Kovács et al. 2002) is that, rather than fitting a boxcar model to a time series, TLS fits a more realistic, fixed transit shape with limb-darkening included, but the same parameters as BLS otherwise. We optimize the TLS algorithm for our search by setting upper and lower limits on the stellar radius and mass to those for M dwarfs (0.1–$0.6 R_{\odot}$, 0.08–$0.5 M_{\odot}$) and the maximum period to correspond to the approximate outer edge of the habitable zone ($\sim$10 days). We rely on our previously

[17] https://photutils.readthedocs.io/en/stable/

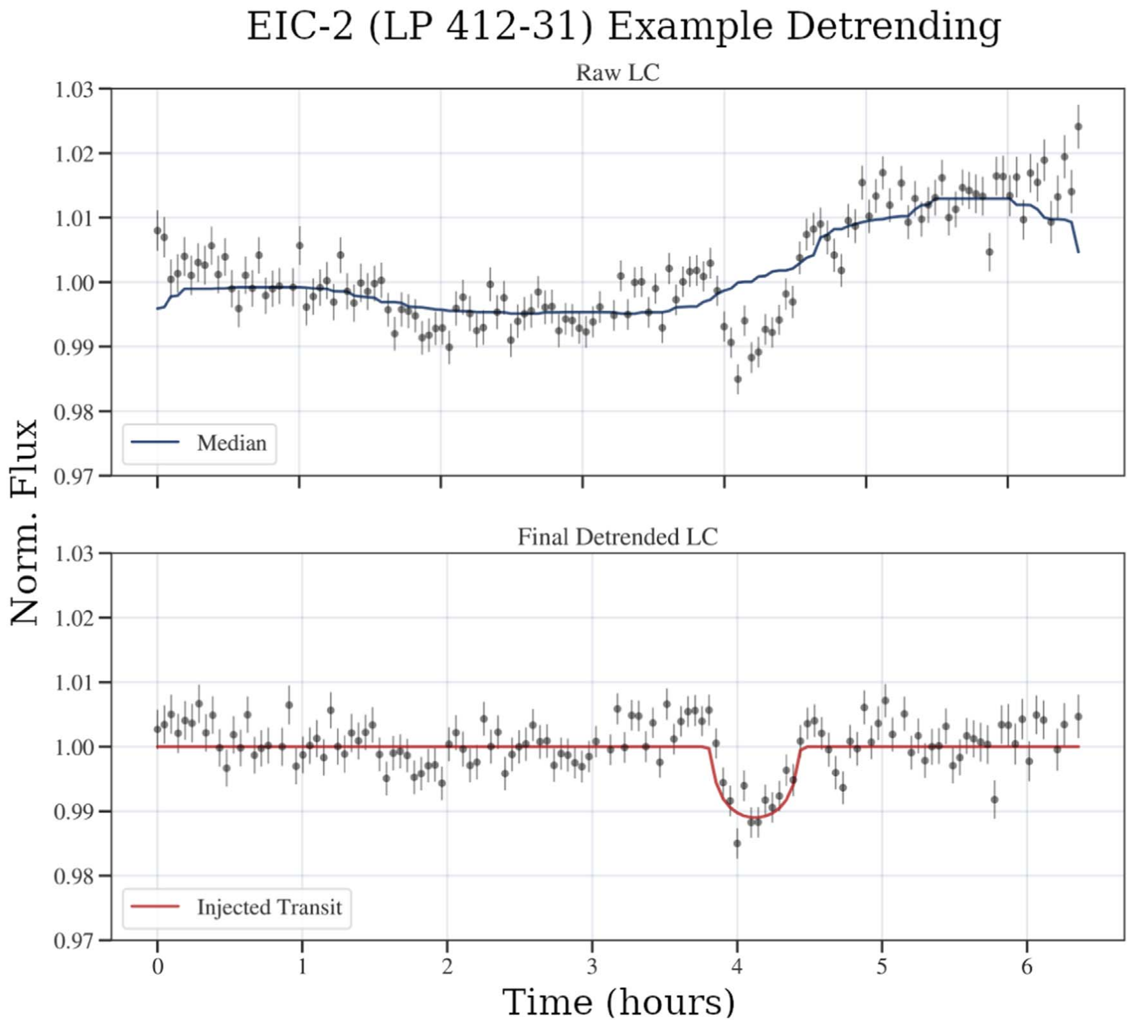

Figure 1. EIC-2 (LP 412-31) example detrending. Data were taken with the Cassini telescope on 2018 December 11. The red line at the bottom shows the injected transit signal (depth ∼1%, TRAPPIST-1 b orbit, with limb-darkening from Claret 1998) compared to the lightcurve after median detrending has been applied. The median shown at the top is affected by some points outside the flux range.

Table 2
EDEN Targets

ID	Name	Spec. Type	Dist. (pc)	*I* Mag	*K* Mag	R.A. (J2000)	Decl. (J2000)
EIC-1	2MASSI J1835379+325954	M8.5V	5.7	13.46	9.17	18:35:37.88	+32:59:53.31
EIC-2	LP 412-31	M8V	14.7	14.48	10.64	03:20:59.71	+18:54:22.77
EIC-3	2MUCD 20263	M8	15.6	14.35	10.84	07:14:03.94	+37:02:46.03

described data-cleaning and detrending steps to remove bad data, and all lightcurves are weighed equally regardless of photometric precision. For each search we save a median-smoothed periodogram, as well as the phase folded model, transit parameters, false alarm probability (FAP), and signal detection efficiency (SDE) for the highest power period.

4.4. Candidate Vetting

Most transit candidates identified by TLS are false positives—and often obvious ones. Currently, vetting is done manually, but it may be automated in the future. The first check of a candidate is inspection of the viability of the TLS output: are the transit parameters physical? Does the phase-folded lightcurve have obvious flares or systematic trends? What are the SDE and FAP values? If these are viable, the interactive data viewer is used to look at systematic trends during transit times, which usually reveal systematic noise sources that introduced the feature. We pursue follow-up observation to eliminate astrophysical false positives (such as eclipsing binaries) only after identifying a promising transit candidate not explainable by other means. We do not specifically set SDE or FAP values to eliminate transit candidates, and consider even those with poor statistics. However, we do perform an analysis in Section 6 of the SDE and FAP values that indicate a robust detection.

5. The First EDEN Targets

EIC-1 (2MASSI J1835379+325954), EIC-2 (LP 412-31), and EIC-3 (2MUCD 20263) are all nearby M8/8.5 ultracool dwarfs (Table 2). They are near the hydrogen-burning limit and

Table 3
Log of Observations

ID	Name	Nights Obs.	Hours Obs.	Median Unbinned Precision (%)	% Used for TLS
EIC-1	2MASSI J1835379+325954	57	205.3	0.163	~70
EIC-2	LP 412-31	56	311.7	0.315	~70
EIC-3	2MUCD 20263	43	297.5	0.380	~85

Note. The Appendix provides a detailed log of the observations.

thus may be either high-mass brown dwarfs or low-mass stars. In this section we will briefly describe their stellar properties and past observations relevant to a search for planets.

5.1. EIC-1

EIC-1 is an M8.5V dwarf located 5.7 pc away (Reid et al. 2003). It was discovered and identified as a nearby dwarf by Lépine et al. (2002) as part of the Digitized Sky Survey. Its brown dwarf status is currently unknown due to differing lines of evidence (Reiners & Basri 2009; Berdyugina et al. 2017; Saur et al. 2018). It is a known radio pulsator with a strong magnetic field and a rapid 2.84 hr rotation period (Berger et al. 2008; Hallinan et al. 2008, 2015; Berdyugina et al. 2017; Kuzmychov et al. 2017). A possible detection of auroral emission has recently been reported for this target (Hallinan et al. 2015).

EIC-1 has been the target of RV observations by CARMENES (Tal-Or et al. 2018) and Keck NIRSPEC (Tanner et al. 2012), some photometric monitoring by MEarth (Dittmann et al. 2016), a wide-orbiting companion search by *Spitzer* IRAC (Carson et al. 2011), and Subaru adaptive optics observations (Siegler et al. 2005), as well as numerous spectroscopic studies from UV to radio wavelengths. We are unaware of any companion candidates from these observations, but note that CARMENES identified it as "active RV-loud," potentially making the detection of habitable planets difficult by RV. EIC-1 was not observed by *K2* and is scheduled to be observed by *TESS* in Sector 26 in 2020 June.

5.2. EIC-2

EIC-2 is an M8V dwarf located 14.7 pc away, identified by Kirkpatrick et al. (1995). It has a rotational period of 0.61 days (Irwin et al. 2011) and is a known flare star with a previously observed giant flare by *XMM-Newton* (Stelzer et al. 2006).

EIC-2 has been the target of RV observations by the Red-Optical Planet Survey (Barnes et al. 2014) and Keck NIRSPEC (Rodler et al. 2012; Tanner et al. 2012), which have 2σ sensitivity to $M \sin i > 3.0\, M_{\oplus}$ throughout the habitable zone. It has also had periodic observations by MEarth (Dittmann et al. 2016). It was not monitored by *K2* or *Spitzer* and is not scheduled to be observed by *TESS* until after the primary mission due to its location near the ecliptic.

5.3. EIC-3

EIC-3 is an M8 dwarf located 15.6 pc away, identified by Lépine & Shara (2005). Compared to EIC-1 and EIC-2, it has been the target of relatively few observations. It has been observed as part of MEarth and the SDSS-III APOGEE Radial Velocity Survey (Deshpande et al. 2013). It was not observed by *K2* or *Spitzer* and is scheduled to be observed by *TESS* in Sector 20 in 2020 January.

6. Planet Detection Limits for EIC-1, EIC-2, and EIC-3

In this section we report the results of our previously described observations, data reduction and detrending pipelines, and transit search for the first three EDEN targets. Both visual and automatic transit injection and recovery tests are performed, described in Sections 6.2.2 and 6.2.3 respectively. We do not detect any convincing planet candidates for these stars, but place sensitive upper limits on the presence of transiting planets around them.

6.1. Description of Lightcurves

EIC-1, EIC-2, and EIC-3 were observed for 200–300 hr each from 2018 June to 2019 February, with 40–60 individual observations per target (see Table 3). The observations are highly clustered in time, with a few periods of continuous or nearly-continuous observations at different observatories lasting 24 hr or more.

Roughly 60%–80% of the cleaned, detrended data are of sufficient quality for a subsequent transit search; the rest is affected by bad weather conditions or technical issues. Durations for the individual high-quality lightcurves range between 2 and 10 hr, depending on target priority, observability, and weather. Some gaps less than 2 hr long exist within longer lightcurves because of passing clouds, temporary technical issues, or manual removal of flares or poor data sections. Cadences vary by a factor of ~2–3 depending on the telescope (with higher cadence for larger primary mirrors) and detector readout times. The average median unbinned precision for lightcurves on a target is ~0.28%. Trends are variable, but most lightcurves have nearly linear or parabolic variations of 1%–3% over their duration, possibly attributable to changing airmass or ponting drift. A sample of detrended lightcurves for EIC-2 for each telescope is shown in Figure 2.

Each target shows evidence for stellar activity, which is expected given their spectral type and previous observations described in Section 5. EIC-2 and EIC-3 have occasional flaring activity above 1%. Lightcurve segments with clearly identifiable flares were removed manually before the transit search. Less than five flares were removed for both targets, representing a negligible loss in time. EIC-1 exhibits regular variability with a 0.5%–1% amplitude, consistent with the rotational period of ~3 hr (Berger et al. 2008). This variation can mimic transit-like signals, and thus reduces our transit detection sensitivity for the target.

6.2. Sensitivity Analysis

To assess the transit detection capability of our observations, we implement a transit injection and recovery routine. We inject realistic transits into our raw target lightcurves using the analytic solutions of Mandel & Agol (2002) as implemented in `batman` (BAsic Transit Model cAlculatioN; Kreidberg 2015), re-select comparison stars with the same procedure described in

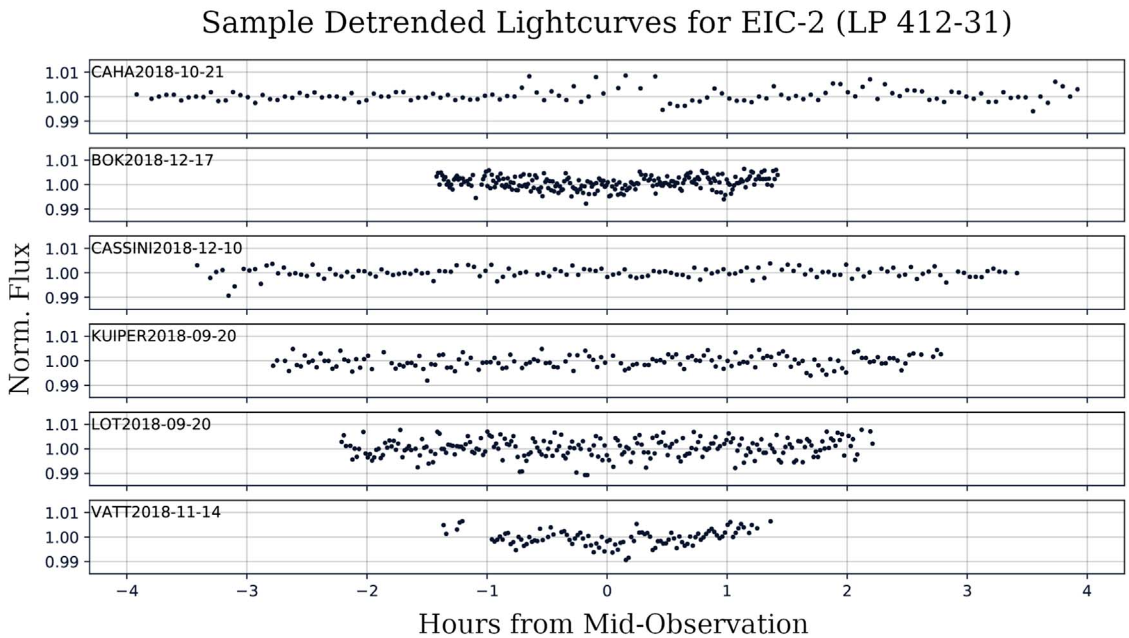

Figure 2. EIC-2 (LP 412-31) sample lightcurves. The data are unbinned so that the relative cadence and raw precision of the instruments can be seen. Telescope and date are shown in the top left for each lightcurve.

Section 3.4, and attempt to recover the transit signals using our detrending and transit search pipeline. We also perform a limited visual transit recovery test to compare the sensitivity of the pipeline to a manual search by eye.

6.2.1. Manual Transit Search

Before injecting any simulated transits, we perform a TLS search and manual inspection of the lightcurves for each target to attempt to identify real transit candidates. Three team members reviewed every lightcurve individually and marked features of interest (transit candidates), which were then compared and vetted together according to Section 4.4, along with the transit candidates identified by TLS. We do not consider any of the transit candidates to be likely planets worthy of follow-up observation; we instead find them to be consistent with stellar variability and systematics. These steps do not definitively exclude the presence of transiting planets, but the probability of detecting a transiting planet is low, and will be quantified through our sensitivity analysis.

6.2.2. Visual Transit Recovery Tests

As a comparison to the following TLS sensitivity results in Section 6.2.3, we also performed a limited, visual transit injection and recovery test. The purpose was to probe what transits team members could find by eye, without prior knowledge of their existence or location.

One team member injected a TRAPPIST-1 b analog (1.1 $R_{\oplus}$, $\sim$0.7% depth, 1.51 day period; Gillon et al. 2017) at a random phase into a fraction of the lightcurves of each target (see Section 6.2.3 for other parameters). Three other team members each received independent sets of these lightcurves with injections at random phase. Nearly half of the lightcurve sets did not contain any injections so that the team would not be compelled to identify transit candidates if they believed none was convincing.

True positives are defined as real injections that are correctly identified, false positives are non-injection features wrongly identified as transits, and false negatives are real injections not identified. Collectively, out of 41 observed injected transits in five different sets of lightcurves, the team had a 1:1 true to false positive ratio, and a 4:1 false negative to true positive ratio. To determine our average visual sensitivity to TRAPPIST-1 b analogs, we consider how many sets of target lightcurves (containing multiple observed transit injections) had at least one true positive, irrespective of false negatives. Four out of five sets of target lightcurves with injections had one or more true positive, therefore we consider our average visual sensitivity to TRAPPIST-1 b analogs to be $\sim$80%. We believe this is limited by conservative transit identification rather than poor data quality. In reality, the false negative ratio is not as high as 4:1 since some of the "observed" transit injections are essentially unidentifiable due to only a small fraction of the transit being observed. While these tests are not a rigorous assessment of our ability to detect transits by eye, they support our argument that Earth-size planets can be correctly identified in our lightcurves without relying on the automated search routine.

6.2.3. Automated Transit Recovery Tests

The purpose of our automatic transit injection and recovery tests is to provide a scalable and objective sensitivity analysis method. For these tests, we simulate transits for planets in a logarithmic grid of period and radius from 0.5 to 10 days and 0.6 to 4 Earth radii, respectively, constituting most of our expected discovery space. The stellar radii of the target stars were determined from available surface gravity measurements (Tsuji & Nakajima 2016; Rajpurohit et al. 2018). Within the grid, orbits are assumed to be circular with random phases and with impact parameters randomly drawn from a uniform distribution between 0.0 and 1.0. While it is technically feasible to detect transits up to an impact parameter of $1 + R_p$, 1.0 is chosen as the upper limit since our detrending and search pipeline is not optimized to search for the very short duration and altered limb-darkening of grazing transits, and will have reduced sensitivity in that parameter space. We empirically find that sensitivity begins to drop significantly around impact parameters of 0.9, with around half the sensitivity to impact parameters between 0.9 and 1.0 compared to the average sensitivity below 0.9. Furthermore, a limit of $1 + R_p$ creates an artificial dependence on planet radius for transit sensitivity analysis, which distracts from more meaningful sensitivity trends.

The transit injections have quadratic limb darkening laws from Claret (1998) for the *I* band. While other limb darkening laws (e.g., logarithmic or exponential) may be more realistic (Espinoza & Jordán 2016), the differences for the sensitivity analysis are negligible in the present noise level regime. We further assume that the limb-darkening laws will be similar in all our NIR and red filters, and thus we use the same law for every injection.

Planets are injected at each grid point until there are 10 potentially detectable planets, i.e., planets with at least one simulated transit within the observing windows. This procedure is adopted to have a sufficient number of detectable planets at longer periods for counting statistics, where many planets may have no observed transits based on their random phase. Combining the grid size (12 by 8) with the requirement of 10 detectable planets means that, for each target, there are a total of 960 potentially recoverable transiting planets in the global sensitivity map.

6.2.4. Positive Identification of Transits

For us to consider a transit detected by TLS to be a true positive result, it must meet one of the following two criteria: (1) the best period is less than 0.5 hr different from the true period of the injected planet, or (2) at least one identified transit midpoint time is within 20 minutes of a real injected transit midpoint (i.e., a transit candidate is correctly identified, but the period is incorrect). All candidates that meet condition (1) naturally meet condition (2).

We make an additional distinction between true positives recovered by TLS and "successful recoveries," which we count in our sensitivity analysis. Successful recoveries are a subset of true positives that also pass a detection significance criterion. We make this distinction because it is possible in a real search to detect a shallow transit only to dismiss it due to low signal. We do not want to consider these cases as successful in our analysis. Therefore, we limit successful recoveries in this analysis to detections that exceed a minimum SDE (Hippke & Heller 2019), corresponding to a detection in a real search that would likely pass vetting and trigger follow-up observations. The SDE is the significance of a period relative to the average significance of all other periods.

We determine the minimum SDE for each target individually based on the global SDE distribution of false positives resulting from our injection recoveries. We set the minimum SDE required for a successful detection as the SDE that is greater than 95% of false positives (i.e., only 5% of false positives have a higher SDE). For our three targets, the minimum robust SDE value ranges for EIC-1, 2, and 3, are roughly 6, 7, and 11.

The true and false positive distributions are shown for EIC-1, EIC-2, and EIC-3 in Figure 3. The differences result from the unique structure of each target's set of lightcurves, which produce higher and lower significance false positives. One noticeable feature of these plots (especially for EIC-3) is that the false positive distribution does not continually increase for lower SDE values, but is instead centered at a specific SDE. This potentially counter-intuitive distribution is caused by both the structure of each target's set of lightcurves, as well as the range and step size of the injection grid. Each target has a dominant false positive signal that is returned when there is no transit injection. Our grid range includes two rows of sub-Earth-size planets that are extremely shallow in depth, and each injection in these rows will return nearly the same false positive SDE as if there were no injection. This leads to a build-up of a high fraction of false positives around the no-injection SDE value, which corresponds roughly to the maximum of the false positive distribution. The higher fraction of true positives at lower SDE values is due to the fact that there is a certain range of injection depths that will only be a marginally higher power than the no-injection false positive and thus will have a low SDE, but they will still be detected successfully at high rates.

It is important to note that the SDE cutoff is not used to determine the significance of transit candidates in the real transit search and is only used in finding the significance of injection recoveries after concluding by other means (Section 6.2.1) that the data contain no real transits. Therefore, it likely provides a conservative sensitivity estimate. Finally, the SDE cutoff cannot be expected to fully capture the probability that a true positive candidate would be followed-up and confirmed, but rather is a best attempt at conservatively estimating the likelihood given subjective human involvement in deciding what is and what is not a convincing candidate. While it would be more desirable to build a completely automatic vetting algorithm, for our observations the algorithm would need to be prohibitively intelligent and complex, and could result in more missed planets.

6.2.5. Pipeline Sensitivity

We illustrate our transit detection sensitivity for EIC-1, EIC-2, and EIC-3 in Figures 4–6, respectively. The top plots show the efficiency of our pipeline in detecting transiting planets, while the bottom plots represent total detection probability for all planets, both transiting and non-transiting, based on our transit detection sensitivity and the geometric transit probability for planets as a function of semimajor axis $\left(P_{\rm tr} = \frac{R_*}{a}\right)$. To calculate the overall sensitivity within a specific range of periods and radii, we simply average the detection sensitivity in that range. Mean sensitivities for select ranges are shown in Table 4.

7. Discussion

7.1. EDEN Sensitivity

The sensitivity maps for EIC-1, EIC-2, and EIC-3 show that we have the potential to successfully detect transiting Earth-sized planets in the habitable zones of nearby, ultracool dwarfs. Furthermore, they show that in a few cases we can detect sub-Earth-sized planets on closer orbits provided two or more transits occur during high-quality observations. To compare these results with *TESS*, the estimated photometric precisions for EIC-1, EIC-2, and EIC-3 are 0.136%, 0.299%, and 0.343% respectively in *one hour* periods of observation (*TESS* Mag. 13.28, 14.35, and 14.52) (Stassun et al. 2018). These are very similar to the median achieved precisions of unbinned EDEN lightcurves typically at a *one minute* cadence (0.163%, 0.315%, and 0.380% respectively). Thus, with long-term targeted observations it is possible we could achieve better sensitivities

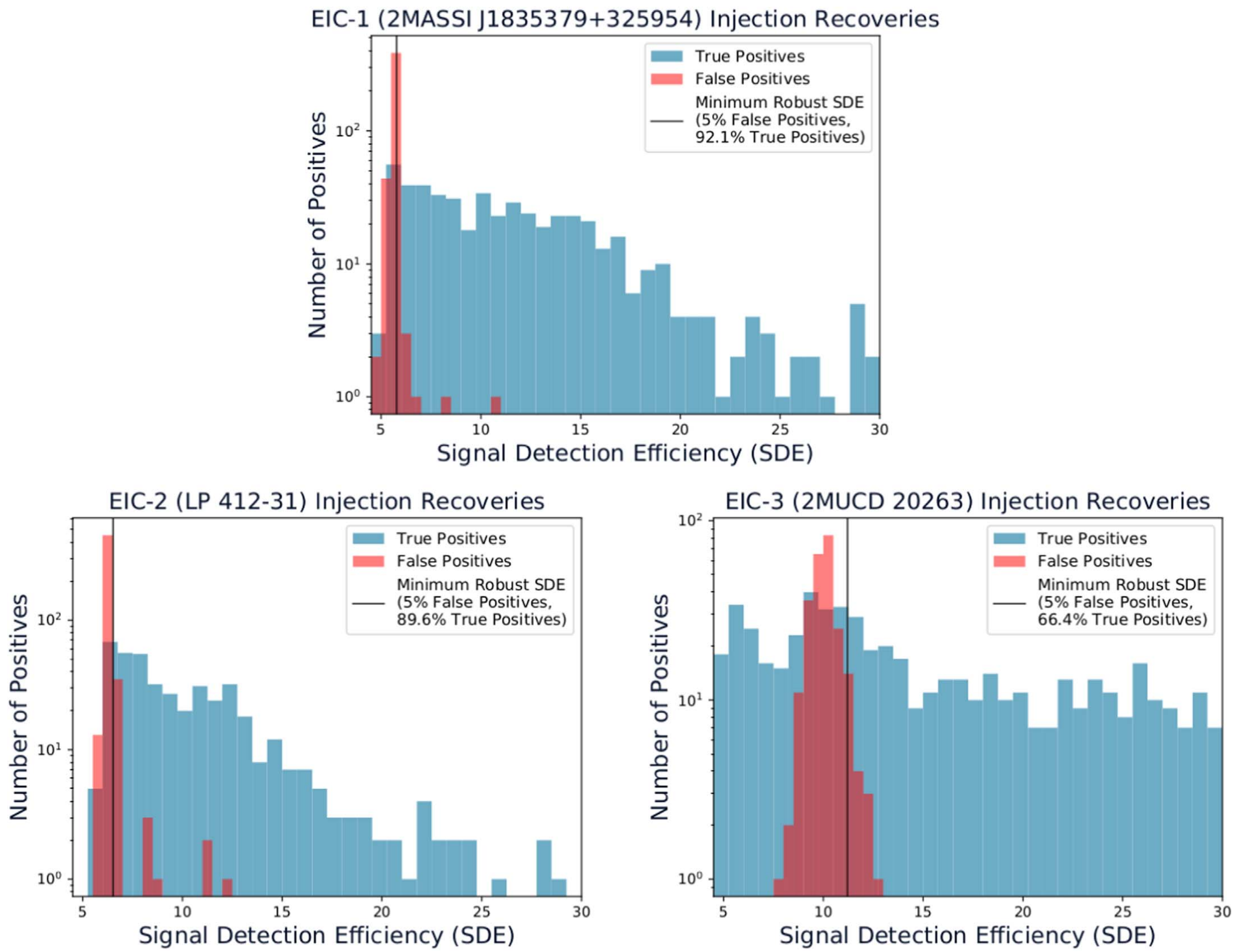

Figure 3. Signal detection efficiency (SDE) distribution for EICs. SDE is calculated as the signal-to-noise of the highest power in the recovery periodogram (Hippke & Heller 2019). The number of false positives does not continue increasing for lower SDE values because of the characteristic false positive unique to each set of lightcurves. Further discussion can be found in Section 6.2.4.

than *TESS* for single targets, in cases where the benefit of our increased photometric precision can outweigh the benefit of *TESS*'s continuous 28 day coverage.

7.2. Sensitivity Analysis and Detection Biases

The primary goal of our sensitivity analysis is setting planetary limits around the target stars that will be useful for future observations. These limits can potentially improve the efficiency of similar transit surveys, and in the case of any future RV companion candidates, help to constrain the inclination. The secondary goal is to help to identify strengths, weaknesses, and biases of our observations and routines. Using this information we can improve our future observations, data reduction, detrending, and search methods. That being stated, we believe our methods are nearly optimized, and only minor improvements can still be expected, which would not significantly change our sensitivity results.

The sensitivity maps in Figures 4–6 show two distinct gradients of decreasing sensitivity. As one would expect, these gradients are for smaller planets ($<1R_{\oplus}$, i.e., lower transit signal-to-noise), and longer periods (>3 days, i.e., fewer observed transits). Both regions of low sensitivity have more true positives than are considered successful, since many detections will have low significance that may not be followed-up. It is possible that some of these true positives would be followed-up, therefore it is likely that the map is somewhat conservative. Furthermore, our manual injection and recovery by eye test estimated that our sensitivity to TRAPPIST-1 b analogs is ∼80%, while the average automated sensitivity is ∼30%. This provides additional evidence that the automated sensitivity is conservative, especially for longer-period planets where one transit can be successfully detected by eye. As a final point, on the right side of the bottom plot of Figures 4–6, where geometric probability is considered, the gradient for longer-period planets becomes steeper, reflecting the decreasing transit probability at greater distance from the host star.

One noticeable aspect of our sensitivity maps is higher noise than similar plots from space-based missions. The noise is due to four primary factors, including the limited grid size, random transit times, the relatively low number of planets injected, and the sporadic and discontinuous schedule of EDEN observations. Most single blocks with relatively high or low sensitivity are simply due to the random sample times. Unlike

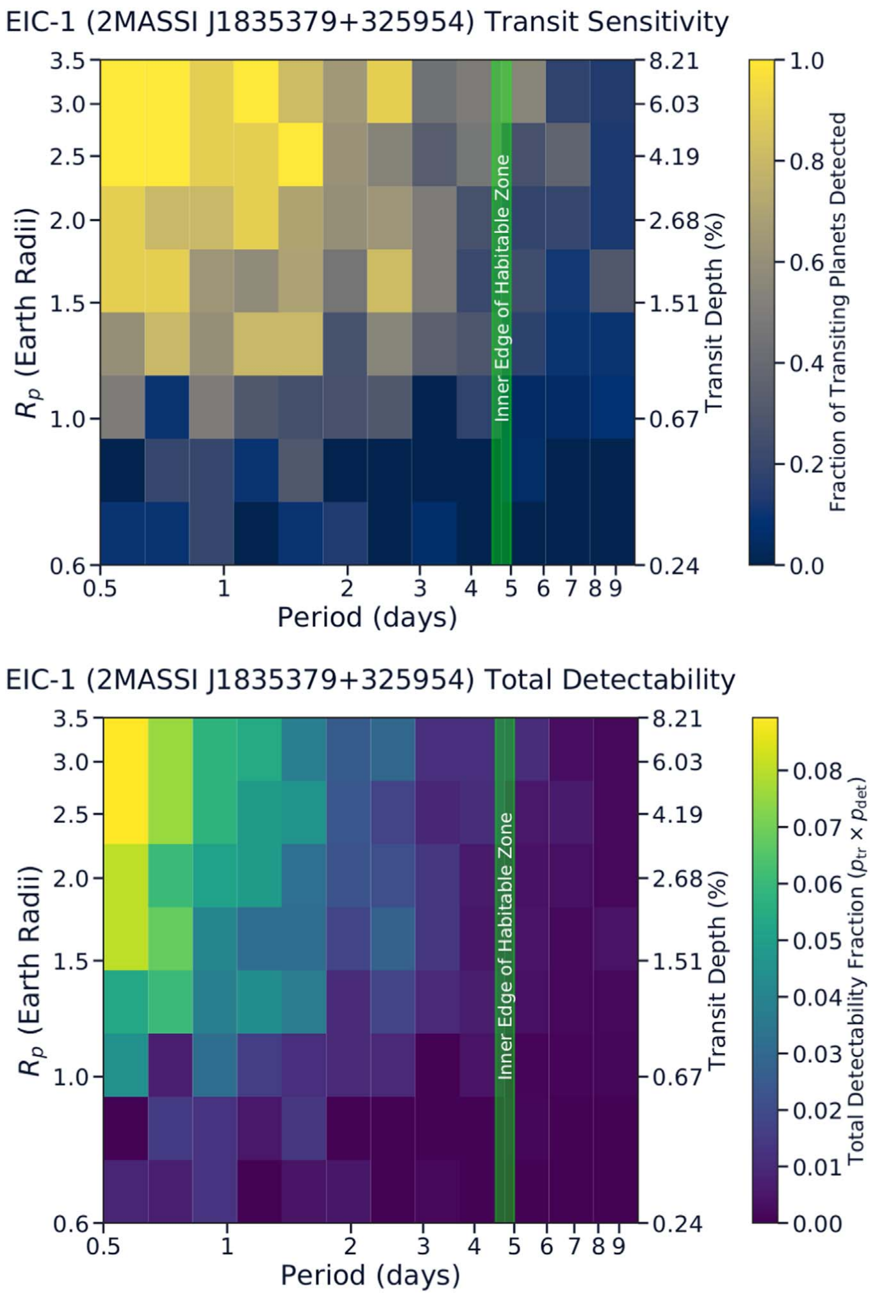

Figure 4. EIC-1 sensitivity maps. Top: pipeline sensitivity to transiting planets. Each grid block represents the fraction of transiting planets recovered out of all injected planets (both recoverable and non-recoverable) for a period and radius centered within the block. Bottom: total detectability considering the geometric transit probability ($p_{\rm tr} \times p_{\rm det}$).

observations from *Kepler*, it is possible that by misfortune a short-period planet never transits during an observation. Some columns may also have lower or higher sensitivity compared to their surroundings depending on whether or not the period is close to a harmonic of the period of observations, and therefore are more or less sensitive to phase.

7.3. Inner Planets and Outer Planets

Our detection limits for inner, shorter-period planets can place significant constraints on the probability of outer, longer-period planets, where observational coverage is lacking, in light of the occurrence rates of small planets around M dwarfs (Mulders et al. 2015a). The strongest example of this is the TRAPPIST-1 system. TRAPPIST-1b and c were detected by ground-based observations that motivated space-based follow-up, which discovered longer-period planets. For our targets, the approximate probability to detect transiting planets analogous to TRAPPIST-1b and c with *one or more transits* is ∼50%. The lack of close-in transiting planets in the extensive data sets on our targets decreases the probability that there are transiting planets at longer periods, and suggests continued observation to increase sensitivity for them is not pragmatic, given the much larger volume of data needed.

7.4. Constraints on Planet Formation Theory

The sample of planets around very cool stars is still small, since late-M dwarfs are too faint for wide-field transit surveys. In addition, higher stellar activity can further complicate the

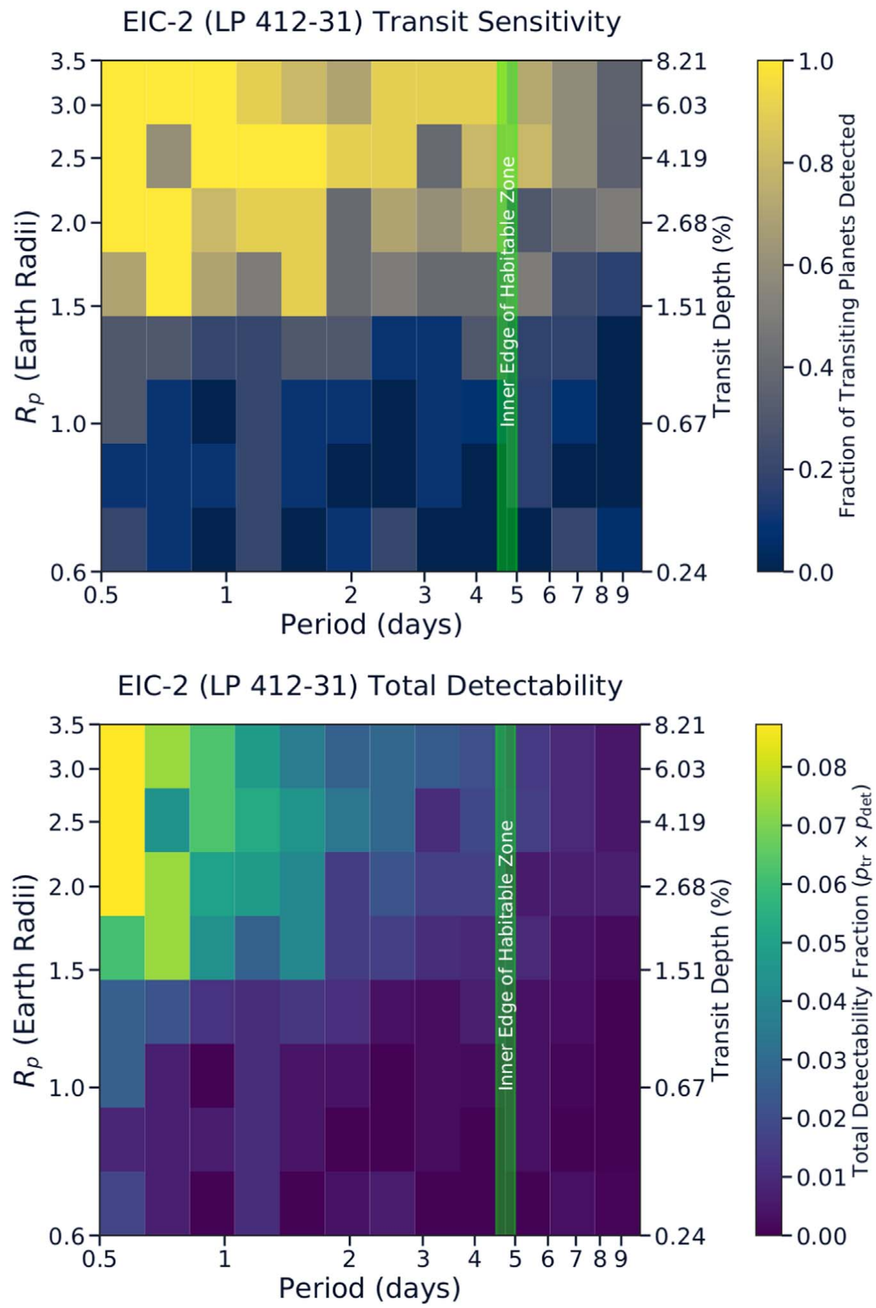

Figure 5. EIC-2 sensitivity maps. Top: pipeline sensitivity to transiting planets. Each grid block represents the fraction of transiting planets recovered out of all injected planets (both recoverable and non-recoverable) for a period and radius centered within the block. Bottom: total detectability considering the geometric transit probability ($p_{tr} \times p_{det}$).

analyses of their lightcurves (e.g., Perger et al. 2017). EDEN has unique capabilities to target these stars and any planet our survey may detect will serve as a valuable addition to this small sample. The examples of TRAPPIST-1 (Gillon et al. 2017) and GJ 3512b (Morales et al. 2019) showed how individual discoveries can challenge our current understanding of planet formation and inform tests of competing formation theories. To assess such discoveries in terms of the actual underlying population of exoplanets, it is crucial to be aware of and able to quantify the relevant selection biases. With a well-defined target selection function, an automated detection pipeline, and the thorough sensitivity analysis presented here, we are prepared to accurately model the EDEN selection biases. Correcting for these biases enables detailed occurrence rate measurements and builds the foundation to study the demographics of late-M-dwarf planetary systems.

The inferred bias can also be applied to synthetic planets from a theoretical formation model. The resulting *observable* synthetic population enables statistical comparisons between theory and observations (e.g., Mordasini et al. 2009). Detailed forward models of well-characterized exoplanet surveys can directly test planet formation models and even optimize free parameters (Mulders et al. 2018, 2019). Such dedicated M-dwarf population syntheses are powerful tools to constrain planet formation in a parameter space different from that around solar-type stars. The predictive power of exoplanet surveys depends on the survey's sensitivity and the number of targets observed: as the number of targets observed by EDEN

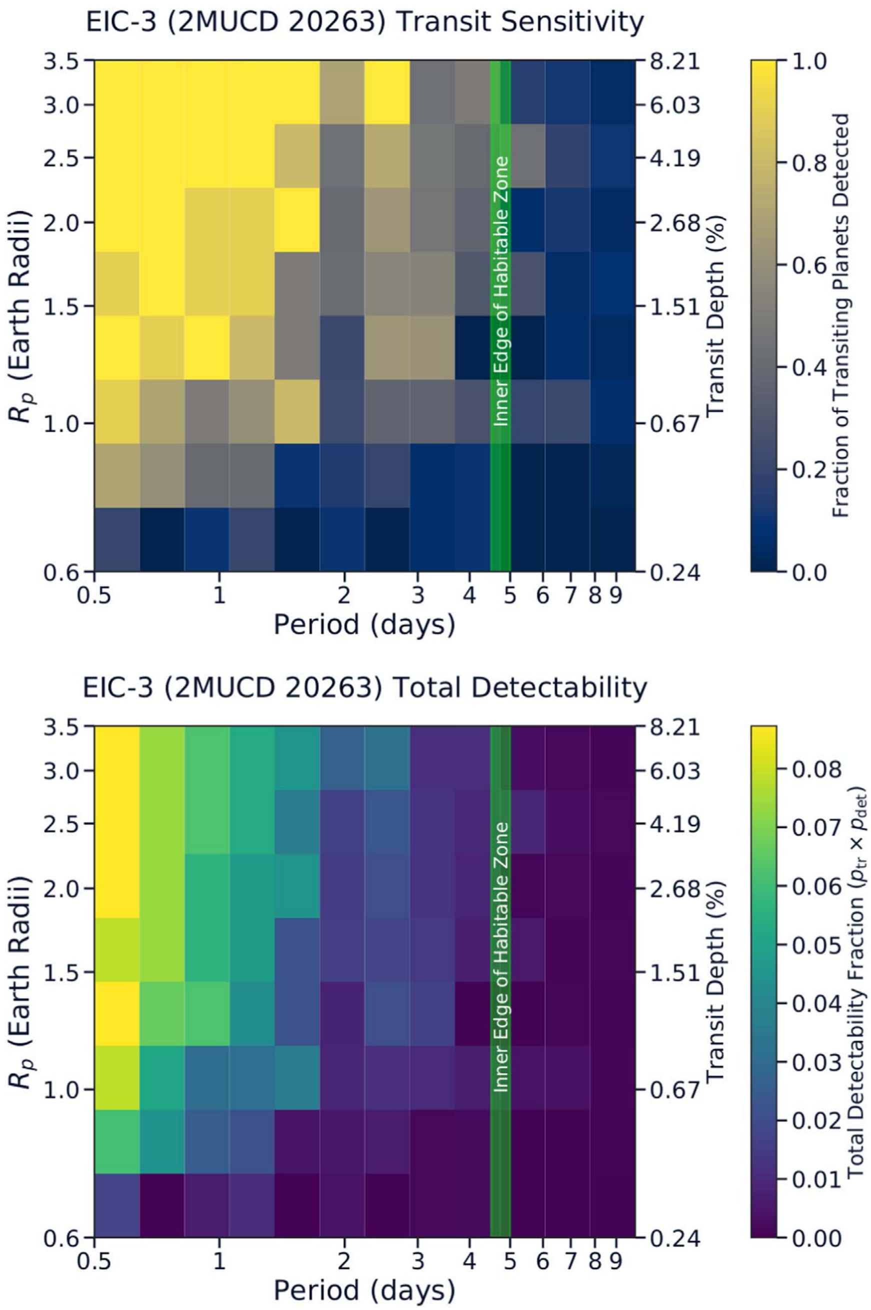

Figure 6. EIC-3 sensitivity maps. Top: pipeline sensitivity to transiting planets. Each grid block represents the fraction of transiting planets recovered out of all injected planets (both recoverable and non-recoverable) for a period and radius centered within the block. Bottom: total detectability considering the geometric transit probability ($p_{\rm tr} \times p_{\rm det}$).

increases, the emerging planet statistics will increase in significance. Currently, we are surveying targets at an increasing rate.

8. Conclusions

We present the first lightcurves and sensitivity analysis from the EDEN transiting exoplanet survey. The key results of our studies are as follows.

(1) EDEN's 0.6–2.3 m diameter telescopes provide very high-quality (median 0.28% precision) red-visual (500–900 nm) lightcurves for late-M-dwarf stars in the solar neighborhood.

(2) We present data on three nearby late-M dwarfs, obtained in the context of a multi-continental transit search campaign. Our observations include 57, 56, and 43 nights of data on the three targets EIC-1, EIC-2, and EIC-3 respectively.

(3) We review the EDEN data reduction and photometry pipeline and our detrending and transit search procedure. Our procedure has been tested, optimized, and validated through transit injection-and-recovery tests.

(4) Our lightcurves reach the sensitivity to detect transits of Earth-sized planets. Of the total of 156 observations on the three targets, no convincing candidate transit events have been identified.

Table 4
EDEN Sensitivity

	Transit Sensitivity (%)			Total Detectability (%)		
ID	0.5–2 days	2–5 days	5+ days	0.5–2 days	2–5 days	5+ days
EIC-1	60 ± 10	35 ± 5	12 ± 1	4.0 ± 0.5	1.1 ± 0.25	0.18 ± 0.05
EIC-2	40 ± 10	22 ± 5	10 ± 1	2.5 ± 0.5	0.6 ± 0.25	0.17 ± 0.05
EIC-3	80 ± 10	40 ± 5	8 ± 1	5.3 ± 0.5	1.1 ± 0.25	0.13 ± 0.05

Note. Reported transit sensitivity and total detectability values are averages for planets between one and two Earth radii. Listed errors are the standard error of the mean.

(5) We describe our transit injection-and-recovery-based approach to assess sensitivity to planetary transits as a function of planet radius and orbital period. We provide a detailed assessment of the sensitivity to transits around our three targets. We show these estimates are conservative compared to manual transit searches by eye.
(6) Our data can confidently exclude the presence of Earth-sized transiting planets with orbital periods shorter than 1 day around each of the targets. Earth-sized planets with 1–2 day periods would have been detected in our data in two transits with ∼60% probability.
(7) EDEN reaches a sensitivity to Earth-sized planets around faint red dwarf stars ($I \approx 15$ mag), which are challenging targets even for NASA's *TESS* mission. Thus, EDEN data on such systems can provide complementary information to *TESS* lightcurves.
(8) Our study demonstrates the potential of the EDEN survey to robustly probe the presence of transiting, Earth-sized planets within the habitable zones of nearby late red dwarfs and inwards, and, in case of non-detection, to set stringent upper limits on the presence of such planets.

The results reported herein benefited from collaborations and/or information exchange within NASAs Nexus for Exoplanet System Science (NExSS) research coordination network sponsored by NASAs Science Mission Directorate. This study used results from the RECONS project (recons.org). T. Henning acknowledges support from the European Research Council under the Horizon 2020 Framework Program via the ERC Advanced Grant Origins 83 24 28. B.V. Rackham acknowledges support from the Heising-Simons Foundation.

This research made use of Photutils, an Astropy package for detection and photometry of astronomical sources (Bradley et al. 2019).

The principal investigators of EDEN are D. Apai, P. Gabor, T. Henning, and W-P. Chen. Initial target selection was performed by A. Mousseau, A. Bixel, and D. Apai. Telescope allocation is organized by D. Apai, L. Mancini, W-P. Chen, C.C. Ngeow, and P. Gabor. Observations have been performed by H. Baehr, A. Bhandare. A. Bixel, R. Boyle (pilot studies as VATT's Telescope Scientist), S. Brown, J. Dietrich, A. Gibbs, M. Häberle, W. Ip, M. Keppler, L. Mancini, V. Marian, K. Molaverdikhani, A. Mousseau, J. Perez Chavez, B. Rackham, P. Sarkis, M. Schlecker, Q.J. Socia, A. Tsai and others. Software has been developed by A. Bixel, N. Espinoza, A. Gibbs, J. Perez Chavez, and B. Rackham. The EDEN automatic pipeline (`edenAP`) was developed by N. Espinoza (precursor pipeline), B. Rackham (bulk development), A. Bixel, J. Perez Chavez (calibration steps), and A. Gibbs. Data organization and collection, and the interactive data viewer were developed by A. Bixel. Detrending, transit search, and sensitivity analysis steps have been implemented and developed by A. Gibbs.

This research has made use of the Cassini 1.52 m telescope, which is operated by INAF-OAS "Osservatorio di Astrofisica e Scienza dello Spazio" of Bologna in Loiano (Italy).

We thank the mountain operations staff at the University of Arizona, Mount Lemmon Sky Center, Lulin Observatory, Calar Alto Observatory, Loaino Telescopes, Mount Graham International Observatory, Vatican Advanced Technology Telescope, and Kitt Peak National Observatory.

Facilities: Mount Lemmon Sky Center, Lulin Observatory, Calar Alto Observatory, Loiano 152 cm Cassini Telescope, Kuiper 61 inch Telescope, Vatican Advanced Technology Telescope (VATT), Bok 2.3 m Telescope.

Software: Numpy (van der Walt et al. 2011), Pandas (McKinney 2010), Scipy (Virtanen et al. 2019), Astropy (Price-Whelan et al. 2018), Photutils (Bradley et al. 2019), astronomy.net (Lang et al. 2010), `TLS` (Hippke & Heller 2019), `batman` (Kreidberg 2015), `edenAP`.

Appendix
Observation Log

In case of future research or discoveries where EDEN data may be useful, we list all periods of observations for EIC-1, EIC-2, and EIC-3 in Tables 5–7.

Table 5
EIC-1 List of Observations

Telescope	Local Date	BJD Start (−245700)	BJD End (−245700)	Hours
CAHA	2018 Jun 26	1296.354	1296.681	7.8
CASSINI	2018 Jun 29	1299.354	1299.612	6.2
CASSINI	2018 Jun 30	1300.342	1300.607	6.4
CAHA	2018 Jun 30	1300.356	1300.433	1.9
CAHA	2018 Jul 1	1301.357	1301.409	1.2
CAHA	2018 Jul 2	1302.349	1302.407	1.4
CASSINI	2018 Jul 2	1302.353	1302.379	0.6
CAHA	2018 Jul 3	1303.354	1303.379	0.6
CAHA	2018 Jul 4	1304.367	1304.652	6.8
KUIPER	2018 Jul 18	1318.743	1318.959	5.2
CASSINI	2018 Jul 19	1319.328	1319.615	6.9
CAHA	2018 Jul 19	1319.346	1319.564	5.2
KUIPER	2018 Jul 19	1319.868	1319.982	2.7
CASSINI	2018 Jul 20	1320.328	1320.599	6.5
CAHA	2018 Jul 20	1320.348	1320.658	7.5
CASSINI	2018 Jul 21	1321.33	1321.562	5.6
CAHA	2018 Jul 22	1322.351	1322.675	7.8
CASSINI	2018 Jul 23	1323.332	1323.615	6.8
CAHA	2018 Jul 23	1323.347	1323.454	2.6
CAHA	2018 Jul 24	1324.346	1324.671	7.8
CASSINI	2018 Jul 25	1325.5	1325.62	2.9
CAHA	2018 Jul 25	1325.507	1325.671	3.9
CAHA	2018 Jul 26	1326.508	1326.671	3.9
LOT	2018 Jul 29	1329.147	1329.211	1.5
KUIPER	2018 Sep 3	1365.658	1365.812	3.7
KUIPER	2018 Sep 4	1366.687	1366.773	2.1
KUIPER	2018 Sep 5	1367.711	1367.802	2.2
KUIPER	2018 Sep 6	1368.624	1368.808	4.4
KUIPER	2018 Sep 7	1369.6	1369.804	4.9
CAHA	2018 Sep 16	1378.308	1378.493	4.5
CAHA	2018 Sep 17	1379.299	1379.303	0.1
BOK	2018 Sep 17	1379.643	1379.753	2.6
LOT	2018 Sep 18	1379.995	1380.147	3.6
LOT	2018 Sep 19	1381.022	1381.144	2.9
LOT	2018 Sep 20	1382.006	1382.143	3.3
CAHA	2018 Sep 20	1382.297	1382.472	4.2
KUIPER	2018 Sep 20	1382.605	1382.777	4.1
CAHA	2018 Sep 21	1383.288	1383.479	4.6
CAHA	2018 Sep 22	1384.287	1384.486	4.8
CAHA	2018 Sep 23	1385.304	1385.482	4.3
CAHA	2018 Sep 24	1386.294	1386.463	4.0
CAHA	2018 Sep 25	1387.299	1387.423	3.0
SCHULMAN	2018 Sep 25	1387.605	1387.714	2.6
CAHA	2018 Sep 28	1390.321	1390.46	3.3
SCHULMAN	2018 Sep 28	1390.59	1390.729	3.3
CAHA	2018 Sep 30	1392.278	1392.417	3.3
CAHA	2018 Oct 17	1409.282	1409.405	3.0
LOT	2018 Oct 19	1411.061	1411.086	0.6
CAHA	2018 Oct 19	1411.341	1411.414	1.8
LOT	2018 Oct 20	1411.964	1412.037	1.8
CAHA	2018 Oct 22	1414.284	1414.364	1.9
CAHA	2018 Oct 24	1416.265	1416.366	2.4
CAHA	2018 Oct 25	1417.253	1417.37	2.8
KUIPER	2018 Oct 31	1423.597	1423.644	1.1
KUIPER	2018 Nov 3	1426.555	1426.645	2.2
KUIPER	2018 Nov 4	1427.55	1427.642	2.2

Table 6
EIC-2 List of Observations

Telescope	Local Date	BJD Start (−245700)	BJD End (−245700)	Hours
KUIPER	2018 Sep 4	1366.798	1367.012	5.1
KUIPER	2018 Sep 5	1367.817	1368.024	5.0
KUIPER	2018 Sep 7	1369.812	1370.013	4.8
LOT	2018 Sep 17	1379.16	1379.372	5.1
CAHA	2018 Sep 17	1379.48	1379.722	5.8
BOK	2018 Sep 17	1379.776	1379.874	2.3
LOT	2018 Sep 18	1380.156	1380.342	4.4
CAHA	2018 Sep 18	1380.54	1380.719	4.3
LOT	2018 Sep 19	1381.151	1381.338	4.5
LOT	2018 Sep 20	1382.15	1382.339	4.5
KUIPER	2018 Sep 20	1382.787	1383.028	5.8
CAHA	2018 Sep 21	1383.505	1383.714	5.0
CAHA	2018 Sep 22	1384.511	1384.716	4.9
CAHA	2018 Sep 23	1385.502	1385.714	5.1
CAHA	2018 Sep 24	1386.482	1386.616	3.2
CAHA	2018 Sep 27	1389.545	1389.712	4.0
CAHA	2018 Sep 28	1390.484	1390.718	5.6
CAHA	2018 Sep 30	1392.433	1392.714	6.7
LOT	2018 Oct 16	1408.199	1408.223	0.6
CAHA	2018 Oct 17	1409.415	1409.636	5.3
CAHA	2018 Oct 18	1410.632	1410.651	0.5
LOT	2018 Oct 19	1411.096	1411.381	6.8
CAHA	2018 Oct 19	1411.433	1411.505	1.7
LOT	2018 Oct 20	1412.142	1412.391	6.0
CAHA	2018 Oct 21	1413.392	1413.723	7.9
CAHA	2018 Oct 22	1414.378	1414.58	4.9
CAHA	2018 Oct 23	1415.392	1415.396	0.1
CAHA	2018 Oct 24	1416.377	1416.734	8.6
CAHA	2018 Oct 25	1417.38	1417.571	4.6
KUIPER	2018 Oct 31	1423.662	1424.016	8.5
KUIPER	2018 Nov 1	1424.66	1425.032	8.9
KUIPER	2018 Nov 2	1425.687	1425.994	7.4
KUIPER	2018 Nov 3	1426.658	1427.037	9.1
KUIPER	2018 Nov 4	1427.683	1428.045	8.7
KUIPER	2018 Nov 9	1432.627	1432.961	8.0
KUIPER	2018 Nov 10	1433.64	1434.041	9.6
KUIPER	2018 Nov 11	1434.605	1435.018	9.9
VATT	2018 Nov 11	1434.632	1435.013	9.1
VATT	2018 Nov 12	1435.665	1436.011	8.3
VATT	2018 Nov 13	1436.664	1437.006	8.2
VATT	2018 Nov 14	1437.84	1438.002	3.9
VATT	2018 Nov 15	1438.656	1438.997	8.2
VATT	2018 Nov 16	1439.767	1440.005	5.7
VATT	2018 Nov 17	1440.709	1441.006	7.1
VATT	2018 Nov 18	1441.665	1442	8.0
VATT	2018 Nov 19	1442.654	1442.997	8.2
CASSINI	2018 Nov 28	1451.28	1451.499	5.3
CASSINI	2018 Nov 29	1452.338	1452.46	2.9
CASSINI	2018 Dec 4	1457.263	1457.537	6.6
KUIPER	2018 Dec 9	1462.559	1462.892	8.0
CASSINI	2018 Dec 10	1463.248	1463.539	7.0
CASSINI	2018 Dec 11	1464.274	1464.545	6.5
BOK	2018 Dec 17	1470.692	1470.811	2.9
CAHA	2018 Dec 20	1473.355	1473.46	2.5

Table 7
EIC-3 List of Observations

Telescope	Local Date	BJD Start (−245700)	BJD End (−245700)	Hours
KUIPER	2018 Dec 9	1462.903	1463.049	3.5
VATT	2018 Dec 18	1471.69	1471.944	6.1
VATT	2018 Dec 19	1472.689	1473.051	8.7
VATT	2018 Dec 20	1473.696	1473.955	6.2
VATT	2018 Dec 28	1481.742	1482.059	7.6
VATT	2018 Dec 29	1482.796	1483.064	6.4
VATT	2018 Dec 30	1483.774	1484.064	7.0
KUIPER	2019 Jan 2	1486.675	1487.041	8.8
KUIPER	2019 Jan 3	1487.762	1488.039	6.6
VATT	2019 Jan 8	1492.596	1493.044	10.8
CAHA	2019 Jan 9	1493.326	1493.735	9.8
CAHA	2019 Jan 10	1494.307	1494.726	10.1
VATT	2019 Jan 10	1494.806	1494.985	4.3
VATT	2019 Jan 11	1495.608	1496.034	10.2
CAHA	2019 Jan 14	1498.27	1498.726	10.9
CAHA	2019 Jan 15	1499.289	1499.717	10.3
CAHA	2019 Jan 16	1500.281	1500.469	4.5
LOT	2019 Jan 17	1500.962	1501.322	8.7
LOT	2019 Jan 18	1502.043	1502.075	0.8
VATT	2019 Jan 19	1503.589	1504.015	10.2
VATT	2019 Jan 20	1504.586	1504.8	5.1
VATT	2019 Jan 22	1506.657	1507.006	8.4
VATT	2019 Jan 23	1507.588	1508.002	9.9
BOK	2019 Jan 24	1508.605	1509.01	9.7
BOK	2019 Jan 25	1509.582	1509.982	9.6
VATT	2019 Jan 26	1510.591	1510.987	9.5
VATT	2019 Jan 27	1511.582	1511.99	9.8
LOT	2019 Jan 28	1511.959	1512.34	9.1
VATT	2019 Jan 28	1512.61	1512.743	3.2
LOT	2019 Jan 29	1512.952	1513.336	9.2
LOT	2019 Jan 30	1513.968	1514.332	8.7
VATT	2019 Jan 30	1514.679	1514.703	0.6
LOT	2019 Jan 31	1514.973	1515.324	8.4
VATT	2019 Jan 31	1515.663	1515.796	3.2
LOT	2019 Feb 7	1521.973	1522.3	7.8
LOT	2019 Feb 8	1523.045	1523.237	4.6
LOT	2019 Feb 9	1524.031	1524.234	4.9
LOT	2019 Feb 10	1524.997	1525.192	4.7
LOT	2019 Feb 11	1526.023	1526.236	5.1
LOT	2019 Feb 12	1526.967	1527.235	6.4
LOT	2019 Feb 13	1528.016	1528.17	3.7
LOT	2019 Feb 14	1528.994	1529.175	4.3

ORCID iDs

Aidan Gibbs https://orcid.org/0000-0002-9027-4456
Alex Bixel https://orcid.org/0000-0003-2831-1890
Dániel Apai https://orcid.org/0000-0003-3714-5855
Néstor Espinoza https://orcid.org/0000-0001-9513-1449
Luigi Mancini https://orcid.org/0000-0002-9428-8732
Wen-Ping Chen https://orcid.org/0000-0003-0262-272X
Quentin Jay Socia https://orcid.org/0000-0002-7434-0863
Chow-Choong Ngeow https://orcid.org/0000-0001-8771-7554
An-Li Tsai https://orcid.org/0000-0002-3211-4219
Victor Marian https://orcid.org/0000-0003-1733-9281
Hans Baehr https://orcid.org/0000-0002-0880-8296
Karan Molaverdikhani https://orcid.org/0000-0002-0502-0428
Paula Sarkis https://orcid.org/0000-0001-8128-3126

References

Bailer-Jones, C. A. L., & Lamm, M. 2003, MNRAS, 339, 477
Barnes, J. R., Jenkins, J. S., Jones, H. R. A., et al. 2014, MNRAS, 439, 3094
Berdyugina, S. V., Harrington, D. M., Kuzmychov, O., et al. 2017, ApJ, 847, 61
Berger, E., Basri, G., Gizis, J. E., et al. 2008, ApJ, 676, 1307
Blake, C. H., Bloom, J. S., Latham, D. W., et al. 2008, PASP, 120, 860
Bradley, L., Sipocz, B., Robitaille, T., et al. 2019, astropy/photutils: v0.6, Zenodo, doi:10.5281/zenodo.2533376
Brown, T. M., Baliber, N., Bianco, F. B., et al. 2013, PASP, 125, 1031
Carson, J. C., Marengo, M., Patten, B. M., et al. 2011, ApJ, 743, 141
Claret, A. 1998, yCat, J/A+A/335/647, 0
de Wit, J., Wakeford, H. R., Gillon, M., et al. 2016, Natur, 537, 69
de Wit, J., Wakeford, H. R., Lewis, N. K., et al. 2018, NatAs, 2, 214
Delrez, L., Gillon, M., Queloz, D., et al. 2018, Proc. SPIE, 10700, 107001I
Deshpande, R., Blake, C. H., Bender, C. F., et al. 2013, AJ, 146, 156
Dittmann, J. A., Irwin, J. M., Charbonneau, D., & Newton, E. R. 2016, ApJ, 818, 153
Dressing, C. D., & Charbonneau, D. 2015, ApJ, 807, 45

Espinoza, N., & Jordán, A. 2016, MNRAS, 457, 3573
Gillon, M., Triaud, A. H., Demory, B. O., et al. 2017, Natur, 542, 456
Grant Williams, G., Olszewski, E. d., Lesser, M. P., & Burge, J. H. 2004, Proc. SPIE, 5492, 787
Greene, T. P., Line, M. R., Montero, C., et al. 2016, ApJ, 817, 17
Hallinan, G., Antonova, A., Doyle, J. G., et al. 2008, ApJ, 684, 644
Hallinan, G., Littlefair, S. P., Cotter, G., et al. 2015, Natur, 523, 568
Hardegree-Ullman, K. K., Cushing, M. C., Muirhead, P. S., & Christiansen, J. L. 2019, AJ, 158, 75
Henry, T. J., Jao, W.-C., Winters, J. G., et al. 2018, AJ, 155, 265
Hippke, M., David, T. J., Mulders, G. D., & Heller, R. 2019, AJ, 158, 143
Hippke, M., & Heller, R. 2019, A&A, 623, A39
Howell, S. B., & Tavackolimehr, A. 2019, Handbook of CCD Astronomy (Cambridge: Cambridge Univ. Press)
Irwin, J., Berta, Z. K., Burke, C. J., et al. 2011, ApJ, 727, 56
Jehin, E., Gillon, M., Queloz, D., et al. 2011, Msngr, 145, 2
Kasting, J. F., Whitmire, D. P., & Reynolds, R. T. 1993, Icar, 101, 108
Kirkpatrick, J. D., Henry, T. J., & Simons, D. A. 1995, AJ, 109, 797
Kopparapu, R. K., Ramirez, R. M., SchottelKotte, J., et al. 2014, ApJL, 787, L29
Kovács, G., Zucker, S., & Mazeh, T. 2002, A&A, 391, 369
Kreidberg, L. 2015, PASP, 127, 1161
Kuzmychov, O., Berdyugina, S. V., & Harrington, D. M. 2017, ApJ, 847, 60
Lang, D., Hogg, D. W., Mierle, K., Blanton, M., & Roweis, S. 2010, AJ, 139, 1782
Lépine, S., & Shara, M. M. 2005, AJ, 129, 1483
Lépine, S., Shara, M. M., & Rich, R. M. 2002, AJ, 124, 1190
Lustig-Yaeger, J., Meadows, V. S., & Lincowski, A. P. 2019, AJ, 158, 27
Mandel, K., & Agol, E. 2002, ApJL, 580, L171
McKinney, W. 2010, in Proc. 9th Python in Science Conf., ed. S. van der Walt & J. Millman (Austin, TX: SciPy), 51
Morales, J. C., Mustill, A. J., Ribas, I., et al. 2019, Sci, 365, 1441
Mordasini, C., Alibert, Y., Benz, W., & Naef, D. 2009, A&A, 501, 1161
Morley, C. V., Kreidberg, L., Rustamkulov, Z., Robinson, T., & Fortney, J. J. 2017, ApJ, 850, 121
Mulders, G. D., Mordasini, C., Pascucci, I., et al. 2019, ApJ, 887, 157
Mulders, G. D., Pascucci, I., & Apai, D. 2015a, ApJ, 798, 112
Mulders, G. D., Pascucci, I., & Apai, D. 2015b, ApJ, 814, 130
Mulders, G. D., Pascucci, I., Apai, D., & Ciesla, F. J. 2018, AJ, 156, 24
Nutzman, P., & Charbonneau, D. 2008, PASP, 120, 317
Perger, M., García-Piquer, A., Ribas, I., et al. 2017, A&A, 598, A26
Price-Whelan, A. M., Sipőcz, B. M., Günther, H. M., et al. 2018, AJ, 156, 123
Rajpurohit, A., Allard, F., Teixeira, G. D. C., et al. 2018, A&A, 610, A19
Reid, I. N., Cruz, K. L., Laurie, S. P., et al. 2003, AJ, 125, 354
Reiners, A., & Basri, G. 2009, ApJ, 705, 1416
Ricker, G. R., Winn, J. N., Vanderspek, R., et al. 2015, JATIS, 1, 014003
Rodler, F., Deshpande, R., Zapatero Osorio, M. R., et al. 2012, A&A, 538, A141
Saur, J., Fischer, C., Wennmacher, A., et al. 2018, ApJ, 859, 74
Savitzky, A., & Golay, M. J. E. 1964, AnaCh, 36, 1627
Siegler, N., Close, L. M., Cruz, K. L., Martin, E. L., & Reid, I. N. 2005, ApJ, 621, 1023
Southworth, J., Hinse, T. C., Jorgensen, U. G., et al. 2009, MNRAS, 396, 1023
Stassun, K. G., Oelkers, R. J., Pepper, J., et al. 2018, AJ, 156, 102
Stelzer, B., Schmitt, J. H. M. M., Micela, G., & Liefke, C. 2006, A&A, 460, L35
Stetson, P. B. 1987, PASP, 99, 191
Tal-Or, L., Zechmeister, M., Reiners, A., et al. 2018, A&A, 614, A122
Tanner, A., White, R., Bailey, J., et al. 2012, ApJS, 203, 10
Tinetti, G., Drossart, P., Eccleston, P., et al. 2018, ExA, 46, 135
Tsuji, T., & Nakajima, T. 2016, PASJ, 68, 13
van der Walt, S., Colbert, S. C., & Varoquaux, G. 2011, CSE, 13, 22
Virtanen, P., Gommers, R., Oliphant, T. E., et al. 2019, arXiv:1907.10121
Wakeford, H. R., Lewis, N. K., Fowler, J., et al. 2019, AJ, 157, 11
Weiner, B. J., Sand, D., Gabor, P., et al. 2018, Proc. SPIE, 10704, 107042H
Zhang, Z., Zhou, Y., Rackham, B. V., & Apai, D. 2018, AJ, 156, 178

工作報告

鹿林天文台觀測時數統計(2003-2020)

林宏欽、蕭翔耀、林啟生、侯偉傑

鹿林天文台自 2002 年 9 月開始人員常駐，2003 年鹿林一米望遠鏡(LOT)上線，開始有正式觀測時數紀錄，可供瞭解鹿林長期的天氣狀況。依 2003-2020 共 18 年的統計結果，鹿林天文台年平均觀測時數為 1146 小時。一年可分為四個觀測季，

- 最佳觀測季：10-12 月。
- 次佳觀測季：1-3 月。
- 最差觀測季：4-6 月。4 月開始進入雨季，5-6 月受梅雨影響，天氣最差。
- 次差觀測季：7-9 月。主要受颱風及西南氣流影響，天氣變化大。此外夏季晝長夜短，每晚可觀測時間比冬季為短。

詳細統計資料及統計如下：

表 1 每月觀測時數統計 (2003-2020)

Month	1	2	3	4	5	6	7	8	9	10	11	12	Total
2003	78.75	142.5	147.5	126.5	129.75	24	222.5	137.75	142	149.25	166.5	271.5	**1738.5**
2004	125	145.98	163	110.5	106.25	133	48	142	116	219.75	214.5	232.45	**1756.43**
2005	163.25	94.75	143	144.75	136.25	45	167.75	76	129.25	210.25	216.25	129	**1655.5**
2006	129	149	126.05	86.8	59.5	39.3	91.57	111.65	60.05	150.6	71.75	132	**1207.27**
2007	127.32	128.55	116.4	53.75	106.6	54	128.88	56.6	69.55	172.63	160.55	261.09	**1435.92**
2008	179	118.25	138.5	85.25	98.25	37	88.4	118.95	59.8	191.38	152.55	211.17	**1478.5**
2009	234.52	165.7	146.75	71.8	167.4	81.75	76.6	6.8	0	175.6	175.8	169.8	**1472.52**
2010	206.9	100.6	181.3	75.8	86.05	26.5	99.85	98.3	109.95	139.8	163.65	169.65	**1458.35**
2011	90.8	123.8	75.9	151.45	56.6	61.5	81.75	97.9	90.1	136.95	87.2	115.25	**1169.2**
2012	113.42	64.88	168.23	32.75	74.3	35.15	106.4	35.7	117.35	214.51	93.81	132.21	**1188.71**
2013	153.58	183.63	134.26	55.83	41.02	80.14	88.05	72.2	107.84	200.57	136.1	86	**1339.22**
2014	269.62	109.8	78.7	135.95	32.4	33.7	114.65	110.9	134.39	232.33	166.15	137.3	**1555.89**
2015	188.55	131.65	111.1	124	64.2	146.9	87.45	45.1	93.25	145.4	197.05	161.2	**1495.85**
2016	75.4	60.25	72.8	82.9	86.05	114.05	123.95	61	42.85	142.2	171.85	193.27	**1226.57**
2017	160.85	105.3	96.4	86.9	84.55	76.1	105.25	139.9	128.2	187.8	134.55	156.7	**1462.5**
2018	110.4	66.7	173.7	125.7	190.7	70.35	80.65	50.35	93.45	142.05	148.15	170.05	**1422.25**
2019	196.3	136.35	124	124.35	39.1	56.55	77.35	58.2	137.45	193.75	200.29	180.2	**1523.89**
2020	234.4	191.1	121.35	98.75	88.35	137.9	102.5	78.3	82.28	163.82	185.65	125.44	**1609.84**
Average	**155.75**	**122.97**	**129.05**	**99.35**	**89.01**	**67.62**	**101.32**	**84.30**	**98.24**	**174.96**	**159.65**	**167.30**	**1455.38**
Average(10yrs)	**159.33**	**117.35**	**115.64**	**101.86**	**75.73**	**81.23**	**96.80**	**74.96**	**102.72**	**175.94**	**152.08**	**145.76**	**1399.39**

* 2009 年因受莫拉克颱風八八風災影響，自八月八日起至十月初約 2 個月期間道路中斷並停電，無法觀測。所以 2009 年之八、九月觀測時數很少，甚至為 0。

**Average 值為扣除最高及最低值後取平均。

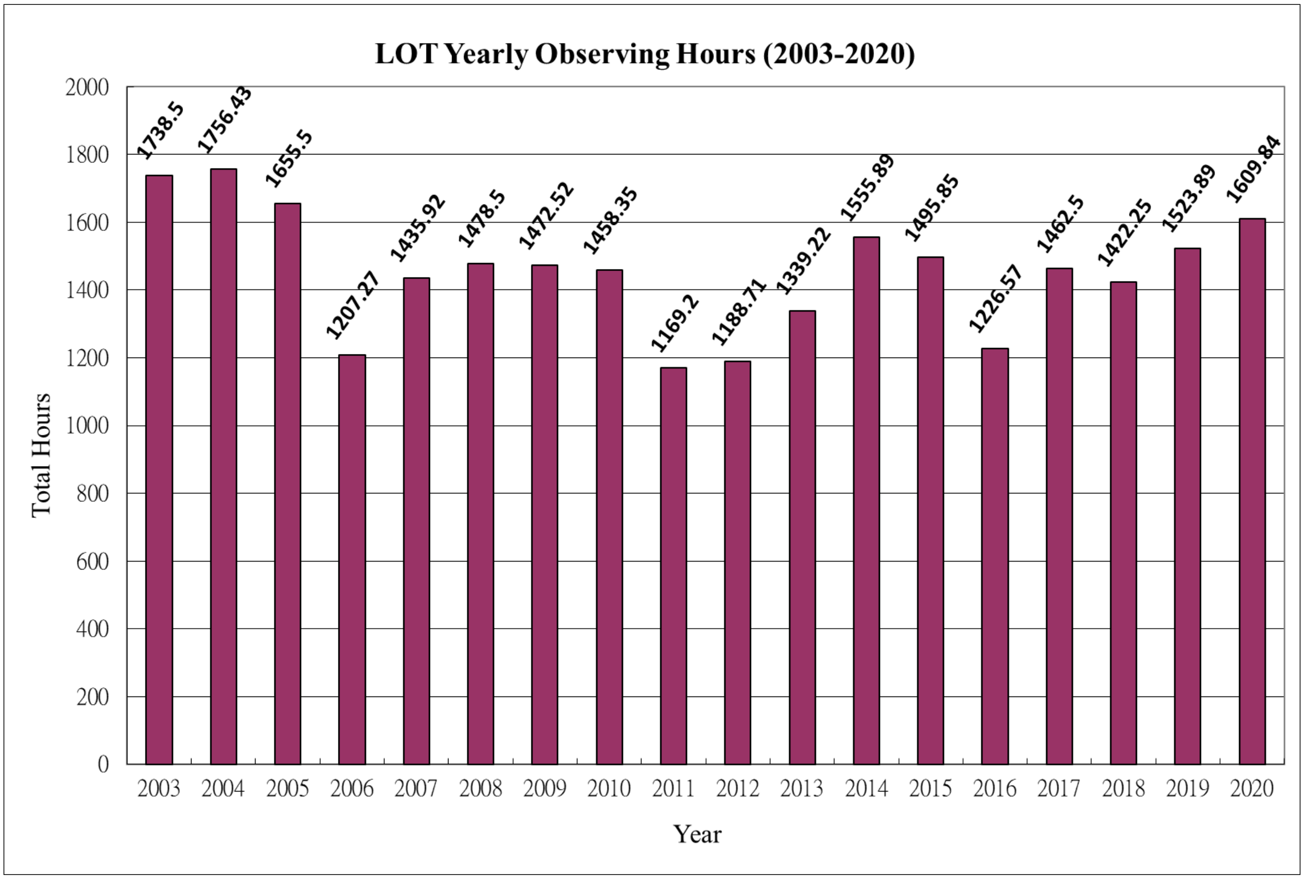

圖 1　鹿林天文台年平均觀測時數統計圖(2003-2020)

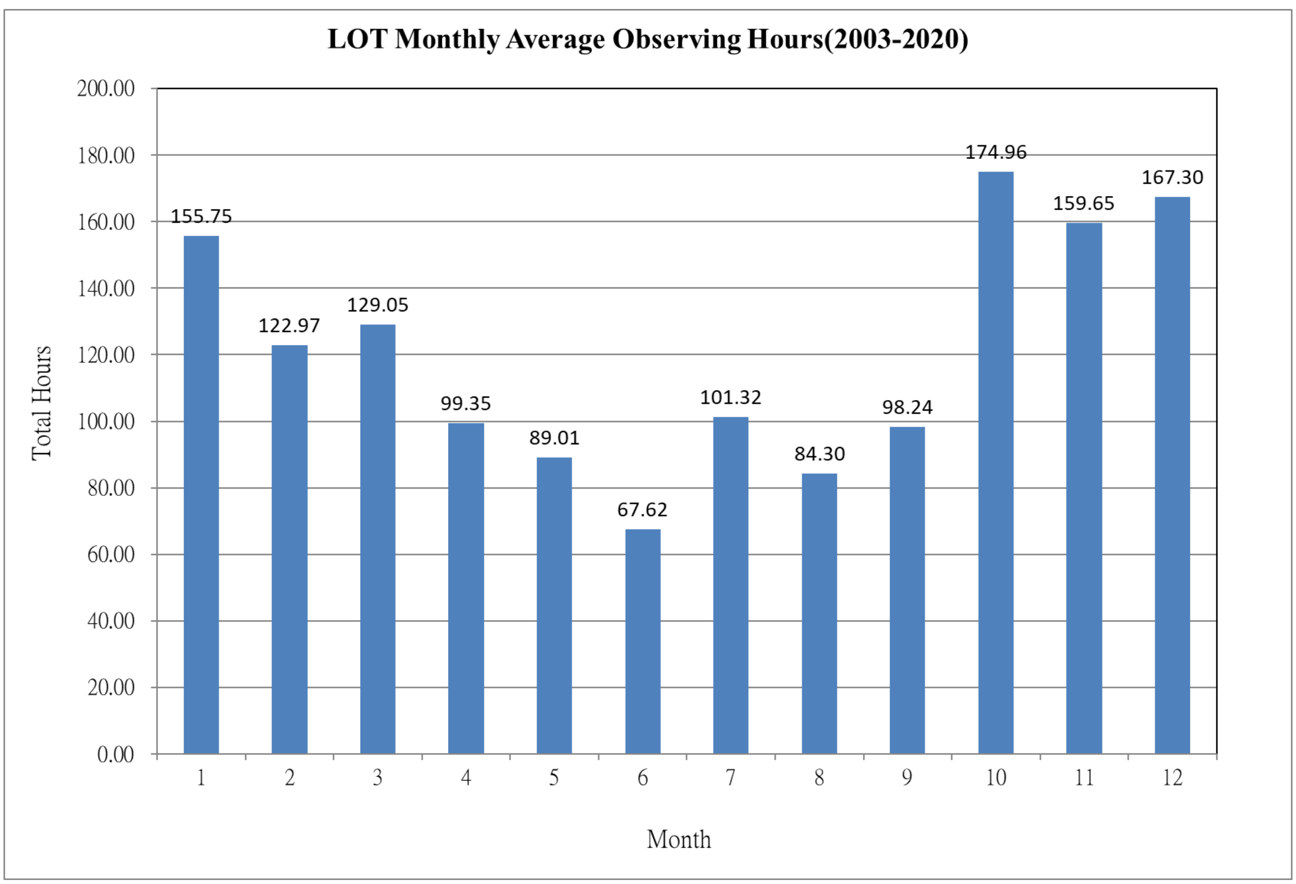

圖 2　鹿林天文台月平均觀測時數統計圖 (2003-2020)

鹿林天文台 LOT 觀測研究計畫統計 (2020)

鹿林天文台一米望遠鏡(LOT)觀測研究計畫時間安排以 4 個月為一個觀測期，一年分為三期（A = 1-4 月、B = 5-8 月、C = 9-12 月），其中字母 E、R 和*R 分別為天文觀測教學、國內研究計畫與國際合作計畫，而大型計畫 EDEN 亦為國際合作計畫。

2020 年的觀測計畫如下，統計結果：E 天文觀測教學有 4 個，佔 10%。R 國內研究計畫有 11 個，佔 29%。*R 國際合作計畫有 23 個，佔 61%。

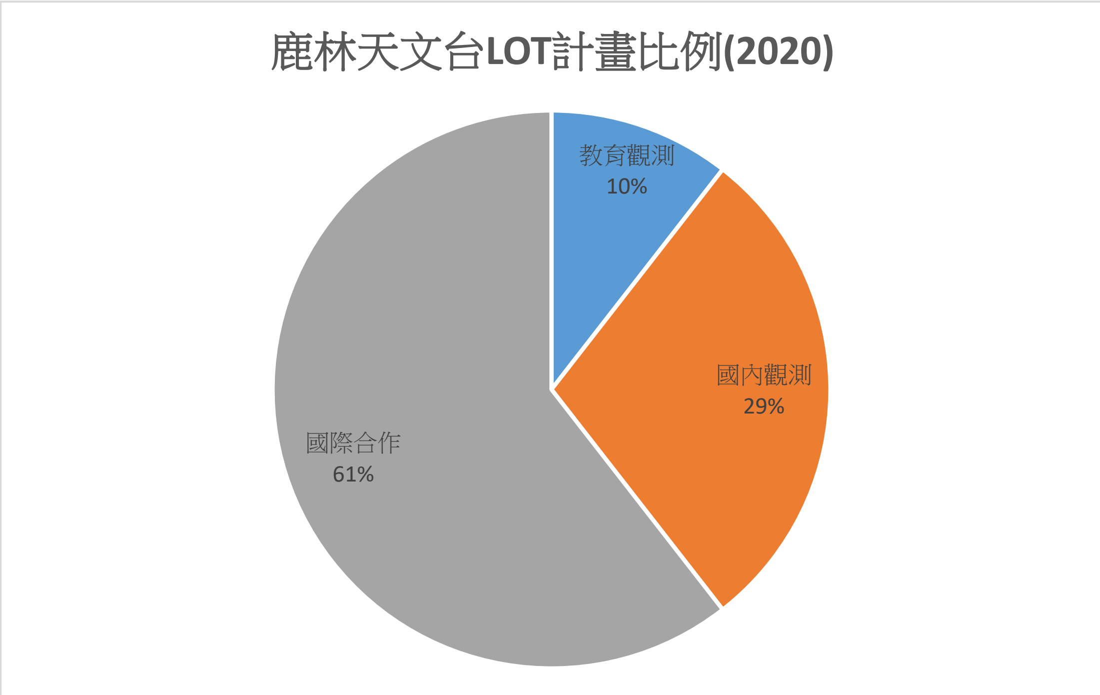

LOT2020A Semester (01 January – 30 April, 2020)

Education Program:

E01 – Observing Training for “Advanced Observational Astronomy” Course

PI: Chow-Choong Ngeow (cngeow@astro.ncu.edu.tw)

Large Program:

EDEN – Exo-earth Discovery and Exploration Network

PI: W-P Chen (wchen@astro.ncu.edu.tw)

Research Program:

*R01 – Dedicated Follow-Up Obseravations of GW Optical Counterparts with LOT

P.I.: Chow-Choong Ngeow (cngeow@astro.ncu.edu.tw)

*R02 – Hα and Hβ narrow bands observation of the UV and FIR resolved local galaxies

P.I.: Cheng Cheng (chengcheng@nao.cas.cn)

*R03 – Narrow-band Imaging of Extended Planetary Nebulae (II) - Abell 24 and Abell 31

P.I.: Chih-Hao Hsia (chhsia@must.edu.mo)

*R04 – Transients within Hours of Explosion

P.I.: Yen-Chen Pan (yenchen.pan@nao.ac.jp)

R05 – ToO Observations of Cosmic Transient Events

P.I.: Albert Kong (akong@phys.nthu.edu.tw)

*R06 – Identifying Gamma-Ray Pulsars Found by Machine Leaning

P.I.: Kwan Lok Li (lilirayhk@gmail.com)

*R07 – Survey of the synchronous binary asteroids in the Solar System

P.I.: Polińska Magdalena (polinska@amu.edu.pl)

*R08 – Visible Taxonomical Classification for Unclassified Near-Earth Asteroids (I)

P.I.: Chih-Hao Hsia (chhsia@must.edu.mo)

*R09 – A Trial to Detect Non-Principal Axis Rotation of Comet 289P/Blanpain

P.I.: Daisuke Kinoshita (kinoshita@astro.ncu.edu.tw)

R10 – The rotation period confirmations for large super-fast rotating asteroids

P.I.: Ting-Shuo Yeh (tsyeh@astro.ncu.edu.tw)

R12 – Monitoring of comet 29P/SW1 and (596) Scheila for activity trends and outburst

P.I.: Zhong-Yi Lin (zylin@astro.ncu.edu.tw)

LOT2020B Semester (01 May – 31 August, 2020)

Education Program:

E01 – Practical Class of ”Fundamentals of Observational Astronomy”

P.I.: Albert Kong (akong@phys.nthu.edu.tw)

E02 – Student Training for NTHU’s “Observational Astronomy” Course

P.I.: Shih-Ping Lai (slai@phys.nthu.edu.tw)

Large Program:

EDEN – Exo-earth Discovery and Exploration Network

PI: W-P Chen (wchen@astro.ncu.edu.tw)

Research Program:

*R01 – Calibrating the griz-Band PLZ Relations using RR Lyrae in Globular Clusters

P.I.: Chow-Choong Ngeow (cngeow@astro.ncu.edu.tw)

*R02 – Visible Taxonomical Classification for Unclassified Near-Earth Asteroids (NEAs) (II)

P.I.: Chih-Hao Hsia (chhsia@must.edu.mo)

R03 – Evaluating the Status of LOT Optical-Axis

P.I.: Yang-Peng Hsieh (m1089002@gm.astro.ncu.edu.tw)

*R05 – Transients within Hours of Explosion

P.I.: Yen-Chen Pan (yenchen.pan@nao.ac.jp)

*R06 – Hunting for Barbarians at Lulin

P.I.: Kang-Shian Pan (m989005@astro.ncu.edu.tw)

*R07 – Searching the Activity of Themis Family Asteroids using LISA

P.I.: Zhong-Yi Lin (zylin@astro.ncu.edu.tw)

R08 – The Study of the Dust to Gas Ratio in Long- and Short-Period Comets

P.I.: Zhong-Yi Lin (zylin@astro.ncu.edu.tw)

R09 – ToO Observations of Cosmic Transient Events

P.I.: Albert Kong (akong@phys.nthu.edu.tw)

*R10 – Identifying Gamma-Ray Pulsars Found by Machine Leaning

P.I.: Kwan Lok Li (lilirayhk@gmail.com)

R11 – Observation of Magnetic Field in RR Lyrae

P.I.: Chow-Choong Ngeow (cngeow@astro.ncu.edu.tw)

R12 – Broadband Monitoring Observations of Mysterious Multiple Bursts

P.I.: Ekaterina Koptelova (koptelova@astro.ncu.edu.tw)

LOT2019C Semester (01 September – 31 December, 2020)

Education Program:

E01 – Practical Class of "Fundamentals of Observational Astronomy"

P.I.: Albert Kong (akong@phys.nthu.edu.tw)

Large Program:

EDEN – Exo-earth Discovery and Exploration Network

PI: W-P Chen (wchen@astro.ncu.edu.tw)

Research Program:

*R01 – Calibrating the griz-Band PLZ Relations using RR Lyrae in Globular Clusters

P.I.: Chow-Choong Ngeow (cngeow@astro.ncu.edu.tw)

*R02 – Visible Taxonomical Classification for Unclassified Near-Earth Asteroids (NEAs) (III)

P.I.: Chih-Hao Hsia (chhsia@must.edu.mo)

R03 – The Study of the Dust to Gas Ratio in Long- and Short-Period Comets

P.I: Zhong-Yi Lim (zylin@astro.ncu.edu.tw)

*R04 – Size and Shape of 2002 MS4 from a Stellar Occultation

P.I.: Xu Fan (fyu922508@gmail.com)

*R05 – Lulin Supernova Program

P.I.: Yen-Chen Pan (ycpan@astro.ncu.edu.tw)

*R06 – LISA Instrumental Testing

P.I.: Hung-Chin Lin (hclin@astro.ncu.edu.tw)

*R07 – Hunting for Barbarians at Lulin

P.I.: Kang-Shian Pan (m989005@astro.ncu.edu.tw)

R08 – ToO Observations of Cosmic Transient Events

P.I.: Albert Kong (akong@phys.nthu.edu.tw)

R09 – Observation of Magnetic Field in RR Lyrae with Blazhko Effect

P.I.: Vaidehi Varma (d1039601@gm.astro.ncu.edu.tw)

鹿林天文台工作報告 2020

1. 具體工作

天文台電力系統改善

鹿林天文台一米望遠鏡 LOT 控制中心自 2002 年完工啟用以來已歷 18 年，由於 儀器設備持續擴充，大量線路重疊不易檢修；此外用電量逐年增加，大型穩壓 器(AVR)也出現不正常跳電情形，所以 2020 年 5 月針對電力系統進行改善，具體項目如下：

1.1 110VAC 大型穩壓器(AVR)更新

110VAC 大型穩壓器(AVR)更新為較大容量機型，並將修復後的舊穩壓器轉為備 援用途。

1.2 新增大電力專用迴路

新增大電力專用迴路專供大電量設備使用，避免因共用同一迴線路過載而導致跳電，影響正常運作。

1.3 望遠鏡及儀器專用梯型電纜線架

建築物原有線路都隱藏在牆壁內，有問題時很難查修。而歷年來陸續增加的線路都是採明 線分布，用新設的鋁製梯型電纜線架將複雜凌亂的線路分類整理，便於將來維護及查修。

LISA 高亮度光譜儀

侯偉傑

LISA 高亮度光譜儀為法國 Shelyak 公司製造，特別適用於如彗星、新星、超新 星、變星、遙遠類星體的紅移或行星狀星雲確認等微弱天體的觀測，光譜範圍涵 蓋了 400-700 nm 整個可見光範圍，並可透過更換元件用於近紅外觀察（650- 1000nm）。2020 年 4 月開始進行基本測試，使用 WO FLT-152 望遠鏡(D=152mm, FL=1050mm, F/7)、0.75x Reducer、主光譜相機 QSI 660 CCD、導星相機 ZWO ASI 174MM。LISA 光譜儀整體配置如下圖，

織女星為 A0 型主序星，曝光時間 5 秒，初步處理後織女星光譜影像，

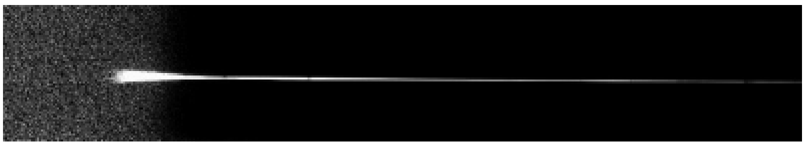

再經過測光與波長校正後，織女星光譜中可見明顯巴爾曼系吸收線。

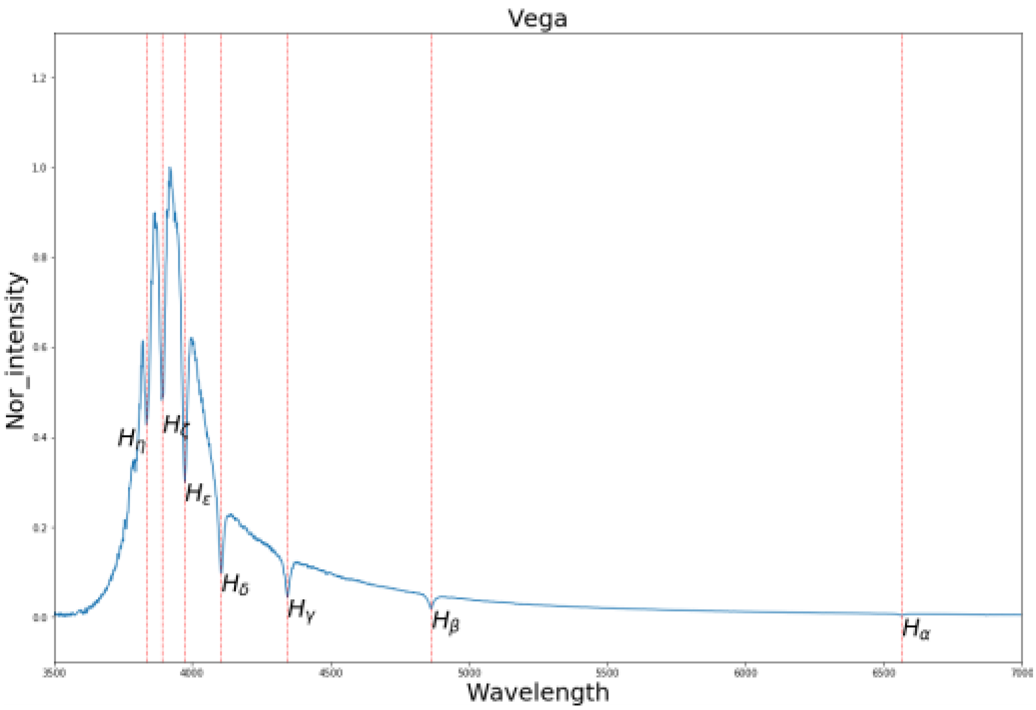

Vega
Nor_intensity
Wavelength
H_η
H_ζ
H_ε
H_δ
H_γ
H_β
H_α

監視錄影系統

張永欣

鹿林天文台位於鹿林前山山頂，屬於玉山國家公園遊憩步道開放區域，不論平日、假日都會有遊客進入。由於天文台房舍分佈多處，平時只有 1～2 位人員駐守，無法全面掌控天文台週邊的安全狀況，所以我們 2020 年 4 月規劃建置監視錄影系統來紀錄並即時反應天文台的維安狀況，包括戶外安全、天文台圓頂開 關狀況及各望遠鏡姿態，總計室外機 17 支，室內機 11 支，詳細位置及視角如 下圖，

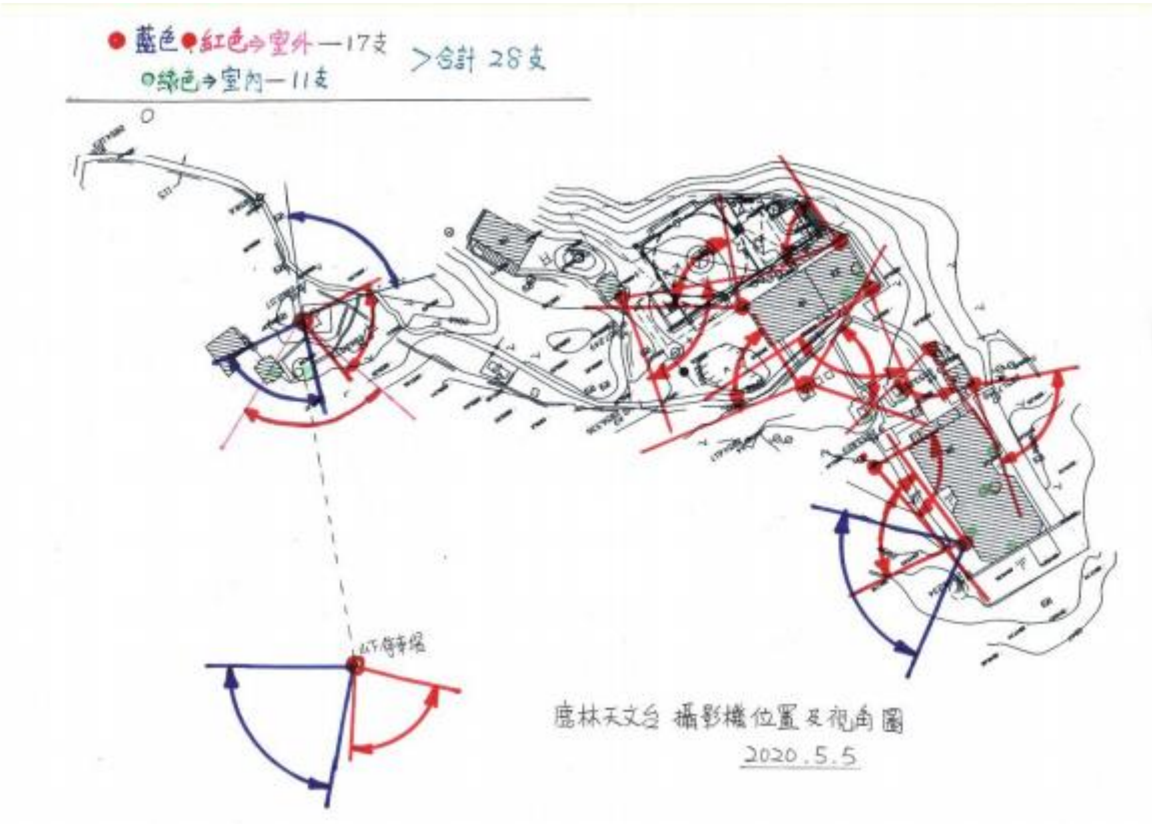

由於天文台區域較廣，受設置地點的供電限制，錄影主機分成 LWT、SLT、LOT 三處置放，各主機配置 10TB 硬碟紀錄，共 30TB 儲存空間，加上影像有變化才 錄影的方式，預計可以提供長達 3 個月以上的錄影時間。系統採用具有網路串接影像功能的錄影機，可將其他 2 台主機的影像匯整到 LOT 的主機上，人員在 LOT 就可以全覽天文台內外各處，藉由此次工程，我們也將有線網路延伸到 800 公尺遠的山下停車場，未來對於此處各項水電設備物聯網自動化，預備了可用的基礎。


6.4TB/9.1TB
5/7/2020 下午 05:04:40
CH01
CH02
CH03
CH04
CH05
CH06
CH07
CH08
CH09
CH10
CH11
CH12
CH13
CH14
CH15
CH16

鹿林天文台 一米望遠鏡室內平場燈製作紀錄

張永欣

起因：

鹿林天文台一米望遠鏡觀測室原設有一投射式的平場屏幕(如圖一)，光源早期由地面二座 500W 無影鎢絲燈漫射照明，由於地面投射燈沒有固定設置，斜射角度無法固定保持，嚴重影響一致性，所以後來將燈源位置改到望遠鏡次鏡架中心，以一磨砂霧面鎢絲燈泡投射，解決了斜角分散不均的差異，但是採用一顆燈泡直接照射，產生了中間強周圍弱的環形不均分佈，始終勉強使用。

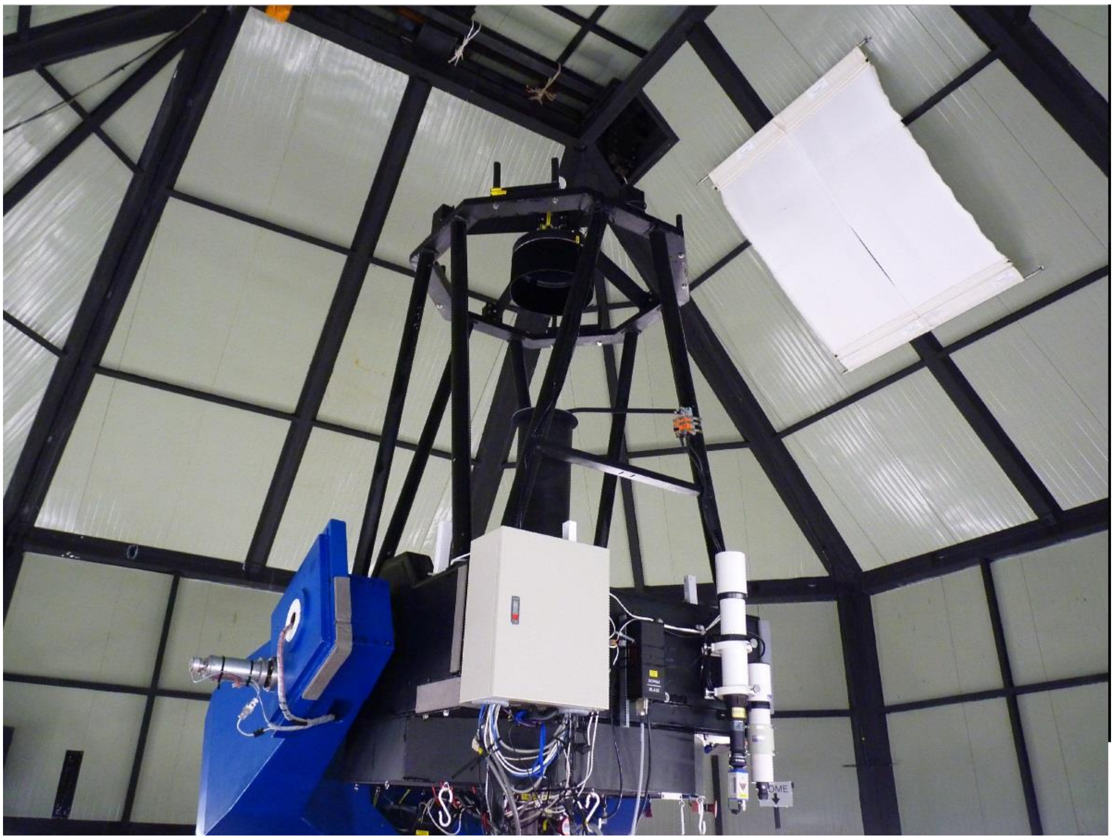

圖一：投射式的平場屏幕

早年只要天氣許可，都盡可能使用天空平場，所以使用室內平場燈的需求似乎不是那麼急迫與要求，但隨著觀測員年紀增長以及勞基法對於連續上班工時限制的要求，在冬天可能有連續上班超過 12 小時的情形發生，於是新平場燈的製作被提起了。

燈具的選擇：

目前市場上買得到的最大 60cm X 60cm 冷光發光板平場燈，但這對於一米口徑是不夠的，加上冷光發光在非常暗情形下的調光作用似乎不是很穩定，均勻性也可

能有問題，另外的問題是大片冷光片及驅動器取得不易，所以將光源轉向市售的 LED 燈，常規的 120cm x 60cm 平板燈二片組合，可以形成約 115 cm X 115cm 的正方形發光面，滿足一米望遠鏡 105cm 圓形覆蓋的範圍。

圖二：側投光源與導光板

圖三：120cm x 60cm 平板燈調暗亮度後不均勻

拆開所上先前購置的新 120cm x 60cm 平板燈，發現是採用側投光式的設計（如圖二），以可調直流電源驅動調暗亮度後，發現導光版造成不均勻性很明顯（如圖三），於是換成 60cmx60cm 平板燈，此型燈是採用點陣背照式設計，由 14x18 陣列＝252 顆 LED 組成（如圖四），沒有導光板的影響，只要單顆 LED 性能差異不大，均勻性影響就會很輕微，但必須是同一批次的 LED 燈珠，恰好有四個暖白光型是同一批的，於是開始測試驅動電路的調整範圍與發光能力。

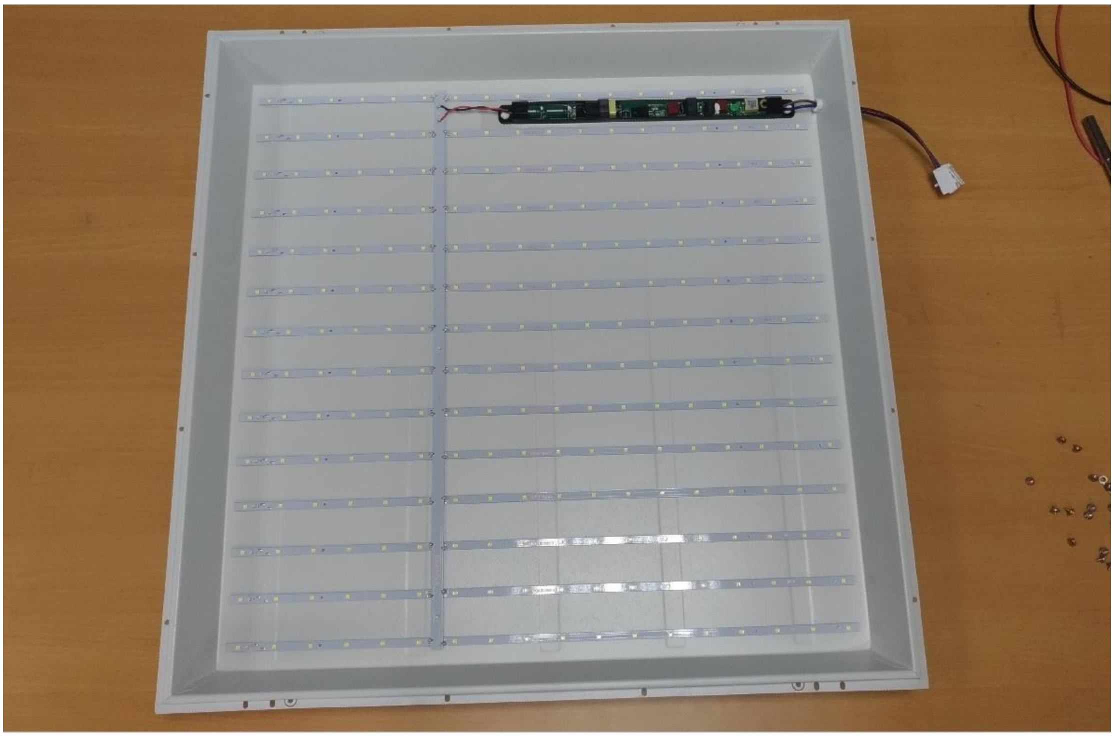

圖四：60cmx60cm 平板燈內部

驅動電壓、電流與亮度：

原燈具是屬於高亮度照明用，驅動的要求要是恆電流安定性，驅動的電壓最高達 65V 左右，經過市售的調光器調到最暗後，仍是太亮。

由於沒有原廠 LED 燈珠的特性數據，所以一開始只能用試誤法測試，此燈具電路採用三顆一組串連再並聯的設計，使用可調直流電源供應器，加上一小限流電阻，確保預設電壓 3V 時不會超過 10mA，最低電壓驅動大約落在 2.01V 左右，此時會明顯看到有些燈珠的亮度是比較暗的，最低電壓電流測試，不知道是可調電源供應器轉鈕不穩，還是 LED 在臨界狀態的特性，電壓一直飄忽不定，電流從 0.015mA 一路測到 0.2mA 左右，取得約 10 組數據後....放棄，等待取得全數位式可調電源供應器再測試。

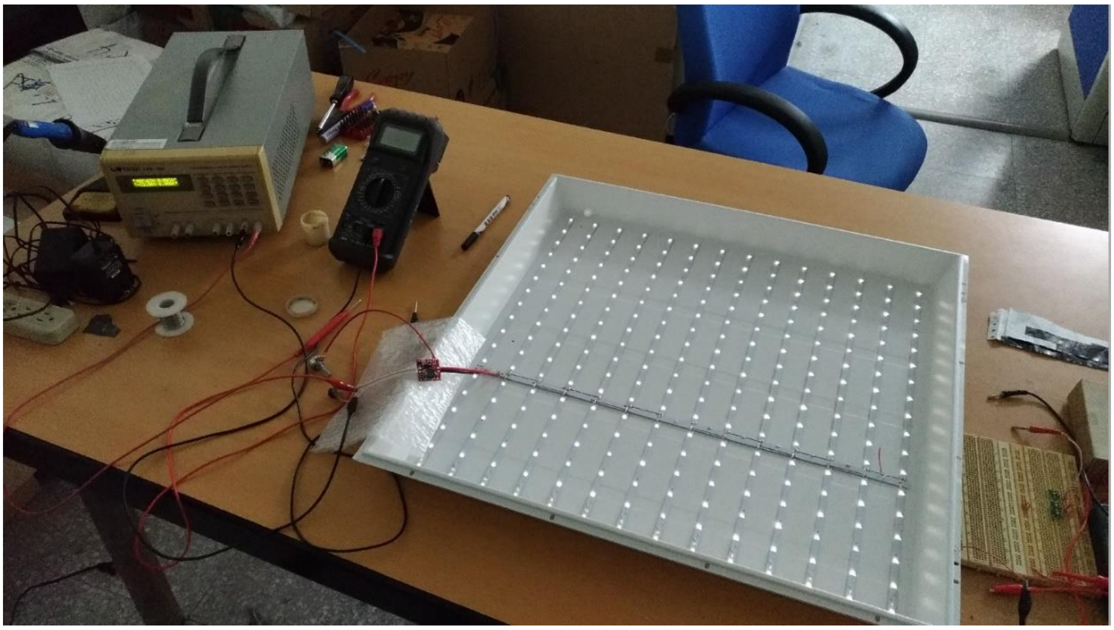

圖五：3W-LED（8v～16v）驅動板與最暗亮度

等待期間又回到原燈具測試，把原廠電路給拆了，斷開主供電路板上的串連銅箔，接上一顆以前買的 3W-LED（8v～16v）驅動板（如圖五），餵給它 12v，成功驅動一排 3 串 6 並，此時電流僅 110mA，接著並接 2 排、3 排一直加到 7 排，驅動器供給電壓為 8.6v 左右，總電流僅上升到 200mA，已經驅動 126 顆 LED 了，應該還是不夠暗，供電壓再降到 9v，驅動板輸出 7.8v，總電流 100mA，蓋上擴散片，效果還不錯，用數位相機拍攝測光，比對鹿林天文台給的 sky-flat 照片資料，距離可用亮度還差 20 倍。（註一：單一座 252 顆 LED 測試最低供電壓 7.63V 時電流 3mA，開始出現發光不均。）

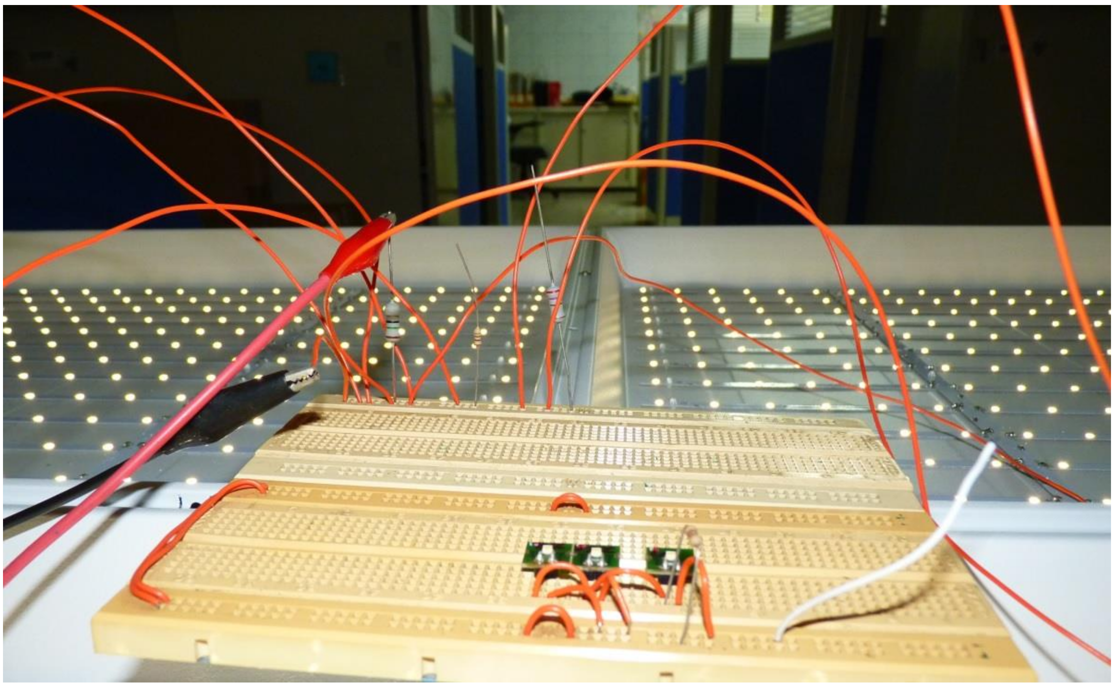

圖六：僅用串接電阻調整亮度

由之前的數據 126 顆 LED，電壓 7.8v 時總電流 100mA，所以單一個燈具 252 顆 LED，耗能約 0.78W，再降低 20 倍乘上 4 具，所以一座平場燈耗電為 0.156W，這樣的耗電是不需要 LED 專用驅動器來求取效能了，只要串接一顆大於 1/4W 電阻就可以穩定且簡單的完成電路（如圖六）；在 12V 電壓供電下選用低亮度以 100Ω-1/2W 電阻，高亮度以 270Ω-1W 電阻串接電路，低亮度時總電流為 0.014A（如圖七），耗能 0.168W。

圖七：電壓 12V 供電，低亮度時總電流為 0.014A，耗能 0.168W。

燈具框架與擴散片：

框架與擴散片是需要配合的，由於沒有材料相關的規格指標，要能發揮擴散片的效能，燈珠與擴散片的深度距離必須大於現有燈具的尺寸，接著進行框架的設計，要求如下：

1. 燈具內部深度大於 5cm。
2. 燈具內框要能嵌入擴散板以及封裝收邊的板材。
3. 燈具屬於倒掛使用，嵌入之擴散板薄片在有限支撐下，面形狀不能因重力而凸出變形。
4. 倒掛安裝的地方是圓頂蒙皮鋼管，不大能承受太重的吊點支撐，所以燈具框架結構要強但重量要輕，現階段山上沒有流籠，採用人力搬運也要要求輕量化。
5. 材料要容易加工，第一座設計免不了還要修修改改。
6. 安裝場合需耐候性，掛上高處後不需要年年粉刷保養。

宗觀幾個需求後，選擇以現成的鋁門窗框來製作是最適合的，於是尋求鋁門窗廠商的協助，從有現貨的量產鋁框材中挑選，還好廠商是熟識多年的好友，願意了解我們這樣非規格化設計配合製作，選用 7.6cm X 2.5cm X 1.3mm20 單邊中央帶突出的框（如圖），取的鋁框型式之後，就開始進行設計繪，燈框尺寸（如圖八）。

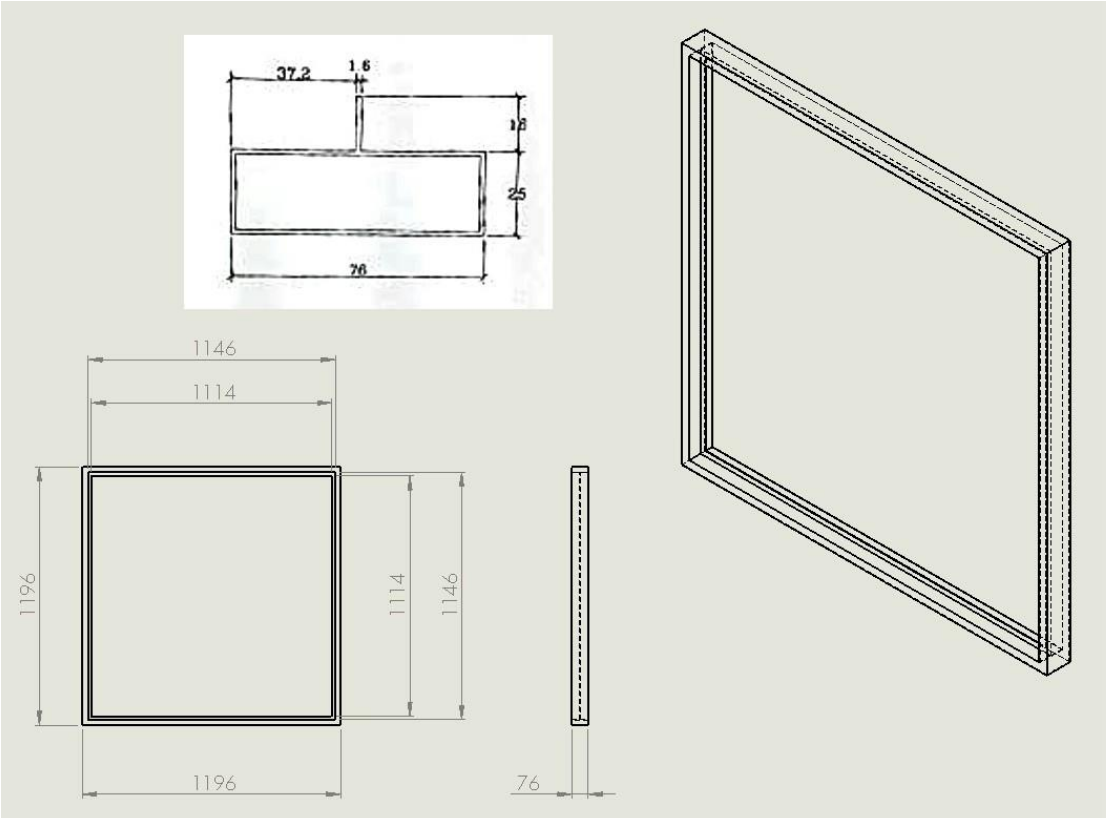

圖八：燈框設計圖

擴散片有找到適用的規格以及可供貨販賣的廠商，量產規格是寬度: 1250 mm X 長度: 1000 Meter，可裁切成 1250 mm X 1250 mm 單片，非常適合此燈具的製作，一次要購買 1 捲＝1 km 長度，所以我會得到 800 片，只能無奈作罷。

回到現有燈具上的擴散片，我有四片 554 mm X 554 mm，2X2 組合成 1108mm X 1108mm 的面，中間有四道縫又不能有支撐遮蔽，又無法上膠黏合，只好採用三明治結構加上中央支撐方式設計，還好 LOT 主鏡前方有一次鏡擋光，中央支撐結構比擋光範圍小即可，三明治結構的上下片是採用廣告壓克力板製作，廣告壓克力板的擴散機制與 LED 燈具擴散片不同，效果比較不好，但均勻度卻相當不錯，所以組合起來應該會更優於只優單一擴散片的效果，要消除擴散片的拼接縫，三片材質不能接觸貼合，但是為了固定為位置與強度，採行內部二片貼合外部隔離的方式製作，拼接縫達肉眼無法辨識（如圖九）。

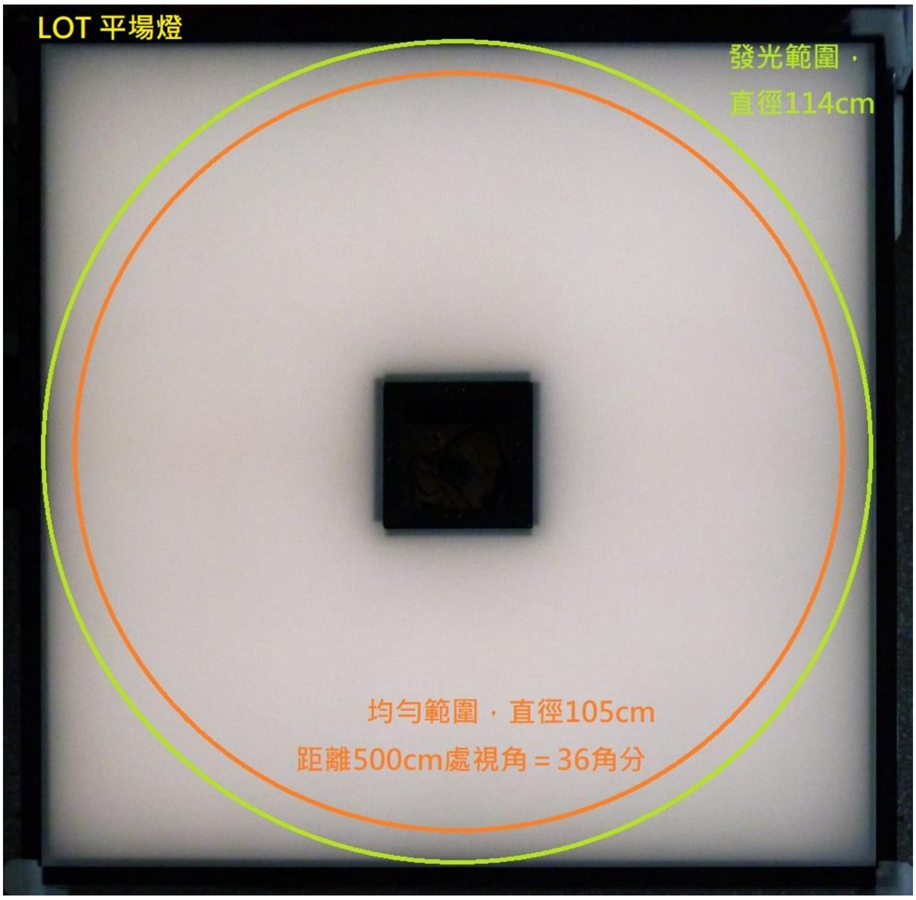

圖九：高亮度時的影像，完全看不出拼接縫。

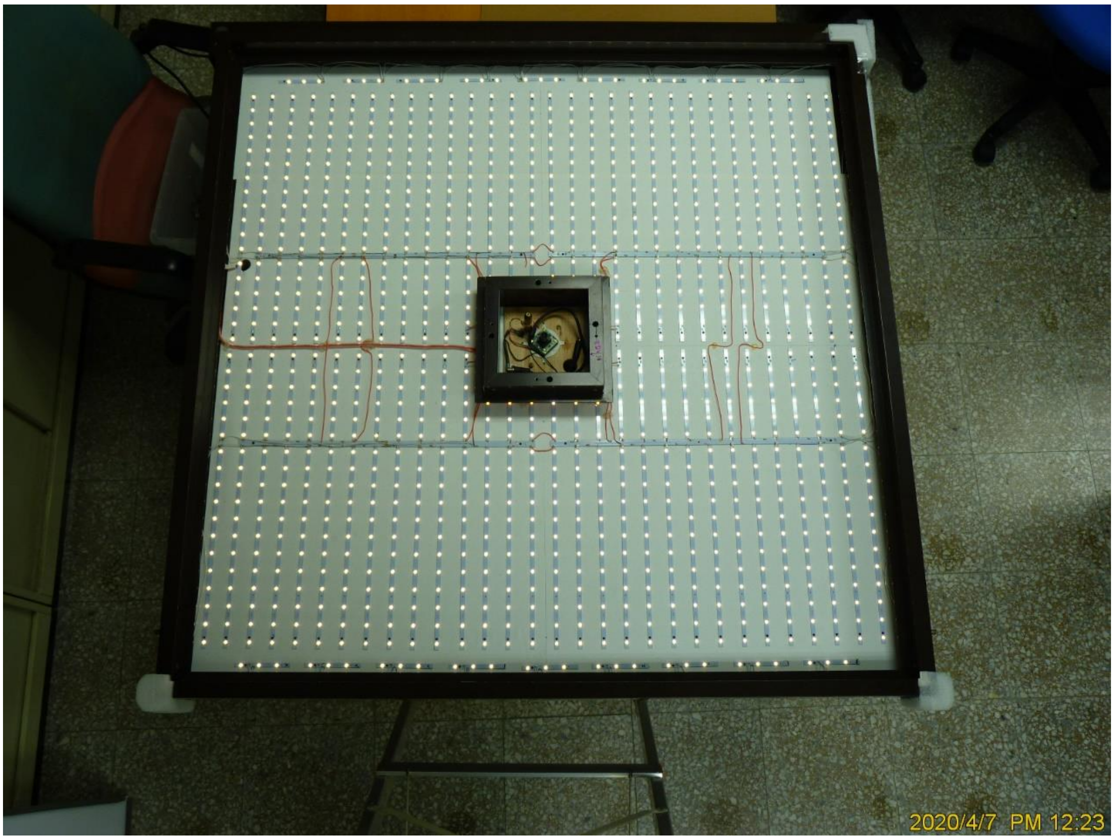

圖十：平場燈低亮度下內部的構造。

燈具安裝架設計：

平場燈除了倒掛安裝於圓頂蒙皮鋼管，還要考慮發光面盡量與望遠鏡光軸垂直，所以要可以微調角度來配合望遠鏡姿態，採用垂直二根鋁框與圓頂結合，一根橫向安裝鉸鍊定位，再由二枝可調伸縮臂調整燈具角度（如圖十一）。

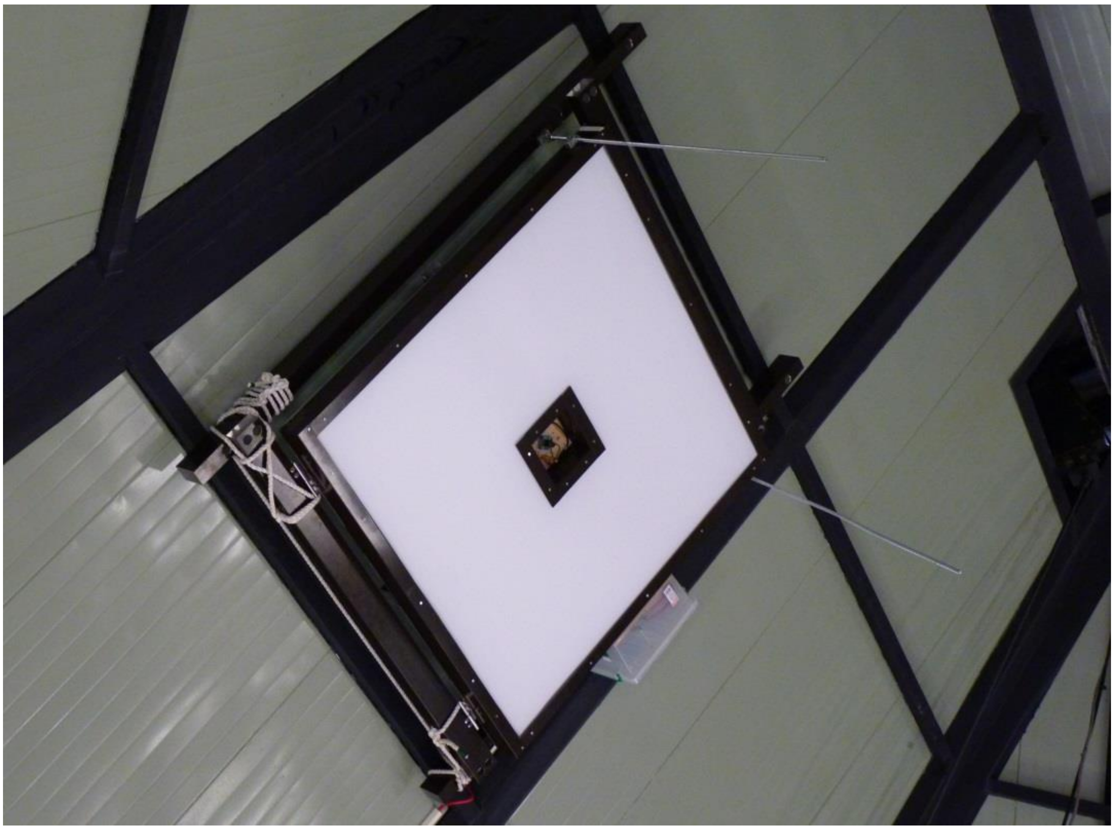

圖十一：安裝於圓頂上之情形。

鹿林天文台 一米望遠鏡室內平場燈安裝報告 2020/07/13

張永欣

室內平場燈於 2020/04/13 安裝在圓頂上，因圓頂鋼管厚度不足，加上圓頂運轉時振動，恐怕有鬆動脫落的危險，所以裝上測試一晚之後，隔天隨即卸下，另謀其他安全安裝方式。

經現場作業方式的考慮後，方案為安裝在專用燈架上，使用時再靠近望遠鏡，但是固定高度的燈架頗高，即使放置到遠離望遠鏡的圓頂邊緣，可能還是會影響到望遠鏡觀測的視野，所以燈架必須能夠升降高低，於是附掛在現有的高空作業車上成為首選，但必須設計一個不影響、不破壞高空作業車的附掛接點。

幾經設計後採用現有 75mmx45mm 方鋼管切割，再板金彎折成轉接座，省去用兩個零件焊接製作方式，對於高空作業車圍欄上的損失空間及干涉情形最少，零件受力方向也最好，但美觀度稍差；另外燈具仰角調整方式改成扁鋼條，於燈架上的固定方式也重新設計，更為強化安全。

7/8 抵達鹿林天文台後，先檢查燈具及零組件的狀況，因夜間可能要觀測，所以等待明日白天再進行改裝。

7/9 作業程序

1. 分解原安裝燈架，更改寬度的跨距，讓仰角調整固定座安裝避免結構干涉。
2. 裝上燈具及調整桿，調整至預先角度。
3. 裝上高空作業車轉接架。
4. 附掛上高空作業車，確認燈具上下、左右均與高空作業車操作不干涉。
5. 燈具電源及控制器安裝，確定燈光控制及攝影機、定位雷射都正常運作。
6. 高空作業車地面位置定位，燈具中心線方向經過望遠鏡不動點。
7. 升高作業車到預定高度，燈具仰角 13 度。
8. 望遠鏡要解除最低角 20 度限制模式，第一次對準。

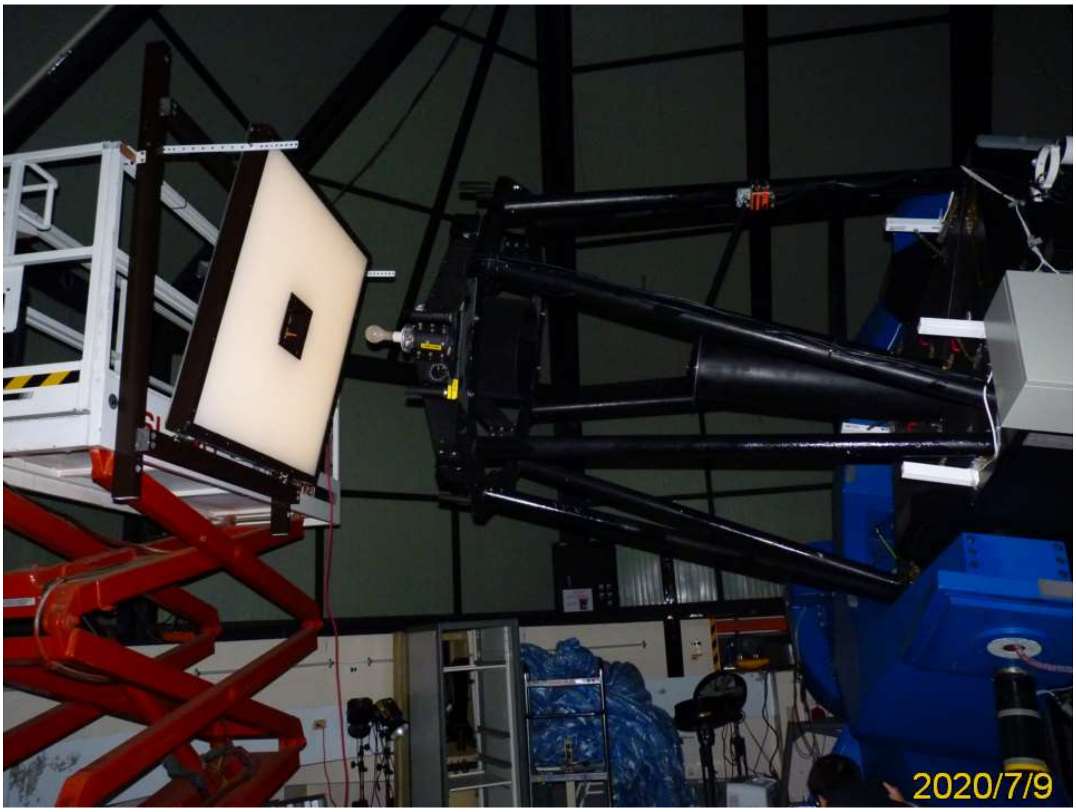

9. 降下燈具重新定位高空作業車位置及角度。

10.升高燈具與望遠鏡第 2 次對準，標定雷射定位點與中心攝影機圖像確認，標定高空作業車高度，評估燈具角度及燈具與望遠鏡距離，避免燈具升降時與望遠鏡移動時干涉撞擊。

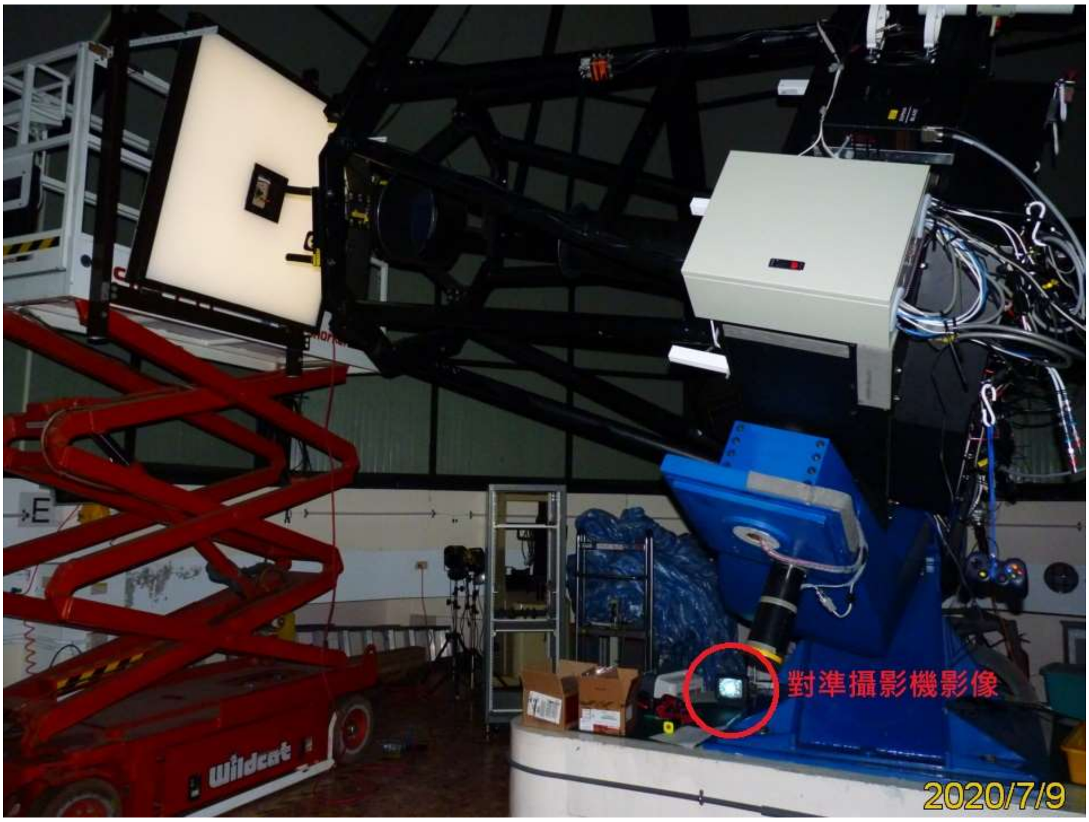

11.確認還有安全操作空件後，降下燈具重新調整燈具角度為 21 度，高於現在設定望遠鏡仰角限制 20 度，可以不必解除軟體安全限制。

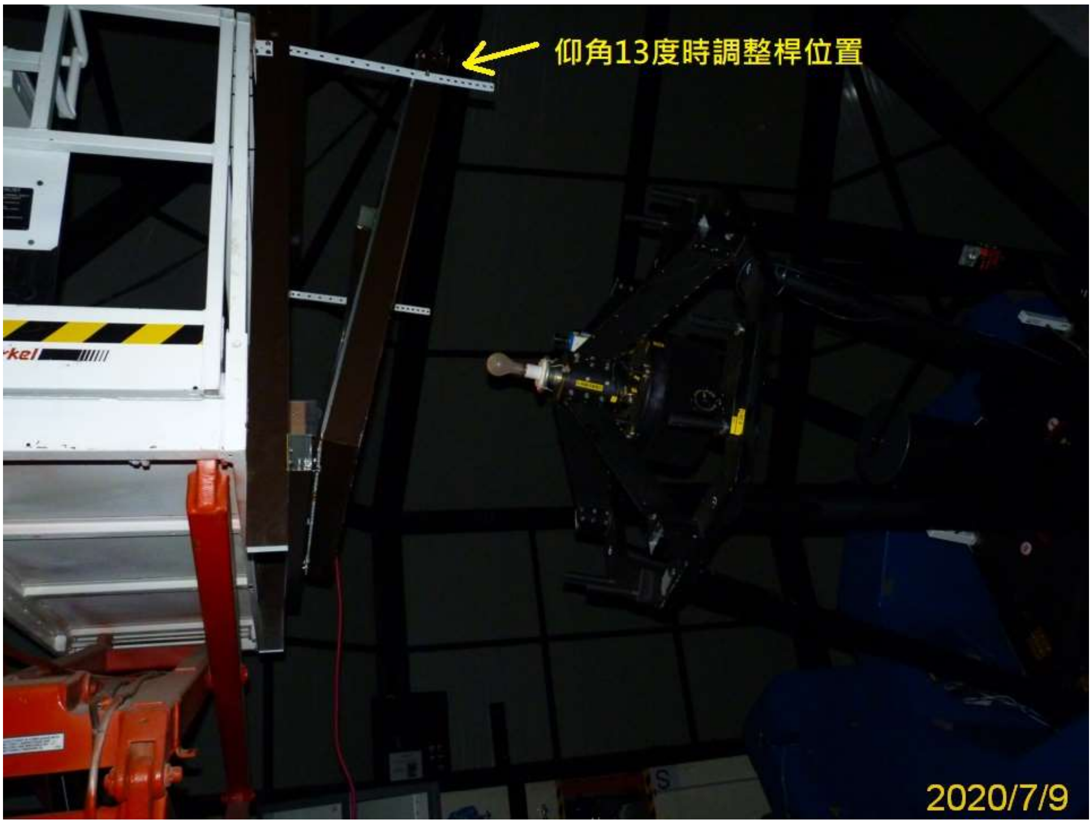

12.升高燈具與望遠鏡第 3 次對準，重新標定雷射定位點與中心攝影機圖像確認。

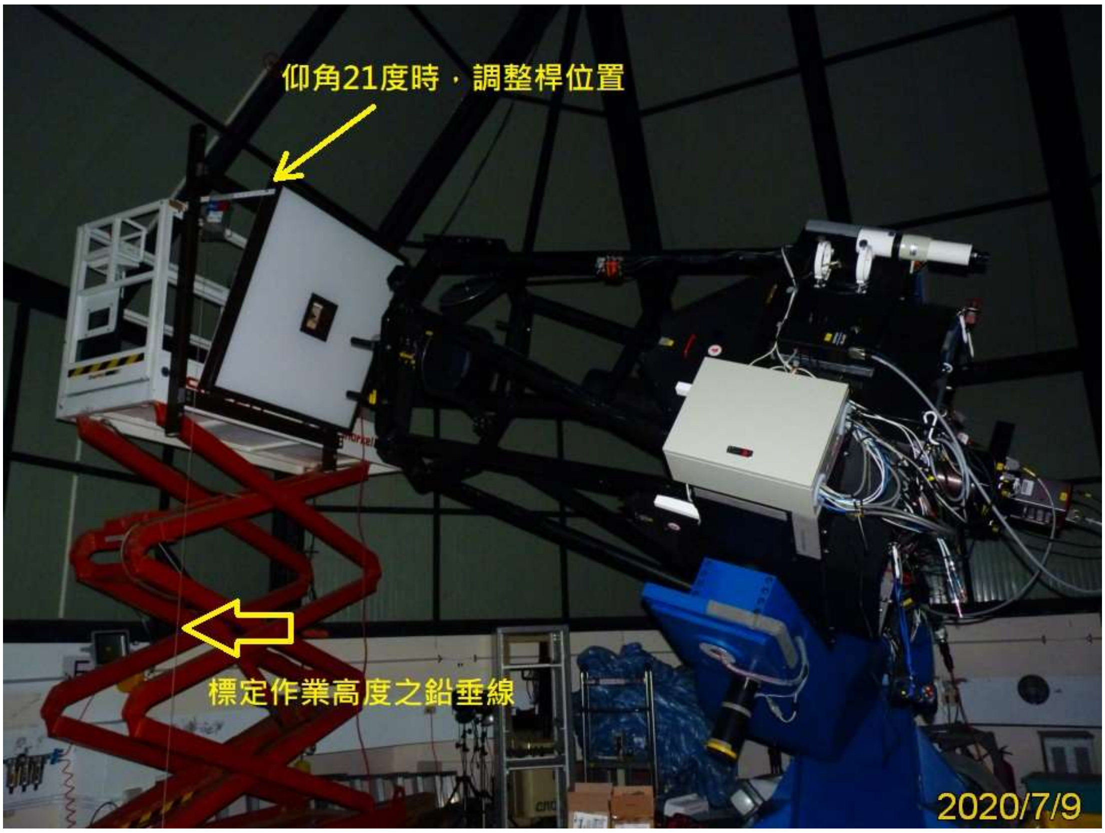

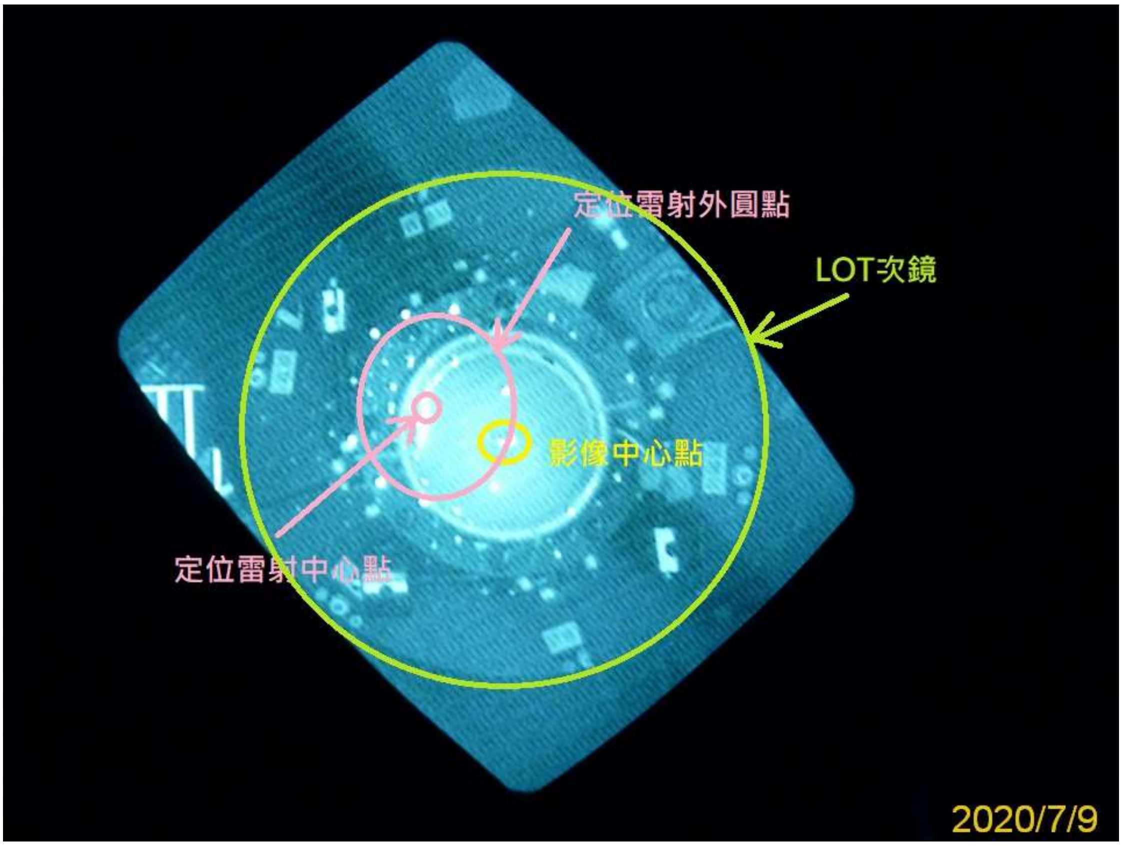

13.定位後進行第 1 次 DomeFlat 拍攝，檔案會交給林忠義博士進行天光平場差異分析，下圖為 LOT 控制室看燈具之影像。

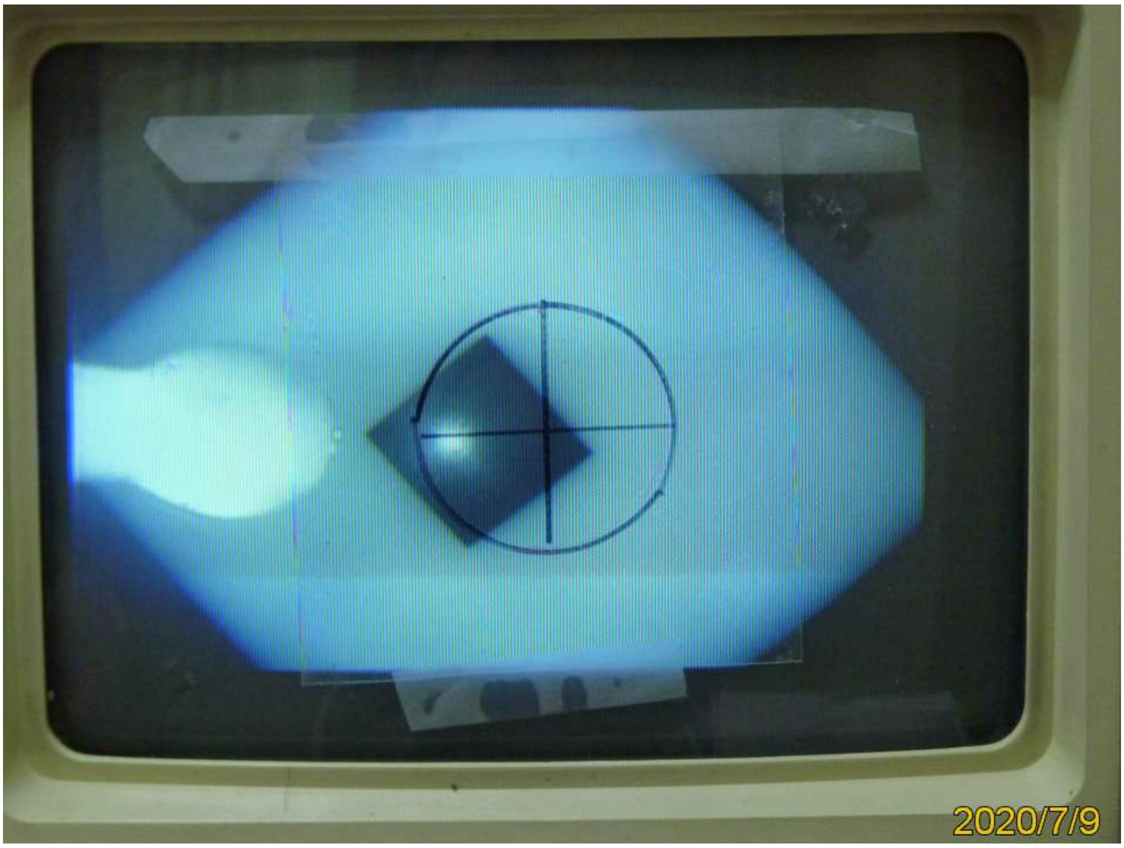

14.標定新的高空作業車工作高度（13 度角與 21 度角作業高度相差 15cm）後，降下燈具。

15.燈具電線及高度鉛垂線收納。

16.更換高空作業車電池為原本 100 AH 大電池組。

7/10 燈具中心攝影機影像是顛倒的，加上雷射點定位點於於 45 度角位置，操作時不直覺，所以重新調整攝影角度及定位點相位，讓往後操作望遠鏡對準時更為直覺容易。

附記：

高空作業車於 7/9 啟用時，發生無法啟動操作之狀況，但是充電機工作正常，更換另一組電池後依然不動，打開底下控制盒檢查電路電路，發現 2 顆保護開關（圓形”5”字樣）其中一顆跳脫，伸出紅色色環，按下歸附之後就順利啟動了。

新、舊平場燈與天光平場比較

侯偉傑

1.1 LOT 平場拍攝介紹

在天文影像處理中，為消除 CCD 像素各自不同的量子效率，與因光路系統上灰塵和暈影所產生的不均勻，必須在觀測前後拍攝平場影像。拍攝平場時必須使用均勻光源，一般會在清晨或黃昏時拍攝暮光平場(twilight flat)。但若是天氣狀況不佳，造成天空光源不均勻，則會使用圓頂內的布幕拍攝圓頂平場(dome flat)。

1. **天光平場**

   在無雲的黃昏或清晨，將望遠鏡指向天頂附近，利用天空均勻光源來拍攝。拍攝當天所使用的濾鏡，每個濾鏡約 5~10 幅影像，每幅影像拍完要作小角度移動，避免影像中星點落在同一位置上。黃昏時濾鏡順序由窄波濾鏡逐漸拍到寬波濾鏡，清晨則反之。

2. **舊圓頂平場**

   在 LOT 圓頂內裝有一布幕，將望遠鏡對準布幕，並開啟望遠鏡前端的燈泡(圖 1)。利用布幕反射燈泡的光近似均勻的光源進行拍攝，與天光平場一樣拍攝當天所使用的濾鏡，每個濾鏡 5~10 幅影像。因圓頂平場沒有星點故不需做小角度移動，且燈泡亮度可調整，所以濾鏡順序也沒有限制。

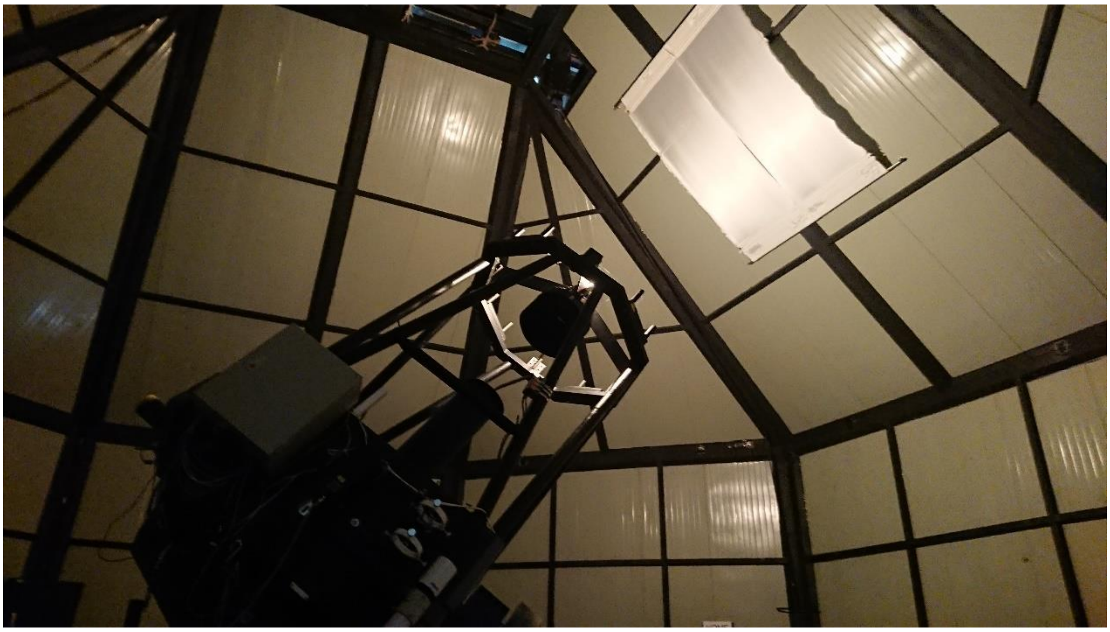

圖 1 舊圓頂平場拍攝

3. 新圓頂平場

2020 年 7 月 9 日安裝新平場燈於升降機上，操作方式詳見新平場燈 SOP。與舊平場燈相似，但安裝時考慮了與望遠鏡指向正交，且平面上無接縫、布幕垂放所造成的凹凸，故光源較舊系統更均勻。拍攝當天所使用的濾鏡，每個濾鏡 5~10 幅影像。因沒有星點故不需做小角度移動，亮度有三段調整，請利用 SOP 提供的模式與秒數調整。

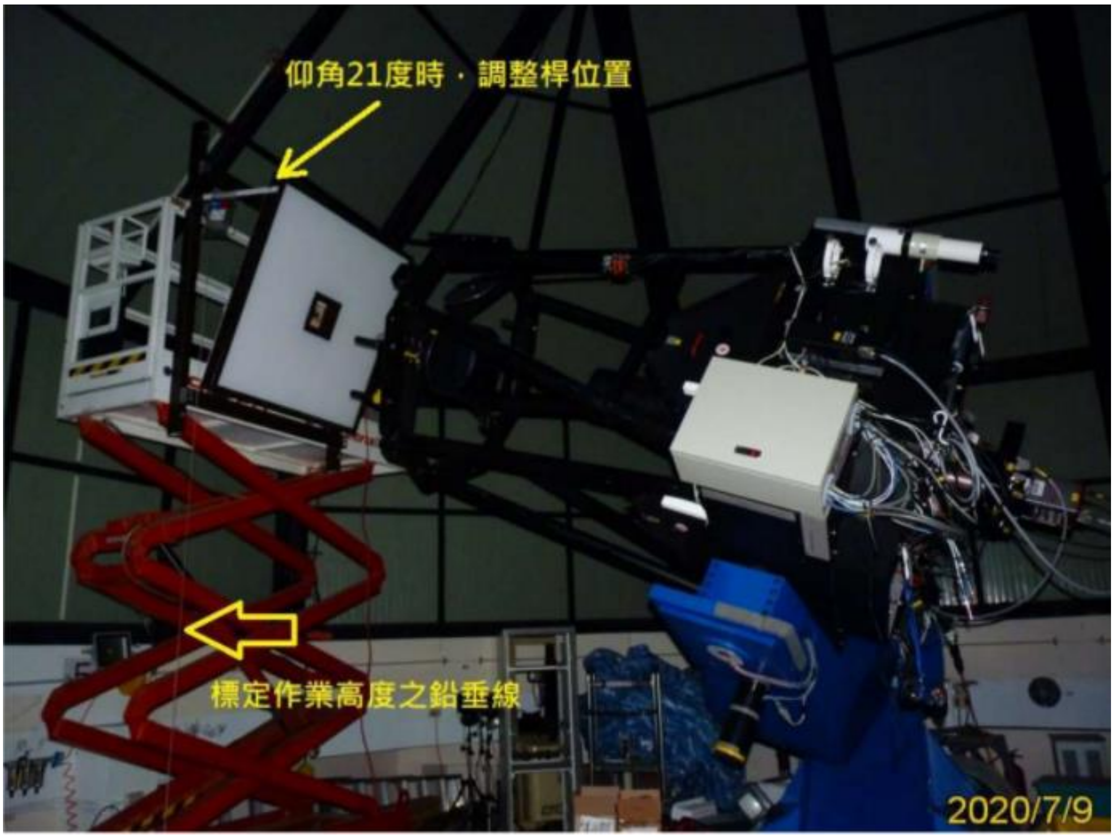

圖 2 新圓頂平場拍攝

1.2 新、舊圓頂平場與暮光平場比較

2021 年 3 月 10 日 LOT 拍攝三種平場，每種平場都拍攝濾鏡 B、V、R 與 I，每個濾鏡都取 7 張影像。

以下將以 B 濾鏡說明，舊圓頂平場曝光時間為 5 秒，每張影像的平均 count 都約為 11500；新圓頂平場曝光時間為 10 秒，每張影像的平均 count 都約為 12100。暮光平場的曝光時間為 5 秒，平均 count 分別約為 18200、19000、19900、20800、21200、22800、23000。圓頂每張影像都由減去了由 10 張 median-combined 合併的 master dark 影像，然後每張影像取中位數作 normalized 後再將 7 張影像做 median-combined 合併，最後得到三種平場的 master flat (圖 4)。

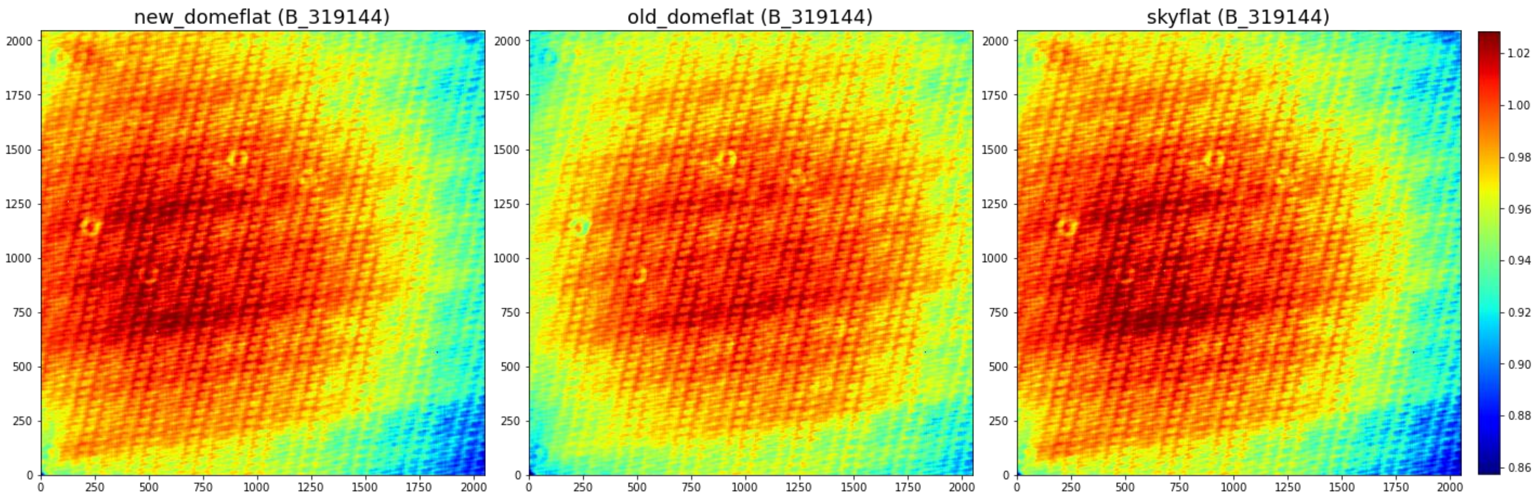

圖 3 三種平場的 master flat

由圖 4 可見新圓頂平場與暮光平場較接近，而舊圓頂平場與暮光平場在 x 方向上有明顯差異。為量化其差異，將圓頂平場除以暮光平場(圖 5)。圖 5 可見新圓頂平場與暮光平場的殘差較舊圓頂平場均勻，而舊圓頂平場在 X 方向與暮光平場差異較大。新平場殘差最高與最低處差異約為 8%，而舊平場約為 14%。為沿著兩軸分別做平均後的亮度輪廓，亦可看出舊平場在 Y 軸上較為不均勻。濾鏡 V、R、I 之結果亦相近於此，結果於此章最後列出。

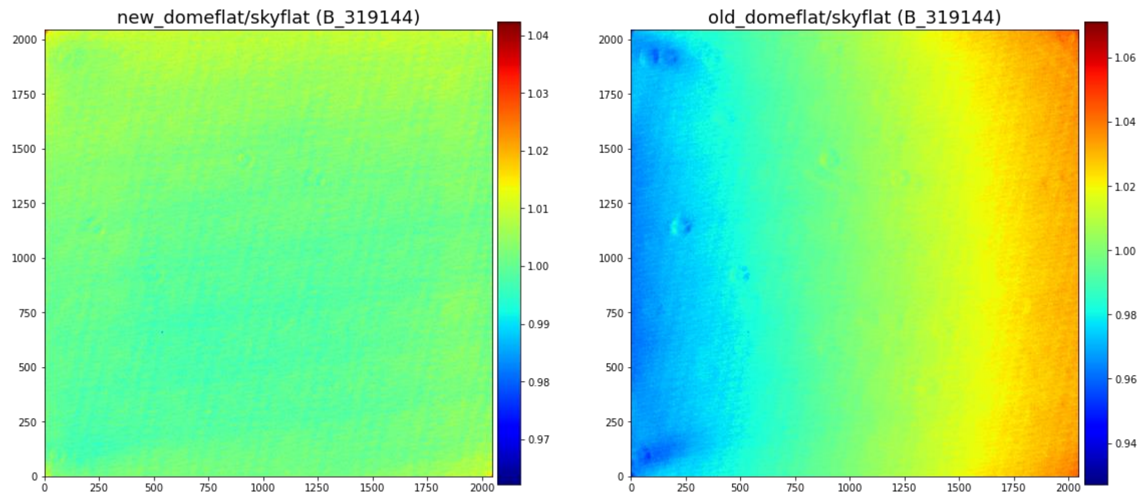

圖 4 圓頂平場除以暮光平場之殘差

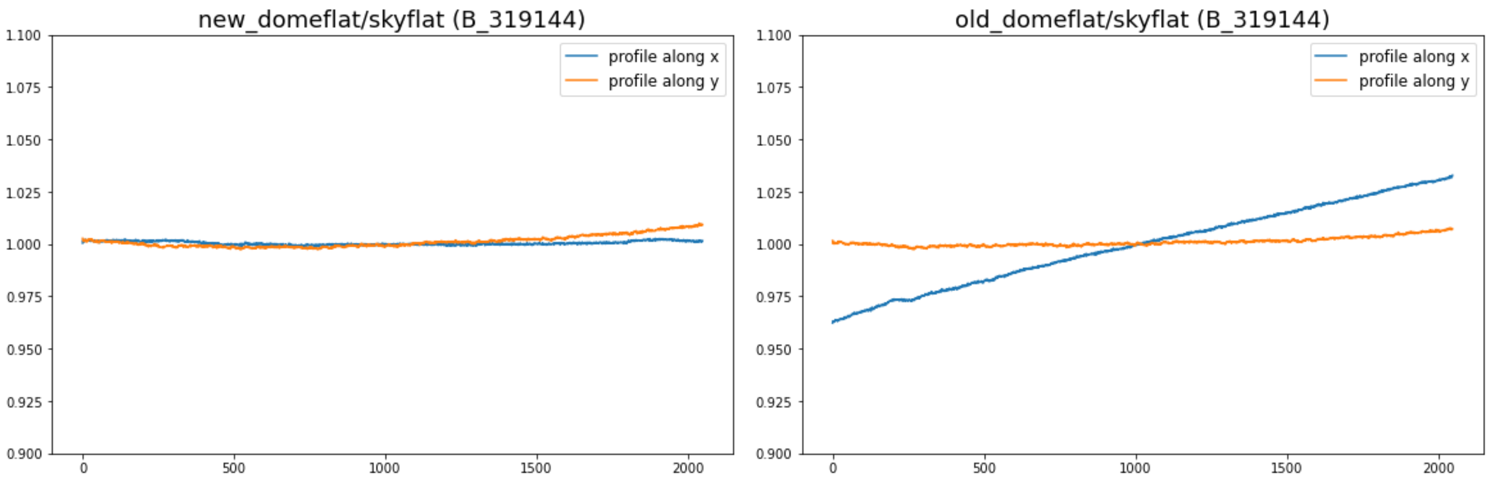

圖 5 殘差沿 x 軸與 y 軸的輪廓

新圓頂平場之結果與天光平場較接近(光源較均勻)，故若天氣不佳時可以使用新圓頂平場代替，不須等下次暮光時間天氣晴朗再補拍。但因為新圓頂平場燈內部光源為 LED，有其特殊譜線不能做為光譜平場源，所以當使用 LISA 光譜儀時，還是選用舊圓頂平場來拍攝。

V-band

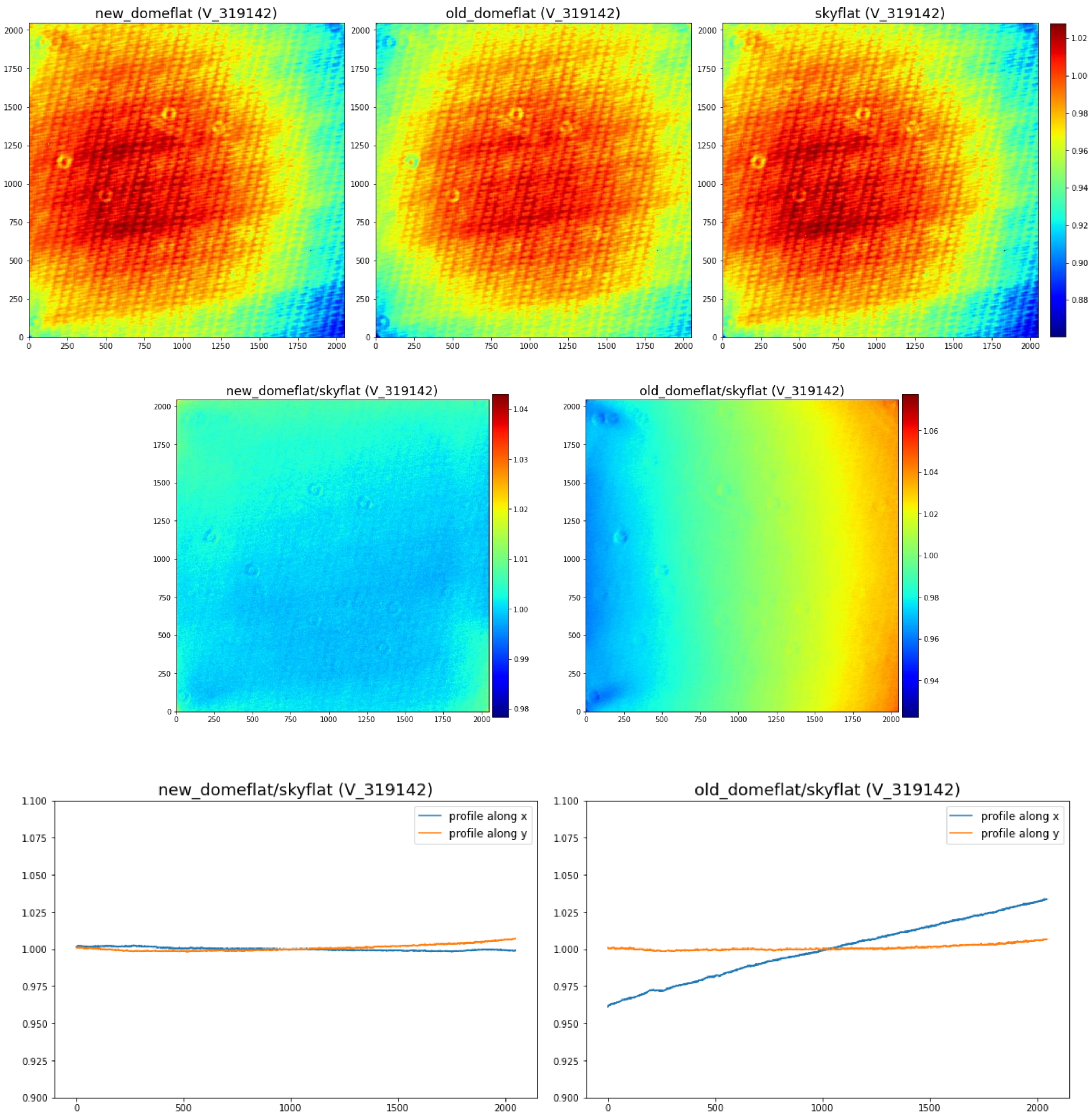
new_domeflat (V_319142)
old_domeflat (V_319142)
skyflat (V_319142)
new_domeflat/skyflat (V_319142)
old_domeflat/skyflat (V_319142)
new_domeflat/skyflat (V_319142)
profile along x
profile along y
old_domeflat/skyflat (V_319142)
profile along x
profile along y

R-band

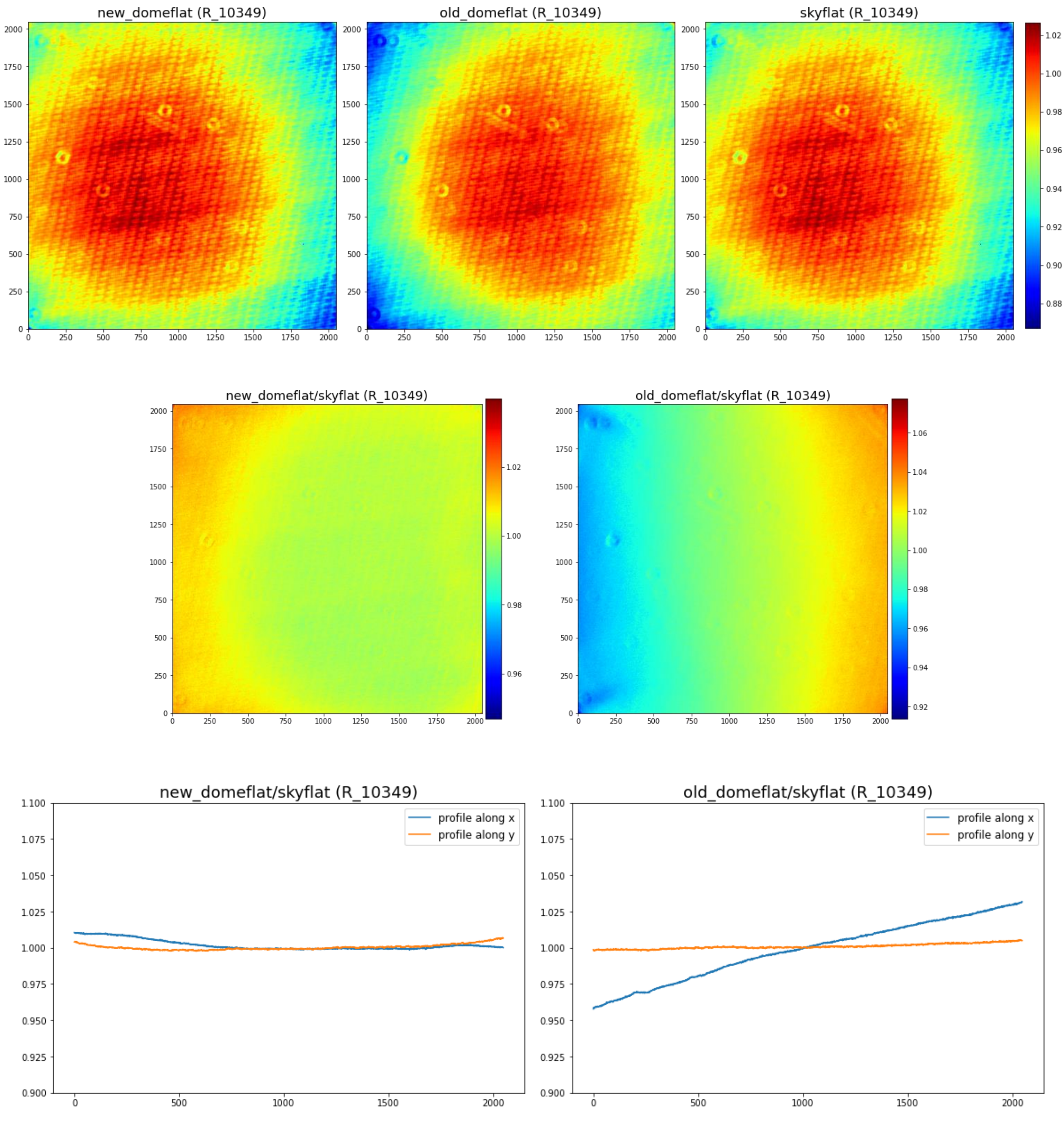
new_domeflat (R_10349)
old_domeflat (R_10349)
skyflat (R_10349)
new_domeflat/skyflat (R_10349)
old_domeflat/skyflat (R_10349)
new_domeflat/skyflat (R_10349)
profile along x
profile along y
old_domeflat/skyflat (R_10349)
profile along x
profile along y

I-band

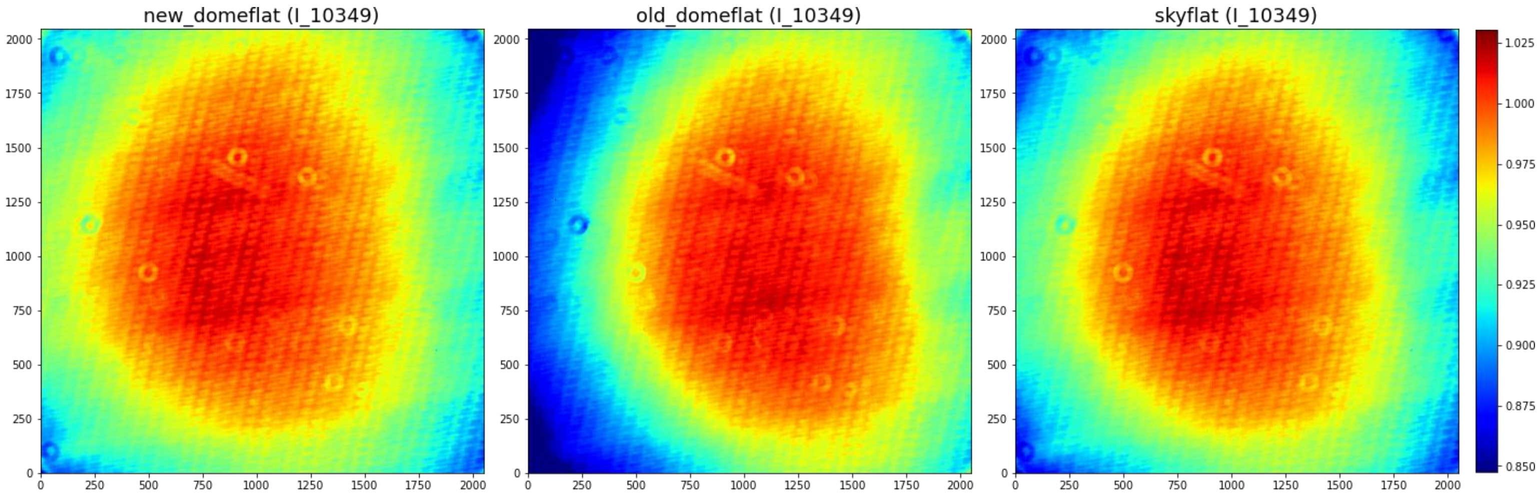

new_domeflat (I_10349)
old_domeflat (I_10349)
skyflat (I_10349)

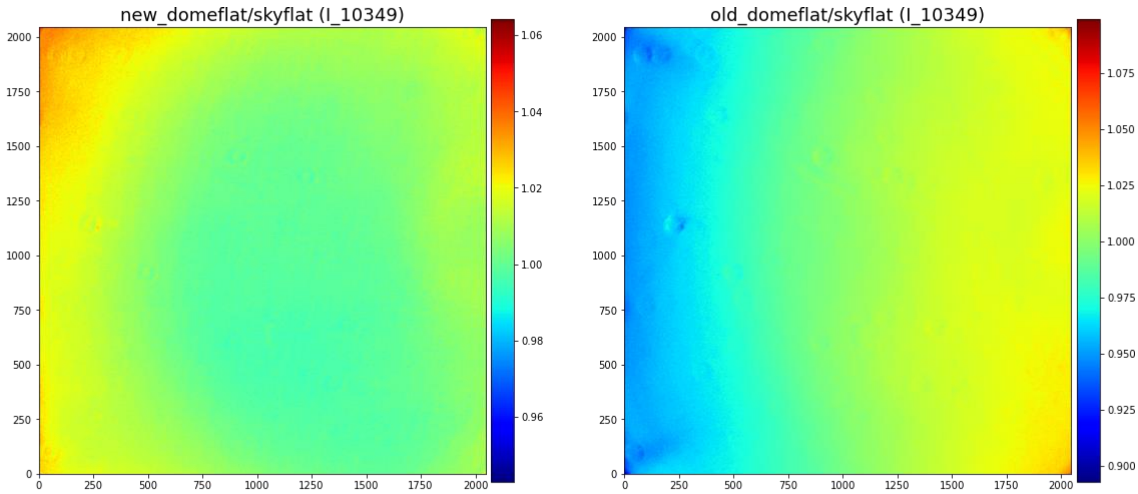

new_domeflat/skyflat (I_10349)
old_domeflat/skyflat (I_10349)

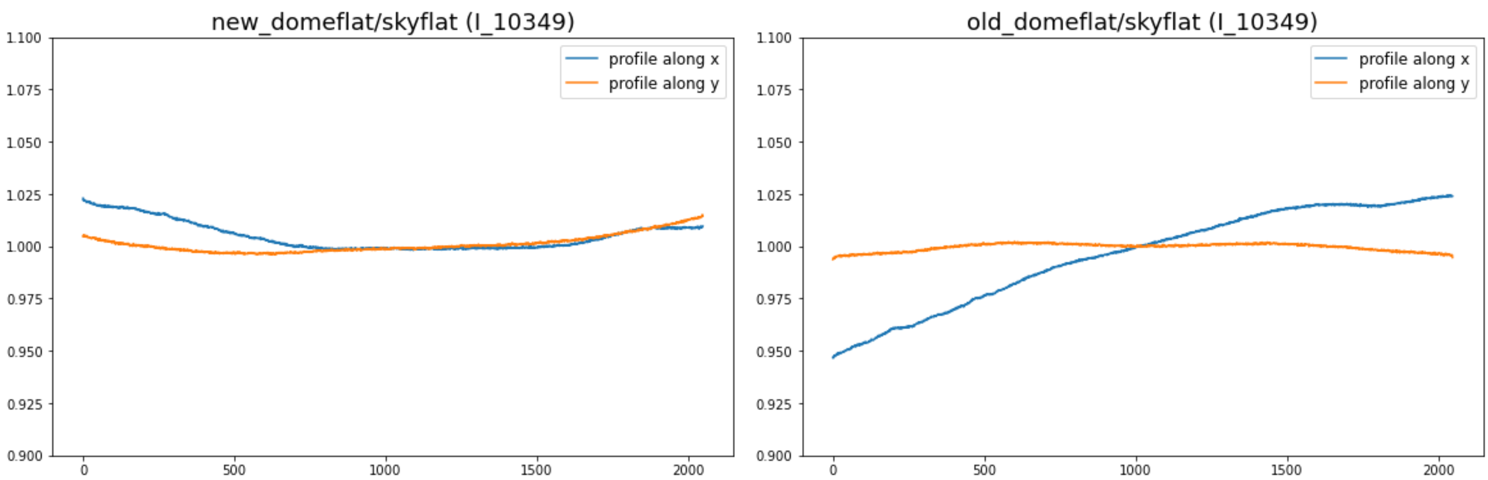

new_domeflat/skyflat (I_10349)
profile along x
profile along y
old_domeflat/skyflat (I_10349)
profile along x
profile along y

2. 科學成果

2.1 Scientific Papers

標題、作者、期刊名稱、卷期、起(迄)頁數、(年/月份)
Title, authors, journal, volume, first page, (year/month)

Solar System/Exoplanets

1. The current development of the Taiwan Meteor Detector System (TMDS) with a dedication to the Geminids 2017 and 2018, Lin, Zhong-Yi; Chi, Hsin-Chang; Wang, Bo-Hao; Lin, et al., Planetary and Space Science, Volume 180, article id. 104763. (202001)
2. Long-term activity of Comet C/2007 N3 (Lulin) as monitored by the SLT at the Lulin Observatory, Lin, Zhong-Yi, Publications of the Astronomical Society of Japan, Volume 72, Issue 2, id.L3 (202004)
3. Characterization of the Nucleus, Morphology, and Activity of Interstellar Comet 2I/Borisov by Optical and Near-infrared GROWTH, Apache Point, IRTF, ZTF, and Keck Observations, Bolin, Bryce T.; Lisse, Carey M.; Kasliwal, Mansi M.; et al., The Astronomical Journal, Volume 160, Issue 1, id.26, 16 pp. (202007)
4. The Asteroid Rotation Period Survey Using the China Near-Earth Object Survey Telescope (CNEOST), Yeh, Ting-Shuo; Li, Bin; Chang, Chan-Kao; et al., The Astronomical Journal, Volume 160, Issue 2, id.73 (202008)
5. A study of the physical properties of an active asteroid (6478 Gault), Lin, Zhong-Yi; Cheng, Yu-Li; Vincent, Jean-Baptiste; Zhang, Xi-Liang; et al., Publications of the Astronomical Society of Japan, Volume 72, Issue 5, id.79 (202010)
6. Low dispersion spectra of lunar impact flashes in 2018 Geminids, Yanagisawa, Masahisa; Uchida, Yuki; Kurihara, Seiya; et al., Planetary and Space Science, Volume 195, article id. 105131., (202101)
7. Initial Characterization of Active Transitioning Centaur, P/2019 LD2 (ATLAS), Using Hubble, Spitzer, ZTF, Keck, Apache Point Observatory, and GROWTH Visible and Infrared Imaging and Spectroscopy, Bolin, Bryce T.; Fernandez, Yanga R.; Lisse, Carey M.; et al. , The Astronomical Journal, Volume 161, Issue 3, id.116, 15 pp. (202103)

Stars/Star Clusters

8. Full orbital solution for the binary system in the northern Galactic disc microlensing event Gaia16aye, Wyrzykowski, Ł.; Mróz, P.; Rybicki, K. A.; et al., A., Astronomy & Astrophysics, Volume 633, id.A98, 21 pp. (202001)
9. The EXOTIME project: signals in the O-C diagrams of the rapidly pulsating subdwarfs DW Lyn, V1636 Ori, QQ Vir, and V541 Hya, Mackebrandt, F.; Schuh, S.; Silvotti, R.; et al., Astronomy & Astrophysics, Volume 638, id.A108, 19 pp. (202006)

Star Formation and Evolution

10. Discovery of extended structures around two evolved planetary nebulae M2-55 and Abell 2, Hsia, Chih-Hao; Zhang, Yong; Zhang, Xi-Liang; et al., Research in Astronomy and Astrophysics, Volume 20, Issue 7, id.107 (202007)

High Energy Astrophysical Phenomena

11. Spitzer Observations of the Predicted Eddington Flare from Blazar OJ 287, Laine, Seppo; Dey, Lankeswar; Valtonen, Mauri; et al., The Astrophysical Journal Letters, Volume 894, Issue 1, id.L1, 6 pp. (202005)
12. Kilonova Luminosity Function Constraints Based on Zwicky Transient Facility Searches for 13 Neutron Star Merger Triggers during O3, Kasliwal, Mansi M.; Anand, Shreya; Ahumada, Tomás; et al., The Astrophysical Journal, Volume 905, Issue 2, id.145, 31 pp. (202012)
13. Revealing a New Black Widow Binary 4FGL J0336.0+7502, Kwan-Lok Li, Y. X. Jane Yap, Chung Yue Hui, et al., arXiv:2103.01557 (202103)

Instrumentation and Methods

14. EDEN: Sensitivity Analysis and Transiting Planet Detection Limits for Nearby Late Red Dwarfs, Gibbs, Aidan; Bixel, Alex; Rackham, Benjamin V.; et al., The Astronomical Journal, Volume 159, Issue 4, id.169, 18 pp. (202004)

2.2 The Astronomer’s Telegram

1. The fragmentation of comet C/2019 Y4 (Atlas) observed at Lulin observatory, Lin, Zhong-Yi; Hsia, Chih-Hao; Ip, Wing-Huen, The Astronomer's Telegram 13629 (202004)
2. The Sodium Emission of comet C/2020 F3 (NEOWISE) observed at KenTing and Lulin observatory, Lin, Zhong-Yi; Wang, Chiahui; Ip, Wing-Huen; et al., The Astronomer's Telegram 13886 (202007)
3. Another major outburst of comet 29P/Schwassmann-Wachmann 1, Lin, Zhong-Yi; Ip, Wing-Huen; Lin, Chi-Sheng; Hsiao, Hsiang-Yao; Hou, Wei-Jir; Lin, Hung-Chin, The Astronomer's Telegram 14207 (202011)

The Astronomer's Telegram

The fragmentation of comet C/2019 Y4 (Atlas) observed at Lulin observatory

ATel #13629; ***Zhong-Yi Lin (IANCU), Chih-Hao Hsia (MUST), Wing-Huen Ip(IANCU)***

*on **13 Apr 2020; 10:38 UT***
Distributed as an Instant Email Notice Comets
Credential Certification: Zhong-Yi Lin (zylin@astro.ncu.edu.tw)

Subjects: Optical, Comet

Referred to by ATel #: 13634, 13651, 13813, 13890

Images on April 9 and 10 taken by the Lulin 40cm telescope (SLT) showed the appearance of a breakup event around the central nucleus. Subsequent R-band images obtained on April 12 by the Lulin on-meter telescope (LOT) showed the presence of at least two fragments. The telescope tracked the apparent motion of the comet and the images with an angular resolution of 0.385"/pixel were stacked at the optical center of the comet. The separation distance between nucleus and 1 is about 3400 km and that of fragments 1 and 2 is about 1600 km. These LOT images of comet C/2019 Y4 (Atlas) can be found at http://www.astro.ncu.edu.tw/people/zylin/2019Y4.html Follow-up observations of C/2019 YA (Atlas), both imaging and spectroscopy, are highly recommended to investigate the cause of this cometary breakup event. This work is based on observations made with Lulin 1m and 40cm telescopes at Lulin observatory (MPC code: D35), operated by Institute of Astronomy, NCU, Taiwan.

C/2019 Y4 (Altas) images

[Previous | Next | ADS]

The Sodium Emission of comet C/2020 F3 (NEOWISE) observed at KenTing and Lulin observatory

ATel #13886; ***Zhong-Yi Lin (IANCU), Chiahui Wang (TCFSH), Wing-Huen Ip (IANCU), Kuo-Pin Huang (NMNS),Chi-Sheng Lin (IANCU), Hsiang-Yao Hsiao (IANCU), Wei-Jir Hou(IANCU), Hung-Chin Lin(IANCU)***
*on **22 Jul 2020; 02:24 UT***
Distributed as an Instant Email Notice Comets
Credential Certification: Zhong-Yi Lin (zylin@astro.ncu.edu.tw)

Related
13897 **CN, C2, C3 production rates of Comet C/2020 F3 (NEOWISE) as observed from Himalayan Chandra Telescope, Hanle, India**
13886 **The Sodium Emission of comet C/2020 F3 (NEOWISE) observed at KenTing and Lulin observatory**

Subjects: Optical, Comet, Solar System Object

Referred to by ATel #: 13897

Tweet

Optical spectra on July 10 taken by the 20cm telescope, Aply 600 spectrograph and Atik 460ex CCD at KenTing observatory showed the strong sodium emission at 5890~5896A around the central nucleus. Follow-up observations on July 11 by the Lulin 15cm telescope, LISA spectrograph and QSI 660 CCD confirmed this identification. The sodium emission in cometary spectra is rare and only a few comets, like comet C/1996 B2 (Hyakutake), and C/1995 O1 (Hale-Bopp), showed this emission. The sodium atoms might be the neutral atoms emitted directly from the cometary nucleus or more likely due to neutral atoms released by dust particles in the coma and dust tail (Cremonese et al. 2002). Unfortunately, the observing window was too small to obtain the image of the sodium tail. Follow-up observations of C/2020 F3 (NEOWISE), both imaging and spectroscopy, are highly recommended to investigate the form of the sodium emission. This work is based on observations made with 20cm telescope at KenTing observatory (MPC code: D34) operated by physics department, NTU, Taiwan and Lulin 15cm telescopes at Lulin observatory (MPC code: D35), operated by Institute of Astronomy, NCU, Taiwan. These spectra images (red line refers to July 10, and blue one is obtained on July 11) of comet C/2020 F3 (NEOWISE) can be found at website http://www.astro.ncu.edu.tw/people/zylin/C2020_F3.html?fbclid=IwAR1lCLTsSTDWnKpSF--FDVZsjjXtsa59QHgjgtrv9INC_irO_BUqngkXxbU

C/2019 Y4 (Altas) images

[**Telegram Index**]

[Previous | Next | ADS]

Another major outburst of comet 29P/Schwassmann-Wachmann 1

ATel #14207; ***Zhong-Yi Lin (IANCU)), Wing-Huen Ip (IANCU),Chi-Sheng Lin (IANCU), Hsiang-Yao Hsiao (IANCU), Wei-Jir Hou(IANCU), Hung-Chin Lin(IANCU)***
*on **24 Nov 2020; 00:59 UT***
Credential Certification: Zhong-Yi Lin (zylin@astro.ncu.edu.tw)

Subjects: Optical, Comet

Referred to by ATel #: 14323

Tweet

We report that a major outburst of comet 29P/Schwassmann-Wachmann 1 was detected by using the images acquired with the SLT (16â Ritchey-Chretien telescope) at Lulin observatory. The outburst was observed to begin on 2020 November 20 with its brightness suddenly increasing by ~2.7 mag, as measured through a 5.6 arcsec (10,000 km) aperture. This outburst event was larger than those previously reported in September and October for which the brightness increases were all less than 0.5 mag (Atel #13110, #13179). Our images obtained before November 20 showed that the V-band magnitude was about 16.1. After the outburst, the central nuclear region was quite concentrated. Photometry of the images was all measured with 10,000 km radius apertures and calibrated to the PS1 catalog.

The lightcurve and images of comet 29P/S-W 1

Related
14323 Outburst of comet 29P/Schwassmann-Wachmann 1
14207 Another major outburst of comet 29P/Schwassmann-Wachmann 1
13179 Additional Outburst of Comet 29P/Schwassmann-Wachmann 1
13164 Possible Fragmentation of Comet 29P/Schwassmann-Wachmann 1
13110 Outburst of Comet 29P/Schwassmann-Wachmann
12994 Outburst of Comet 29P/Schwassmann-Wachmann 1

[**Telegram Index**]

R. E. Rutledge, Editor-in-Chief rrutledge@astronomerstelegram.org
Derek Fox, Editor dfox@astronomerstelegram.org

2.3 Progress Reports

1. Survey of the synchronous binary asteroids in the Solar System, Polińska M., Bartczak P., Dudziński G., Podlewska-Gaca E.
2. Survey of the synchronous binary asteroids in the Solar System, Chia-Lung Lin, Li-Ching Huang, Yu-Chi Cheng, Wei-Jie Hou

Survey of the synchronous binary asteroids in the Solar System - progress report

Polińska M.[1], Bartczak P.[1], Dudziński G.[1], Podlewska-Gaca E. [1]

[1] *Institute Astronomical Observatory, Adam Mickiewicz University in Poznań, Poland*

In the Solar System among the 424 binary asteroids we currently know only 18 synchronous binary small objects, the systems with two bodies having similar size and with the same rotational and orbital periods. In our project we are concentrating on creating models for this unique binary objects with major parameters about asteroid systems, such as non-convex shape, spin axis orientation. Models are calculated, on the same way as for the 90 Antiope (Bartczak et al., 2014) and 809 Lundia (Bartczak et al., 2017, Kryszczyńska et al., 2008), using the genetic-algorithm-based modelling method SAGE (Shaping Asteroids with Genetic Evolution). The SAGE method based on photometric observations, for modelling process are required data from several apparitions (in particular observations obtained with different and evenly distributed ecliptic longitudes).

1. Photometric observations of synchronous binary systems.

Photometric observations are still the main source about physical properties of asteroids. Lightcurve for synchronous binary system, is not quasi-sinusoidal as for most asteroids, but with very characteristic typical U-V shape (Fig. 1.B, 2.B) due to the rotation of nonspherical bodies and caused by mutual eclipses. Analyzing asteroid lightcurves from a few nights of observations, we can estimate their rotation periods. If we collect data from a few apparitions, over several years, we can determine major parameters about asteroid systems. Adding new data to the already obtained dataset will allow us to compute their models for the first time. Below are very shortly presented examples of reduced data from 2020 year for two binary asteroids observed with the LOT telescope.

1.1. 1139 Atami

The Atami is a Mars-crossing synchronous binary asteroid. Its binary nature was revealed by photometric observations in 2005 (Manzini et al., 2006), components have dimensions around 5 kilometers and maximum separation of 15 km. Rotation and orbital period of the system was calculated to 27.45 hours. Since 1986 Atami has already been observed during its ten apparitions (Fig 1. A). Observations obtained for Atami by the LOT and the RBT (Roman Baranowski Telescope) telescopes during the last opposition in 2020 show lightcurve with visible mutual eclipses of different depths. In Fig. 1. B is presented composite lightcurve from 16 nights in January and March 2020 and shows a total amplitude of around 1.0 mag, 0.6 mag for the eclipsing and 0.4 mag for the rotational components. Different depths of minima, caused by mutual eclipses, are due to various phase angles of observations and ecliptic longitudes. The orbital as well as the rotational periods were calculated to 27.469 ± 0.001 h. It is predicted that during nearest apparition in July 2021 we are able to observe eclipses events as well.

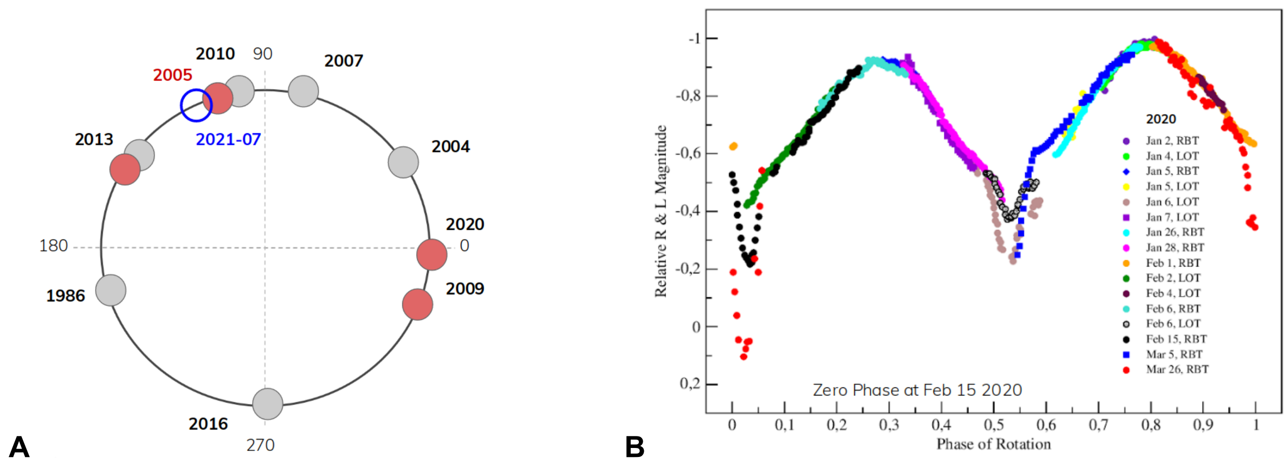

Figure 1. A. Comparison of the ecliptic longitudes of the Earth in the reference frame of the asteroid Atami: observations without eclipses (gray circles), oppositions with visible eclipses (red circles) and future apparition in 2021

(blue ring). **B.** The preliminary composite lightcurves of 1139 Atami from its 2020 opposition (V=14.7 mag). Observations obtained with 1-m LOT telescope at Lulin Observatory in Taiwan and with 0.7 m RBT telescope in Winer Observatory, Arizona, USA.

1.2. 2478 Tokai

Tokai is a binary asteroid from the main asteroids belt. Photometric observations obtained in 2007 showed that it is a synchronous binary system with a period of 25.885 +/- 0.007 hours (Higgins et al., 2007). Since 2007, the system was observed only during five apparitions (Fig. 2.A). The last observations of the Tokai system from 13 nights, when the object was observed from December 2019 to March 2020, also show eclipses/occultation of components. The received composite lightcurve is presented in Fig. 2. B and it shows a total amplitude of around 0.9 mag, 0.6 mag for the eclipsing and 0.3 mag for the rotational components. Unfortunately, the lightcurve from apparition 2019/2020 is incomplete.
All collected lightcurves for Tokai have visible eclipses which may suggest that we can observe the system orbit edge-on at the time of the observation.

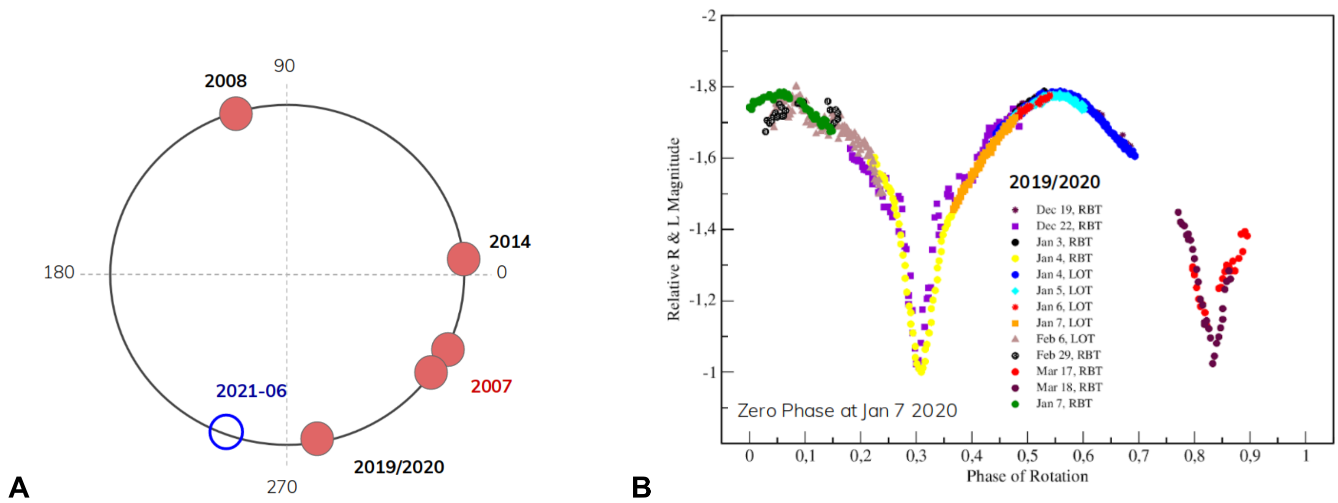

Figure 2. A. Positions of the Earth in the reference frame of the Tokai asteroid. Red dots represent positions with observed occultation events. Open blue circle represents future observing geometry in 2021. **B.** The preliminary composite lightcurves of 2478 Tokai from its 2019/2020 opposition (V=15 mag). Observations obtained with the LOT and RBT telescopes. The calculated rotational period is to 25.897 +/- 0.004 h.

2. Future works

The main goal of our project is determination for the first time models with its uncertainty for all synchronous binary asteroids. The data obtained with the LOT telescope (for the four asteroids: 854 Frostia, 1089 Tama, 1139 Atami, 2478 Tokai) additionally with observations from various telescopes and the yet unpublished dataset collected in the database of Poznan Astronomical Observatory will enable us to calculate models of this unique binary asteroids in the near future.

References:

Bartczak P., Kryszczyńska A., Dudziński G., Polińska M., et al., (2017), A new non-convex model of the binary asteroid (809) Lundia obtained with the SAGE modelling technique, MNRAS, 471, 1, 941-947
Bartczak P., Michałowski T., Santana-Ros T., Dudziński G., (2014), MNRAS, 443, 1802
Higgins, D., Pravec, P., Kusnirak, P. et al., 2007, Central Bureau Electronic Telegrams, No. 824, (2478) Tokai
Kryszczyńska A., Colas F., Descamps P., Bartczak P., Polińska M., Kwiatkowski T. et al., (2008), New binary asteroid 809 Lundia – I. Photometry and modelling, A&A 501, 769-776
Manzini, F., Behrend, R., Klotz, A., et al., 2006, Central Bureau Electronic Telegrams, No. 430, (1139) Atami

Spectral variation of M dwarf during the flare and flare temperature measurement

Chia-Lung Lin, Li-Ching Huang, Yu-Chi Cheng, Wei-Jie Hou

1. Introduction

The temperature of the flare determines the intensity of high-energy radiation such as ultraviolet, which in turn determines the impact on the biosphere on Earth-like exoplanets in the habitable zone. The flare temperature also affects the results of the flame energy calculations. Furthermore, the heating of the chromosphere during a flare can affect the behavior of the radiation in the entire spectrum of the star.

Many previous spectroscopic/photometric (e.g. Kowalski et al. 2010, 2016) studies on the color index of flare have found that the temperature of white light flare is around 9000 to 10000 K. However, the recent study carried out by Howard et al. (2020) has found that the temperature can reach 25,000 K.

Assuming that a 25000 K flare occurs on an M dwarf star with the temperature of 2800 K, and the area of the flare explosive region is 0.001% of the projected circular area of the star, the overall blackbody emission of the star should change as in Figure 1, and the relative intensity of light at short wavelength would increase significantly. If we can observe a flare event on an M dwarf with a spectrometer, we can subtract the spectrum of the M dwarf during the flare occurs from the spectrum of the stellar quiescent to obtain the blackbody radiation contributed by the flare, and then deduce the temperature of the flare.

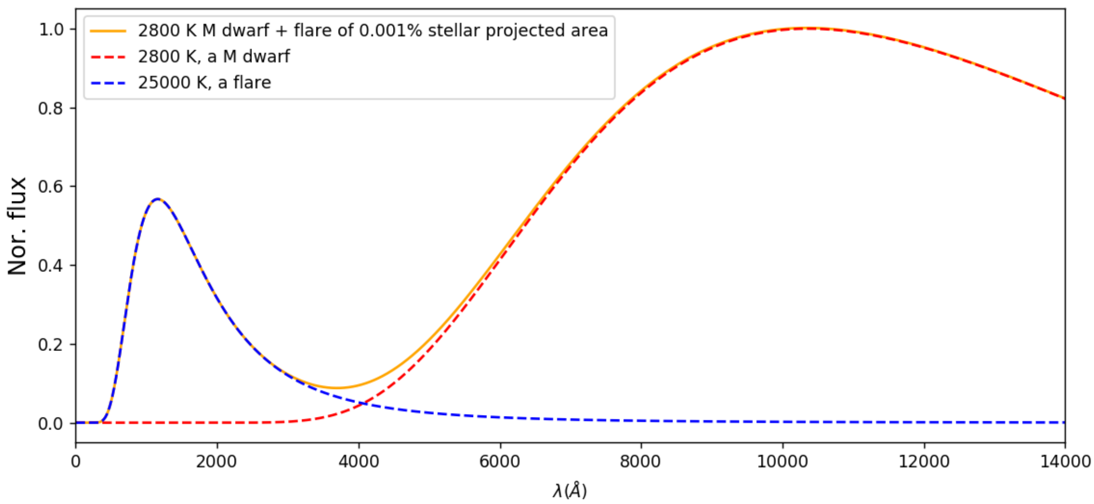

Figure 1. Simulation of the variation of the blackbody radiation of a flare with the temperature of 25000 K and the area of 0.001% stellar disk erupting on an M dwarf with the temperature of 2800 K. The red dashed curve is the blackbody radiation of an M dwarf with 2800 K, and the orange curve is that of the M dwarf spectra plus the blackbody radiation of the flare. The blue curve represents the flare's blackbody radiation obtained by subtracting orange curves from the red dashed curve.

2. Observation and a quick result.

We will use the LISA spectrometer on the Lulin 1-m telescope (LOT) at the Lulin Observatory for flare spectroscopic observations. We will also perform simultaneous photometric follow-up with the SLT 41-cm telescope. Our intended target is Wolf 359 because of its high flare occurrence frequency, which allows us to obtain enough samples of the flare spectra in a limited time. Since Wolf 359 cannot be observed from the Lulin Observatory during this semester (i.e. LOT 2020B), we have selected an M-type flare star, EPIC 210651981, for a three-night test observation this semester. The sampling frequency was 30 seconds for SLT 41-cm in r band and 5 minutes for LOT LISA. We captured a flare at midnight on October 30 (Figs. 2 and 3), but we unfortunately missed the peak of the flare in the spectroscopic observations and only recorded the decay phase, which lasted about 20 minutes and emitted an energy of about 31.7 Log erg in r band. The Balmer lines also increase during the flare (see Fig. 4 and Fig. 5), especially the H-beta line.

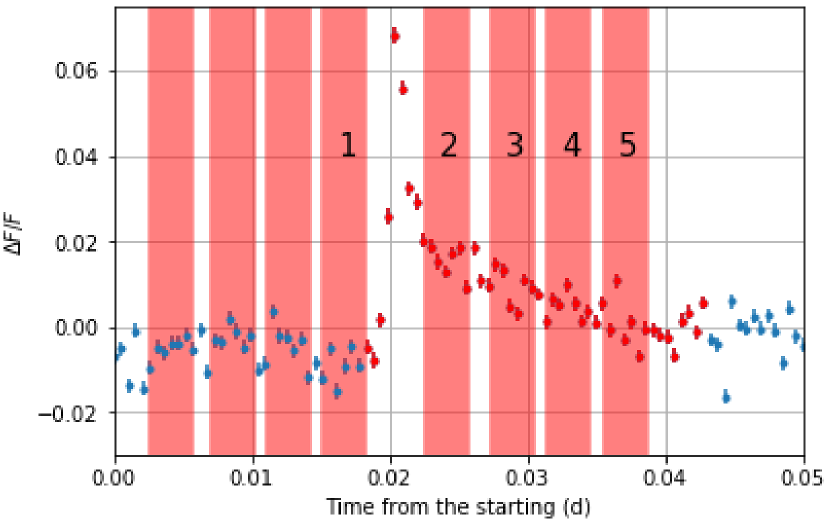

Figure 2. The flare profile of EPIC 210651981 in the light curve observed by the SLT 41-cm telescope with sampling frequency of 30 seconds. The flare peak amplitude is ~ 0.065 and the flare energy is ~ 31.7 Log erg in r band. It lasted about 20 minutes. The red-covered area is the exposure coverage time range of the LOT LISA spectrometer (five minutes for one exposure). The spectra of 1, 2, 3, 4 and 5 are shown in Fig. 3.

3. A brief discussion and summary

From the comparative spectra shown in Figure 3, one of the biggest challenges is that the wavelength range of the spectra seen by the LISA spectrometer does not cover at least 4000 angstrom in the short wavelength. This means that flare that are too low in temperature or too small in area will be difficult to detect from LISA observations. Our observation program will be relatively sensitive on relatively high temperature and

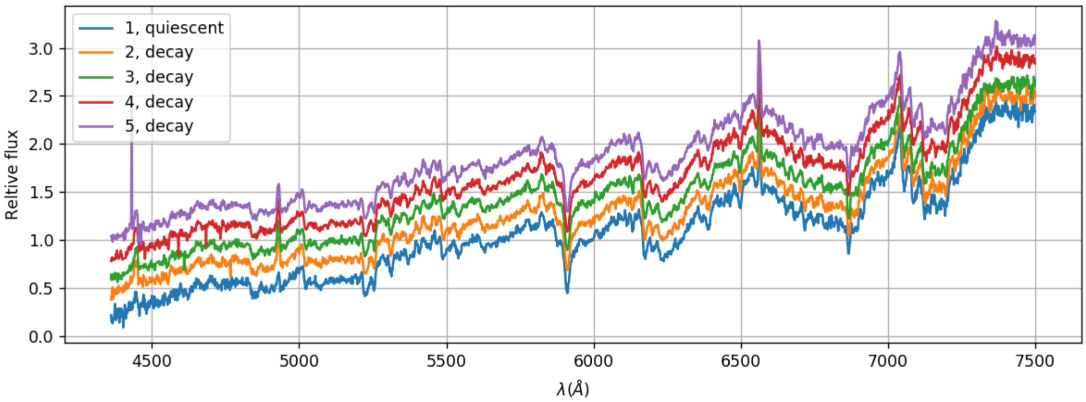

Figure 3. The stellar spectra of the quiescent and flare state.

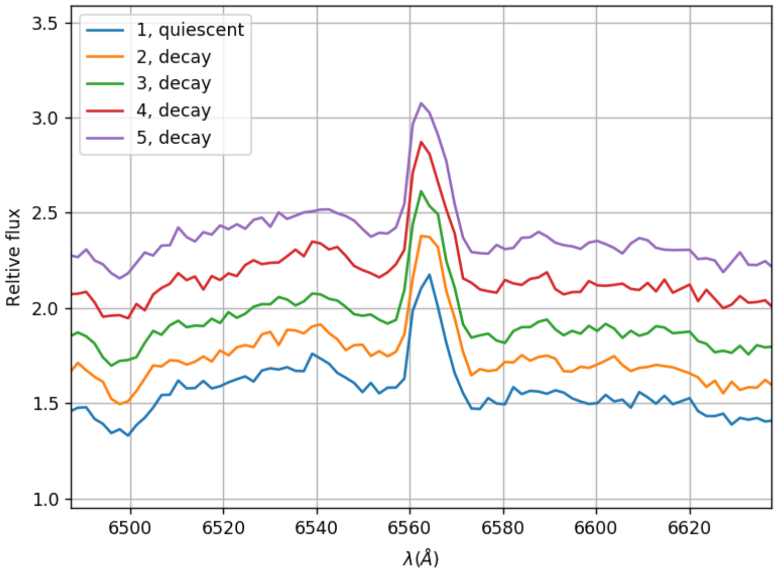

Figure 4. The H-alpha line variation from quiescent to flaring states.

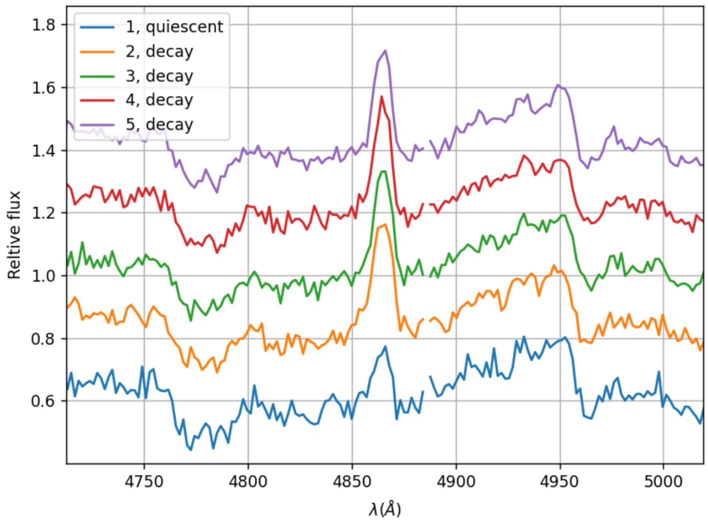

Figure 5. H-beta line variation from quiescent to flaring state. The increasing of H-beta emission is more significant than that of H-alpha line.

large flare. Moreover, the simultaneous SLT 41-cm photometric observation will be conducted using shorter wavelength band such as u band for the color-temperature study of flare combining photometric and spectroscopic observations.

We have submitted a LOT observational proposal for next season 2021A and have been given more than 10 nights in April to focus on Wolf 359. We expect to capture the complete spectrum of the flare from impulsive to decay phase and look forward to the SLT 41-cm simultaneous photometric observation in shorter band can contribute to color-temperature flare study in the new season.

References:

Kowalski, A. F., Hawley, S. L., Holtzman, J. A., et al. 2010, ApJL, 714, L98. doi:10.1088/2041-8205/714/1/L98

Kowalski, A. F., Mathioudakis, M., Hawley, S. L., et al. 2016, ApJ 820, 95. doi:10.3847/0004-637X/820/2/95

Howard, W. S., Corbett, H., Law, N. M., et al. 2020, ApJ, 902, 115. doi:10.3847/1538-4357/abb5b4

3. 其他成果

3.1 目前參與之國際合作計畫

台灣位處太平洋西側，由於廣大的太平洋上（橫跨 6 個時區）只有夏威夷有天文台，對於觀測隨時間變化的天文現象或是全球不同經度的天文台（甚至太空望遠鏡）針對特定天體的聯合觀測，鹿林天文台扮演舉足輕重的角色。多年來鹿林天文台積極參與國際合作計畫，與各國天文台建立良好合作模式，並取得優良成果。這一年我們參與的幾個主要國際合作計畫如下：

1. 全球蠍虎 BL 類星體聯合觀測計畫（The Whole Earth Blazar Telescope - GLAST-AGILE Support Program, WEBT-GASP）：監測活躍星系核，藉此研究黑洞與噴流的性質。
2. 史維基瞬變探測器計畫（Zwicky Transient Facility, ZTF）：將天文研究推進到時間加上空間的 4D 階段，可望對可見光時域天文學作出重大的科學貢獻。
3. 伊甸園觀測網（Exoearth Discovery and Exploration Network, EDEN）：搜尋鄰近太陽之 M 型恆星可能位於適居區內的系外行星。
4. 年輕超新星巡天計畫 (Young Supernova Experiment) ：使用 Pan-STARRS telescopes 在 ZTF 天區進行巡天，藉由兩者之間經度的差距來探測瞬變天體早期的演化。

GLAST-AGILE Support Program (GASP) project

Tsai, An-Li & Chen, Weng-Ping

This project

Blazars are known as one type of AGNs with strong relativistic jets. They have rapid and large-amplitude flux variability from radio to γ-ray with time-scales from hours to years.

The Whole Earth Blazar Telescope (WEBT) has been organizing the GLAST-AGILE Support Program (GASP) to become the WEBT-GASP consortium which the WEBT-GASP consortium provides data at optical, near-infrared, and radio with high-temporal-density monitoring of blazars to be compared with the UV and X-ray data from Swift, and the γ-ray data from the AGILE and GLAST satellites. The aim is to understand the connection among emissions at different frequencies and to derive information on the emitting jet.

Our NCU Lulin 45 cm Telescope, a member of the WEBT-GASP consortium, has been a part of the project for years, and will continue to contribute to. I will be responsible for processing the Lulin data and submit the results for this project and provide image and photometric data for further studies on light curves, spectral energy distribution, and so on.

Lulin observations in 2020

In 2020, Lulin SLT 40 cm telescope obtained 6664 fits data for 26 GASP targets, including 3C273, 3C279, 3C345, 3C371, 3C454-3, 3C66A, 4C29-45, 4C38-41, 4C51-37, 4C71-07, AO0235+16, CTA102, DA406, ES2344+514, PKS1510-08, L-Lacertae, Mkn421, Mkn501, OJ248, OJ287, OJ49, ON231, PKS0735+17, PKS2155-304, S4 0954+65, and S5 0716+71.

The light-curve of each target is shown in Figure 1.

About 533 fits data are not usable. About 92% data are available. There are 333 days have executed this project. Only 231 days have observations, and 102 days have no observation due to bad weather. The succeed rate is about 69%.

Paper published in 2020

- Weaver, Z. R., Williamson, K.E., Jorstad, S. G., et al. (including Chen, W.-P. and Tsai, A.-L.), "Multiwavelength Variability of BL Lacertae Measured with High Time Resolution ", *ApJ*, 900, 137W (2020)

- Raiteri, C.M., Villata, M., Carosati, D., et al. (including Chen, W.-P. and Tsai, A.-L.), "The dual nature of blazar fast variability: Space and ground observations of S5 0716+714 ", *MNRAS*, 501, 1100 (2020)

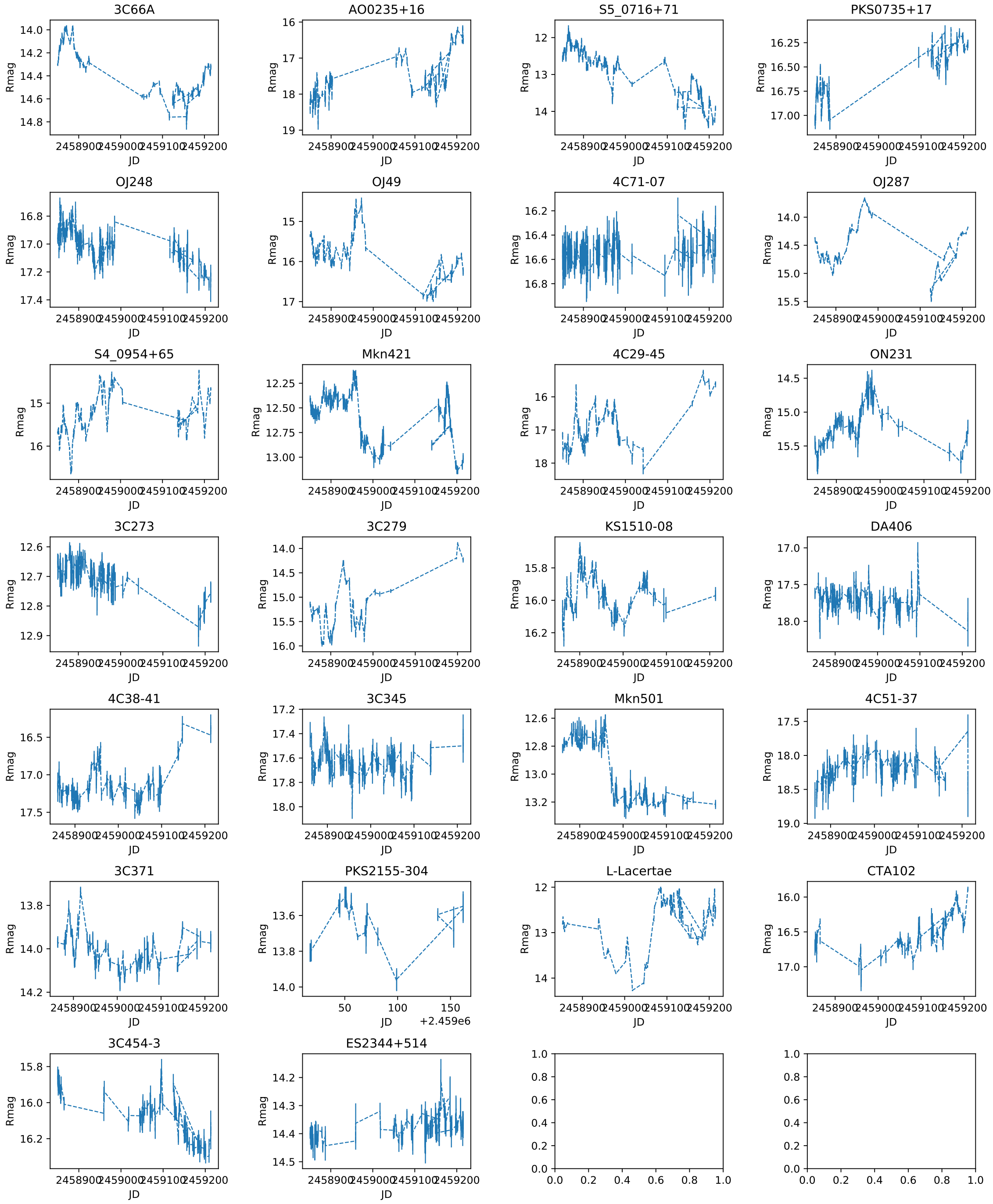

Figure 1 Lulin observations in 2020 with 26 GASP targets2

Exo-earth Discovery and Exploration Network (EDEN)

Tsai, An-Li & Chen, Weng-Ping

This project

The Exo-earth Discovery and Exploration Network (EDEN) project aims to identify and characterize habitable planets within 50 lightyears. Our NCU Lulin One-meter Telescope (LOT) is one of the eight telescopes in the EDEN sites. With eight telescopes in North America, Europe, and Asian, EDEN allows to have a longitudinal coverage in the northern sky. The typical EDEN telescopes have several hundred times more light-gathering power than the wide-field cameras of NASA's Transiting Exoplanet Survey Satellite (TESS) mission, allowing EDEN telescopes to probe the habitable zones of nearby but very faint red dwarf stars inaccessible to NASA's TESS mission, or to most other ground-based transit surveys that utilize small telescopes. In addition to exploring planets around host stars too faint for TESS, project EDEN will also be a powerful system for following up the most exciting planet candidates identified by TESS.

I will be in charge of using LOT for transit surveys and follow-up observations. The LOT will contribute the telescope time of ∼10 days a month. The main goal is to monitor nearby M-type stars and search for possible transiting earth-like planets in the habitable zone.

Lulin observations in 2020

In 2020, Lulin One-meter Telescope obtained 20190 fits data for 15 EDEN targets, including 2MASS_J0515+5911, 2MUCD11188, LP 229-30, LP 271-25, LP 310-34, LP 315-53, LP 326-21, LP 335-12, LP 388-55, LP 647-13, LSPM J0140+2701, LSPM J0419+4233, LSPM J0510+2714, LSPM J1055+0808, and TOI 736.

One light-curve of the EDEN targets is shown in Figure 1. There are 121 days have executed this project. Only 96 days have observations, and 25 days have no observation due to bad weather. The succeed rate is about 79%.

Paper published in 2020

- Gibbs, A., Bixel, A., Rackham, B., et al. (including Chen, W.-P. and Tsai, A.-L.), "EDEN: Sensitivity Analysis and Transiting Planet Detection Limits for Nearby Late Red Dwarfs", ApJ, 159, 169G (2020)

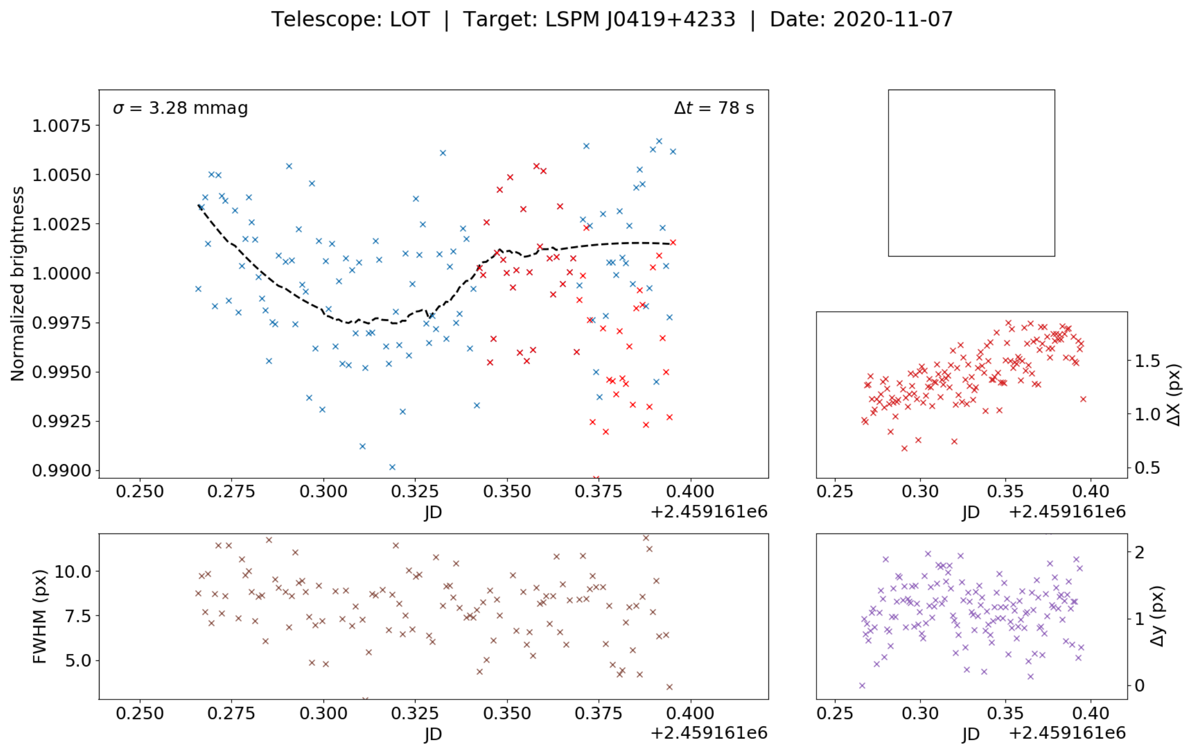

Figure 1 The light-curve of LSPM J0419+4233 on Nov. 17, 2020.

TRANSIENTS WITHIN HOURS OF EXPLOSION

Yen-Chen Pan
Graduate Institute of Astronomy, National Central University

1. Abstract

Transient surveys are now consistently finding transients within hours of explosion. These observations provide rare opportunities to investigate the explosion and progenitor system, and probe the circumstellar environment surrounding the SN. Interaction with a potential companion star is also visible in the first hours. We have started an international collaboration to detect extremely young explosions since 2019. Using a novel technique to combine our data with public data, we will clearly identify interesting targets as they rise, detecting transients within hours of explosion. The Lulin observatory is part of the collaboration and plays a critical role in constraining the properties of these young transients. Here I will briefly describe the program and report the current status.

2. Description of the Program

Early observations of transients place unique constraints on their progenitor systems and explosion mechanisms. To increase the number of transients detected within hours of explosion, we are starting a new survey, the Young Supernova Experiment (YSE). YSE is the collaboration between DARK (University of Copenhagen), UC Santa Cruz, University of Illinois, University of Toronto, and Northwestern University. YSE will survey $\sim 1000\,\mathrm{deg}^2$ of equatorial sky on a 3-day cadence (in $griz$) using the Pan-STARRS (PS) telescopes. We will also shadow other public transient surveys, such as ASASSN, ATLAS and ZTF, which can improve our detection and selection of SNe within hours of explosion. Because of different observatory longitudes, there will be a lag of a few hours between the public survey and PS observations. During this time, some transients will explode and rise to a point of being detectable, and more will be barely detectable in the public surveys and rise considerably in a few hours. When PS detects a new transient, we will immediately query these public surveys to determine if the transient is young. With the expected cadence of PS observations, our detected transients will be 3 days old at most, and we expect to discover $\sim$2 transients within hours of explosion per month.

We ask for Lulin ToO observations to obtain the multi-color photometry of YSE transients, and to watch the objects quickly develop. Being another few hours lag from the PS telescope, the location of Lulin observatory will be critical to constrain the extremely young transients discovered by YSE. Any young transients detected by PS telescope can be monitored by Lulin within hours, which will greatly reduce the cadence of our photometric observations. This is crucial given the light-curve evolution is expected to be dramatic within the first few days after explosion. The early Lulin observations will play an important role in catching this fast evolution and provide better constrain on the transient age.

3. Program Status

We were able to observe 15 transients with Lulin 1-m telescope from 2019 to 2020. Five objects were classified as Type Ia supernovae (SNe Ia). Two were classified as Type Ibc supernovae (SNe Ibc). Seven were classified as Type II supernovae (SNe II). One was classified as Luminous Blue Variable (LBV). Many of these events are interesting and exciting. For example, we observed SN 2018ivc, a young core-collapse SN discovered in M77. Lulin successfully caught this SN within 12 hours after the discovery. We also observed SN 2019np, an extremely nearby and young SN Ia discovered in

NGC 3254. Our collaboration (including Lulin) were able to obtain the photometry only couple of hours after the explosion. Another interesting object is SN 2020bio, a core-collapse SN with shock-breakout feature detected by YSE. This kind of feature is rare and can only be detected at extremely early times.

All the Lulin data has been reduced and processed to create excellent light curves. Examples can be found in Figure 1. Detailed studies are still at work.

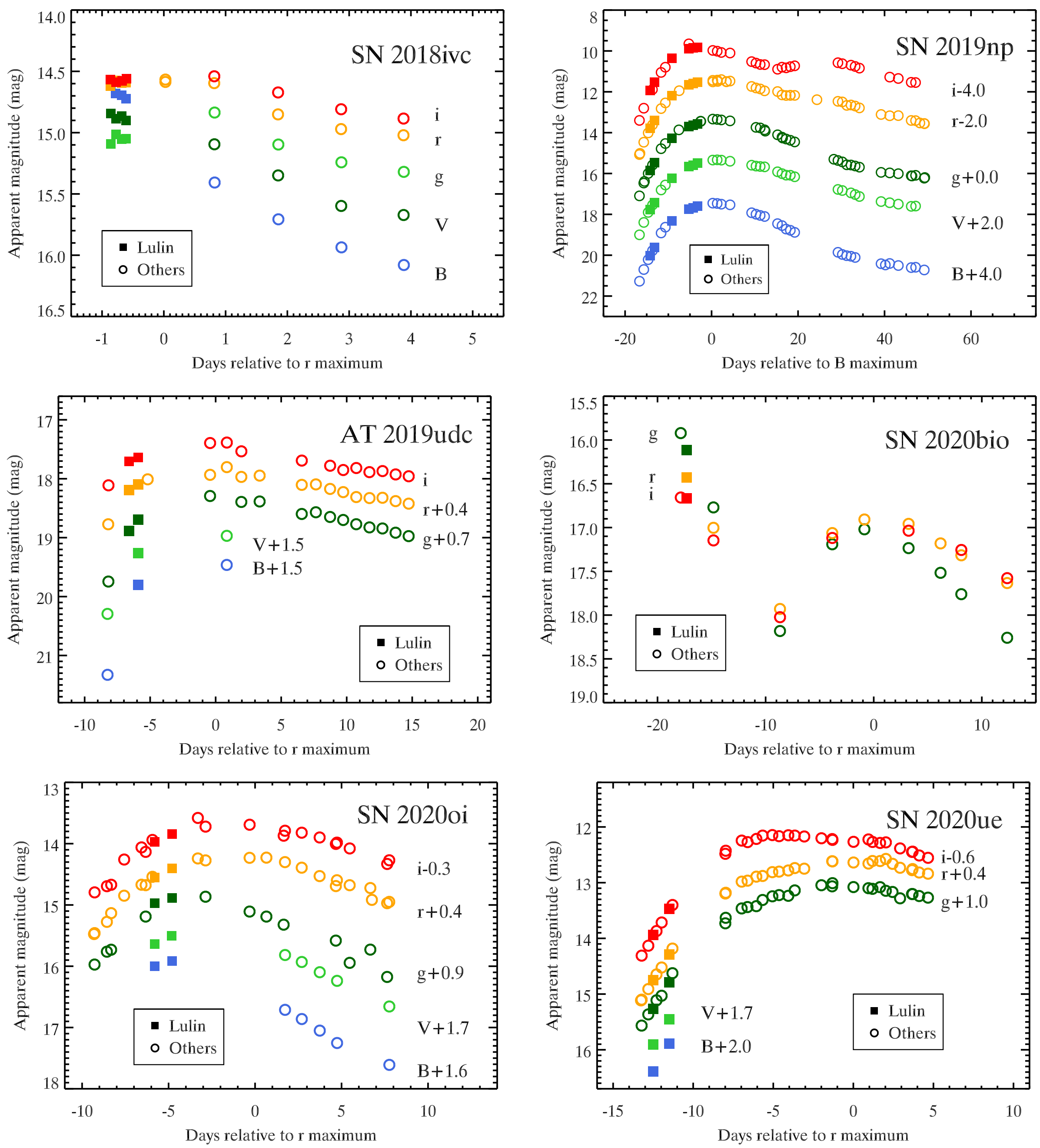

Figure 1: Multi-color light curves of some nice SNe observed by our YSE collaboration. For all panels, the photometry observed by Lulin 1-m telescope is shown in filled squares, while other telescopes in our collaboration are shown in open circles.

鹿林天文台參訪團體統計(2020)

日期	單位	人數
1 月 13 日	全國大學天文聯盟	9
1 月 18 日	台達電	9
1 月 21 日	成功高中天文社	23
1 月 22 日	建國中學	50
1 月 29 日 6 月 15 日	因疫情暫停參觀	
6 月 25 日	玉管處保育科	13
6 月 28 日	警察小隊來賓	6
7 月 14 日	中大科學日文課	13
7 月 18 日	逢甲大學天文社	8
7 月 19 日	二水國中	25
7 月 25 日	中原天文社	15
7 月 27 日	瑞祥高中	9
8 月 2 日	台師大菁英團隊	13
8 月 11 日	台南社大攝影班	15
8 月 15 日	高雄新莊、道明、中正高中	40
8 月 29 日	文山社大	20
9 月 17 日	中大理學院院長等	4
9 月 26 日	台灣山岳文教基金會	4
10 月 9 日	親子觀星會	24
10 月 17 日	全國大學天文聯盟	53
10 月 17 日	台北天文協會	24
10 月 21 日	玉管處、金管處	6
11 月 14 日	台南社大、永康社大	30
12 月 5 日	嘉中嘉女天文社	39
12 月 6 日	新竹高中天文社	12
12 月 11 日	中一中中女中天文社	19
12 月 14 日	中大國際處	13
12 月 19 日	惠文高中	21

LISA 使用手冊

鄭宇棋、侯偉傑

安裝前調整

確認波長範圍

將光譜儀主 CCD 連接電腦 (cooling 可有可無), 並且接妥 calibration kit box 中譜燈的 12V 電源, 拍攝 300 秒譜燈, 檢查波長範圍是否合乎需求. MaxIm DL 的 horizontal profile 可對照手冊的 Ne/Ar 發射譜線(附件 x)確認波長. LISA 的建議可用範圍為 X=500-2750.

調整波長範圍

若需調整 grating angle, 先移除 1 顆保護蓋螺絲, 並鬆開撥桿的 2 顆螺絲, 中間螺絲為 grating 轉軸勿動！請注意手部清潔, 盡可能防止塵埃掉入光譜儀內部. 撥桿向上為移向紅端, 反之則往藍端, 調整時主 CCD 以 10 秒連續曝光, 監看波長範圍變化, 調整主 CCD 的波長範圍無誤後, 鎖緊撥桿螺絲, 並再次曝光確認波長範圍是否因螺絲鎖緊而產生些許改變

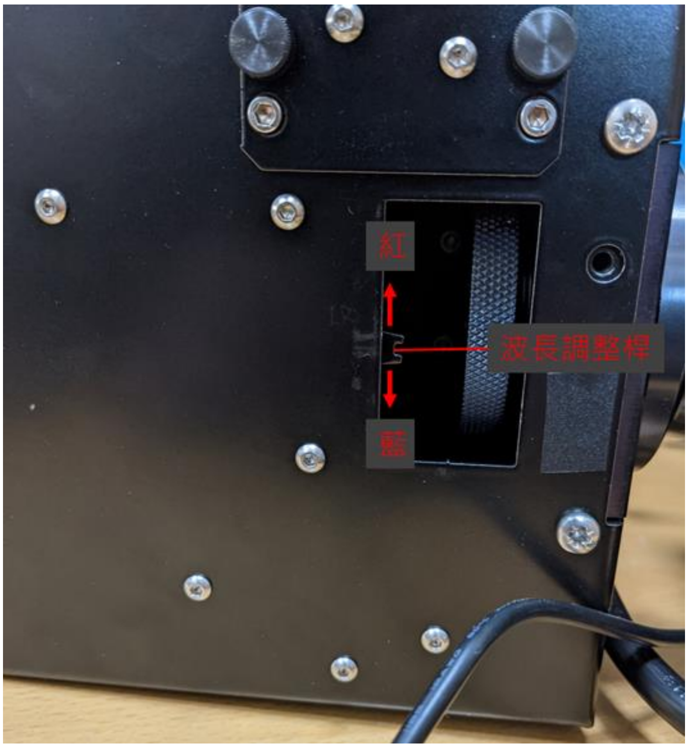

主 CCD 後續調整與對焦

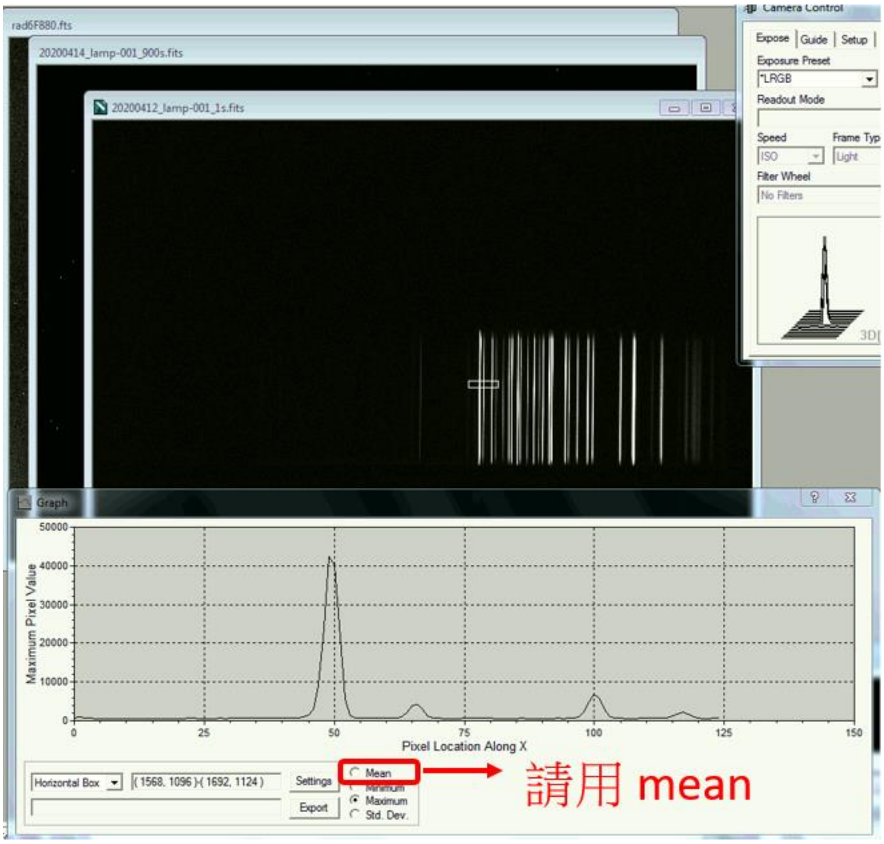

圖 2

波長調整完成後，鬆開主 CCD 固定螺絲，持續連續拍攝譜燈(5 秒即可)，微調 CCD 角度使色散軸對齊主 CCD 的長軸，並前後移動約略調整焦點位置．鎖定主 CCD 後，再利用光譜儀內部的調焦機構(見圖)，來微調主 CCD 的對焦狀況，受到成像面彎曲的影響，對焦請對在 CCD 中間偏右約 1500-2000 pixel 之間的譜燈發射線．在妥善對焦的狀況下，發射線的半高全寬大致小於 5 pixel．完成後裝回光譜儀兩側蓋板．

Check List

- ❏ 波長範圍是否符合需求
- ❏ 主 CCD 對焦狀況
- ❏ 主 CCD alignment

光譜儀安裝與電腦設定

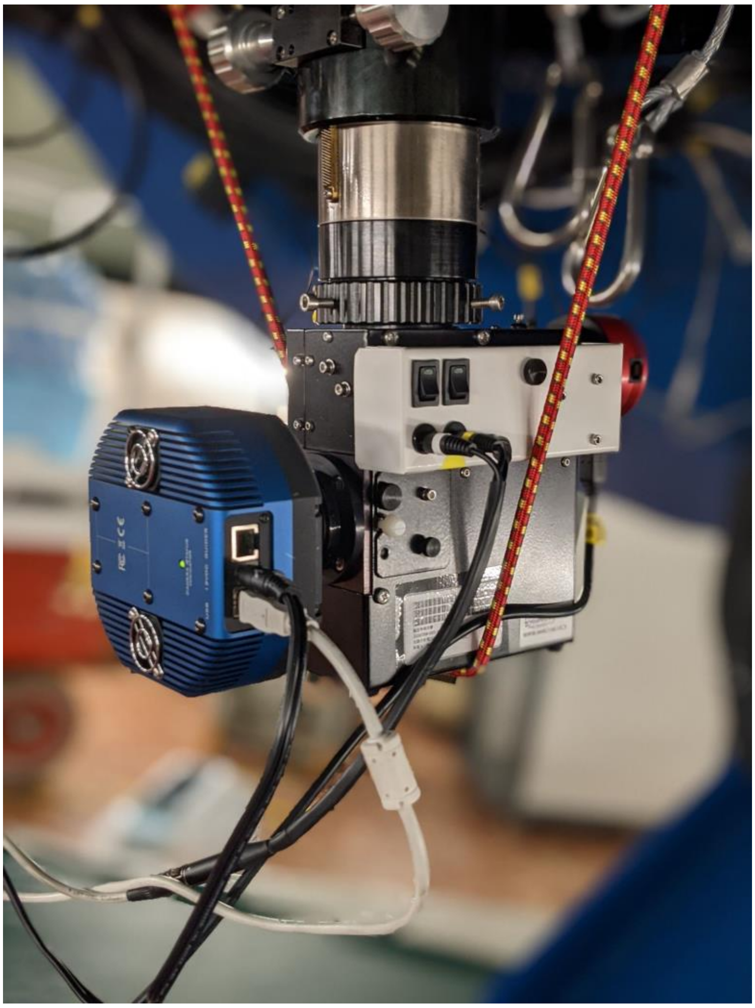

圖 3

光譜儀安裝

如圖 3, 安裝時主 CCD 朝端北, QSI 660 CCD 接 12V 電源線與 USB 線 (連接線接口朝西), guiding camera 接 USB 線 (連接線接口朝下), calibration kit box 12V 電源線白左黃右. 若有安裝減焦鏡, 對焦座長度轉到最短, 若無減焦鏡, 對焦座則拉長至約 5 公分(?). 適當調整防護用彈性束帶長度, 切記束帶固定點不要越過對焦座！

電腦設定與 CCD 連線

Main CCD：

MaxIm DL > ASCOM > QSI CCD Camera (圖 4 上)

Coolor：-15℃ (設定太低會降不下去，或是早上溫度會回升)

Guiding camera：

PHD2 > ASI Camera > ZWO ASI120MM(ID0) (圖 4 下)

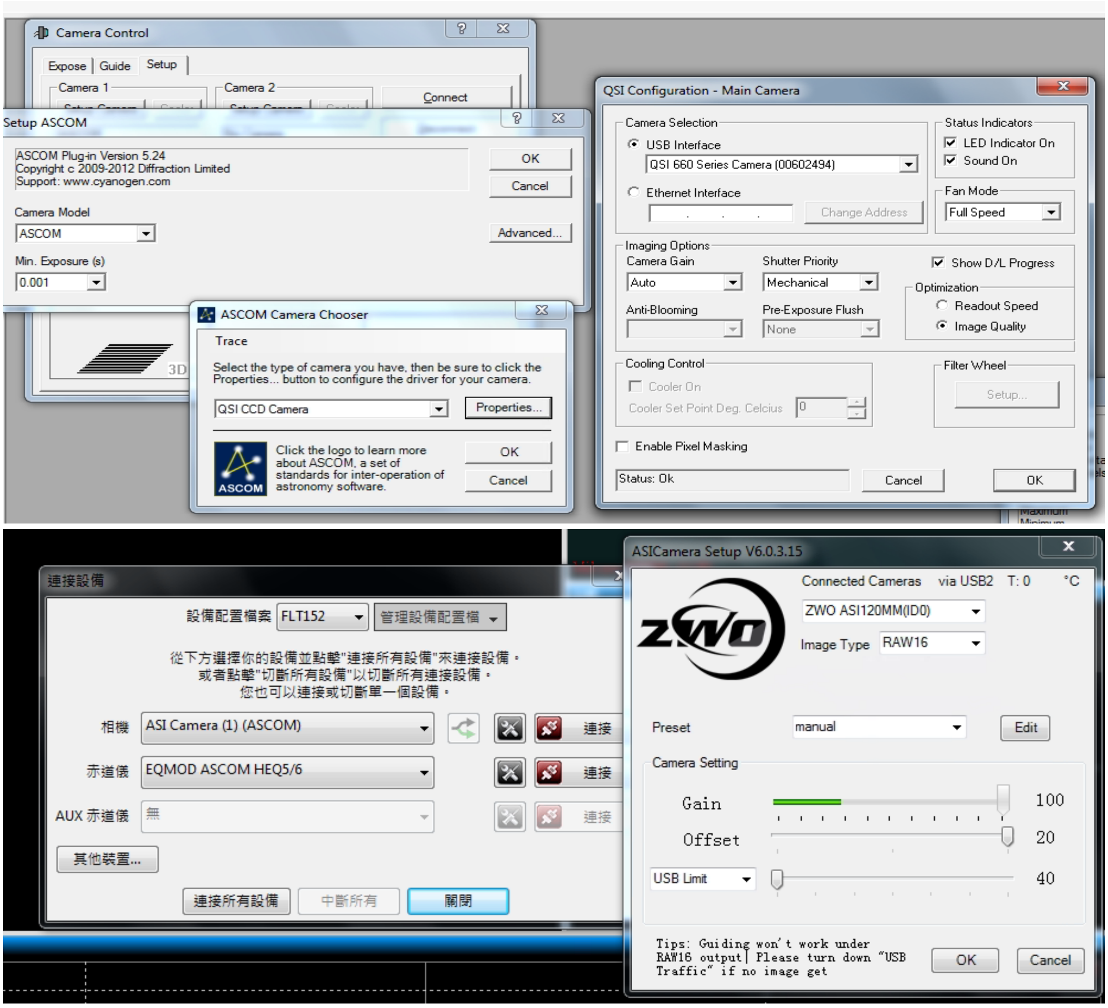

圖 4

導星相機調整(需在圓頂進行)

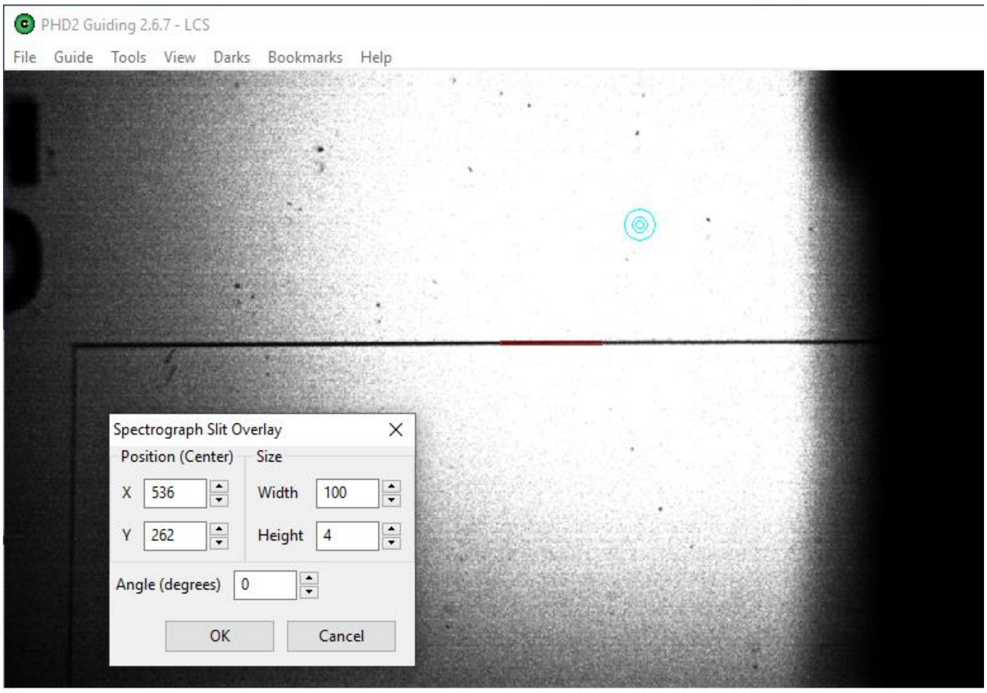

圖 5

攜帶一台可連接 guiding CCD 的電腦至圓頂，開啟平場燈並連線 guiding CCD，以 PHD2 導星軟體監控狹縫對焦情形與旋轉角度，盡可能將狹縫調整至水平方向. 完成後排線接回控制室電腦，在導星軟體 PHD2 的 view 選單，點選'spectrograph slit'以開啟狹縫標記，若有需要可在'slit position'修改狹縫位置. 狹縫位置可開啟平場燈來進行確認.

Check List

- ❑ 導星 CCD 方向與對焦調整 (排線朝下)
- ❑ 安全束帶沒有跨越電動對焦座
- ❑ 手動對焦座位置正確 (有減焦鏡：轉到最短，沒有減焦鏡：長度約 x 公分)
- ❑ 線材接妥, toolkit box 開關開啟
- ❑ CCD 溫度設定在-15 度
- ❑ 導星軟體狹縫設定
- ❑ MaxIm DL telescope 連線

觀測前準備

望遠鏡對焦

選取一顆 10 等亮星，設定 guiding CCD 一秒連續曝光，以 PHD2 軟體監看星點的對焦情形，並且以 auto slew 電腦調整焦距.

譜燈拍攝

使用預設的 Ne/Ar 譜燈，切換後等待至少五分鐘讓光源穩定，原則上至少拍攝 7 張 300 秒影像，每晚拍攝一次即可.

Dome flat

關閉 dome slit，打開 mirror cover，把望遠鏡指向 flat screen，打開平場燈，原則曝光 60s*7，與 60s dark 交錯拍攝，開始拍攝時開啟望遠鏡 sidereal tracking，讓望遠鏡視野掃過 flat screen，降低光源和布幕不均勻造成的影響，不建議使用內建的平場燈

bias/dark

QSI CCD 的 cooling 效率只能達到 ΔT=-25 度，請盡量在白天圓頂升溫前完成拍攝

Special note

Maxim DL 連接 QSI CCD 在曝光過程中會暫時凍結無法操作，若要取消曝光，請使用額外小技巧來解決

Check List

- ❑ 望遠鏡對焦
- ❑ 譜燈拍攝
- ❑ 平場拍攝

光譜拍攝

bad pixel mask

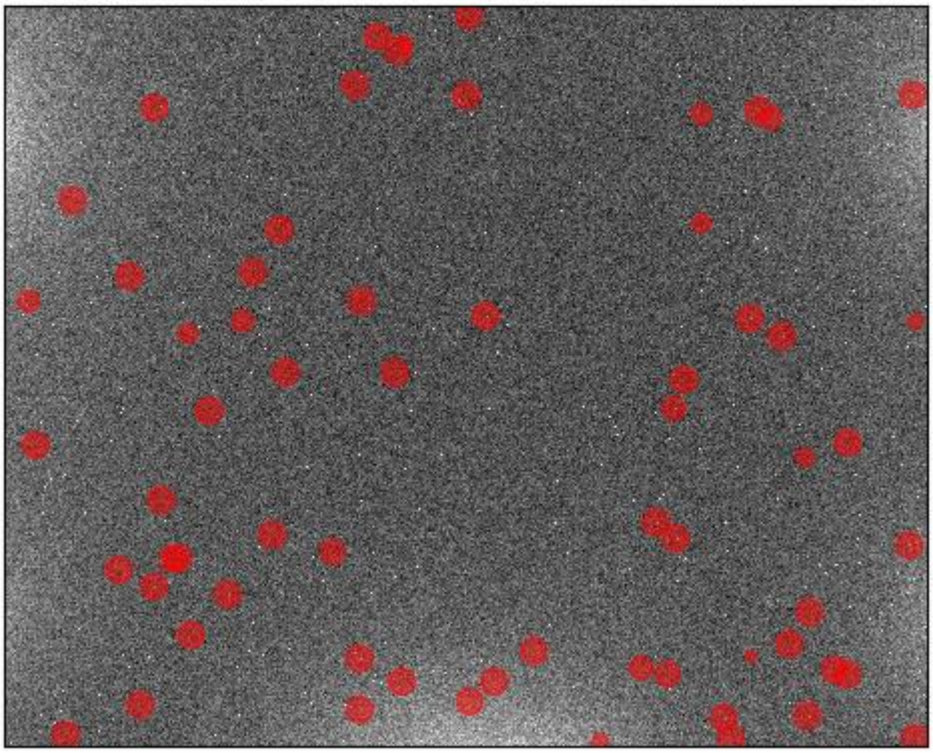

圖 6

拍攝光譜時，若需要長時間曝光(> 600s)，盡量避開已知的 CCD hot pixel，圖 6 為曝光 600 秒, pixel count > 60000 的 bad pixel. 此類 pixel 加上 bias/dark 之後會接近飽和，而造成無法彌補的後果.

自動導星設定-PHD2 Guiding

裝好儀器後第一次使用導星一定要先做一次 calibration，第一次 calibration 做完之後，之後直接導星即可。若覺得自動導星不太準確可以再做一次 calibration，不過若狀況依舊，可能是天氣狀況，或是 seeing 不佳，就要使用手動導星。

calibration 方法：在 guiding camera 影像上點選一顆星，然後 shift + click guiding button，畫面星點旁會出現黃色虛線十字，並開始做 calibration。等到黃色虛線十字變成綠色實線十字時代表已完成 calibration 並開始 guiding。而畫面下方 History 欄的修正量趨於穩定後就可開始拍攝。

停止 guiding：在移動望遠鏡前必須先停止 guiding ，否則 PHD2 會干擾望遠鏡 slew。可以用 re-looping exposure 或是 stop 來停止 guiding。

流星觀測與月撞觀測 (2016~)

林忠義(NCU)、紀信昌(NDHU) 、李瑾(TAM)、林宏欽(NCU)、
吳秉勳(Hui-Wen High school)、廖家賢(KTO)、馬學輝(KTO)

2013 年至 2015 年期間，東華大學之流星觀測實驗室架設 Dong Hwa Meteor System 持續與中央大學的阿部新助教授合作進行流星觀測，擷取臺灣東部東南至東北面向的即時 Meteor 觀測數據，進行三角定位軌道分析，定位流星軌道。另一方面，也同時拍攝流星光譜，進行分光光譜分析，探討流星組成成份。自 2016 年起，我與東華大學之流星觀測實驗室開始與合作，並著重於中央大學鹿林一米與其它望遠鏡的近地天體資料與流星事件的對應互補關係。自 2016 年起，我們開始與臺北市立天文科學教育館助理研究員李瑾研究員發展流星共同觀測計劃。台北市陽明山湖田國小、墾丁天文台、福壽山農場與合歡山小風口的流星觀測站在團隊的努力下於 2016 年八月、2017 年九月、2018 年三月與 2020 年六月開始與現行架設於鹿林天文台的流星觀測站(北、東、南面共六架攝影機)進行同步觀測，目的在流星光譜拍攝以及流星軌道三角定位，在決定流星軌道這方面，這方面我們已得到初步值得參考的豐富資料。從 2017 年開始，東華大學流星組學生(表一)已陸續在國內年會與國際會議中發表的許多相關的壁報論文(如附件)，我們團隊也從這幾年的觀測資料收集到許多軌道資訊，尤其是三大流星雨中的英仙座與雙子座流星雨，雖然天氣因素仍影響著觀測數據的多寡，但我們仍可從任兩個以上的測站對同一個流星事件中量測出流星的軌道、速度等，由此計算出的軌道與其對應的母體軌道也相當符合，對此，我們已經發表了一篇 Sci 學術論文

除流星觀測外，從 2017 年 12 月我們還針對月面撞擊閃焰事件做觀察，目的在瞭解星塵中的粒子大小分布情形，以流星體觀測大小的限制(雷達幾公分到幾公尺、流星觀測幾十公尺到幾百公尺)，月面撞擊事件觀測統計可以知道大小在幾公尺到幾十公尺的分布，結合兩者數據，我們就可以了解地球附近星塵中的粒子大小分布情形。針對月閃事件的聯合觀測，我們參與由日本 Ryuhei Yamada 所領導觀測團隊，提供 2018 年 12 月雙子座流星雨觀測其間所拍攝到的事件於日本團隊，從共同事件中探討不同流星群的撞擊概率、計算撞擊坑洞大小與能量分布情形，最後也參與論文討論與撰寫。

表一 東華大學參與流星資料處理與月面撞擊觀測學生

劉智晟	應數系
林宗誼	物理系
吳仲恩	材料系
洪梓惟	電機系
劉俊佑	自資系

林奕廷	光電系
林榮勝	光電系
張晏薰	應數系
王柏皓	應數系
金天慈	物理系
陳諺平	物理系
鄭宇伶	物理系
陳文豐	光電系
陳柏翰	光電系
郭仁傑	光電系
劉力魁	材料系
簡廷州	資工系

發表論文

1. Zhong-Yi Lin et al. 2020 The current development of the Taiwan Meteor Detector System (TMDS) with a dedication to the Geminids 2017 and 2018. Planetary and Space Science Volume 180, January 2020, 104763
2. Masahisa Yanagisawa et al. 2020 Low dispersion spectra of lunar impact flashes in 2018 Geminids (PSS, revised)

發表壁報論文

(1) 2019 年中華民國天文學會年會，05/17 ~ 05/19 2018，台中
(2) The 50th Lunar and Planetary Science Conference，3/18–22, 2019，Texas, USA
(3) 2019 中華民國物理年會海報，01/23~01/25 2019，台北
(4) 2018 年中華民國天文學會年會，05/18 ~ 05/20 2018，金門
(5) 2018 年中華民國天文學會年會，05/18 ~ 05/20 2018，金門
(6) *Synchronous Surveillances of Meteor Events using the Taiwan Meteor Detection System*
2017 年中華民國天文學會年會，05/19~05/21 2017，苗栗
(7) *Recent Meteor Observations of the Taiwan Meteor Detection System*
13th Asian-Pacific Regional IAU Meeting (APRIM 2017), July 3-7, 2017, Taipei

支援鹿林經費

1. 支援鹿林觀測費用 60k (由林忠義 MOST 助理研究學者支出)
2. 支援鹿林與所上經費 200k (由林忠義 MOST 助理研究學者節餘款支出)

山頂上的眼睛
——鹿林天文臺

文/周修麒、唐偉哲
鹿林星空圖：廖政霖

中央大學因於鹿林前山（海拔2862公尺）之顛，設有全臺最高且望遠鏡口徑最大的天文臺，而有「全臺最高學府」之稱。要到鹿林天文臺，首先要乘車到塔塔加上東埔停車場，接著要經過大約4公里的林道，只有經許可的車輛與接駁車可以行駛，但若用走的上山，徜徉於山林之間，也是個不錯的選擇。沿途最先抵達的著名地標就是樹齡800年大鐵杉，接著向右轉是往鹿林前山的方向，途中還會經過麟趾山鞍部，此處一片遼闊的山谷很值得駐足欣賞。沿著林道一直走到底，之後就會看到上天文台木棧道登山步道了，這段0.6公里的陡峭步道只能步行，清晨或是下雨天步道潮濕走起來要更加小心，是通往天文臺最辛苦的過程。

玉山國家公園導覽地圖：https://www.ysnp.gov.tw/page.aspx?path=445&2

崎嶇蜿蜒的路途，讓人不禁好奇當初天文臺建設的過程，以下是鹿林天文臺林宏欽臺長與我們分享的興建歷程與觀測生活：

開疆闢土，蓋天文臺

台長在中大唸碩士時跟的是蔡文祥教授。當時蔡教授的主要研究計畫之一是台灣天文選址，台長跟著指導教授到處跑，最後選定玉山國家公園鹿林前山。一般天文台基礎建設是從水、電、路三通開始，鹿林前山最大的問題是沒有路。因經費有限，先蓋鐵皮屋當臨時測站，請當地原住民幫忙揹水、揹油（發電機用）、揹建材等上去。發電機只有在晚上觀測時才會啟動，所以白天是沒電的，水也只夠飲用，洗臉用濕紙巾擦，不可能洗澡。在這麼簡陋的環境下，通常一個月去個1-2次、一次只能待個3-4天。後來真正蓋天文台時，望遠鏡鏡片、架台、鋼筋水泥等重物，則是從山下拉一個索道到山上，利用流籠來吊運。早期通訊主要是靠無線電，但觀測資料傳輸需要網路，所以自行架設了一套特規無線網路設備，用天線打到對高岳，再從對高岳打到阿里山的香林國中上TANet（台灣學術網路）。由於當時設備不穩定，一出問題就必須三個點都有人去檢修。「那個時候網路常常壞掉，每個禮拜都要跑阿里山好幾次」台長笑著說。後來內政部長去爬玉山時，發現手機收不到訊號，為了登山安全便找了幾家電信業者協力改善玉山國家公園的通訊品質，因附近山頭只有鹿林前山有電，因此基地台便在此，從此天文台手機、網路通訊問題就徹底解決了，不用再勞師動眾大費周章跑阿里山。

觀測生活

臺長的工作是望遠鏡的運作、維護，以順利執行觀測收集資料，讓老師、學生能夠利用望遠鏡的觀測資料進行各種不同的研究計畫。

因為鹿林天文臺沒有可讓車通行的路，山上的一切食衣住，通通都要用搬的上去。前一陣子天文台洗衣機壞掉，洗衣機一百公斤要怎麼搬？在山上要住那麼多天衣服也不能不換，不能洗衣服怎麼辦？還有床被、單套這些也要洗，以前搬運都靠原住民同事幫忙，他們說年輕時可以，但現在也有點年紀了，沒辦法背這麼重。最後就去部落裡面找年輕人來背這一百公斤的洗衣機。從這個故事中，我們不禁感嘆山上生活起居的打理是如此辛苦，感謝天文臺所有人員的努力，現今的鹿林天文臺環境相當舒適，有房間、客廳、廚房、浴室，生活起來都與平地上沒有差別，客廳有沙發、餅乾、咖啡茶飲，還許多天文相關書籍可以閱讀，是很溫馨的空間。現在比較辛苦的就是食物日常用品還是需要靠人力背上去，或是下次可能需要換冰箱的時候。

介紹完鹿林天文臺的生活，現在就讓我們來認識一下天文臺以及對於天文臺來說最重要的望遠鏡吧！

鹿林一米望遠鏡

（Lulin One-meter Telescope，LOT）

LOT是蓋賽格林反射式光學望遠鏡，口徑一公尺，焦長八公尺，是臺灣最大的望遠鏡。由於地球自轉，星星持續地在天空中由東向西移動，為了追蹤特定的目標，望遠鏡需架在赤道儀上，一般我們常看到的是T字型掛有重錘的德式赤道儀，然而鹿林天文臺所用的是叉式赤道儀，外型與經緯儀類似，但叉臂轉軸朝向北天極，可用電腦控制並自動追蹤。LOT設有自動導入系統，利用天文軟體便能輕易讓望遠鏡對到我們想要觀測的目標。而感光元件部分，鹿林天文臺所使用的高靈敏度冷卻CCD相機，可將CCD冷卻至零下80度，幾乎可以忽略熱雜訊對影像的影響。

TOAS 0.5米超廣角望遠鏡陣

這四座50公分口徑的望遠鏡，是為了中美掩星計畫（TAOS）而興建的。這個計劃的主要目的是為了研究古柏帶天體，利用掩星觀測法來估計這些小型天體的數量，TAOS監測遠方恆星的亮度，當恆星被古柏帶天體遮掩的時候，恆星的亮度便會有所變化。而之所以需要四座望遠鏡，是為了同時觀測以減少誤判的機率。TAOS從2005年開始進行觀測，由於臺灣氣候多雲霧、望遠鏡不夠靈敏等因素，觀測結果不如預期。因此新一代TAOS-2計畫改到墨西哥興建三座1.3米的望遠鏡，而中央大學天文所也持續參與這項計畫。

除了LOT和TAOS外，鹿林天文臺還有0.4米鹿林巡天望遠鏡，協助進行觀測。

鹿林天文臺簡介

國立中央大學天文研究所「鹿林天文台」位於台灣中部玉山國家公園塔塔加地區的鹿林前山，海拔2862 m，是台灣最重要的光學天文基地。此台址較不受冬季東北季風、夏季西南氣流和颱風的影響；加上位處高山，空氣污染很少，大氣透明度高，幾乎沒有光害，天光背景暗，大氣寧靜度較好。每年平均可觀測約180 夜，較好的觀測季節是每年的秋季與冬季。

1990 年在國科會(科技部前身)支持下，蔡文祥教授開始進行台灣天文選址計畫，於鹿林前山設置一個臨時觀測站進行選址調查及天文研究教學。歷經3 年的視寧度（seeing）、氣候、夜天光背景等條件調查後，確定玉山國家公園的鹿林前山為優良的天文台址。1997 年獲得太空計畫室（太空中心前身）資助，興建鹿林第一座天文台（SLT），1999 年完工，安裝自行設計製造的76 cm 超輕型望遠鏡(SLT76)；2000 年開始進行觀測，是鹿林天文台早期最重要的觀測設備。在教育部追求學術卓越發展計畫的挹注下，2002 年建置台灣最大的鹿林1 m 望遠鏡（LOT），同年冬季開始觀測。目前基地內有1 m 望遠鏡（LOT）、0.4 m 望遠鏡（SLT40）、0.4 m廣角巡天望遠鏡（LWT）。此外還有成功大學極低頻無線電波偵測系統（ELF）、中央大學太空所的大氣輝光全天相機、紅色精靈高速相機及環保署鹿林山空氣品質背景站（LABS）等地科、大氣、太空相關的研究設施。

鹿林天文台的主要策略是應用小型望遠鏡和台灣觀測條件優勢。因為小型望遠鏡的運作及時間分配，比中大型望遠鏡更具彈性；而台灣緯度較低，因此可以觀測較大的南天區，且地理經度上與

天文研究計畫，例如中美掩星計畫（TAOS）、泛星計畫（Pan-STARRS）、全球望遠鏡聯合觀測(WET)、全球蠍虎BL類星體聯合觀測（WEBT）、年輕系外行星掩星計畫（YETI）。每年約有十多個研究計畫同時進行，成立以來已產出逾百篇相關研究論文。除研究外，也支援國內大學及科教天文觀測實習。在台灣近代天文發展史上，鹿林天文台締造了多項紀錄：首度發現小行星、首度發現超新星、首度發現彗星、首度發現近地小行星及首度進行小行星命名。

2006年開始進行的鹿林巡天計畫（LUSS）搜尋太陽系小天體，3年期間共發現800多顆小行星。其中已有400多顆軌道確認獲得永久編號，小行星發現數排名世界前50。鹿林天文台發現的小行星目前已有101顆得到永久命名，小行星名遍佈全台灣，涵蓋台灣的自然科學及人文地理。2007年鹿林巡天首度發現彗星（C/2007 N3） 與近地小行星（2007 NL1），該彗星後來命名為鹿林彗星（Comet Lulin）。2009年鹿林彗星最接近地球時，肉眼可見，全世界天文界及天文愛好者也因此曉得「鹿林天文台」。

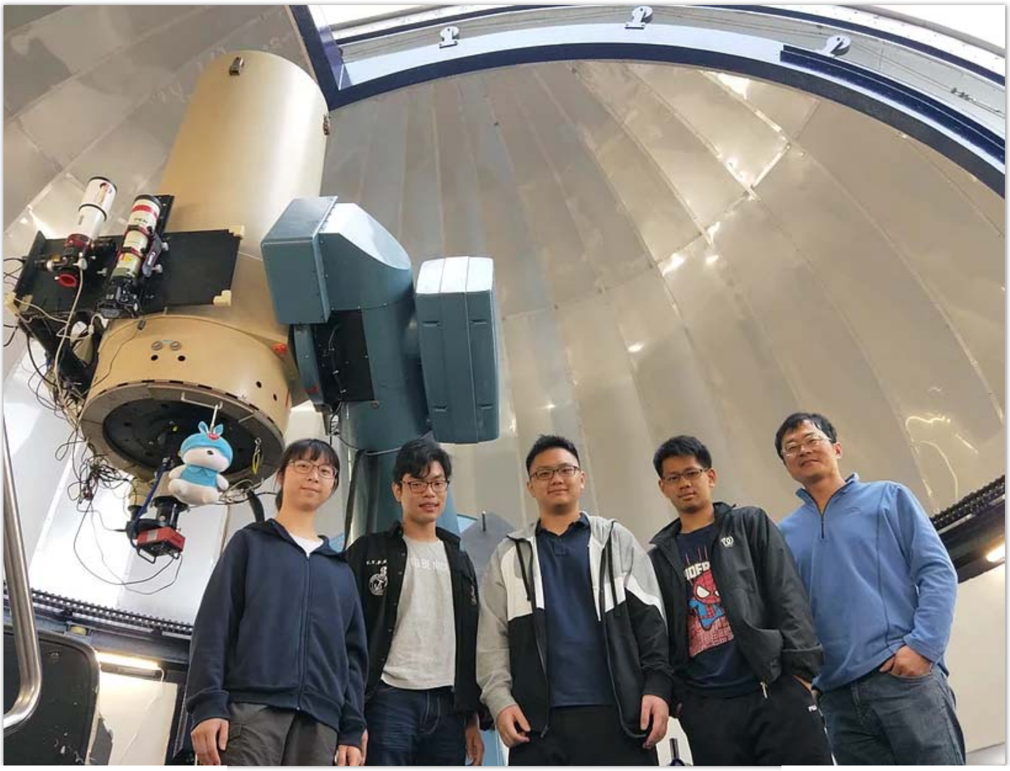

鹿林天文臺林宏欽臺長專訪：

邁向鹿林之路

臺長在高中參加天文社後，開始瘋天文。當時在社團就是看天文書、玩望遠鏡、去野外觀星拍照，夢想是將來到圓山天文臺（臺北市立天文科學教育館前身）工作。玩著玩著便玩到了大學，中原大學那時候有一個天文臺，晚上天文社大夥常在裡面觀測聊天。大二那年，正好是1986年哈雷彗星回歸，全世界都在追彗星，臺灣也掀起哈雷風潮。大學畢業後考上中大天文所，玩當時全國最大的60公分望遠鏡，畢業後在竹科工作了一年半。1997年進入臺北市立天文科學教育館，夢想成真，在天文館工作的五年裡，參與了45公分望遠鏡的建置及館內資訊網路的建設。2002年鹿林天文臺落成，因臺北光害嚴重，觀測效果很差，於是離開臺北去鹿林玩一米望遠鏡直到現在。

飛向宇宙，浩瀚無垠

訪談最後我們與臺長聊到了人類的未來與夢想，在天文這個領域，探索整個宇宙可說是人們最大的嚮往，於是便問了臺長：「假如有一張可以到宇宙任何角落的機票，你最想去哪裡？」

對於這個問題，臺長笑了笑說，如果他有這個機會，他想要去看一下外星人長甚麼樣子。當然，這些目前都只是紙上談兵，以現在的航太科技，連我們自己的太陽系都還出不去，是不可能達成的。臺長補充說，雖然現在到不了，但我們可以在天文觀測方面有所斬獲，現在已經發現了許多系外行星，假以時日有機會可以飛出我們的太陽系，去到更遙遠的星球，現在這些觀測可以說是在為未來鋪路。

3 展望宇宙的臺灣之眼：鹿林天文臺

文／陳文屏、林宏欽、張光祥

鹿林天文臺位於臺灣南投縣與嘉義縣交界之鹿林前山，緊鄰玉山國家公園，是臺灣最重要的光學天文基地，兼具研究與教育功能。

▲圖 1　俯瞰鹿林天文臺的全貌（Credits：國立中央大學天文研究所）

為什麼選在高山上建立鹿林天文臺？

此地受冬季東北季風、夏季西南氣流和颱風的影響較小；受惠於國家公園的優越環境，加上位處高山，空氣汙染和塵埃少，大氣透明度高，光害也較小；由於海拔高、大氣稀薄，所以消光較小，大氣寧靜度[1]較好，秋冬兩季尤其適合觀測。

鹿林天文臺的基本檔案

- 地理位置：東經 120°52′25″，北緯 23°28′07″
- 海拔：2,862 公尺
- 夜天光背景[2]：每平方角秒的視星等為 21.28 星等
- 大氣寧靜度：星點平均視角為 1.39 角秒
- 年平均觀測時間：1,450 小時（約 180 個夜晚，以每晚 8 小時計）

鹿林天文臺的開發緣起於 1990 年，由當時任職於中央大學天文所的蔡文祥教授與張光祥先生，考量臺灣各地的晴天率、海拔、後勤支援等因素，並歷經 3 年的大氣寧靜度、氣候、夜天光背景等條件調查後才選定臺址。

天文臺所使用的電力由臺電提供，玉山國家公園和中華電信的基地臺則分別提供用水和網路通訊服務。此外，天文臺內也設有自動氣象站、全天域相機以及雲量監測儀等儀器設備，可作為觀測參考。

1. 大氣寧靜度：大氣擾動對星光成像的影響程度。以星點的視角表示，視角愈小表示大氣寧靜度愈好，觀測到的星像愈清晰。
2. 夜天光背景：夜空背景的亮度。星等數字愈大，表示亮度愈低，意即光害愈小，能夠觀測愈暗的天體。

鹿林天文臺有哪些設備？

基地內設置了數座小型可見光望遠鏡 。 除了有鹿林一米望遠鏡（Lulin One-meter Telescope，簡稱 LOT）、中美掩星計畫（Taiwanese-American Occultation Survey，簡稱 TAOS）的 4 座 0.5 米自動望遠鏡、0.4 米超輕型望遠鏡（Super Light Telescope，簡稱 SLT40）、鹿林廣角望遠鏡（Lulin Wide-field Telescope，簡稱 LWT）進行天文觀測外，另有成功大學的紅色精靈[3] 地面觀測與極低頻無線電波偵測系統 (ELF)、中央大學的氣暉全天相機、土石流偵測預警系統，以及環保署的鹿林山大氣背景測站 (LABS) 等設備，記錄大氣、環境、太空、地震等觀測數據，為我國珍貴的高山科學基地。

(1)鹿林一米望遠鏡 (LOT)：

鹿林天文臺最大的望遠鏡——LOT，同時也是目前臺灣口徑最大的通用型光學望遠鏡。LOT 具備良好的光學成像品質、指向和追蹤精度，並配備高靈敏儀器，包括專業天文相機，以取得天體影像，並測量在不同可見光波段的亮度。另外也配置低色散光譜儀及偏振儀等，藉以取得天體光譜或偏振訊息。

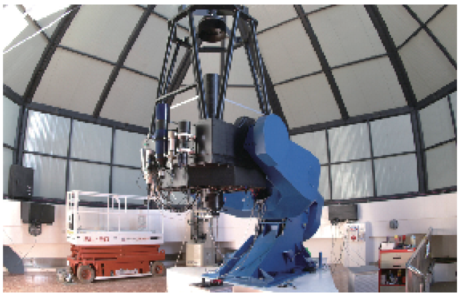

▲圖 2　鹿林天文臺的一米望遠鏡
（Credits：國立中央大學天文研究所）

LOT 由德國 APM 公司製作，屬於卡塞格林反射式望遠鏡，由於採用鏡後端對焦座，因此卡焦儀器限重 50 公斤 。LOT 觀測目標包括太陽系天

3.紅色精靈：積雨雲層上方發生的放電現象，由於主要發出紅光，而且發生的時間非常短暫不易捉摸，因此被稱為紅色精靈。

▼表 1　鹿林天文臺配置的小型可見光望遠鏡（依口徑大小排列）

望遠鏡	口徑	種類	焦比[4]	運作期間
LOT	100 cm	卡塞格林 (Cassegrain) 反射式望遠鏡	F/8	2003–
SLT76	76 cm	里奇－克萊琴 (Ritchey-Chrétien) 反射式望遠鏡	F/9	2000–2002
TAOS	50 cm × 4	反射式望遠鏡	F/2	2005–2016
SLT40	40 cm	里奇－克萊琴反射式望遠鏡	F/8.4	2006–
LWT	40 cm	反射式望遠鏡	F/3.8	2018–
L35	35 cm	施密特－卡塞格林 (Schmidt-Cassegrain)	F/8.25	2012–2017
LELIS	10 cm × 3	攝影鏡頭	F/1.8	2002–2008

體、銀河系中的恆星、變星、星團及鄰近星系等，除了提供中央大學師生研究與教學之用，也開放國內、外學者申請使用。

某些宇宙現象有時效性，例如星球爆發、掩星等，隨著地球自轉，只有面對該天體的觀測者才能夠看到。由於臺灣位處西太平洋，向東 6 個時區內缺乏其他天文臺，因此對於會隨時間變化，需連續監測的天象，或是國際間需要位在不同經度的天文臺（或太空望遠鏡）針對特定天體聯合觀測時，鹿林天文臺便扮演著舉足輕重的角色。

多年來，鹿林天文臺的望遠鏡積極參與此類計畫，例如：全球望遠鏡聯合觀測（Whole Earth Telescope，簡稱 WET）聯合不同時區的望遠鏡，接力監測恆星的亮度變化，以星震[5]手段探討恆星內部結構；

4. 焦比：口徑與焦距的比值。詳情請參〈IV-1 星夜集光者：光學望遠鏡〉篇。

5. 星震：利用亮度變化或光譜都卜勒效應研究天體的震動，藉此瞭解無法直接觀測的恆星內部結構，其原理類似利用地震波研究地球的內部結構。

全球蝎虎 BL 類星體聯合觀測 （Whole Earth Blazar Telescope ， 簡稱 WEBT）監測活躍星系核，藉此研究黑洞與噴流的性質[6]；年輕系外行星掩星觀測計畫（Young Exoplanet Transit Initiative，簡稱 YETI）則監測星團成員、搜尋系外行星造成的凌星事件等，均與國際天文臺建立良好合作模式，並取得優良成果。

啟用至今，鹿林天文臺的望遠鏡共發現 15 顆超新星、800 餘顆小行星，以及一顆彗星。每年通常約有十幾個研究計畫利用 LOT 執行，使用 LOT 數據發表的研究論文已超過百篇。除了研究之外，LOT 也支援大學、高中及社教機構進行觀測教學實習，另有多座小型望遠鏡提供特定課題使用。

⑵中美掩星計畫 (TAOS)：

天文臺原來設有 4 座 TAOS 望遠鏡，由中央研究院天文所、中央大學天文所、美國哈佛史密松天文物理中心，以及韓國延世大學共同合作。每座望遠鏡的口徑 50 公分，具備 3 平方度[7]的超廣角視野，全年監測可能由柯伊伯帶天體造成的掩星事件，藉以估計分布在太陽系外圍的小型天體數量。

TAOS 計畫自 2005 年開始運行，累積 6 年的觀測結果一共收集超過 10 億筆恆星光度的測量數據，因為沒有偵測到任何掩星事件，提供了柯伊伯帶天體的數量上限。第一代 TAOS 的設備已於 2016 年拆除、撤離，第二代的海王星外自動掩星普查計畫 （Transneptunian Automated Occultation Survey，簡稱 TAOS-II）選在墨西哥的聖彼德羅

6. 詳情請參〈I-4 大大小小的時空怪獸：黑洞面面觀〉、〈V-8 內在強悍的閃亮暴走族：活躍星系〉篇。

7. 平方度：一度乘以一度的天空範圍。例如滿月的張角約半度，3 平方度相當於 10 個滿月的天空面積。

瑪蒂爾天文臺 (San Pedro Mártir Observatorio) 落腳，一共有 3 座口徑 1.3 米的望遠鏡。

⑶**超輕型望遠鏡 (SLT)：**

中央大學天文研究所於 1997 年獲得太空計畫室（現在的國家太空中心）補助，興建鹿林第一座天文臺 “SLT”。1999 年 SLT 完工後，內部安裝自行設計、製造的 76 公分超輕型望遠鏡 (SLT76)，並從 2000 年開始進行觀測，是鹿林天文臺初期最重要的觀測設備。SLT76 於 2005 年換裝口徑 40 公分的超輕型望遠鏡 (SLT40)，並自 2006 年開始進行鹿林巡天計畫（Lulin Sky Survey，簡稱 LUSS），搜尋太陽系小天體。計畫進行 3 年期間共發現 800 多顆小行星，其中有 400 多顆已獲得永久編號，小行星發現數量排名世界第 47。

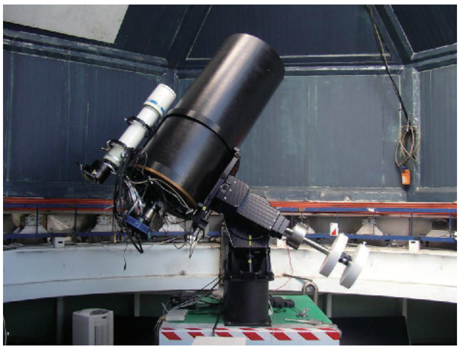

▲圖 3　鹿林天文臺的 40 公分超輕型望遠鏡（Credits：國立中央大學天文研究所）

目前鹿林天文臺發現的小行星已有 100 多顆得到永久命名，名稱涵蓋臺灣的代表性人物、團體、地理、山水及原住民族等。2007 年 LUSS 首度發現彗星 (C/2007 N3) 與近地小行星 (2007 NL1)，該彗星後來被命名為**鹿林彗星** (Comet Lulin)。LUSS 計畫結束後，自 2010 年起 SLT40 投入變星、彗星的長期監測工作。

⑷**善用地理優勢的觀測策略：**

鹿林天文臺的主要策略是利用小型望遠鏡的機動性，以及臺灣本身的觀測條件優勢，與其他的天文臺合作、競爭。臺灣的地理位置緯度較低，因此可以觀測範圍較大的南半球天空；而經度方面則可以跟

國際間的其他天文臺互補。對於需要長期監測或瞬變的天文現象（如超新星及伽瑪射線爆等），鹿林天文臺參與跨國合作，在全球天文觀測網和太空與地面的聯合觀測中占據不可或缺的位置。比如 2006 年中央大學天文所參加夏威夷大學主導的**泛星計畫** (Pan-STARRS) ， 另外近年加入由加州理工學院主導的**茲威基瞬變探測利器**（Zwicky Transient Facility ， 簡稱 ZTF）， 並加入**伊甸園觀測網** （Exoearth Discovery and Exploration Network，簡稱 EDEN），以搜尋鄰近太陽之 M 型恆星周圍可能位於適居區內的系外行星[8]等，都因為地理位置的優勢，能藉由鹿林天文臺的設備追蹤並確認新的科學發現。

在臺灣近百年的天文發展史上，鹿林天文臺締造了多項紀錄，包括首度發現小行星、首度發現超新星、首度發現彗星、首度發現近地小行星及首度進行小行星命名。天文臺的望遠鏡口徑雖然小，但做為天文教育與基本研究工具，多年來配合規劃的課題立基，亦取得良好的成果。

8. 詳情請參〈V-1 遙遠的鄰居：系外行星〉篇。

Globe at Night - Sky Brightness Monitoring Network

2016年中華民國天文學會年會 天文教育及業餘天文活動報告 E3

Performance and Results from Globe at Night - Sky Brightness Monitoring Network 表現及初步結果

潘振聲 Chun Shing Jason PUN[1]

江國興 Albert K.H. KONG[2], 蘇柱榮 Chu Wing SO[1], 張桂蘭 Kuei Lan CHANG[3], 楊曄群 Yeah Chun YANG[3], 張師良 Sze Leung CHEUNG[4]

[1]香港大學 The University of Hong Kong,

[2]國立清華大學 National Tsing Hua University,

[3]臺北市立天文科學教育館 Taipei Astronomical Museum,

[4]日本國立天文台 國際天文學聯合會天文普及辦公室 IAU Office for Astronomy Outreach, National Astronomical Observatory of Japan

國立成功大學

15.5.2016


::: 中文 English 網站導覽
南瀛天文館
TAINAN ASTRONOMICAL EDUCATION AREA
TAEA
認識園區 館設介紹 參觀服務 活動學習 志工園地 互動交流 資訊公開
認識園區
現在位置：臺南市南瀛科學教育館 > 認識園區 > 使命與展望
字級大小： 小 中 大 登出
使命與展望
展望
南瀛天文館座落於金黃色曾文溪畔自然生態環境中，被白堊地形包圍，遠離都市光害，挾其地利與天候上的優勢，成為全台灣唯一可以直接進行夜間星空導覽解說的天文館，在臺灣不斷推動與國際接軌及提升學生國際競爭力之際，南瀛天文館的設立，成為一個重要的天文科學教育場所，創造與都市天文館截然不同的「星」體驗，在未來發展上，除推廣天文教育特色外，更將串起鄰近的自然人文景觀、豐富的生態自然資源，創造一個結合天文、科學、人文與生態之多面向教育價值，並帶動社區營造天文特色，打造大內區成為「南瀛星故鄉」。

遠離都市光害

2

全島

（2015年4月16日晚上11時由國際太空站拍攝）

Credit: Science and Analysis Laboratory, NASA-Johnson Space Center, The Gateway to Astronaut Photography of Earth, ISS043-E-122279

3

臺北

(2013年

晚上11

空站拍

4

Cr
ISS

高雄

(2013年3月27日
晚上11時由國際太
空站拍攝)

5

Credit: Science and Analysis Laboratory, NASA-Johnson Space Center, The Gateway to Astronaut Photography of Earth, ISS035-E-11406

光污染

- 「**光污染**(Light Pollution)」(又稱**光害**)是一種因**不正確使用**人為室外照明，而對自然環境和生態等引起的負面影響
- 光線直接照射或反射上天空，大氣中的雲、霧、懸浮粒子等污染物會將這些光線散射(scatter)開，**導致夜空被照亮**。

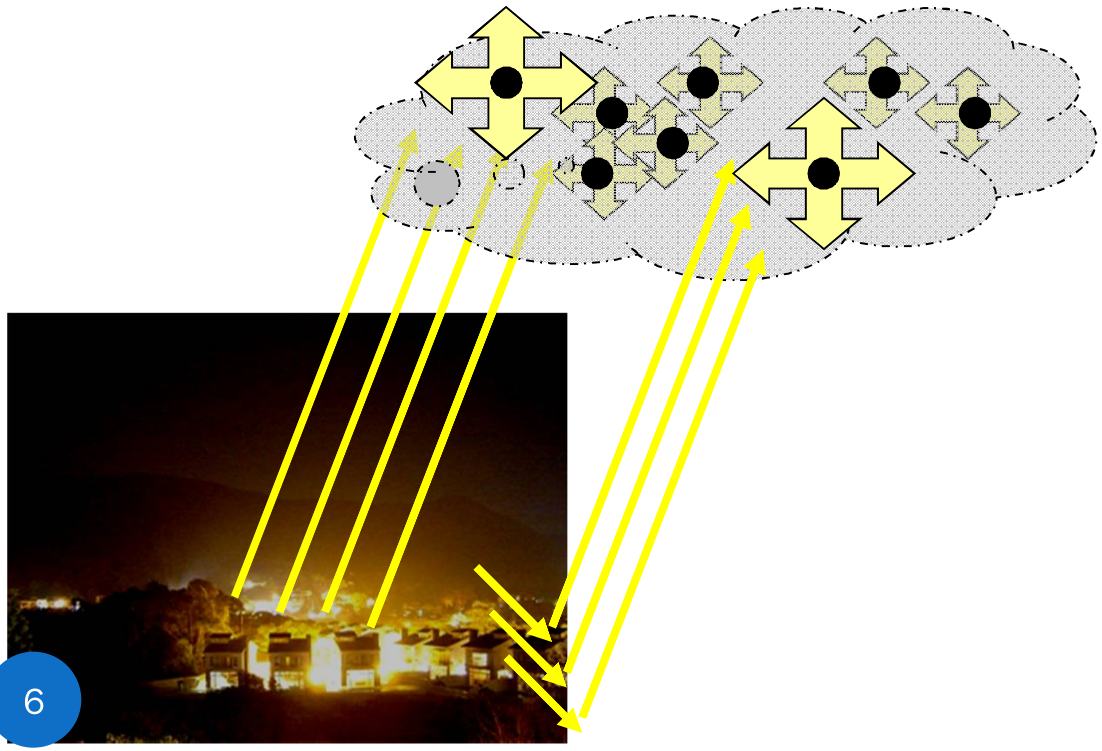

6

夜空光度測量錶 Sky Quality Meter (SQM)

Figure source: Unihedron

- 製造：加拿大 Unihedron 公司
- 感光元件：TAOS TSL237 High-Sensitivity Light-to-Frequency Converter
- 近紅外線濾鏡：Hoya CM-500
- 大小：3.6 x 2.6 x 1.1 in.
- 由5-6V DC供電
- 測量天頂夜空光度
- 量度單位：等每平方角秒 (mag arcsec^{-2})
- 準確性約為 ±0.1 mag arcsec^{-2}
- 價格合理(~US$350) 及耐用

香港光害調查 (2007-2009)

- 公民科學項目
- 邀請中學生(28間中學的148位學生)和義工(天文愛好者、營舍管理員)參與
- 透過網頁報告夜空光度讀數

8

香港大學物理學系 香港光害調查 A Survey of Light Pollution in Hong Kong, Department of Physics, HKU

香港夜空光度分佈圖 Hong Kong Light Pollution Map

09年6月
June, 09

- 2009年6月: 首張「香港夜空光度分佈圖
- 近2000次量度、199個測量地點、171位義工
- 市區的平均夜空光度，高於最黑的郊區100倍

測量夜空光度：評估光污染(2010-now)

- 研究項目： 香港夜空光度監測網絡(***Hong Kong Night Sky Brightness Monitoring Network, NSN***)協辦：香港太空館、香港天文台、可觀自然教育中心暨天文館

- 結果與「**IAU黑暗天空國際標準**」**IAU Zenith Dark Sky Standard** (NSB = 21.6 mag arcsec^{-2}) 比較

測量夜空光度：評估光污染(2010-現時)

- 「香港夜空光度監測網絡」由18個分佈各區的監測站組成
- 監測站每晚**自動**收集夜空光度數據，再透過無線電話網絡將數據**即時傳送**回香港大學

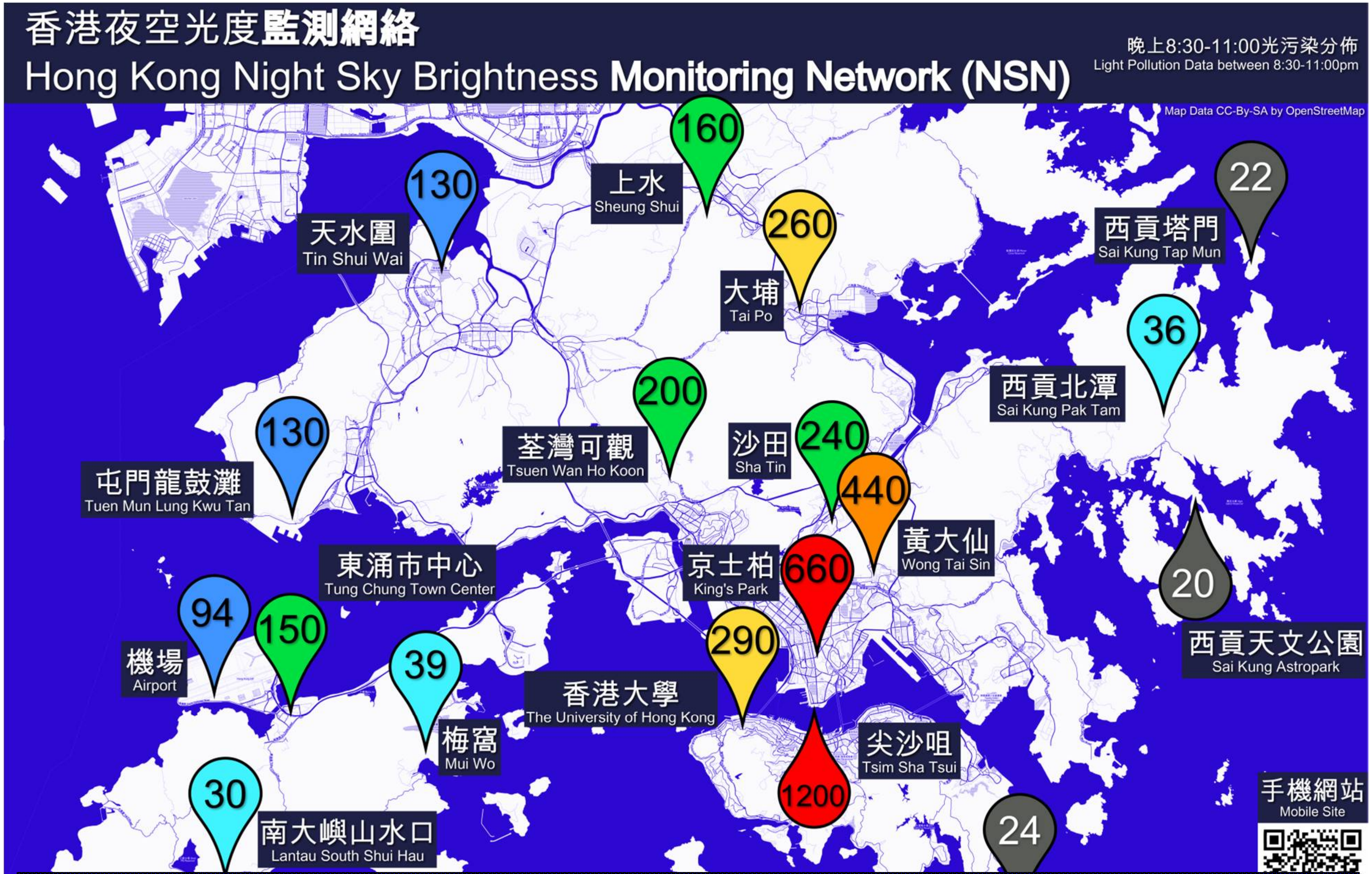

- 2013年3月：商業中心晚上8 時半至11 時的平均夜空光度，高於「IAU黑暗天空國際標準」1200倍
- 市區的平均夜空光度，高於郊區15 倍

12

The Globe at Night - Sky Brightness Monitoring Network (GaN-MN) (2015-現在)

- 合辦：
  - 國際天文學聯合會(IAU)天文普及辦公室
  - 日本國立天文台
  - 香港大學
  - The Globe at Night 計劃

13

The Globe at Night - Sky Brightness Monitoring Network (GaN-MN) (2015-現在)

- 本計劃為國際天文學聯合會2015國際光之年工作小組**確認的主要Cosmic Light program**
  - 致力將夜空測量國際標準及星空保育公眾教育推廣至全球
  - 國際天文學聯合會確認信提及：“Suggestions were to “*coordinate … with others who are pursuing the educational aspect in other regions*.” 「*鼓勵…積極聯系在其他地區的教育工作者*。」
  - **歡迎參加！**

INTERNATIONAL YEAR OF LIGHT 2015

COSMIC LIGHT

IAU

14

The Globe at Night - Sky Brightness Monitoring Network (GaN-MN) (2015-現在)

- 專案目的：
  - 以統一的方法測量夜空光度研究全球的光污染
  - 向公眾和政府展示因使用燈光而引致的光污染的害處
  - 透過展示實時和全球性的夜空光度數據，作為公眾光污染教育的平台

15

The Globe at Night - Sky Brightness Monitoring Network (GaN-MN) (2015-現在)

- 方法：
  - 夜空光度測量的統一方法：
    - SQM-LE
      - 價格合理(~US$350) 及耐用
    - 使用由生產商提供的保護機殼
    - 30秒測量頻率
    - 統一的校準計劃

@ 鹿林天文台 (LUO)

16

紅：現有監測站(截至2016年4月有16個)
藍：候選監測站(截至2016年4月有3個)

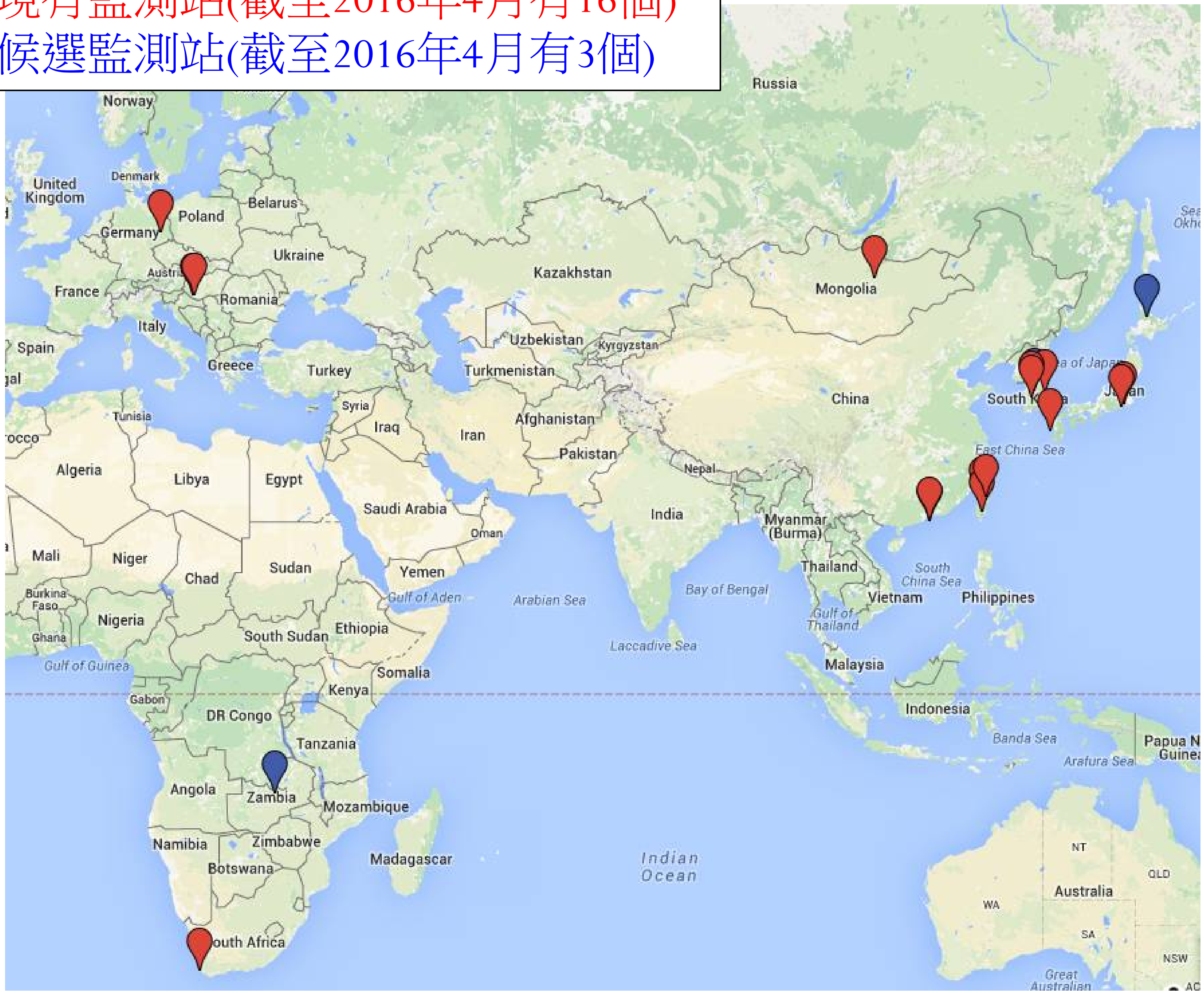

[redacted]

[redacted]

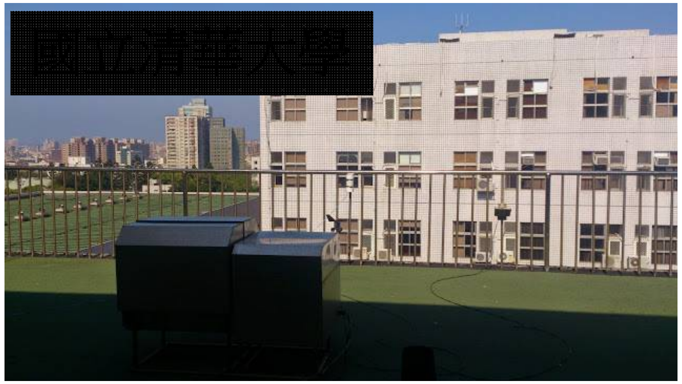

[redacted]

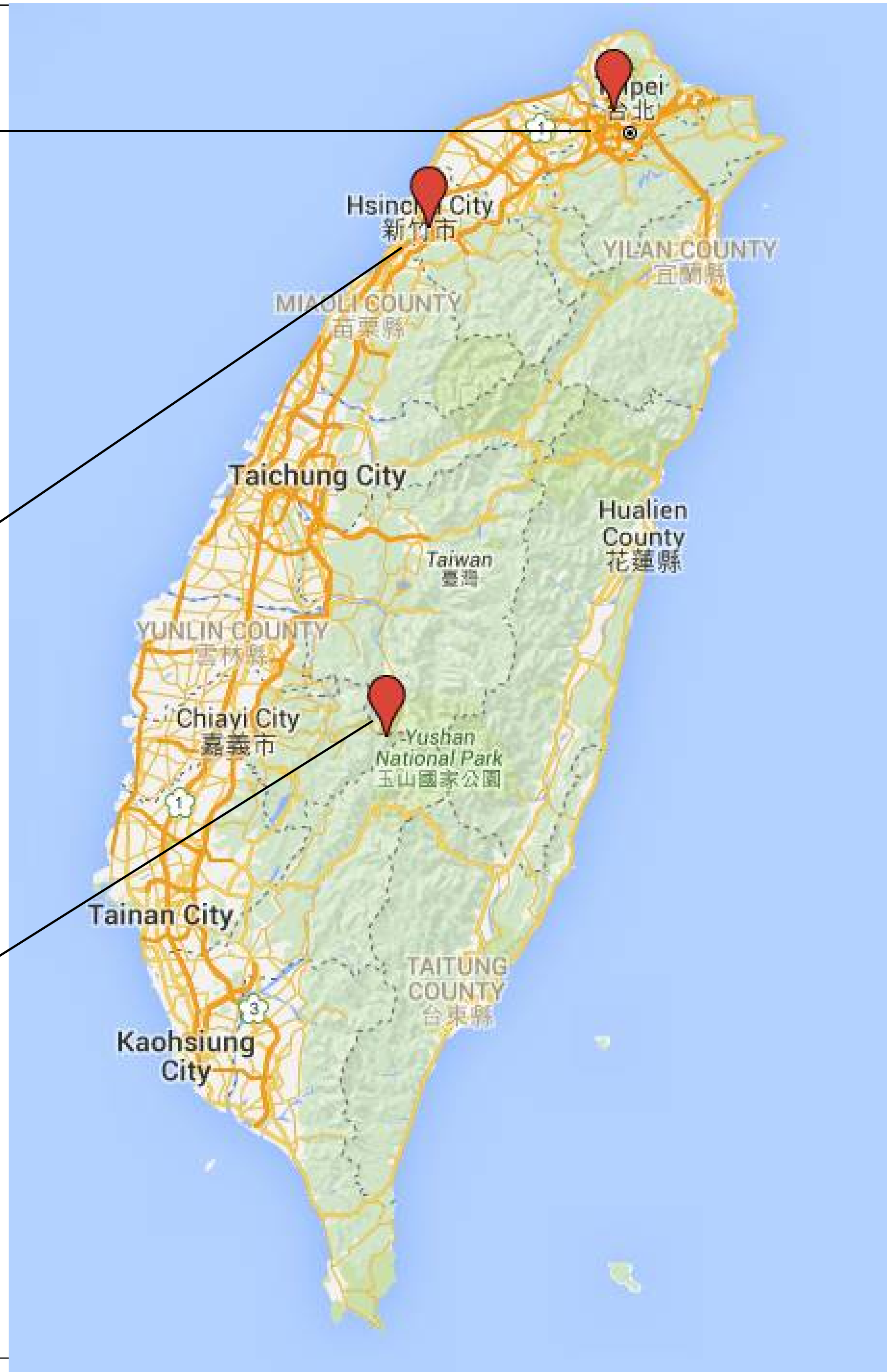

26

GaN-MN公眾網頁：

http://globeatnight-network.org/map.html

- 在Google Map上的光污染地圖：
  - ➢實時光污染數據(晚間)
  - ➢昨晚夜空光度中位數值(日間)

GaN-MN初步結果– 晚間天空光度變化

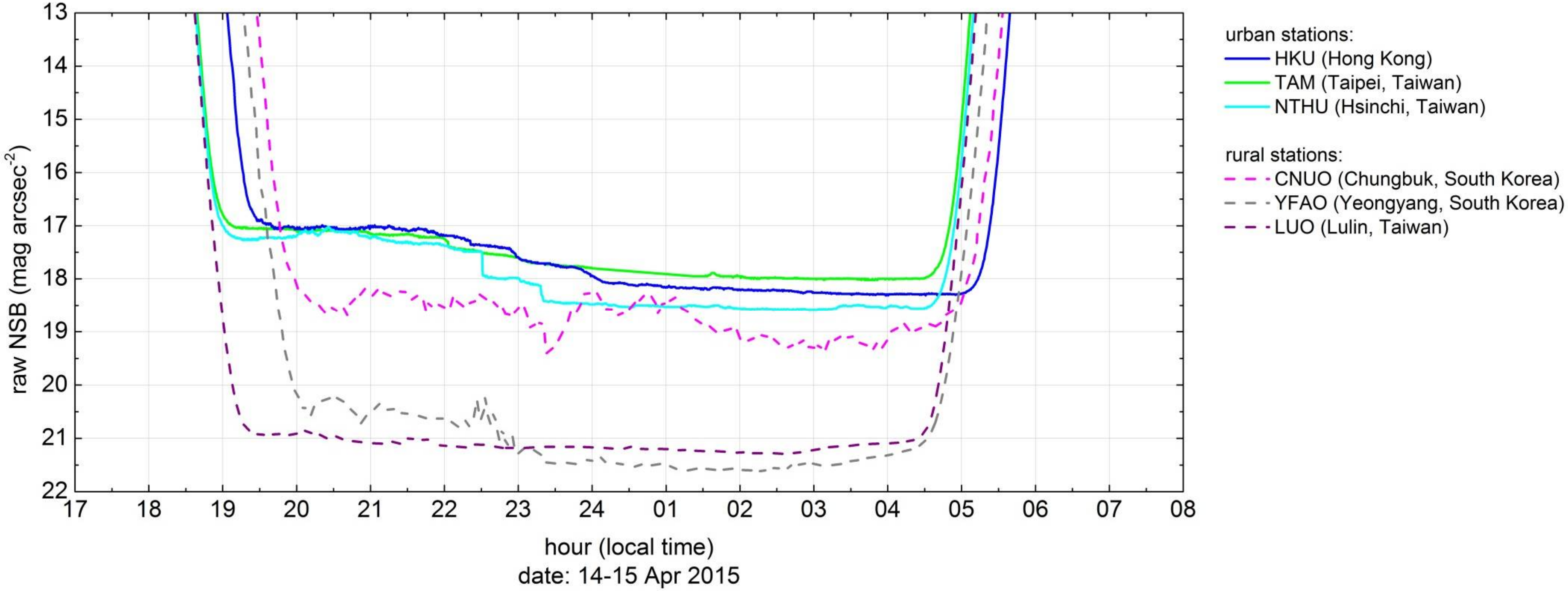

- 後半晚比前半晚黑暗
- 市區比郊區光亮

29

$$\Delta NSB_{late\text{-}early} = NSB_{late} - NSB_{early}$$

[redacted]

Average NSB between 01:00-03:00 = NSB_{late}

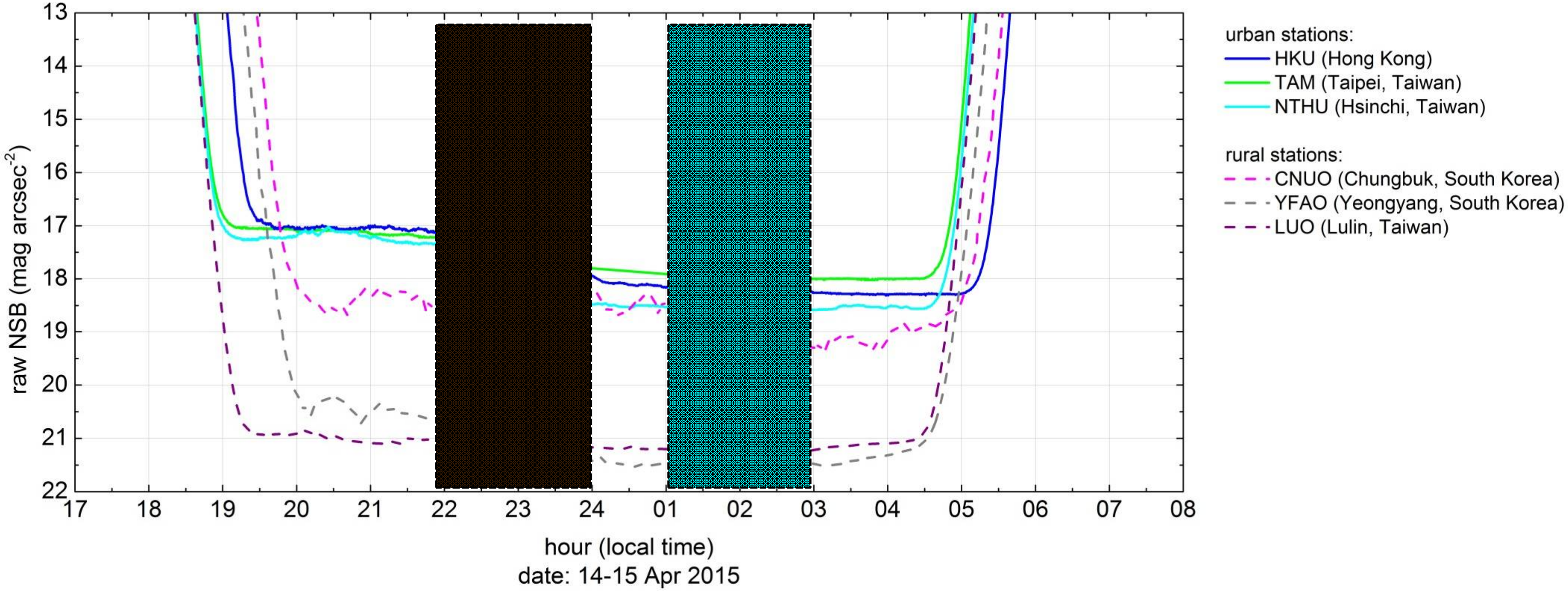

30

GaN-MN初步結果 –
晚間天空光度變化

前半晚
比
後半晚
光亮程度

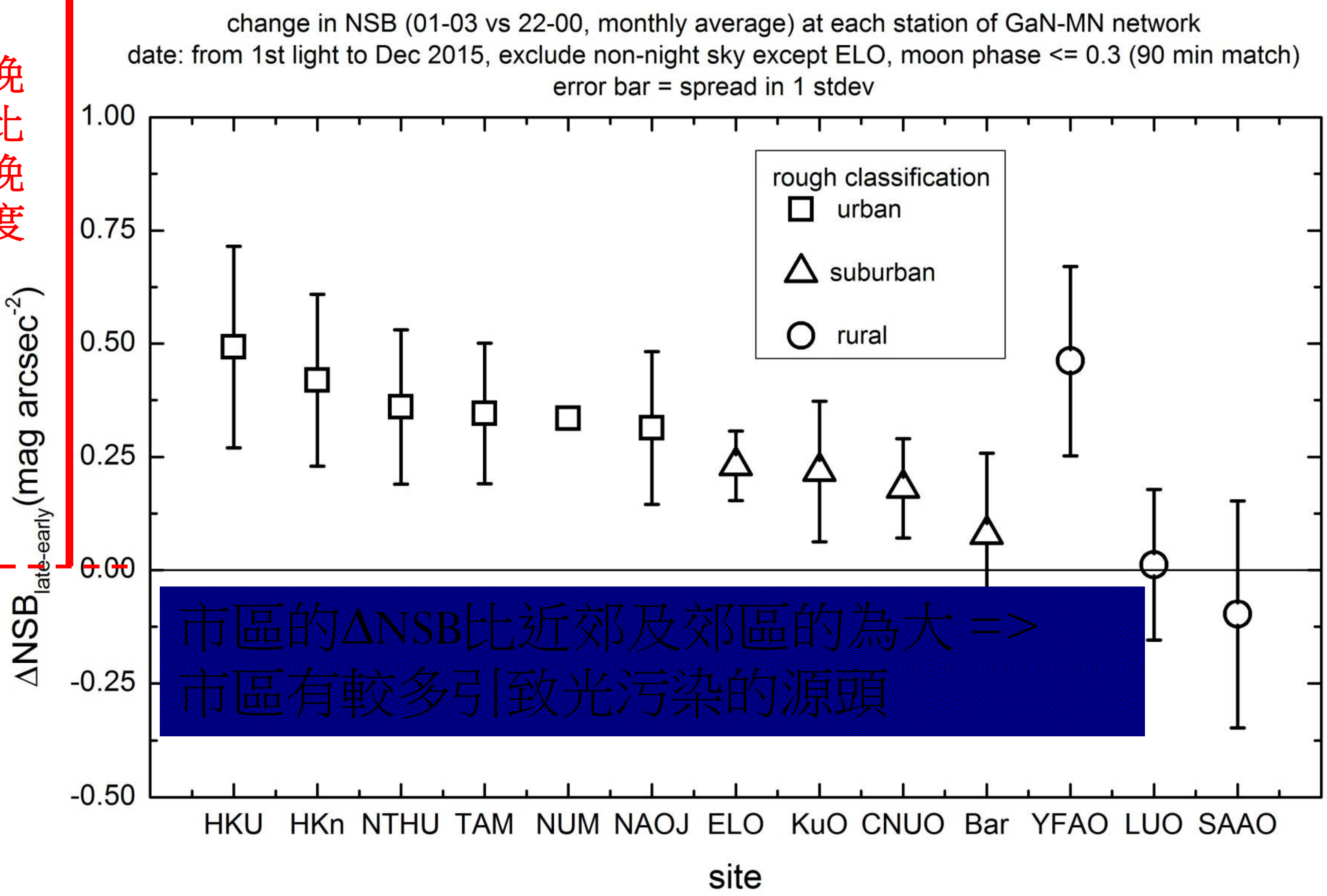

[redacted]

33

GaN-MN初步結果 –
晚間天空光度變化

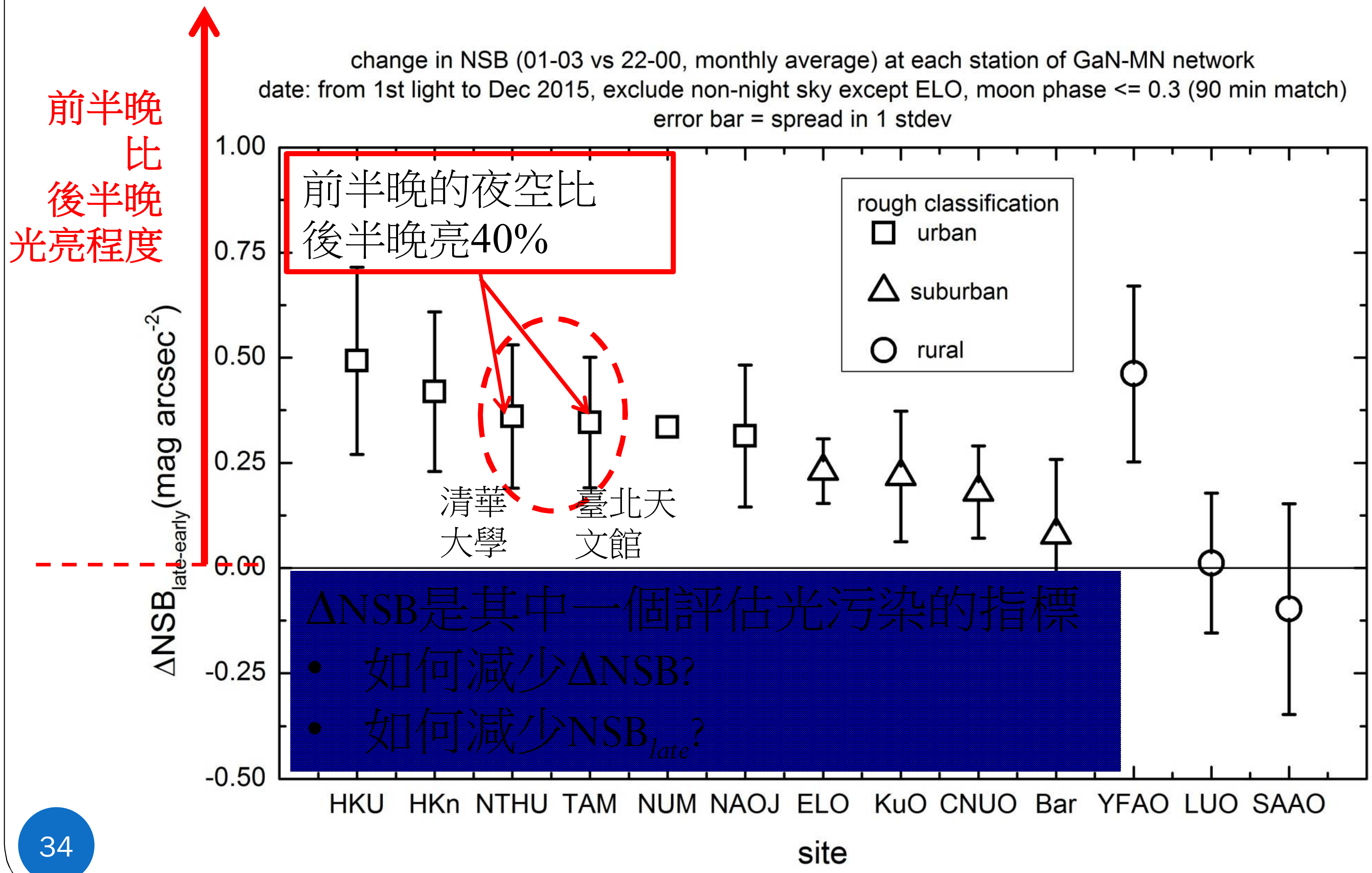

ΔNSB是其中一個評估光污染的指標

- 如何減少ΔNSB?
- 如何減少NSB_{late}?

34

如何減少光污染？

- 光污染主要元凶：
- 減少光污染
  - 避免濫用照明
  - 改裝照明
  - 節省能源
  - 立法 / 監管
  - **教育 / 推廣**

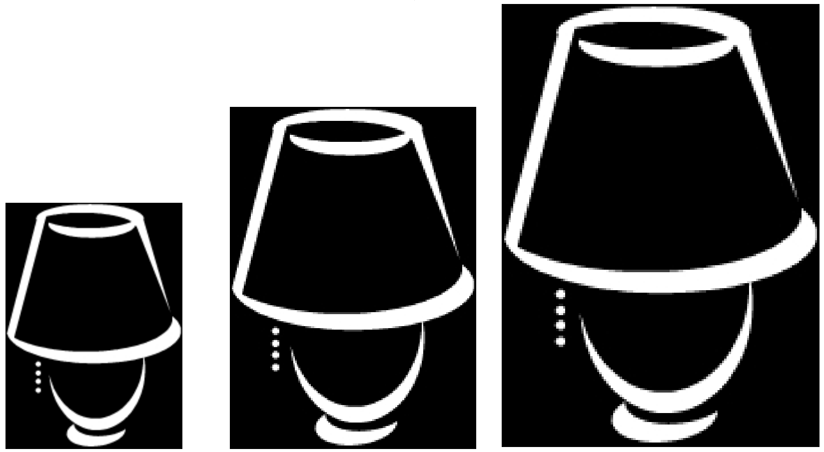

社區光污染認知活動(2012-13)：學校活動

- 舉行了多場中學工作坊
- 教育學生光污染的科學和其對環境的影響
- 工作坊內容：
  - 講座
  - 測量體驗
  - 流動天象廳
  - 展覽
  - 鼓勵學生進行科研專案

37

社區光污染認知活動：「光污染研究科學巡禮」(2013)

- 在「**地球一小時**」期間於星光大道(旅遊熱點)舉行科學巡禮
- 教育公眾光污染對環境的影響
- 向社會推廣香港大學進行的光污染研究
- 活動內容：
  1. 實時夜空光度量度
  2. 示範
  3. 影片播放 (https://www.youtube.com/watch?v=CgomX5ha4h4)
  4. 展覽

38

「星．夜．行」光污染實地考察 (2015-16)

活動內容：

- 光污染講座
- 比賽簡介會
- 透過實地考察親身體驗光污染的影響
  - 旅程始於**市區**
  - 郊野公園**觀賞螢火蟲**
  - 天文公園**觀星**

39

光污染研究比賽 & 光污染短片製作比賽 (2015-16)

得獎作品欣賞
https://youtu.be/TUN5ildjCjg

The Globe at Night - Sky Brightness Monitoring Network (GaN-MN)

- 易於加入
- 你只需要：
  - 一套SQM-LE及保護機殼
  - 電源供應及互聯網
- 好處：
  - 將你的數據實時放上互聯網
  - 獲取世界其他地方的光污染數據
  - 一同為減少光污染出力！

42

謝謝

GaN-MN由香港大學知識交流計劃支持

欲了解更多GaN-MN

1) Visit: http://globeatnight-network.org/

2) Email us at: globeatnight.network@gmail.com or gan-mn@qq.com

新聞報導

中央大學葉永烜院士獲傑拉德·科伊伯獎　終身成就綻放國際

2020-08-15 文／秘書室

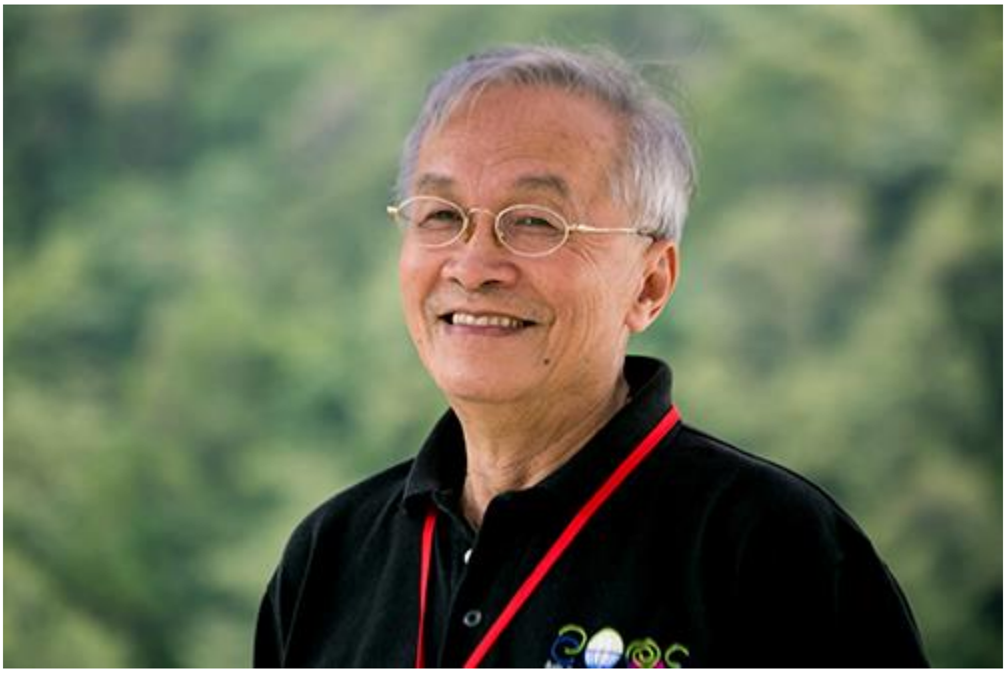

中央大學葉永烜院士獲頒傑拉德·科伊伯獎殊榮。照片天文所提供

2020 年的傑拉德·科伊伯獎(Gerard P. Kuiper Prize)(註)，經美國天文學會(American Astronomical Society)的行星科學分會 (Division of Planetary Science) 嚴格審議，頒發給中央大學天文研究所葉永烜教授，以表彰他在行星科學領域的貢獻。

中央大學校長周景揚說，葉永烜教授在彗星電漿物理學、太陽系動力學、行星及衛星 大氣層與固體表面的磁層相互作用等領域貢獻卓著，早耀眼於國際，此次美國天文學會特頒贈此一獎項，肯定葉教授的終身成就，對葉教授而言，實為實至名歸。

葉永烜教授自 1998 年起開始於中大任教，除了擁有豐富的教學及行政資歷外，也積極參與多項國際太空計畫，並以科學團隊成員的身分加入許多行星探索任務，他發表在《Nature》和《Science》之論文篇數更為華人科學家之最。中央大學在美國新聞與世界報導（U.S. News & World Report）中所列出的國際合作指標排名得以連續五年蟬聯全國第一，葉教授功不可沒。

葉永烜教授致力於推動美國、歐洲及亞洲對太陽系的科學探索，是 NASA 和歐空局(ESA)合作的卡西尼土星任務的三位創議者之一。同時也是亞洲大洋洲地球科學學會(Asia-Oceania Geosciences Society)的創始主席，該學會更團結了地球

科學界社群，在亞洲及大洋洲地區紮根行星研究，自此成為了世界領先的國際科學組織之一，在地球科學各領域之間建立起嶄新的合作關係。

此外，葉永烜教授曾獲頒美國太空總署「特殊公共服務」榮譽勳章、卡西尼土星計畫團隊成就獎、伽利略木星計畫團隊成就獎，美國地球物理聯會會士，教育部國家講座， 更榮膺中央研究院第 31 屆數理科學組院士。此次獲頒美國天文學會傑拉德·柯伊伯獎，正是其教育家精神與對學術的貢獻，在行星科學領域中發揮了強大影響力的例證。

註：傑拉德·科伊伯獎(Gerard P. Kuiper Prize) 傑拉德·柯伊伯獎是美國天文學會的行星科學分會每年頒發一次的獎項，獎勵在行星科學領域有突出貢獻的天文學家，該獎是以天文學家傑拉德·柯伊伯的名字命名，為終身成就的獎項。

葉永烜院士喜歡與年輕學子為伍，提攜後進不遺餘力。照片天文所提供

讓世界「看見台灣」 永恆的飛船─齊柏林小行星

2020-08-07 文／秘書室

感念齊柏林導演一生關注台灣土地發展的堅持與勇氣，中央大學周景揚校長特將齊柏林小行星銘版，頒贈給齊柏林之子齊廷洹。陳如枝攝。

「齊柏林飛船」，是人類對飛行夢想的初探，為感念空拍導演齊柏林先生對台灣的卓越貢獻，中央大學特將鹿林天文台所發現的編號 281068 號小行星，經國際天文學聯合會（IAU）通過，命名為「齊柏林 (Chipolin)」小行星，象徵一艘永恆的飛船，深情地望著台灣，守護著台灣。

8 月 7 日在齊柏林空間舉辦的《逐岸》開展記者會中，特舉辦齊柏林小行星頒贈儀式，由中央大學校長周景揚頒贈小行星銘版給齊柏林導演之子齊廷洹先生，感念齊柏林導演一生關注台灣土地發展的堅持與勇氣，希望大家記得齊柏林的精神及對台灣環境的關懷。

中央大學校長周景揚表示，美麗的福爾摩沙台灣，你我的共同家園，透過齊柏林導演的空拍視角，可以跨越種族和文化的藩籬，撼動人心。中央大學希望將他的精神化為永恆，如同星光般燦爛，普照大地。

周景揚校長指出，齊柏林導演除讓人看見台灣之美外，同時也喚醒我們更疼惜自己生長的土地。中央大學以地球科學起家，長期致力於環境永續之研究。從地球、海洋、大氣、水文，乃至太空、天文，以科學的專業全方位守護著台灣和地球，為人類永續生存的明天而努力，無疑將他的精神作了永續的傳揚！

齊柏林小行星，2006 年 7 月 18 日由鹿林天文台林宏欽台長及美國馬里蘭大學葉泉志博士共同發現，2017 年 11 月 4 日正式通過命名。大小約為 4.9 公里，發現時位在魔羯座，目前已運行到獅子座。繞行太陽一圈 5.6 年（軌道週期），離太陽最近時（近日點）為 4.3 億公里，最遠時（遠日點）為 5.1 億公里。

中央大學從 2006 年開始的鹿林巡天計畫，不但曾發現台灣史上的第一顆彗星，同時也發現了 800 多顆小行星，使台灣成為亞洲發現小行星最活躍的地方之一。卓越的天文研究成果，充份展現台灣人「以小搏大」的精神，也讓世界真正「看見台灣」！

中央大學周景揚校長、天文所黃崇源所長、齊柏林小行星發現者林宏欽和齊家人、看見・齊柏林基金會歐晉德董事長、萬冠麗執行長等人共同合影。陳如枝攝。

齊柏林導演「看見台灣」電影的最後，布農族孩童在玉山頂上高歌，讓中央大學天文所葉永烜教授深受感動，以此畫作來表達對齊柏林導演的敬意。葉永烜教授提供。

台灣參與之 ZTF 計畫　發現了第一顆金星軌道內的小行星

2020-01-14 文／天文所

中央大學天文所與清華大學天文所共組的「探高（TANGO）」團隊參與美國加州理工學院主導之「史維基瞬變設備」（簡稱為 ZTF），於今年初發現了第一個位於金星軌道內的小行星─2020 AV2。照片天文所提供

中央大學天文所與清華大學天文所共組的「探高（TANGO）」團隊參與美國

加州理工學院主導之「史維基瞬變設備」(Zwicky Transient Facility，簡稱為 ZTF)，於今年初發現了第一個位於金星軌道內的小行星—2020 AV2。此類小行星軌道非常特殊，須藉由行星的重力擾動才能從太陽系其他地方進入金星軌道內。

史維基瞬變設備(ZTF)為加州理工學院主導的國際合作計畫，已於 2018 年 3 月開始科學觀測，該望遠鏡利用 47 平方度超廣視野相機進行各類的巡天計畫。透過前所未有的廣視野觀測，可捕捉到充滿動態的夜空。

太陽系的小行星主要位於主小行星帶(火星與木星之間)，極少數的小行星軌道位於地球軌道內，被稱為 Atira，而 2020 AV2 又被細分為 Vatira (運行軌道全在於金星軌道內的小行星，V 代表金星)。Vatira 曾被預測，但由於其特殊軌道位置，因此非常不易被觀測 (類似水星、金星只能在晨昏被觀測)，為了尋找地球特洛伊小行星與 Atira，ZTF 太陽系小天體團隊進行了多次暮光巡天觀測(Twilight survey)，發現了多顆地球軌道內的小行星，且陸續刷新了最短軌道周期紀錄。2020 AV2 的發現除了證明 Vatira 的存在，更進一步幫助天文學者了解太陽系小天體的模型。

在科技部補助下，中央大學天文所和清華大學天所合組的「探高」團隊是 ZTF 國際合作隊伍的一員。主要科學目標在於太陽系小物體、變星、超新星和重力波的光學對應體的追蹤觀察。暮光巡天是由馬里蘭大學的葉泉志博士與中央大學天文所葉永烜教授所建立的觀測計畫。

馮元楨校友享年百歲　被譽為「生物力學之父」

2019-12-27 文／秘書室

中央大學名譽博士馮元楨校友，以 100 歲的高齡辭世。他的國際學術地位崇高，被譽為「生物力學之父」。秘書室檔案照片。

2002 年獲頒中央大學名譽博士的馮元楨院士，今(2019)年 12 月 15 日以 100 歲的高齡辭世。他的國際學術地位崇高，畢業於中央大學大陸時期航空系，雖然讀的是航空領域，卻在生物力學領域深受世人肯定，被譽為「生物力學之父」。

馮元楨院士為 20 世紀科學的開創性人物，為國際學術界所仰望。除為台灣中央研究院士和中國科學院院士之外，同時是美國國家工程院、醫學院及科學院三科院士。2000 年獲美國總統頒贈「國家科學獎章」。

馮院士 1941 年畢業於大陸中央大學航空系，1943 年取得航空碩士學位，後赴美留學，獲美國加州理工學院航空博士。隨後任教於美國加州理工學院航空系，成為國際著名力學專家。

馮院士雖然是航空領域出身，但在生物工程成就卻更為顯著。1966 年於美國加州大學聖地牙哥分校首創生物工程系，並延攬知名的錢煦教授前往任教。錢煦說，馮院士將流體力學應用在生物醫學上，以更精確、更實際的方式來思考人類健康，他接連發表多篇具有里程碑意義的學術論文，奠基了當代生物工程學。

馮院士從航空跨足到生物工程，其實背後來自對家人的深度關懷。馮元楨在

自傳中曾提及，因母親罹患青光眼，促使他想對生物醫學有更多認識的渴望。他在 2007 年一場演講中曾說，他轉向以「人」為本的生物工程，是覺得儘管對飛機了解很多，但對自身卻了解得不夠透徹。

他治學態度嚴謹，誠樸創新的精神，深深地影響國內外學術的發展。除 2002 年曾獲頒中央大學名譽博士之外，中大並將 2008 年 12 月 20 日在鹿林天文台所發現的編號 210434 小行星，以「馮元楨（Fungyuancheng）」來命名，並獲國際天文學聯合會（IAU）的小天體命名委員會審查通過，以感念他對世人的卓越貢獻。

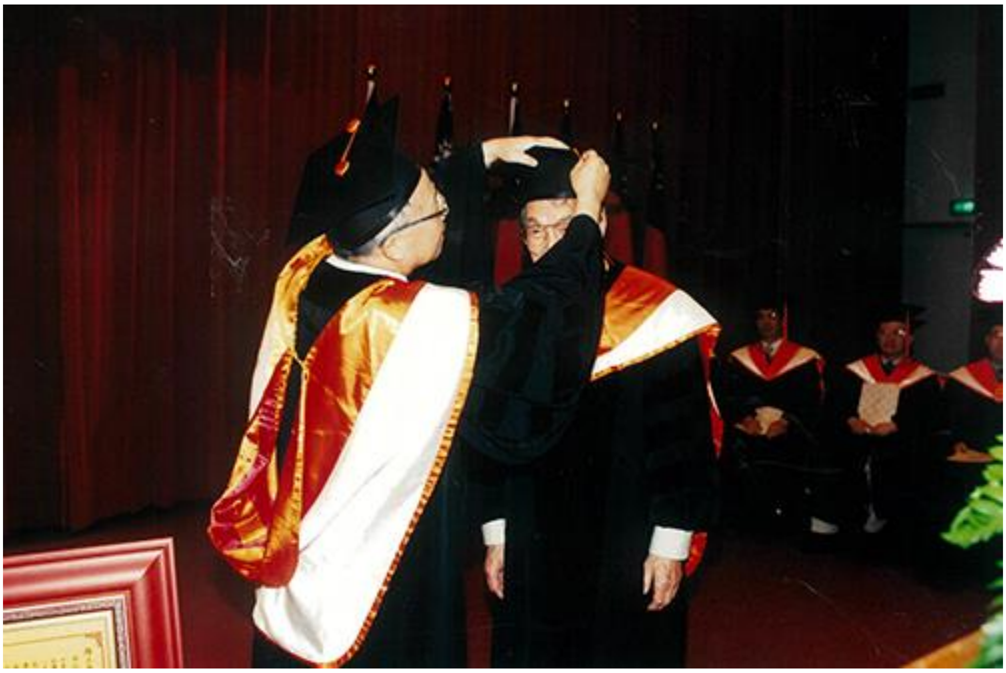

馮元楨院士校友 2002 年在劉兆漢校長任內，獲頒中央大學名譽博士。秘書室檔案照片

馮元楨院士校友（左三）2002 年蒞校參與「中大力學與生物科技」論壇，與校內的師長一同合影。秘書室檔案照片

中研院學者葉永烜、陳瑞華獲頒世界科學院科學獎

2020/12/31 中時新聞網 中大新聞

國際學術組織「世界科學院」（The World Academy of Sciences, TWAS）日前宣布 2021 年科學獎獲獎名單，中研院生物化學研究所特聘研究員陳瑞華獲生物科學獎，中研院院士葉永烜則獲得地球、天文及太空科學獎。

陳瑞華以研究細胞訊息路徑和蛋白修飾如何操控細胞凋亡、細胞自噬、以及腫瘤進程的重要貢獻而獲獎。她曾獲李天德醫藥基金會卓越醫藥科技獎、台灣生技醫藥發展基金會生技講座、教育部學術獎、吳健雄教育基金會臺灣傑出女科學家獎。

葉永烜為彗星及行星科學專家，現任中央大學天文所及太空科學所專案教授。葉永烜在太陽糸大型结構之動力學起源、彗星離子層物理及行星衛星與磁層電漿作用等研究領域上均有先驅性的傑出貢獻。葉院士也是教育部永久國家講座教授、美國地球物理聯會會士，曾獲 NASA 共服務特殊獎章、亞洲及大洋洲地球科學會阿斯福特獎、美國天文學會行星科學分會之科伊伯獎。

世界科學院科學獎頒給對學術研究有傑出貢獻之科學家。領域包括農業、生物、化學、數學、醫學、物理、社會科學及地球、天文及太空科學等，各領域一至二名獲獎者。

TWAS 成立於 1983 年，旨在協助發展中國家從事科學研究與開發應用，當選該科學院院士或獲頒相關獎項，不僅代表學者個人的成就，更代表該國對於全球推展科學之持續關懷與付出。
媒體報導

達爾文主義對宇宙演化的重要含義

2020/12/21 中時新聞網

本書獲選為紐約時報 1997 年度最佳圖書
如史詩般優雅，卻又令人屏息的宇宙的演化故事
天文物理學大師 丘宏義教授 專文推薦
中央大學物理與天文研究所 曹耀寰博士校訂

《預知宇宙紀事》建造起宇宙的全貌，把天文物理學描寫得有如童話故事一般，帶領讀者馳騁現代宇宙學的無限風光，從大爆炸理論、宇宙膨脹、統一場論到超弦理論。書中字字珠璣，而又發人深省。費瑞斯的文字透露了人類探究深邃無垠星空的渴望；他也告訴讀者已及其他的科學家，宇宙的探索同時也是哲學的、宗教的和藝術的課題。

【精彩書摘】

達爾文主義對於我們宇宙演化的問題，有三個特別重要的含義。

首先，達爾文說所有的生物都是祖先的產物，因而排除了靜態世界的概念，而以歷史的軸線為萬物的核心。歷史學家勒文伯格（Bert James Loewenberg）寫道：「他成功地把整個過去的生命收納到現在生命的每個層面和形式裡。」

其次，他的理論不只是援引了時間，而且是「很多的」時間。生物從單純的生命形式分化為現在地球上的數百萬個物種，這需要數億年的時間；時間這麼久，使得數學不是很好的達爾文有時候乾脆攤著手說，過去是無限的久遠。即使有些誇張，不過它背後的動力是可以理解的。演化的歷史不僅是世界的核心，而且也是浩瀚無垠的。

第三，當達爾文豎起了歷史的「五朔節花柱」(maypole)而發現它出乎意料的高，

焦點就轉到恆星上。在《物種起源》裡，他談到行星長久以來是「根據萬有引力循環不已」，這並不是隨便說說的。當我們知道地球已經這麼老了，萬物也經歷

了綿延互涉的歷史過程，也就發現我們自己的故事其實是和宇宙演化的劇本交織在一起的。

在宇宙演化的穹廬裡，有許多高樓大廈。在這裡我只談談其中規模較大的幾幢。

在地球的層次上，大量的絕種（massive extinction）中斷了化石的紀錄。最近我們把這現象歸因於彗星或小行星撞擊地球，導致地震、洪水和大火，所形成的霾害使得地球幾十年的時間沒有日光照射。我們發現有七次全球性絕種與彗星或小行星撞擊地球的時間吻合。其中最戲劇化的研究個案，是從白堊紀（Cretaceous period）到第三紀（Tertiary period）之間，也就是六千五百萬年前，恐龍和其他生物集體滅亡的故事。墨西哥灣的猶卡坦半島附近，有個「證據確鑿」的隕石坑，是由石油地質學家（oil geologist）所發現的，最初他們也不知道那是什麼東西，後來的學院裡的科學家才提出撞擊假說，解釋這個大洞的來源。（這隕石坑埋在比較新的地層下，直徑有一百英里。）這場浩劫對於生物環境有個戲劇性的影響，它為新物種的誕生鋪路，否則他們幾乎不可能取代那些在生態上佔據有利位置的舊有生命形式。既然我們是從這其中的物種演化而來的（像狐猿一樣的生物，當恐龍轟然走過時，瑟縮地躲在樹上），我們或許也該謝謝彗星在六千五百萬年前把地球搞得天翻地覆吧。

在早期的太陽系裡，地球被彗星像冰雹一樣地轟炸，反而是有好處的（儘管這在科學上很不可思議）。原始的彗星可以形成海洋，賜給地球生命誕生所需的胺基酸（amino acid）。彗星是否帶來醞釀生命的水和胺基酸，從現代彗星、土衛六，以及銀河系的分子雲的光譜裡偵測到的含碳分子（complex carbon molecules），可以作為證據。

演化論的觀點使我們對於所有事情都想要追尋歷史事件的證據。太陽系裡關於太陽及其行星形成的方式，有非常多的線索。我們看看行星間的相對大小。靠近太陽的軌道上，是個巨石嶙峋的世界，有水星、金星、地球和火星。再遠一些，是雲翳氤氳的氣體巨行星，有木星、土星、天王星和海王星。每個巨行星有岩石核心，再裹著冰層和雲氣。在冥王星（可能是從海王星逃逸的衛星，其軌道與海王星軌道相交）之外，是彗星的領域，由冰雪和岩屑組成。我們讓這些太陽系的組成分子排成一列，站在前頭的是嬌小的岩石行星；然後是冰冷的、籠罩在氣層裡的巨行星；最後是更冷的冰凍彗星層。這有什麼演化上的意味呢？

人類應該是宇宙中最寂寞的生命吧。我們直到最近，才開始去認識宇宙，還不很清楚怎麼去解釋它，也沒有別人可以一起討論。所以我們只有自言自語，完全從人類的角度去看。就此而論，我們的對話只是獨白而已，這樣的獨立蒼茫使我們感到困擾。我們只和擁有同樣認知的生命對話，只和同一種生命，因為地球上的

所有生命都是一家人，而所觀察的宇宙也只有一個。這樣子我們又如何去計算機率和必然性，好理解在自然的法則和常數裡，什麼是必然的，什麼是偶然的，並且判斷生命和智慧在萬物的宇宙架構裡的重要性，是核心的還是周邊的？

在文藝復興之前，我們住在一間愜意的宇宙小屋裡，我們的居所似乎是很安詳的。前科學的時代裡的宇宙是圍繞在我們四周的：它由我們周遭的環境所組成（不多不少），我們也隸屬於它，和它相處融洽。哥白尼革命改變了這一切，但是它的震撼還不至於像教科書所說的，「罷黜」我們的核心地位，而只是使宇宙看起來不再圍繞在我們身邊罷了。哥白尼式的廣袤宇宙，即使不是無生命跡象，也似乎是毫無用處、不著邊際的。（哲學家阿古奇〔Giovanni Agucchi〕在給伽利略的一封信裡，特別提出這一點，以反駁哥白尼的理論。）如果它是有生命跡象的，那麼我們就不得不想想，我們是否和其他的生命分享我們這個宇宙穹廬，這些生命會不會比我們更聰明、更先進、更值得上帝去關愛。

如此我們進入一個意見分歧的時代，科學的普及化像俱樂部一樣地風行起來，試圖去駕馭可怕的無垠宇宙。所謂的科學嬉皮，便是誇耀他毫不猶豫接受的「中肯」命題，說我們只不過是一團泥土，附著在星系裡的一顆塵沙上面，盲目地穿過那佈滿無心的星球的死寂空間。金斯爵士（Sir James Jeans）抓準了人們的這種心態，寫了一本天文學的暢銷書，殘酷地強調萬物的龐大和渺小、極熱和極凍，使得人們不禁要問他是要教育人類，還是要嚇死他們。

(本文摘自《預知宇宙紀事》/商周出版)

【作者簡介】

提摩西·費瑞斯（Timothy Ferris）

著名的科學作家，NASA 顧問，在四所大學任教，是加州柏克萊大學的榮譽教授。他的著作曾獲提名美國國家圖書獎和普立茲獎。著有《預知宇宙紀事》以及暢銷書《星系：銀河的未來》（1989 年獲美國物理學院獎、提名普立茲獎）、《新的天空》（1992 年紐約時報年度好書）。

【譯者簡介】

林淑貞

政大外交系畢業。譯有《牛頓的蘋果》、《性、演化、達爾文》、《探索大地之

心》、《生命中的戒指與蠟燭》、《如果中共跨過台灣》、《海蒂報告》、《林村的故事》、《母親與女兒的戰爭》、《作父母，也要作情人》。

林宏濤

台灣大學哲學系碩士，德國弗來堡大學博士研究。譯著有：《鈴木大拙禪學入門》、《啟蒙的辯證》、《菁英的反叛》、《詮釋之衝突》、《體會死亡》、《美學理論》、《法學導論》、《愛在流行》、《隱藏之泉》、《神在人間》、《眾生的導師：佛陀》、《南十字星風箏線》、《神話學辭典》、《與改變對話》、《死後的世界》、《正義的理念》、《與卡夫卡對話》等作品。

十月底有獵戶座流星雨、天王星衝　天文迷不要錯過

2020/10/21 yahoo 奇摩新聞

喜愛天文的天文迷，10 月底還有獵戶座流星雨、天空之神天王星衝可觀賞，在沒有光害的情況下，流星雨每小時可以看見約莫 20 顆；天王星是以躺著的姿勢繞太陽運行，可以透過望遠鏡尋找蹤影。(李明朝報導)

獵戶座流星雨觀賞期又來臨，中央大學天文所博士後研究員林忠義表示，這次極大期日期是在 10 月 21 日晚上，位於東北方輻射點獵戶座，升起後（約莫晚上 9 點 30 分）已經不受月光影響，所以這次觀測條件非常好，然而今年預期的 ZHR (天頂每小時出現率)只有 15 至 20 顆，同時，獵戶座流星雨母體是哈雷彗星，地球經過著名的哈雷彗星在太陽內側留下碎散的塵埃粒而產生，塵埃粒相對大，造成亮流星多，峰值流量持續時間長且相對速度快，極大期前後（10 月 19 日、20 日、22 日、23 日等）夜間都可以觀測獵戶座流星雨，觀測地點要遠離城市光害與視野大的地方觀看。

另外，10 月底也是觀測天空之神天王星日子，林忠義表示，在望遠鏡發明後所發現的第一顆行星-天王星(Uranus, 希臘神話譯成拉丁文的意思是天空之神)-也即將在 10 月 31 日達到肉眼可見亮度 5.7 等、視直徑約 3.8 角秒，也就是所謂的「天王星衝」的日子，這時候天王星與太陽正好分處於地球兩側，也是離地球最近的時候，只不過肉眼可見需要在極度理想的觀測條件下。

林忠義表示，天王星與其它行星相比，有一個的奇特之處，在於它的自轉軸幾乎與軌道平面平行，也就是說天王星是以躺著的姿勢繞太陽運行，天王星也有環，只不過它的環沒有土星來的壯觀，不過對於喜愛天文的天文迷來說，也是值得觀賞。

中大鹿林天文台監視器　台灣水鹿山羌悠閒同框

中大新聞

2020/09/16 中廣新聞網

位於海拔 2862 公尺的國立中央大學鹿林天文台，架設多支監視器，意外拍攝到水鹿覓食的畫面，天文台人員表示，附近算是水鹿棲息地，由於水鹿生性敏感，稍有驚動就會離開，目前以監視器觀察，不去驚擾牠們。(李明朝報導)

鹿林天文台加裝監視器，主要是曾經在鹿林小屋附近發現黑熊足跡，由於距離天文台不遠，基於安全考量，天文台把廚餘、垃圾桶都放置在屋內，集中後再帶往山下處理，並於天文台區域內增設監視器，可以掌握屋外動態。

雖然一直沒有看到黑熊，不過，台灣水鹿、山羌卻一直入鏡，鹿林天文台人員表示，當地也算是台灣水鹿的棲息地，以往可能常常出現，只是當時沒有拍到，在新增的監視器，確實一直拍到水鹿在附近吃草等畫面，除了水鹿，附近也有山羌出現，原本以為牠們會互相迴避，卻各自吃草，非常難得拍到同框畫面。

鹿林天文台人員進一步表示，因為台灣水鹿只要聽到風吹草動，立即會離開，所以到目前並沒有人、鹿相遇的情形，都是透過監視器畫面在入夜後拍到，同仁也不會去驚擾牠們，讓牠們在附近可以好好吃草。

中央大學葉永烜院士獲傑拉德·科伊伯獎　終身成就綻放國際

2020/08/17 中央通訊社

2020 年的傑拉德·科伊伯獎(Gerard P. Kuiper Prize)(註)，經美國天文學會(American Astronomical Society)的行星科學分會 (Division of Planetary Science) 嚴格審議，將頒發給中央大學天文研究所葉永烜教授，以表彰他在行星科學領域的貢獻。

中央大學校長周景揚說，葉永烜教授在彗星電漿物理學、太陽系動力學、行星及衛星大氣層與固體表面的磁層相互作用等領域貢獻卓著，早耀眼於國際，此次美國天文學會特頒贈此一獎項，肯定葉教授的終身成就，對葉教授而言，實為實至名歸。

葉永烜教授自 1998 年起開始於中大任教，除了擁有豐富的教學及行政資歷外，也積極參與多項國際太空計畫，並以科學團隊成員的身分加入許多行星探索任務，他發表在《Nature》和《Science》之論文篇數更為華人科學家之最。中央

大學在美國新聞與世界報導（U.S. News & World Report）中所列出的國際合作指標排名得以連續五年蟬聯全國第一，葉教授功不可沒。

葉永烜教授致力於推動美國、歐洲及亞洲對太陽系的科學探索，是 NASA 和歐空局(ESA)合作的卡西尼土星任務的三位創議者之一。同時也是亞洲大洋洲地球科學學會(Asia-Oceania Geosciences Society)的創始主席，該學會更團結了地球科學界社群，在亞洲及大洋洲地區紮根行星研究，自此成為了世界領先的國際科學組織之一，在地球科學各領域之間建立起嶄新的合作關係。

此外，葉永烜教授曾獲頒美國太空總署「特殊公共服務」榮譽動章、卡西尼土星計畫團隊成就獎、伽利略木星計畫團隊成就獎，美國地球物理聯會會士，教育部國家講座，更榮膺中央研究院第 31 屆數理科學組院士。此次獲頒美國天文學會傑拉德·柯伊伯獎，正是其教育家精神與對學術的貢獻，在行星科學領域中發揮了強大影響力的例證。

註：傑拉德·科伊伯獎(Gerard P. Kuiper Prize)
傑拉德·柯伊伯獎是美國天文學會的行星科學分會每年頒發一次的獎項，獎勵在行星科學領域有突出貢獻的天文學家，該獎是以天文學家傑拉德·柯伊伯的名字命名，為終身成就的獎項。

中央大學葉永烜院士獲傑拉德·科伊伯獎　終身成就綻放國際

2020/08/17 PChome 新聞
2020 年的傑拉德·科伊伯獎(Gerard P. Kuiper Prize)(註)，經美國天文學會(American Astronomical Society)的行星科學分會 (Division of Planetary Science)嚴格審議，將頒發給中央大學天文研究所葉永烜教授，以表彰他在行星科學領域的貢獻。

中央大學校長周景揚說，葉永烜教授在彗星電漿物理學、太陽系動力學、行星及衛星大氣層與固體表面的磁層相互作用等領域貢獻卓著，早耀眼於國際，此次美國天文學會特頒贈此一獎項，肯定葉教授的終身成就，對葉教授而言，實為實至名歸。

葉永烜教授自 1998 年起開始於中大任教，除了擁有豐富的教學及行政資歷外，也積極參與多項國際太空計畫，並以科學團隊成員的身分加入許多行星探索任務，他發表在《Nature》和《Science》之論文篇數更為華人科學家之最。中央大學在美國新聞與世界報導（U.S. News & World Report）中所列出的國際合作指標排名得以連續五年蟬聯全國第一，葉教授功不可沒。

葉永烜教授致力於推動美國、歐洲及亞洲對太陽系的科學探索，是 NASA 和歐空局(ESA)合作的卡西尼土星任務的三位創議者之一。同時也是亞洲大洋洲地球科學學會(Asia-Oceania Geosciences Society)的創始主席，該學會更團結了地球科學界社群，在亞洲及大洋洲地區紮根行星研究，自此成為了世界領先的國際科學組織之一，在地球科學各領域之間建立起嶄新的合作關係。

此外，葉永烜教授曾獲頒美國太空總署「特殊公共服務」榮譽勳章、卡西尼土星計畫團隊成就獎、伽利略木星計畫團隊成就獎，美國地球物理聯會會士，教育部國家講座，更榮膺中央研究院第 31 屆數理科學組院士。此次獲頒美國天文學會傑拉德·柯伊伯獎，正是其教育家精神與對學術的貢獻，在行星科學領域中發揮了強大影響力的例證。

註：傑拉德·科伊伯獎(Gerard P. Kuiper Prize)傑拉德·柯伊伯獎是美國天文學會的行星科學分會每年頒發一次的獎項，獎勵在行星科學領域有突出貢獻的天文學家，該獎是以天文學家傑拉德·柯伊伯的名字命名，為終身成就的獎項。

中央大學葉永烜院士獲傑拉德·科伊伯獎　終身成就綻放國際

2020/08/17 蕃新聞

2020 年的傑拉德·科伊伯獎(Gerard P. Kuiper Prize)(註)，經美國天文學會(American Astronomical Society)的行星科學分會 (Division of Planetary Science) 嚴格審議，將頒發給中央大學天文研究所葉永烜教授，以表彰他在行星科學領域的貢獻。

中央大學校長周景揚說，葉永烜教授在彗星電漿物理學、太陽系動力學、行星及衛星大氣層與固體表面的磁層相互作用等領域貢獻卓著，早耀眼於國際，此次美國天文學會特頒贈此一獎項，肯定葉教授的終身成就，對葉教授而言，實為實至名歸。

葉永烜教授自 1998 年起開始於中大任教，除了擁有豐富的教學及行政資歷外，也積極參與多項國際太空計畫，並以科學團隊成員的身分加入許多行星探索任務，他發表在《Nature》和《Science》之論文篇數更為華人科學家之最。中央大學在美國新聞與世界報導（U.S. News & World Report）中所列出的國際合作指標排名得以連續五年蟬聯全國第一，葉教授功不可沒。

葉永烜教授致力於推動美國、歐洲及亞洲對太陽系的科學探索，是 NASA 和歐空局(ESA)合作的卡西尼土星任務的三位創議者之一。同時也是亞洲大洋洲地球

科學學會(Asia-Oceania Geosciences Society)的創始主席，該學會更團結了地球科學界社群，在亞洲及大洋洲地區紮根行星研究，自此成為了世界領先的國際科學組織之一，在地球科學各領域之間建立起嶄新的合作關係。

此外，葉永烜教授曾獲頒美國太空總署「特殊公共服務」榮譽勳章、卡西尼土星計畫團隊成就獎、伽利略木星計畫團隊成就獎，美國地球物理聯會會士，教育部國家講座，

更榮膺中央研究院第 31 屆數理科學組院士。此次獲頒美國天文學會傑拉德·柯伊伯獎，正是其教育家精神與對學術的貢獻，在行星科學領域中發揮了強大影響力的例證。

註：傑拉德·科伊伯獎(Gerard P. Kuiper Prize)

傑拉德·柯伊伯獎是美國天文學會的行星科學分會每年頒發一次的獎項，獎勵在行星科學領域有突出貢獻的天文學家，該獎是以天文學家傑拉德·柯伊伯的名字命名，為終身成就的獎項。

淡水「逐岸」特展開跑　小行星命名齊柏林

2020/08/14 udn 聯合新聞網

新北市淡水區齊柏林空間，從見山開展之後，耗時一年籌備的第 2 檔期，作品「逐岸」正式開展，會中中央大學為感念齊柏林，特別將一顆小行星命名「齊柏林」，希望大家記得齊柏林的精神及對台灣環境的關懷。

淡水區齊柏林空間《逐岸》正式開展，齊柏林基金會董事長歐晉德、教育部綜合規劃司副司長王明源、新北市淡水古蹟博物館館長柏麗梅、以及台東縣指定為造舟國寶的達悟族人張馬群與兒子張世凱，為了感念齊柏林，特別划拼板舟，在觀潮廣場上岸。

張世凱表示，他曾經與齊柏林承諾，要在蘭嶼飛魚季拍攝地方耆老用拼板舟捕魚的畫面，雖然齊柏林已離去，但他仍計畫乘著拼板舟環島，用齊導演關注環境的角度出發。

另外在會中，特舉辦齊柏林小行星頒贈儀式，中央大學校長周景揚感念齊柏林導演一生關注台灣土地發展的堅持與勇氣，希望大家記得齊柏林的精神及對台灣環境的關懷。

中央大學校長周景揚表示，中央大學從 2006 年開始的鹿林巡天計畫，發現了 800 多顆小行星，而齊柏林小行星是 2006 年由鹿林天文台林宏欽台長及美國馬里蘭大學葉泉志博士共同發現，2017 年正式通過命名。透過齊柏林導演的空拍視角，可以跨越種族和文化的藩籬，撼動人心。

柏林兒子齊廷洹表示，許多年輕人對於海岸環境乾淨的了解程度有限，希望透過父親的影像，還有展覽，讓大家重視了解這些議題。而第二號作品《逐岸》，有大投影沉浸式的展現手法，互動多媒體式的推移牆面，讓民眾以一起「飛閱海岸線」，這次策展最大特點，邀集了在環境生態領域的專家，設計出「對談人空間」，讓他們的作品用深入淺出的方式與齊導的作品相呼應，讓展覽更具廣度。

極大期來了！英仙座流星雨找到沒？

2020/08/14 中廣新聞網

天文迷熱愛的英仙座流星雨，極大期就在這兩天(12、13 日)，中央大學鹿林天文台在合歡山已經捕捉到一顆極亮的火流星。一般觀星民眾可以在沒有光害地點，稍加注意，或許就能找到。

英仙座流星雨的極大期是位在 8 月 12、13 日，不過，城市想要看流星雨的機率不高，主要是光害等因素，所以想要看流星雨，山區的地點比較能捕捉到。

另外，英仙座流星雨是從 7 月中旬到 8 月 24 日之間，目前中央大學鹿林天文台在日前也拍攝到一顆流星雨相當明亮，猶如火流星，雖然時間短暫，卻也讓天文迷感到興奮。

為什麼稱為英仙座流星雨？因彗星繞行太陽時，會有一些物質漂流在運行軌道上，天文所張光祥老師表示，地球公轉接近彗星軌道留下的物質時就能形成流星雨，而其流星雨輻射點剛好於英仙座星座方向時稱之英仙座流星雨。

極大期雖然沒有找到流星雨，也不要灰心，張光祥老師表示，只要到較為高處，再往英仙座方向，也許就能找到一顆流星，其實也相當浪漫。

一起飛閱海岸線　中大發現小行星命名「齊柏林」

2020/08/10 蘋果新聞網

看見‧齊柏林基金會，今天（7 日）在淡水齊柏林空間展出「逐岸」特展。將已

故導演齊柏林生前拍攝的台灣海岸，以五大主題分區做論述，觀眾跟著齊柏林鏡頭一起「飛閱海岸線」，感受台灣海岸美麗與哀愁。蘭嶼達悟族張世凱划著與父親張馬群（台東縣定造舟國寶）完成的傳統拼板舟，從大直划向淡水，實現當年與齊柏林的約定。國立中央大學天文所也將發現的小行星，以「齊柏林」命名，紀念其精神與對台灣環境的關懷。

紀錄片導演齊柏林，2017 年 6 月 10 日在空拍時因直升機墜落不幸罹難，為了紀念齊柏林對台灣環境的關懷，隔年（2018 年）「齊柏林空間」在淡水正式成立。今天在淡水區中正路 298 號「齊柏林空間」，展出「逐岸」特展，看見・齊柏林基金會表示，這次逐岸特展耗時 1 年籌備，透過層層推地的展示手法，讓民眾感受台灣海岸的美麗與震撼。

蘭嶼達悟族男子張世凱表示，與已故導演齊柏林當年在拍攝「看見台灣二」時結識，雙方約定要在飛魚季節前往蘭嶼，拍攝地方耆老乘著拼板舟捕魚的畫面，齊柏林過世後，張世凱不曾忘記這個承諾，特別與父親張馬群先生（台東縣定造舟國寶），一同完成蘭嶼傳統拼板舟，昨天從大直基隆河划向淡水，在觀潮廣場前的沙灘上岸，今天記者會時還特別舉行傳統「拋舟儀式」，親身實現當年與齊柏林的約定。

國立中央大學校長周景揚周景揚表示，中央大學天文所林宏欽與葉泉志，2006 年 7 月 18 日在鹿林天文台觀測時，發現了一個大小約 4.9 公里，軌道周期 5.5 年的璀璨小行星，因有感於齊柏林導演一生關注台灣土地發展的堅持與勇氣，特別將新發現的行星以「齊柏林（Chipolin）」命名，並將命名證書頒給齊柏林兒子齊廷洹，希望讓大家記得齊柏林的精神與對台灣環境的關懷。

齊柏林基金會表示，此次特展以關心台灣海洋為主軸，特別展出齊柏林的空拍作品，希望民眾能踴躍前來參觀「逐岸」特展，親身體驗台灣海岸的風情。

小行星以齊柏林命名　兒指像爸爸在天上看見台灣

2020/08/10　中央通訊社

為紀念已故導演齊柏林，中央大學天文所鹿林天文台將發現的小行星命名為「齊柏林」。齊柏林的兒子齊廷洹指出，爸爸曾經的夢想是當機師，這次命名就像是爸爸在天上看著台灣。

齊廷洹受訪時表示，「爸爸生前就有當機師的夢想，礙於身材與近視無法圓夢。這次的小行星命名就像是讓他夢想成真，可以一直在天上看著我們、看著他愛的台灣。」

齊廷洹指出，小時候爸爸常帶著家人到海邊玩，今天見到記者會安排達悟族人張世凱等與拼板舟一起入場儀式，讓他想起父子倆曾一起划獨木舟的美好記憶。

對於父親節將至，齊廷洹笑著說，「想跟他說我瘦 15 公斤了。」也希望父親知道，大家沒有忘記父親，期待透過展覽讓更多人珍愛台灣這片土地。

齊柏林於民國 106 年 6 月 10 日為電影「看見台灣 II」搭乘直升機勘景，不幸在花蓮山區墜機過世。

財團法人看見・齊柏林基金會為紀念齊柏林及持續推廣環境教育所規劃的「齊柏林空間」去年 4 月開幕，並舉辦開幕首展「見山」，今天則宣布第二場展覽「逐岸」正式開展及進行齊柏林小行星「頒贈」儀式。

看見・齊柏林基金會董事長歐晉德、教育部綜合規劃司副司長王明源、新北市淡水古蹟博物館館長柏麗梅、國立中央大學校長周景揚、台東縣指定為造舟國寶的達悟族人張馬群與兒子張世凱今天出席記者會。

張世凱分享指出，他曾經與齊柏林立下要在蘭嶼飛魚季拍攝地方耆老乘著拼板舟捕魚的畫面，雖然齊柏林已離去，但他仍希望有日能乘著拼板舟環島，讓大家看見從蘭嶼視角出發的台灣。

配合今天的記者會，張世凱與族人在前一天乘著拼板舟自大直划向淡水，記者會當天也在淡水河划到觀潮廣場前的沙灘上岸，到達記者會現場時並舉行傳統「拋舟儀式」，張馬群也在現場吟唱蘭嶼傳統古調。

「齊柏林空間」自第二檔展覽開始，基金會將邀請各界人士呼應齊柏林作品主題進行一系列對談。

其中，包括財團法人中央通訊社董事長劉克襄以詩對話、社團法人台灣海洋環境教育推廣協會秘書長郭兆偉以步行對話、RE-THINK 創辦人黃之揚以海廢對話及公視節目「我們的島」以環境對話。

感念「看見臺灣」精神　中央大學命名「齊柏林小行星」贈齊家

2020/08/10 yahoo 奇摩新聞

中央大學為感念空拍導演齊柏林對臺灣的卓越貢獻，將鹿林天文台所發現的編

號 281068 號小行星，命名為「齊柏林 （Chipolin）」小行星。並於 7 日在淡水齊柏林空間舉行頒贈儀式，由中央大學校長周景揚頒贈小行星銘版給齊柏林兒子齊廷洹，感念齊柏林一生關注臺灣土地發展的堅持與勇氣，希望大家記得齊柏林的精神及對臺灣環境的關懷。

「齊柏林飛船」是人類對飛行夢想的初探，「齊柏林」小行星更是象徵一艘永恆的飛船，深情地望著臺灣，守護著臺灣。周景揚表示，透過齊柏林的空拍視角，可以跨越種族和文化的藩籬，撼動人心。中央大學希望將他的精神化為永恆，如同星光般燦爛，普照大地。

周景揚指出，齊柏林除讓人看見臺灣之美外，同時也喚醒我們更疼惜自己生長的土地。中央大學以地球科學起家，長期致力於環境永續之研究。從地球、海洋、大氣、水文，乃至太空、天文，以科學的專業全方位守護著臺灣和地球，為人類永續生存的明天而努力，無疑將他的精神作了永續的傳揚。

齊柏林小行星是 2006 年 7 月 18 日由鹿林天文台台長林宏欽及美國馬里蘭大學博士葉泉志共同發現，2017 年 11 月 4 日經國際天文學聯合會（IAU）通過命名。大小約為 4.9 公里，發現時位在魔羯座，目前已運行到獅子座。繞行太陽一圈 5.6 年（軌道週期），離太陽最近時（近日點）為 4.3 億公里，最遠時（遠日點）為 5.1 億公里。

中央大學從 2006 年開始的鹿林巡天計畫，不但曾發現臺灣史上的第一顆彗星，同時也發現了 800 多顆小行星，使臺灣成為亞洲發現小行星最活躍的地方之一。卓越的天文研究成果，充份展現臺灣人「以小搏大」的精神，也讓世界真正「看見臺灣」。

感念「看見臺灣」精神　中央大學命名「齊柏林小行星」贈齊家

2020/08/10 立報傳媒

中央大學為感念空拍導演齊柏林對臺灣的卓越貢獻，將鹿林天文台所發現的編號 281068 號小行星，命名為「齊柏林 （Chipolin）」小行星。並於 7 日在淡水齊柏林空間舉行頒贈儀式，由中央大學校長周景揚頒贈小行星銘版給齊柏林兒子齊廷洹，感念齊柏林一生關注臺灣土地發展的堅持與勇氣，希望大家記得齊柏林的精神及對臺灣環境的關懷。

「齊柏林飛船」是人類對飛行夢想的初探，「齊柏林」小行星更是象徵一艘永恆的飛船，深情地望著臺灣，守護著臺灣。周景揚表示，透過齊柏林的空拍視角，可以跨越種族和文化的藩籬，撼動人心。中央大學希望將他的精神化為永

恆，如同星光般燦爛，普照大地。

周景揚指出，齊柏林除讓人看見臺灣之美外，同時也喚醒我們更疼惜自己生長的土地。中央大學以地球科學起家，長期致力於環境永續之研究。從地球、海洋、大氣、水文，乃至太空、天文，以科學的專業全方位守護著臺灣和地球，為人類永續生存的明天而努力，無疑將他的精神作了永續的傳揚。

齊柏林小行星是 2006 年 7 月 18 日由鹿林天文台台長林宏欽及美國馬里蘭大學博士葉泉志共同發現，2017 年 11 月 4 日經國際天文學聯合會（IAU）通過命名。大小約為 4.9 公里，發現時位在魔羯座，目前已運行到獅子座。繞行太陽一圈 5.6 年（軌道週期），離太陽最近時（近日點）為 4.3 億公里，最遠時（遠日點）為 5.1 億公里。

中央大學從 2006 年開始的鹿林巡天計畫，不但曾發現臺灣史上的第一顆彗星，同時也發現了 800 多顆小行星，使臺灣成為亞洲發現小行星最活躍的地方之一。卓越的天文研究成果，充份展現臺灣人「以小搏大」的精神，也讓世界真正「看見臺灣」。

中央大學今贈齊柏林行星之名　齊廷洹：相信爸很高興

2020/08/10 udn 聯合新聞網

「希望齊柏林精神可以化為永恆，守護台灣」，中央大學校長周景揚今在齊柏林空間展覽「逐岸」茶會中，代表頒贈以齊柏林為命名的小行星銘版給齊柏林之子齊廷洹。齊廷洹說，相信爸爸會很高興，也感謝今天茶會多人前來，沒有忘記爸爸，希望爸爸的善緣可以繼續發揚。

齊廷洹也感動說，小行星比人類生命更長，有一個接近永恆的行星紀念爸爸，好像抬頭就能看到爸爸。

「齊柏林飛船」是人類對飛行夢想的初探，為感念已故空拍導演齊柏林對台灣的卓越貢獻，中央大學特將鹿林天文台所發現的編號 281068 號小行星，是 2006 年 7 月 18 日由時任台長及美國馬里蘭大學葉泉志博士共同發現，經國際天文學聯合會（IAU）通過，在 2017 年正式命名為「齊柏林 (Chipolin)」小行星，象徵一艘永恆的飛船，深情地望著台灣，守護著台灣。

周景揚表示，感念齊柏林導演一生關注台灣土地發展的堅持與勇氣，希望大家記得齊柏林的精神及對台灣環境的關懷，將他的精神化為永恆，如同星光般燦爛，普照大地。

周景揚指出，中央大學以地球科學起家，長期致力於環境永續之研究，從地球、海洋、大氣、水文，乃至太空、天文，以科學的專業全方位守護著台灣和地球，為人類永續生存的明天而努力，無疑將齊導的精神作了永續的傳揚。

齊柏林小行星，大小約為 4.9 公里，發現時位在魔羯座，目前已運行到獅子座。繞行太陽一圈 5.6 年（軌道週期），離太陽最近時（近日點）為 4.3 億公里，最遠時（遠日點）為 5.1 億公里。

中央大學表示，從 2006 年開始的鹿林巡天計畫，不但曾發現台灣史上的第一顆彗星，同時也發現了 800 多顆小行星，使台灣成為亞洲發現小行星最活躍的地方之一，充份展現台灣人「以小搏大」的精神，也讓世界真正「看見台灣」。

與齊柏林的約定　達悟划船到淡水

2020/08/10 yahoo 奇摩新聞

導演齊柏林生前與蘭嶼達悟族好友張世凱約定將拍攝蘭嶼飛魚祭，然而齊柏林卻突然離世，張於是帶著拼板舟，從遙遠的河岸划船至淡水河找上「齊柏林基金會」；齊柏林基金會董事長歐晉德表示，導演齊柏林《看見台灣》著重山林環境，7 日開展的《逐岸》重點放於海岸環境。

齊柏林基金會昨舉行「齊柏林小行星暨蘭嶼《逐岸》開展儀式」，現場由達悟族人震撼拋舟儀式，張世凱父親、造舟國寶張馬群吟唱蘭嶼古調為展覽《逐岸》祈福，此外，國立中央大學校長周景揚還特別將天文所發現的行星以「齊柏林」命名證明贈與齊柏林兒子齊廷洹。

中央大學校長周景揚表示，中央大學天文所教授林宏欽、葉泉志 2006 年 7 月 18 日在鹿林天文台觀測時，發現一個大小約 4.9 公里，軌道周期 5.5 年的璀璨小行星，有感於齊柏林關注台灣土地的堅持與勇氣，特別將新發現的行星以「齊柏林（Chipolin）」命名，希望讓大家記得齊柏林愛台的精神。

達悟族張世凱表示，當年在齊柏林拍攝「看見台灣二」時結識，雙方約定要在飛魚季節前往蘭嶼，拍攝地方耆老乘著拼板舟捕魚畫面，齊柏林過世後，他不曾忘記這個承諾，特別與父親張馬群完成蘭嶼傳統拼板舟，從大直基隆河划向淡水從觀潮廣場前的沙灘上岸，實現與齊柏林的約定。

小行星命名齊柏林　永恆守護臺灣也讓世界「看見臺灣」

2020/08/10 台灣英文新聞

為感念空拍導演齊柏林先生對臺灣的卓越貢獻，中央大學特將鹿林天文台所發現的編號 281068 號小行星，經國際天文學聯合會（IAU）通過，命名為「齊柏林 (Chipolin)」小行星，象徵一艘永恆的飛船，深情地望著臺灣，守護著臺灣。

8 月 7 日在齊柏林空間舉辦的《逐岸》開展記者會中，特舉辦齊柏林小行星頒贈儀式，由中央大學校長周景揚頒贈小行星銘版給齊柏林導演之子齊廷洹先生，感念齊柏林導演一生關注臺灣土地發展的堅持與勇氣，希望大家記得齊柏林的精神及對臺灣環境的關懷。

齊柏林小行星，2006 年 7 月 18 日由鹿林天文台林宏欽台長及美國馬里蘭大學葉泉志博士共同發現，2017 年 11 月 4 日正式通過命名。大小約為 4.9 公里，發現時位在魔羯座，目前已運行到獅子座。繞行太陽一圈 5.6 年（軌道週期），離太陽最近時（近日點）為 4.3 億公里，最遠時（遠日點）為 5.1 億公里。

小行星以齊柏林命名　兒指像爸爸在天上看見台灣

2020/08/10 自由時報

為紀念已故導演齊柏林，中央大學天文所鹿林天文台將發現的小行星命名為「齊柏林」。齊柏林的兒子齊廷洹指出，爸爸曾經的夢想是當機師，這次命名就像是爸爸在天上看著台灣。

齊廷洹受訪時表示，「爸爸生前就有當機師的夢想，礙於身材與近視無法圓夢。這次的小行星命名就像是讓他夢想成真，可以一直在天上看著我們、看著他愛的台灣。」

齊廷洹指出，小時候爸爸常帶著家人到海邊玩，今天見到記者會安排達悟族人張世凱等與拼板舟一起入場儀式，讓他想起父子倆曾一起划獨木舟的美好記憶。

對於父親節將至，齊廷洹笑著說，「想跟他說我瘦 15 公斤了。」也希望父親知道，大家沒有忘記父親，期待透過展覽讓更多人珍愛台灣這片土地。

齊柏林於民國 106 年 6 月 10 日為電影「看見台灣 II」搭乘直升機勘景，不幸在花蓮山區墜機過世。

財團法人看見·齊柏林基金會為紀念齊柏林及持續推廣環境教育所規劃的「齊柏林空間」去年 4 月開幕，並舉辦開幕首展「見山」，今天則宣布第二場展覽

「逐岸」正式開展及進行齊柏林小行星「頒贈」儀式。

看見·齊柏林基金會董事長歐晉德、教育部綜合規劃司副司長王明源、新北市淡水古蹟博物館館長柏麗梅、國立中央大學校長周景揚、台東縣指定為造舟國寶的達悟族人張馬群與兒子張世凱今天出席記者會。

張世凱分享指出，他曾經與齊柏林立下要在蘭嶼飛魚季拍攝地方耆老乘著拼板舟捕魚的畫面，雖然齊柏林已離去，但他仍希望有日能乘著拼板舟環島，讓大家看見從蘭嶼視角出發的台灣。

配合今天的記者會，張世凱與族人在前一天乘著拼板舟自大直划向淡水，記者會當天也在淡水河划到觀潮廣場前的沙灘上岸，到達記者會現場時並舉行傳統「抛舟儀式」，張馬群也在現場吟唱蘭嶼傳統古調。

「齊柏林空間」自第二檔展覽開始，基金會將邀請各界人士呼應齊柏林作品主題進行一系列對談。

其中，包括財團法人中央通訊社董事長劉克襄以詩對話、社團法人台灣海洋環境教育推廣協會秘書長郭兆偉以步行對話、RE-THINK 創辦人黃之揚以海廢對話及公視節目「我們的島」以環境對話。

小行星命名齊柏林　永恆守護臺灣也讓世界「看見臺灣」

2020/08/10 新住民全球新聞網

為感念空拍導演齊柏林先生對臺灣的卓越貢獻，中央大學特將鹿林天文台所發現的編號 281068 號小行星，經國際天文學聯合會（IAU）通過，命名為「齊柏林 (Chipolin)」小行星，象徵一艘永恆的飛船，深情地望著臺灣，守護著臺灣。

8 月 7 日在齊柏林空間舉辦的《逐岸》開展記者會中，特舉辦齊柏林小行星頒贈儀式，由中央大學校長周景揚頒贈小行星銘版給齊柏林導演之子齊廷洹先生，感念齊柏林導演一生關注臺灣土地發展的堅持與勇氣，希望大家記得齊柏林的精神及對臺灣環境的關懷。

齊柏林小行星，2006 年 7 月 18 日由鹿林天文台林宏欽台長及美國馬里蘭大學葉泉志博士共同發現，2017 年 11 月 4 日正式通過命名。大小約為 4.9 公里，發現時位在魔羯座，目前已運行到獅子座。繞行太陽一圈 5.6 年（軌道週期），離太陽最近時（近日點）為 4.3 億公里，最遠時（遠日點）為 5.1 億公里。

小行星命名「齊柏林」　兒：像爸爸在天上看台灣

2020/08/10 三立新聞網

為紀念已故導演齊柏林，中央大學天文所鹿林天文台將發現的小行星命名為「齊柏林」。齊柏林的兒子齊廷洹指出，爸爸曾經的夢想是當機師，這次命名就像是爸爸在天上看著台灣。

齊廷洹受訪時表示，「爸爸生前就有當機師的夢想，礙於身材與近視無法圓夢。這次的小行星命名就像是讓他夢想成真，可以一直在天上看著我們、看著他愛的台灣。」

齊廷洹指出，小時候爸爸常帶著家人到海邊玩，今（7）日見到記者會安排達悟族人張世凱等與拼板舟一起入場儀式，讓他想起父子倆曾一起划獨木舟的美好記憶。

對於父親節將至，齊廷洹笑著說，「想跟他說我瘦 15 公斤了。」也希望父親知道，大家沒有忘記父親，期待透過展覽讓更多人珍愛台灣這片土地。

齊柏林於民國 106 年 6 月 10 日為電影「看見台灣 II」搭乘直升機勘景，不幸在花蓮山區墜機過世。

財團法人看見・齊柏林基金會為紀念齊柏林及持續推廣環境教育所規劃的「齊柏林空間」去年 4 月開幕，並舉辦開幕首展「見山」，今日則宣布第二場展覽「逐岸」正式開展及進行齊柏林小行星「頒贈」儀式。

看見・齊柏林基金會董事長歐晉德、教育部綜合規劃司副司長王明源、新北市淡水古蹟博物館館長柏麗梅、國立中央大學校長周景揚、台東縣指定為造舟國寶的達悟族人張馬群與兒子張世凱今日出席記者會。

張世凱分享指出，他曾經與齊柏林立下要在蘭嶼飛魚季拍攝地方耆老乘著拼板舟捕魚的畫面，雖然齊柏林已離去，但他仍希望有日能乘著拼板舟環島，讓大家看見從蘭嶼視角出發的台灣。

配合今日的記者會，張世凱與族人在前一日乘著拼板舟自大直划向淡水，記者會當日也在淡水河划到觀潮廣場前的沙灘上岸，到達記者會現場時並舉行傳統「拋舟儀式」，張馬群也在現場吟唱蘭嶼傳統古調。

「齊柏林空間」自第二檔展覽開始，基金會將邀請各界人士呼應齊柏林作品主題進行一系列對談。

其中，包括財團法人中央通訊社董事長劉克襄以詩對話、社團法人台灣海洋環境教育推廣協會秘書長郭兆偉以步行對話、RE-THINK 創辦人黃之揚以海廢對話及公視節目「我們的島」以環境對話。

齊柏林小行星　讓世界「看見臺灣」

2020/08/10 HiNet 生活誌

「齊柏林飛船」，是人類對飛行夢想的初探，為感念空拍導演齊柏林先生對台灣的卓越貢獻，中央大學特將鹿林天文台所發現的編號 281068 號小行星，經國際天文學聯合會（IAU）通過，命名為「齊柏林（Chipolin)」小行星，象徵一艘永恆的飛船，深情地望著臺灣，守護著臺灣。

8 月 7 號在齊柏林空間舉辦的《逐岸》開展記者會中，特舉辦齊柏林小行星頒贈儀式，由中央大學校長周景揚頒贈小行星銘版給齊柏林導演之子齊廷洹先生，感念齊柏林導演一生關注台灣土地發展的堅持與勇氣，希望大家記得齊柏林的精神及對台灣環境的關懷。

中央大學校長周景揚表示，美麗的福爾摩沙臺灣，你我的共同家園，透過齊柏林導演的空拍視角，可以跨越種族和文化的藩籬，撼動人心。中央大學希望將他的精神化為永恆，如同星光般燦爛，普照大地。

周景揚校長指出，齊柏林導演除讓人看見台灣之美外，同時也喚醒我們更疼惜自己生長的土地。中央大學以地球科學起家，長期致力於環境永續之研究。從地球、海洋、大氣、水文，乃至太空、天文，以科學的專業全方位守護著台灣和地球，為人類永續生存的明天而努力，無疑將他的精神作了永續的傳揚！

齊柏林小行星，2006 年 7 月 18 日由鹿林天文台林宏欽台長及美國馬里蘭大學葉泉志博士共同發現，2017 年 11 月 4 日正式通過命名。大小約為 4.9 公里，發現時位在魔羯座，目前已運行到獅子座。繞行太陽一圈 5.6 年（軌道週期)，離太陽最近時（近日點）為 4.3 億公里，最遠時（遠日點）為 5.1 億公里。

中央大學從 2006 年開始的鹿林巡天計畫，不但曾發現台灣史上的第一顆彗星，同時也發現了 800 多顆小行星，使台灣成為亞洲發現小行星最活躍的地方之一。卓越的天文研究成果，充份展現臺灣人「以小搏大」的精神，也讓世界真正「看見臺灣」！

小行星以齊柏林命名　兒指像爸爸在天上看見台灣

2020/08/10 HiNet 生活誌

為紀念已故導演齊柏林，中央大學天文所鹿林天文台將發現的小行星命名為「齊柏林」。齊柏林的兒子齊廷洹指出，爸爸曾經的夢想是當機師，這次命名就像是爸爸在天上看著台灣。

齊廷洹受訪時表示，「爸爸生前就有當機師的夢想，礙於身材與近視無法圓夢。這次的小行星命名就像是讓他夢想成真，可以一直在天上看著我們、看著他愛的台灣。」

齊廷洹指出，小時候爸爸常帶著家人到海邊玩，今天見到記者會安排達悟族人張世凱等與拼板舟一起入場儀式，讓他想起父子倆曾一起划獨木舟的美好記憶。

對於父親節將至，齊廷洹笑著說，「想跟他說我瘦 15 公斤了。」也希望父親知道，大家沒有忘記父親，期待透過展覽讓更多人珍愛台灣這片土地。

齊柏林於民國 106 年 6 月 10 日為電影「看見台灣 II」搭乘直升機勘景，不幸在花蓮山區墜機過世。

財團法人看見・齊柏林基金會為紀念齊柏林及持續推廣環境教育所規劃的「齊柏林空間」去年 4 月開幕，並舉辦開幕首展「見山」，今天則宣布第二場展覽「逐岸」正式開展及進行齊柏林小行星「頒贈」儀式。

看見・齊柏林基金會董事長歐晉德、教育部綜合規劃司副司長王明源、新北市淡水古蹟博物館館長柏麗梅、國立中央大學校長周景揚、台東縣指定為造舟國寶的達悟族人張馬群與兒子張世凱今天出席記者會。

張世凱分享指出，他曾經與齊柏林立下要在蘭嶼飛魚季拍攝地方耆老乘著拼板舟捕魚的畫面，雖然齊柏林已離去，但他仍希望有日能乘著拼板舟環島，讓大家看見從蘭嶼視角出發的台灣。

配合今天的記者會，張世凱與族人在前一天乘著拼板舟自大直划向淡水，記者會當天也在淡水河划到觀潮廣場前的沙灘上岸，到達記者會現場時並舉行傳統「拋舟儀式」，張馬群也在現場吟唱蘭嶼傳統古調。

「齊柏林空間」自第二檔展覽開始，基金會將邀請各界人士呼應齊柏林作品主題進行一系列對談。

其中，包括財團法人中央通訊社董事長劉克襄以詩對話、社團法人台灣海洋環境教育推廣協會秘書長郭兆偉以步行對話、RE-THINK 創辦人黃之揚以海廢對話及公視節目「我們的島」以環境對話。

齊柏林小行星守護台灣　逐岸特展高空視角看寶島

2020/08/10　中央廣播電臺

「看見˙齊柏林基金會」今天(7 日)起在淡水藝術工坊舉辦「逐岸」特展，展覽內容是從數千小時齊柏林影像檔案中，精選出台灣海岸線的珍貴紀錄。在開幕典禮上，國立中央大學也將「齊柏林小行星」的命名證書，頒贈給齊柏林的兒子齊廷洹，期盼眾人永遠記得他的精神與對台灣環境的關懷。

「逐岸」特展在新北淡水藝術工坊的「齊柏林空間」展出，讓已故紀錄片導演齊柏林再次帶領國人，以廣闊、客觀的高空視角，用心看見台灣海岸的故事與真相，並同時看到北部岬灣、東部斷層、南部珊瑚礁及西部平坦沙質等不同海岸之美。

「看見˙齊柏林基金會」執行長萬冠麗表示，為了讓觀展者身歷其境，這次特別透過超大螢幕的設計，讓民眾一進展場，就能感受被天空環繞的感覺。萬冠麗：『(原音)挑高 2 米 9、寬有 515 公分的一個大畫面，因為它是完整的一個畫面，所以你站在的那個角度，就是齊柏林拍攝的角度，你就可以從那邊看到空中的齊柏林曾經看到的影像，所以你就會感受到那個移動之美。』

為了感念齊柏林對台灣的貢獻，中央大學將鹿林天文台所發現的編號 281068 小行星，命名為「齊柏林」(Chipolin)，中央大學校長周景揚特別在特展開幕典禮上，將命名證書頒給齊柏林的兒子齊廷洹。周景揚：『(原音)在這個場合，也讓我們向世界宣布，我們的「齊柏林」小行星已經經過國際天文學聯合會的命名的通過，正式就在我們宇宙中，永遠在那邊看護著我們台灣。』

齊廷洹笑著說，相信爸爸會很高興。齊廷洹：『(原音)大家沒有忘記他，就看到今天還這麼多人願意前來，大家還記得他，他以前結的這些善緣都還在繼續發揚下去，所以希望他能夠站在更高的角度，繼續默默的推動。』

齊廷洹認為，小行星比人的生命更長遠，能有個接近永恆的東西來紀念爸爸，好像抬頭看就能看到爸爸一樣，對他來說很感動。

讓世界「看見台灣」永恆的飛船─齊柏林小行星

2020/08/10 臺灣時報

「齊柏林飛船」，是人類對飛行夢想的初探，為感念空拍導演齊柏林先生對台灣的卓越貢獻，中央大學特將鹿林天文台所發現的編號 281068 號小行星，經國際天文學聯合會（IAU）通過，命名為「齊柏林 (Chipolin)」小行星，象徵一艘永恆的飛船，深情地望著台灣，守護著台灣。

8 月 7 日在齊柏林空間舉辦的《逐岸》開展記者會中，特舉辦齊柏林小行星頒贈儀式，由中央大學校長周景揚頒贈小行星銘版給齊柏林導演之子齊廷洹先生，感念齊柏林導演一生關注台灣土地發展的堅持與勇氣，希望大家記得齊柏林的精神及對台灣環境的關懷。

中央大學校長周景揚表示，美麗的福爾摩沙台灣，你我的共同家園，透過齊柏林導演的空拍視角，可以跨越種族和文化的藩籬，撼動人心。中央大學希望將他的精神化為永恆，如同星光般燦爛，普照大地。

周景揚校長指出，齊柏林導演除讓人看見台灣之美外，同時也喚醒我們更疼惜自己生長的土地。中央大學以地球科學起家，長期致力於環境永續之研究。從地球、海洋、大氣、水文，乃至太空、天文，以科學的專業全方位守護著台灣和地球，為人類永續生存的明天而努力，無疑將他的精神作了永續的傳揚！

齊柏林小行星，2006 年 7 月 18 日由鹿林天文台林宏欽台長及美國馬里蘭大學葉泉志博士共同發現，2017 年 11 月 4 日正式通過命名。大小約為 4.9 公里，發現時位在魔羯座，目前已運行到獅子座。繞行太陽一圈 5.6 年（軌道週期），離太陽最近時（近日點）為 4.3 億公里，最遠時（遠日點）為 5.1 億公里。

中央大學從 2006 年開始的鹿林巡天計畫，不但曾發現台灣史上的第一顆彗星，同時也發現了 800 多顆小行星，使台灣成為亞洲發現小行星最活躍的地方之一。卓越的天文研究成果，充份展現台灣人「以小搏大」的精神，也讓世界真正「看見台灣」！

讓世界「看見台灣」　永恆的飛船─齊柏林小行星

2020/08/10 蕃新聞

「齊柏林飛船」，是人類對飛行夢想的初探，為感念空拍導演齊柏林先生對台灣的卓越貢獻，中央大學特將鹿林天文台所發現的編號 281068 號小行星，經國際天文學聯合會（IAU）通過，命名為「齊柏林 (Chipolin)」小行星，象徵一艘永恆的飛船，深情地望著台灣，守護著台灣。

8 月 7 日在齊柏林空間舉辦的《逐岸》開展記者會中，特舉辦齊柏林小行星頒贈儀式，由中央大學校長周景揚頒贈小行星銘版給齊柏林導演之子齊廷洹先生，感念齊柏林導演一生關注台灣土地發展的堅持與勇氣，希望大家記得齊柏林的精神及對台灣環境的關懷。

中央大學校長周景揚表示，美麗的福爾摩沙台灣，你我的共同家園，透過齊柏林導演的空拍視角，可以跨越種族和文化的藩籬，撼動人心。中央大學希望將他的精神化為永恆，如同星光般燦爛，普照大地。

周景揚校長指出，齊柏林導演除讓人看見台灣之美外，同時也喚醒我們更疼惜自己生長的土地。中央大學以地球科學起家，長期致力於環境永續之研究。從地球、海洋、大氣、水文，乃至太空、天文，以科學的專業全方位守護著台灣和地球，為人類永續生存的明天而努力，無疑將他的精神作了永續的傳揚！

齊柏林小行星，2006 年 7 月 18 日由鹿林天文台林宏欽台長及美國馬里蘭大學葉泉志博士共同發現，2017 年 11 月 4 日正式通過命名。大小約為 4.9 公里，發現時位在魔羯座，目前已運行到獅子座。繞行太陽一圈 5.6 年（軌道週期），離太陽最近時（近日點）為 4.3 億公里，最遠時（遠日點）為 5.1 億公里。

中央大學從 2006 年開始的鹿林巡天計畫，不但曾發現台灣史上的第一顆彗星，同時也發現了 800 多顆小行星，使台灣成為亞洲發現小行星最活躍的地方之一。卓越的天文研究成果，充份展現台灣人「以小搏大」的精神，也讓世界真正「看見台灣」！

齊柏林小行星　讓世界「看見臺灣」

2020/08/10 新浪新聞

「齊柏林飛船」，是人類對飛行夢想的初探，為感念空拍導演齊柏林先生對台灣的卓越貢獻，中央大學特將鹿林天文台所發現的編號 281068 號小行星，經國際天文學聯合會（IAU）通過，命名為「齊柏林 (Chipolin)」小行星，象徵一艘永恆的飛船，深情地望著臺灣，守護著臺灣。

8 月 7 號在齊柏林空間舉辦的《逐岸》開展記者會中，特舉辦齊柏林小行星頒贈儀式，由中央大學校長周景揚頒贈小行星銘版給齊柏林導演之子齊廷洹先生，感念齊柏林導演一生關注台灣土地發展的堅持與勇氣，希望大家記得齊柏林的精神及對台灣環境的關懷。

中央大學校長周景揚表示，美麗的福爾摩沙臺灣，你我的共同家園，透過齊柏

林導演的空拍視角，可以跨越種族和文化的藩籬，撼動人心。中央大學希望將他的精神化為永恆，如同星光般燦爛，普照大地。

周景揚校長指出，齊柏林導演除讓人看見台灣之美外，同時也喚醒我們更疼惜自己生長的土地。中央大學以地球科學起家，長期致力於環境永續之研究。從地球、海洋、大氣、水文，乃至太空、天文，以科學的專業全方位守護著台灣和地球，為人類永續生存的明天而努力，無疑將他的精神作了永續的傳揚！

齊柏林小行星，2006 年 7 月 18 日由鹿林天文台林宏欽台長及美國馬里蘭大學葉泉志博士共同發現，2017 年 11 月 4 日正式通過命名。大小約為 4.9 公里，發現時位在魔羯座，目前已運行到獅子座。繞行太陽一圈 5.6 年（軌道週期），離太陽最近時（近日點）為 4.3 億公里，最遠時（遠日點）為 5.1 億公里。

中央大學從 2006 年開始的鹿林巡天計畫，不但曾發現台灣史上的第一顆彗星，同時也發現了 800 多顆小行星，使台灣成為亞洲發現小行星最活躍的地方之一。卓越的天文研究成果，充份展現臺灣人「以小搏大」的精神，也讓世界真正「看見臺灣」！

小行星命名「台北天文館」　距離地球約 5 億 3000 萬公里

2020/07/20 ETtoday 新聞雲

為了表彰台灣成立最早、規模最大的天文專業博物館，在天文教育及推廣上的貢獻，國際天文學聯合會（IAU）正式通過，將編號 300300 號小行星命名為「台灣天文館」。

這顆小行星是由國立中央大學天文研究所林宏欽與美國加州理工學院博士後研究員葉泉志，於 2007 年 8 月 6 日在中大天文所「鹿林天文臺巡天計畫」拍攝的影像中發現，經過長期觀測確認後，賦予永久編號第 300300 號。

根據天文館表示，由中央大學推薦，經審核通過後正式命名為 TAM，記為 (300300) TAM，即臺北天文館（Taipei Astronomical Museum）的英文縮寫。

「台北天文館」小行星為一顆位於主小行星帶內的天體，軌道半長軸約 2.446 天文單位，相當於 3 億 6600 萬公里，以 3.83 年的週期繞太陽公轉，直徑約 1.4 公里，目前在巨蟹座方向，距離地球約 5 億 3000 萬公里處，亮度僅 22 等，必須以大型天文望遠鏡才能拍到。

表彰博物館成立　小行星命名「台北天文館」

2020/07/17 東網

台灣台北市天文館周三（15 日）指出，國際天文學聯合會（IAU）日前正式通過，將編號 300300 號小行星命名為「台北天文館」，表彰台灣成立最早、規模最大的天文專業博物館，以及在天文教育及推廣上的貢獻。

天文館指出，由台灣的國立中央大學推薦，並經過審核後，該小行星正式命名為 TAM，即台北天文館的英文縮寫「Taipei Astronomical Museum」。小行星發現者同樣是國立中央大學天文研究所的鹿林天文台台長林宏欽，以及與美國加州理工學院博士研究員葉泉志；2 人在 2007 年 8 月 6 日在鹿林天文台巡天計劃中拍攝的影像中發現，經長期觀測及確認，給予永久編號第 300300 號。

該小行星位於主小行星帶內的小天體，軌道半長軸約 2.446 天文單位，相當於 3 億 6600 萬公里，以 3.83 年的周期繞太陽公轉，直徑約 1.4 公里；目前在巨蟹座方向，距離地球約 5 億 3000 萬公里處，亮度僅 22 等，須以大型天文望遠鏡才能見到其身影。

13 年前發現小行星　以「台北天文館」為名

2020/07/16 udn 聯合新聞網

國際天文學聯合會（IAU）通過，將編號 300300 號小行星命名為「台北天文館」，這顆小行星由現任鹿林天文館台長林宏欽與葉泉志發現，長時間確認行星軌道後，賦予永久編號，經由中央大學向 IAU 推薦，正式命名為 TAM，即台北市立天文館（Taipei Astronomical Museum）的英文縮寫，表彰台灣成立最早、規模最大的天文專業博物館在天文教育及推廣上的貢獻。

過去許多行星，常以人名、地名命名，比如陳樹菊、雲門，甚至還有林書豪，都是小行星的名稱。天文館表示，這些名稱都是由發現者向 IAU 提出申請，經審核確認無重複名稱，才能通過命名。

去年 IAU 通過「科博館」與「孫維新」，與這次的「台北天文館」同樣是由林宏欽與葉泉志發現，天文館表示，這顆小行星是他們在 2007 年，於中央大學大天文所鹿林天文台巡天計畫（LUSS）拍攝的影像中發現，經過長期觀測確認後，賦予永久編號第 300300 號，再由中央大學推薦，經審核通過後正式命名。

天文館表示，「台北天文館」是一顆位於主小行星帶內的小天體，軌道半長軸約 2.446 天文單位，相當於 3 億 6 千 6 百萬公里，以 3.83 年的周期繞太陽公轉，其直徑約 1.4 公里。目前在巨蟹座方向距離地球約 5 億 3 千萬公里處，亮度僅約 22 等，必須以大型天文望遠鏡才能拍攝到它。

天文館也說，300300 號小行星屬於王后星族（Massalia family）中 6000 多個成員之一，估計是約 1.5 至 2 億年前因王后星（20 Massalia）的前身遭撞擊後形成，最大成員是直徑約 150 公里的王后星，屬矽質的 S 型小行星。

天文館表示，中央大學與台北天文館將於 7 月 18 日 13 時 30 分在台北天文館演講廳舉辦命名授贈儀式，並由發現人林宏欽進行專題演講，重現 13 年前發現這顆小行星的過程，現場也將舉辦解說導覽，民眾於 7 月 18 日至 8 月 16 日間皆可持優待票進入展示場參觀這顆以館為名的小行星。

土星衝、木星衝　7 月中旬最接近地球

2020/07/14 yahoo 奇摩新聞

天文迷最近很忙，除了八月的英仙座流星雨值得期待外，中央大學天文所博士後研究員林忠義提到 7 月 14 日與 7 月 21 日，可先觀測 1 年出現 1 次的木星衝與土星衝，只要所看的位置不要有過高建築或其他物體遮擋，還有光害不嚴重，用肉眼就可以看到。（李明朝報導）

喜愛觀賞天文的天文迷，8 月份的英仙座流星雨絕對不能錯過，因為從歷年來英仙座流星雨觀察，出現火流星數量比其它流星雨數目還多，平均亮度也比較亮，推測與流星母彗星的大小有關，英仙座流星雨的母彗星為編號 109 號週期彗星ㄧ史威福-塔托彗星有關，它的直徑約為 26 公里，繞太陽公轉一周約 133 年，前一次最接近太陽時間是在 1992 年。

至於 7 月間也有其它比較特別的天文景象，如 7 月 14 日木星衝、7 月 21 日的土星衝，中大天文所博士後研究員林忠義表示，7 月 14 木星衝約每 399 天出現一次，觀測時木星在人馬座,亮度約負 2.8 等,至於 7 月 21 日土星衝現象約每 378 天出現一次, 今年衝時亮度約 0.1 星等，觀測時土星位置從摩羯座到人馬座，由於外行星[衝]時是是太陽、地球，土星或木星成一直線，也是外行星最接近地球與觀測外行星的最理想時間，但也不是這段期間才能看到木星與土星，到年底前都可以觀測到，只是觀測時間不再整晚皆可觀測，而是傍晚日落後，而且位置越來越偏西，亮度越來越暗，因此在[衝]時藉由望遠鏡觀測將會欣賞到視直徑最大的木星與土星，其著名的木星大紅班與土星環也相對較為顯著。

想看木星衝、土星衝的天文迷，在當天往南方尋找，同時只要當地沒有過高建築或其他物體遮擋，有機會可以看到。

肉眼可見期間限定！新彗星出沒北半球　縮時記錄超美時刻

2020/07/13 yahoo 奇摩新聞

國外天文望遠鏡日前發現尼歐懷茲彗星（NEOWISE Comet, 天文編號 C ／ 2020 F3)，北半球均有機會看見。因尼歐懷茲彗星在北半球肉眼即可觀測，引起許多天文迷熱議追蹤，預估將會是繼上個月的日環食之後，再次掀起一波天文觀星熱。中央氣象局表示：彗星將在 2020 年 7 月 23 日最接近地球，肉眼即可觀測。國外已有不少天文迷拍到它的身影，並用縮時攝影紀錄下這一刻。

中央大學天文所博士研究員林忠義表示這次是繼海爾波普與百武彗星之後，北半球難得能有如此明亮的彗星。在 7 月中旬之前，觀賞時間是在日出前，只要朝著東北東方的御夫座方向尋找，若是等到 7 月下旬，則要日落後，往西北西方的大熊星座尋找，此時彗星可觀測時間越來越長，但亮度將越來越暗。而氣象局指出，「彗星」是太陽系形成之初遺留下來的小天體，會環繞太陽運行，當彗星接近太陽時，太陽的光和熱會使彗星表面的揮發物質蒸發，形成彗髮與彗尾；「流星」則是太空中的小石塊或塵埃，因地球重力吸引而往地面落下的過程，與地球大氣發生碰撞摩擦產生的燃燒現象。

新彗星 C/2020　F3　NEOWISE 來了　一般望遠鏡就看得見

2020/07/09 經濟日報

國外天文學家用太空望眼鏡發現一新彗星，編號為 C/2020 F3 （NEOWISE），北半球包括台灣用一般望遠鏡就都可以觀賞，有高倍鏡頭更佳，預估繼上個月日環食之後，這次追星有機會再掀起另一波天文熱。

中央大學天文所博士後研究員林忠義也在追蹤，他說要觀看這顆彗星，7 月中旬以前最好的時段為日出前，朝東北東，中旬以後就要等日落後朝西北西方，除了望遠鏡，運氣好在光害低的地方肉眼也有可能看見彗星。

不僅國外已經觀測到 C/2020 F3 （NEOWISE）彗星，台灣目前也有業餘天文學家像台灣親子觀星會拍到，中央大學鹿林山天文台因為玉山山脈擋住視角，目前觀測角度不好，不過還是有拍到彗星行蹤。林忠義說，觀察這彗星的最佳時間為七月下旬，是北半球經過海爾波普、百武彗星之後，再一次出現難得亮度和距離用肉眼可以看見的彗星。

林忠義接受媒體訪問時表示，現在（7 月中旬）要觀賞 C/2020 F3 NEOWISE 彗星是日出前，朝東北東方向的御夫座尋找，可以明顯看見托著「尾巴」的彗星；到 7 月下旬要等日落後往西北西方大熊星座尋找，這時候可以觀測彗星的時間會一天比一天長，但是亮度越來越暗。

林忠義說明，過去許多彗星被發現的時候，雖然預測肉眼可見，但是這些彗星經過太陽前後時分裂或亮度低於預期而看不見，C/2020 F3 NEOWISE 在北半球肉眼看得見，因此引起天文迷熱情追蹤和討論。

台灣親子觀星會理事長江英瑞說，他這幾天在高雄市鳳山區鳳鼎路，用一般雙孔望遠鏡就可以很清楚看見彗星，最好的時間為凌晨 4 點至 4 點半，往東北方約 10 點半位置，只要還平面 10 度以上沒建築物或雲層阻礙都看得見，不過如果碰上曙光或其他光源干擾，可能沒辦法用肉眼直接看見彗星。

江英瑞表示，這是一顆新的彗星，當初是美國太空總署衛星太空望遠鏡拍到畫面，公布以後全世界天文迷開始追蹤，台灣很幸運在 7 月用一般望遠鏡就可以找到這顆彗星，其實就像林忠義研究員說的，每年都有彗星，但是能用一般望遠鏡觀賞的不多，台灣過去較有名的是觀賞「海爾波普」彗星，這次媒體採用 C/2020 F3 NEOWISE 照片，是台灣親子觀星會會員在新竹寶二水庫拍的畫面，另一個觀星社團還有人 PO 縮時攝影和會員分享。

天空新發現彗星　不需天文望眼鏡即可見

2020/07/09　中廣新聞網

國外用太空望眼鏡發現一顆 C/2020 F3 (NEOWISE) 彗星，只要是北半球都可以觀賞，中央大學天文所博士後研究員林忠義表示，這顆彗星 7 月中旬之前在日出前朝著東北東方，七月下旬在日落後，朝著西北西方向，都可用肉眼看見。

中央大學天文所博士後研究員林忠義表示，有關這顆彗星，不僅國外已經觀測到，台灣目前也有業餘天文學家拍到，然而中大鹿林天文台受限位置有玉山山脈阻擋，所以一時之間還難以觀測到。

至於觀察這個彗星的最佳時間為七月下旬，林忠義表示，繼海爾波普與百武彗星之後，北半球難得有這麼明亮的彗星，這次想看這顆彗星，在 7 月中旬之前，觀賞時間是在日出前，只要朝著東北東方的御夫座方向尋找; ;若是等到七月下旬，則需等到日落後往西北西方大熊星座尋找，此時彗星可觀測時間越來越長，但亮度將越來越暗。

林忠義表示，以往曾有許多預測肉眼可見的彗星，但這些彗星在經過太陽之前或之後發生分裂或亮度不如預期，所以這顆彗星的發現，也引起國內外熱烈的討論。

台灣親子觀星會表示，目前已有會員陸續拍到這顆彗星並且分享。

8 月英仙座流星雨　仰望天空就可能找到

2020/07/07 yahoo 奇摩新聞

日環食結束之後，天文迷可以接著期待 8 月間的英仙座流星雨，中央大學天文所博士後研究員林忠義表示，今年英仙座流星雨極大期將在 8 月 12、13 日兩天達到最高峰，預估每小時可能達到 100 顆左右;此外，根據往年觀測資料發現英仙座流星雨也是一年當中出現火流星數量最多的一群流星雨，一般肉眼可見火流星，但當天能否見到數目如此多的流星，就要看觀測地點有沒有受到視野被遮蔽與光害的影響。（李明朝報導）

每年三大流星雨分別是象限儀座流星雨、英仙座流星雨，以及雙子座流星雨，天文所林忠義表示，英仙座流星雨從歷年的觀察， 出現火流星數量比其它流星雨數目還多，平均亮度也比較亮，推測與流星母彗星的大小有關，英仙座流星雨的母彗星為編號 109 號週期彗星—史威福-塔托彗星有關，它的直徑約為 26 公里，繞太陽公轉一周約 133 年，前一次最接近太陽時間是在 1992 年。

英仙座流星雨今年預估在 8 月 12、13 日兩天流星數最多，觀測時間建議選在上半夜，林忠義表示，觀測流星雨不需要望遠鏡等特殊器材，也不限於特定景點，只要挑選視野開闊，光害較少的地方以肉眼欣賞即可，若觀測條件好，屆時每小時可能會有 100 顆的流星雨從夜空劃過。

觀測流星雨的主要目的？林忠義表示，由台灣流星觀測網所觀測到流星雨的軌跡可重組流星體的軌道並從資料庫找尋相對應的天體，從光譜分析可知流星群的成份比例，藉此可以與已知母體的成分做比較，除此之外，還可以探索未知的流星雨群。

中大天文團隊發現星團瓦解的證據中

2020/07/03　中廣新聞網

中央大學天文研究所陳文屏教授的研究團隊，觀察鄰近太陽的星團，包括后髮座星團以及 Blanco 1　星團，首度發現潮汐尾結構，表示這些星團正在瓦解。

恆星在太空中群聚誕生，然後逐漸瓦解。年輕的星球常聚集成星團，而像太陽這樣中年的恆星，當年跟它一起形成的星球現在已經四處分散，無法指認。

陳文屏教授研究團隊，發現有星團出現瓦解現象，陳文屏教授說，他與合作學者利用蓋婭太空望遠鏡精確測量恆星的距離與運動數據，研究距離只有 300 光

年，年齡約 8 億年的后髮座星團，陳文屏教授表示，首度發現這個離我們第二近的星團由於受到外部力量干擾，成員星多半已經被拉扯，形成潮汐尾結構。而另外一個距離 750 光年，年齡只有 1 億年的 Blanco 1 星團，則剛開始展現瓦解的現象。

中大團隊的下一步，是研究位於銀河系不同位置，年齡各異，更多的星團樣本，探討星團瓦解的詳細過程。

中大團隊表示取得更靈敏的數據，分析不同質量的成員星從星團中逃脫的差異。

【日食千萬不可直視】也不能戴太陽眼鏡、底片觀測　都會傷害視網膜

2020/06/22 上報

天文盛事日環食將於 21 日下午登場，在嘉義、台東、金門澎湖等地可觀測到日環食、台灣其他地區則可見大規模日偏食。專家提醒，在觀測日食時，千萬不可直視太陽，也不可以使用太陽眼鏡、底片觀測，必須使用專用的太陽濾鏡，以免對眼睛造成永久傷害。

嘉義市天文協會理事長莊明娟表示，觀測日環食除透過適當遮減光器材、專業濾光設備；另外，使用手機、相機拍攝日環食時，也必須透過減光鏡、濾光鏡，否則容易過曝，或造成感光元件受損。

中央大學天文所專任助理張永欣提醒，要觀測日食，最重要的就是保護自己的眼睛。過去民間流傳，用 2 層曝光底片就可以觀測日食，然而這是錯誤資訊，太陽的紅外線可以穿透底片，眼睛一樣會受傷。另外，也不可以用天文望遠鏡直視太陽。

他建議民眾應該到望遠鏡專賣店購買有減光措施的工具，如日食觀測眼鏡或攝影用高濃度減光鏡，或者也可以到五金行購買「電焊保護鏡」，如此才能安心觀賞日食。

眼科醫師指出，在沒有保護下，肉眼只要直視太陽短短幾分鐘，眼睛內的黃斑部視網膜就可能被陽光紫外線燒灼受傷，造成永久性的視力減損，嚴重可能失明。

醫師也提醒，正在點散瞳劑矯正近視的學童，尤其是長效型的藥物，如果前 1 周沒有先停藥，瞳孔用藥後會持續放鬆，無法適時收縮自我保護，也不適合參加觀看日食教學活動，家長要特別注意。

想看完整日環食又不想出門？中央大學推薦 5 直播網站

2020/06/22 udn 聯合新聞網

中央氣象局天文站預報台灣今天下午可以看見日環食，下一次再出現的時間是 195 年以後，不少人都不想錯過這次天文奇景。

台灣中南部、東部合計 10 縣市看得到完整的日環食，北部雖然只能看見偏食，不過中央大學為大家整理出 5 個直播網站，不想出門的人一樣不會錯過兩世紀難得的機會，中大呼籲記得不要用眼睛直視陽光。

5 個直播網可以在 YouTube 輸入以下關鍵字：全國大學天文聯盟、2020 夏至日環食全國網路聯播（中央氣象局與澎湖吉貝國小合作）、台北市立天文科學教育館、日環食直播金門金城國中天文台、2020 台灣日環食 In 嘉義縣新港鄉咬仔竹。

氣象局預估最早看見日環食「初虧」地點在金門，今天下午 2 點 44 分 4 秒，金門「初虧」揭開序幕，5 點 26 分 43 秒台東「復圓」，環食帶地區都可以看見完整的環食過程，其他地區只能看見偏食。

在環食帶 10 個縣市為金門、澎湖、花蓮、台東、高雄、台南、嘉義縣市、雲林、南投，完整環食時間由西向東為金門下午 4 點 10 分開始，到台東成功下午約 4 點 16 止。

錯過等 195 年！天文奇景日環食下午登場　全台直播免出門

2020/06/22 yahoo 奇摩新聞

錯過再等 195 年！今天（21 日）是夏至，台灣下午有難得一見的日環食可觀賞，在 10 個縣市可見，其他地區則可見日偏食。許多民眾早早出門卡位觀賞天文奇景，不過懶得出門的民眾在家也可透過 5 個直播頻道觀看。

今天下午 2 點 44 分 4 秒，日環食「初虧」在金門揭開序幕，最後結束於下午 5 點 26 分 43 秒台東的日面「復圓」。氣象局表示，本次日環食將會出現在金門縣、澎湖縣北側、雲林縣南部、嘉義縣、嘉義市、台南市北側、高雄市北側、南投縣南側、花蓮縣南側及台東縣北側共 10 個縣市。

環食帶地區可見環食的時間由西而東，約為金門的下午 4 點 10 分至台東成功的下午 4 點 16 分左右，環食帶中心至邊緣地區各可見約 1～58 秒不等的環食景象。

氣象局提醒，日環食觀測及攝影須注意安全，相機或望遠鏡未加減光鏡看日環食，會造成眼睛燒傷，導致視力永久受損，一定要加裝適當的濾光裝置。

中央大學在臉書分享 5 個直播網站，讓民眾不用出門也能觀賞天文奇景，也提醒大家不要用眼睛直視陽光。

日環食 6 月 21 日登場　專家：別用兩層底片看太陽

2020/06/18 udn 聯合新聞網

天文奇觀日環食將於 6 月 21 日登場，一旦錯過就要再等 195 年，直到 2215 年 6 月 21 日才看得到，讓不少民眾蓄勢待發，準備觀測天文奇觀。中央大學天文所專任助理張永欣提醒，觀測時應配戴有減光措施的觀測眼鏡及減光鏡，或到五金行尋找「電焊保護鏡」，千萬不能用肉眼直視，否則將對眼睛造成嚴重傷害。

張永欣表示，該次日環食從非洲內陸至西太平洋，能觀測到日環食的環食帶僅寬約 47 公里，最特別的是台灣也位於其中，由西向東通過金門、澎湖北方、雲林、嘉義、高雄、南投、花蓮、台東等局部鄉鎮，尤其雲林水林鄉更是第一個可觀賞到日環食「初虧」的地點。

無論天文奇觀多麼特別，最重要的是保護自己的眼睛，張永欣指出，不少民眾和網路皆流傳，透過 2 層曝光底片能觀測日食，他直呼這是錯誤觀念，太陽的紅外線能穿透底片，眼睛一樣會受熱受傷，另外望遠鏡也被禁止觀測太陽。他說，望遠鏡集光力強，一瞬間會使鏡片燃燒，甚至傷害眼睛，天文望眼鏡上都會註明「禁止觀測太陽」，連天文台望眼鏡的自動導引程式，只要靠近太陽便會跳出警告。

該如何觀測日食？張永欣表示，望遠鏡專賣店有販賣安全減光措施工具，如合乎安規的日食觀測眼鏡或攝影用高濃度減光鏡，減光程度需達到數萬至十萬倍，才能安全又舒適的觀看日食；另還有替代方案，可至五金行購買「電焊保護鏡」，號數選擇 12 至 14 號，其中以 14 號最合適，他說，配戴 14 號觀看日光燈會完全呈現黑暗，最能保護眼睛。

張永欣說，觀看日食初虧時間約莫在當天下午 2 點 49 分左右開始，結束時間是 5 點 27 分左右，各地時間有些微差異，桃園市（市政府）則於下午 2 點 49 分 36 秒初虧（太陽仰角 51 度，方位 277 度），下午 4 點 13 分 22 秒食甚（太陽仰角 32 度，方位 283 度），下午 5 點 24 分 28 秒復圓（太陽仰角 16 度，方位 289 度），提醒民眾觀測前需做好防護措施。

日環食 6/21 出現　觀看切記保護眼鏡

2020/06/16 yahoo 奇摩新聞

日環食即將在 6 月 21 日出現，環食帶僅寬約 47 公里，環食帶內可以觀賞到壯觀的日環食，但環食帶以外地區就僅能看見日偏食，不過中央大學天文所助理張永欣提醒，太陽的光線強烈，觀測日食一定要做好保護眼睛，在沒有安全的減光措施下，絕對不能肉眼直視太陽，更不能使用望遠鏡做為觀看工具，強大的能量會瞬間造成眼睛永久的傷害。（李明朝報導）

難得一見的日環食會在 6 月 21 日出現，一旦錯過可能要再等 2215 年 6 月 21 日，根據台北市天文館表示，本次日環食從非洲內陸至西太平洋，整個亞洲幾乎都在可見食的範圍，臺灣位於環食帶上，由西向東通過金門、澎湖北方、雲林、嘉義、高雄、南投、花蓮、台東等幾縣的局部鄉鎮，全臺食分皆超過 0.92（月面掩入日面的視直徑比），下一次發生環食帶大範圍覆蓋臺灣的日環食，可要等到將近 200 年之後的 2215 年。

在觀看日環食的安全減光措施不可少，張永欣表示，安全的減光措施，指的是經過第三方認證，合乎安規的日食觀測眼鏡或是攝影用高濃度減光鏡，減光程度必須達到數萬至十萬倍，才能安全舒適的觀看日食；以肉眼觀測時，還要考慮到減光材質對於紅外線及紫外線穿透律的等級，例如攝影用的 ND2～ND400 濾鏡以及塑膠類染色的軟碟片、光碟片等等，即使可見光的減光濃度達到安全範圍，但是仍然無法阻擋紅外線，會讓眼睛受傷，所以僅能用於攝影；紅外線及紫外線皆為肉眼無法辨識的光譜段，必須由儀器來測定，所以第三方的認證很重要，不要輕易相信廠商的數據。適用於肉眼觀測太陽的減光鏡，是鍍金屬膜材質的，比較普遍的巴德膜（baader planetarium Astro-Solar Film/ Solar Film）及 Thousand Oaks Optical 鍍鎳鉻濾鏡，都是屬於這一類的，由於是金屬膜，所以使用前切記要檢查是否有氧化腐蝕的針孔亮點，使用含金屬的銀漆筆將腐蝕孔塗掉封閉，才能安全使用。

觀看日食初虧時間約莫在當天下午 2 點 49 分左右開始，結束時間是 5 點 27 分左右，各地時間都會有些微差異，張永欣表示，桃園市（市政府）則是在下午 2 點 49 分 36 秒初虧（太陽仰角 51 度，方位 277 度），下午 4 點 13 分 22 秒食

甚（太陽仰角 32 度，方位 283 度），下午 5 點 24 分 28 秒復圓（太陽仰角 16 度，方位 289 度），最大食分是 0.942，所以只要頭頂到西方偏北 20 度（方位 290 度）開闊，看得到太陽的地方都適合觀測。

嘉義市迎接 6 月 21 日環食！64 架無人機飛上空

2020/06/15 udn 聯合新聞網

眾所期待的日月地三星連線「日環食」天文奇景即將在 6 月 21 日登場，嘉義市府指出，位於環食帶上的嘉義市，是最棒的觀賞地點，為了迎接日環食，在 20 日北香湖公園安排「無人機飛舞秀」，以 64 架無人機飛上天空，排出 621 嘉義日環食等圖像，每次 8 分鐘的 2 場演出為日環食拉開序幕。

市府教育處表示，在北香湖公園湖面上空，將有 64 架無人機飛上夜空，逐一變化出 2020、0621、愛心、Taiwan、Chiayi、噴水圓環吳明捷投球、日環食與虎尾科大等 8 個圖案。

無人機將在北香湖湖面的上空，優雅的展演兩次，每一次 8 分鐘、每次變化 8 個圖案，來展現嘉義市之美。展演的表演時間是 20 日晚間 6 點 50 分和 9 點 05 分，也是嘉義市首次夜空無人機秀，大家千萬不可錯過。

本次的無人機展演，高度將在 20 到 120 公尺，運用排列與不同的顏色，呈現出 2D 影像效果，例如「愛心」圖案就會從最內圈閃耀到外圈，仰望天空就像是愛心在天空閃爍。

也會利用顏色排列出日環食「月亮接近太陽」過程，一如日環食是天空中最美麗的金戒指，20 日唯二兩場無人機展演，也將是嘉義市夜空中最美麗的星空點點。

市府教育處表示，無人機展演秀是「2020 嘉義日環食系列活動大師講座第一場」的開場與結尾，講座將由中央大學天文所博士李昫岱主講，以日環食與太陽系為主題，帶領大家一起來認識日食，讓民眾了解宇宙天文與日環食的點點滴滴。

迎接日環食　嘉義市 20 日晚無人機秀拉開序幕

2020/06/15　中央通訊社

嘉義市政府為了迎接 21 日將發生的日環食，20 日先在北香湖公園安排「無人機飛舞秀」，以 64 架無人機飛上天空，排出 621 嘉義日環食圖像，為日環食拉

開序幕。

嘉義市府教育處長林立生今天指出，無人機 20 日晚間僅展演 2 次，高度將在 20 到 120 公尺，運用排列與不同的顏色，呈現出 2D 影像效果，每一次 8 分鐘、變化 8 個圖案，來展現嘉義市之美。

64 架無人機飛上北香湖公園湖面上空，在夜間逐一變化出「2020、0621、愛心、Taiwan、Chiayi、噴水圓環吳明捷投球、日環食與虎尾科大」等 8 個圖案。

嘉義市府教育處表示，無人機展演秀是「2020 嘉義日環食系列活動大師講座第一場」的開場與結尾，講座將由中央大學天文所博士李昫岱以日環食與太陽系為主題，帶領大家一起來認識日食。

嘉義市府教育處歡迎民眾在 20 日晚間 6 時 30 分到北香湖公園聆聽大師講座，探索宇宙天文與日環食的點點滴滴，並欣賞夜空無人機秀。

星際訪客 Oumuamua 是不是外星飛船？科學家又來解謎

2020/04/20 科技新報

Oumuamua（音似台語「黑麻麻」），1I/2017 U1，是已知第一顆造訪太陽系的星際天體，於 2017 年 10 月 18 日被中央大學共同參與的「泛星 1 號」望遠鏡發現，因極端的雙曲線軌道而認證為源自太陽系外的天體。Oumuamua 詭異的長短軸比例（約 6：1）使外型就像一根雪茄，通過太陽後又出現預期外的加速度，當時引起部分科學家及媒體懷疑 Oumuamua 可能不是自然天體。

近年天文學家一直嘗試研究 Oumuamua 的形成機制，4 月 13 日發表在《自然：天文學》期刊的新研究提供了第一個完整理論。中國科學院國家天文台的張韻與美國加州大學聖克魯茲分校的林潮提出，Oumuamua 的形成可能與母恆星的潮汐作用有關。

研究團隊以超級電腦計算，當形成 Oumuamua 的原型天體接近母恆星時，會被巨大的潮汐力扯碎，如同「舒梅克–李維九號彗星」接近木星，被母恆星的高溫融化，拋離至遠處時再冷卻為長形碎片，形成極端的長短軸比例，甚至可高達 10：1。

這個過程也使大量高揮發物質耗散，符合 Oumuamua 沒有任何可見的彗星活動現象（如彗尾），不過昇華溫度較高的水冰能在表面下保存完好，當 Oumuamua 經過太陽附近時，揮發的水冰可能產生與觀測相符的加速度。

Oumuamua 國際研究團隊負責人 Matthew Knight 也表示這個研究相當傑出，模型完善，未來將透過更多像 Oumuamua 這樣的星際訪客驗證此理論的正確性。

合歡山暗空公園專業觀星　昆陽派出所將成最高天文台

中大新聞

2020/03/13 udn 聯合新聞網

合歡山國際暗空公園旅遊，打造專業觀星導覽更進一步，南投縣政府獲交通部觀光局補助 1500 萬元改善服務據點設施，南投縣長林明溱到昆陽會勘後，再與清境地區民間團體業者討論，敲定合歡山暗空公園將以昆陽與鳶峰兩處最佳觀星據點，也將結合天文學術團隊提供專業觀星導覽服務。

林明溱說，暗空公園五大觀星熱點昆陽、鳶峰、松雪樓、小風口及武嶺中，尤以鳶峰、昆陽設立旅遊服務及天文望遠鏡等專業觀星設施的條件最佳，經觀光處與清境永續環境發展協會及中央大學顧問團隊評估，確立鳶峰為普及性觀星據點而昆陽則提供專業國際級的觀星設備及導覽解說服務。

觀光局重視也肯定南投縣府合歡山國際暗空公園改善相關計畫，之前補助兩期 2500 萬元經費，主要針對鳶峰暗空公園旅服務中心，施設天文及觀星平台、休憩平台及攤商平台各一座，並增設改善既有公廁及無障礙、跨性別廁所，預計今年 8 月底完工。

而這次增加 1500 萬元補助，將進一步針對昆陽旅遊服務中心、鳶峰旅服務中心修繕、台 14 甲線路燈「暗空不暗地」減少光害及翠峰、鳶峰公廁修繕，預計 4 月完成規劃設計、明年 1 月前峻工。

合歡山是經國際認證的暗空公園，環境維持及旅遊服務充實改善十分重要，這三期工程的後續規劃，都將徵詢民間社團及學術團體，將改善的硬體能夠與新增的天文望遠鏡等專業觀光設備充分結合，包括屋頂如何拆除打造觀星窗等等，真正打造出吸引各層面觀星大眾前往的魅力與價值。

昆陽旅遊服務中心原為派出所，但舊建築仍無使用執照，將儘速由觀光處接手向林務局承租，並依法申請合法建照、使照，讓暗空公園的觀光發展全面推動，打造專業嶄新的觀星旅遊服務，讓南投縣的觀光更多元豐富。

合歡山暗空公園　鳶峰、昆陽最佳觀星據點

2020/03/11 中時電子報

籌備中的合歡山國際暗空公園，再獲交通部觀光局補助 1500 萬元，將用於旅遊服務、暗空環境營造；縣長林明溱 10 日到昆陽會勘，並決定以昆陽與鳶峰兩處最佳觀星據點，結合民間團體與天文學術團隊，做專業觀星導覽。

林明溱指出，暗空公園 5 大觀星熱點，包括昆陽、鳶峰、松雪樓、小風口及武嶺，其中以鳶峰、昆陽設立旅遊服務，及天文望遠鏡等專業觀星設施的條件最佳，經觀光處、清境永續環境發展協會及中央大學顧問團隊評估，將以鳶峰為普及性觀星據點，昆陽則提供專業國際級的觀星設備及導覽解說服務。

林明溱表示，交通部觀光局先前補助 2500 萬元經費，主要針對鳶峰旅遊服務中心施設天文及觀星平台、休憩平台及攤商平台，並增設改善既有公廁及無障礙、跨性別廁所，預計今年 8 月底完工；此次再增加 1500 萬元補助，將針對昆陽旅遊服務中心修繕、台 14 甲線路燈「暗空不暗地」減少光害，及翠峰、鳶峰公廁修繕，預計 4 月完成規畫設計、明年 1 月前竣工。

林明溱說，合歡山暗空公園後續規畫，將徵詢民間社團及學術團體，讓改善的硬體能夠與未來新增的天文望遠鏡等專業觀星設備充分結合，包括屋頂如何拆除打造觀星窗等。

另外，昆陽旅遊服務中心原為派出所，但屬舊建築未取得使用執照，將由觀光處向林務局承租，並依法申請合法建照及使用執照，未來提供嶄新的觀星旅遊服務。

中大、清大團隊　發現第一顆金星軌道內的小行星

2020/01/17 udn 聯合新聞網

中央大學天文所與清華大學天文所共組的「探高（TANGO）」團隊參與美國加州理工學院主導的「史維基瞬變設備」（Zwicky Transient Facility，簡稱為 ZTF），今年初發現了第一個位於金星軌道內的小行星—2020 AV2。此類小行星軌道非常特殊，須藉由行星的重力擾動才能從太陽系其他地方進入金星軌道內。

中央大學表示，史維基瞬變設備（ZTF）為加州理工學院主導的國際合作計畫，已於 2018 年 3 月開始科學觀測，該望遠鏡利用 47 平方度超廣視野相機進行各類的巡天計畫。透過前所未有的廣視野觀測，可捕捉到充滿動態的夜空。

太陽系的小行星主要位於主小行星帶(火星與木星之間)，極少數的小行星軌道位於地球軌道內，被稱為 Atira，而 2020 AV2 又被細分為 Vatira (運行軌道全在於

金星軌道內的小行星，V 代表金星)。

中央大學表示，Vatira 曾被預測，但由於其特殊軌道位置，因此非常不易被觀測（類似水星、金星只能在晨昏被觀測）。為了尋找地球特洛伊小行星與 Atira，ZTF 太陽系小天體團隊進行了多次暮光巡天觀測(Twilight survey)，發現了多顆地球軌道內的小行星，且陸續刷新了最短軌道周期紀錄。2020 AV2 的發現除了證明 Vatira 的存在，更進一步幫助天文學者了解太陽系小天體的模型。

在科技部補助下，中央大學天文所和清華大學天所合組的「探高」團隊是 ZTF 國際合作隊伍的一員。主要科學目標在於太陽系小物體、變星、超新星和重力波的光學對應體的追蹤觀察。暮光巡天是由馬里蘭大學的葉泉志博士與中央大學天文所葉永烜教授所建立的觀測計畫。

100 年前，人們眼中的宇宙還很小

2020/01/14 臺灣新浪網

我們可以想像得出 100 年後人類的生活嗎？那時的人類科學和科技進步到了何種程度？我們是否已經成了星際居民遨遊宇宙？而當 2120 年來臨時，那時的人們回望現在的我們，就好像我們回看 1920 年的歷史一樣。

1920 年不能算是尋常的一年。當時，第一次世界大戰剛剛以《凡爾賽條約》的簽署為標誌而結束，各國正在從戰爭中逐漸恢復。1920 年的科學界也並不平靜，這一年科學界發表了許多深刻改變人類的發現，科學界送走了一些科學家，也迎來了一些新生命，日後成長為科學研究中的關鍵人物。

現在，讓我們把時間撥回到 100 年前。。。。。。

1920 年，新年剛過不久，科學界傳來一個噩耗，丹麥著名數學家鄒騰去世。在這一年中，一些大師永遠地離開了我們，但他們的思想即使到今天仍在流傳。

丹麥數學家鄒騰

1920 年 1 月 6 日，丹麥數學家鄒騰去世

雖然鄒騰（H。 G。 Zeuthen）這個名字對大多數人而言還很陌生，但他

在丹麥乃至世界數學史上具有重要影響，他在圓錐曲線的枚舉幾何學、代數曲面理論以及數學史等領域都做出了傑出的貢獻。鄒騰從小在數學方便表現出了天賦，彷彿「不需要花時間去學」。進入大學后，他有機會前往巴黎師從法國幾何學泰鬥沙勒，並開始自己的枚舉幾何學研究。後來，他又出版了數學史著作《古代圓錐曲線的歷史》，同時代的著名數學家評價這本書「開啟了一個新的時代」。多年來，他在哥本哈根大學教學的同時編寫數學課本和講義，並在大學開設數學史等課程。他的整個職業生涯幾乎都在哥本哈根度過，他為丹麥登上世界數學的舞台做出了巨大貢獻。

印度數學家拉馬努金

1920 年 4 月 26 日，拉馬努金去世，享年 32 歲

拉馬努金（Srinivasa Ramanujan）是一位天才的傳奇數學家，他是英國皇家學會最年輕的會員之一，也是劍橋大學三一學院的第一位來自印度的院士。他出生在印度一個沒落的婆羅門家庭，幾乎沒有受過正規的高等數學教育和訓練，卻憑藉出眾的數學直覺和不懈的耐心鑽研，在數學分析、數論、無窮級數和連分數等領域作出了重大貢獻。1913 年，他開始與劍橋大學著名數學家哈代通信，哈代隨後邀請他到英國，開始了兩人富有成果的合作。拉馬努金一生提出了上千個公式和命題，併為後人的研究指明了方向。1973 年數學家德利涅證明了最著名的「拉馬努金猜想」，並因此獲得菲爾茲獎。

然而，科學不會停下向前的腳步。在這一年裡，人們通過實驗、觀測等當時一切可用的科技手段，在各個領域收穫了許多令人欣喜的發現，其中有一些深刻地改變了我們的生活。

提取胰島素

班廷提出一種提純胰島素的方法

胰島素的發現是現代醫學史的一個裡程碑。20 世紀初，一些醫生髮現胰腺中的提取物具有降糖作用。但由於無法製備高純度的製劑，相關研究一度陷入困境。1920 年，年輕的外科醫生班廷（Frederick Banting）向糖尿病領域的權威教授麥克萊德（John Macleod）提出了一種提純胰島素的方法。班廷建議通過結紮狗胰管，再對其進行分離和提取。胰島素的提純工作就是從那時開始的。

到 1921 年，班廷提取胰島素的來源從狗的胰腺轉向牛的胚胎，使得實驗發生了飛躍性的進展。1923 年，班廷和麥克萊德二人因在胰島素方面作出的貢獻而獲得諾貝爾生理學及醫學獎。

測量獵戶座 α

獵戶座 α 的光球角直徑首次被測量

1920 年，威爾遜天文台的邁克爾孫測星干涉儀首次測量出了獵戶座 α 的光球角直徑，獵戶座 α 成為除太陽之外第一顆被測出光球的角直徑的恆星。獵戶座 α 又名參宿四，距離地球超過 600 光年，它是一顆紅超巨星，也是已知的裸眼可見的最大和最亮的恆星之一。後續的研究報導它的角直徑約在 0.042 到 0.056 角秒之間。紅超巨星是恆星演化過程中「臨近終章」的階段，處於這個階段的恆星會出現忽明忽暗的現象。2019 年年底，獵戶座 α 亮度突然變暗，但尚不確定這種亮度變化是否與超新星爆發有關。科學家正在密切關注這顆恆星亮度的後續變化。

小艾伯特實驗

心理學家約翰·沃森和助手

進行了著名而極具爭議的「小艾伯特實驗」

1920 年，心理學家約翰·沃森和助手進行了著名而極具爭議的「小艾伯特實驗」。在實驗中，11 個月大的小艾伯特起初對在身邊活動的白鼠並未表現出恐懼。隨後，當艾伯特觸摸白鼠時，實驗人員就在他身後製造出巨大而刺耳的聲音，艾伯特隨即大哭並表現出恐懼。重複數次后，即使沒有雜訊，小艾伯特在面對白鼠，甚至其他毛茸茸的物品時，也表現出了恐懼和不安。由於錄像顯示小艾伯特有痴獃的跡象，實驗結果的可靠性被質疑。而在實驗完成後，沃森並未除去嬰兒的條件反射，這也違反了學術道德。曾有後續研究試圖調查實驗對嬰兒後來的影響，他們發現小艾伯特在 6 歲時因病夭折，實驗的後續影響也無從而知。

薩哈電離方程

天體物理學家薩哈提出了薩哈電離方程

薩哈電離方程描述的是恆星光譜與溫度之間的關係。這個方程最早由印度天體物理學家薩哈（Meghnad Saha）提出，它表示了在一顆恆星中，任何一種特定元素的電離狀態會如何隨著溫度和壓力的變化而變化。這個方程的一個重要應用是解釋了恆星的光譜分類。薩哈也因此分別在 1930、1937、1939、1940、1951、1955 年被提名為諾獎物理學獎候選人，然而他的提名卻一再被諾獎委員會拒絕，給出的原因是薩哈電離方程是一個有用的「應用」而非「發現」。但在天體物理學領域，學者認為薩哈方程打開了恆星天體物理學之門，是天文研究來說是諾獎級別的貢獻。

當然，我們還有很多沒有搞清楚的事情。當時的人們甚至還不清楚，銀河系是不是宇宙的全部，併為此進行了一場世紀辯論。科學家提出了很多假說和「預言」，但尚沒有能力驗證它們，有些假說甚至在半個多世紀后才通過更先進的技術手段被證實。科學就是在以這樣的方式不斷前進。

世紀大辯論

20 世紀最偉大的一場科學辯論

發生在 1920 年 4 月 26 日

20 世紀最偉大的一場科學辯論發生在 1920 年 4 月 26 日，當時，天文學家沙普利和柯蒂斯在華盛頓的史密森尼國家自然歷史博物館中為宇宙究竟有多大展開了辯論。沙普利主張銀河系就是整個宇宙，認為像仙女座星雲等螺旋星雲都是一些小的天體，是銀河系的一部分；而柯蒂斯認為，通過望遠鏡觀測到的那些螺旋狀星雲實際上是可以與銀河系相媲美的星系或島宇宙，他爭辯道仙女座星雲中的新星比銀河系中還要多。這場辯論的真正獲勝者直到 1924 年才得以揭曉：哈勃計算出仙女座星系中的一顆造父變星的距離，得出它不在銀河系內，最終證明柯蒂斯是對的。

中子的存在

盧瑟福首次預言了原子核中

應當還存在著一種中性核子——中子

1920 年，盧瑟福首次預言了中子的存在，但直到 1932 年查德威克才在實驗中找到了它。1934 年茲威基和巴德提出當一顆大質量恆星耗盡燃料時，它的核心會在引力作用下坍縮，以至於大部分電子和質子會擠壓在一起形成中子，最終形成了一個極端緻密的中子星。無論是中子還是中子星都包含了許多秘密，其中一個與中子有關的大謎題是：它的壽命究竟有多長？近年來，有兩種同樣精確的測量中子的方法卻給出了相差 9 秒的結果！這讓一些物理學家非常憂慮，他們仍在試圖用最新的研究來理解和解釋這一差異。

米蘭科維奇循環

地球物理學家米蘭科維奇

在專著中提出了「米蘭科維奇循環」

1920 年，塞爾維亞地球物理學家米蘭科維奇（Milutin Milanković）出版了專著《太陽輻射造成的熱現象的數學理論》，詳細闡述了有關地球公轉與自轉的各種參數及地球氣候模式之間的關係，也就是後來著名的「米蘭科維奇循環」。米蘭科維奇發現有三個循環周期主要影響地球與太陽之間的關係，分別是偏心率、轉軸傾角和歲差。在很長一段時間里，這個理論缺乏足夠的證據支持，直到約半個世紀后，科學家開始有能力在海底等處進行取樣分析，才找到了更多支持證據。全球氣候的自然變化還有其他許多影響因素，而自工業革命后不可忽視的人為因素同樣是目前學界的共識。

同樣在這一年，世界也迎來了許多新的生命。他們當中有許多日後成長為科學家，用他們有限的生命在科學的海洋中不斷探索，一步步推動科學與人類文明向前邁進。

羅莎琳德·富蘭克林

1920 年 7 月 25 日，羅莎琳德·富蘭克林出生於英國

羅莎琳德·富蘭克林（Rosalind Franklin）作為一位著名的物理化學家為諸多領域做出了突出貢獻，包括對煤和病毒的研究。更重要的是，她所拍攝的 DNA

的 X 光衍射圖「照片 51」是揭開 DNA 結構之謎的關鍵。但遺憾的是，這項工作在她生前並沒有獲得應有的認可。1962 年，諾貝爾生理學和醫學獎被授予沃森、克里克和威爾金斯，以表彰他們在 DNA 雙螺旋結構研究中所做的貢獻，此時富蘭克林已經去世。在富蘭克林生活的年代，女性進入科學界仍然不是一件容易的事情。當 1941 年富蘭克林從劍橋大學本科畢業時，劍橋大學甚至尚未開始授予女性學位。但她一生仍在科學上做出了不可磨滅的貢獻。

湯定元院士

1920 年 5 月 12 日，湯定元出生於江蘇金壇縣

湯定元是中國科學院院士，我國紅外物理的奠基者，他開拓了我國半導體學科和半導體光電器件的研究。湯定元 22 歲時從國立中央大學物理系畢業后留校任教，后赴美留學。學成歸國后開始在中科院應用物理所等機構工作。20 世紀 50 年代，他帶領的研究小組首次進行了鍺光電導光譜分佈的定量研究。隨後他又領導進行了一系列紅外研究，建立起我國紅外研究的學科體系，並成功研製多種先進的紅外光電探測器，應用於遙感探測中，為「兩彈一星」等項目做出了重要貢獻。2019 年 6 月，湯定元因病在上海與世長辭。